The effect of stone protrusion on the incipient motion of rock armour under the action of regular waves

Hela Perakum Viduragomi Vithana

A thesis submitted in partial fulfilment of the requirements for the Degree of Doctor of Philosophy in the University College London

Department of Civil, Environmental & Geomatic Engineering

University College London

January 2013

To gods I have seen.

To gods I have not seen.

Declaration

I, Hela Perakum Viduragomi Vithana, confirm that the work presented in this thesis is my own. Where information has been derived from other sources, I confirm that this has been indicated in the thesis. No part of this work has been submitted for any other degree or diploma.

Hela P. V. Vithana
January 2013.

ABSTRACT

Rock armour units forming coastal bed protection are often dumped "randomly" from a side stone dumping vessel, barge or flexible fall pipe. Random placement may create more protrusions (projections) of stones above mean bed level giving stones more exposure to the flow and making them more prone to displacement. If a bed protection can be laid to an optimum protrusion level, storm damage can be reduced lowering maintenance costs over the design life.

Fenton & Abbot (1977) and Chin &Chiew (1993) concluded that Shields critical shear stress for a fully exposed stone is as low as 0.01 (i.e., protrusion, p=0.82d where d is the stone diameter). They showed that the threshold value of 0.06 originally proposed by Shields (1936) refers to a 'levelled' bed of between p=0 and 0.2d. However, those observations were based on tests using uni-directional currents.

This thesis describes a laboratory study to investigate the effect of stone protrusion on threshold stone movement under regular waves. Tests were carried out to investigate the incipient motion of light weight test spheres of differing density and diameter in the range 9.5mm-31.8mm, resting on a rough bed of 19mm spheres in a wave flume. Protrusion of the test stones was varied by changing the space between three supporting spheres. In past studies, researchers have used turbulence measurements, shear plate apparatus, hot film techniques etc., to quantify bed shear stress. In the present study, it was deduced from direct measurements of the pressure on

the surface of a typical bed element. Advance flow measurement techniques such as Laser Doppler Velocimetry and Volumetric Three-component Velocimetry (V3V) were also used for flow measurement and visualisation.

It was found that the threshold shear stress is strongly related to stone protrusion and followed an exponential relationship in the range of conditions considered. For each wave period a different Shields shear stress versus protrusion curve was obtained. When the wave period increased the curve shifted towards that for the currents suggesting that for longer wave periods under the field conditions where high Reynolds number flows exist, the curve obtained for currents will be applicable.

Light weight stones (specific gravity=1.19) with protrusion, p =0, 0.17d and 0.21d showed remarkable stability even for the largest bed shear stresses. A model bed protection made of crushed natural rocks (anthracite) showed that the damage to a “levelled” bed is 50% less than in a randomly placed bed.

Measured bed shear stress data were consistent with the published results [Kamphuis (1975), Simons *et al.* (2000)] for a rough bed. The results suggested that the theoretical bed level is located 0.35d below the crests of the roughness elements.

The method of rock armour placement crucially influences the stability of a bed protection. Significant reduction in bed damage can be achieved by placing stones to an optimum protrusion above mean bed level.

ACKNOWLEDGEMENTS

I would first like to express my heartfelt gratitude to Prof. Richard Simons, my principal supervisor, for his enthusiastic support, advice, guidance and supervision that helped me throughout this difficult journey. Balancing the study, work and family commitments as a part time student has not been easy. I am particularly grateful to Prof. Simons for his understanding and patience.

I would like to thank Dr Eugeny Buldakov, my secondary supervisor, for his suggestions and especially, for extending support and cooperation while carrying out experiments in the fluids laboratory.

This project benefitted from the experience and excellent technical support from Mr. Leslie Ansdell and Mr. Keith Harvey who took a keen interest in the project and enthusiastically supported the work. Their workmanship and commitment to the work were par excellence.

I want to thank the Technical Resources Manager, Mr. Ian Seaton for making the resources available without interruption, for his inputs and suggestions. Special thanks are to Mr. Les Irwin for his help. I want to thank Mr. Paul Mennell for his suggestions during tests and for his trademark jokes which elevated British humour to a new level. I will always cherish the happy moments and delightful conversations that brought warmth to the cold, damp basement life.

I am grateful to Dr Martin Hyde of TSI who made available V3V measurement system on a loan. I was fortunate to have this state-of-the art equipment which was very crucial for understanding the flow processes. I would also like to thank Dr Dan Troolin of TSI for his help.

At last, but not least, I am grateful to my family who stood by me through great debacles, trials and tribulations to see the completion of this thesis.

Table of Contents

List of Figures

List of Tables

List of Symbols

A	Cross-sectional area
A_e	Eroded area
A_p	Projected frontal cross sectional area
$A\tau$	Turbulent mixing coefficient
a	Horizontal amplitude of particle motion at the bed, shortest dimension of a natural rock armour unit
b	Intermediate dimension of a rock
C	Phase velocity of surface gravity waves, empirical constant
C_D	Morison's drag coefficient
C_H	Horizontal force transfer coefficient
C_M	Morison's inertia coefficient
C_V	Vertical force transfer coefficient
C_L	Lift coefficient
D	Diameter of the monopile
D_e^{-2}	Initial diameter of the laser beam
d	Diameter of sphere

d_1	Spherical test stone diameter
d_2	Diameter of the spheres on the bed
d_e^{-2}	Diameter of the laser beam at the measurement volume
d_f	Laser beam fringe spacing
d_m	LDV measurement volume width
d_n	Nominal diameter
d_{n50}	50% passing nominal diameter
e	Exposure, eccentricity, gap/proximity to the bed
F	Force
F_d	Drag force
F_H	Horizontal (in-line) force
F_i	Inertia force
F_L	Vertical (lift) force
F_W	Force due to gravity
f	Focal length
f_d	Doppler frequency shift
f_e	Energy dissipation factor
f_s	Introduced frequency shift

f_w	Wave friction factor
g	Acceleration due to gravity
H	Wave height
H_s	Significant wave height
h	Water depth
h_m	LDV measurement volume height
i	Number of stones/ protrusions in the bed, i=1...
j	Number of waves, j=1 to M
F_H	Horizontal (in-line) force
F_i	Inertia force
F_L	Vertical (lift) force
F_W	Force due to gravity
f	Focal length
f_d	Doppler frequency shift
f_e	Energy dissipation factor
f_s	Introduced frequency shift
f_w	Wave friction factor
g	Acceleration due to gravity

H	Wave height
H_s	Significant wave height
h	Water depth
h_m	LDV measurement volume height
i	Number of stones/ protrusions in the bed, i=1...
j	Number of waves, j=1 to M
KC	Keulegan-Carpenter number
k	Roughness height, wave number, turbulent kinetic energy
k_s	Nikuradse's equivalent roughness height
L	Wave length, length scale of flow
L_0	Deep water wave length
l	Largest length scale of the turbulence
ℓ	Prandtle's mixing length
l_m	LDV measurement volume length
M	Mass, measured parameter
M_D	Disturbing moment around a pivot point caused by fluid forces on a stone
M_R	Restoring moment (resistance) offered by the submerged

	weight of a stone
N	Scale ratio(=prototype dimension/model dimension)
P	Pressure, probability
P_0	Dynamic wave pressure amplitude
p	Stone protrusion above mean bed level
p/d	Relative stone protrusion
q	Bed load transport rate
R	Radius of a sphere or pipe, correlation coefficient
Re*	Grain Reynolds number (u_*d/ν)
Re_d	Reynolds number (U_md/ν)
r	Number of turbulent events per wave cycle, r = 1...R
S_d	Damage level parameter
s	Specific gravity
t	Time
U	Horizontal particle velocity
U_m	Maximum value of horizontal orbital velocity
u	Instantaneous horizontal velocity
u’	Turbulent fluctuation in the horizontal velocity

	component, u'=u-<u>
u_*	Shear velocity
$\widehat{u_*}$	Peak shear velocity
V	volume
V_m	LDV measurement volume
V_p	Tracer particle velocity perpendicular to the fringes at the laser beam intersection
v	Instantaneous vertical velocity
v'	Turbulent fluctuation in the vertical velocity component
W′	Submerged weight
W_{50}	Median weight of stones
x	Horizontal co-ordinate
y	Vertical co-ordinate
y^+	$= yu_*/\nu$
y_0	Height at u=0 from the origin of the y co-ordinate
y_1	Height to theoretical bed level from the flume bed
Δy	Vertical distance to theoretical bed from roughness apex
z	Coordinate in the crosswise direction

3D	Three dimensional
2D	Two dimensional
α	Structure slope, empirical constant
β	Slope angle, empirical constant
δ'	Boundary layer thickness
δ_s	Stokes boundary layer thickness
ε	Eddy viscosity
η	Water surface elevation
η_b	Bed elevation
κ	Von Karman constant, half angle of the laser beams
λ	The horizontal spherical co-ordinate
λ_l	Laser beam wave length
$\lambda_{\Psi\text{-cr}}$	Coefficient to account for rock shape
λ_{UL}	Ratio (τ_{nt}/τ_m)
μ	Sample mean
ν	kinematic viscosity
ξ	Stone hiding factor
κ	Von Karman constant, half angle of the laser beams

λ	The horizontal spherical co-ordinate
λ_l	Laser beam wave length
$\lambda_{\Psi\text{-}cr}$	Coefficient to account for rock shape
π	Value of 3.141593
ρ	Density of water
σ	Sample standard deviation
ρ_s	Density of stones
τ	Mean shear stress
τ_m	Peak shear stress amplitude
τ_R	Reynolds stress
τ_{cr}	Critical shear stress
τ'	Turbulent fluctuation in shear stress
τ_t	Instantaneous shear stress, $\tau+\tau'$
τ_n	Mean normal stress
τ_{nm}	Peak normal stress amplitude
τ_n'	Turbulent fluctuation in normal stress
τ_{nt}	Instantaneous normal stress, $\tau_n+\tau_n'$
τ_0	Constant shear stress near the bed

φ	The vertical spherical co-ordinate
ϕ	Pivot angle of a stone, angle of repose of granular material
ω	Angular frequency (=2π/T)
Ψ	Shields parameter
Ψ_{cr}	Shields critical shear stress
Φ_E	Stone transport rate
Δ,δ	Small increment
ΔS	An elemental area

Subscripts:

15	15 % passing sieve size
85	85 % passing sieve size
50	50 % passing sieve size
90	90% passing sieve size
max	Maximum
max+	Positive maximum
min	Minimum
rms	Root mean square

x,y,z	x, y, z directions
n	Nominal
p	Prototype
m	Model
s	Standard normal

Operators:

$\bar{M}$	Mean value
<M>	Ensemble average
dM	Ordinary differential
∂M	Partial differential

1 Introduction

1.1 Background and Motivation

Rip-rap scour protections are employed around offshore marine structures such as offshore oil rigs, undersea cables and pipes, wind farms, tidal power generators etc. Scour protection aprons are also provided as toe protection to coastal structures like breakwaters and revetments. Due to lack of understanding of the behaviour of rock armour on a scour protection, engineers often have to optimise a design using physical model tests as shown in the Figure 1.1. Each physical model test costs a significant amount of money. If there is a reliable method to quantify the stable rock size and bed damage without physical model tests, the optimisation process could be made cost effective.

Rock armour units forming coastal bed protection are often dumped "randomly" from side stone dumping vessel, a barge or a flexible tube whereas rock armour on coastal structures like breakwaters and revetments are placed individually by crane. Random placement creates protrusions (projection) above mean bed level giving stones more exposure to the flow. The more a single armour unit projects above mean bed level the more it is exposed to flow and the greater are the disturbing forces due to lift, drag and inertia. The increased protrusion causes an increase in the destabilising moment and a reduction in the resisting moment. This would, therefore,

reduce the threshold shear stress that needs to be applied to dislodge a rock element out of its pocket.

On the other hand, smaller protrusion will increase the stability of a stone. If a bed protection can be levelled mechanically to achieve an optimum protrusion, the bed damage can be reduced to a desirable level.

Figure 1.1: Scour protection around offshore mono-piles.

Hofland (2005) devised an influence factor (IF) reflecting the importance of the various geometric parameters (orientation, protrusion, size, shape etc.) of a natural rock that influences its displacement. This is the multiplication factor of the critical shear stress in response to a change in the parameter within the typical range of the bed. Hofland found that the orientation has an IF =10 and protrusion has an IF=5, making the latter the second most important parameter. However, incipient motion test data for different orientations (i.e., angle of flow attack) published by Chin & Chiew (1993) showed that the orientation is less important having an IF =1.5 (see Section

2.6.2.6). Nevertheless, stone protrusion is a dominant parameter affecting stone displacement.

Shields (1936) critical shear stress for rough turbulent flow (Ψ_{cr}=0.06) is often used as the threshold criterion to determine stable rock size. However, Fenton & Abbot (1977), based on tests on uni-directional currents, concluded that the Shields critical shear stress depends on the particle protrusion above mean bed level (p) and a value of Ψ_{cr}=0.06 corresponds to a relative protrusion (p/d) value between 0 and 0.2 where d is the particle diameter, i.e. Shields used a levelled bed in the original tests. Based on new laboratory flume tests, Fenton & Abbot recommended a value of Ψ_{cr}=0.01 corresponding to a fully exposed element (p/d $\approx$ 0.82) for the design of a scour protection. Therefore, the extent of stone protrusion above mean bed level plays a dominant role in the stability of an armour unit.

Design of bed protection in the marine environment becomes more complex due to the existence of waves. Therefore, the results of Fenton & Abbot (1977) for uni-directional currents should not be adopted for coastal engineering applications without further scientific inquiry. In contrast to currents in an open channel, wave stirring on a tidal current can generate additional turbulence. Due to the steep gradient of the oscillatory boundary layer, wave-induced shear stress amplitude should be larger and hence, dominate the bed damage. Shields criterion is only valid for steady uniform flows like in an open channel with constant cross-section whilst unsteady non-uniform conditions exist in the marine environment, i.e., near roughness elements on the bed and close to coastal structures. The unsteady nature of

the oscillatory flow induces inertia forces on an element in addition to form drag.

To the best knowledge of the author, the influence of stone protrusion on the critical shear stress and bed damage under oscillatory flow has not been investigated before. Based on a literature survey, it was identified that there is a gap in knowledge that needs to be filled in this area of research.

Appreciating the importance of stone protrusion for the incipient motion and bed damage of scour protection and also its relevance towards advancing the knowledge on sediment transport, this PhD research project was designed to focus on variable stone protrusion, its impact on the critical bed shear stress and damage to a rock bed protection under the action of regular waves. This considers both the stability of the elements and the detailed hydrodynamics that act to destabilise them.

The methodology consists of (i) the observation of the first movement of idealised spherical stones of different density on a rough bed (ii) measurement and integration of pressure on the surface of a spherical bed element of 50mm diameter to compute in-line and uplift forces/shear stress for varying protrusion levels (iii) visualisation of flow structures contributing to the forces on stones using state of the art V3V three-dimensional PIV system (iv) bed damage observation on a model scour protection consisting of anthracite coal representing rock armour in the wave flume and stochastic modelling of bed damage using the Monte Carlo Simulation.

It is hoped that the research methodology and the results can find useful applications in coastal engineering practice including in the design of rock scour protections, toe protection in breakwaters, revetments etc., as well as in coarse sediment transport modelling and contribute to further understanding of the fluid-bed interaction under the action of regular waves.

1.2 Aims and Objectives of the present study

- To understand the effect of stone protrusion on the critical bed shear stress under the action of regular waves.
- To determine the bed shear stress through integration of pressure on the surface of an idealised rock armour unit (i.e., sphere).
- To understand the effect of stone protrusion on horizontal and uplift forces on a bed element.
- To study the flow structures that induce forces on an armour stone at the time of the incipient movement through flow visualisation.
- To understand the influence of stone protrusion on wave-induced damage to a model bed protection consisting of rock armour.
- To make recommendations to coastal engineering practitioners on measures to reduce wave-induced damage to bed protection consisting of rock armour.

1.3 Outline of the Thesis

Physical processes and past experimental/theoretical research relevant for the present study were reviewed in Chapter 2.

Chapter 3 consists of three main sections: experimental apparatus, instrumentation and data analysis. The section on apparatus describes the wave flume, experimental set up designed for the incipient motion tests and pressure measurement. Information on the operation procedure and principles behind the data capturing mechanism of Laser Doppler Velocimetry, Volumetric Three-component Velocimetry (3V3) and wave probes are given in the section on instrumentation. Analysis of data is described in the last section.

Wave-induced forces on a sphere resting on a coplanar bed of similar spheres is described in Chapter 4. Horizontal and uplift forces on a sphere were calculated for three different exposure levels: fully exposed, small finite protrusion and a coplanar (zero protrusion). The measured forces were compared with the calculated using the Morison's equation.

Chapter 5 describes the wave induced oscillatory shear and normal stresses at the bed. It also presents the turbulence intensity and Reynolds stresses over the course of the wave cycle calculated based on LDV measurements.

The results of the incipient motion tests are presented in Chapter 6. Shields critical shear stress at the time of the inception of stone motion was calculated for a number of stone protrusion levels based on visual observation of the initial particle displacement.

Chapter 7 presents the results of the flow visualisation tests obtained using V3V. It reveals the three dimensional features of the flow and vorticity around a sphere at the moment of its initial movement. The V3V images

also show the formation and ejection of coherent vortices from the roughness elements over the wave cycle.

Chapter 8 details the experiments on a model bed protection constructed using crushed natural rocks (anthracite coal) to study the extent of wave-induced damage to a scour protection. A stochastic model was devised using a Monte Carlo simulation method to predict the bed damage. Knowledge gathered through experiments described in all preceding chapters was utilised to formulate this model.

The dissertation is concluded with Chapter 9. It provides an overview of the experimental study, a summary of the principal research findings and suggestions for further work.

2. Literature Review

2.1 Introduction

Understanding the point and process of the “first movement” or incipient motion of an armour unit is crucial to the design of a stable, robust scour protection. This research particularly focuses on the effect of one, important geometric parameter - stone protrusion - on the incipient motion and, hence, resulting bed damage. It is the objective of this chapter, first, to review the current state of knowledge relating to incipient motion of armour stones with emphasis to the effect of variable stone protrusion and, second, to identify the existing theories governing the physical processes of incipient motion of armour stones on which the present research will be founded, through the review of previously published studies.

2.2 Scour protection in engineering practice

There are two types of design approach:

Statically stable design: This is the conventional approach where no movement of individual elements are allowed for the design event.

Dynamically stable design: This approach allows the initial configuration of the bed protection to undergo limited reshaping. Rip-rap toe protection is provided for coastal structures like revetments, groynes, breakwaters etc., to provide safety against scouring and undermining of a structure and support

against sliding. Coastal structures are often constructed using land based methods, i.e. dump trucks, placement by cranes etc.

Rock Manual (CIRIA, 2007) mentions three main requirements for rock fill bed protection in the offshore.

- Rock protection to pipelines and cables
- Scour protection of slender structures like mono-piles (e.g. offshore wind farms or jacket type structures such as oil/gas platforms)
- Scour protection for massive structures such as concrete gravity structures

There are at least three methods of offshore stone dumping:

- From a side stone-dumping vessel or a barge - stones can be considered to fall individually.
- From a split-hopper barge - stones fall as a single mass exceeding the fall velocity of a single stone.
- From a vessel through a (flexible) fall pipe in order to achieve greater accuracy.

Better control can be achieved in the rock placement process by crane than in offshore dumping of rocks where rocks will settle on the bed in a random fashion. Therefore, a relatively flat, levelled surface can be achieved in land based construction, i.e. breakwater, revetment slopes, than in offshore scour protection construction. For individually placed rocks, vertical construction tolerance of $\pm 0.3 d_{n50}$ for dry (above low water) construction and $\pm 0.5 d_{n50}$ in depths less than 5m is recommended by the CIRIA Rock Manual (1991) where d_{n50} is the 50% passing nominal stone diameter. Enhanced vertical

rock placement accuracy can be achieved using an advanced Closed Fall Pipe System even in depths of 1000m. The procedure called “scrading” consisting of dynamic tracking system to control the position of the pontoon and the pipe, conveyor belt to control rock feeding rate and screed plate at the end of the pipe to level the placed material, offers vertical placement accuracy in the order of 0.1m for coarse gradings and $0.5d_{n50}$ for light gradings (CIRIA, Rock Manual, 2007).

Figure 2.1: Methods of stone dumping in offshore (CIRIA, 1991).

A field example: The rock sizes used in scour protection for offshore mono piles have been reported to be in the *O(200kg)*. Rock Manual (CIRIA, 2007), in Section 6.4.4.7 gives an example of a scour protection apron for an

offshore platform at a depth (h) of 30m with design wave heights up to H=10m and currents of 1.5m/s. The armour grading specified in this instance was 60-400kg and the installation was performed using a flexible fall-pipe system (FFP).

Assuming a median stone size of 230kg, nominal diameter, d_n was found to be 0.44m using the definition $d_n=(M/\rho)^{1/3}$ and $\rho_s=2650kg/m^3$. This would give a relative roughness ratio of $a/k_s=2.46$ (based on a 10 second wave period) which is in the same order of magnitude, i.e. O(1), as in the tests carried out in the wave flume described later in this thesis, where *a* is horizontal wave orbital amplitude at the bed and k_s is Nkuradse equivalent roughness height.

2.3 Currently available stability formulae to estimate stable stone size

This section reviews existing stability formulae for determining the stable rock size in a bed protection. They broadly fall into two categories: (i) empirical and (ii) process based formulae. The following discussion is based on the review of existing design guidance on the scour assessment and protection near marine structures (i.e., Whitehouse, 1998; Sumer & Fredsoe, 2002; Coastal Engineering Manual, 2006; CIRIA Rock Manual, 2007).

2.3.1 Empirical formulae

There are a number of empirically derived equations to determine the stable stone size. However, these are often applicable to a defined structure type, slope, water depth and cross-section within a narrow parameter range. While some of them like Van der Meer (1988, 1993) and Hudson (1959) are

famous and widely accepted within the coastal engineering community, their usefulness is limited as they cannot be employed in every situation. A change to the design or location may render the empirical equations inapplicable.

2.3.1.1 Emergent structures

Unit size for concrete armour on an emergent structure (i.e. breakwater, revetment) can be assessed by the Hudson (1959) formula. $N_s = H_s/\Delta d_n$ is known as the *stability number* where H_s is the significant wave height, $\Delta = (\rho_s/\rho) - 1$, ρ_s is the density of rock/concrete armour, ρ is the density of water and d_n is nominal diameter. The stability number has been related to structure slope and porosity, wave steepness, the number of waves in a storm, damage number etc., by various researchers (for instance, Van der Meer, 1988).

The Hudson formula has been derived by substituting $u = \sqrt{gh}$ and $H_b = \gamma h$ at the point of wave breaking in a Morison type force formulation, $F_d \propto u^2$, where K_D is the stability number, α is the slope angle of the structure, H_b is the wave height at breaking and h is the water depth:

$$\frac{H_s}{\Delta \mathrm{d_n}} = (K_D \cot \alpha) \qquad (2.1)$$

This equation has been used successfully over decades. However, the disadvantage is that the empirical coefficient K_D is not constant and depends on the armour type, wave type (breaking, non-breaking) and structure slope. It also does not take into account the effect of wave period, storm duration,

porosity of the structure and damage level (The Coastal Engineering Manual, USACE, 2006).

Van der Meer (1988) derived formulae to predict the stability of rock armour stones on uniform armour stone slopes with crests above the maximum run-up level. In contrast to the Hudson formula, these formulae included the effects of storm duration or number of waves (N), wave period (T_m), the structure's permeability (P) and a clearly defined damage level (S_d).

There has been more research since Van der Meer introduced his famous equation in 1988 for rock slopes. Van der Meer (1993), De Jong (1996), Burcharth & Liu (1993) and Holtzhauzen (1996) presented stability equations for different concrete armour types relating stability number with damage number N_{0d}, number of waves, wave steepness and packing density coefficient (see CIRIA, 2007 for more details).

2.3.1.2 Toe and scour protection

Van der Meer (1993) carried out tests for the 1995 edition of the Rock Manual to study the breakwater toe stability (CIRIA, 2007). He derived a relationship between h_t/h and H_s/d_{n50}. h_t is the water depth at the toe and h is the water depth in front. This relation was valid for h_t/h > 0.5 and a damage level, S_d = 0 - 3% (no or minor movement), S_d > 3% and up to 10% (acceptable damage) and >20% (failure). This study was confined to depth limited wave breaking conditions and hence, would not be applicable for large water depths, i.e. 20-25m.

The damage level parameter is defined as:

$$S_d = \frac{A_e}{d_{n50}^2} \tag{2.2}$$

where A_e is the eroded area and d_{n50} is the sieve size (nominal diameter) passing 50% of the rock sample.

Figure 2.2: Toe stability as a function of relative toe depth.

2.3.2 Process based formulae

Unlike empirical formulae, process based equations are derived from first principles of physics and, hence, can be applied anywhere irrespective of the location, structure type, design etc. As general feature of these process based formulae is that they use the threshold value of the physical parameters like bed shear stress (Shields, 1936), velocity (Izbash & Khaldre, 1970), discharge (USACE, 2007) etc, to estimate the stable rock size.

2.3.2.1 Shields critical bed shear stress

Shields (1936) is the best known stability formula to describe the initiation of motion. Non-dimensional Shields parameter is defined by:

$$\Psi = \frac{u_*^2}{\Delta g d} \tag{2.3}$$

Where u_* is shear velocity and $\Delta = (\rho_s/\rho)-1$. Shields found that the non-dimensional critical shear stress (Ψ_{cr}) approaches an asymptotic value of 0.06 for rough turbulent flows. Bed protections are characterised by very low mobility of bed material and fully rough turbulent flow, i.e. Re_*>1000. Fenton and Abbot (1977) recommended a value of Ψ_{cr}=0.01 for a fully exposed stone based on experiments. This contrasted with the Shields threshold value of 0.06 for a small finite rate of particle transport as originally observed by Shields and with the values of 0.03 – 0.07 at high Reynolds numbers for the first displacement reported by Breusers & Schukking (1971).

Rock Manual (CIRIA, 2007) recommended following values for the design of armour stone layers and rockfill:

- Ψ_{cr}= 0.03 - 0.035 for the point at which stones first begin to move
- Ψ_{cr}= 0.05 - 0.055 for limited movement

Shields (1936) stability parameter is based on mean flow velocities. Recently, Jongeling *et al*. (2003), Hofland (2005) and Hoan (2008) attempted to incorporate turbulent kinetic energy into a Shields type stability parameter. This approach is discussed in Section 2.12.1.3.

2.4 Incipient motion of stones

Shields (1936) said ‘‘Considering the grains in a bed of uniform grain sizes, the question is: When will the grain be dislodged from the bed and set into motion?.” The initiation of movement of a particle is defined as the instant when the forces applied by the fluid flow (drag and lift) exceed the stabilising force due to particle weight (Raudkivi, 1998).

Shields discussed two methods for determining threshold shear stress at the inception of motion - reference and visual methods. Most authors report that Shields might have used the reference method, i.e. extrapolating the bed load transport to zero level. However, Kennedy (1995) disagrees and claims that Shields used Kramers (1932, 1935) criteria for general motion for visual observation (Buffington, 1999).

Shields defined that the “beginning of the movement” occurs when the (non-dimensional) shear stress just exceeds a certain critical value of 0.06. The dimensionless shear stress or Shields parameter, Ψ is defined by:

$$\Psi = \frac{\tau}{(\rho_s - \rho)gd} \qquad (2.4)$$

where, τ is shear stress, ρ_s is density of the particles, ρ is density of water, g is acceleration due to gravity, d is mean grain diameter. Shields parameter is roughly equal to the ratio of the tractive force applied by the flow on a particle ($\propto \rho u^2 d^2$) to the gravitational force on the particle that resists the movement ($\propto g(\rho_s-\rho)d^3$). The Shields critical shear stress, Ψ_{cr} for grain Reynolds number, Re_*>1000 is defined by:

$$\Psi_{cr} = \frac{\tau_{cr}}{(\rho_s - \rho)gd} = 0.06 \qquad (2.5)$$

Figure 2.3: Shields Curve (1936). The hatched area depicts the critical shear stress as a function of grain Reynolds number.

Shields parameter represents incipient motion in steady uniform flow. Therefore, for oscillatory flow, there are limitations for using this formula which will be discussed in Section 2.9.

2.5 Previous studies on incipient motion

The classical work of Shields (1936) on steady uniform currents led to a relationship between the threshold value of the non-dimensional shear stress Ψ_{cr}, and the grain Reynolds number, Re_* (Figure 2.3). Ψ_{cr} can also be expressed as a function of non-dimensional stone diameter, D_* :

$$\mathrm{Re}_* = \frac{\mathrm{u}_* \mathrm{d}}{\nu} \tag{2.6}$$

and

$$\mathrm{D}_* = \left(\frac{\mathrm{Re}_*^2}{\Psi_{\mathrm{cr}}}\right)^{1/3} = \left[\frac{\mathrm{g(s-1)}}{\nu^2}\right]^{1/3} \mathrm{d} \tag{2.7}$$

where, specific gravity $s = \rho_s/\rho$ and ν is kinematic viscosity.

Soulsby & Whitehouse (1997) compared data from various studies on incipient motion with the Shields curve, i.e. for waves; Willis (1978); Bagnold (1946); Manohar (1955); Vincent (1957); Goddet (1960); Rance and Warren (1969); Rigler and Collins (1984). Data for currents for D*>100 were below the Shields asymptotic value lying around 0.02-0.03 whilst for waves, data sit above the Shields curve. The authors concluded that this discrepancy of the data could be due to (i) different methods used to calculate friction factor, f_w, in estimating critical shear stress (ii) the use of the shear stress amplitude, τ_m, as an appropriate measure of the force on the bed (iii) neglecting of horizontal pressure gradient due to wave. Analysis of Soulsby & Whitehouse is shown in Figures 2.4 and 2.5.

Terrile *et al*. (2006) carried out flume tests to understand incipient motion of coarse uniform ($D_{90}/D_{10} \cong 1.25$) particles of D_{50} = 8.8mm and 11.4mm under shoaling regular waves. Their data confirmed that acceleration plays a role for the initiation of motion, since combinations of similar orbital velocity and varying acceleration magnitude resulted in no motion, some motion and motion as acceleration increased. The authors found qualitatively, that the

initiation of motion occurs at or is very close to the maximum shear stress due to the combined effects of drag/lift and acceleration.

Figure 2.4: Threshold of motion by currents in comparison with the Shields Curve (Soulsby & Whitehouse, 1997).

Figure 2.5: Threshold of motion by waves in comparison with the Shields Curve (Soulsby & Whitehouse, 1997).

2.6 Parameters affecting stability of armour stones

2.6.1 Bottom turbulence

Bottom turbulence, is the single most important factor in the incipient motion of stones and will be manifested in shear stresses, for without a hydrodynamic traction force, a stone will remain stationery. Some of the key studies on bottom turbulence and shear stress on rough beds relevant for this study are; Grass (1971), Kamphuis (1975), Kemp & Simons (1982*, 1983*), Sleath (1987), Simons *et al*. (2000). Turbulent flow processes are discussed in more detail in Sections 2.8 and 2.9.

2.6.2 Geometric parameters; stone size, shape, position, orientation, bed slope

2.6.2.1 Stone Size

The size of a stone, most often indicated by the diameter, is an important parameter that determines its stability. The characteristic size commonly used for bed protections is the nominal diameter, defined as the side of an equivalent volume cube, d_n (CIRIA, 1991).

$$\mathrm{d_n} = \sqrt[3]{\mathrm{M}/\rho_\mathrm{s}} \qquad (2.8)$$

The diameter of an equivalent volume sphere is defined as $d_s = \sqrt[3]{6/\pi} \approx 1.24 d_n$.

When graded materials are used size and weight parameters are represented by median and average. When the particles are small enough

(i.e., less than 200mm) statistical averages are derived by sieve analysis. The median sieve size d_{50} on the percentage passing cumulative curve is related to median weight, W_{50}.

The 50% passing nominal diameter d_{n50} is the size of the cube with equivalent volume to the stone with median weight and is given by:

$$\mathrm{d_{n50}} = \sqrt[3]{\mathrm{W_{50}}/\rho_s \mathrm{g}} \qquad (2.9)$$

The conversion factor relating d_{50} to d_{n50} has been determined experimentally. The most extensive study is by Laan (1981) for which following relationship was obtained:

$$\frac{\mathrm{d_{n50}}}{\mathrm{d_{50}}} = 0.84 \qquad (2.10)$$

The grading of rocks is their size distribution. It is usually quantified by the parameter d_{85}/d_{15} where m percent of the stones in a sample of stones is smaller than d_m, i.e., d_{15} is the sieve size through which 15% of the stones by weight in a sample will pass. For most design applications for specifying the top armour layers, the grading used is classified as narrow, $d_{85}/d_{15} < 1.5$.

2.6.2.2 Stone Shape

The Rock Manual (CIRIA, 1991) defines the stone shape by an aspect ratio, c/a. c is maximum axial length (given by the maximum distance between two points on the block of stone), a is the thickness or minimum axial breadth (given by the minimum distance between two parallel straight lines between which the block could just pass).

The Rock Manual gives five rock shape classifications based on the aspect ratio. Irregular rocks have a c/a of between 2.0-3.0. The Rock Manual states that not more than 20% of the number of rocks should exceed an aspect ratio c/a = 3.0. Chien & Wan (1999) give an overview of the factors available to describe stone shape. Many of them are difficult and time consuming to determine.

A shape factor often used for classifying the stone shape is defined as:

$$\mathrm{SF} = \frac{\mathrm{a}}{\sqrt{\mathrm{bc}}} \tag{2.11}$$

Ratio of the three principal body axes a, b, c (respectively, shortest, intermediate, and longest) give an idea of the shape. Typically SF = 0.6 for crushed rock.

On average, the Shape Factor for graded stones is defined in the Rock Manual (CIRIA, 1991) as:

$$\mathrm{SF_s} = \frac{\mathrm{W_{50}}}{\rho_s \mathrm{g d_{50}^3}} = 0.6 \tag{2.12}$$

Laan's (1981) study used several different rock types and sizes of stone and found that the Shape Factor, SF_s varied between 0.34 and 0.72. Latham *et al.* (1988) using different shape classes of Limestone fragments found that SF_s fell between 0.66 and 0.7.

Gogus and Defne (2005) carried out tests on particles of different shapes and sizes to determine the effect on incipient motion. They concluded that the shape of a particle has a significant effect on its incipient motion. They

found that the particle Reynolds number Re_* corresponding to the initiation of motion increases as the shape factor decreases.

Objects such as rectangular cylinders and crushed stones have sharp edges where flow separation point would be fixed. For such geometries the drag is relatively independent of the Reynolds number (Sumer & Fredsøe, 2006). On the contrary, the flow separation point of circular cylinders and spherical objects would depend on the Reynolds number and could experience drag crisis at supercritical flow regime, i.e. drag coefficient drops off suddenly as Re increases. As shown in Figure 2.28, the drag crisis occurs for an ellipsoid earlier than for a sphere. Therefore, variations in the shape of a stone could induce changes to the critical shear stress.

The scale of this variation is of practical importance. Carling *et al*. (1992) observed that the critical shear stress varied by a maximum of approximately 20% for single differently shaped stones of same nominal diameter placed on rough beds with varying roughness.

2.6.2.3 Stone position

The position of a stone in a bed can be described by several factors. Three often used parameters that can provide information about the position of a stone are (Kirchner *et al*., 1990; Hofland, 2005):

- **protrusion, p:** the height of the apex of a rock particle relative to the mean bed level. The mean bed level is determined by averaging the elevation at the apex of a large number of stones in the bed.

- **exposure, e:** the height of the apex of the particle relative to the local mean upstream bed level.
- **pivoting angle, ϕ:** the maximum angle at which the bed can be tilted without movement of the particle. Unlike the friction angle or angle of repose this is a quantity that refers to a single stone.

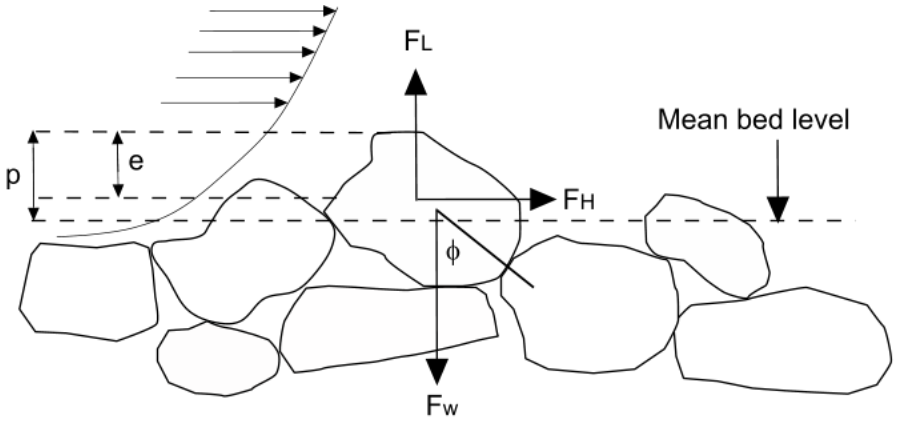

Figure 2.6: Forces on a stone - definition sketch.

When the relative protrusion, p/d ≈1.0, the stone is fully exposed to flow and a large drag force exists. p is the protrusion and d is the stone diameter. When, p/d ≈1.0, a smaller pivoting angle, ϕ, and a relatively large drag (due to large exposed area) give a large disturbing moment around the pivot point (≅ $(1/2)F_H d\cos\phi$) and small resisting moment (≅ $(1/2)F_W d\sin\phi$) due to gravity where F_H is the horizontal force, F_L is the uplift force and F_w is the submerged weight of the stone. When p/d decreases, the resisting moment increases relative to the disturbing moment and hence, the stability of the stone will increase.

Fenton & Abbott (1977) showed that the critical shear stress for a fully exposed sphere (p/d=0.82), is Ψ_{cr}=0.01, which is much lower than the value Shields (1936) obtained in the fully turbulent flow regime, i.e. Ψ_{cr}=0.06 in Re*>1000. They concluded that Ψ_{cr}= 0.06 refers to a relative protrusion value between p/d=0 and 0.2 which represents the case where the bed is well levelled (nearly coplanar). Based on these observations the authors recommended a value of Ψ_{cr}= 0.01 for scour protection design. Coleman (1967) carried out tests in a water tunnel to measure the drag and lift forces on an over-riding sphere (p/d=0.82) placed at an interstice of a hexagonal array of spheres. His observations matched with those of Fenton & Abbott (1977) for a fully exposed sphere, i.e. Ψ_{cr}= 0.01.

Chin and Chiew (1993) found that the non-dimensional critical shear stress reached a low value of 0.006 for p/d= 0.94. At low values of p/d, critical shear stress increased rapidly beyond Shields' asymptotic value with Ψ_{cr} rising up to 0.1.

Figure 2.7 shows the relative protrusion values and the test results of Fenton & Abbot (1977) in comparison with the classical Shields curve. Figure 2.8 shows the combined results of both Fenton & Abbot (1977) and Chin & Chiew (1993) plotted on the same figure.

Figure 2.7: Non-dimensional Shields parameter against grain Reynolds number. Different asymptotic curves for relative protrusion values were identified (Fenton & Abbot, 1977).

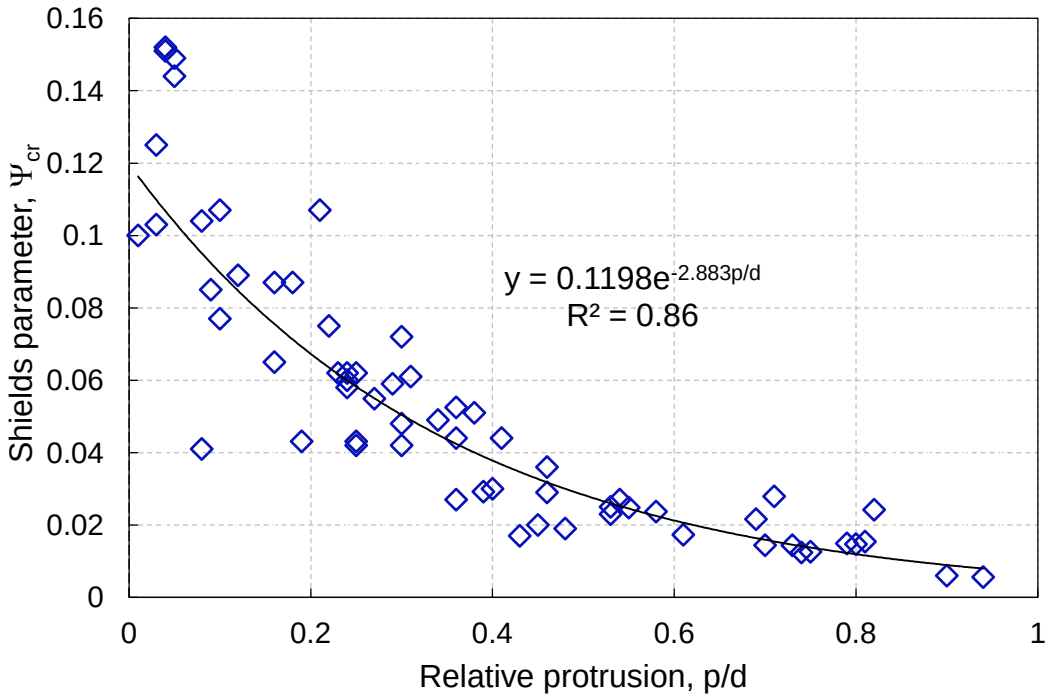

Figure 2.8: Shields critical shear stress against relative protrusion (Fenton & Abbot, 1977; Chin & Chiew, 1993).

Analytical predictions of friction angle and grain protrusion would only be possible for simplified bed geometries such as identical spheres on a

hexagonal packing arrangement (see Chin & Chiew, 1993). For natural beds these variables must necessarily be characterised by empirical relationships derived from direct measurements. Miller & Byrne (1966) proposed that the mean friction angle for natural beds could be described by the relationship:

$$\phi_s = \alpha\left(d/\bar{d}\right)^{-\beta} \qquad (2.13)$$

where, ϕ_s is the average friction angle in degrees, d is the size of a fraction of grains, $\bar{d}$ is the average diameter of the bed grains and α, β are empirically determined parameters.

Kirchner *et al.* (1990) concluded that the critical shear stress, Ψ_{cr} is strongly dependent on grain protrusion, exposure and friction angle, all of which vary from point to point on a bed.

Therefore, the critical shear stress of a stone on a rough bed strongly depends on the stone protrusion as shown by the exponential relationship in Figure 2.8. Ψ_{cr} of a single grain size on a rough bed is not a single value, but a probability distribution. Therefore, an assumption of a single critical shear stress value of $\Psi_{cr} = 0.01$ (Fenton & Abbot, 1977) or $\Psi_{cr} = 0.03$ – 0.035 (CIRIA, 2007) may lead to an unacceptable damage level in the case of scour protection.

Therefore, to address the uncertainty posed by the use of a single threshold stress value, the CIRIA Rock Manual (2007) recommended to follow a probabilistic design approach or to accept a certain amount of bed damage. The Rock Manual recommended the use of Monte Carlo Simulation for probabilistic analysis of damage to coastal structures with the input of

probability distributions to represent different parameters. These input parameters should be stochastically independent.

2.6.2.4 Stone orientation

For gravel river beds it is sometimes seen that the stones have their longest axis predominantly in the spanwise direction (Nikora *et al*., 1998). However, gravel beds are subject to armouring and stones can be locked into a cluster. A stone minimises its exposure by burying itself in the scour hole created around it. However, a stone in a flume would have to follow a different strategy to maximise the stability. De Boer (1998) noted that the angular stones in a flume experiment were predominantly orientated with the longest axis in the direction of the flow after water-working. Carling *et al*. (1992) measured critical shear stress in their experiments with differently shaped stones on beds of different roughness. They found that the stones placed with their long axis perpendicular to the flow moved sooner than when placed parallel.

Chin and Chiew (1993) observed the initiation of movement of a spherical stone [d=16.5mm, R_*=O(1000)] supported on three similar stones glued to a rotating disk on the flume bed to understand the effect of the horizontal orientation on critical shear stress. The experiment showed that the stability of a spherical test stone increased when the angle of attack, reference to the direction of flow (i.e. flume axis) increased from 0^0 to 60^0. They concluded that the horizontal orientation affects the particle stability.

Therefore, available evidence suggests that, in nature, stones would be aligned to the direction where the exposure is the least, or it would reduce the exposure by hiding amongst other stones or burying itself in sand.

Unlike natural beds, for the construction of scour protection, for example, stones are placed with the longest axis vertical to minimise the area exposed to the flow (Hofland, 2005). Therefore, stones in a scour protection are designed to be immobile.

2.6.2.5 Bed slope

On the sloping face of scour protection or a submerged rock fill embankment, a component of the gravity force on a stone acts down slope. If the bed is tilted gradually, the stone will be displaced when the slope angle just exceeds the angle of repose. Therefore, only a fraction of the gravity force perpendicular to the slope acts to create a restoring moment. Therefore, the critical shear stress on a slope is less than that on a flat bed. Whitehouse (1995) and Soulsby & Whitehouse (1997) derived a shear stress reduction factor to take account of the effect of the bed slope.

2.6.2.6 Relative influence of orientation, protrusion, size and shape on the inception of motion of stones

It is important to understand what parameters are most dominant comparatively in the inception of motion of stones, so that those dominant parameters can be included in a predictive model of incipient motion and bed damage.

Hofland (2005) estimated an approximate influence factor (IF) of the above mentioned characteristic parameters on the stability of an element. The multiplication factor of the critical shear stress in response to a change in the parameter (protrusion, orientation etc.) within the typical values for a bed, was determined based on available literature and flume tests. The following Table is reproduced from Hofland (2005):

Table 2.1: Approximate influence of stone characteristics on stone stability (Hofland, 2005).

Characteristic/parameter	Approximate influence factor	Source(s)
Protrusion, p/d=0 - 0.5	5	Fenton & Abbot (1977)
Orientation	>10	Carling *et al.* (1992)
Size (d_{85}/d_{15}=1.5)	2	Shields (1936)
Shape (when d_n is used)	0.2	Breusers(1965), Carling (1992)

According to the above Table the stone orientation has the highest influence. Chin & Chiew (1993) carried out incipient motion tests in a flume varying the angle of attack of a current on a fully exposed 16.5mm glass marble resting on 3 similar marbles. For zero degree orientation, the critical shear stress was 0.0142 and for 60 degrees this value was 0.0207. Therefore, when the orientation was changed from 0 to 60 degrees the critical shear stress increased only by a factor of 1.5. Therefore, the influence factor of 10 obtained by Hofland (2005) based on the data of Carling *et al.* (1992), needs further review.

Nevertheless, it is clear from the published experimental evidence that the stone protrusion is one of the most significant factors that determines the initiation of motion of the stones.

2.7 Wave theory

2.7.1 Introduction

In the calculation of the wave-induced bed shear stress, $\tau_m = (1/2) f_w \rho U_m^2$ and relative bed roughness, a/k_s, pre-determination of the bottom wave orbital velocity, U_m and orbital amplitude, a is required. Here, wave friction factor is defined by f_w. Moreover, the wave-induced pressure, P, on the surface of a bed element is also an important parameter relevant for this study. These physical parameters can be calculated using a number of wave theories. Particularly, linear wave theory (Airy waves) is of importance due to its simplicity for use in engineering applications. Therefore, wave theories and their validity for use in different relative water depth ranges are reviewed in this section.

Literature on the historical development of wave theory is extensive (see Lamb, 1932; Ippen, 1966; Phillips, 1974, 1977; Horikawa, 1978; Schwartz & Fenton, 1982; Mei & Liu, 1993; Craik, 2004). However, there is no single general solution that covers all wave and water depth ranges.

Therefore, due to the assumptions made in their derivation, the wave theories available can be used to predict wave motion for certain ranges of the wave parameters; wave height, H, defined as the vertical distance from

the wave trough to wave crest; the wavelength, L, defined as the distance between successive crests; and the wave period, T, defined as the time between successive crests passing a given point. In addition, the following parameters are also important for this study; wave celerity, $C = L/T$, angular frequency, $\omega = 2\pi/T$, and wave number, $k = 2\pi/L$.

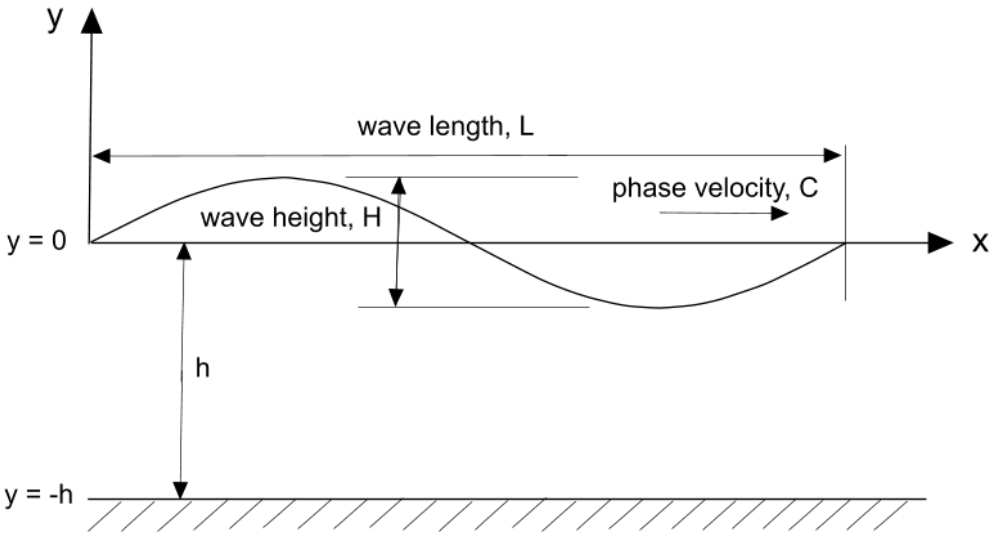

Figure 2.9: Definition sketch of a two dimensional free surface sinusoidal wave.

Le Méhauté (1976) categorised free surface waves into deep, intermediate and shallow water regions based on the ratio of water depth to wavelength. Values for the depth parameter, h/gT^2, and the ratio of water depth to wavelength, h/L for different wave regimes are presented in Table 2.2.

Table 2.2: Classification of wave regimes by Le Méhauté (1976).

Classification	h/gT^2	h/L	Wavelength, L
Deep water waves	>0.08	>1/2	$(L_0 =)gT^2/2\pi$
Intermediate waves	0.0025 to 0.08	1/20 to 1/2	$L_0 \tanh(kh)$
Shallow water waves	<0.0025	<1/20	$T\sqrt{gh}$

Le Méhauté (1976) produced a summary of the ranges of applicability of different wave theories based on wave height and water depth parameters, H/gT^2 and h/gT^2. The illustration is reproduced in Figure 2.10.

Figure 2.10: Ranges of validity for various wave theories as suggested by Le Méhauté (1976).

Robinson (2010) discussed Le Méhauté's wave classification in detail. He observed that Dean (1965) showed similar validity regions. He also noted that Le Méhauté's classification has not been disputed by any one. Moreover, Le Méhauté's figure has been included in the Coastal Engineering Manual (2002). However, Robinson (2010) found, during his literature review, some discrepancies between Le Méhauté's wave theory limits and other theoretical validity limits. Nevertheless, the Le Méhauté

classification of wave regimes is presented here on the basis of its wide acceptance by the coastal engineering community.

2.7.2 Small amplitude (linear) wave theory

The most simple of the wave theories is linear or Airy (1841) wave theory. Its derivation starts with the Navier-Stokes equations and makes a number of assumptions including incompressible, frictionless flow. Secondly, conservation of mass or continuity of the fluid is assumed. The problem was linearised by assuming that the wave height, H, is much smaller than the wavelength L, and water depth, h, i.e. H<<L, h.

2.7.3 Wave generated currents (steady streaming)

Stokes (1847) was the first to discuss the concept of a net wave-induced velocity. A fundamental difference between Stokes and Linear wave theory is that the Stokes orbital motions of water particles do not close but instead lead to a non-periodic current or mass transport of water in the direction of wave advance. The associated *Stokes drift* current is given by

$$U_s = \frac{H^2 \omega k \cosh[2k(y+h)]}{8 \sinh^2(kh)} \tag{2.14}$$

The solution presented by Longuet-Higgins (1953) showed a net flow in the direction of wave advance near the water surface and at the bottom, balanced by a return flow in the opposite direction at mid depths.

$$U_s = \frac{5}{4}\left(\frac{\pi H}{L}\right)^2 C \frac{1}{\sinh^2(kh)} \tag{2.15}$$

Measurements by Russell and Osorio (1957) of the vertical distribution of mass transport velocities in a laboratory wave tank found reasonable agreement with the theoretical relationships.

Based on velocity measurements in wave flume, Dixen *et al.* (2008) found a maximum streaming current of O(4cm/s) for h = 0.4m, T=1.6sec and H=14.2cm. Due to the small scale of the velocities, steady streaming should be of lesser importance than the instantaneous large scale velocity in the order of bottom orbital velocities, i.e., O(20 cm/s) for the removal of large stones.

2.7.4 Comparison of wave theories

Soulsby *et al.* (1993) noted that, historically, many comparison studies have focused on the prediction of the horizontal velocity under the crest, which is one of the most important quantities used for design purposes (e.g., Dean and Perlin, 1986; Kirkgoz, 1986). Soulsby *et al*. (1993) observed that linear wave theory gives the best overall agreement of bottom orbital velocity with data for flat and sloping beds (slopes between 1:100 and 1:4.45) up to the breaking point and within the surf-zone. However, this comparison cannot be extrapolated to the overall velocity profile. In particular, velocities under the trough are overestimated by a factor up to 1.5 to 2 near the breaking point due to asymmetry in the wave profile. The asymmetry can be very important in determining the direction and magnitude of the net sediment transport due to the waves. This weakness in predicting velocity asymmetries can be overcome by Stokes higher order models in intermediate water depths.

Figure 2.11 shows a comparison of velocity data and linear and convocoidal wave theories presented by Isobe & Horikawa (1982) obtained from Soulsby *et al.* (1993). The wave parameters for the two cases (a) and (b) are shown in Table 2.3 below.

Table 2.3: Wave parameters - experiments of Isobe & Horikawa (1982) on wave orbital velocity.

Test	H(cm)	T(sec)	h(cm)	Bed Slope	h/gT^2	Wave Regime
(a)	9.16	0.97	10.4	0.05	0.0113	Intermediate depth
(b)	6.75	2.0	8.8	0.05	0.0021	Shallow depth

Linear wave theory predicted the measured peak velocity well both in the intermediate and shallow water depths. However, the phase of the wave is not predicted.

Figure 2.11: Comparison of computed and measured near-bed water particle velocity profiles of shoaling waves on a 1:20 plane beach (Isobe & Horikawa, 1982). (a) intermediate depth (b) shallow depth. Measured □ , Linear theory - - -.

.

2.8.1 Laminar boundary layer

Most theoretical investigations in fluid mechanics are based on the concept of a perfect, i.e. frictionless (inviscid) and incompressible fluid. In the motion of such a perfect fluid, two contacting layers experience no tangential forces (shearing stresses) but normal (pressure) forces. That is a perfect fluid will not offer internal resistance to change in shape, i.e. tangential stress is not proportional to the strain.

However, in contrast to a perfect fluid, a Newtonian fluid exhibits a linear stress strain relationship. Newton (1642-1727) postulated that, for the straight and parallel motion of a given fluid, the tangential stress between two adjoining layers is proportional to the velocity gradient in a direction perpendicular to the layers, that is:

$$\tau = \frac{\mathrm{F}}{\mathrm{A}} \propto \frac{\partial u}{\partial y} \tag{2.16}$$

or

$$\tau = \mu \frac{\partial u}{\partial y} \tag{2.17}$$

where, the constant of proportionality, μ is constant for a particular fluid at a particular temperature, and is known as the coefficient of viscosity.

Near a solid wall a perfect fluid would not apply a shear stress on the wall and hence, no opposite stress on the fluid layer above (Newton's Third Law) to retard the motion. That is, there will be slip.

However, in a real fluid due to inter molecular attractions the fluid will adhere to the wall creating strain of the fluid layers (or velocity gradient) and hence, there will be a shearing stress.

2.8.2 Turbulent boundary layer

Due to the difficulty in explaining turbulent shear flows analytically, scientists have used semi-empirical hypotheses to describe turbulent shear stresses.

Boussinesq (1877), in analogy with the coefficient of viscosity in equation (2.17) introduced a *mixing coefficient*, A_τ, for the Reynolds Stress in turbulent flow by putting:

$$\tau = -\rho\overline{u'v'} = A_\tau \frac{d\bar{u}}{dy} \tag{2.18}$$

From Prandtl's mixing length hypothesis (Schlichting,1968):

$$\tau = \rho\ell^2 \left|\frac{d\bar{u}}{dy}\right| \frac{d\bar{u}}{dy} \tag{2.19}$$

Prandtl assumed that the turbulent shearing stress at the wall is zero owing to the disappearance of the fluctuations and hence, the mixing length, ℓ is proportional to distance from the wall, y.

$$\ell = \kappa y \tag{2.20}$$

κ is known as the Von Karman constant. After substituting in eqn. (2.19):

$$\tau = \rho\kappa^2 y^2 \left(\frac{du}{dy}\right)^2 \tag{2.21}$$

Comparing eqn. (2.18) with eqn. (2.21) we find the following expression for the virtual viscosity:

$$A_\tau = \rho\ell^2 \left|\frac{d\bar{u}}{dy}\right| \tag{2.22}$$

and for the virtual kinematic viscosity or eddy viscosity:

$$\varepsilon = \ell^2 \left|\frac{d\bar{u}}{dy}\right| \tag{2.23}$$

The mixing length is assumed to be independent of the magnitude of velocity and is considered to be a local function and not a property of the fluid like viscosity (Schlichting, 1968).

Hence, substituting eqn. (2.23) into eqn. (2.19)

$$\tau = \rho\varepsilon\frac{d\bar{u}}{dy} \qquad (2.24)$$

The eddy viscosity is as shown in eqn. (2.24) is dependent on the time-mean velocity. Eqn. (2.23) is still unsatisfactory as the eddy viscosity vanishes when $d\bar{u}/dy = 0$, i.e. at minimum and maximum. In reality this is not true. Therefore, Prandtl introduced a simpler relationship for the eddy viscosity. Thus:

$$\varepsilon = \kappa_1 b\,(\bar{u}_{max} - \bar{u}_{min}) \qquad (2.25)$$

Prandtl assumed that the lumps of fluids that move in a transverse direction during turbulent mixing are of the same order of magnitude as the width of the mixing zone, b. κ_1 is a non-dimensional coefficient to be determined experimentally. $\bar{u}_{max} - \bar{u}_{min}$ is the maximum difference in the time-mean flow velocity.

At this stage Prandtl assumed a far reaching assumption, i.e., at the bed the shearing stress remains constant, i.e. $\tau = \tau_0$.

Introducing the friction velocity, u_*

$$u_* = \sqrt{\frac{\tau_0}{\rho}} \qquad (2.26)$$

Substituting equation (2.26) in (2.21)

$$\frac{du}{dy} = \frac{u_*}{\kappa y} \tag{2.27}$$

After integrating we have

$$u = \frac{u_*}{\kappa} \ln y + c \tag{2.28}$$

The constant of integration, c should be determined experimentally and depends on the conditions at the wall.

Assuming that at a certain height, $y = y_0$, the velocity, $u = 0$

$$\frac{u}{u_*} = \frac{1}{\kappa}(\ln y - \ln y_0) \tag{2.29}$$

2.8.3 Turbulent boundary layer over rough beds

Nikuradse (1933) carried out very systematic and extensive measurements on flow through rough pipes with their inside wall covered with sand of a known grain size glued on the wall for varying pipe diameters and roughness size. Assuming $y_0 = \gamma k_s$ where k_s is the Nikuradse roughness height and the Von Karman constant, $\kappa = 0.4$.

$$\frac{u}{u_*} = \frac{1}{\kappa}\left(\ln \frac{y}{k_s} - \ln \gamma\right) \tag{2.30}$$

Nikuradse found that for a completely rough flow regime

$$\frac{u}{u_*} = 5.75 \ln \frac{y}{k_s} + 8.5 \tag{2.31}$$

and

$$y_0 = \frac{k_s}{30} \tag{2.32}$$

Based on Nikuradse's data, after comparing with data for smooth pipes, three flow regimes have been identified (Schlichting, 1968).

- *Hydraulically smooth regime:*

$$0 \leq \frac{\mathrm{k_s u_*}}{\nu} \leq 5, \qquad \lambda_\mathrm{k} = \lambda_\mathrm{k}(\mathrm{Re} = \bar{\mathrm{u}}\mathrm{d}/\nu) \tag{2.33}$$

Where, $\lambda_\mathrm{k} \propto (\mathrm{k}/\mathrm{R})^{0.314}$, k/R is relative roughness, R is the radius of the pipe and λ_k is friction coefficient defined as $\tau_0 = \lambda_k \rho \bar{u}^2/8$. In this case size of the roughness is so small that all protrusions are contained within the laminar sub layer.

- *Transition regime:*

$$5 \leq \frac{\mathrm{k_s u_*}}{\nu} \leq 70, \qquad \lambda_\mathrm{k} = \lambda_\mathrm{k}(\mathrm{k_s}/\mathrm{R}, \mathrm{Re}) \tag{2.34}$$

Protrusions extend partly outside the laminar sub-layer and additional resistance, as compared with a smooth pipe, is mainly due to the form drag experienced by the protrusions in the boundary layer.

- *Fully rough turbulent regime:*

$$\frac{\mathrm{k_s u_*}}{\nu} > 70, \quad \lambda_k = \lambda_k(k_s/R) \tag{2.35}$$

All protrusions reach outside the laminar sub-layer. By far the largest part of the resistance to flow is due to the form drag. For this reason the law of resistance becomes quadratic.

2.8.3.1 Nikuradse roughness height, k_s

The value of k_s is a function of the size of the bed particles as well as the bed geometry (grain spacing, shape and size distribution). Kamphuis (1975)

observed that k_s= 2d_{90} for natural sand and rock particles of the size, d_{90}=0.5, 2.2, 4.22, 12.2 and 46mm. Following Engelund and Hansen (1972), Nielsen (1992) adopted a value of k_s= 2.5d_{50} for use in Swart's (1974) wave friction factor formula.

Dixen *et al*. (2008) reported that k_s= 2.3d_{50} and 2.0d_{50} for 3.85cm and 1.4cm diameter natural stones, respectively. For ping-pong balls of 3.6cm diameter glued to the flume bed, they estimated a value of k_s= 2.5d_{50}.

The stone sizes used in the present study varied from1.9cm to 5.0cm and of the scale as the roughness measured in previous studies, Hence, k_s= 2.5d_{50} was assumed in the calculations.

2.8.4 Theoretical bed level

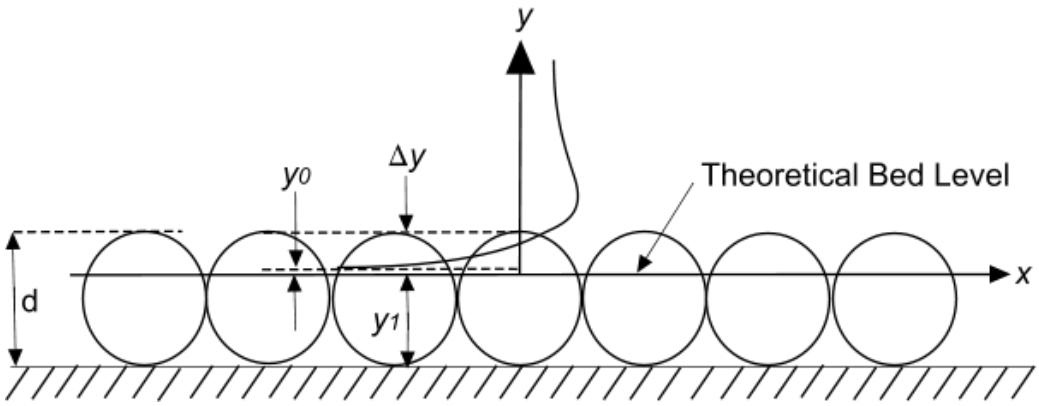

Figure 2.12: Definition sketch of the theoretical bed level.

In contrast to a smooth bed, the choice of the origin of the y axis, $y = 0$, is not obvious. It is generally defined as the level of the origin which leads to the best fit of eqn. 2.29 to measured current profiles (Nielsen, 1992). It can also be considered as the level at which the mean drag on the surface appears to act. In many commonly encountered types of roughness, the

expression, $y_1 = 0.7$ times roughness height (d), gives a good estimate (Jackson, 1981). Bayazit (1976, 1983) found that, $y = 0$ is located (0.15-0.35)d below the top level of the elements.

For oscillatory flow over rough beds, Sleath (1987) and Dixen (2008) discussed about the theoretical bed level. Sleath(1987) quoting Einstein (1950) suggested that the origin should be taken 0.35d below the crest level of the roughness elements or y_1=0.65d. Dixen reported that the theoretical bed level for ping-pong balls (3.6cm diameter) glued to the flume bed and stones (1.4cm and 3.85cm) is located 0.23d and 0.25d below the top level of the roughness elements, respectively.

Therefore, from available literature, a value of y_1=0.65d provides a lower bound for the displacement height to define the theoretical bed level.

2.9 Shear stress in oscillatory flow over rough beds

2.9.1 Introduction

Jonsson (1966) concluded from dimensional analysis that the structure of oscillatory boundary layers depends mainly on the Reynolds number:

$$Re = \frac{a^2\omega}{\nu} = \frac{aU_m}{\nu} \tag{2.36}$$

and relative roughness, a/k_s, where a is wave orbital amplitude at the bed and ω is wave angular frequency.

In this section, physical processes and parameters related to oscillatory boundary layer and shear stress are discussed.

2.9.2 Nature of oscillatory boundary layer

In the study of stone movement, the bottom boundary layer, through which the main flow will exert shear stress on the bed, is the most important part of the flow. When compared to a tidal current, the wave boundary layer, due to its short time-scale, is thin and hence, will have a steep velocity gradient and high shear stress. If superimposed on a weak current, wave-induced oscillatory shear stress will enhance the combined maximum shear stress amplitude (Soulsby *et al.*, 1993). Therefore, even if the tidal velocity is much larger than the wave-induced velocity, the wave velocity amplitude will dominate the shear stress near the bed.

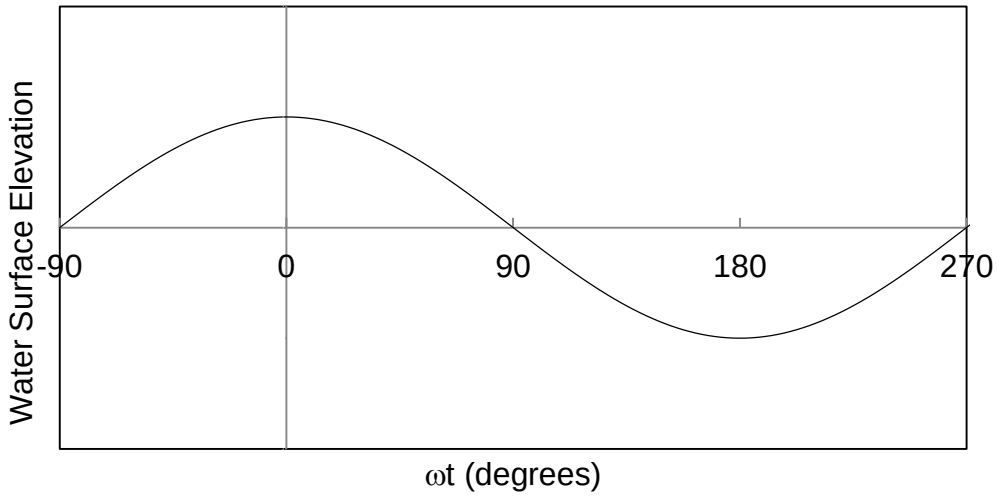

(a)

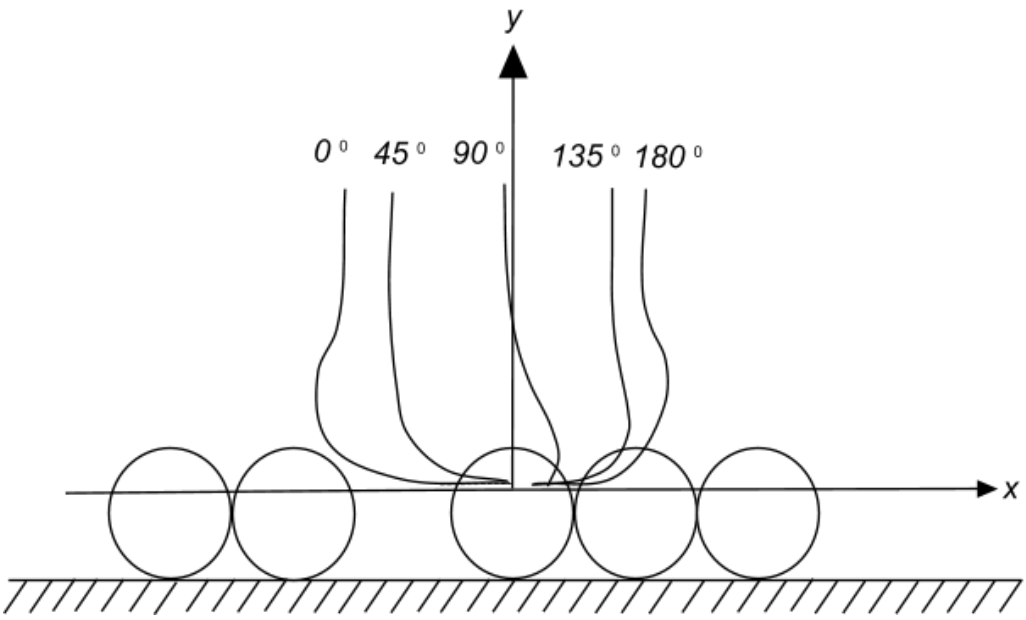

(b)

Figure 2.13: Definition sketch of the boundary layer development. (a) water surface elevation against phase angle, ωt (b) flow reverses at $\omega t \approx 90^0$ near the bed.

The wave boundary layer has a steep velocity gradient and, therefore, induces a large bed shear stress when compared to a current making the waves more dominant of the two in the incipient motion of stones (see Figure 2.14).

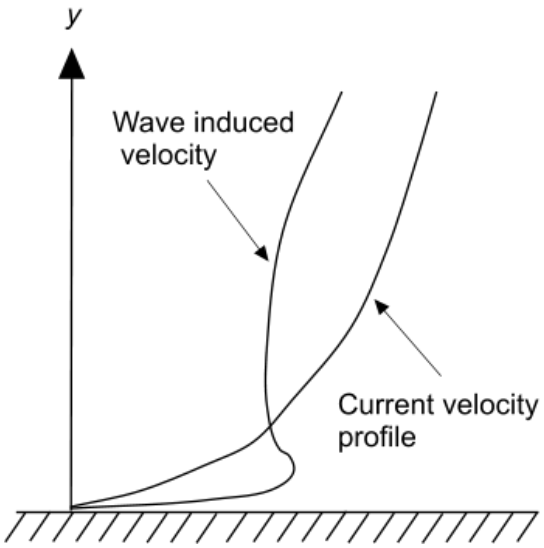

Figure 2.14: Sketch showing wave and current boundary layers.

It is conventional to define the wave-induced shear stresses and forces in terms of the maximum free stream velocity amplitude, U_m.

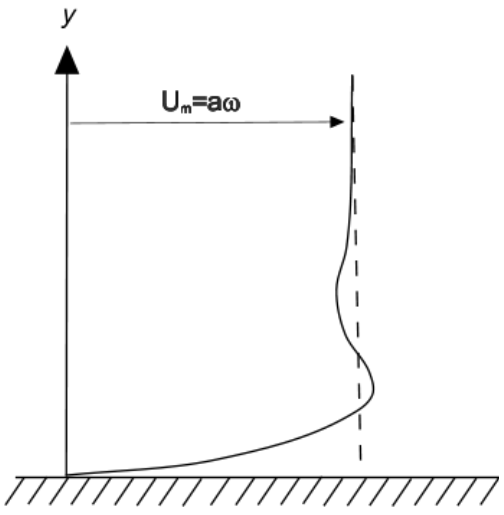

Figure 2.15: Definition sketch showing maximum velocity amplitude.

2.9.3 Boundary layer thickness

There are different definitions for the boundary layer thickness. However, boundary layer thickness, δ', is defined here as the distance from the theoretical bed level to the point where U$(y, \omega t)$ is maximum at $\omega t = 0$.

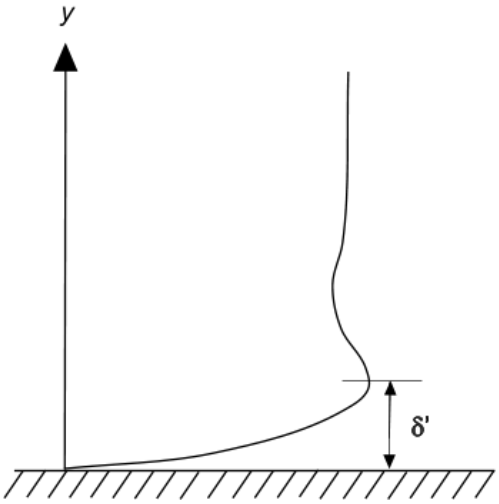

Figure 2.16: Definition sketch showing the boundary layer thickness.

For laminar flow Stokes boundary length scale is defined as:

$$\delta_s = \sqrt{\frac{2\nu}{\omega}} \tag{2.37}$$

The practical limit for measuring boundary layer thickness lies around the level where the velocity defect is one percent of the free stream amplitude, i.e., 0.01U_m (Nielsen, 1992).

$$\delta_{0.01} \approx 4.5\delta_s \tag{2.38}$$

Sleath (1987) based his definition for the top of the boundary layer on experiments using sand (0.2mm, 1.63mm), gravel (8.12mm) and pebbles (30mm) and presented the following relation:

$$\frac{\delta'}{a} = 0.27\left(\frac{a}{k_s}\right)^{0.67} \tag{2.39}$$

and is defined as the position where the amplitude of the velocity defect has dropped to 5% of the velocity amplitude.

For rough turbulent flow, researchers have found a correlation between δ'/k_s and a/k_s. Dixen *et al*. (2008), based on stone and ping-pong ball (glued to the flume bed) tests, concluded that for relative roughness a/k_s = O(1) or smaller, the boundary layer thickness δ'/k_s= O(0.5d) or smaller. Dixen *et al*. (2008), after fitting test results with published data of Jonsson and Carlsen (1976), Sleath (1987), Jensen *et al.* (1989), found an empirical expression for δ'/k_s:

$$\frac{\delta'}{a} = 0.08\left[\left(\frac{a}{k_s}\right)^{0.82} + 1\right] \tag{2.40}$$

2.9.4 Eddy viscosity and mixing length

Relationships used for the prediction of shear stresses within the boundary layer for steady uniform flow are commonly used to predict shear stresses under oscillatory flow. However, the assumptions on which theses relationships have been based, i.e., zero pressure gradient, eddy viscosity, ε, and mixing length, ℓ, are constants at a certain height of the boundary layer and proportional to the height from the bed, are not directly applicable to oscillatory flows. In oscillatory flow over rough beds, vortices formed behind the roughness elements are ejected at each half cycle. These ejected vortices will interact with other vortices and with previous vortices to

produce a pattern of turbulent eddies which decay with height above the bed. It seems probable that the vortices formed and released into the flow will have a significant effect on the turbulence within the boundary layer (Sleath, 1991) and hence, on the eddy viscosity and mixing length.

Sleath (1987) used sand, gravel and pebbles of median diameters 0.2mm, 1.63mm (sand, a/k_s= 24.8-1112), 8.12mm (gravel, a/k_s= 2.34-27.7) and 30.0mm (pebbles, a/k_s= 0.74-8.69). 30.0mm pebbles were laid on the bed while other sediments were glued to plates fixed on the tunnel bed. He found that both eddy viscosity and mixing length vary significantly over a wave cycle.

Figure 2.17: Variation of eddy viscosity during the course of the wave cycle. x- x, y=3.5mm; o-o, y=30mm. Eddy viscosity has been normalised using its cycle mean, $\bar{\varepsilon}$ (Sleath, 1987).

Figure 2.18: Variation of time mean (cycle averaged) eddy viscosity with distance from the theoretical bed located 0.35d below the crest level of the elements (Sleath, 1987).

In analogy with the Prandtl's relationship for eddy viscosity (eqn. 2.63), Kajiura (1968) assumed that for rough beds, cycle averaged eddy viscosity:

$$\bar{\varepsilon} = \ constant;\ 0 \leq y \leq \frac{1}{2}k_s \tag{2.41}$$

$$\bar{\varepsilon} = \kappa \hat{u}_* y;\ \frac{1}{2}\ k_s < y \leq 0.05\hat{u}_*/\omega \tag{2.42}$$

$$\bar{\varepsilon} = constant;\ y > 0.05\hat{u}_*/\omega \tag{2.43}$$

where, $\hat{u}_*$ is peak shear velocity, $\omega = 2\pi/T$ is angular frequency and T is wave period.

As seen from the data of Sleath (1987) in Figure 2.18, there is indeed an intermediate range where, $\bar{\varepsilon} \propto \hat{u}_* y$. He observed that Von Karman constant κ during the wave cycle was considerably lower (0.059 - 0.078). When he used a mean value of the shear velocity, $\bar{u}_*$ (i.e. $\bar{\varepsilon} = \kappa \bar{u}_* y$), this value increased to 0.13 though still lower than the theoretical value of 0.4.

Figure 2.19: Variation of mixing length during the course of the wave cycle. x- x, y=3.5mm; o-o, y=30mm (Sleath, 1987).

Figure 2.20: Variation of mean mixing length with distance from the bed (Sleath, 1987).

As seen from the Figure 2.19 the mixing length varies over the wave cycle at a particular height from the bed. The measured data is in agreement with the

linear variation proposed for steady flow when the cycle average shear velocity was considered. However, observed Von Karman constant was still smaller than 0.4 (i.e., 0.14 - 0.17).

Therefore, due to the deviation in behaviour of both eddy viscosity and mixing length parameters from the steady flow, the fitting of boundary layer velocity data to a logarithmic relationship for all phases of the oscillatory flow will not be practical.

Nielsen (1992) reported that better agreement of the velocity distribution with the logarithmic relation is obtained for smooth beds such as that of Jensen (1989) where the relative roughness, a/k_s is >33. Agreement was also observed for the data of Jonsson & Carlsen (1976) for a/k_s = 28 – 125.

Dixen *et al.* (2008) showed (Figure 2.21) that for large roughness elements, the velocity data satisfied the logarithmic law when the thickness of the boundary layer develops sufficiently to accommodate the logarithmic boundary layer. This happens when the phase angle $\omega t > 40^0$ for the roughness, a/k_s=O(0.5).

Figure 2.21: Logarithmic fit of velocity data for (a) crest (b) trough half periods. Water depth =0.4m, H=14.2cm, T= 1.6sec, a/k_s=0.72 (Dixen et al., 2008).

2.9.5 Shear stress

Based on experiments, Sleath (1987) concluded that the mean horizontal force on a unit area obtained through the momentum integral approach (eqn. 2.44) is about a factor ten larger than the periodic Reynolds shear stress, $< \tau_R >= -\rho < u'v' >$.

Total shear stress,

$$\tau = \rho \int_y^\infty \frac{\partial}{\partial t}(u_\infty - u)dy \qquad (2.44)$$

which says that the shear stress at level y is equal to the fluid density times the total acceleration defect above y.

Sleath (1987) attributed this phenomenon to the mean pressure gradient in oscillatory flows with rough beds and to the momentum transfers associated with vortex ejection on flow reversal.

Dixen *et al.* (2008) found that the shear stress obtained from ensemble and space-averaged Reynolds stress is slightly less than that obtained from the log-fit method. This is because the maximum of the Reynolds stress occurs not at the bed level, but slightly below the top of the roughness elements. However, the shear velocity, u_*, obtained by the momentum integral method and log-fit method tallied well. They used natural stones of 1.4cm, 3.85cm and ping-pong balls of 3.6cm glued to the flume bed. These observations by Dixen *et al.* (2008) are consistent with those of Sleath (1987).

2.9.6 Wave friction factor

Direct determination of the bed shear stress is not possible for practical engineering designs. Therefore, researchers have tried to develop semi-empirical relationships to define bottom shear stress. It is accepted that the drag force on a bed element is proportional to the square of the velocity, $F \propto \rho u^2$. On this basis, Jonsson (1966) defined a transfer function, f_w linking the square of the peak orbital velocity to the bed shear stress

$$\tau_m = \frac{1}{2} f_w \rho U_m^2 \qquad (2.45)$$

Jonsson showed, from dimensional analysis, that the wave friction factor can be expected to depend on the Reynolds number $a^2\omega/\nu$ and relative bed roughness, a/k_s.

The wave friction factor appears to be related to energy dissipation. The time average energy dissipation is given by

$$D_E = \overline{\tau(t) U_\infty(t)} \qquad (2.46)$$

where $U_\infty(t)$ is velocity just above the boundary layer. Jonsson (1966) defined the energy dissipation factor, f_e, by:

$$D_E = \frac{2}{3\pi} \rho f_e (a\omega)^3 \qquad (2.47)$$

Nielsen (1992) plotted f_w, f_e data of several studies (Riedel, 1972; Kemp & Simons, 1982; Sleath, 1987; Jensen, 1989; Jonsson & Carlsen,1976) for rough turbulent flow. Lofquist (1980, 1986) reported comprehensive measurements of bed shear stress over natural sands. Both these authors

concluded that though there is considerable scatter of data, for practical purposes, it can be assumed that $f_w \approx f_e$.

The wave friction factor,f_w, due to its practical relevance, has been subject to considerable research effort in the past. Some of the equations available in the literature to compute the wave friction factor are discussed below.

Jonsson (1966) proposed:

$$\frac{1}{4\sqrt{f_w}} + \log_{10}\frac{1}{4\sqrt{f_w}} = -0.08 + \log_{10}\frac{a}{k_s} \tag{2.48}$$

Kajiura's (1968) equation:

$$\frac{1}{4.07\sqrt{f_w}} + \log_{10}\frac{1}{4\sqrt{f_w}} = -0.253 + \log_{10}\frac{a}{k_s} \tag{2.49}$$

Kamphuis (1975) used an oscillating water tunnel to measure shear stress on a smooth bed and five rough beds made of particles of diameter, d_{90}= 0.5, 2.2, 4.22, 12.2 and 46 millimetres. He used oscillation periods from 2.5 sec to 15 sec and amplitudes between 0.5m and 3m. For the rough turbulent flow regime (i.e., $u_* k_s/\nu$ > 70), Kamphuis proposed a simple relationship for the wave friction factor:

$$f_w = 0.4\left(\frac{a}{k_s}\right)^{-0.75} ; \frac{a}{k_s} \leq 100 \tag{2.50}$$

Kamphuis (1975) argued, based on his test results, that for rough turbulent flow regime where there is no effect of viscosity, friction factor for a particular a/k_s value, is independent of the flow Reynolds number (Re).

Swart (1974) suggested the following formula:

$$f_w = exp\left[5.213\left(\frac{a}{k_s}\right)^{-0.194} - 5.977\right] \tag{2.51}$$

Sleath (1987) calculated the friction factor based on his experiments using sand, gravel and pebbles of median diameter 0.2mm, 1.63mm (sand, a/k_s= 24.8-1112), 8.12mm (gravel, a/k_s= 2.34-27.7) and 30.0mm (pebbles, a/k_s= 0.74-8.69). The friction factor data obtained from momentum integral method tallied well with the curves of Jonsson (1963) and Kamphuis (1975). Data obtained from the Reynolds stress method fell well below the above curves giving the relationship:

$$f_w = 0.0067\left(\frac{a}{k_s}\right)^{-0.22} \tag{2.52}$$

Simons *et al*. (2000) measured the shear stress directly using UCL Shear Cell apparatus (described in Grass *et al.*, 1995 in more detail) for regular oscillatory flow over 2D roughness elements of 6mm square placed at 25mm centres perpendicular to the flow direction. They found the following relationships:

$$f_w = 0.33\left(\frac{a}{k_s}\right)^{-0.84};\ \frac{a}{k_s} < 30 \tag{2.53}$$

and

$$f_w = 0.001exp\left[6.1\left(\frac{a}{k_s}\right)^{-0.2}\right];\ \frac{a}{k_s} > 30 \tag{2.54}$$

Figure 2.22: Friction factor, f_w against relative roughness, a/k_s (Simons et al., 2000).

Figure 2.23: Friction factor, f_w against Reynolds number (Kamphuis, 1975).

Figure 2.24: Friction factor, f_w against Reynolds number (Kamphuis, 1975).

Dixen *et al.* (2008) measured bed shear stress using the logarithmic boundary layer and momentum integral methods. The rough bed consisted of stones (1.4cm and 3.85cm) and ping-pong balls (3.6cm) glued to the flume bed. They plotted the test data and compared with results of various researchers, i.e. Bagnold (1946), Kamphuis (1975), Sleath (1987), Simons *et al*. (2000), and found that the data fitted the equation

$$f_w = 0.32\left(\frac{a}{k_s}\right)^{-0.8} \; ; \; 0.2 < \frac{a}{k_s} < 10 \qquad (2.55)$$

This relation is very similar to the equation (2.53) proposed by Simons *et al*. (2000).

2.9.6.1 Scale effects and field measurements of friction factor

Not many field studies that calculated wave friction factor of coarse particles in the field scale can be found in the literature.

Thompson *et al*. (2012) carried out experiments in the Delta Flume under irregular waves. Waves heights ranged from 0.8-1.3m, peak periods 3-10 sec and water depths, 1.75-3.75m. They used several methods to estimate the shear stress (i.e., Reynolds Stress, TKE, Inertial Dissipation) and found that only the mean values of f_w agreed with previous studies (i.e., Kamphuis,1975; Kemp & Simons, 1982; Sleath, 1987).

Experiments of Kamphuis (1975) were conducted in an oscillating tunnel with amplitudes of oscillation varying from 0.5m to 3.0m and period 2.5 sec to 15 seconds.

Myrhaug *et al*. (1998) analysed velocity data at two locations (i.e. Strait of Juan de Fuca, Washington State in 18m water depth and at a location named EDDA, North Sea at a water depth of 70m). The seabed material at the Strait of Juan de Fuca site consisted of rock and gravel of average diameter 5cm. The seabed at the North Sea site mainly consisted of fine sand with d_{50}=0.2mm. The predicted shear stress agreed well with that for the Strait of Juan de Fuca site. The agreement was attributed to the absence of suspended material at this location.

Whilst the number of tests at field scale that quantified friction factor is sparse, the existing few seem to agree with the earlier laboratory scale studies (i.e., Kamphuis,1975; Kemp & Simons, 1982; Sleath, 1987, Simons *et al*., 2000).

2.10 Wave Forces on a single stone

2.10.1 Profile drag

Skin friction and pressure drag on a 3D object together constitute the profile drag. When Re_d approaches zero, the skin drag is about two thirds of the total drag. When separation of the boundary layer occurs, the pressure drag makes a proportionately larger contribution, about 90% when Re_d > 200. The present experiments will be conducted in the region of $Re_d=U_m d/\nu$ > 1000, and hence, are outside the region where skin friction drag is important. For a sphere, a stable separation position is achieved at $\psi = 80^0$ from the front stagnation point when $Re_d \cong 1000$. Unlike 2D bodies (i.e.,

cylinders), 3D objects do not form a vortex street, but a vortex ring which becomes unstable and moves downstream when 200 < Re_d < 2000. The drag coefficient, C_D gradually becomes independent of Reynolds number from Re_d = 2000 (see Figure 2.28).

Figure 2.25: Flow past a sphere at subcritical Reynolds number (Schlichting, 1968).

At $Re_d \approx 3X10^5$ the boundary layer becomes turbulent before separation, so the separation point moves further downstream, the wake becomes smaller, and the value of C_D drops sharply from about 0.5 to below 0.1 (Massey and Ward-Smith, 1998). This phenomenon is called the drag crisis.

At supercritical flow (i.e., transition at $Re_d \sim 3.9X10^5$), the point of separation, which lies near the equator of the sphere (i.e., $\psi = 0^0$) for laminar boundary layer, moves over a considerable distance in the downstream direction (see Figure 2.26). This will result in a reduced wake area, and the pressure distribution becomes more like that for a frictionless motion.

Figure 2.26: Flow past a sphere at supercritical Reynolds number (Schlichting, 1968).

Figure 2.27: Pressure distribution around a sphere in the subcritical and supercritical range of Reynolds numbers with angle $\psi = 0$ degrees at the nose of the sphere (Schlichting, 1968).

Figure 2.28: Drag coefficient against Reynolds number for a sphere and few other objects (Massey and Ward-Smith, 1998).

Concluding remarks

The above Figures from 2.25-2.28 refer to steady uniform flow and the effect of the proximity to a solid boundary on flow is not included. Nevertheless, they shed light on the flow separation process and variation of drag with the Reynolds number on a solid sphere. As the Reynolds numbers (Re_d) are in the $O(10^3 - 10^4)$ under the present experimental conditions, they fall within the subcritical flow range. Therefore, the drag crisis will not affect the test results. The drag coefficient for a free sphere within this range is 0.4-0.5.

2.10.2 In-Line Force; quasi-steady drag and inertia

For steady currents, the drag force acting on a sphere in the direction of flow

is given by

$$F = \frac{1}{2} C_D A_p U|U| \tag{2.56}$$

Where, C_D is the drag coefficient and A_p is the cross-sectional area perpendicular to the flow direction. U is measured positive in the flow direction.

In the case of oscillatory flows, however, there will be two additional contributions to the total in-line force.

$$F = \frac{1}{2} C_D A_p U|U| + m' \frac{dU}{dt} + \rho V \frac{dU}{dt} \tag{2.57}$$

$m'(dU/dt)$ is defined as the hydrodynamic mass force and $\rho V(dU/dt)$ is called the Froude-Krylov force.

The hydrodynamic mass force is caused by the acceleration of the fluid in the immediate surroundings of the body. This could be best explained by a plate moved in still water (instead of stationary plate) in the direction perpendicular to its plane with an acceleration a. Here, not only the plate but the fluid in the immediate neighbourhood of the plate has to be accelerated due to the pressure from the plate. If the hydrodynamic mass is denoted by m', the force to accelerate the total mass, is $F = (m + m')a$, where, m is the mass of the plate.

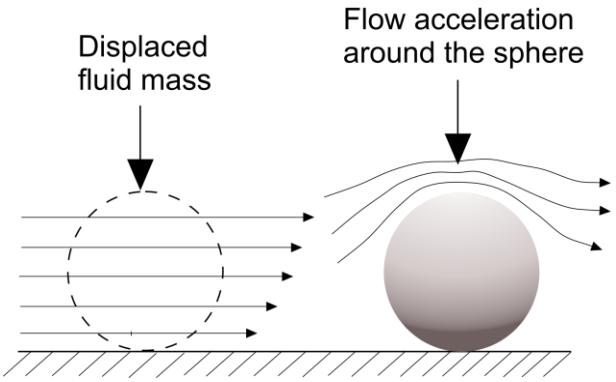

Figure 2.29: Sketch showing acceleration of displaced fluid around a sphere.

The second effect is that the accelerated motion of the fluid in the outer flow region will generate a pressure gradient according to:

$$\frac{\partial P}{\partial x} = -\rho \frac{dU}{dt} \tag{2.58}$$

The pressure gradient in turn will produce an additional force which is termed the Froude-Krylov force. Replacing, m' in eqn. (2.57) with the mass coefficient C_m, the in-line force can be re-written as:

$$F = \frac{1}{2} C_D A_p U|U| + C_m \rho V \frac{dU}{dt} + \rho V \frac{dU}{dt} \tag{2.59}$$

By defining a new coefficient, $C_M = C_m + 1$

$$F = \frac{1}{2} C_D A_p U|U| + C_M \rho V \frac{dU}{dt} \tag{2.60}$$

This equation is known as the Morison equation (Morison *et al*., 1950). The term $C_M \rho V (dU/dt)$ is called the inertia force and C_M is called the inertia coefficient.

For smaller Keulegan-Carpenter (KC) number flows of the O(1), the potential flow value of C_m for a sphere is 0.5. C_M tends to 1.5. KC is defined as:

$$KC = \frac{U_m T}{d} \tag{2.61}$$

where, U_m, T and d are as defined previously.

Most of the experimental work relating to forces on a submerged body is focused on cylinders due to their wide practical use (Sarpkaya & Issacson, 1981; Sumer & Fredsøe, 2006). Studies on small spheres without diffraction effects (i.e. in the D/L < 0.2 region) in a wave environment, are limited. Out of the studies undertaken, only a very few of them relate to small spheres resting on a solid boundary. The majority of the studies on drag, inertia and lift coefficients relate to objects that lie away from a solid boundary. The limitation of the Morison's equation (1950) is that it is valid for the calculation of the in-line force when diffraction effects are negligible.

Hofland (2005) listed a number of studies looking at stones resting on a channel bed for steady uni-directional currents. These defined C_D at various positions (i.e., $C_{D,0.15}$ - mean velocity (U) measured 0.15d above the top of the sphere, $C_{D,0}$ - U measured at the centre of the sphere and $C_{D,*}$ - for u_* (friction velocity). These studies are by:

- Watters and Rao (1971); $C_{D,*}$ ≈2:2, $C_{D,0.15}$ ≈0.3±0.05 for spheres in a hexagonal bed arrangement
- Xingkui and Fontijn (1993); $C_{D,0.15} = 0.36$ for natural stones
- Chepil (1958); $C_{D,0.15}$=0.26 for hemispheres
- Coleman (1967, 1972), Patnaik *et al*. (1992); $C_{D,0} \approx 0.4$ for a single sphere sitting on top of other similar spheres

Hofland (2005) concluded that the use of $U = U_{0.15}$ in $(1/2)\rho C_D A U|U|$ gives a reasonably constant drag coefficient $C_{D,0.15} \approx 0.23 – 0.3$ for all protrusions. Moreover, Xingkui & Fontijn (1993) found that the correlation between the instantaneous velocity at this height and the drag force is a maximum. Einstein & El-Samni (1949) found a constant C_L for different flow velocities at this height.

Dixen *et al*. (2008) made a comparison of in-line force coefficients for oscillatory flow using a bed of ping-pong balls (glued to the flume bed, 3.6cm diameter) and natural stones (1.4cm-3.85cm) in a wave flume. Based on the least-square-fit they found that the C_D = O(0.5) and C_M = O(0.1) with the exception that C_M = 0.5 for the 45^0 arrangement of ping-pong balls and C_M = 0.4 for the stones. For the same test conditions with KC = 12, they cited values of C_D = 0.6 and C_M = 1.2 for a free sphere from Sarpkaya (1975). The reason given by the authors for this significant reduction in C_M (or negative values of hydrodynamic mass coefficient, C_m) is due to the wash of the lee-wake water over the roughness element when the flow reverses. The second reason given is that the space around the roughness element is limited for the water around to accelerate when compared with a free sphere/object. The difference in observed C_M values in the tests was attributed to the variation in the stone arrangement.

Iwata and Mizutani (1989) studied wave forces on a submerged sphere. They found that for KC < 10, C_M has an almost constant average value of 1.2. Flow separation occurs in almost all cases when KC > 10 and the drag force dominates. The estimated average drag coefficient C_D = 0.7. They

concluded that the uplift forces due to horizontal velocity-induced vortex shedding dominate at the bottom and hence, the Morison equation is not applicable to estimate the vertical wave force. The range of applicability for the Morison equation to estimate vertical wave force is when the ratio of vertical velocity to horizontal velocity is larger than 1/3. However, it is not clear whether the test sphere rested on the bed.

Torum (1994) conducted direct measurements of wave-induced parallel and normal forces on an armour unit on a berm breakwater. He found that the parallel force could be rather accurately modelled using the Morison equation. Average force coefficients were calculated as C_D =0.35 and C_M = 0.2. However, the attempt to model the normal force using the same equation was not successful.

Wolfram and Naghipour (1999) concluded that the force coefficients obtained from different methods varied significantly. However, there is a clear trend that the addition of a current (to a wave) significantly decreased the drag coefficient and to a lesser extent the inertia coefficient. For KC > 10 the use of mean values for drag and inertia coefficients (about 1.7 and 2, respectively) for heavily marine roughened cylinders in (irregular) waves without current seemed reasonably satisfactory.

Concluding remarks

Therefore, the force coefficients change depending on whether flow is oscillatory or uni-directional, Re - KC flow regime, wall proximity, stone

arrangement, stone protrusion, surface roughness, whether a superimposed current is present etc.

The results of Dixen *et al*. (2008) and Torum (1994) show that for a stone resting on a rough bed of similar stones in a wave dominated environment (i.e. regular oscillatory rough turbulent flow regime), the inertia coefficient reaches a low value, i.e. C_M=O(0.1) while drag coefficient remains in the region, C_D = O(0.5).

2.10.3 Uplift force

Sources of the uplift force are (1) vortex shedding (2) stones falling within the influence of the low pressure wake region of upstream stones (3) moving eddies (4) quasi-steady upward directed drag due to the wall proximity effect.

The flow around a near-wall sphere is not symmetric. Therefore, a quasi-steady upward directed mean lift must exist in contrast to a free sphere located away from the wall (i.e. gap ratio, $e/d > 1$) where the pressure distribution around the sphere is symmetric. Here, *e* is the distance from the wall, *d* is diameter of the sphere. Uplift forces are also due to asymmetry in the wake vortices which start when KC $\approx$ 4. Well established lift force regimes are formed when KC > 6 - 7.

Based on research on cylinders, Sumer & Fredsøe (2006) concluded that the vortex-induced oscillating lift and drag will cease to exist in the case when the gap ratio (e/d) is smaller than about 0.3 (with the object being close to the bed) due to the suppression of vortex shedding. Therefore, if the

same phenomena is true for a stone resting on the bed the wall-induced quasi-steady lift force should be more important than the irregular lift force.

There are two approaches in quantifying the uplift force. In one, the maximum value of the lift force, F_{Lmax} is considered, while in the other an r.m.s value of the lift force, F_{Lrms} is adopted (Sumer & Fredsøe, 2006).

$$F_{Lmax} = \frac{1}{2}\rho C_{Lmax} A_y U_m^2 \tag{2.62}$$

$$F_{Lmax} = \frac{1}{2}\rho C_{Lrms} A_y U_m^2 \tag{2.63}$$

$$C_{Lmax} = \sqrt{2} C_{Lrms} \tag{2.64}$$

Torum (1994) in his direct measurement of normal force on an armour unit on the flat side of a berm breakwater reported that the lift coefficient was scattered in the test range KC = 25 - 100 varying between C_L = 0.1 and -0.1. The particle Reynolds number $Re_* = u_* d_{n50}/v$ = 1.5 X 10^4 and $Re_d = U_m d_{n50}/v$ = 4.0 X 10^4. Therefore, the measurements were in the fully turbulent flow regime.

Rosenthal & Sleath (1986) observed that the positive (measured upward from the bed) lift coefficient increased when the gap ratio (e/d) reduced. They tested a sphere for different gap ratios including a test sphere sitting on similar spheres on an oscillating tray and a pendulum rig (for high Re_d > 2000). When the sphere diameter d is large relative to viscous boundary layer length scale $1/\beta=(2\nu/\omega)^{1/2}$, the amplitude and maximum positive values of C_L initially increased with increasing Re_d, reached a maximum and then progressively decreased. For the rough bed, for a relatively large

sphere (βd = 8.3) maximum positive C_L reduced from 0.2 to 0.1 when Re_d = $U_m d/\nu$ increased from 0 to 3000. C_L is fairly constant at high Re numbers.

Iwata & Mizutani (1991) reported that the vertical wave force is magnified and becomes irregular when the submerged sphere is at the bottom boundary. Close to the bed, the measured vertical wave force deviated from the calculated values. Therefore, they concluded that the use of the Morison equation is not valid at the bottom and surface boundaries, most likely due to the unsteady random behaviour of the forces. In another study, Mizutani and Iwata (1993) concluded that the irregular lift force could be estimated stochastically using a Weibull probability distribution.

Previous results for uni-directional flow seem to agree well with those for oscillatory flow. At high Re_*, $C_{L,0.15}$ values of 0.15 to 0.22 were found when the test particle is placed between other particles (Einstein & El-Samni, 1949; Xingkui & Fontijn, 1993; Benedict & Christensen, 1972). The measurements of Chepil (1958) indicate that $C_{L,0.15}$=0.23 for the configuration with hemispheres spaced three diameters apart. Based on the same data Wilberg & Smith (1985) estimated $C_{L,t}$ = 0.2 at the top of the spheres.

Concluding remarks

Therefore, based on available literature, a lift coefficient of C_L = 0.1 – 0.2 would be typical for a stone resting on a rough bed in turbulent oscillatory flow. Vortex shedding is suppressed when an object is close to a solid boundary and hence, quasi-steady uplift force dominates. However, the

effect of the irregular lift force on top of the quasi-steady lift force due to vortex shedding does not totally diminish as suggested by the experimental observations of Hofland (2005) (see Section 2.12.2). The Morison equation is not useful in predicting the uplift force.

2.11 Flow structures, turbulence and their length scales

The turbulence in shear flow comprises of a sea of eddies (lumps, blobs, tubes, sheet of vorticity). These vortices are stretched and twisted by the velocity field, which is itself dictated by the instantaneous vorticity distribution. Vortical structures evolve in the velocity field induced by itself and all the other vortical structures. Diffusion of vorticity is restricted to regions where there are large gradients in vorticity. It remains coherent (localised) for a certain time because vorticity can spread only by material movement (advection) or else by diffusion. This is unlike linear momentum where the pressure force can instantly re-distribute the linear momentum throughout all space (Davidson, 2004).

In the following subsections the length scale of turbulence and the processes that contribute to the production of near-bed turbulence, are reviewed with the objective to find a relationship later on, between the critical shear stress of the stone and the large scale turbulence that is primarily responsible for the dislodging of a stone from the bed.

2.11.1 Length scale of turbulent eddies

There is a broad spectrum of eddy sizes in a fully developed turbulence which are associated with a cascade of energy. At the large scale, there are energy containing eddies. In pipe flow these eddies are of the size of the radius of the pipe and in open channel flow, these eddies are of the size of the water depth. On the lower level of the cascade, there are the smallest eddies where viscous dissipation takes place. The Reynolds number of these smallest eddies are of the order of unity and their size is as small as 0.1mm or even smaller (Davidson, 2004).

Hofland (2005) argued that large scale turbulent structures (eddies) of the order of the water depth have a larger chance of reaching the bed sporadically, bringing fluid parcels of large velocity magnitude to the bed. These fluctuations are rare and intermittent, and therefore, hardly alter the intensity of turbulence near the bed, while the probability of occurrence of extreme forces is increased.

According to Hofland (2005) two types of flow structures are primarily responsible for the entrainment of stones and they vary in size - i.e., quasi-steady force fluctuations (QSF) and turbulent wall pressure fluctuations (TWP). The QSF depend on the near-bed streamwise velocity. Turbulent sweep events present at the time of initial stone movement are 2 – 4h in length (order of the water depth, h). Nezu and Nakagawa (1993) reported that this size is usual of large scale flow structures in open channel flow. The origin of TWP can be small-scale vortices. TWP with a length scale of the

order of the stone diameter, d, are most effective in generating forces on a stone; a vortex centre at 0.5-2d above a stone will probably induce the largest (lift) force.

Davidson (2004) noted that in the outer region (of the boundary layer) viscous stresses are negligible. The velocity gradients scale with the water depth, *h*, since the largest eddies, which are most effective at transporting momentum, are of the order of *h*.

In oscillatory flow, the orbital excursion has been considered to be an important length scale for large-scale turbulence. Losada & Desire (1985) assumed that the large-scale turbulence and length scales can be defined in terms of mean flow parameters:

$$\frac{U}{L} \sim \frac{u}{l} \tag{2.65}$$

Here, Losada & Desire assumed that $U = U_m$ and $L = a$.

Then,

$$Re = \frac{UL}{\nu} = \frac{U_m a}{\nu} = \frac{\omega a^2}{\nu} \tag{2.66}$$

Loasada and Desire also hypothesised quoting Jonsson & Carlsen (1976) that for oscillatory flow the length scale, l, is in the order of the boundary layer thickness, δ'.

Dixen *et al*. (2008) based on their study and other studies (Jonsson & Carlsen,1976; Sleath, 1987; Jensen *et al.*, 1989) on oscillatory flow over rough beds found that:

$$\frac{\delta'}{k_s} \propto \left(\frac{a}{k_s}\right)^{0.82} \tag{2.67}$$

Arnskov *et al*. (1993) reported that the current has a significant influence on sediment transport due to the increase in wave-current combined mean bed shear stress. This increase is due to the wave-induced oscillatory flow which enhances the momentum exchange between the layers of fluid in the current boundary layer. Consequently, the momentum-rich, high velocity fluid in the outer layers will be carried into the neighbourhood of the bed in larger quantities with the introduction of waves resulting in a substantial increase in the bed shear stress.

It is possible to establish a simple relation between the mixing length, ℓ, and a characteristic length of the respective flow. For example, in flows along rough walls the mixing length near the wall must tend to a value of the same order of magnitude as the solid protrusions (Schlichting, 1968).

2.11.2 Sources of turbulence affecting bed shear stress

2.11.2.1 Inrush and ejection of fluid

Using the hydrogen bubble technique, Grass (1971) visually identified two well defined features of the flow structures close to the boundary of smooth and rough beds in free surface channel flow, i.e. inrush and ejection. The ejection phase corresponded with the ejection of low momentum fluid outwards from the boundary while inrush phases were associated with transport of high momentum fluid inwards towards the boundary. These two features were present irrespective of the roughness of the boundary. Whilst

coherent effects of the inrush phases appeared to be mainly confined to a region close to the boundary, the influence of the ejection phases is far more extensive. The ejected low momentum fluid elements, drawn from the viscous sub-layer and from between the interstices of the roughness elements, travel outward from the boundary into the body of the flow and give rise to very large positive contributions to Reynolds stress at points remote from the boundary.

2.11.2.2 Turbulent Bursting

Kline *et al*. (1967) observed through visual studies, the presence of surprisingly well-organised spatially and temporally dependent motions within the ‘laminar sublayer’. These motions lead to the formation of low-speed streaks in the region very near the wall. The streaks interact with the outer portions of the flow through a process of gradual ‘lift-up’, then sudden oscillation, bursting, and ejection. They concluded that these processes play a dominant role in the production of new turbulence and the transport of turbulence within the boundary layer on smooth walls.

Runstadler *et al*. (1963) hypothesized that the production of turbulence in the inner layers was largely due to the bursting of the observed flow model, and more particularly to the eruptions of the low-speed streaks.

Kim *et al*. (1971) studied the structure of the incompressible smooth surface boundary layer over a flat plate in a low-speed water flow using hydrogen-bubble measurements and also hot-wire measurements with dye visualisation. Particular emphasis was placed on the details of the process

of turbulence production near the wall. They reported that in the zone $0 < y^+ < 100$ (i.e., from the viscous sub-layer to the log law of the wall region) the data show that essentially all turbulence production occurs during intermittent 'bursting' periods. Here, y^+ is equal to $u_* y/\nu$.

Carstensen *et al*. (2010) carried out detailed experiments in an oscillating water tunnel to investigate oscillatory boundary layers over smooth beds. The experiments revealed the existence of two significant coherent flow structures: (i) Vortex tubes, essentially two dimensional vortices close to the bed extending across the width of the boundary layer flow, caused by an inflectional-point shear layer instability. The imprint of these vortices in the bed shear stress is a series of small, insignificant kinks and dips. (ii) Turbulent spots, isolated arrowhead-shaped areas close to the bed in an otherwise laminar boundary layer where the flow 'bursts' with violent oscillations. The emergence of the turbulent spots marked the onset of turbulence. Turbulent spots caused single or multiple violent spikes in the bed shear stress signal.

The authors observed that the emergence of the turbulent spots at a critical point of the flow development, i.e. Re>1.5 X 10^5, marks the onset of turbulence. The authors further observed that turbulent spots appear at the deceleration phase of the wave cycle. Turbulent spots can cause single or multiple spikes in the bed shear stress which can be a factor of 3 or 4 larger than the maximum shear stress, τ_m.

2.11.3 Concluding remarks

The length scale of large scale turbulence, which can induce sweep movements to dislodge a stone, is in the order of the boundary layer thickness and water depth. In addition, small eddies with the length scale of the stone diameter, with the vortex centre at 0.5-2d from the stone, can induce lift forces on the stone.

Two mechanisms can contribute to a large positive enhancement of the Reynolds stress. (i) the in-rush of momentum rich parcels of fluid to the bed from the upper water column; and (ii) turbulent spots – low momentum streaks drawn from the viscous sub-layer, which are gradually lifted, then undergo sudden oscillation, bursting and ejection into the upper region of flow. The bursting process has been identified in the literature as the main mechanism for the production of turbulence in the near wall region and will be important for fine sediment transport. However, the impact of the turbulence generated by the bursting process on the forces on larger stones remains to be investigated.

2.12 Stone entrainment, transport and bed damage modelling

There are two approaches to stone transport and bed damage modelling (i) deterministic methods using the mean tractive force concept on a stone, and (ii) stochastic methods which are based on the probability of exceedance of a threshold value by the applied force/shear stress at the initiation of motion.

2.12.1 Stone entrainment and transport (deterministic approach)

The use of (dimensionless) bed load transport (Φ) as a bed damage indicator is conventional for uniform flow (Paintal, 1971a). However, bed load transport is dependent on upstream hydraulics; all the stones passing a certain section have been entrained upstream of that section. Bed load transport is, therefore, considered a non-local parameter. Stability parameters like Shields (Ψ), are local parameters. Some researchers in the past (Meyer-Peter & Müller, 1948; Parker, 1979 and others) have defined bed load transport rate, $\Phi = q/\sqrt{\Delta g d^3}$ as a function of Shields shear stress, i.e., Φ=f(Ψ). This would make Ψ - Φ a relationship of local and non-local parameters. Such a relationship can only be valid for uniform flow where the flow condition is unchanged along the channel. To adapt to various flow conditions, Hofland (2005) proposed that the dimensionless entrainment rate (Φ_E) could be used as a bed damage indicator because it is completely dependent on the local hydrodynamic parameters. The dimensionless entrainment rate is expressed as:

$$\Phi_E = \frac{E}{\sqrt{\Delta g d}} \tag{2.68}$$

where, $E = nd^3/A$, n is the number of pick-ups per unit time. N is number of pick-ups during time T from the area A. $n = N/T$.

This way of defining entrainment rate is different to the damage definition given in the Rock Manual (CIRIA, 1991) for rock slopes because it measures the eroded area, not the number of extractions. The damage number S_d is thus defined as:

$$S_d = \frac{A_e}{d_{n50}^2} \quad (2.69)$$

Where, A_e is the eroded area. Initial damage is defined as when S_d = 2 – 3, and will depend on the slope of the structure.

2.12.1.1 Stone transport formulae based on excess shear stress concept

There are several widely used equations to predict bed load transport. Most take the form $q_s = m(\Psi - \Psi_{cr})^n$ defining the sediment transport rate in terms of excess shear stress, i.e. $\Psi - \Psi_{cr}$. Most classical sediment transport formulae are based on the excess shear stress concept.

The disadvantage of these relationships is that they are based on a single threshold stress assuming that the stone transport would start when the applied stress just exceeds the threshold value. The threshold shear stress varies spatially on a bed depending on the stone protrusion. For a fully exposed particle the critical shear stress could be as low as 0.01 whilst a grain with zero protrusion could be more stable with a threshold stress as large as 0.1 (Fenton & Abbot, 1977).

Meyer-Peter and Müller (1948) used a critical shear stress value of Ψ_{cr}= 0.047 in their equation:

$$\frac{q_s}{\sqrt{\Delta g d^3}} = 8(\Psi - 0.047)^{3/2} \quad (2.70)$$

Parker (1979) used a lower value for Ψ_{cr}= 0.03:

$$\frac{q_s}{\sqrt{\Delta g d^3}} = 11.2\frac{(\Psi - 0.03)^{4.5}}{\Psi^3} \quad (2.71)$$

The majority of the bed load transport formulae for unsteady flow have been adapted from those formulae developed for steady flow assuming that the sediment is advected at a mean orbital velocity.

Madsen and Grant (1976) adapted the Einstein-Brown formula for the averaged transport rate q_s during half the wave period as:

$$\frac{q_s}{wd^2} = 12.5\Psi^3 \qquad (2.72)$$

Where, w is the fall velocity of grains and, $\Psi = (1/2) f_w \rho U_m^2 \,/\, \Delta g d$.

Sleath (1978) described his experimental data by

$$\frac{q_s}{\omega d^2} = 47(\Psi - \Psi_{cr})^{3/2} \qquad (2.73)$$

Where, ω=$2\pi/T$.

Bailard and Inman (1981), based on the work of Bagnold (1963) and Komar & Inman (1970) assumed that the volume of solids mobilized, Λ, is assumed proportional to the energy dissipation rate where:

$$\Lambda = \frac{1}{\tan\phi}(\Psi - \Psi_{cr})d \approx 1.6(\Psi - \Psi_{cr})d \qquad (2.74)$$

Assuming, ϕ = 32^0. If it is advected at the mean orbital velocity, $(2/\pi)U_m$, then the transport rate for the half period is:

$$q_s \approx (\Psi - \Psi_{cr}) d U_m \qquad (2.75)$$

Concluding remarks

The above list of sediment transport formulae is far from complete. The common characteristic of these formulae is that they are based on an excess shear stress concept. The majority of the transport formulae have

been developed for uni-directional currents and applicable for sand and gravel. Some bed load transport models for currents have been adapted for waves assuming that the sediment is advected by the mean orbital velocity. As each stone on a bed protection has a different critical shear stress value depending on the level of protrusion (Fenton & Abbot,1977; Chin & Chiew,1993) the use of one single value for Ψ_{cr} in the bed load transport formulae would not be appropriate. Rather, the critical shear stress can be more appropriately represented by a probability distribution function.

2.12.1.2 Stone transport rate, Φ_E, incorporating local turbulence

Jongeling *et al*. (2003) empirically derived the following stone transport formula, which showed that the modified Shields parameter, Ψ_{WL}, strongly correlated with the non-dimensional entrainment rate, Φ_E:

$$\Phi_E = 5.4\,X\,10^{-14}\Psi_{WL}^{4.89}; \quad 18 < \Psi_{WL} < 39, \qquad R^2 = 0.78, \alpha = 6 \tag{2.76}$$

Jongeling *et al*. (2003) averaged the local turbulent kinetic energy, $\sqrt{k}$ within a height above the bed equal to $h_m=5d_{n50}+0.2h$. α refers to the turbulence magnification parameter.

The modified Shields parameter was defined as:

$$\Psi_{WL} = \frac{\langle(\bar{u} + \alpha\sqrt{k})^2\rangle_{hm}}{\Delta g d_{n50}} \tag{2.77}$$

Hofland (2005) also averaged the turbulent kinetic energy over the mixing length, L_m, and defined a new stability parameter

$$\Psi_{Lm} = \frac{max\left[\langle\bar{u} + \alpha\sqrt{k}\rangle_{Lm}\frac{Lm}{y}\right]^2}{\Delta g d} \tag{2.78}$$

Hofland's stone transport formula:

$$\Phi_E = 1.15\ X\ 10^{-9}\Psi_{\mathrm{WL}}^{4.53};\quad 2.5 < \Psi_{\mathrm{Lm}} < 5.5,\qquad \mathrm{R}^2 = 0.77, \alpha = 6 \qquad (2.79)$$

Hoan *et al*., (2008) in their experiments for currents, laid stripes of light weight stones made of epoxy resin (d_{n50}=0.82cm, d_{n85}/d_{n15} = 1.11, ρ_s = 1320 – 1971 kg/m^3) surrounded by natural stones (d_{n50}=0.8cm, d_{n85}/d_{n15} = 1.27, ρ_s = 2700kg/m^3) having a rough permeable layer thickness of 4cm. They used a tapering flume to create expanding non-uniform flow conditions. Their study showed that the non-dimensional entrainment rate Φ_E, has a poor correlation with the Shields non-dimensional shear stress, Ψ.

However, the relationship they derived using Φ_E and the modified Shields stability Parameter, $\Psi_{u\text{-}\sigma(u)}$ agreed well with the measured data. $\Psi_{u\text{-}\sigma(u)}$ is a parameter that accounts for the turbulence intensity at the bed as opposed to the mean velocity used by Shields.

Jongeling *et al*. (2003), Hofland (2005) and Hoan (2008), plotted stone transport data against the modified Shields parameter incorporating local near-bed turbulence and found a strong correlation of the type, $\Phi_E = \alpha_1 \Psi^{\beta_1}$.

Concluding remarks

It is clear from the above three studies that the inclusion of the local turbulence fluctuation (and the resulting fluctuation in the shear stress) is very important in describing local stone entrainment/transport. As special characteristic of the above three studies is that, the authors attempted to average the turbulent kinetic energy over the mixing length or equivalent. However, the incipient motion is caused by the interaction of protruding bed

elements with the turbulent events at the bed and hence, the turbulence statistics gathered over a sufficient time period close to the bed would capture the effect of high momentum water parcels moving towards the bed from the upper part of the water column (inrush) as well as 'bursting' of turbulent spots and ejection of vortices from the bed elements. In the present study, therefore, instead of averaging the turbulence over the mixing zone, the maximum turbulence fluctuation (and hence, maximum fluctuation in shear stress) near the bed will be used to find a correlation with the observed bed damage.

2.12.1.3 Semi-empirical studies on stone transport/bed damage

Naheer (1979) carried out tests in a wave flume to study the damage of a bed protection consisting of natural rocks (5.44 and 5.7mm) and coal (8 and 11.1mm). In these test he used solitary waves. Naheer observed that the bed damage has a linear correlation with the maximum dimensionless shear stress.

$$\frac{N_P}{N_{PT}} = -6.36\,X10^{-4} + 0.0121\tau_{max} \qquad (2.80)$$

Where N_P is the number of particles moved by the wave in the test area, and N_{PT} is the total number of particles in the uppermost layer in the test area. Therefore, this parameter is equivalent to the percentage of stones moved.

Losada *et al*. (1987) followed an energy dissipation approach to derive a stability equation. After fitting published incipient motion data of various researchers, they found the following relationship:

$$\frac{a}{d} = \alpha'\left(Re^{2/3}/D_*\right)^{6/5} \qquad (2.81)$$

Where, a is wave orbital amplitude at the bed, d is grain size, $Re = \omega a^2/\nu$ and D_* is non-dimensional grain diameter. α' is an empirical coefficient to be determined by experiment.

2.12.2 Stochastic modelling of stone entrainment/bed damage

Kalinske (1942, 1947), Einstein (1942, 1950) and Frijlink (1952) pioneered the probabilistic approach of bed load transport calculation. Einstein departed from the mean tractive force concept. In turbulent flow the fluid forces acting on a particle vary with respect to time and space and, therefore, movement of any particle depends upon the probability, P, that at a particular time and place the applied forces exceed the resisting forces (Raudkivi, 1998).

Papanicolaou *et al*. (2002) used a stochastic model to study the probabilistic aspects of the incipient motion. The effect of the intermittent nature of the near- bed turbulence and bed packing on the commencement of sediment motion was studied. In order to isolate the near-bed turbulence effects from other parameters like size, shape, etc., uni-sized spherical particles were chosen.

The instantaneous velocities u, v were represented by a Gaussian probability distribution. The conventional approach is to represent the flow parameters, i.e. normal and shear Reynolds stress components, hydrodynamic forces and their moments, by a normal distribution (Einstein, 1950; Paintal, 1971*a,b*; Cheng and Chiew, 1998). However, recent experimental evidence suggests that the Reynolds normal stress in natural

streams is represented well by a gamma distribution and that the Reynolds shear stress is represented well by a "peaky shaped" density function. Following this new approach using a probability distribution function (PDF) of instantaneous velocities instead of other flow parameters, Papanicolaou *et al.* (2002) showed that the conventional approach over predicts the critical condition by at least a factor of 2.

The force on an exposed particle was modelled by the drag and lift forces. The stability of a particle as determined by the balance of the disturbing and restoring moments:

$$F_D l_3 + F_L l_2 \geq W' \cos(\beta) l_2 f_h \qquad (2.82)$$

Where, $l_2 = d/4\sqrt{3}$, $l_3 = d/\sqrt{6}$, β is the angle of the bed with the horizontal (Figure 2.30).

This was simplified and re-arranged in terms of u, v:

$$\Theta = A_1 u^2 + A_2 v^2 \geq C f_h \qquad (2.83)$$

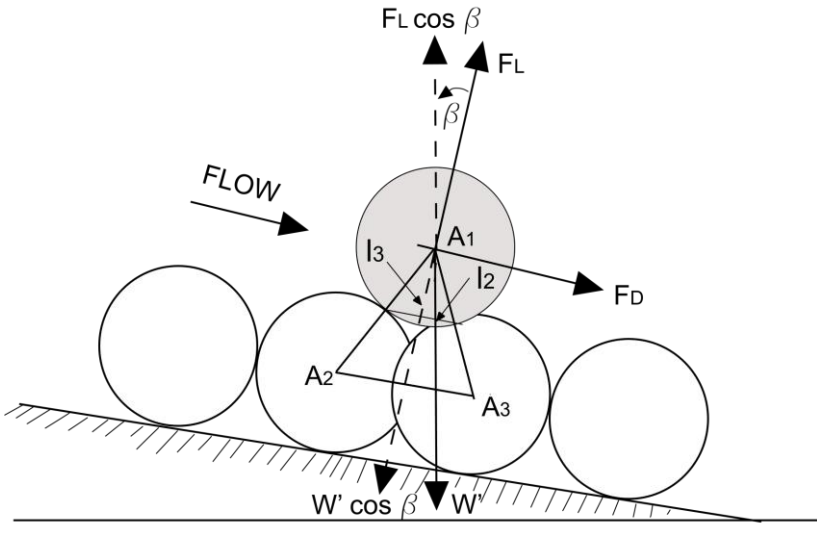

Figure 2.30: Definition sketch of inter-particle geometry for an exposed particle (Papanicolaou et al., 2002).

For the exposed particle, the probability of exceedence, P_E was defined as

$$P_E = P(\Theta \geq C f_h) \tag{2.84}$$

For the fully packed particles (Figure 2.31) movement can only occur, if the lift force is greater than or equal to the submerged weight.

$$F_L = \frac{1}{2} C_L \frac{\pi d^2}{4} \rho u_b^2 \tag{2.85}$$

The authors concluded that a C_L = 0.4 is the best value for fully developed turbulence after carrying out a sensitivity test. u_b is the instantaneous velocity atop the bed.

$$u_b^2 \geq \frac{\mathrm{W}'}{\mathrm{A}_3} \cos(\beta)\, f_h \tag{2.86}$$

As u_b follows a Gaussian distribution, its square follows a chi-square distribution of the type $f(u_b^2) = \exp(-u_b/2)/\sqrt{2\pi u_b}$.

For the fully packed case, the probability of exceedence is denoted by:

$$P_E = P[\mathrm{F_L} \geq W' \cos(\beta) f_h] \tag{2.87}$$

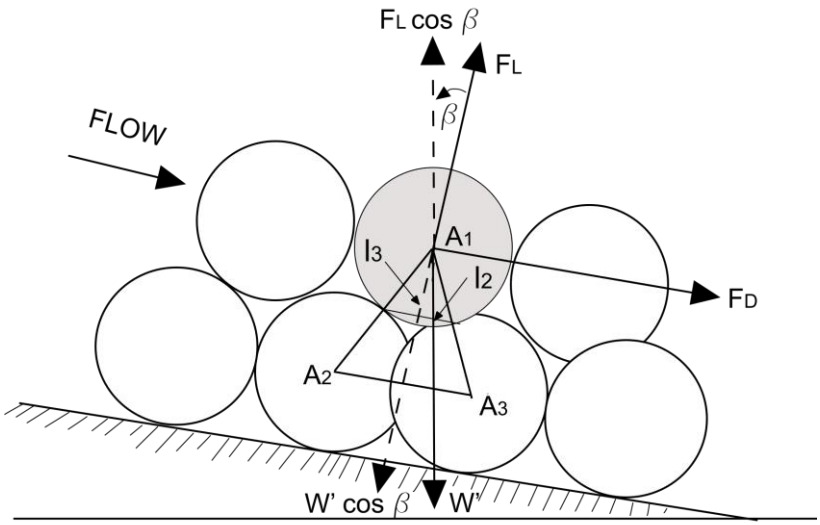

Figure 2.31: Definition sketch of inter-particle geometry for a fully packed bed (Papanicolaou et al., 2002).

Papanicolaou *et al.* (2002) conducted incipient motion tests for spherical particles for different packing conditions, i.e. 2%, 50% and 70%. For the 2 percent case (exposed), the spacing among the particles was 6 diameters. The 70 percent case represented the fully packed condition. They concluded that assuming a normal PDF for the near-bed velocity resulted in only 33% over prediction to the critical condition in the 2 percent (exposed) case while for the 50 percent condition (partially packed - one diameter spacing between elements) this over prediction was 360%. Use of a Gaussian PDF for u, v resulted in only 7% and 29% over prediction, respectively.

Wu & Yang (2002) calculated the entrainment probabilities of mixed size sediments. They observed that, to date, two key factors affecting the incipient motion of natural sediments still remain to be incorporated into the theoretical formulation of entrainment probabilities: the effects associated with near-bed coherent flow structures and randomly configured mixed-size sediments. The former is typically characterized by the periodic bursting events such as sweeps, ejections, and inward/outward interactions; the latter is represented by the random grain protrusion, friction angle, and hiding-exposure effect. Wu & Yang assumed the exposure as a probability distribution. The applied shear stress on smaller and larger particles were distributed according to the relation, $\tau = \xi\tau_0$ where the hiding factor ξ was determined probabilistically.

$$\tau_i = \xi\tau_0 \tag{2.88}$$

Einstein (1942, 1950) related the probability of erosion to the ratio between the effective weight of a grain and the instantaneous lift. He determined,

empirically, a hiding factor to account for sheltering or trapping of smaller particles.

$$\xi_i \approx 0.89\left(\frac{d}{d_{50}}\right)^{-2.255} \tag{2.89}$$

Egiazaroff (1965) defined a hiding or exposure factor for finer sediments in terms of the dimensionless Shields critical shear stress for mean d_m or d_{50}:

$$\xi_i = \frac{\Psi_{cr,i}}{\Psi_{cr,\ d50,\ Shields}} \tag{2.90}$$

Hofland (2005), Hofland *et al*. (2005) and Hofland & Battjes (2006) carried out pressure measurements on a hollow 30cm cube, located in a bed of natural stones (rough bed). Hofland argued that, due to the sharp edges, a cube represents natural rocks better. The PDF of the measured near-bed velocities was not perfectly Gaussian, but could be approximated quite well by such a distribution (Figure 2.32). The shape of the measured drag force PDF fitted well with that obtained theoretically assuming the normal distribution for the near- bed velocity, u_b (Figure 2.33). The prediction was quite good for the highest exposure.

Figure 2.32: Measured near-bed velocity compared with Gaussian PDF (Hofland, 2005).

Figure 2.33: Normalised PDF of measured drag force on linear (left) and semi-logarithmic (right) scale for different exposures and uniform flow (Hofland, 2005). Solid line represents theoretically derived PDF.

Figure 2.34: Measured normalised uplift force PDF compared with theory (Hofland, 2005).

Assuming that the lift force is due to the quasi steady mechanism, the lift force, F_L was taken to be proportional to u^2. The resulting theoretical curve for the uplift force PDF, followed a Gaussian distribution. However, Hofland (2005) observed that the measured uplift forces for most exposures followed a normal distribution (Figure 2.34) indicating that there is another mechanism, other than the quasi-steady mechanism, involved in the fluctuating lift forces on bed material. Therefore, it can be concluded that the

influence of vortex-induced lift is still influential for a stone lying on a solid boundary.

2.12.2.1 Exceedance probability of the critical shear stress

The mobility of stones occur when the applied shear stress on a bed of stones exceeds the critical shear stress. As the shape, size, protrusion, exposure and orientation of a single element vary, the critical shear stress is not a single value, but a probability distribution function even for a single stone size.

Grass (1970) observed that the initial instability of fine sediment particles depends on the critical shear stress distribution and the mean shear stress distribution applied by the current. Grass argued that the critical bed shear stress distribution is an “intrinsic property” of the bed material just like the terminal fall velocity, which will be independent of the near-bed turbulence. Therefore, at the moment of incipient motion, the applied shear stress, τ, should just exceed, the critical shear stress, τ_{cr}.

$$\tau > \tau_{cr} \tag{2.91}$$

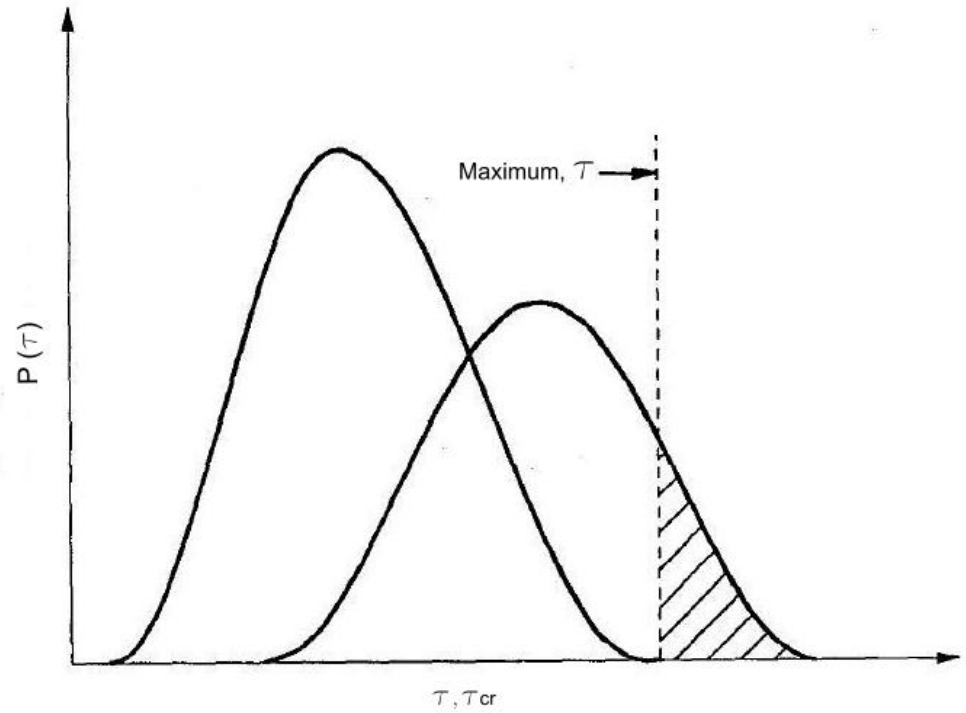

Figure 2.35: Probability density functions of the shear stress applied by the flow on the bed, τ, and critical shear stress of stones, τ_{cr}.

2.12.2.2 Concluding remarks

Stochastic modelling of the incipient motion, would offer a more realistic approach for the design of a bed protection than designing for an extreme case (i.e., single fully exposed stone) deterministically, as such an approach will not take into account the variability of the critical shear stress in space and time.

From the results of the previous studies on the subject, it appears that a Gaussian distribution is a better candidate to model near-bed flow velocities. However, all those studies cited are for uni-directional currents and hence, the applicability of their findings for oscillatory flow needs to be verified by measurement.

3 Experimental apparatus, instrumentation and data analysis

3.1 Introduction

Experiments were carried out to understand the effect of stone protrusion on the critical shear stress and the forces on a stone in a model bed protection. Stones were idealised as solid spheres (except in bed damage tests described in Chapter 8 where crushed natural rocks were used). The main apparatus consisted of the wave flume at the Fluids Laboratory at the Civil, Environmental and Geomatic Engineering Department of the UCL. The 90cm long, 45cm wide model bed protection was located at the middle of the flume. Wave heights of between 3.5-16.5cm, wave periods between 1-2.5s and a still water depth of 40cm mainly (and 30cm for some tests) were used.

Incipient motion tests were carried out changing the stone protrusion above mean bed level. The bed consisted of 19mm glass marbles. The test sphere, with diameter 9.5 - 25.3mm, specific gravity 1.19 - 2.53, was placed over three similar spheres fixed to a plate on the flume bed. The stone protrusion was varied by changing the space between the supporting spheres.

Forces on a stone in a bed protection were quantified by measuring and integrating the pressure on a 50mm sphere located over a coplanar bed of similar spheres (billiard balls). A special apparatus was made for this purpose.

Resistance type wave probes were used to synchronise the water surface elevation with the pressure signal from Honeywell 40PC001B2A pressure sensors.

Laser Doppler Velocimetry was used to measure the turbulence parameters at the bed. A novel method, Volumetric Three-component Velocimetry, was used to compute the three dimensional velocity and vorticity fields to visualise the flow patterns near the rough bed and around a sphere (i.e. idealised stone).

3.2 Experimental apparatus

3.2.1 Description of the wave flume

The experiments were carried out in the UCL wave-current flume, schematically illustrated in Figure 3.1. The flume was 14.5m long with wave paddles located at either end. Therefore, excluding the lengths of the wave paddles, the test section was 9m long. The width and height of the flume are 45cm and 65cm respectively.

The side walls of the flume are constructed of 1cm thick plate glass. The bed consists of 183cm long and 45.7cm wide cast aluminium sections. The flume is supported along its full length by an iron structure with U-shaped cast aluminium sections that provided support at 91.5cm intervals. The water supply was provided from an overhead storage tank located above the laboratory. The flume was slowly filled via a 150mm diameter supply pipe. Tests were conducted about 1 hour after filling the flume to allow for settling.

3.2.2 Description of the wave paddles

The novel aspect of the facility is that the wave flume is equipped with two identical wave generators with force-feedback wave absorption, one at either end of the flume. These are particularly effective in absorbing low frequency waves. Simons *et al*. (2000) noted that when used in conjunction with a short , horizontal, perforated metal “beach” suspended below the wave trough level at the non-wave generating end, it is possible to maintain reflection coefficients less than 5% for waves with periods across the range 0.8 sec<T<3.0 sec. The 917mm long 450mm wide perforated plate was positioned 38cm from the downstream paddle and was suspended 5cm below the still water level. The beach attenuated the incoming waves sufficiently with any remaining residual waves being absorbed by the wave paddle.

The paddles were controlled to generate surface waves using OCEAN software developed by Edinburgh Designs Ltd. Regular sinusoidal waves as well as irregular, random waves can be generated for chosen wave parameters by instructing the paddles through the software.

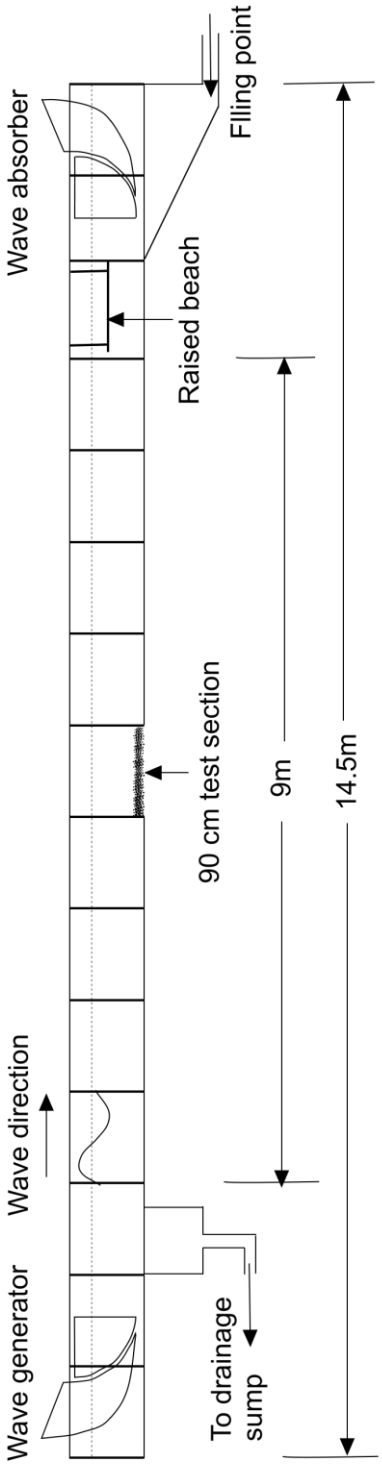

Figure 3.1: Wave-current flume at Civil, Environmental and Geomatic Engineering Department of the UCL. Approximate dimensions 1450cm X 45cm X 65cm.

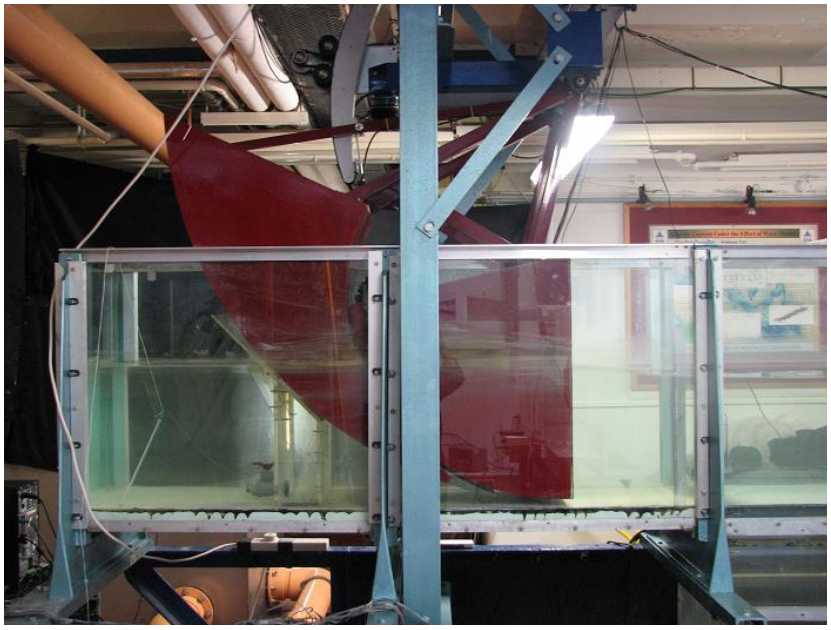

(a)

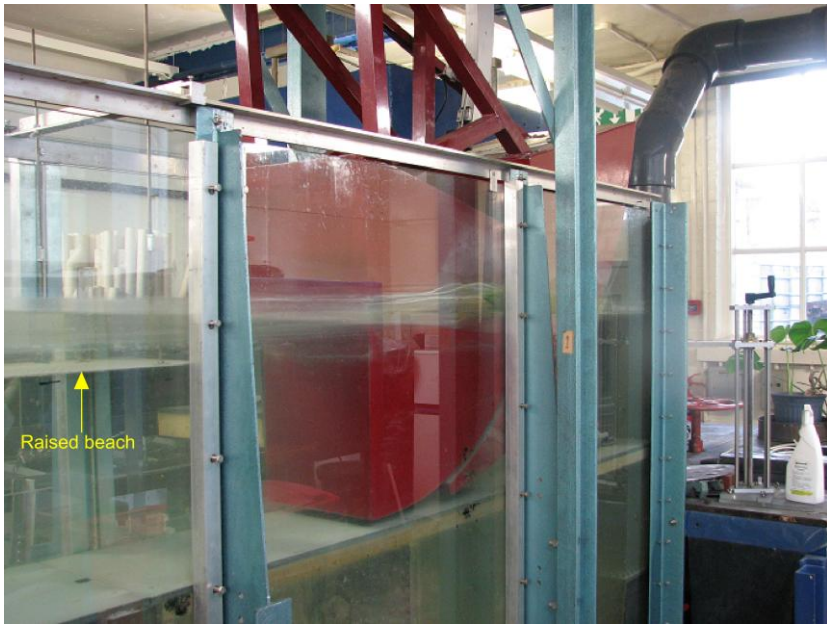

(b)

Figure 3.2: Wave flume - (a) wave generator (b) wave absorber and raised beach in front.

3.2.3 Incipient motion tests

Incipient motion of spherical stones of different density was observed varying the relative particle protrusion. Three 19mm spheres were screwed to a plate, which was, in turn, fixed to the flume bed flush with the floor. The movable test stone was placed to rest on the three spheres fixed at the middle of the plate as shown in Figure 3.3.

The test section was 90cm long, spread across the 45cm width of the flume. After fitting the plate in to the circular slot on the flume bottom, glass marbles were laid in one layer around the three supporting stones, following a hexagonal pattern as shown in Figures 3.4 and 3.5. Marbles at the two edges of the coplanar bed were glued using epoxy resin to contain the glass marbles within the 90cm long section.

The flume was then gradually filled with water to a 40cm depth (some tests at 30cm water depth were also conducted initially). Several test runs were conducted before the proper tests to obtain the approximate wave height at which displacement occurs.

The wave height and period were defined within the wave maker software developed by Edinburgh Design Ltd to generate a sinusoidal wave pattern. The wave height at the start of the tests was chosen to be a low value under which the stone was very stable. This wave height was gradually increased in 0.5cm increments until the stone starts a rocking movement and then the first displacement occurs. At the first displacement, the wave height and

period were recorded. 3-4 tests per each case were run to obtain average/representative wave conditions at the threshold of movement.

A sketch showing the inter-particle geometry of the test sphere and the three supporting particles (spheres) is shown in Figure 3.6.

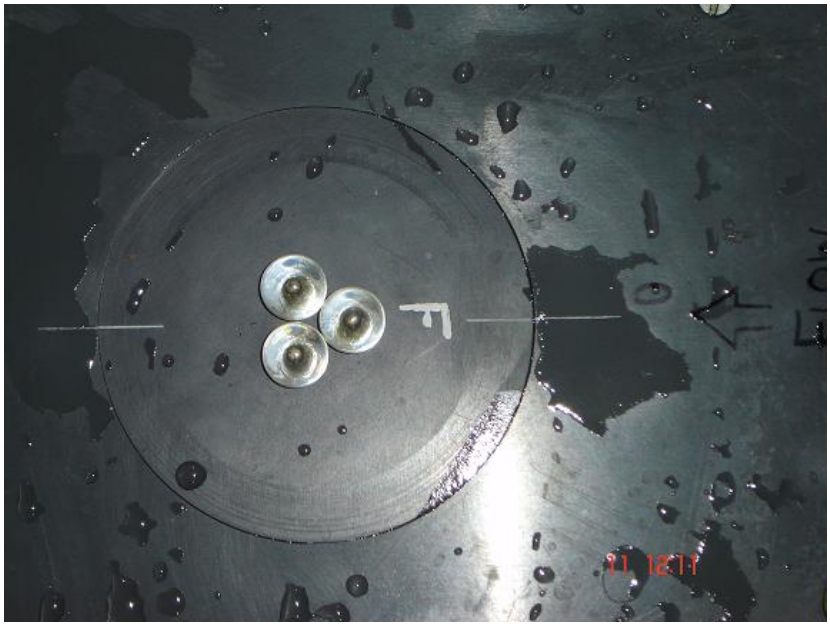

(a)

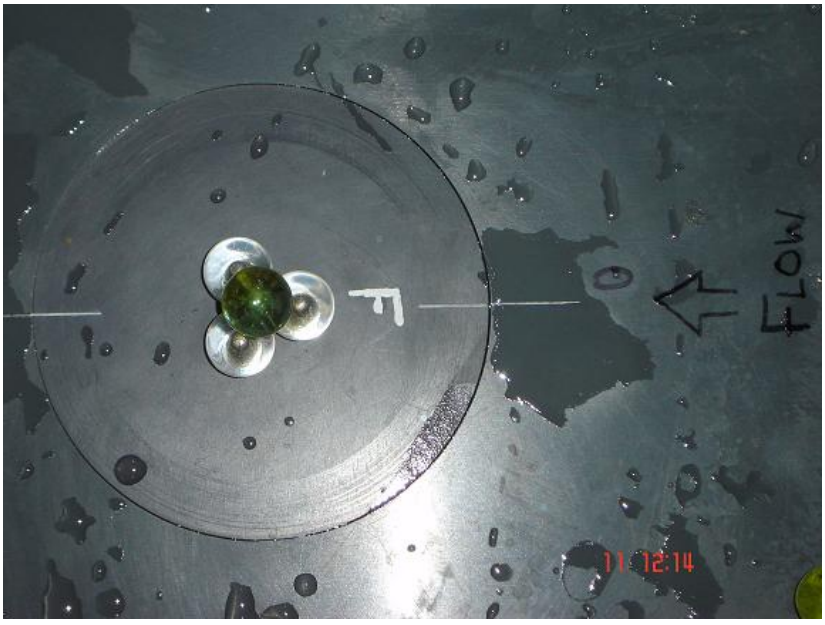

(b)

Figure 3.3: Apparatus for incipient motion tests - (a) Three spheres screwed to the plate (b) test stone (sphere) resting on the supporting spheres. Wave direction is shown by an arrow pointed towards the left.

(a)

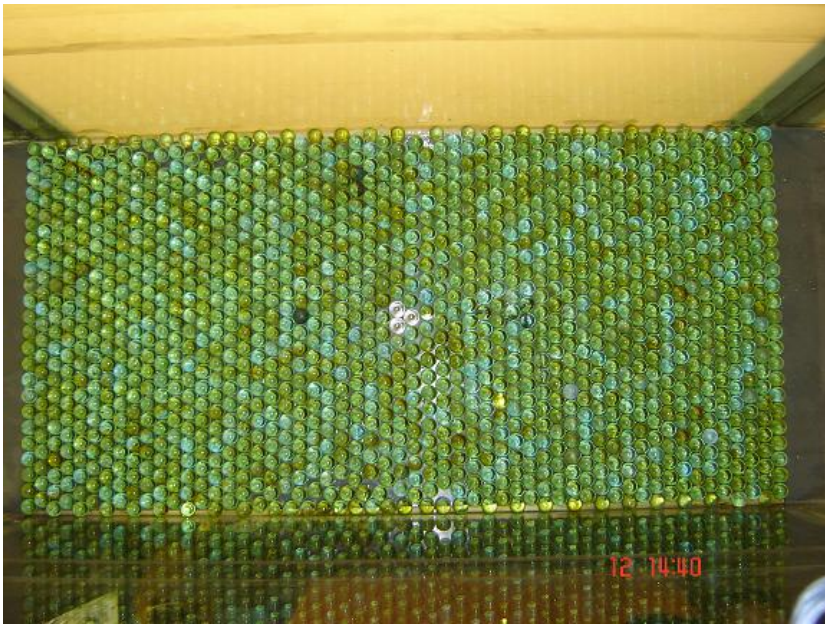

(b)

Figure 3.4(a),(b): Bed of 19mm glass marbles with three supporting stones (white) in the middle.

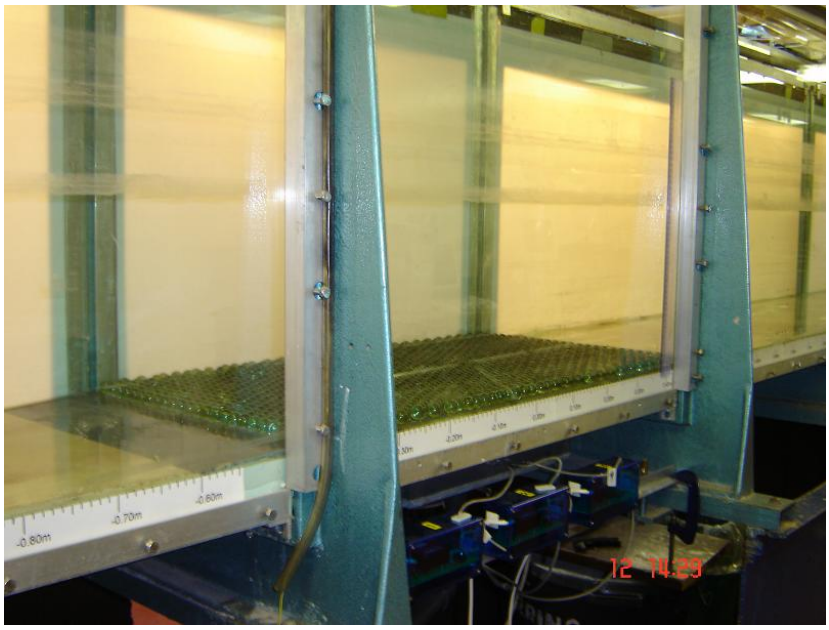

Figure 3.5: Test section in wave flume.

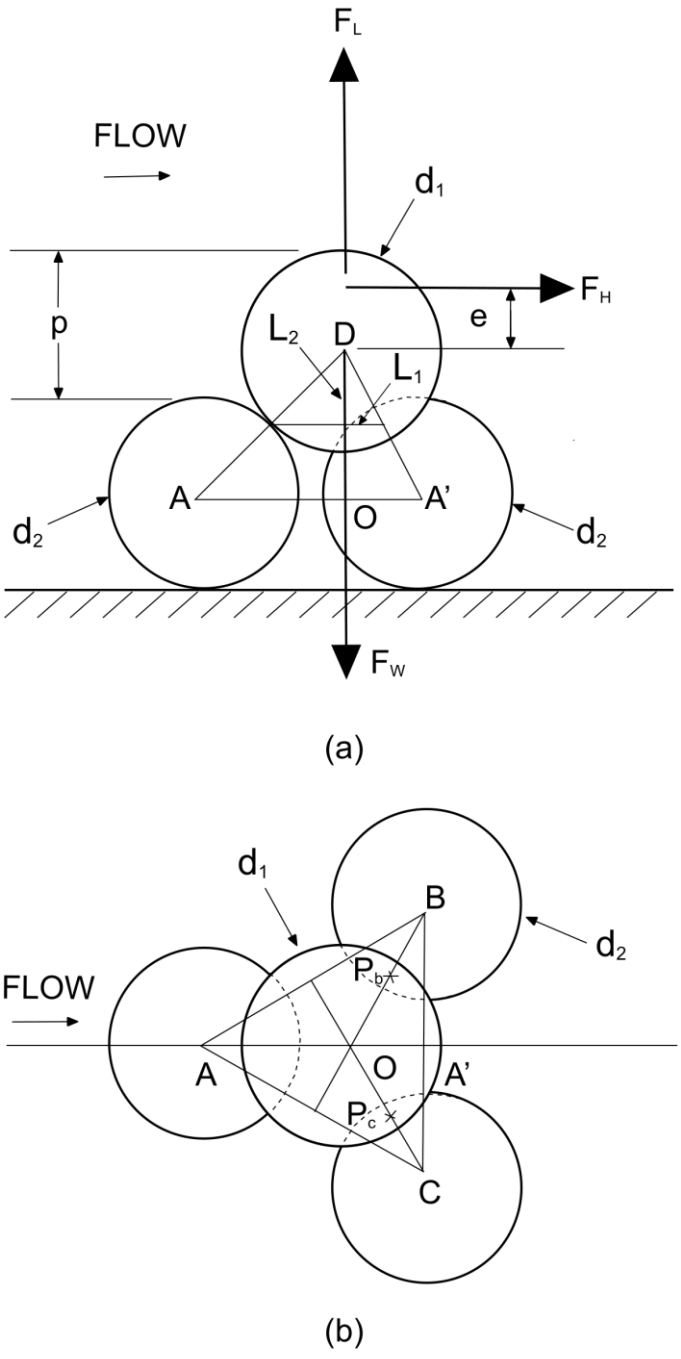

Figure 3.6: Definition sketch of inter particle geometry (a) section (b) plan.

3.2.4 Pressure measurement

A special device was designed for the measurement of pressure around a sphere. The pressure measuring sphere is shown resting on a bed of similar spheres in Figures 3.7-3.9 (fully exposed position). Figure 3.10 shows the measuring sphere located within a coplanar bed the pressure data of which were used to calculate bed shear stresses. The device was designed as a sphere. This device consisted of a 50mm hollow sphere made of two hemispheres as shown in Figures 3.11 and 3.12. The upper hemisphere was designed to tightly dovetail into the groves of the lower hemisphere. 1.5mm tappings on a meridian of the sphere surface spaced at 30^0 angles were connected to Honeywell 40PC001B2A pressure sensors via high strength silicone flexible tubes, with the tubes having a 2mm internal diameter (see Figures 3.13 - 3.15). Flexible tubes were run through a built-in solid pipe (internal diameter 7.5mm and outer diameter 12mm) located at the bottom of the lower hemisphere and then connected to the sensors. After filling the wave flume slowly, water was bled from the flexible tubes for some time to remove any air bubbles that might have trapped inside. Bleeding was also carried out while waves were running before the tests.

Sensors were energised and connected to the Datatranslation data logger. The output signal from an analogue wave probe stationed right above the measuring sphere in the flume, was also connected to the same data logger. DT Measure Foundry software was used to define the capture rate at 625Hz. The length of the record was defined between 100 to 200 wave cycles.

When the sensors were connected to the data logger using ordinary copper wires significant background noise was observed distorting the wave profile. Signal quality significantly improved when ordinary wires were replaced with coaxial cables. 50 Ohm BNC Crimp connecters were used at both ends of the coaxial cable.

The pressure sensor chosen was the Honeywell 40PC001B2A (40PC series) which is temperature compensated and supply regulated with its own internal amplifier. The analogue output voltage of 0.5V (at atmospheric) to 4.5V is linearly proportional to input pressure. The model used had a measuring range from 0 to ±50mmHg. The sensor's dimensions measured 13.2mm x 11.2mm x 9.6mm plus a 10.2mm long funnel at the top. The device required an input DC voltage of 4.75-5.25V and current of 10mA. It had an operating temperature range of between -45°C and 125°C with a response time of 1ms.

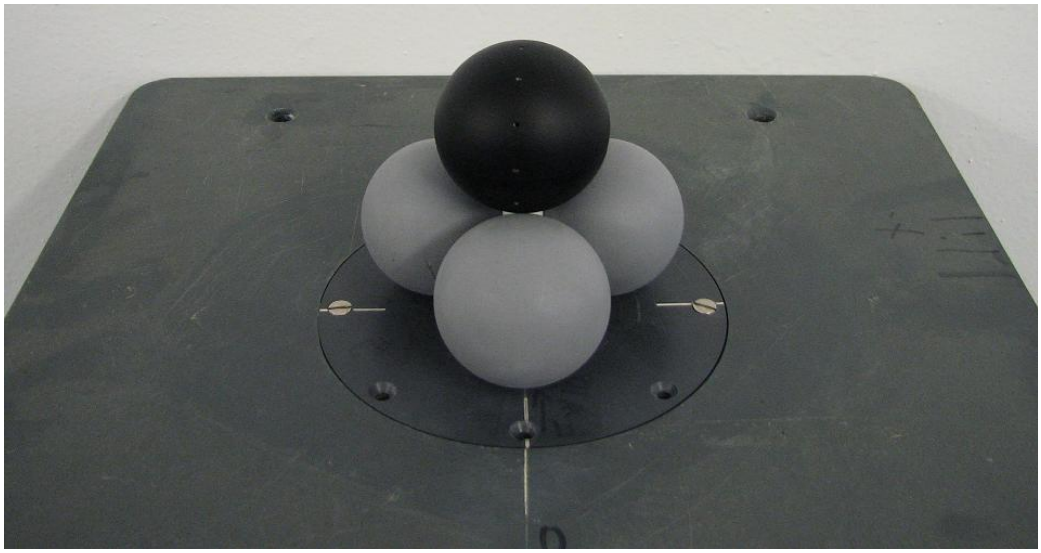

Figure 3.7: Sphere (black) with pressure tappings on the surface. Supporting three spheres fixed to the plate.

Figure 3.8: Measuring sphere (black) over the rough bed of 50mm billiard balls.

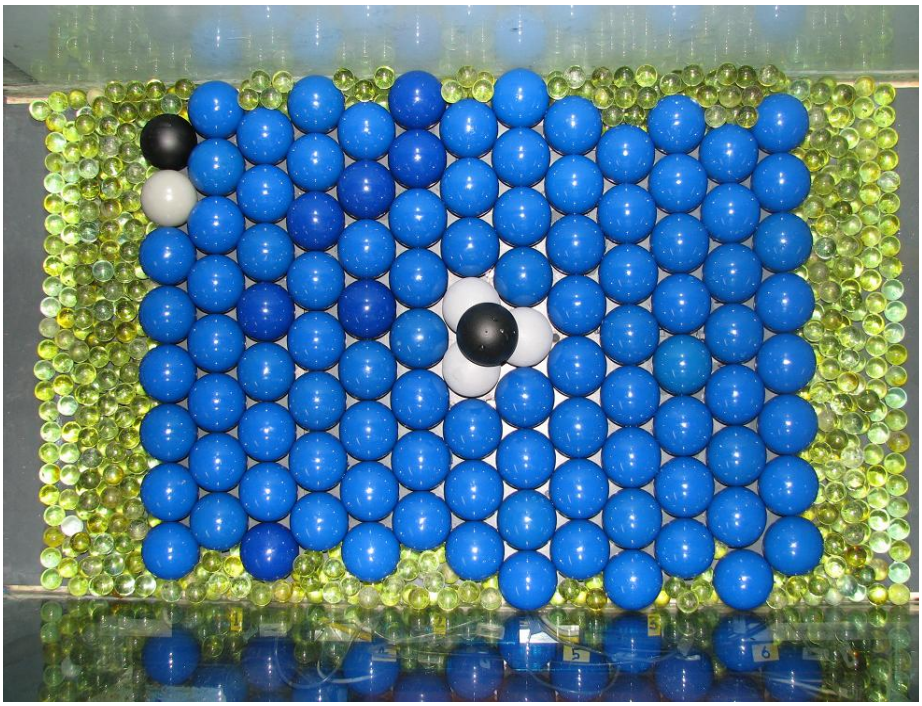

Figure 3.9: Plan view of the rough bed of 50mm spheres.

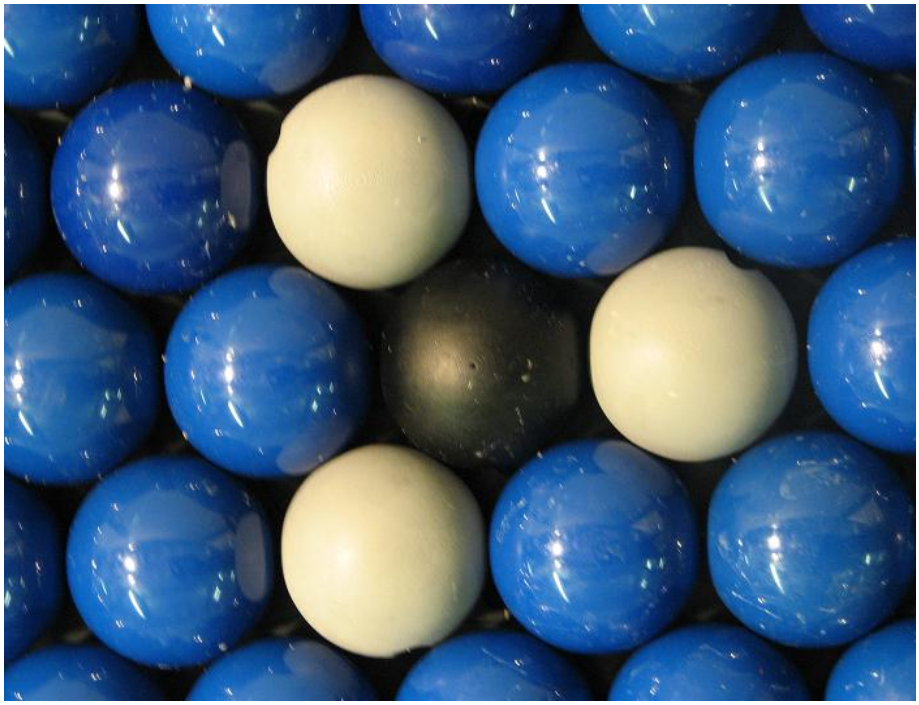

Figure 3.10: Measuring sphere with pressure tappings (black) in a Coplanar bed.

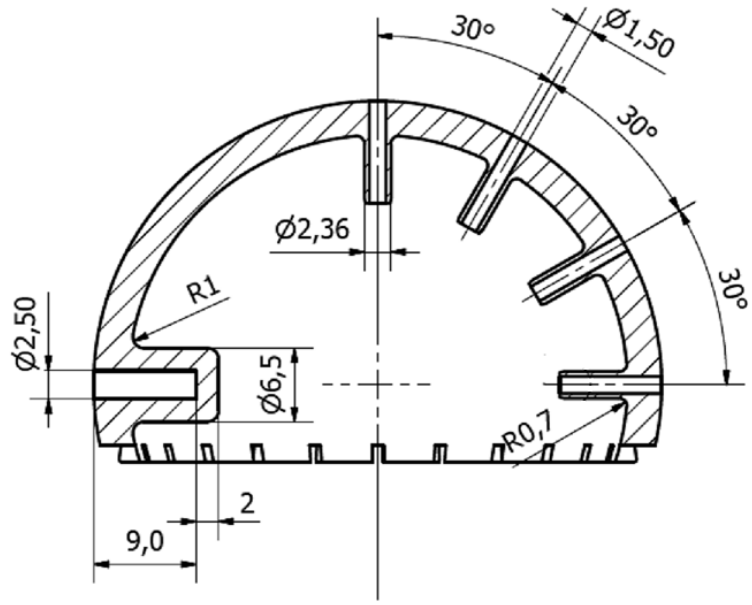

(a)

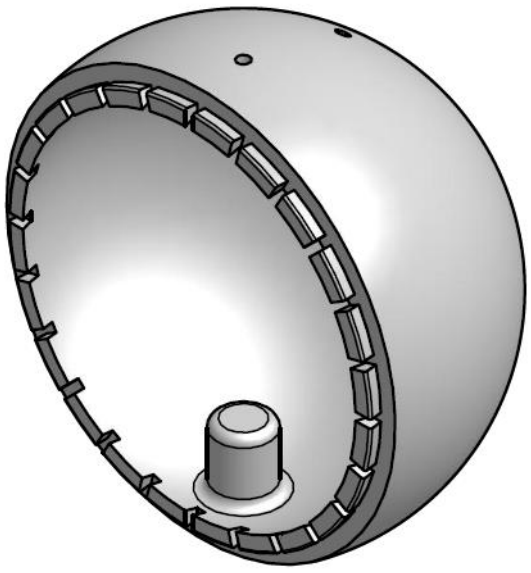

(b)

Figure 3.11: Upper half of the measuring sphere (a) section (b) 3D model. All dimensions in millimetres.

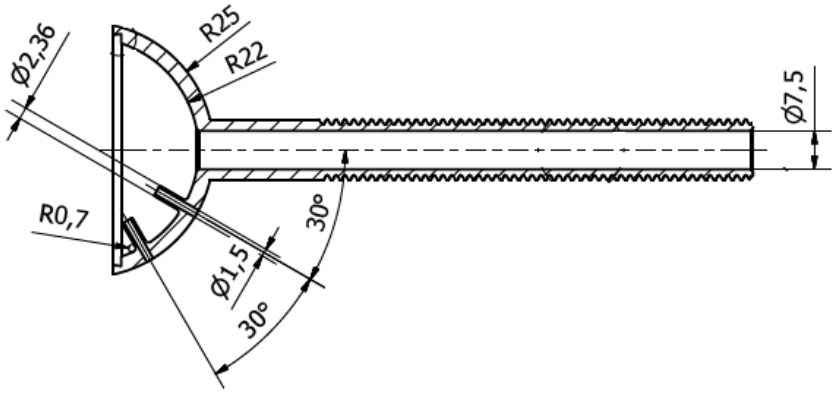

(a)

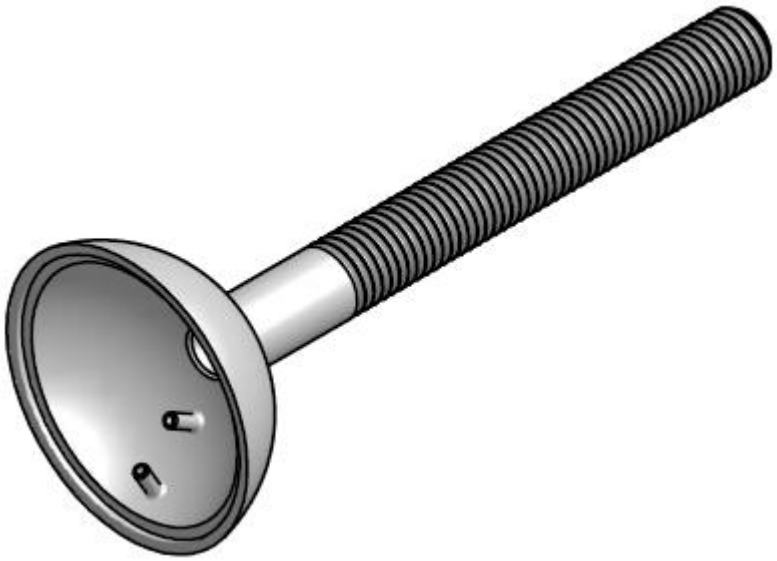

(b)

Figure 3.12: Lower half of the measuring sphere (a) section (b) 3D model. All dimensions in millimetres.

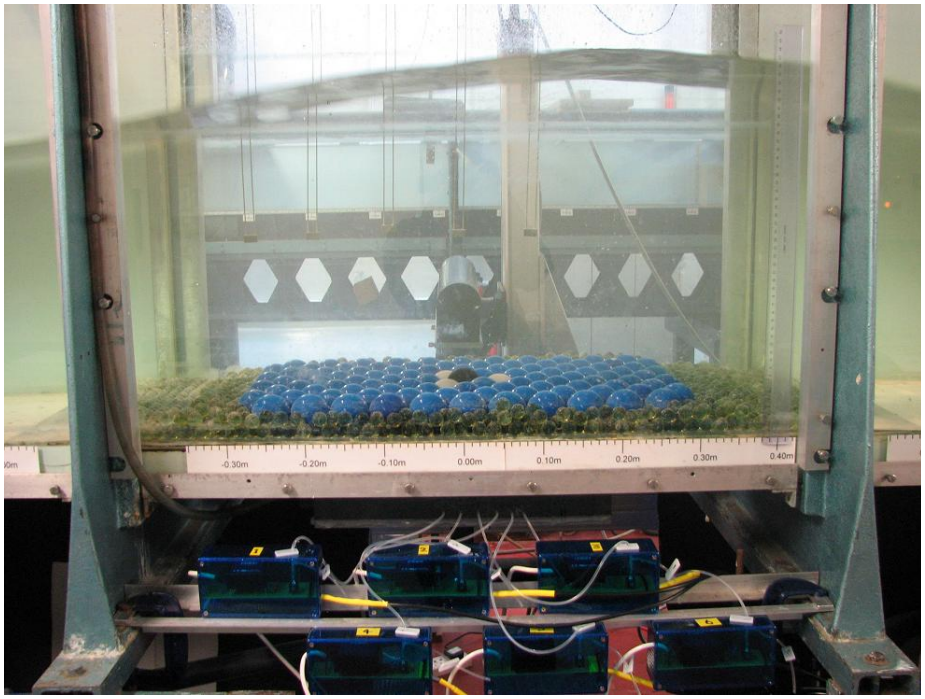

Figure 3.13: Waves running over the rough bed. Pressure tappings are connected to Honeywell 40PC001B2A type pressure sensors housed in the boxes below.

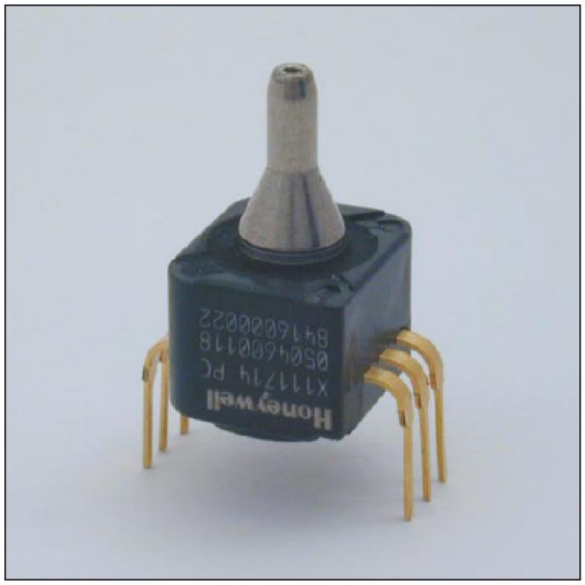

Figure 3.14: Honeywell 40PC001B2A pressure sensor.

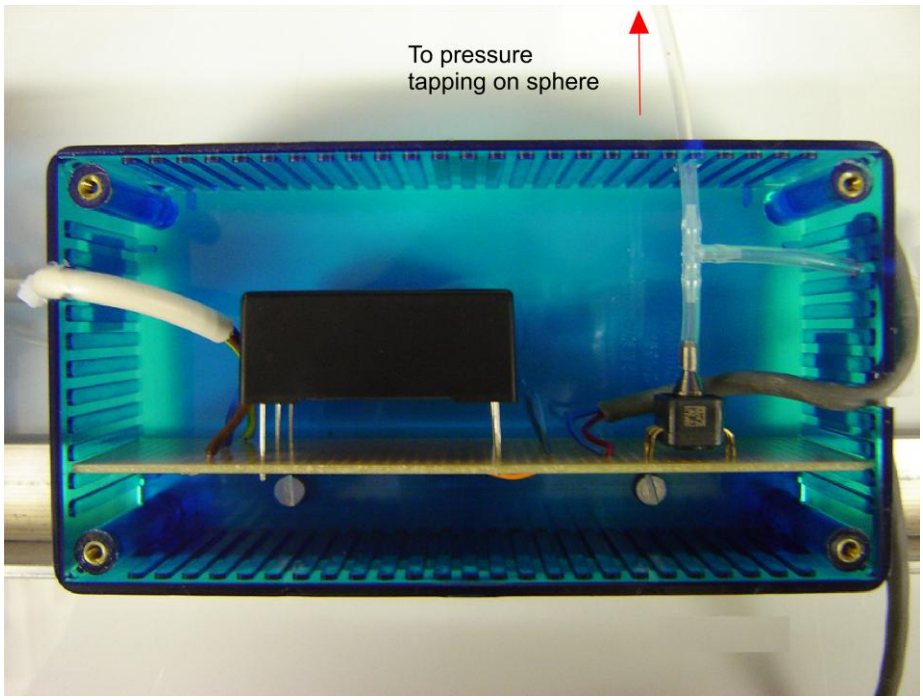

Figure 3.15: Honeywell 40PC001B2A pressure sensor inside the casing.

3.3 Instrumentation

3.3.1 Wave probes

Three mobile wave probes were used to monitor the surface profile of the waves. The principle of operation is based on the change in electrical resistance of the probe in response to a change in the depth of immersion. The probes were energised with a high frequency voltage. As the resistance between the pairs of vertical stainless steel wires change, the output voltage from the probes also changes. The output voltage is proportional to the depth of immersion.

Three mobile probes, WP1, WP2 and WP3 were set up in a group as shown in Figure 3.16. One probe (Ch2.) was placed right above the measuring sphere connected to six pressure transducers. The objective was to synchronise the wave probes with the pressure transducer. The distance between the probes remained constant throughout the tests.

The voltage output produced by the wave probes was analysed via the wave monitor modules and then channelled into the Datatranslation data logger simultaneously with the pressure sensor output from the test sphere. The DT Measure Foundry software was used to visualise and capture the signal from the wave probes. An example of the measured voltage for Channel 2 is shown in Figure 3.32. It shows that the signal was not affected by the background noise.

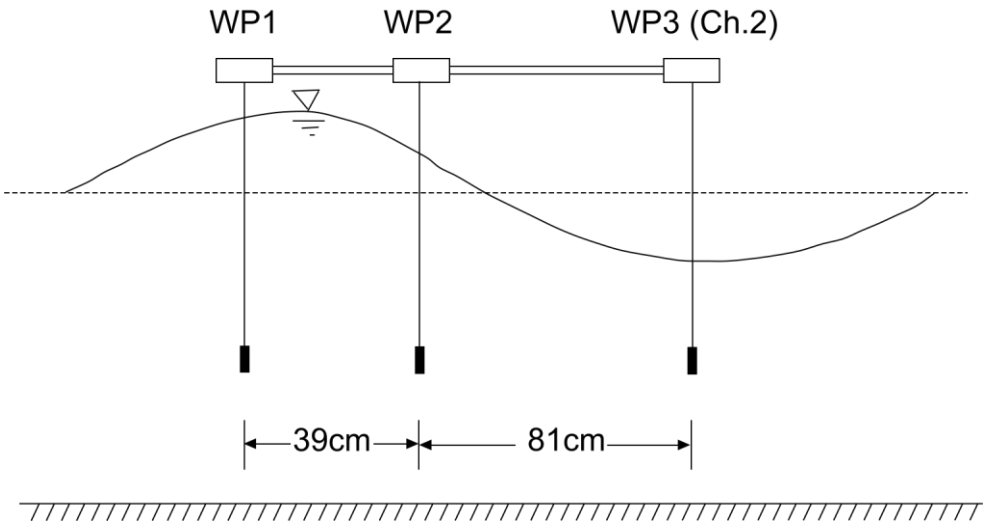

Figure 3.16: Schematic of the mobile wave probes WP1, WP2 and WP3.

3.3.2 Laser Doppler Velocimetry

Laser Doppler Velocimetry is a technique used for measuring fluid velocities by detecting the Doppler frequency shift of light scattered by small moving neutrally buoyant seeding particles. The Doppler frequency shift, f_d, is the difference between that of the incident laser beams and the scattered light frequencies. When light is reflected from a moving object, the frequency of the scattered light is shifted by an amount, f_d, proportional to the speed of the object. Therefore, the speed of a moving tracer particle in water can be estimated by observing the frequency shift. The main advantages of the LDV are the non-intrusive nature of the technique and the accuracy of the measurements.

An incident laser beam is split into two beams of the same frequency and intensity, and refocused to intersect at a point in the flow, as shown in Figure 3.17.

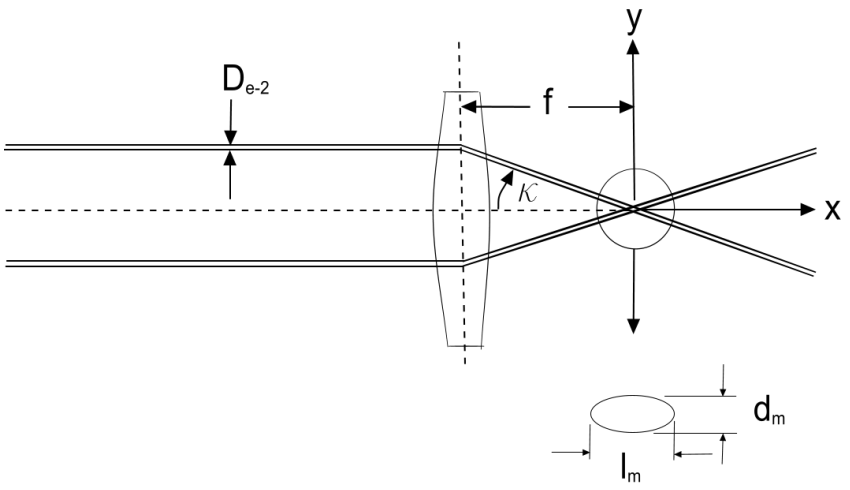

(a)

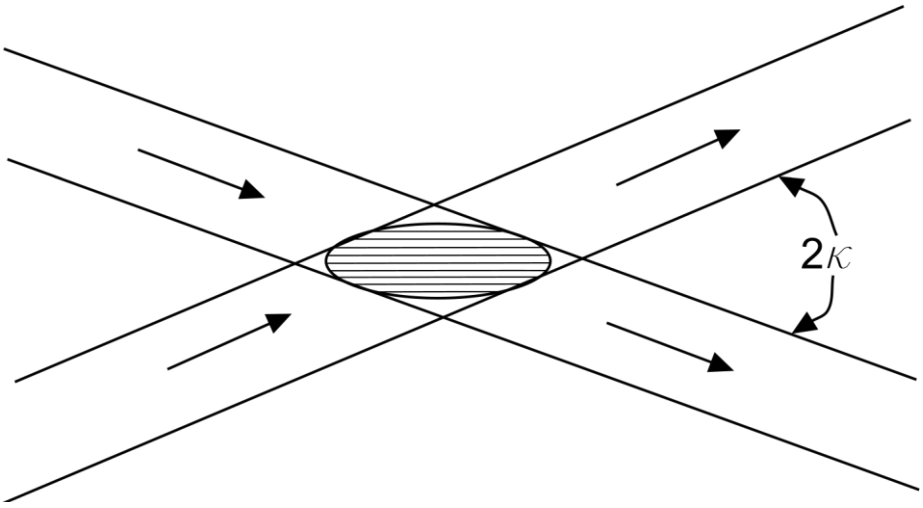

(b)

Figure 3.17(a),(b): Schematic of the laser optics and the measuring volume.

At the intersection of the two coherent light beams, an interference fringe pattern consisting of alternating zones of brightness and darkness is created. This intersected area is referred to as the control volume or measuring volume. The dimensions of the measuring volume were given by Durst *et al*. (1981) as:

$$l_m = \frac{d_{e^{-2}}}{\sin \kappa} \tag{3.14}$$

$$d_m = \frac{d_{e^{-2}}}{\cos \kappa} \tag{3.15}$$

$$h_m = d_{e^{-2}} \tag{3.16}$$

Where, l_m, d_m and h_m are the length, width and height of the measurement volume, respectively.

The measurement volume, V_m is given as:

$$V_m = \frac{\pi d_{e^{-2}}}{6 \cos \kappa \sin \kappa} \tag{3.17}$$

Where $d_{e^{-2}}$ is the diameter of the laser beam at the measurement volume. This is defined as:

$$V_m = \frac{4\lambda_l f}{\pi D_{e^{-2}}} \tag{3.18}$$

Where λ_l is the beam wave length, f is the focal length and $D_{e^{-2}}$ is the initial diameter of the light beam.

The fringe spacing, d_f, is the distance between the sequential bright (or dark) zones. When a tracer particle travels through the fringe pattern it reflects

light alternatively. The scattered light is collected by a photo detector. Assuming the two beams intersect at an angle of 2κ, the dark fringes are separated by a distance:

$$d_f = \frac{\lambda_l}{2 \sin \kappa} \tag{3.19}$$

Where κ is half-angle between the laser beams.

Fast Fourier Transform (FFT) and autocorrelation techniques are used to obtain the burst frequency. A high pass filter removes the intensity 'pedestal' from the middle of the burst, and a low pass filter then removes high frequency noise from the signal. Once the Doppler burst is isolated, the dominant frequency is measured and related to the velocity of the particle passing through the fringes.

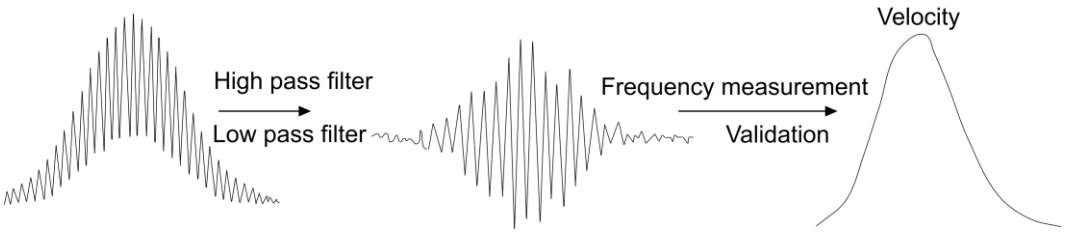

Figure 3.18: Steps in signal processing.

The amplitude of the signal burst varies with time and provides a measure of the particle velocity perpendicular to the fringe pattern. The frequency of the amplitude modulation is given by Durst *et al*. (1981) as:

$$f_d = \frac{2V_p}{\lambda_l} \sin \kappa \tag{3.20}$$

Where V_p is the particle velocity perpendicular to the fringes.

Doppler frequency depends only on the magnitude of V_p, not direction, i.e., positive and negative values of V_p will produce the same Doppler frequency. To correct for this directional ambiguity, the frequency of one of the incoming beams is shifted by a known value, f_s. This causes the fringe pattern to move at a speed $V_s = f_s\ d_f$ towards the incoming unshifted beam (Figure 3.19). The frequency recorded by the photodetector is now:

$$f_d = \left| f_s + \frac{2V_p}{\lambda_l} \sin \kappa \right| \tag{3.21}$$

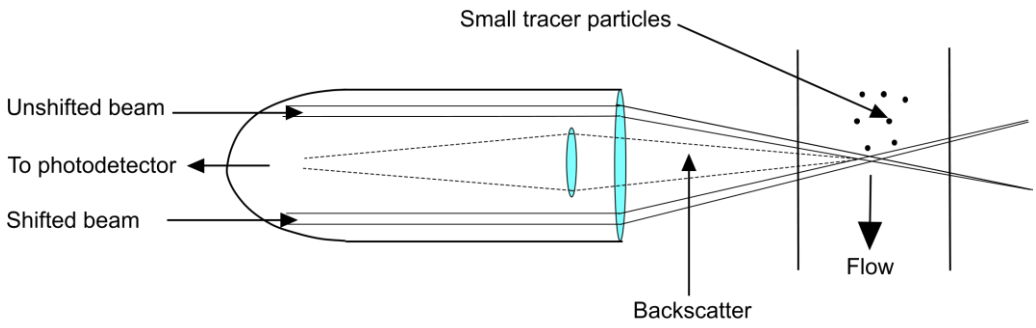

Figure 3.19: Transmitting and receiving optics in the same probe head.

The LDV system at UCL consists of an INNOVA 70C, 5 Watt Argon-ion laser and a two-component TSI laser anemometer. The two colour dual beam LDV system is capable of measuring horizontal (streamwise direction) and vertical components of the velocity.

The green and blue beams (colour due to different wavelengths) from the argon-ion laser were each split and re-focused to form two mutually orthogonal planes at a common intersection point, i.e., two blue beams form one plane and two green beams form the second plane normal to the former. Both focusing lenses and photodetector were inside the single laser

probe head as shown in Figure 3.19 operating in the backscatter mode. The signal processing was carried out within the TSI IFA-650 signal processor. Seeding material (Titanium dioxide) was added to the water to improve the data burst rate which was monitored on the oscilloscope and software.

The LDV system used in the present tests has the following parameters. l_m=2.4mm - 3.2mm, d_m=0.118 - 0.157mm, κ=2.8^0, f=512mm, $D_{e^{-2}}$=0.47mm.

In a multi-channel LDV system, simultaneous measurement of the velocity components is obtained by ensuring that the data-ready signals become available within a time window termed the coincidence window. This window should be of the order of the fluid transit time through the measuring volume and significantly smaller (by an order of magnitude) than the average time between data (Kang, 2001). The larger the coincidence window the higher the probability that the signal processors will validate Doppler bursts from different particles, causing loss of correlation. This value was chosen between 500-2000μs in the present tests based on earlier trials.

Because the arrival of each particle is random, the time between the velocity estimates is random. Therefore, the velocity is not evenly sampled in time. Before most analysis techniques can be applied to the data the record must be re-sampled onto an equi-spaced time grid. This can contribute uncertainty to the final analysis. Munekata *et al*. (2001) carried out Reynolds stress measurement using different sampling methods and concluded that equal time interval method with coincidence data is suitable for the accurate measurement of the accurate Reynolds shear stress.

3.3.4 Volumetric Three-component Velocimetry

Volumetric Three-component Velocimetry (V3V) is a state of the art technique for instantaneous volumetric measurement of the 3D velocity fields. The instrument consists of a unique single-body, three-aperture, 12 mega-pixel camera for 3D imaging. V3V uses volume illumination with Nd:YAG laser so that particles inside a large cubic volume up to 120x120x100 mm^3 can be recorded based on two-frame double-exposure at a 7.25Hz capture rate.

The raw particle images were processed to obtain the 3D positions of tracer particles using a fast and parallel triangle search algorithm. Then a 3D particle tracking technique was used to obtain velocity vectors for moving a tracer particle from position A at time t to position B at time $t+\Delta t$. Image processing is described in more detail under the section on data analysis.

3.3.4.1 System description

The system consists of the 3D camera probe, a dual head Nd:YAG double pulsed laser with optics to generate the volumetric illumination, a synchronizer as timing control unit and a computer system with the Insight V3V software. The intersection of the viewing region of the camera probe and the laser illumination beam determines the size, shape and location of the measurement volume (see Figure 3.20).

Figure 3.20: V3V Schematic representation (Pothos et al, 2009).

3.3.4.2 Operation procedure

Figures 3.21-3.25 show the V3V set up in the present tests. The laser probe was mounted over the wave flume above the test section as shown in Figure 3.22. The camera was setup on the side of the flume as shown in the figures, with the viewing direction orientated perpendicular to the wave direction. The volumetric domain was 120 x 120 x 100 mm^3. Two laser beams emitting from the probe crossed at a location 670mm in front of the camera probe (reference/focal plane) to allow positioning of the probe. The measurement region was taken as that region between the reference plane and the camera probe.

The operation of the V3V system and 2D PIV system are quite similar. The camera is synchronized with the pulsed laser and images of tracer particles are captured during two successive laser pulses separated by a pre-determined time interval (e.g., 0.005 sec). The velocity of the flow should be taken into account in determining the separation interval, as it is common practice to allow the particles to move a distance of 4 to 8 pixels between

two images. At the time of generating the laser pulses that trigger the capture of images (frames) A and B, a TTL (Transistor-transistor logic) signal was sent simultaneously to one of the channels connected to the data logger measuring the wave surface profile. This was done to determine the phase of the wave at the recording of each image frame.

Before each test, a small amount of concentrated mixture of tracer particles (Polyamide with 11% Titanium dioxide, 55 microns mean diameter) dissolved in water, was poured upstream and along the flume over the test section and allowed to sink and diffuse uniformly into the water column by running waves. The flow visualisation test was carried out only after the diffusion of particles uniformly over the water depth had occurred.

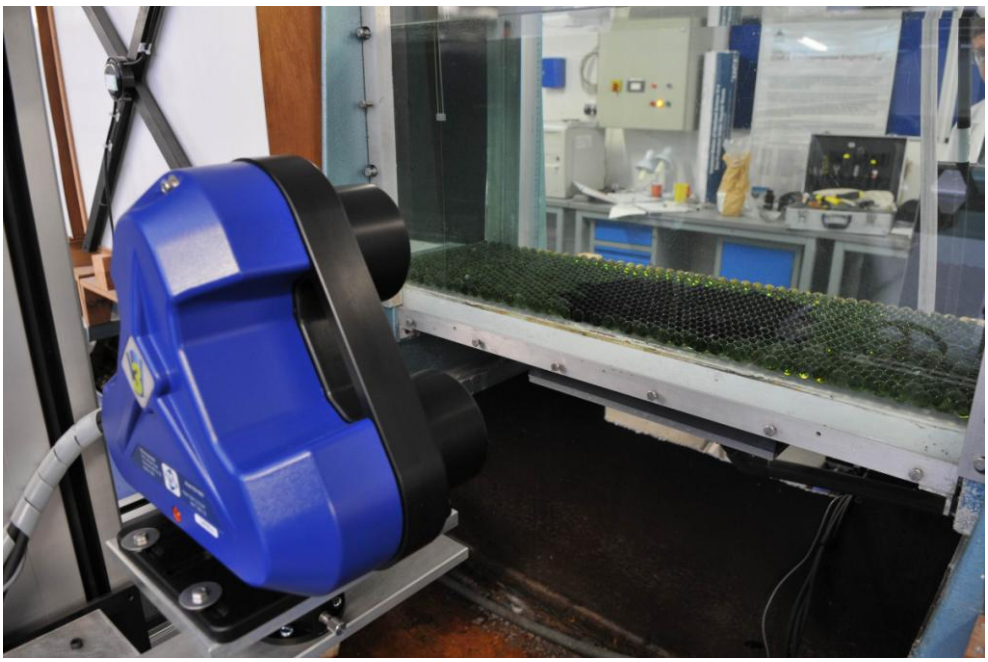

Figure 3.21: V3V camera mounted in front of the rough bed of glass marbles.

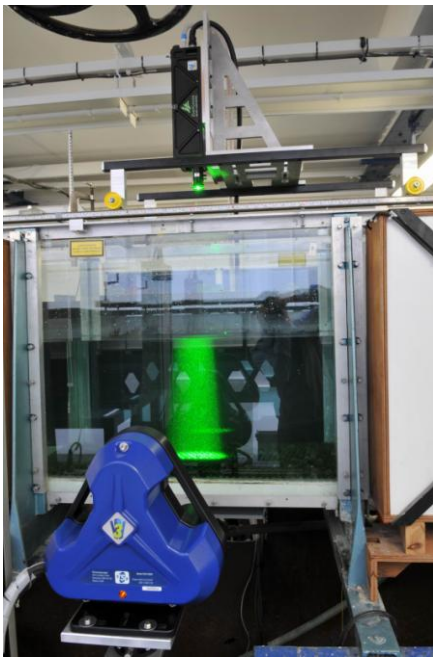

Figure 3.22: Laser illumination beam.

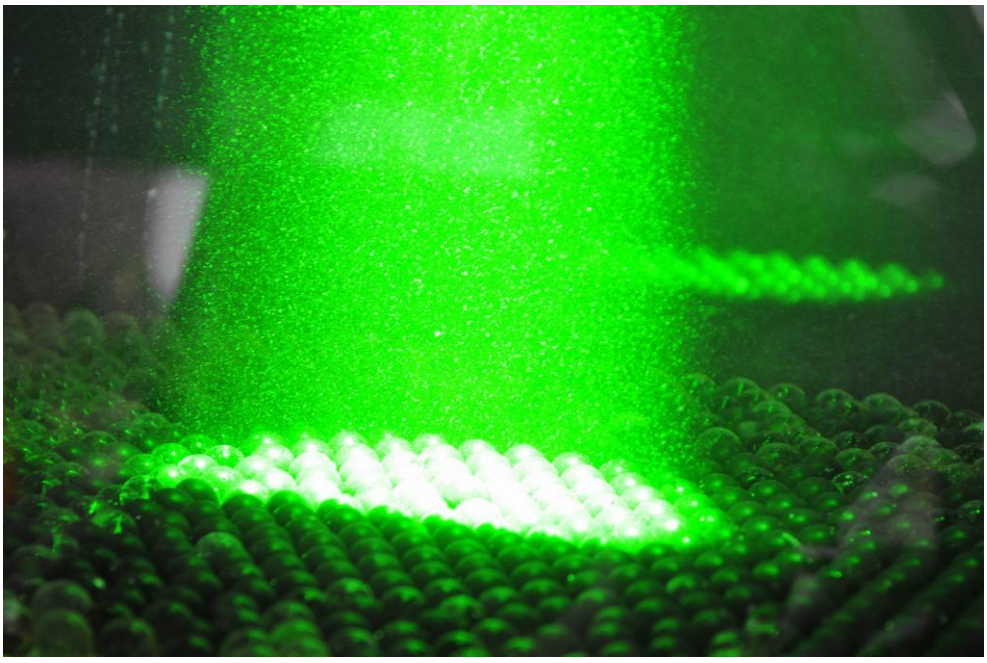

Figure 3.23: Illuminated tracer particles inside the laser beam.

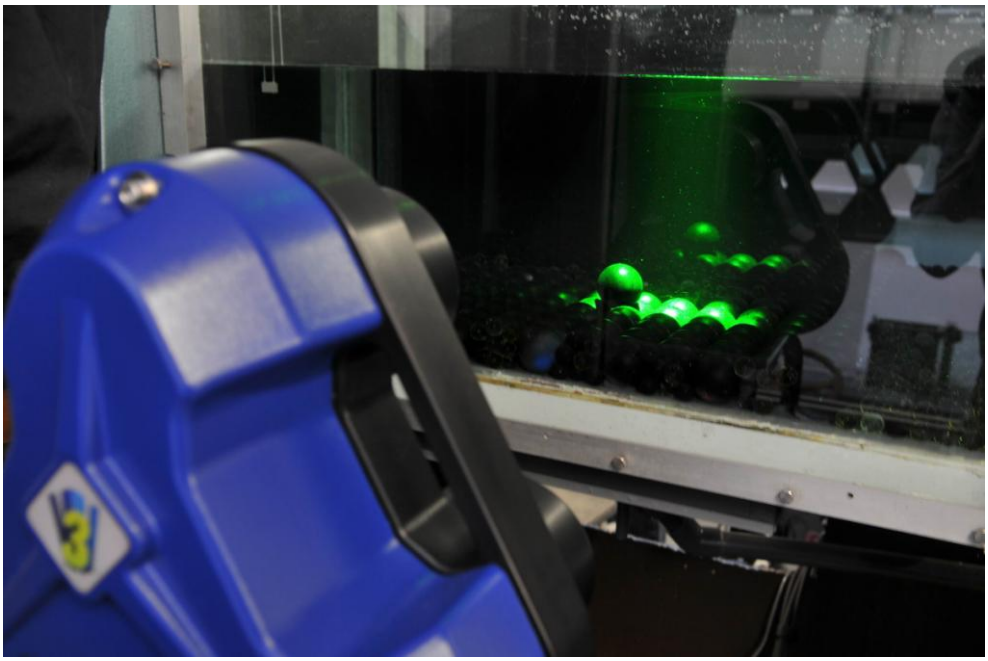

Figure 3.24: Fully exposed 50mm sphere illuminated by the laser beam.

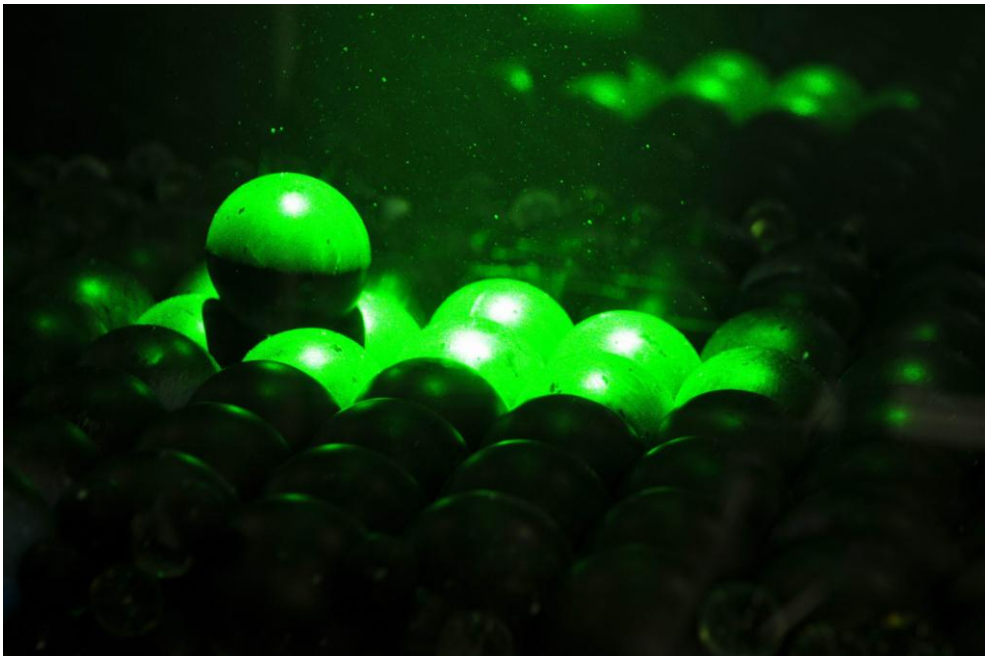

Figure 3.25: A close up view of a fully exposed sphere illuminated by the laser beam.

3.3.4.3 3D imaging principle

Three image sensors are mounted on a single body in a coplanar triangular pattern. The mapping region of the camera is measured from the camera to the point where the three image sensors intersect. The image of a particle within this mapping region is recorded by the camera from three different angles producing three images of the particle. These images form a triangle (a triplet) in the image plane as shown in Figures 3.26 and 3.27.

The size of the triangle depends on the depth position. Particles close to the camera faceplate will produce a larger triangle than one located further away from it. The centre of the triangle determines the *x* and *y* positions of the particles. *z* is obtained through the calibrated results that relate the size of the triplet triangle to the distance from the focal/reference plane (Figure 3.29).

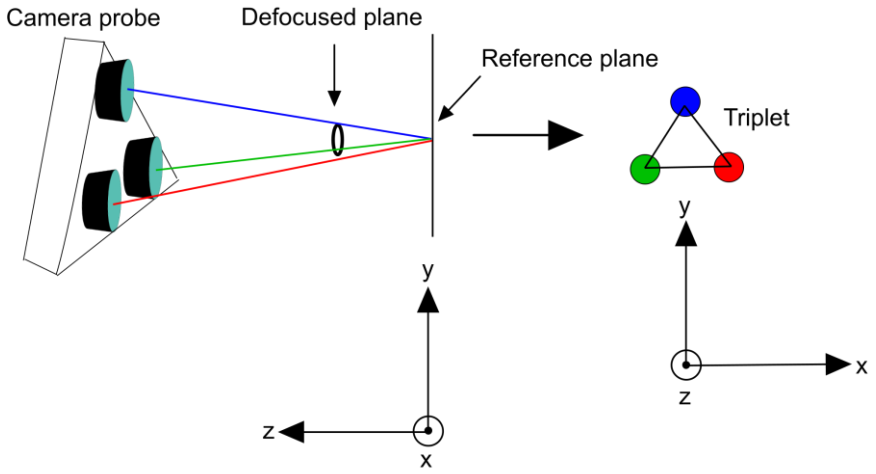

Figure 3.26: Sketch showing the formation of a 'triplet' in V3V.

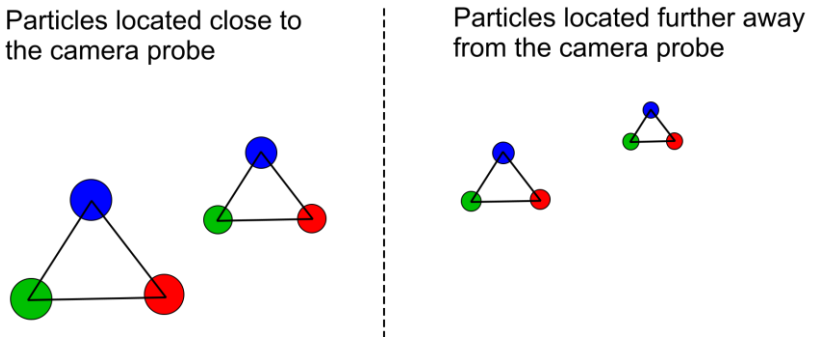

Figure 3.27: Sketch showing particle images in the image domain.

3.3.4.4 System calibration

The aim of the calibration was to minimise the errors caused by mechanical misalignment of the camera, optical distortion and deviations from pin hole optics (Pothos *et al.*, 2009). A calibration target as shown in Figure 3.28 consisting of a high precision grid of dots was gradually moved in stages across the flume through the measurement volume. Data capture was done

one plane at a time. The captured 2D calibration images were analysed and a Gaussian fit was used to find the (x, y, z) positions of the dot locations. After the calibration was carried out the system was used for actual experimental measurements.

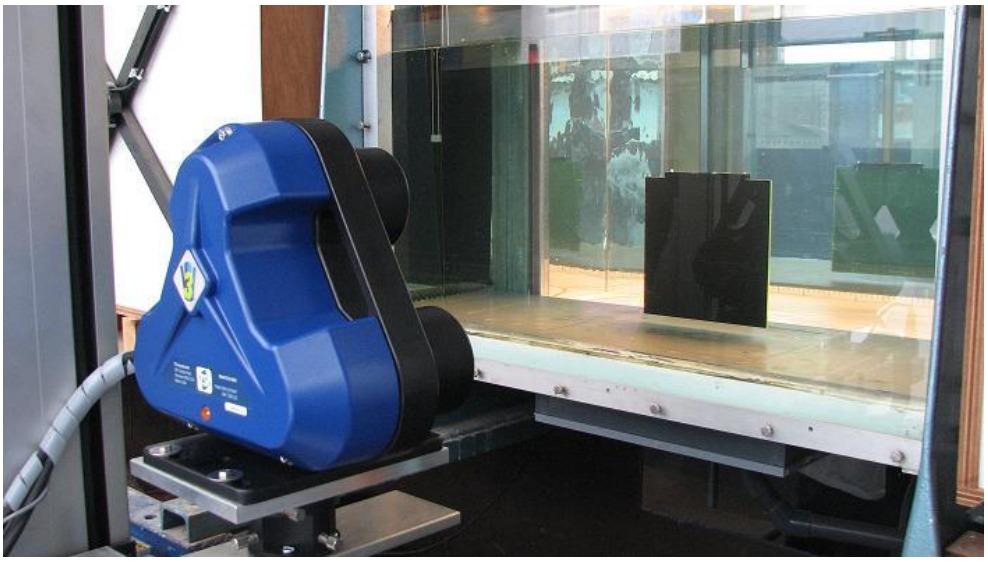

Figure 3.28: Calibration target in V3V system calibration.

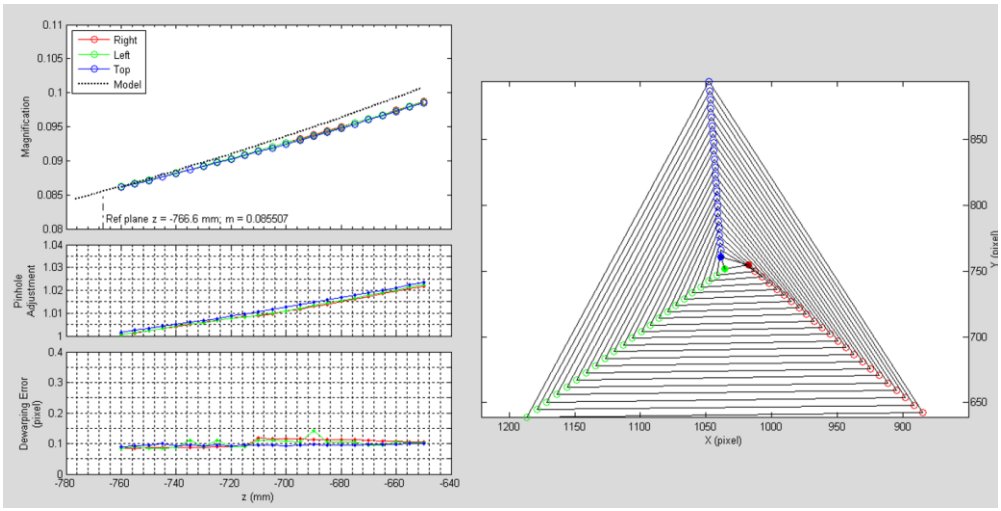

Figure 3.29: Spatial calibration data from the present V3V tests.

3.3.5 Acquisition of digital images in the bed damage tests

Damage progression to a granular bed protection consisting of light weight natural rocks (anthracite), was observed using an overhead camera connected to a computer. Software was used to trigger the start and end of the capturing of photographic data with data capture carried out at 10 second intervals. The images were automatically saved to the computer's hard drive.

An Artec laser scanner (Figure 3.31) was used to obtain a 3D digital surface elevation map of the rock armour bed protection. The bed surface was later re-digitised to obtain the surface elevation of cross-sections, taking measurements at the crest of the bed elements.

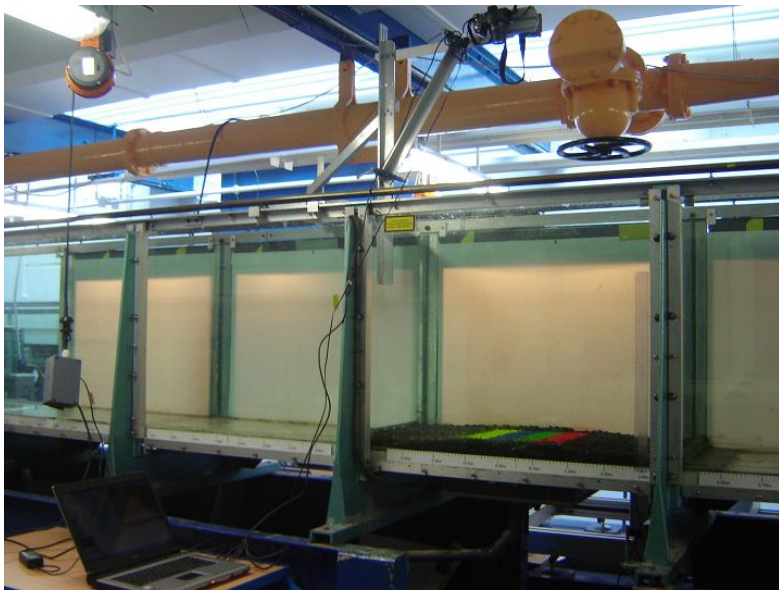

Figure 3.30: Overhead photo camera linked to the computer.

Figure 3.31: Artec scanner used for 3D scanning to obtain a digital surface elevation map of the model bed protection.

3.4 Data analysis

The laboratory tests provided information on the incipient motion of the stones, forces, turbulence parameters, bed shear stresses etc. The measured data were analysed using various quantitative methods; both stochastic and deterministic. Special software as well as automated excel sheets were employed in the analysis. Details of the analysis are provided in this section under various sub headings.

3.4.1 Ensemble-averaging

Ensemble-averaging is a technique that was used throughout this study. Instantaneous data of a quantity, M, for example, wave surface elevation, velocity, pressure or shear stress etc., were ensemble-averaged using the following relationship to obtain the average profile of the quantity over the wave cycle.

$$\bar{M} = \frac{1}{N}\sum_{n=0}^{N-1} M(t + nT) \tag{3.1}$$

The turbulent fluctuation is

$$M' = M - \bar{M} \tag{3.2}$$

Where N, is the number of wave cycles and n=0,1,2,3…N-1.

3.4.2 Wave profile data

The free surface wave profiles were obtained from the analysis of the wave probe measurements, as described in Section 3.3.1. The data acquisition sampling rate for the test on a coplanar bed was 625Hz. Data was ensemble- averaged over 50 wave cycles as a minimum. Figure 3.32 shows the analogue signal obtained for the wave probe located just above the measuring sphere (channel 2).

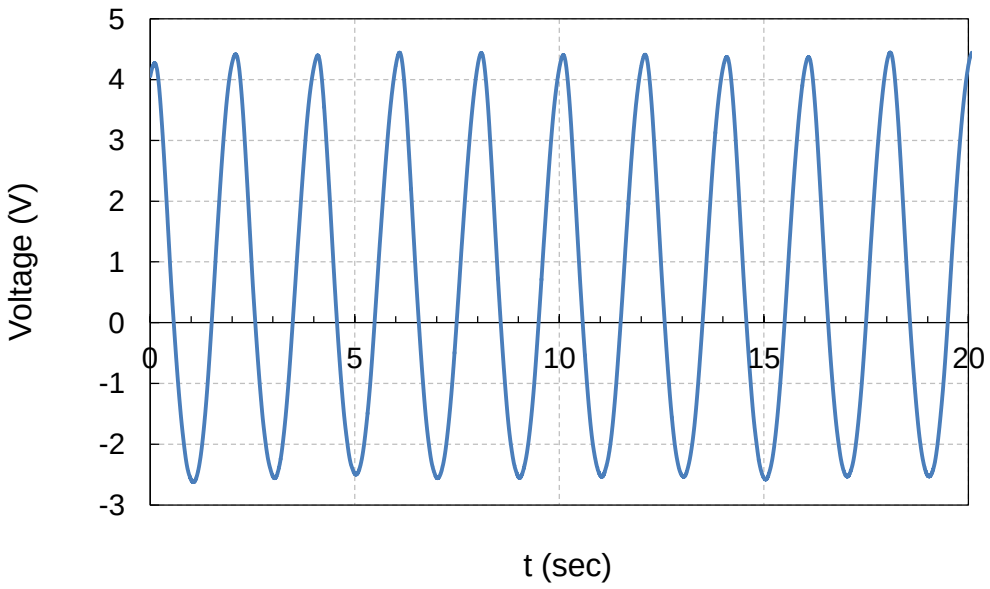

Figure 3.32: Analogue signal from the wave probe positioned right above the test sphere (Ch.2).

The voltage measurement was related to the water elevation through a simple calibration assuming that the water level and the voltage are related linearly. A calibration graph was produced by plotting the measured voltage versus the water level by lowering the water level in the flume when the water was static prior to generating waves.

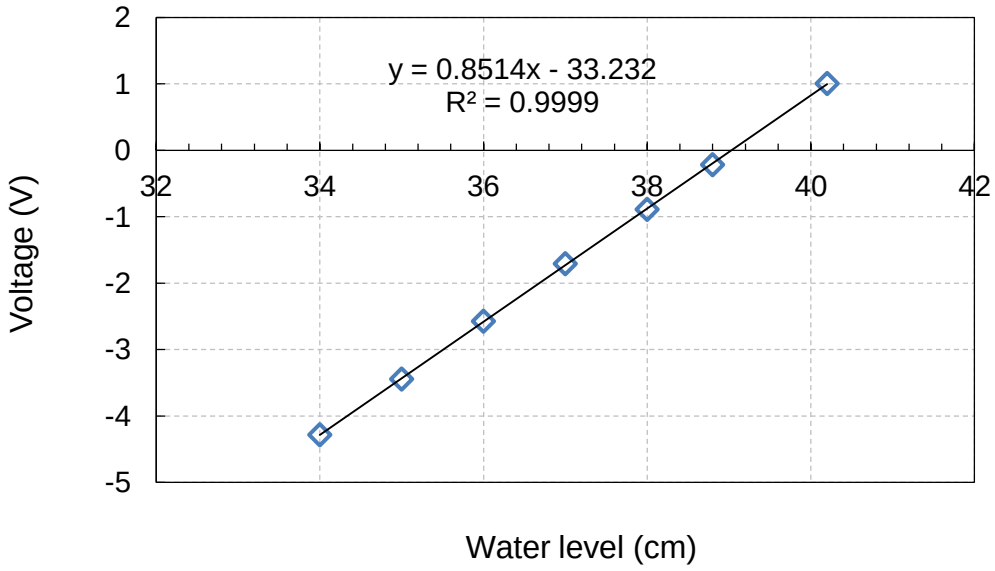

Figure 3.33: Wave probe calibration graph for channel 2. Water temperature, T=20 deg. 01/10/2010.

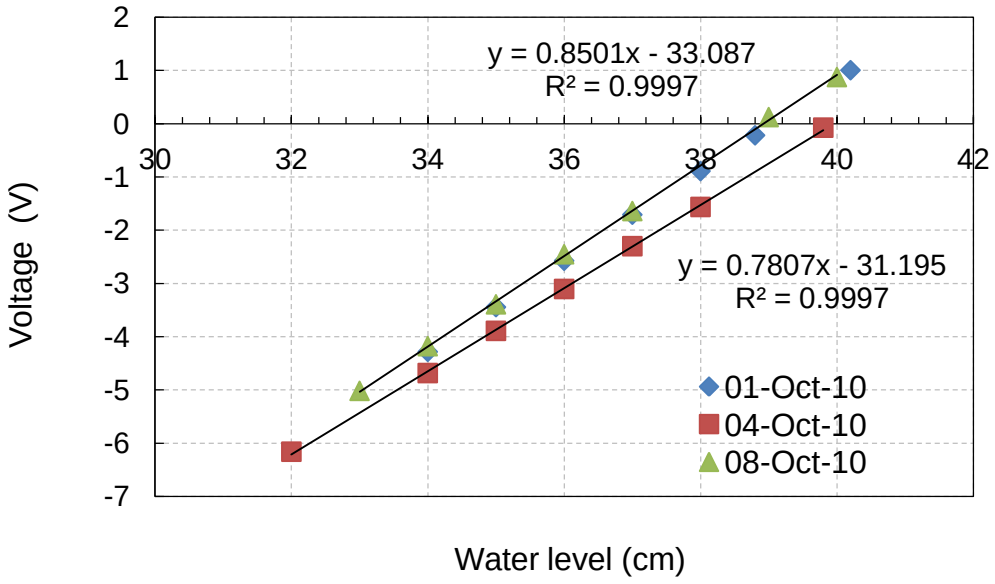

Figure 3.34: Wave probe calibration graph for channel 2 on different dates.

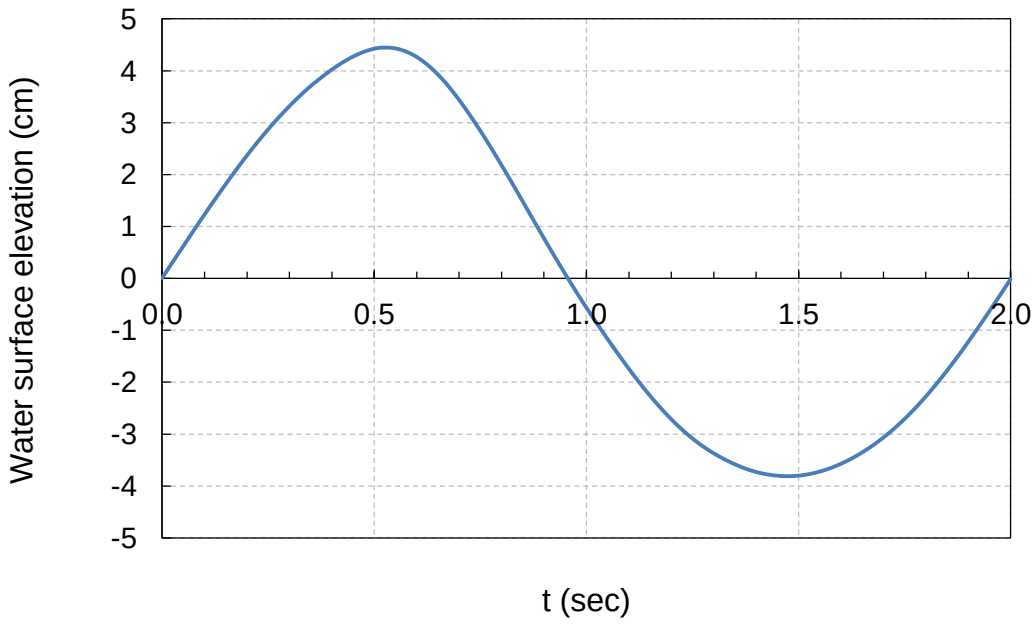

Figure 3.35: Ensemble averaged wave surface profile.

A least square fit to the measured voltage data in Figure 3.32 showed a correlation coefficient of 0.9999 (R^2=1 and 0 refer to a perfect fit and no correlation, respectively).

This correlation could change due to a change in the conductivity of the water caused by a change in the water temperature or contamination of the water. Therefore, calibration tests were carried out each day prior to undertaking any tests. The graph for the test on 4 October 2010 did not coincide with the graphs for other two days. This could be due to the drop of the water temperature to 18^0C from 20^0C on 1 October.

The ensemble-averaged wave surface profile over a wave cycle obtained using the derived calibration coefficients is shown in Figure 3.35.

3.4.3 Pressure transducer data

Similar to the calibration of the wave probe, the output voltage from the pressure transducers was found to follow a linear relationship when plotted against the water depth. Figure 3.36(*a)* shows the transducer locations on a meridian and Figure 3.36*(b)* shows the horizontal angles at which the measurements were carried out. Calibration tests were conducted on each day prior to undertaking the tests to ascertain whether there was any effect due to a change in water temperature etc.,. However, the position of the calibration curve did not change (see Figures 3.37-3.39). In order to convert the voltage output from the pressure sensor into hydrostatic pressure during calibration, $P=\rho gh$ was used.

Figure 3.40 shows the pressure profiles for all channels at vertical angles, φ=-60,-30, 0, 30, 60, 90 degrees at the horizontal angle position, λ=0. The angle, $\lambda=180^0$ refers to the direction of wave propagation.

The pressure was measured at λ=0, 30, 60, 90, 120, 150 and180 degrees on the right hemisphere. In order to ascertain whether the symmetry of forces can be assumed in the calculation of forces on the right hemisphere, one test on both the left and right hemispheres was carried out. The Figures from 3.43 to 3.46 show a comparison of pressure profiles from the transducers on the left and right hemispheres at symmetrical positions.

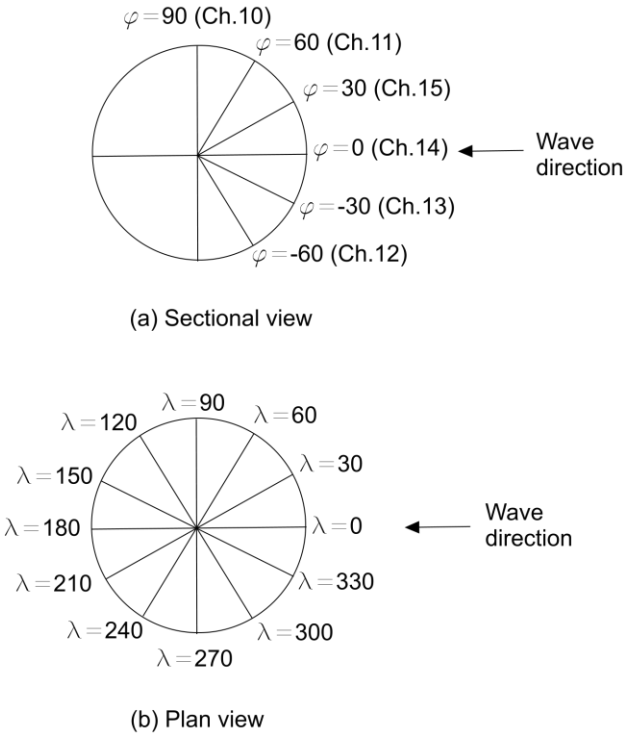

Figure 3.36: Definition sketch of the pressure measuring sphere showing (a) pressure sensor locations on a meridian (b) horizontal angle of the meridian.

Pressure profiles for symmetrical positions on the sphere measured by channel 11 on the top hemisphere (Figures 3.43 and 3.44) and channel 13 on the bottom hemisphere (Figure 3.45) agreed well. Good agreement was also found for the symmetrical positions for channel 14 at the midpoint (Figure 3.46). Therefore, on the basis of the observed symmetry in the pressure data, it was decided that the measurements on the left hemisphere can be assumed to hold true for the right hemisphere also.

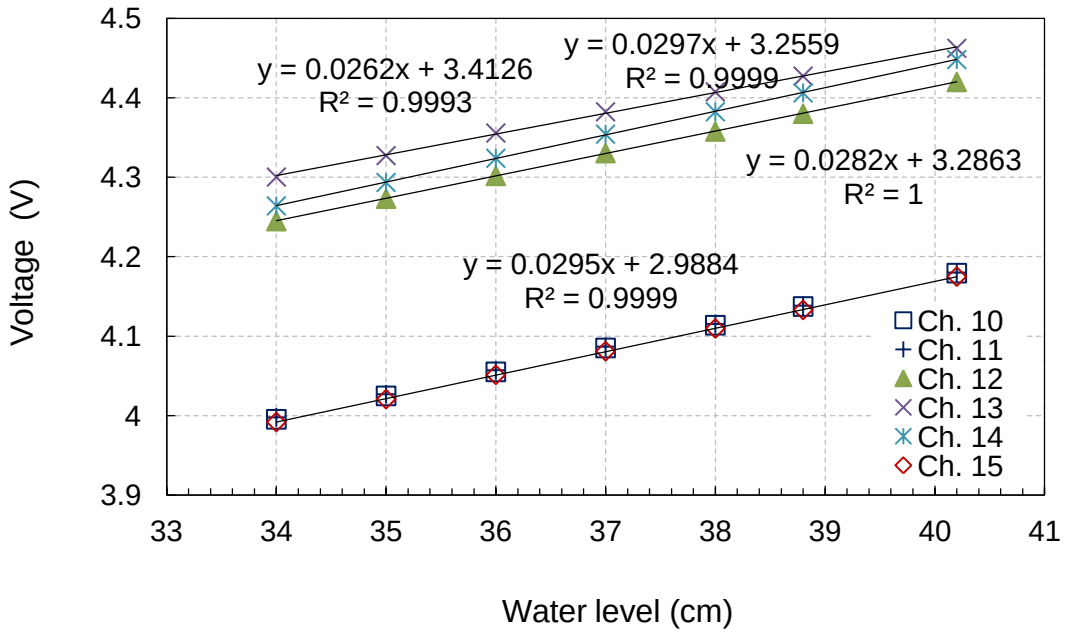

Figure 3.37: Pressure transducer calibration graph for channels 10 to 15. Water temperature, T=20 deg. 01/10/2010.

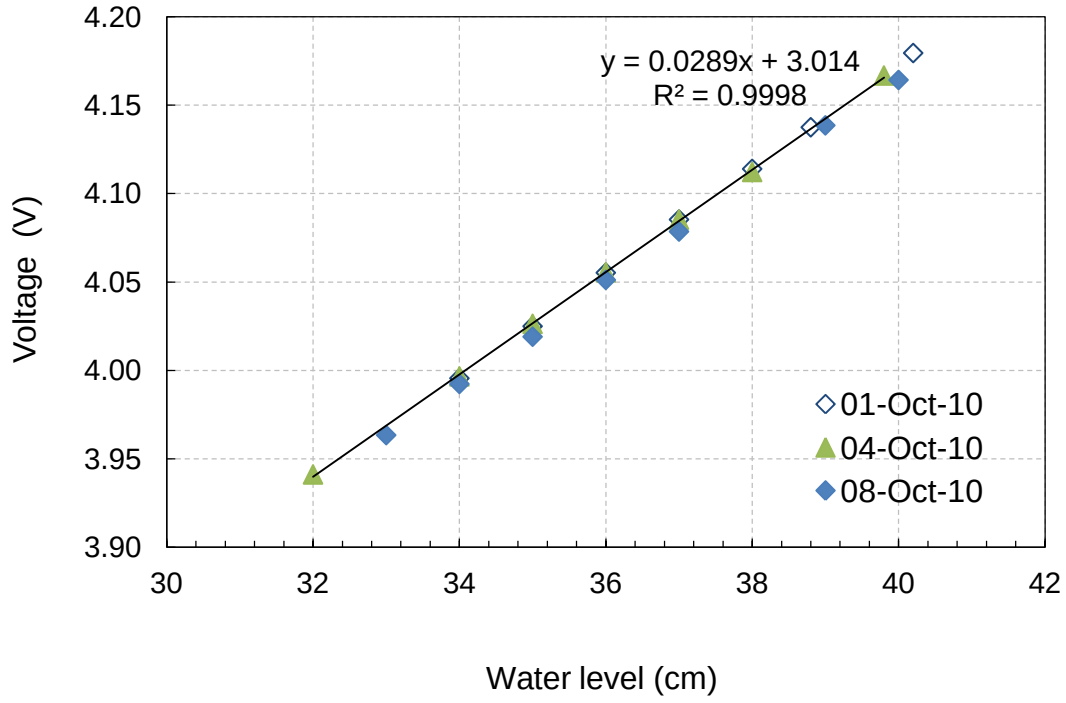

Figure 3.38: Pressure transducer calibration graph for channel 10 on different days.

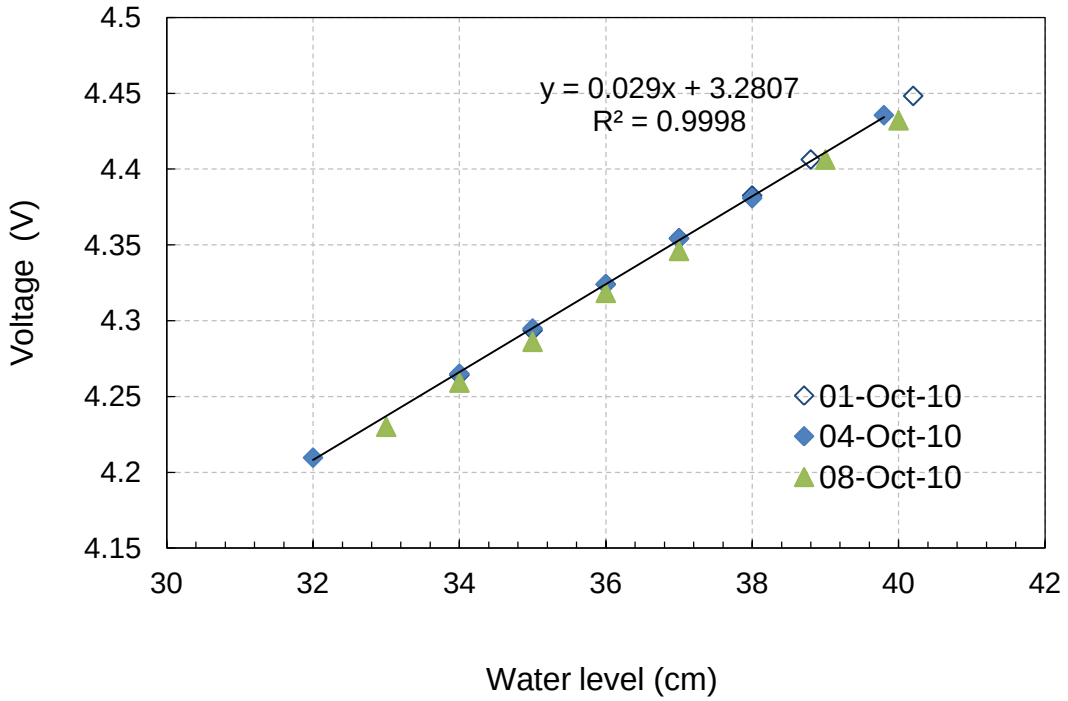

Figure 3.39: Pressure transducer calibration graph for channel 14 on different days.

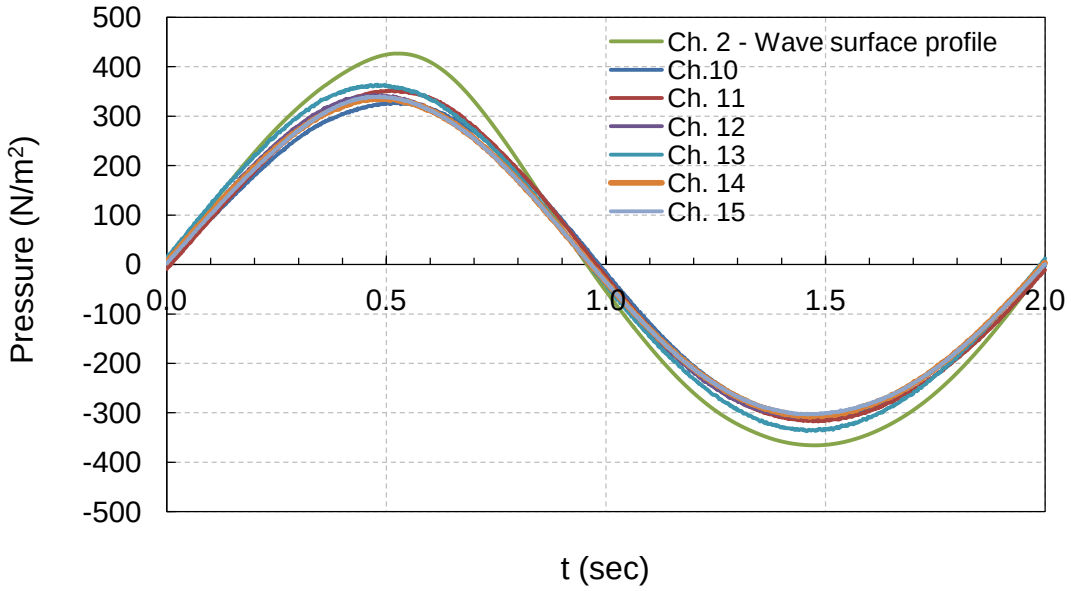

Figure 3.40: Ensemble-averaged pressure variation at the bed level for all channels on a meridian at λ=0 deg.

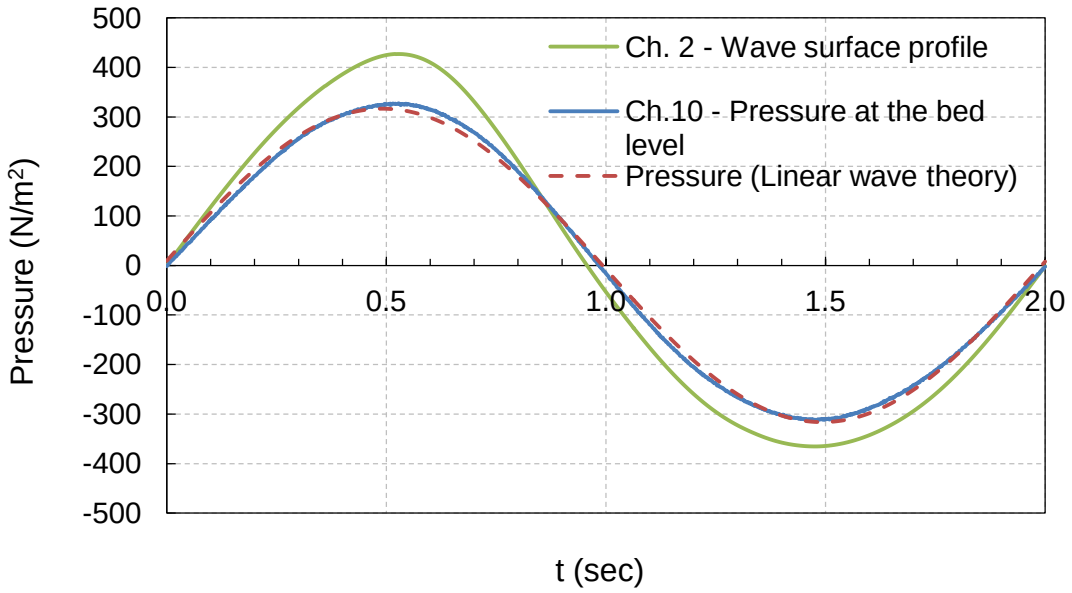

Figure 3.41: Ensemble-averaged pressure variation on a meridian at λ=0 deg.

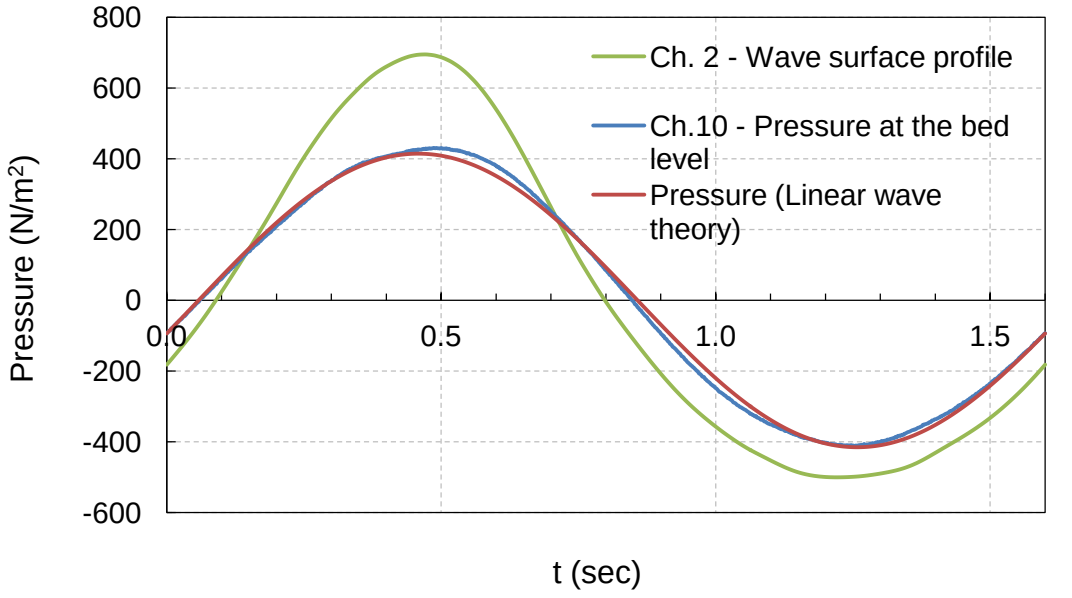

Figure 3.42: Ensemble averaged pressure variation on a meridian at λ=0 deg for channel 10.

Figure 3.41 refers to a generated wave of H=8cm and T=2 sec. The measured pressure profile for channel 10 at the bed level (roughness apex) agreed well with linear wave theory. It is of interest to note that the pressure variation for a steeper wave of H=12cm and T=1.6sec (Figure 3.42) also matched well with linear wave theory at the bed level.

The measured pressure distribution around a 50mm sphere for a fully exposed and coplanar bed conditions under a regular wave of H=8cm and T=2 sec, is shown in Figure 3.47. Readings correspond to ($\lambda=0^0$ and 180^0 at the centre of the sphere). The pressure was normalised by the dynamic pressure amplitude at the bed, $P_0=0.5\rho gH/\cosh(kh)$.

The pressure distribution around a sphere having a finite relative protrusion, i.e., p/d=0.216 is compared with a sphere in a coplanar bed for the same wave condition in Figure 3.48. Origin (0^0) refers to the nose of the sphere at the equator (i.e., $\lambda=0$, $\varphi=0$ as shown in Figure 3.36). As striking feature to note is that the pressure distribution around the sphere with p/d=0.216 behaves in an approximately similar manner to a sphere in a coplanar bed. The pressure distribution is only marginally higher for a stone with p/d=0.216 compared to one in the coplanar bed.

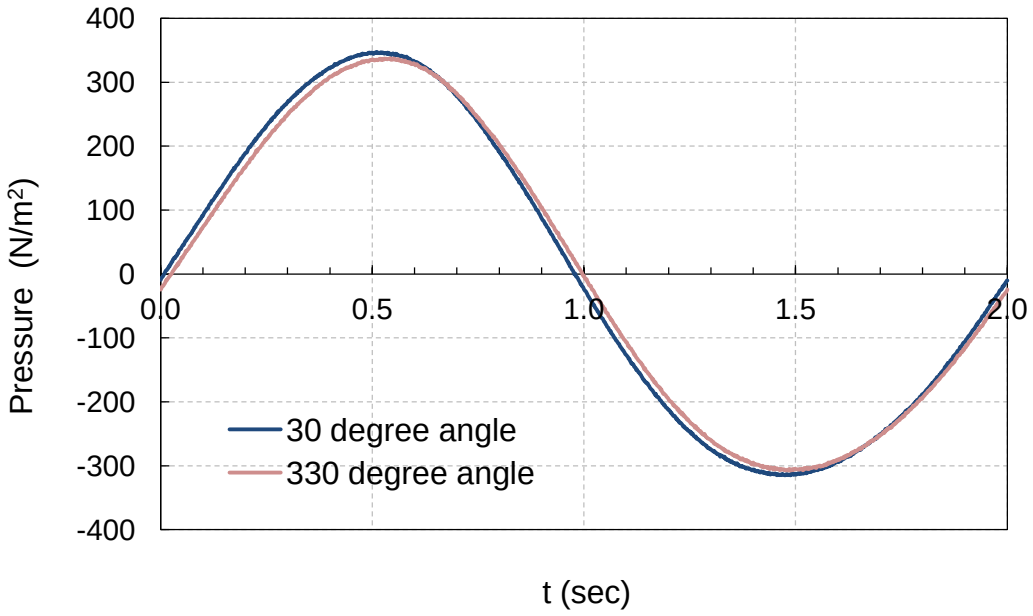

Figure 3.43: Comparison of symmetry in pressure reading for Channel 11.

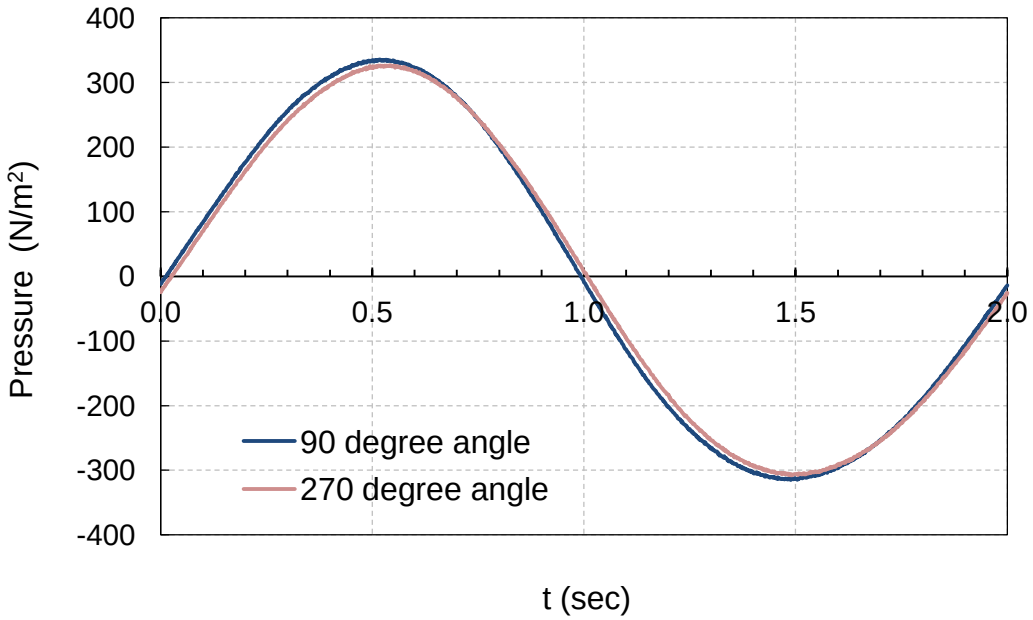

Figure 3.44: Comparison of symmetry in pressure reading for Channel 11.

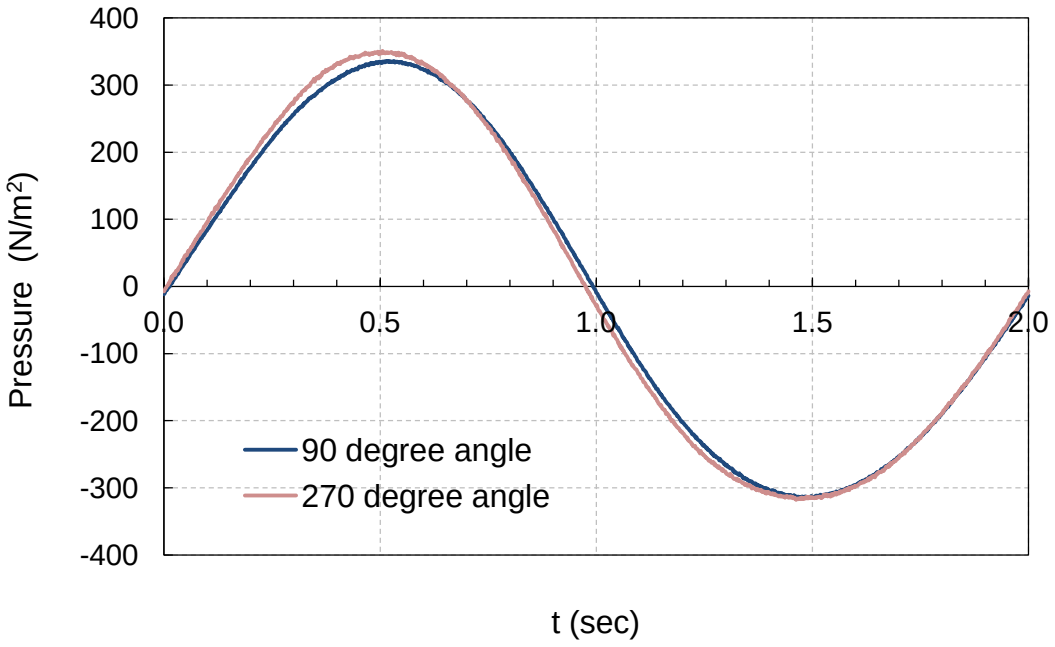

Figure 3.45: Comparison of symmetry in the pressure reading for Channel 13.

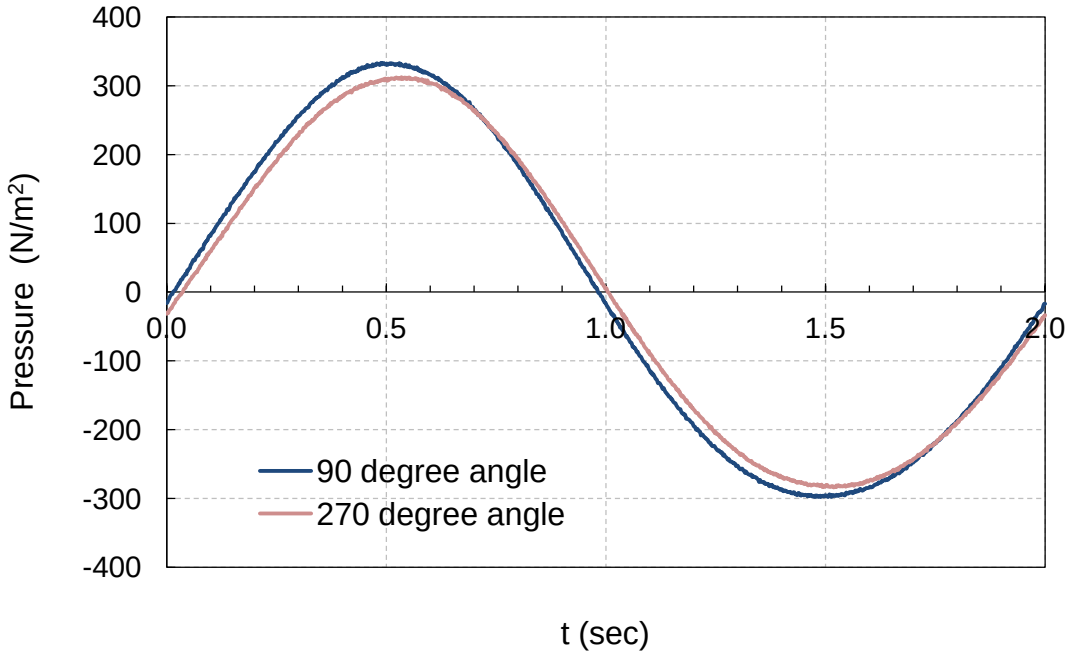

Figure 3.46: Comparison of symmetry in the pressure reading for Channel 14.

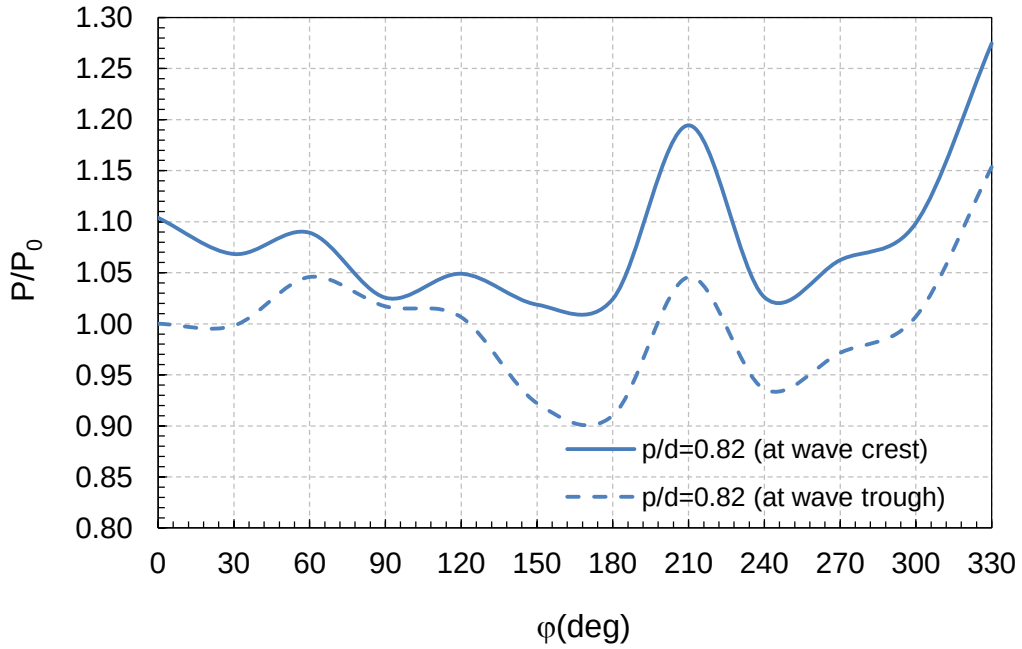

(a)

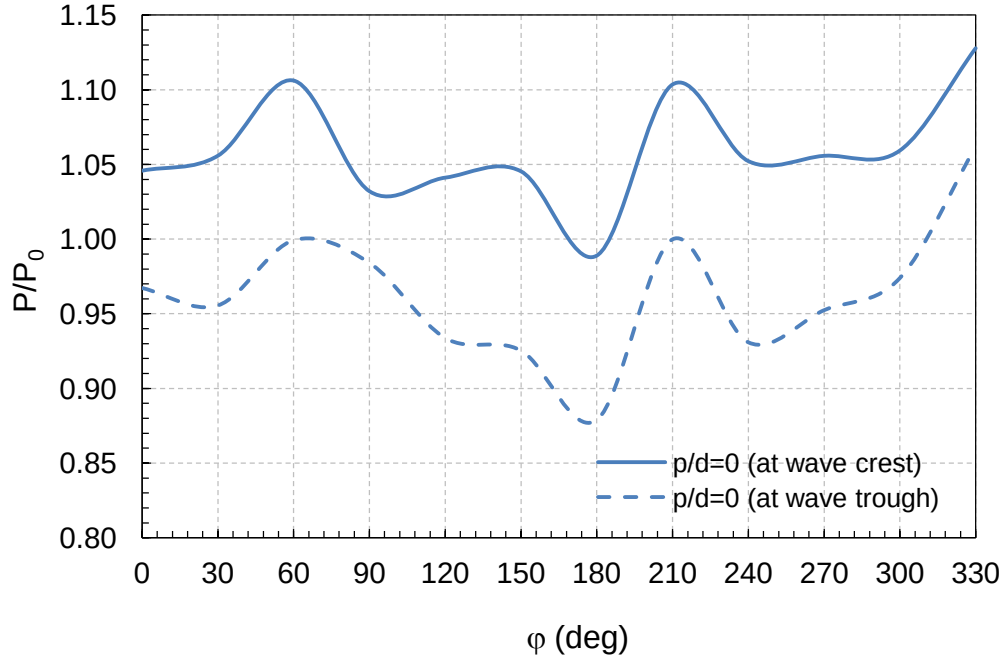

(b)

Figure 3.47: Pressure distribution around a sphere for (a) p/d=0.82 (b) p/d=0.

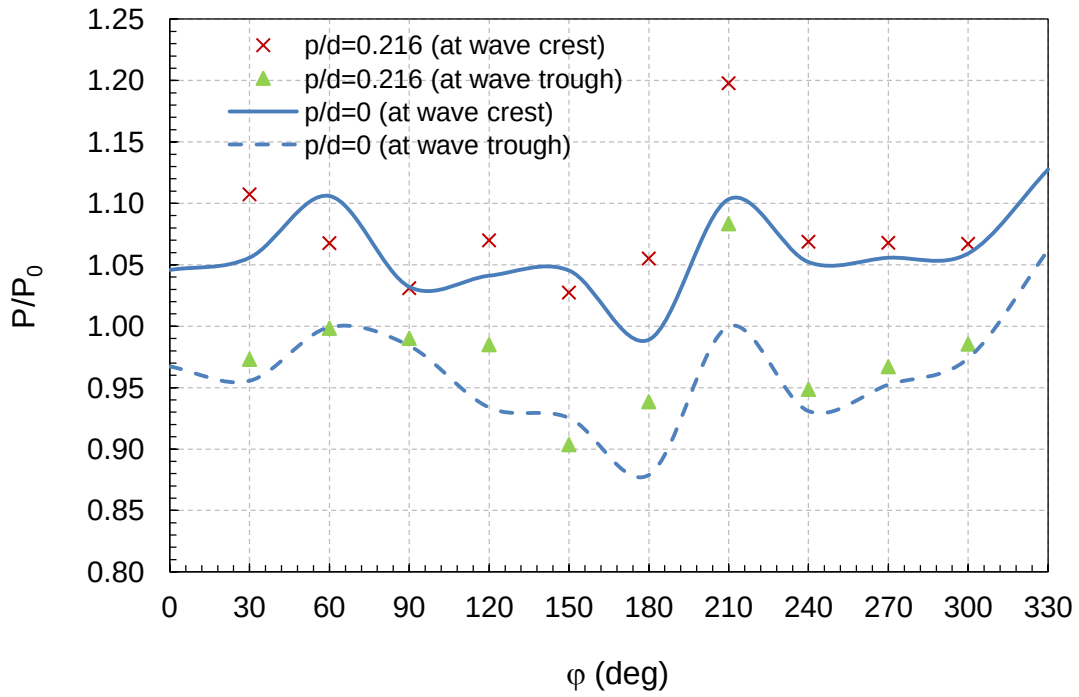

Figure 3.48: Pressure distribution around a sphere in a coplanar bed (p/d=0) and a sphere with finite protrusion, p/d=0.216.

3.4.4 Force integration on a sphere

The force, δF on an elemental area, ΔS was computed.

$$\delta F = \Delta S \frac{1}{4}(P_1 + P_2 + P_3 + P_4) \tag{3.3}$$

The pressure readings at the four corners of the elemental area, P_1, P_2, P_3 and P_4 were averaged to obtain the force on the elemental area.

The surface area of the elemental area

$$\delta(\Delta S) = (r\delta\lambda)(R\delta\varphi) \tag{3.4}$$

$$\Delta S = R^2 \iint \cos\varphi \, d\varphi \, d\lambda \tag{3.5}$$

Which results in the solution:

$$\Delta S = R^2(\sin\varphi_2 - \sin\varphi_1)\,(\lambda_2 - \lambda_1) \tag{3.6}$$

Therefore, the total horizontal (in line) force

$$\mathrm{F_H} = \sum \delta F \cos\bar{\varphi}\ \cos\bar{\lambda} \tag{3.7}$$

The vertical (uplift) force

$$\mathrm{F_V} = \sum \delta F \sin\bar{\varphi} \tag{3.8}$$

Where, $\bar{\varphi} = (\varphi_1 + \varphi_2)/2,\quad \bar{\lambda} = (\lambda_1 + \lambda_2)/2,\ \lambda_i, \varphi_i = n30^0,\ n = 0{,}1{,}2..11$ (i.e. $\lambda_{i+1} - \lambda_i = 30^0$ and $\varphi_{i+1} - \varphi_i = 30^0$).

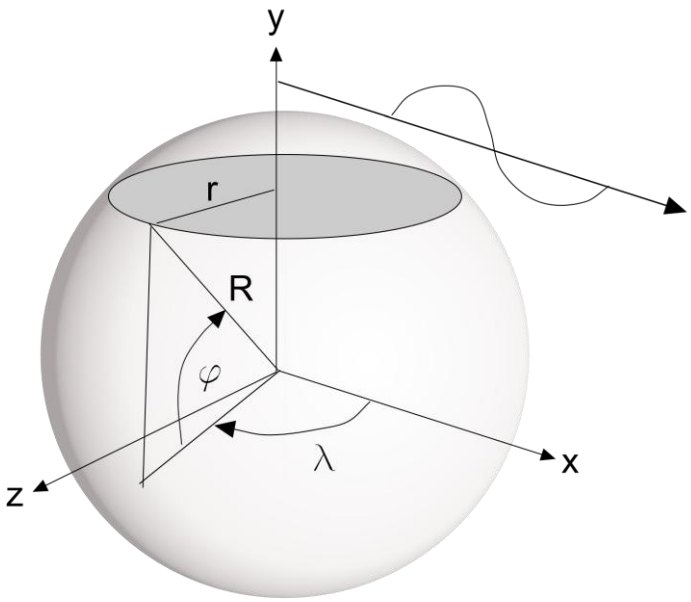

Figure 3.49: Definition sketch of the spherical coordinates.

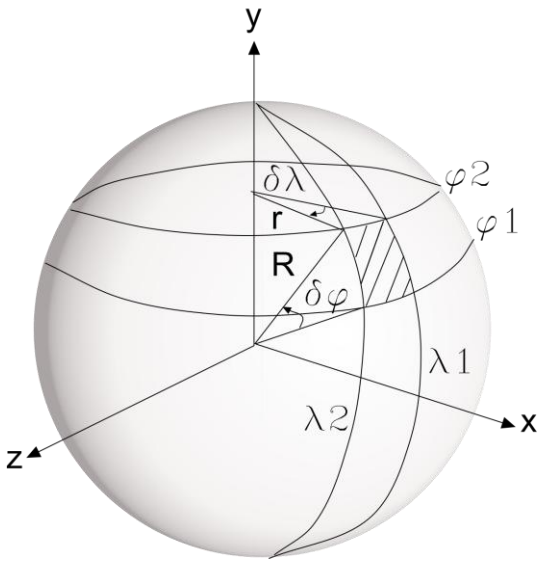

Figure 3.50: Small elemental area (hatched), ΔS, on a sphere.

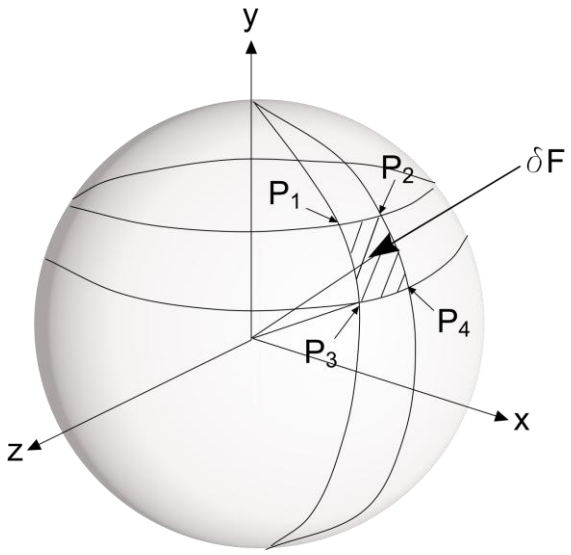

Figure 3.51: Pressure readings on a sphere - P_1, P_2, P_3 and P_4.

3.4.5 Velocity data

LDV data sampled at 100Hz were ensemble-averaged following the procedure stated in Section 3.4.1. The measured velocity data for a point

1mm above the bed is shown in Figure 3.52. The wave height, period and water depth were 8cm, 2 seconds and 40cm, respectively.

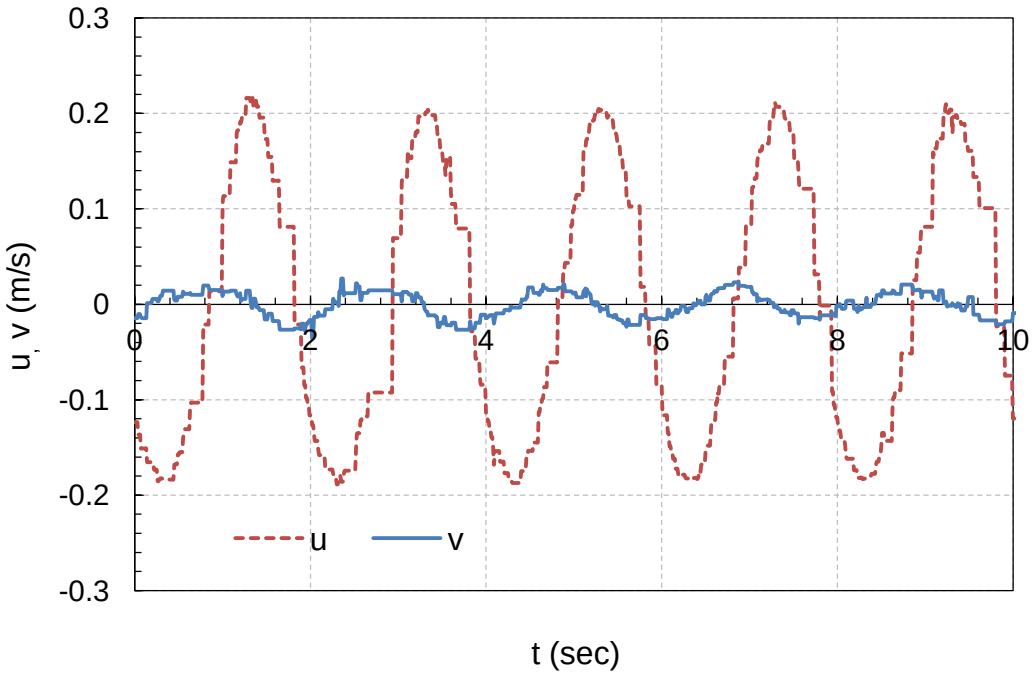

Figure 3.52: A typical set of velocity data.

3.4.6 Incipient motion data

Data on the incipient motion consisted of the size and specific gravity of the spherical particle, wave height, period and water depth at the time of the initiation of motion. The peak orbital velocity amplitude at the bed, U_m was calculated using linear wave theory. The critical shear stress was found using the relationship, $\tau_{cr}=0.5f_w\rho U_m^2$.

3.4.7 V3V Image processing

Raw images from the 3D camera probe, total six images, were analysed using Insight 3V3 software. That is two images each from the three image sensors corresponding to time, t=t (Frame A) and t=t+Δt (Frame B).

The V3V camera probe has a large depth of field which makes the images look identical to typical PIV images. However, the images record particles in a large cubic volume in contrast to a thin planar sheet. The objective of image processing is to obtain 3D positions of the particles from raw images captured by the calibrated system. The data processing consisted of four steps: (1) 2D Particle Identification (2) 3D Particle Identification (Triplet Search) (3) 3D Particle tracking and (4) Grid Interpolation (Pothos *et al.*, 2009).

3.4.7.1 2D particle identification

Firstly, 2D particles in the images were identified. This was done by setting two parameters in the software. The first is a baseline intensity threshold. It was assumed that any valid particle would have a peak intensity above this threshold. This narrowed down the search area to include valid particles and thus eliminating background noise. The second parameter defined the local particle peak intensity relative to local background intensity. Lastly, a Gaussian intensity profile was fitted, the peak of which represents the centre of the particle.

3.4.7.2 3D particle identification (triplet search)

Images from each of the apertures were combined to determine the location of each particle in 3D space. Each ‘triplet’ represents a single particle in the flow. *x,y* location of the particle is represented by the centroid of the triangle and the depth (*z*) is represented by the size of the triangle via the calibration data (see Figures 3.26 and 3.27).

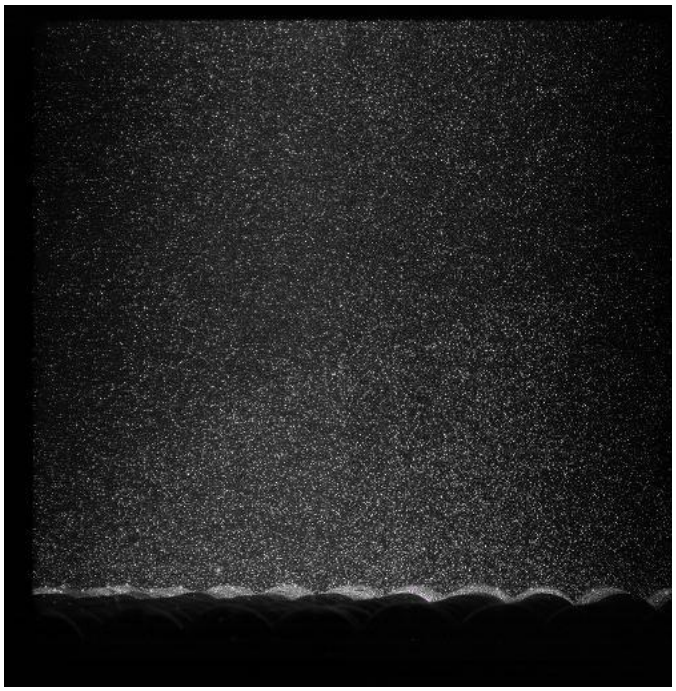

Figure 3.53: Raw data (illuminated tracer particles) from the present V3V tests.

3.4.7.3 3D particle tracking

The third stage of data processing involved searching for particle pairs in two successive images to obtain 3D velocity vectors. In the previous stages the particle positions were identified. Three algorithms are available for 3D particle tracking: the nearest neighbour method, the relaxation method, and

the particle matching method. Pothos *et al*. (2009) and Lai *et al*. (2008) observed that the relaxation method proposed by (Pereira *et al.*, 2006) is the most robust and efficient. Therefore, the relaxation method was used in the present analysis.

The particle matching procedure is described in Pothos *et al*. (2009) in more detail. Once the volumetric particle locations were determined in frame A (at t=t) and frame B (at $t=t+\Delta t$), the particles were divided into subgroups called clusters according to their spatial locations. Clusters here can be thought of as similar to interrogation regions in PIV. Clusters in B are larger in volume than corresponding clusters in A because particles may move out of the cluster area. Within a cluster, each pair of corresponding particles is assigned a number representing match probabilities. For example, P(m,n) is the match probability between particle m in frame A and particle n in frame B. Initially each particle pair has the same probability, 1/N, where N is the number of possible pairs between A and B for each cluster. The probability computation is based on the assumption that neighbouring particles move similarly. These probabilities are then iteratively recomputed for all particles in the cluster, until they converge. For particle m in frame A, the maximum match probability P(m,n) is found among P(m,1), P(m,2), …If this maximum probability is greater than a given threshold, then (m,n) is considered a matched pair.

Figure 3.54 shows a sketch demonstrating the matching procedure as described in Pothos *et al*. (2009). As shown in the schematised volume to the left, the probability is high when, if the displacement from particle m to

particle n is applied to the other particles in the cluster, a matching particle is nearby. The probability is low when the displacement of other particles in the cluster results in no nearby particle matches as shown in the volume to the right.

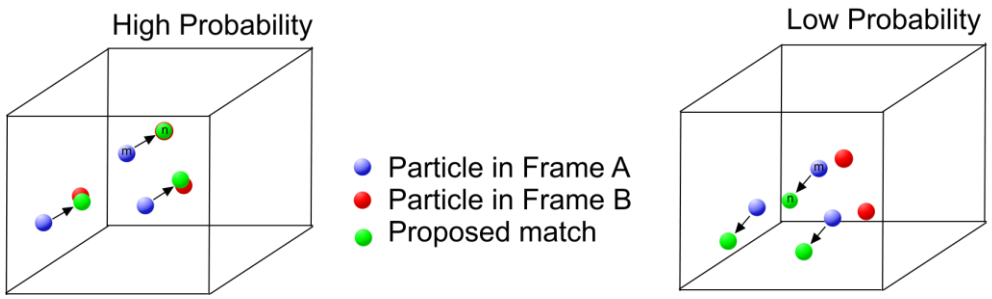

*Figure 3.54: Illustration of 3D particle matching procedure between two successive camera frames (*Pothos *et al*., 2009).

3.4.7.4 Grid interpolation

The final stage of the image processing exercise involved grid interpolation. After the 3D particle tracking step, the vectors are located randomly according to particle locations. It is beneficial to have vectors on a rectangular grid in order to compute the flow quantities such as vorticity. Therefore, this was carried out through interpolation using a Gaussian-weighted method. The vectors from an interpolated grid from the present experiments and are shown in Figure 3.55.

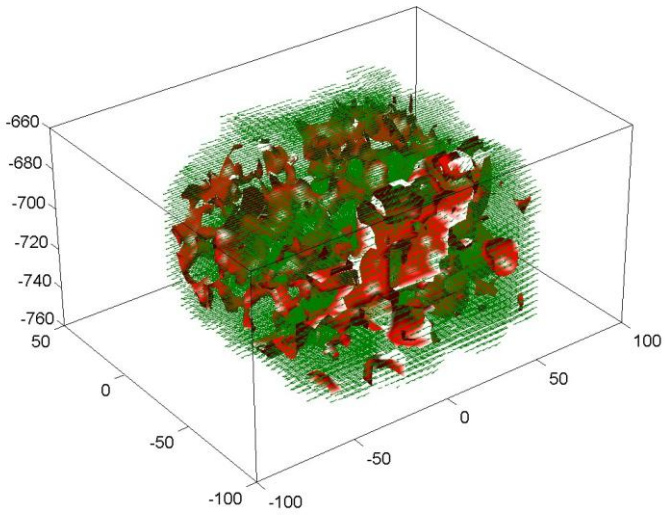

Figure 3.55: Vectors (green) in an interpolated grid from the present tests.

3.4.8 Analysis of photographic images

Photographs of the model bed protection consisting of natural rocks (crushed anthracite) were analysed to find the number of rocks moved during the 30 minute wave test run time. The photographs were used to count the displaced rocks based on visual observation. The displaced rock positions are painted white in Figure 3.56 below for easy identification during counting.

A camcorder was used to video the incipient motion of the spherical particles. A scale glued to the side of the flume in line with the test stone was used to find the phase of the threshold of movement. A frame from a video clip corresponding to the incipient movement is shown in Figure 6.15.

Figure 3.56: Damage to a model bed protection – rock count.

3.4.9 Laboratory model scale effects

Achieving complete hydraulic similitude where all the force ratios are constant and equal is impossible except at prototype scale. Two important criteria used to measure hydraulic similitude are Froude ($U/\sqrt{gL}$) and Reynolds (UL/ν) scaling.

Here, the field example mentioned in Section 2.2, i.e., a wave of H=10m, T=10 sec in a water depth of h=30m, is compared with the physical model. The rock size was d_n=0.44m. Here, the Froude number is defined as $Fr = U_m/\sqrt{gh}$ and Reynolds number, given as $Re = aU_m/\nu$. The Froude time-scale based on the wave dispersion relationship is given as $N_T = \sqrt{N_L}$ (Hughes, 1993) where; the time-scale is $N_T = t_p/t_m$; and the length scale is $N_L = L_p/L_m$.

For the prototype case, the relative depth parameter, h/gT^2=0.031, and hence, the waves are classed as being in the intermediate depth (Le Mehaute, 1976). The model tests were carried out in the range, h/gT^2=0.01-0.04 which also falls into the intermediate water depth range.

The vertical scale, $N_{Ly}=h_p/h_m$=30m/0.4m=75. As the horizontal orbital amplitude at the bed is a function of both H and h, it was used to find the horizontal model scale $N_{Lx}=a_p/a_m$=2719mm/55mm=49.4.

The time scale of the waves is $N_T=T_p/T_m$=10/2=5. The time-scale satisfying the Froude criteria is $N_T = \sqrt{N_L}$=$\sqrt{N_{Lx}}$ =7.03. As the model time-scale and the Froude time-scale are equal approximately this is consistent. As shown in Tables 3.1 and 3.2, the Froude number for the prototype is approximately equal to that of the model. Therefore, it can be concluded that the model satisfies the Froude similarity criterion for a typical prototype example.

However, the Reynolds number similarity has not been achieved. The model flow Reynolds number, $Re=U_m a/\nu$, is much smaller than that of the prototype which could induce viscous effects if the flow is in the laminar region.

The roughness Reynolds number in the model, $u_* k_s/\nu \cong 2700$. This should be ≥ 200 for rough turbulent flow when $a/k_s \leq 100$. For a relative roughness of the O(1) in the present tests, rough turbulent flow occurs at $Re=aU_m/\nu > 1.0 \times 10^3$ (Kamphuis, 1975). In the model $Re \cong 8200$.

The stone Reynolds number $Re_d=U_m d/\nu$ is 2850. Transition to turbulence from laminar flow occurs somewhere around Re=2000 for an individual

stone (Schlichting, 1968; Davidson, 2004). Therefore, the flow is outside the laminar region and hence, the viscous effects would not be critical.

Table 3.1: Example prototype parameters.

H	T (sec)	h(m)	U_m (m/s)	a (mm)	Fr	Re	$u_* k_s/\nu$	Re_d
10	10	30	1.7	2710	0.1	4.65×10^6	4.6×10^5	6.6×10^5

Table 3.2: Laboratory model parameters.

H	T (sec)	h(m)	U_m (m/s)	a (mm)	Fr	Re	$u_* k_s/\nu$	Re_d
8	2	0.4	0.17	55	0.086	8200	2700	2850

4 Wave-induced forces on a single stone

4.1 Introduction

In this chapter the effect of stone protrusion on wave-induced horizontal (in-line) and vertical (uplift) forces on a 50mm spherical test stone is investigated. Tests were carried out for three different protrusion levels of the stone, i.e. p/d=0 (coplanar bed), 0.216 and 0.82 (fully exposed). The pressure on the surface of the sphere was measured using transducers connected to tappings on the sphere surface. The pressure was then integrated over the full surface of the sphere calculating the force on a small elemental surface area formed by 30 degree horizontal and vertical angles to obtain the net in-line and uplift forces.

Table 4.1: Pressure measurement on a stone - test conditions.

Test no.	H (cm)	T(s)	h(cm)	U_m (m/s)***	KC
PM3	8	1.6	40	0.16	5.2
PM4	10	1.6	40	0.20	6.4
PM5	12	1.6	40	0.23	7.4
PM6	5	2	40	0.11	4.4
PM7	8	2	40	0.17	6.8
PM8	10	2	40	0.21	8.4
PM9	12	2	40	0.26	10.4

Note: *** Derived from linear wave theory.

The measured forces are normalised by the dynamic wave pressure amplitude at the bed. Chakrabarti (1973) analytically determined the forces on small objects one order of magnitude smaller than the wave length using

linear wave theory. The present experimental research follows a similar approach.

4.2 Wave-induced forces

4.2.1 Fully exposed sphere

Figure 4.1 shows the measured horizontal and uplift forces on a fully exposed sphere. The force was normalised by P_0A_p, where P_0 is the amplitude of the dynamic wave pressure at the bed given by linear theory and A_p is projected frontal area of the sphere.

$$P_{wd} = P_0 \cos(kx - \omega t) \tag{4.1}$$

$$P_0(y) = \frac{1}{2}\rho g H \frac{\cos k(y+h)}{\cosh(kh)} \tag{4.2}$$

At the bed level dynamic pressure amplitude is

$$P_0(y=-h) = \frac{1}{2}\frac{\rho g H}{\cosh(kh)} \tag{4.3}$$

Figures 4.1 and 4.2 refer to the forces on a fully exposed (relative protrusion, p/d=0.82) 50mm sphere resting on a coplanar bed of similar spheres in a hexagonal, bed arrangement. Figure 4.1 shows the time variation of the forces induced by H=8cm, T=2 sec waves ensemble-averaged over 50 cycles.

The maximum horizontal force, $F_{H\text{-}max}$, and maximum positive uplift force ($F_{L\text{-}max+}$) correlate well with the dynamic wave pressure amplitude, P_0. Particularly, the vertical force has a near perfect agreement (Figure 4.2).

$$F_{H-max} = C_H P_0 A_{px} \tag{4.4}$$

$$F_{L-max+} = C_v P_0 A_{py} \tag{4.5}$$

It should be noted that C_H and C_V are not coefficients in Morison's equation. A_{px} and A_{py} are the projected frontal areas in the x,y directions, which were assumed approximately as $\pi d^2/4$ for a fully exposed sphere.

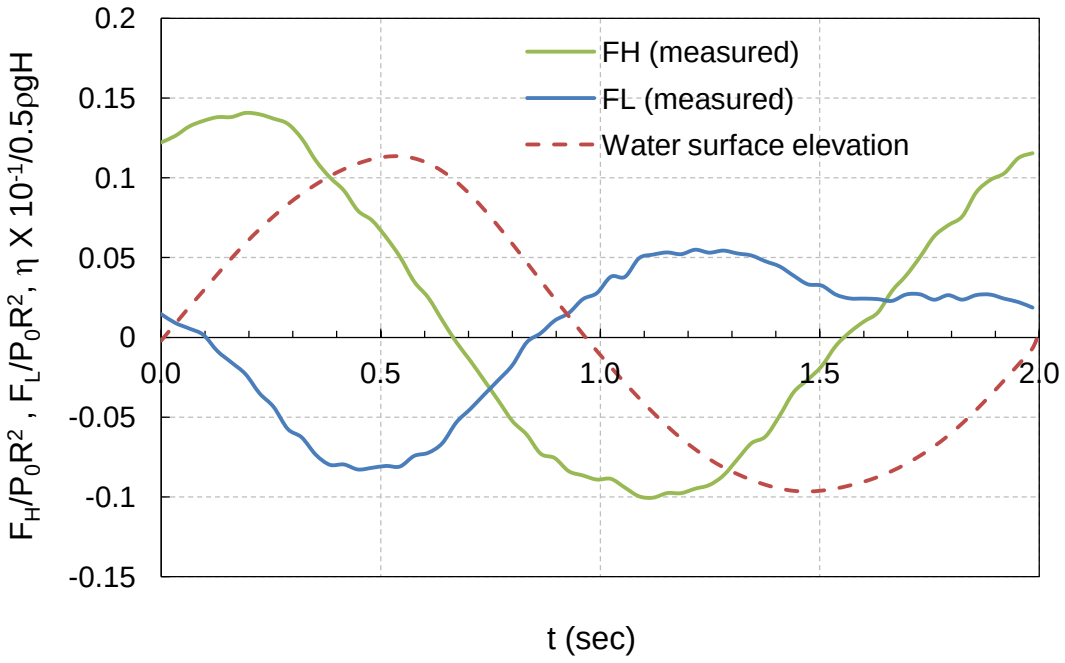

Figure 4.1: Measured horizontal force (F_H) and uplift force (F_L) variation on a fully exposed (p/d=0.82) 50mm sphere.

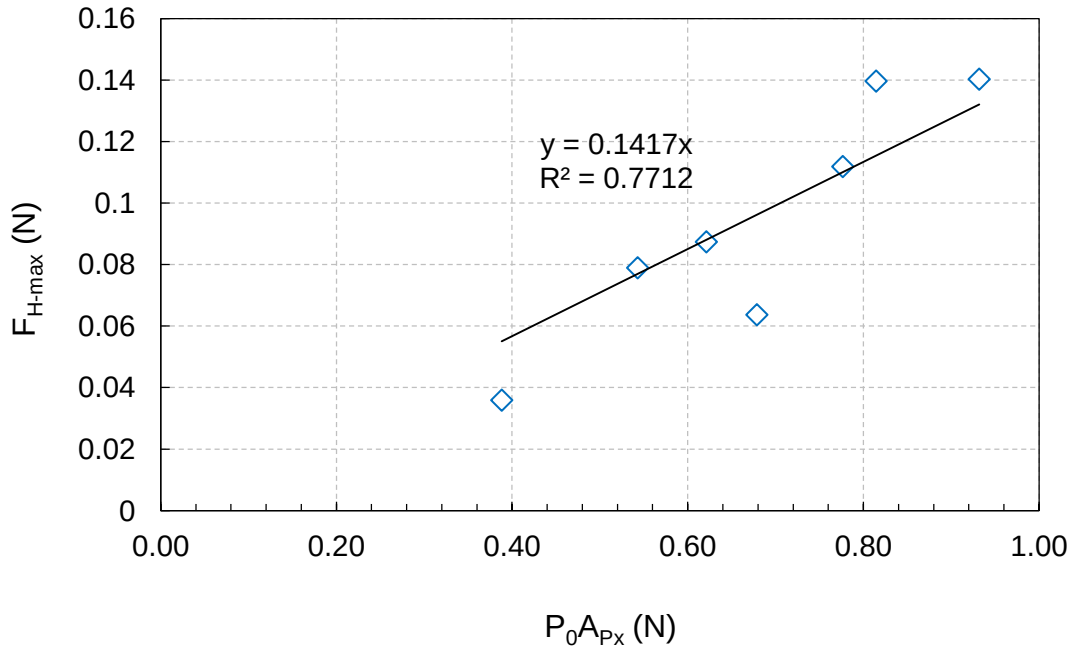

(a)

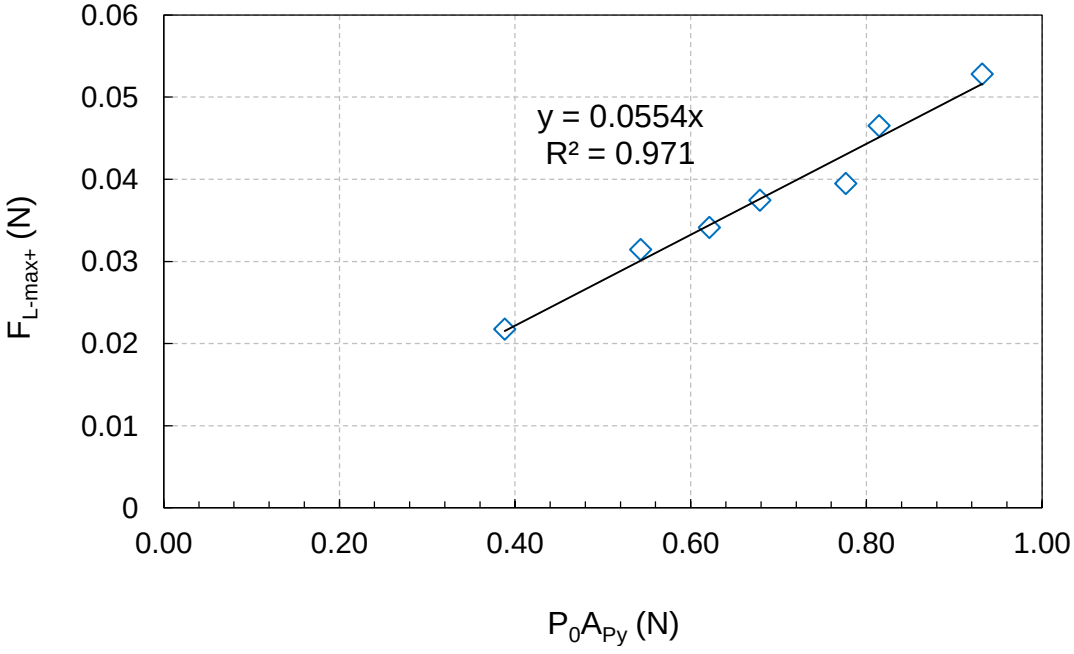

(b)

Figure 4.2: Measured (a) Maximum horizontal force ($F_{H\text{-}max}$) and (b) maximum positive uplift ($F_{L\text{-}max+}$) on a fully exposed sphere.

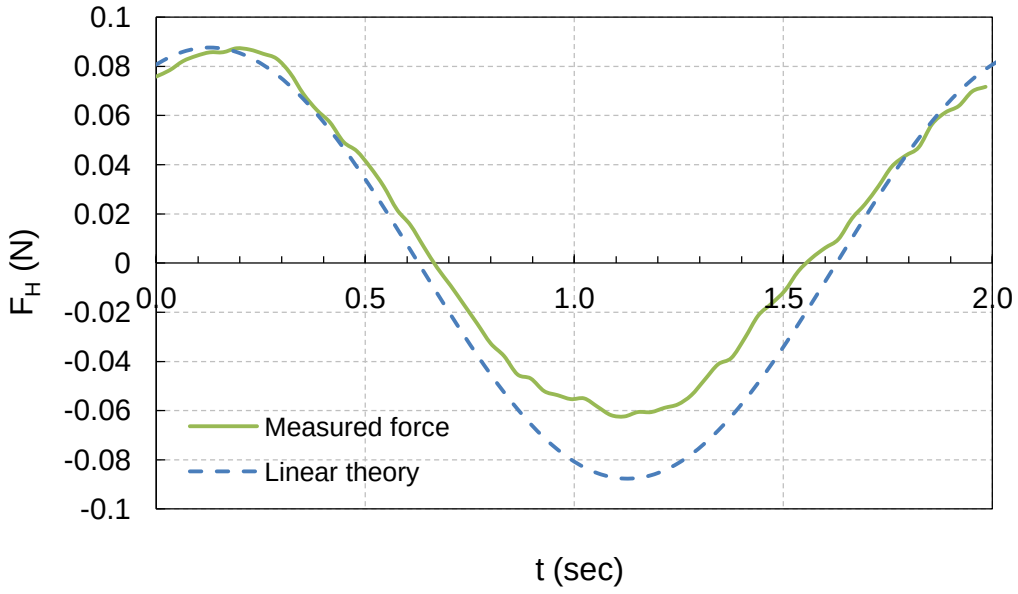

(a)

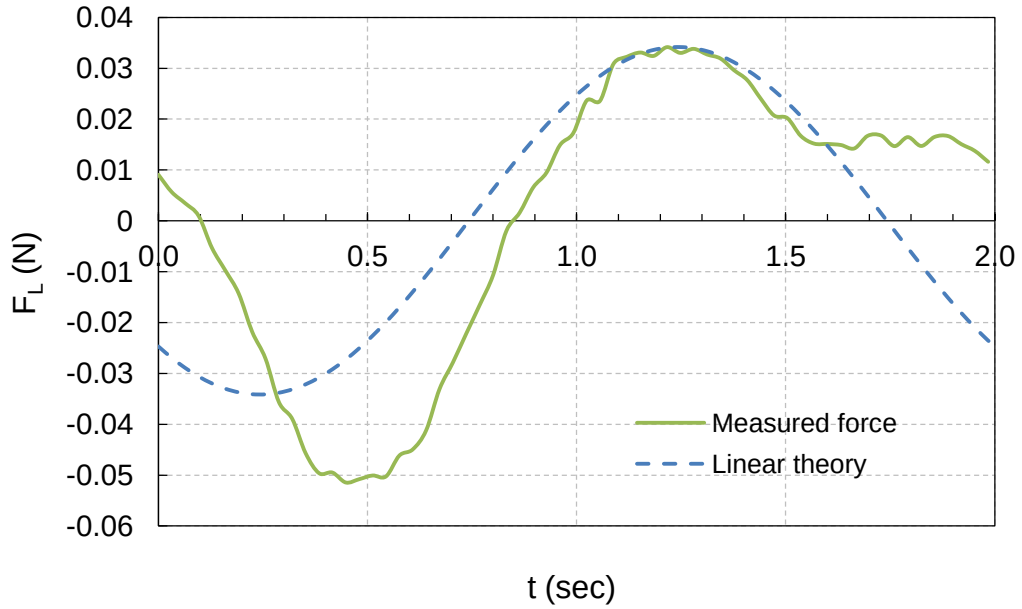

(b)

Figure 4.3: Measured (a) horizontal and (b) vertical force variation compared with linear theory, i.e. $F=CP_0A_p\cos(\omega t)$.

The semi-empirical relationships in equations (4.4) and (4.5) obtained for the peak horizontal and vertical forces were plotted in Figures 4.3 assuming a cosine variation. It was observed that, even though the time variation is not represented accurately, the magnitude of the maximum horizontal force amplitude ($F_{H\text{-}max}$) and the maximum positive uplift force amplitude ($F_{L\text{-}max+}$) can be modelled reasonably well with these equations for a fully exposed sphere. In terms of the forces on a stone, it is the peak value that is important for engineering design.

It was also observed that the maximum positive uplift force ($F_{L\text{-}max+}$) on a sphere resting on the bed is about 40% that of the maximum horizontal force, $F_{H\text{-}max}$ (Figure 4.1).

4.2.2 Sphere on a coplanar bed

The force coefficients, C_H and C_V were calculated for a sphere in a coplanar bed using best fit to the measured data (Figure 4.4). The projected frontal area, A_{px} for the calculation of horizontal force, was assumed to be that part of the sphere above the theoretical bed level perpendicular to the flow direction (i.e. $A_{px}=6.13 \times 10^{-4}$ m^2). In calculating the vertical force, $A_{py}=\pi d^2/4$ was assumed.

The fit of the equation $F=CP_0A_p\cos(\omega t)$ to the measured data over a wave cycle is shown in Figure 4.5. Linear wave theory over predicted the measured maximum horizontal force by 19% whilst the maximum positive uplift force was under predicted by 35.4%. Therefore, for a stone on a

coplanar bed the error in the prediction of the horizontal and vertical forces is larger than for a fully exposed stone (compare Figures 4.3 and 4.5).

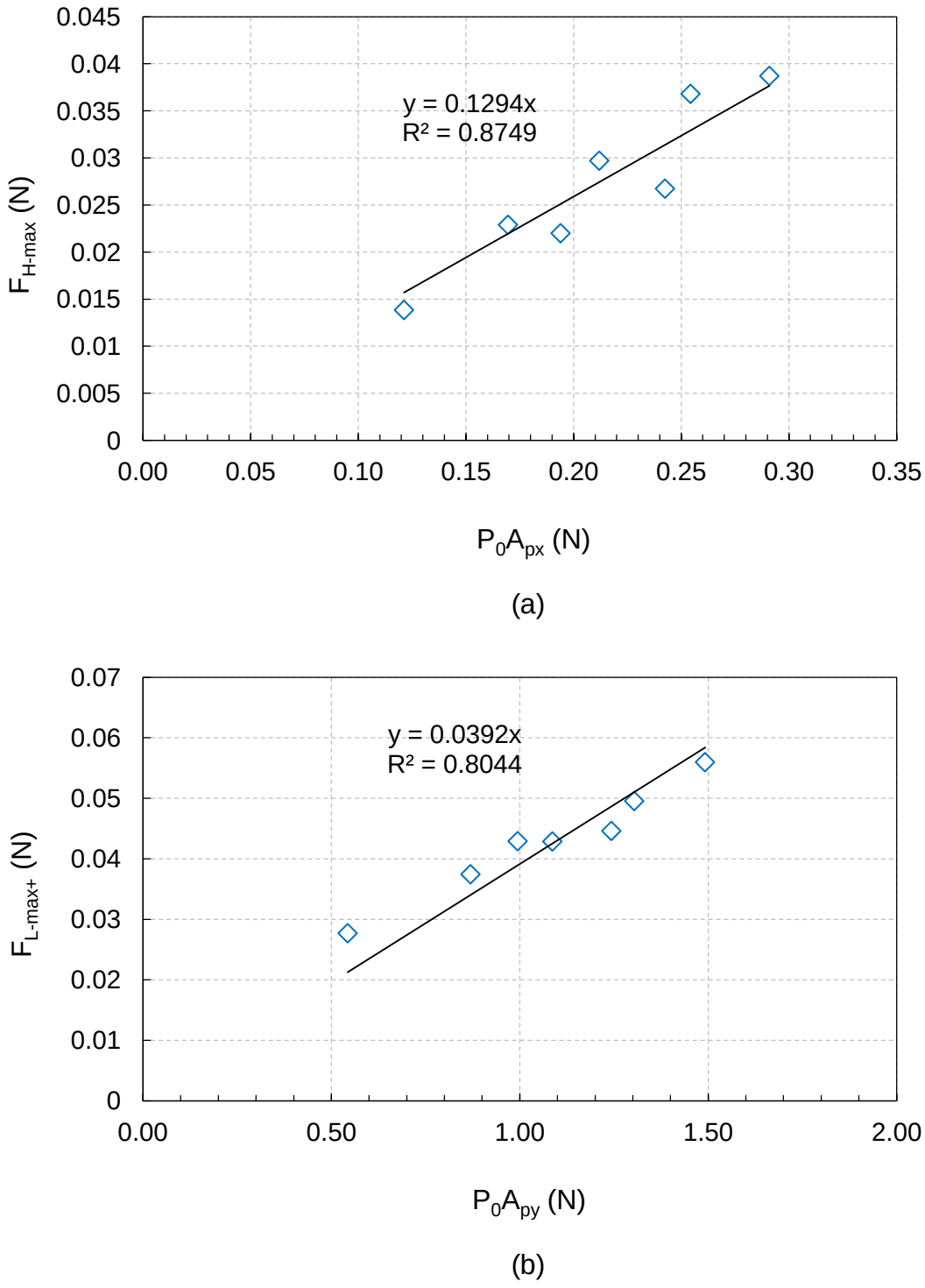

Figure 4.4: Measured (a) Maximum horizontal force ($F_{H\text{-}max}$) and (b) maximum positive uplift ($F_{L\text{-}max+}$) on a 50mm spherical element in a coplanar bed.

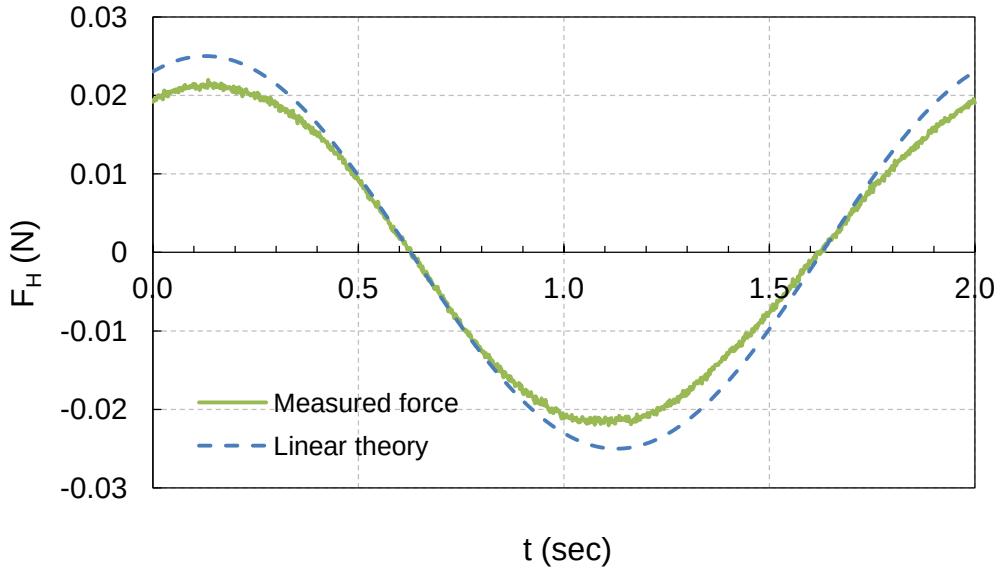

(a)

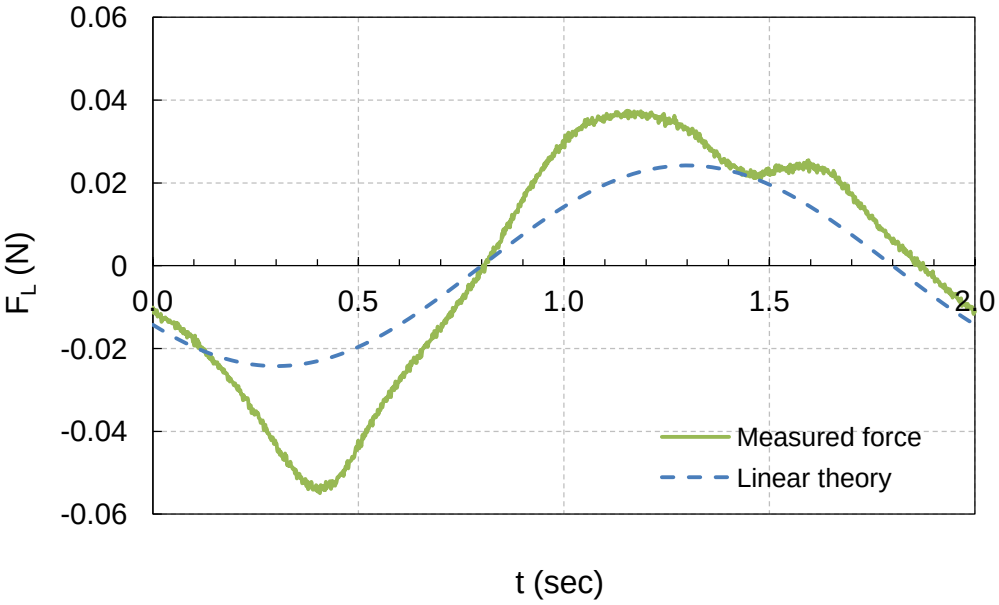

(b)

Figure 4.5: Measured (a) horizontal and (b) vertical force variation on a spherical stone in a coplanar bed (p/d=0) compared with linear theory, i.e. $F=CP_0A_p\,\mathrm{Cos}(\omega t)$.

4.2.3 Summary of force coefficients

Table 4.2 summarises the values obtained for the force coefficients C_H and C_V in the equation, $F=C\ 0.5\rho g H A_p/\cosh(kh)$. For both cases of relative protrusion, the coefficients appear to be relatively constant within the tested KC number range from 4.4 to 10.4. C_H varied between 0.09-0.17 and C_V varied between 0.05-0.057 for a fully exposed sphere.

It would be interesting to investigate these coefficients further for higher KC number flows as force coefficients insensitive to variation in KC number would be favoured over Morison's force coefficients which are a function of many variables such as type of flow, flow regime, stone position, surface roughness etc.

Table 4.2: Summary of the force transfer coefficients deduced from linear wave theory.

p/d	C_H	C_V
0.82 (fully exposed)	0.141	0.055
0 (coplanar bed)	0.129	0.039

4.3 Morison's force coefficients

4.3.1 Fully exposed sphere

The measured forces in tests P3 to P9 (Table 4.1) were fitted to the drag, $0.5\rho A_p U_m^2$ and inertia, $\rho V(dU/dt)$ terms of Morison's equation, where A_{px} and A_{py} are the projected frontal area in the x and y directions and V_x and V_y are the displaced volumes of the stone in the x,y directions. For a fully exposed sphere, A_{px}, $A_{py}=\pi d^2/4$ and $V_x=V_y=\pi d^3/6$ were assumed.

For the maximum horizontal force, a reasonably good fit of the data was obtained for the drag term with a correlation coefficient of 0.79. The data fit to the inertia term is slightly less with a correlation coefficient of 0.64 (Figure 4.7). Interestingly, a better fit of the data was obtained for the quasi-steady uplift force (Figure 4.8).

In these tests the data fell within KC = 4.4 and 10.4. Based on previous publications (Sarpkaya & Issaacson, 1981; Iwata & Mizutani, 1989), the inertia term dominates over the form drag when KC<10. When Morison's drag (C_D) and inertia (C_M) coefficients, obtained by dividing the maximum in-line force by $0.5\rho A_{px}U_m^2$ and $\rho V(du/dt)$ terms, were plotted against the KC number (Figures 4.9), a better fit was obtained for the inertia term than for the drag term indicating the relative importance of inertia within this range.

In Figure 4.1, the maximum horizontal force occurred on average 30 degrees after the maximum horizontal acceleration/deceleration. This indicates the dominance of inertia over drag. However, the quasi-steady uplift force appears to be less affected by inertia.

Morison's force coefficients are sensitive to wave theories used for the calculation of forces. In this study linear wave theory was used to obtain the bottom particle velocity. Figure 4.6 shows the bottom horizontal particle velocity obtained from linear wave theory compared with measured data at a point 100mm above the bed level (i.e. two stone diameters above). The velocity obtained from linear wave theory, U_m, under predicted the measured peak velocity by approximately 13% in Figure 4.6(a). For a slightly steeper wave in Figure 4.6(b) this error is 8.5%. Whilst the prediction error can be

reduced if a higher order wave theory is used, it was decided that for the purpose of this study, this accuracy would be sufficient.

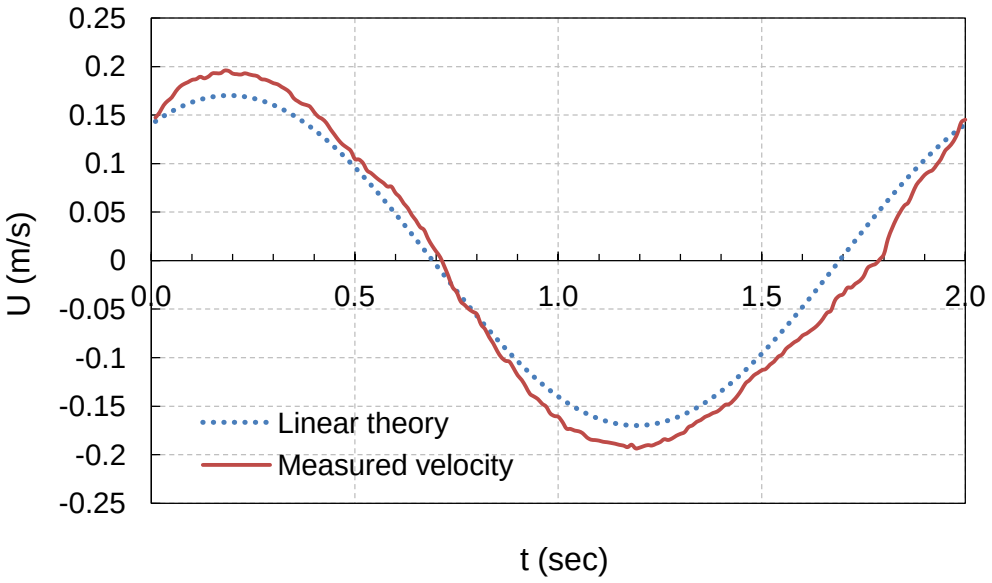

(a)

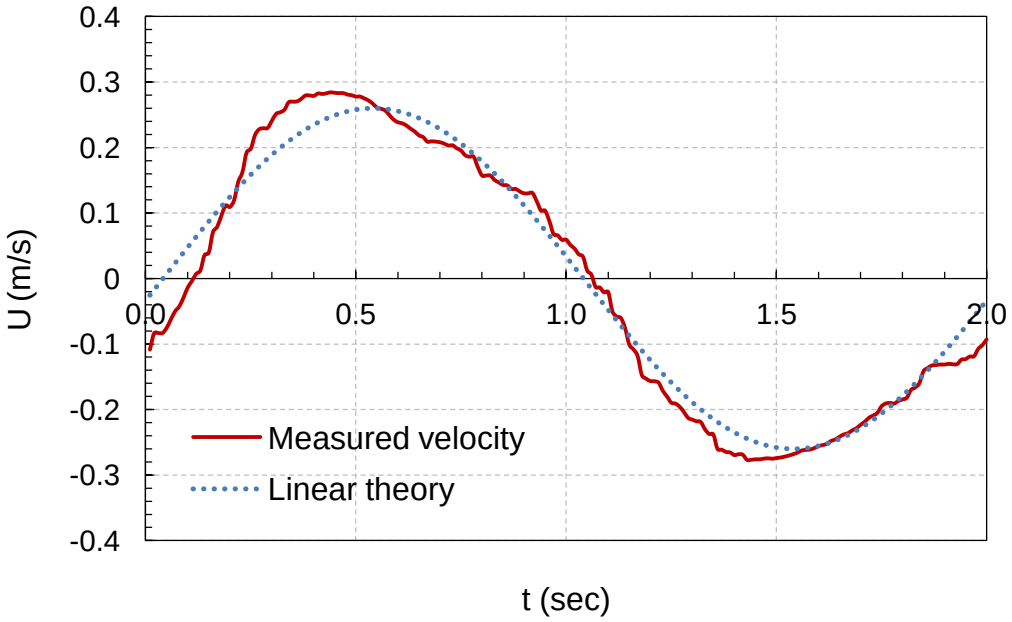

(b)

Figure 4.6: Measured bottom particle velocity compared with linear wave theory (a) H=8cm, T=2 sec, H/gT^2=0.002 (b) H=12 cm, T=2 sec, H/gT^2=0.0031.

Table 4.3 shows the typical wave conditions used for the pressure measurements as well as in the other experiments described within this thesis. Based on Le Mehaute (1976) the type of waves was classified using the wave steepness parameter (H/gT^2) and the dimensionless depth parameter (d/gT^2). All tested waves were within the Intermediate depth region. The recommended wave theories to calculate water particle velocity, pressure etc., for the waves in this depth are Stokes 2nd, 3rd and Stream function V. Nevertheless, it was found that linear theory matched reasonably well with the measured velocity and pressure data.

Table 4.3: Pressure measurement on a stone - wave parameters and relative depth classification.

Test	H(cm)	T(s)	h(cm)	h/gT^2	H/gT^2	Wave type	Recommended
PM1	6	1	40	0.041	0.006	Intermediate	Stokes 3rd
PM2	8	1	40	0.041	0.008	Intermediate	Stokes 3rd
PM3	8	1.6	40	0.016	0.003	Intermediate	Stokes 2nd
PM4	10	1.6	40	0.016	0.004	Intermediate	Stokes 3rd
PM5	12	1.6	40	0.016	0.005	Intermediate	Stream function
PM6	5	2	40	0.010	0.001	Intermediate	Stokes 2nd
PM7	8	2	40	0.010	0.002	Intermediate	Stokes 2nd
PM8	10	2	40	0.010	0.003	Intermediate	Stream function
PM9	12	2	40	0.010	0.003	Intermediate	Stream function

Based on best fit to the measured data, the drag and inertia coefficients for the maximum horizontal force were found to be C_D=1.92 and C_M=2.48 (for the crest half cycle). The drag and inertia coefficients for the maximum positive uplift force were found to be C_D=0.55 and C_M=0.72 respectively (for the trough half cycle).

Dixen *et al.* (2008) quoted C_D=0.6 and C_M=1.2 from Sarpkaya (1975) for a free sphere (unaffected by boundaries) at KC=12. Fischer *et al.* (2002)

observed a much higher value for the drag coefficient, C_D=1.9, for a bottom mounted sphere at Re=500.

The observed C_D and C_M values are larger than the typical values obtained by previous researchers for a free sphere. For a bottom mounted smooth cylinder Sarpkaya & Isaacson (1981) observed based on the study of Sarpkaya (1977), that C_D reached 2.0 at KC=10. For the same tests, C_M approached its potential flow value of 3.29. Sarpkaya attributed this to the wall proximity effects - early separation of flow, inhibition of regular vortex shedding and the influence of vortices shed in the previous cycles – larger forces cause larger force coefficients. Flow visualisation tests on a 50mm sphere and flow over rough beds in the present study seem to support this view (see flow details in Figures 7.15-7.17 and Appendix C). Similar to Sarpkaya's study, the KC number remained under 10.4 in the present tests. The flow separated early and the influence of vortices shed from the previous half cycle increased as they were being swept back by the reversing flow.

The physical meaning of the KC number can be given as the stroke length of the water particles relative to the size of the stone. Small KC numbers mean that the orbital motion of the water particles is smaller than the size of the stone. This may result in non-separation of the flow whereas a large sweep could induce flow separation.

Increased turbulence intensity after the addition of artificial turbulence may increase the force coefficients (Cheung & Melbourne, 1983). The bottom

mounted sphere, therefore, will be subjected to more turbulence, than one unaffected by the proximity to a wall.

Figure 4.9 shows C_D and C_M values for individual tests. The drag coefficient decreased from 3.0 to 2.1. This reduction is considered to be due to the gradual reduction in skin friction drag when the KC number approached 10, whilst the inertia coefficient increased to 2.7.

Using the force transfer coefficients deduced in this study, Morison's force was calculated and compared with the measured horizontal (F_H) and vertical forces (F_L) during the course of a wave cycle. Morison's formula over predicted the maximum horizontal force by 17.9% (Figure 4.10a) and under predicted the peak positive uplift force by 13.5% (Figure 4.10b).

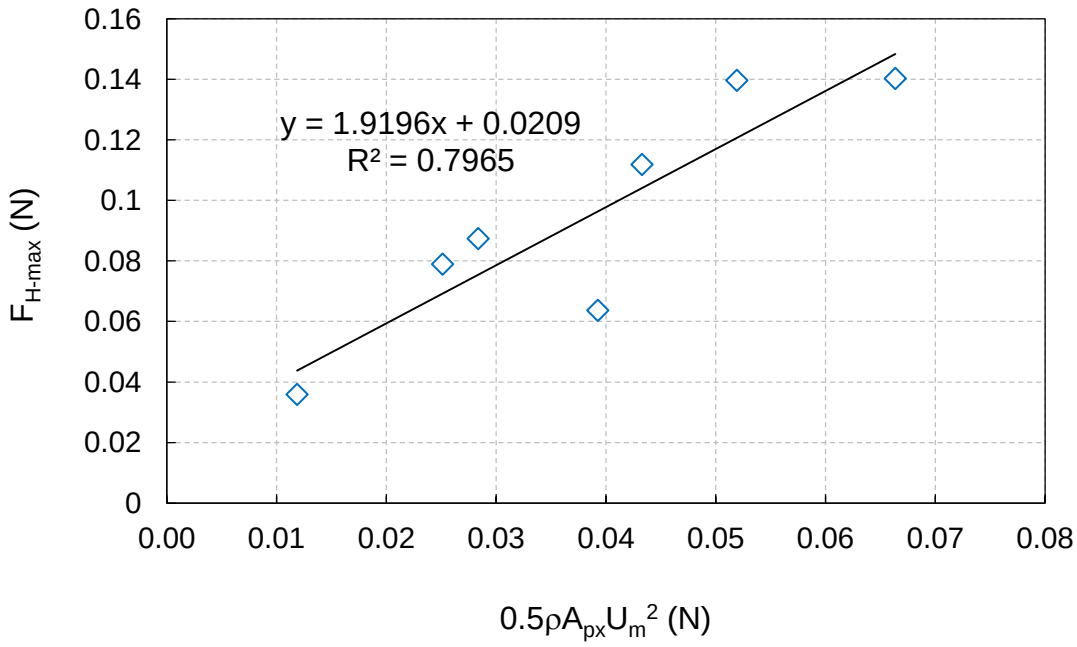

(a)

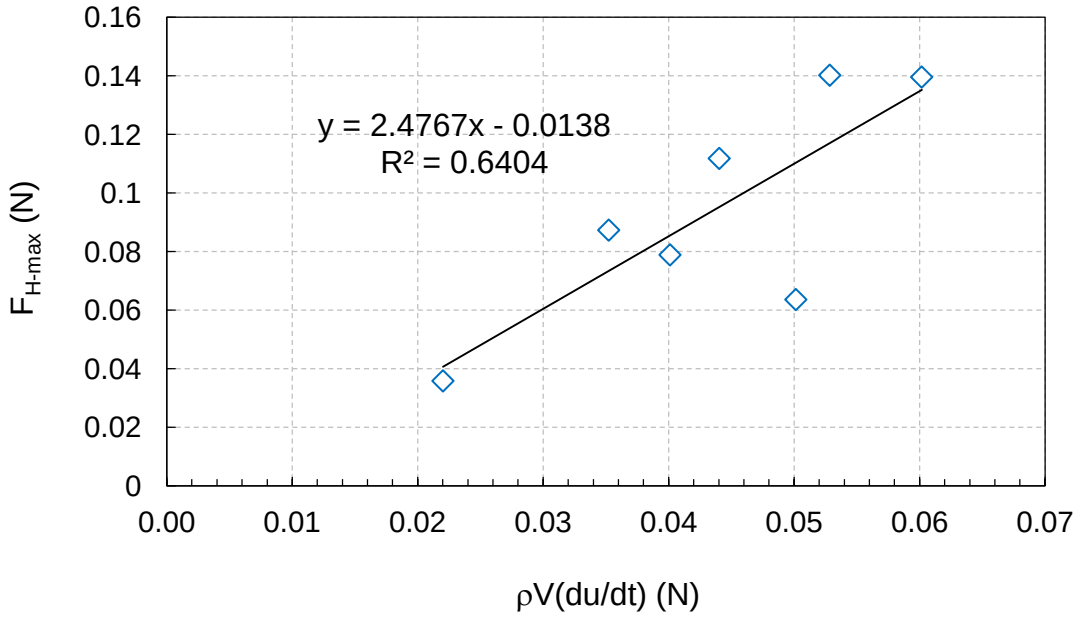

(b)

Figure 4.7: Best fit of (a) drag and (b) inertia terms to measured maximum horizontal force to find Morison's force coefficients, C_D and C_M.

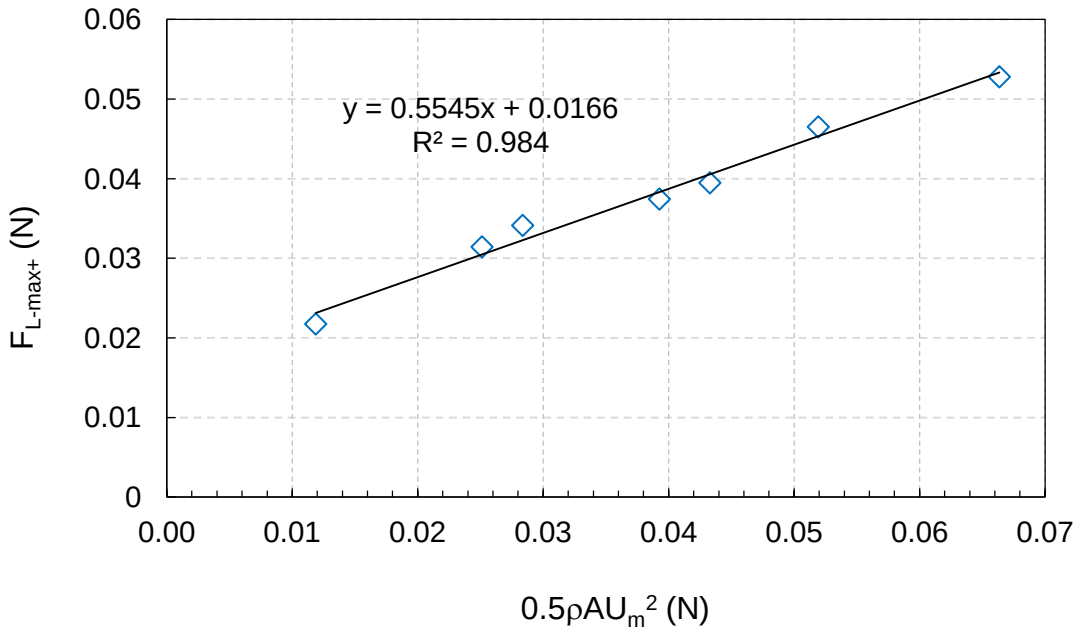

(a)

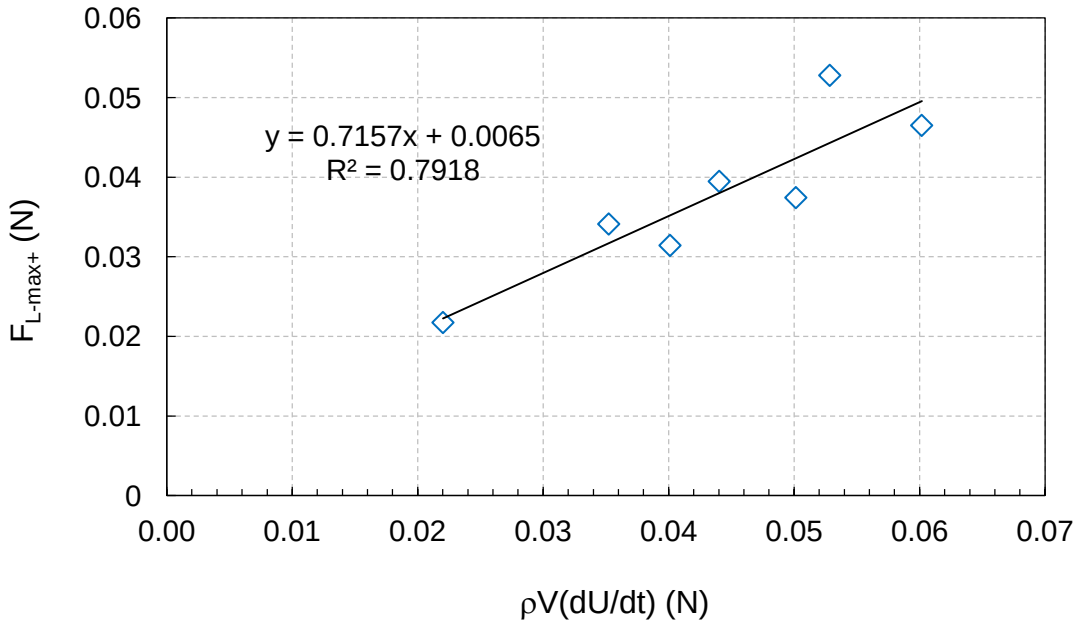

(b)

Figure 4.8: Best fit of (a) drag (b) inertia terms to measured maximum positive uplift force to find Morison's force coefficient, C_D and C_M.

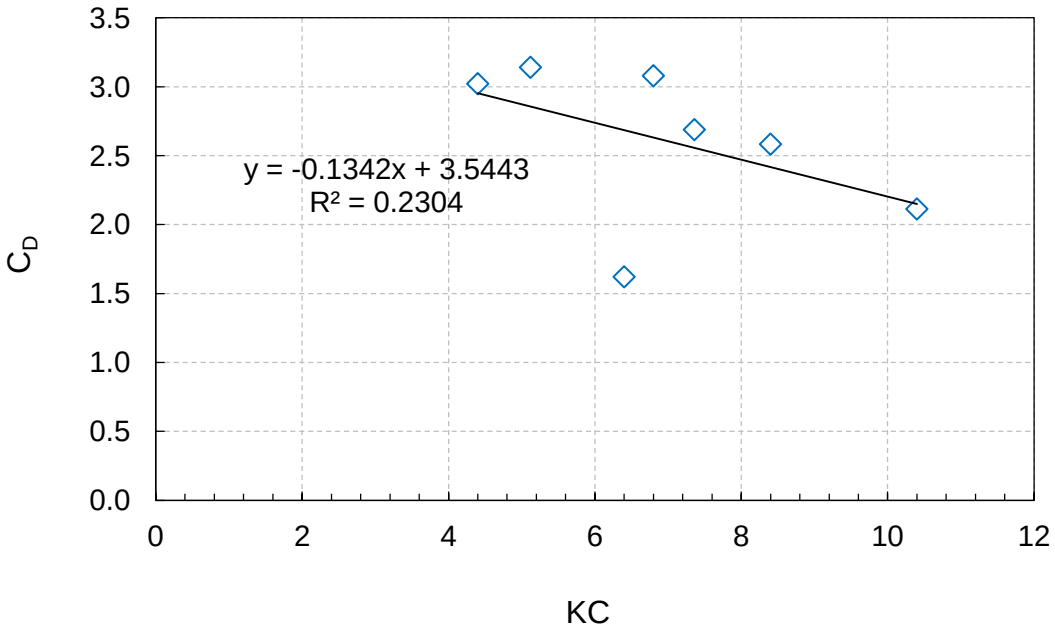

(a)

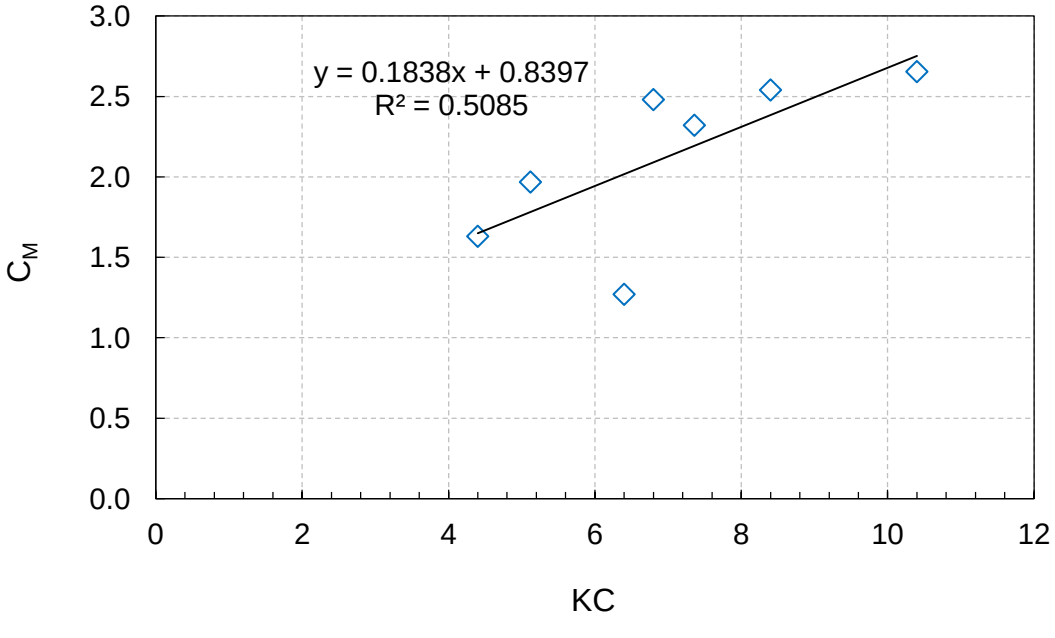

(b)

Figure 4.9: Variation of (a) C_M and (b) C_D with KC for individual tests.

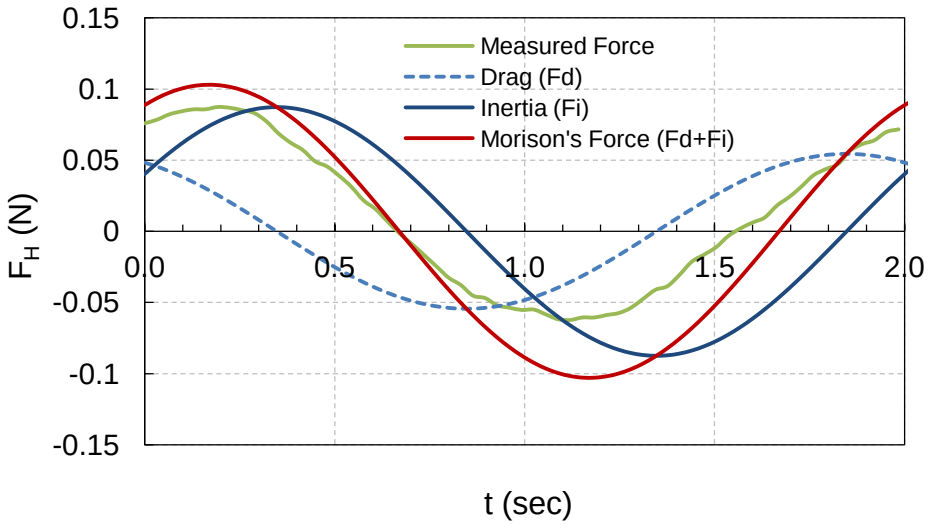

(a)

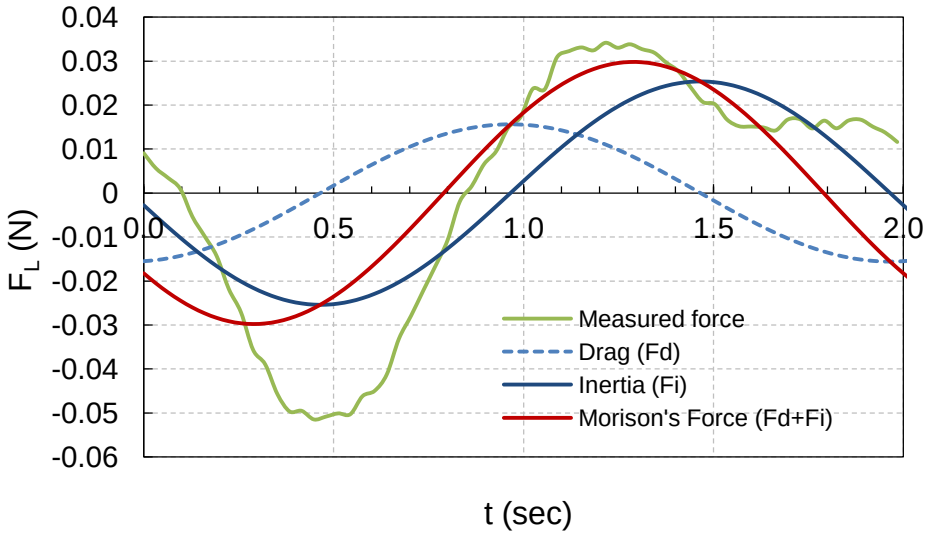

(b)

Figure 4.10: Measured (a) horizontal and (b) uplift force variation on a fully exposed sphere compared with the Morison's force.

In order to check the influence of the inertia on the horizontal force, Morison's force was plotted omitting the drag term. The match between the

measured force and the prediction improved indicating the dominance of the inertia term for low KC number flow (Figures 4.11 and 4.15). However, such an improvement was not possible for the uplift force.

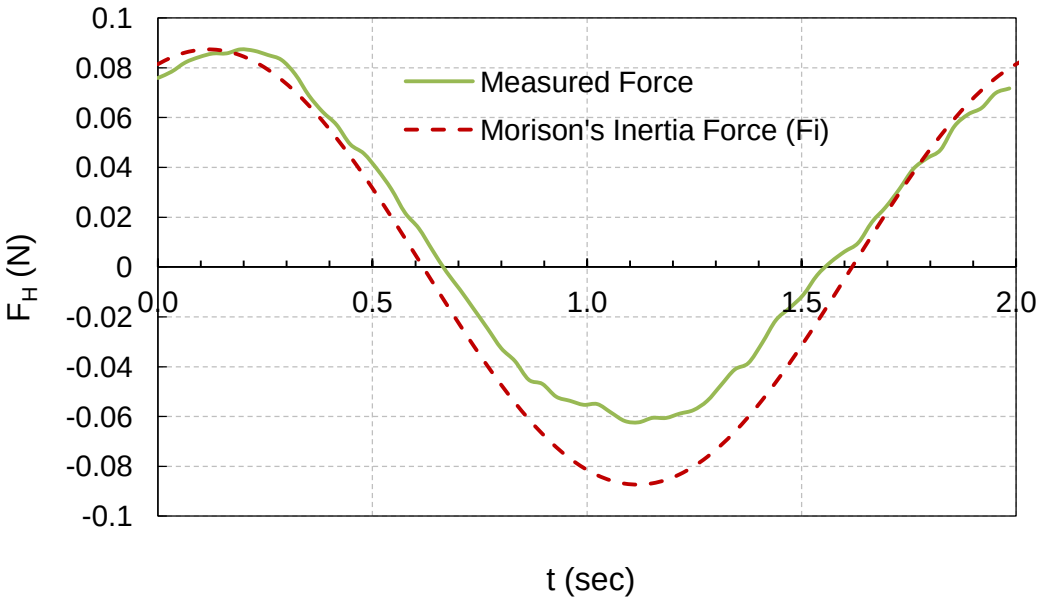

Figure 4.11: Measured horizontal force variation on a fully exposed sphere compared with the Morison's inertia force.

4.3.2 Sphere in a coplanar bed

Figures 4.12 and 4.13 show the C_D and C_M values obtained by fitting the measured maximum horizontal and positive uplift forces to the drag and inertia terms of Morison's equation.

In calculating the horizontal force, the projected frontal area, A_{px}, and the displaced Volume, V_x, were taken as that part of the sphere located above the theoretical bed level assumed to be at 0.35d below the crest of the

roughness elements, i.e. A_{px}=6.13 X 10^{-4} m^2 and V_x=1.8113 X 10^{-5} m^3. $A_{py}=\pi d^2/4$ and $V_y=\pi d^3/6$ were assumed in the calculation of the vertical force.

For the horizontal force, C_D=1.49 and C_M=2.39 were obtained. C_D=0.42 and C_M=0.7 were calculated for the uplift force. It is noteworthy that the values obtained were very similar to those for a fully exposed sphere.

The force transfer coefficients deduced from curve fitting were used to predict the force on a stone in a coplanar bed (Figure 4.14). Morison's equation over predicted the maximum horizontal force amplitude by 27.1%. It under predicted the maximum positive uplift force by 26.0%.

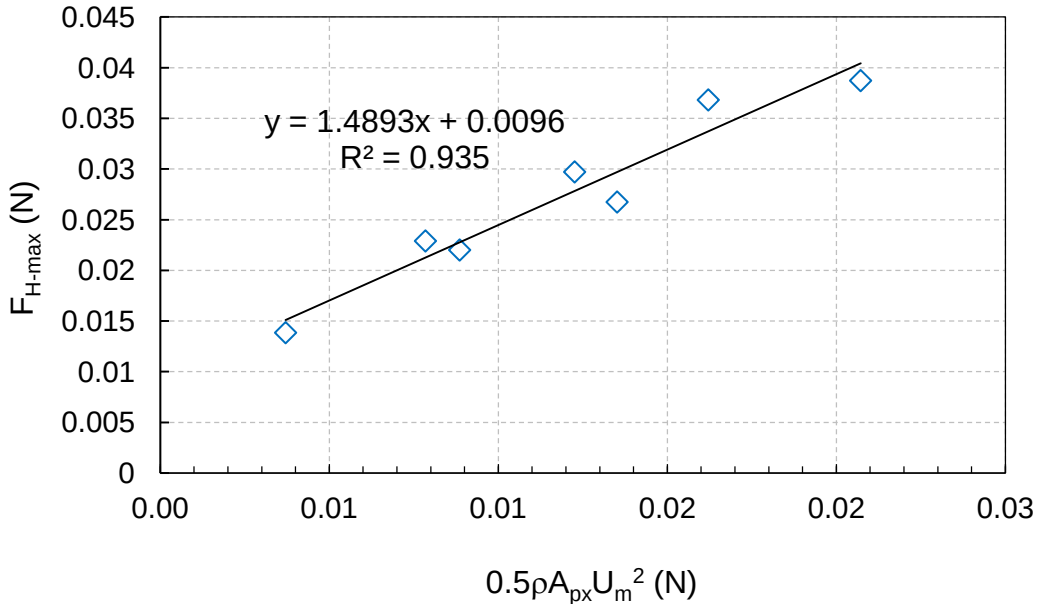

(a)

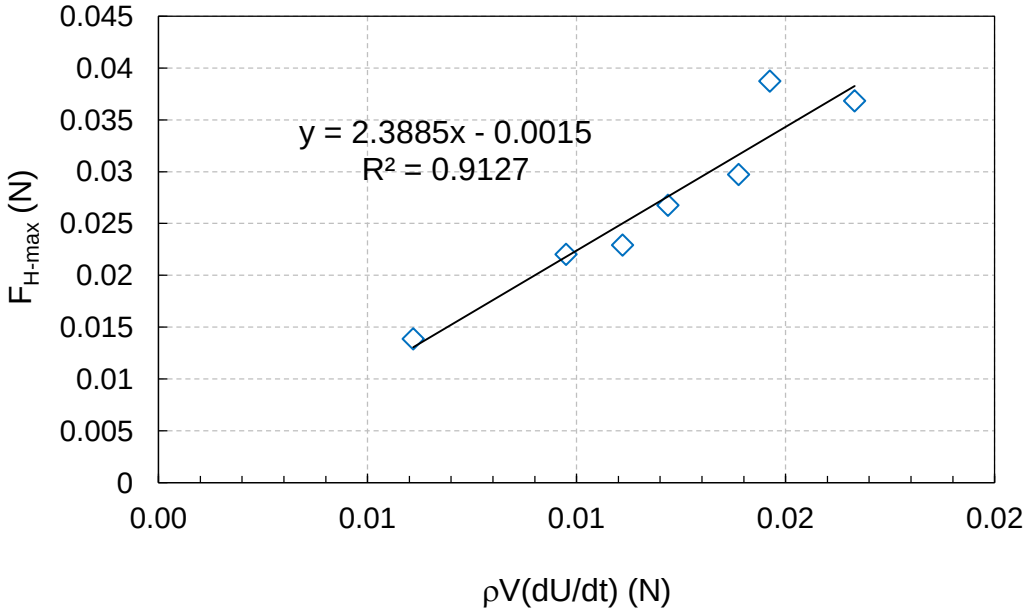

(b)

Figure 4.12: Best fit of Morison's (a) drag and (b) inertia terms to measured maximum horizontal force.

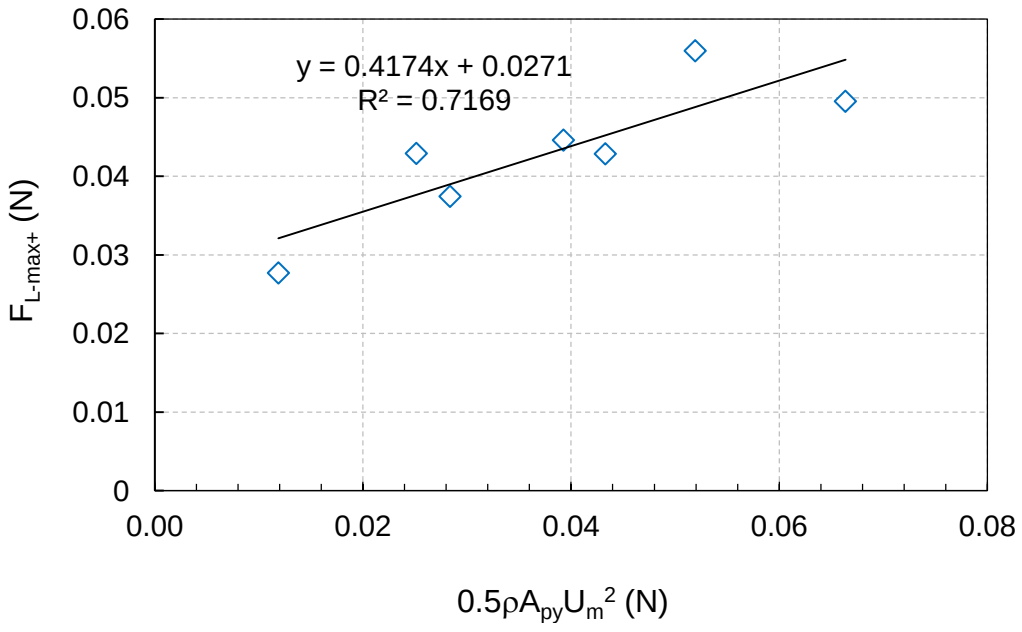

(a)

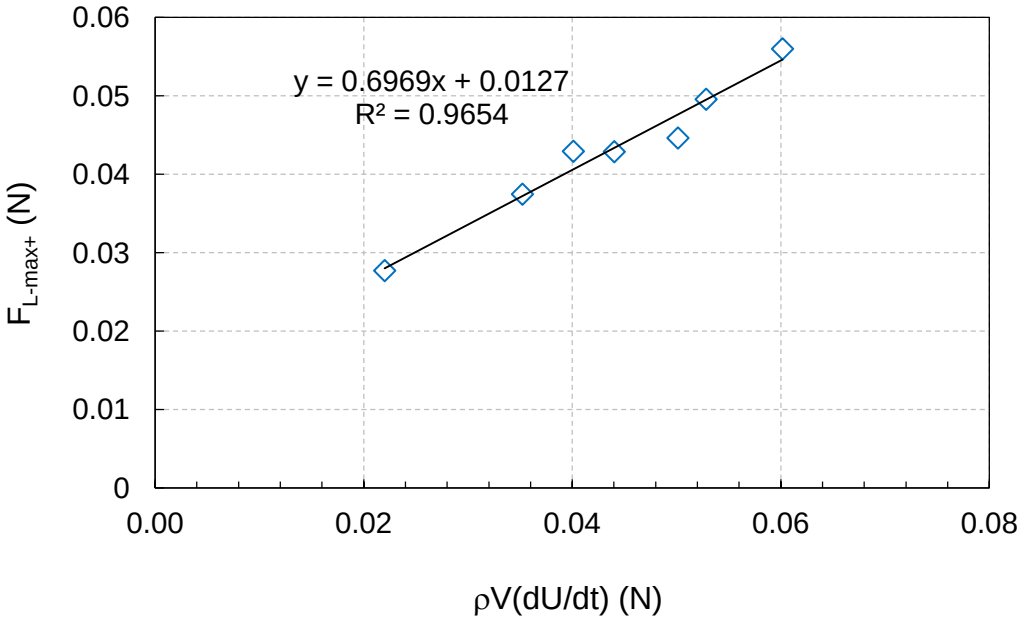

(b)

Figure 4.13: Best fit of Morison's (a) drag and (b) inertia terms to measured maximum positive uplift force.

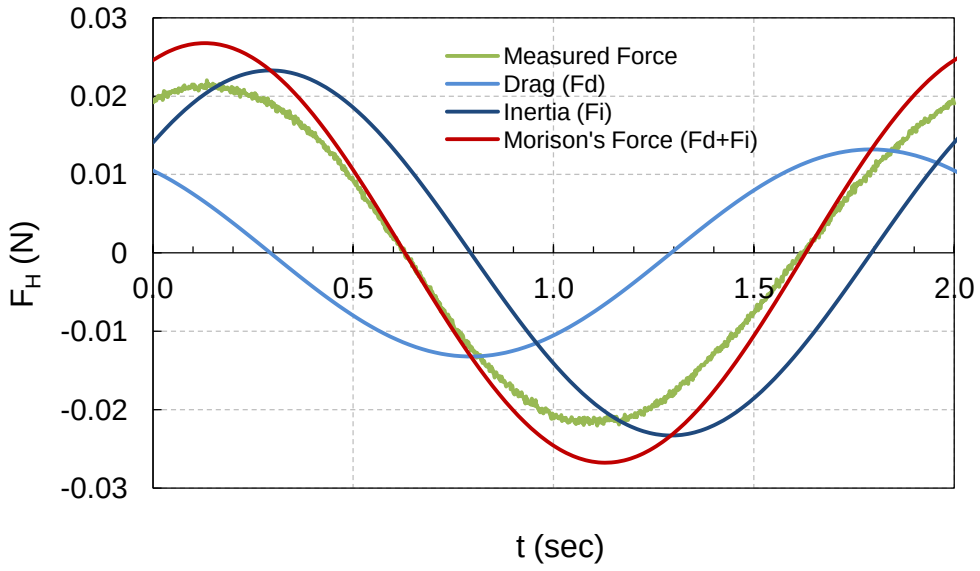

(a)

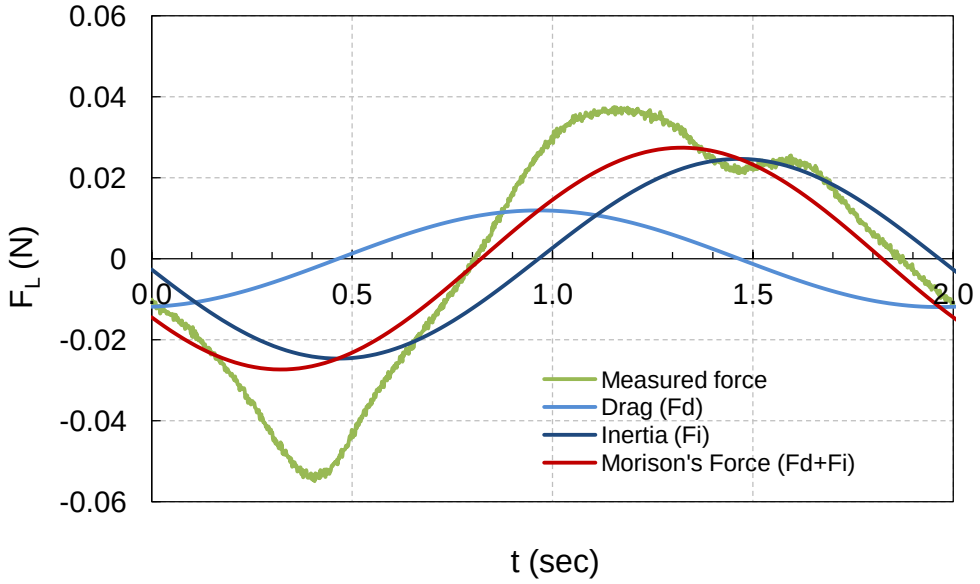

(b)

Figure 4.14: Measured (a) horizontal and (b) uplift forces on a spherical stone in a coplanar bed (i.e., p/d=0) compared with the Morison's force.

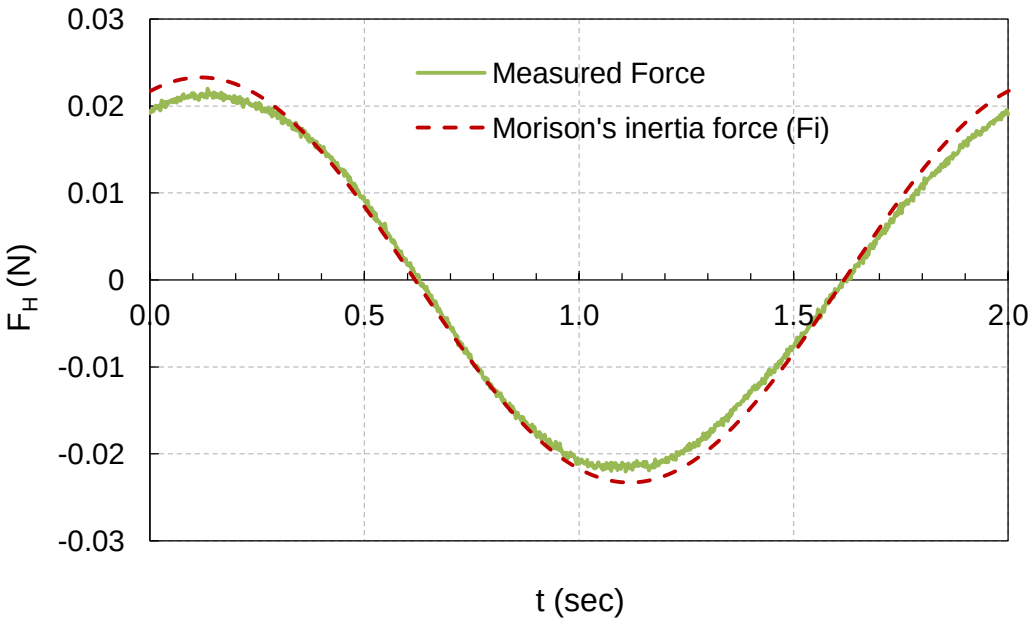

Figure 4.15: Measured horizontal force variation on a coplanar bed (i.e., p/d=0) compared with the Morison's inertia force.

4.3.3 Summary of Morison's force coefficients

Tables 4.4 and 4.5 show a summary of the force transfer coefficients obtained by curve fitting to the measured forces. Irrespective of the amount of stone protrusion, Morison's coefficients assumed similar values within the tested KC number range (4.4 to 10.4). Dixen *et al.* (2008) found that C_D=0.5-0.7 and C_M=0.1-0.2 for a coplanar bed of ping pong balls (d=3.6cm) glued to the flume bed under regular waves at KC=12. The authors relied on turbulence measurements to determine the force transfer coefficients as opposed to current pressure measurements.

The drag and inertia coefficients observed in the present tests for a coplanar bed, i.e. C_D=1.49 and C_M=2.39, using billiard balls (d=50mm) are significantly larger than those observed by Dixen *et al*. (2008). However, the

observation of Fischer *et al.* (2002) that the drag coefficient approached 1.9 for a bottom mounted sphere at Re=500 and the results of Sarpkaya (1977) (as quoted in Sarpkaya & Isaacson, 1981) for a bottom mounted cylinder with C_M reaching 3.29 seem to agree with the present results.

Therefore, the large force transfer coefficients observed in the present tests can be attributed to (i) the effect of proximity to the bed (ii) early flow separation at low KC numbers <10.

Table 4.4: Summary of Morison's horizontal (in-line) force coefficients.

p/d	C_D	C_M
0.82 (fully exposed)	1.92	2.48
0 (coplanar bed)	1.49	2.39

Table 4.5: Summary of Morison's uplift force coefficients.

p/d	C_D	C_M
0.82 (fully exposed)	0.55	0.72
0 (coplanar bed)	0.42	0.70

4.4 Effect of stone protrusion on forces

It is one of the primary objectives of this chapter to investigate the effect of different stone protrusion levels on wave-induced forces on a stone in a bed protection. That would help better understand and interpret the phenomena observed in the incipient motion tests described in Chapter 6.

Figure 4.16 shows the variation of the horizontal and vertical forces over a wave cycle for different protrusion levels. p/d=0.82 refers to a fully exposed stone and p/d=0 corresponds to a coplanar bed. The most significant feature observed is that the forces on a spherical element with relative

protrusion, p/d=0.216, are only marginally larger than the forces on a sphere in a coplanar bed. It appears that the stone with p/d=0.216 does not protrude enough to perturb the flow to significantly alter the pressure gradient around it. Therefore, it behaves almost in a similar manner to a stone in a coplanar bed. The incipient motion tests showed that a coplanar bed is remarkably stable. A stone with p/d=0.2 exhibited the same degree of stability. Therefore, approximately similar pressure distribution and forces measured on a stone in a coplanar bed and one with a finite protrusion of 0.216 explain the reason why light weight marbles (i.e. specific gravity, s=1.19) with p/d<0.2 did not move in the incipient motion tests.

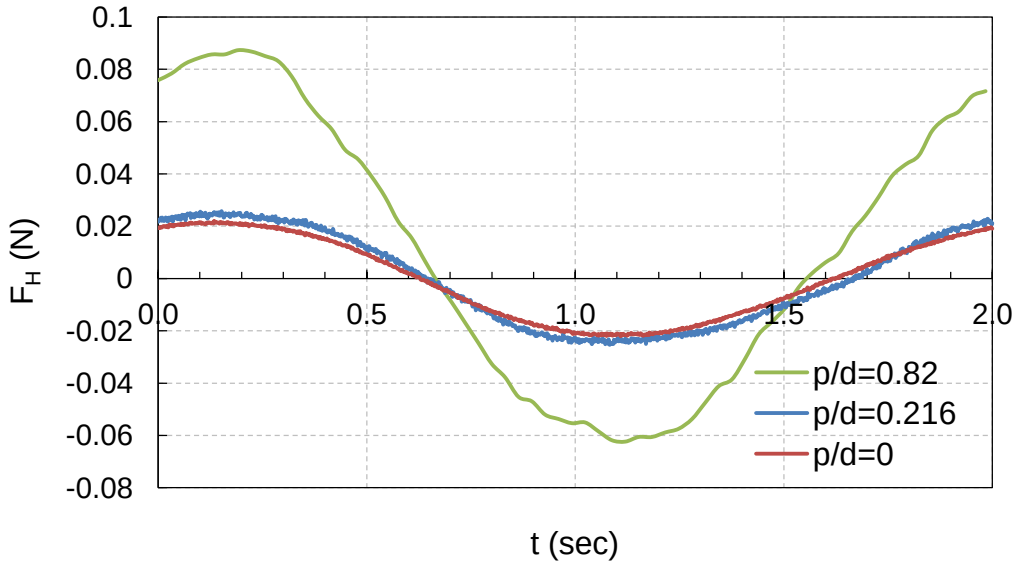

(a)

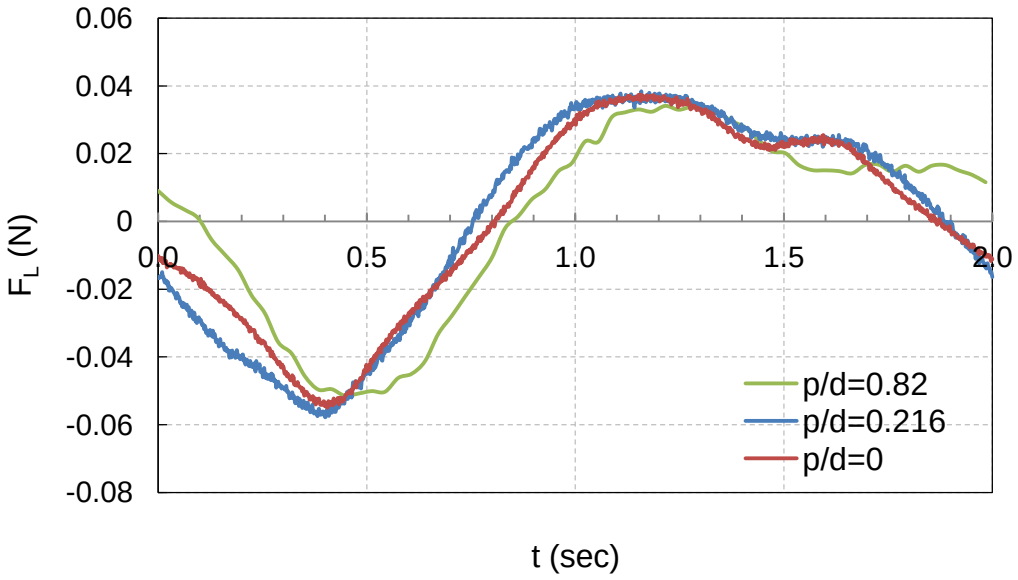

(b)

Figure 4.16: Measured (a) horizontal and (b) vertical force variation on a 50mm spherical stone of different relative protrusion.

4.5 Summary

In this chapter the effect of stone protrusion on the wave-induced horizontal (in-line) and vertical (uplift) forces on a 50mm spherical test stone was investigated. It was found that the forces on a stone strongly depend on the exposure above mean bed level. The key findings in this chapter were:

1 Horizontal and uplift force variation on a stone of relative protrusion, p/d=0.216 over a wave cycle was only slightly larger than the forces on a stone in a coplanar bed (i.e. p/d=0). The pressure distribution on the stone followed the same trend.

2 Peak values of the in-line ($F_{H\text{-}max}$) and positive uplift ($F_{L\text{-}max+}$) forces on a fully exposed spherical element (i.e., p/d=0.82) was predicted well by the use of the dynamic pressure amplitude at the bed obtained from linear wave theory, i.e., $F_{H\text{-}max}=C_H 0.5\rho g H A_{px}/\cosh(kh)$ and $F_{L\text{-}max+}=C_V 0.5\rho g H A_{py}/\cosh(kh)$. However, for a stone on a coplanar bed the prediction error increased.

3 Morison's drag and inertia coefficients assumed similar values for a fully exposed stone and one in a coplanar bed, irrespective of the exposure level.

4 Morison's horizontal drag and inertia coefficients for a fully exposed sphere were found to be C_D=1.92 and C_M=2.48 respectively. The values for the uplift force were C_D=0.55 and C_M=0.72.

5 Morison's force coefficients for a stone in a coplanar bed were found to be C_D=1.49 and C_M=2.39. For the uplift force, these were C_D=0.42 and C_M=0.7.

6 The large force transfer coefficients observed in the present tests relative to a free sphere are due to the effect of proximity to the bed and early flow separation under low KC numbers.

7 Under low KC number flow (i.e., KC<10 in the present tests), the inertia force is more dominant. The measured horizontal force agreed well with Morison's inertia force term within this range.

8 Morison's equation poorly predicted the lift force. Therefore, it is not a good predictor for modelling uplift forces.

5 Shear stress and friction factor

5.1 Introduction

Accurate determination of the shear stress applied by oscillatory waves on a rough bed is crucial in predicting damage to a granular bed protection. Researchers in the past have used several methods to estimate shear stress in laboratory experiments. i.e. (i) momentum integration (ii) Reynolds stress (iii) direct measurement using a shear cell, hot film techniques (iv) energy dissipation method. In the present work, a different method, that is the measurement and integration of pressure on the surface of a spherical element of 50mm diameter set in a coplanar hexagonal bed of similar spheres (billiard balls), was used to quantify shear stresses.

Table 5.1: Measurement of shear and normal stresses - test cases.

Test	H (cm)	T (s)	h (cm)	U_m (m/s)	d (cm)	a (cm)	a/k_s	f_w	u^*k_s/ν	$Re=aU_m/\nu$
PM1	6	1	40	0.07	5	1.13	0.09	2.49	9289	7.5E+02
PM2	8	1	40	0.09	5	1.50	0.12	1.96	10583	1.3E+03
PM3	8	1.6	40	0.16	5	4.00	0.32	0.86	12462	6.1E+03
PM4	10	1.6	40	0.2	5	5.00	0.4	0.71	14184	9.5E+03
PM5	12	1.6	40	0.23	5	6.00	0.48	0.61	15109	1.3E+04
PM6	5	2	40	0.11	5	3.38	0.27	0.99	9201	3.5E+03
PM7	8	2	40	0.17	5	5.50	0.44	0.66	11583	8.9E+03
PM8	10	2	40	0.21	5	6.88	0.55	0.55	13029	1.4E+04
PM9	12	2	40	0.26	5	8.13	0.65	0.47	15038	2.0E+04

5.2 Measurement of forces on a spherical roughness element

Pressure transducers were located at points where the latitude at angle, φ = -90, -60, -30, 0 (equator), 30, 60, 90 degrees cross the meridian. The sphere was rotated 180 degrees (half a circle) horizontally at λ=30 degree intervals each time, running a number of wave cases. Each elemental area formed by 30 degree arcs in (λ, φ) directions would have 4 pressure sensors at the four corners. The average pressure is $P=(P_1+P_2+P_3+P_4)/4$. An elemental surface area of the sphere enclosed by two latitude and two longitude circles 30 degrees apart, is used to find the force on that element, i.e. $\delta F_H = P.\delta A$. The force on all elements are summed up in x (direction of wave propagation) and y (vertical) directions to find the net horizontal and vertical forces. The experimental arrangement and calculation methodology are discussed in more detail in Chapter 3.

5.3 Shear stress

The shear stress is defined here as the net horizontal force per unit area. In order to find the shear stress, the net horizontal force, ΔF_H was divided by the effective planar area of the sphere, $2\sqrt{3}\ R^2$ or $1.1(\pi d^2/4)$, on the coplanar bed where the billiard balls were arranged in a hexagonal array.

Figures 5.1 and 5.2 show the measured (ensemble-averaged over a 50 cycles) shear stress, $<\tau>$, for two wave conditions: a wave height, H=8cm, period, T=2 sec and H=8cm, period, T=1 sec at a water depth of h=40cm,

respectively. The predicted oscillatory shear stress determined using the relation, $\tau_m=0.5f_w\rho U_m^2 cos(\omega t)$ was superimposed on the measured shear stress profiles. In this equation, the wave friction factor, f_w, was computed using the eqn. $f_w=0.33(a/k_s)^{-0.84}$ (Simons *et al*., 2000).

As shown in Figure 5.3, the shear stress leads the wave surface elevation by an average 64 degrees. The instantaneous shear stress, τ, is presented in Figure 5.4.

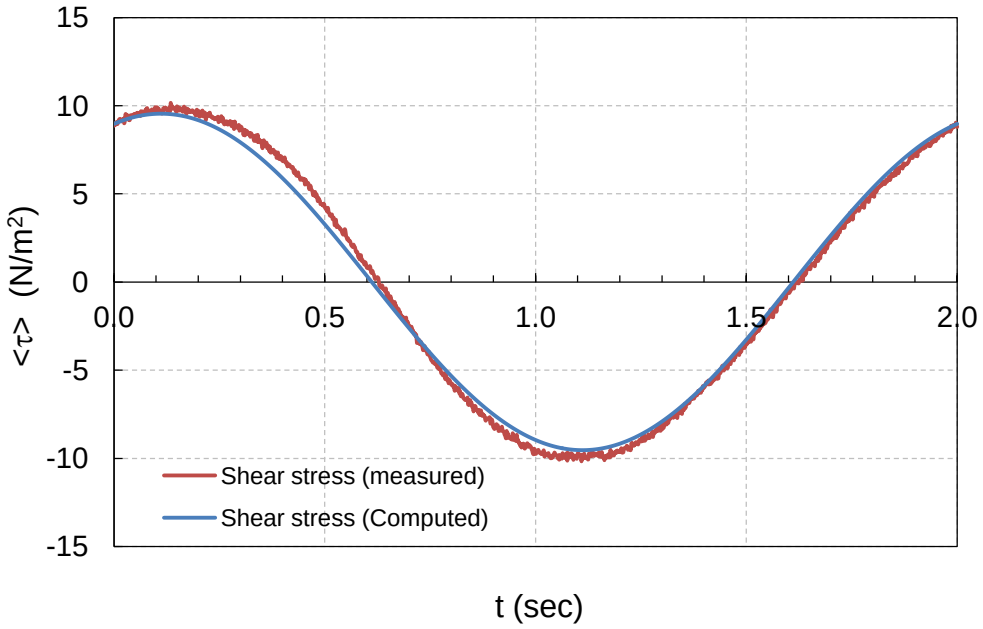

Figure 5.1: Shear stress computed using $<\tau>=0.5f_w\rho U_m^2 cos(\omega t)$ superimposed on measured shear stress profile, $<\tau>$ for H=8cm, T=2.0 sec., h=40cm.

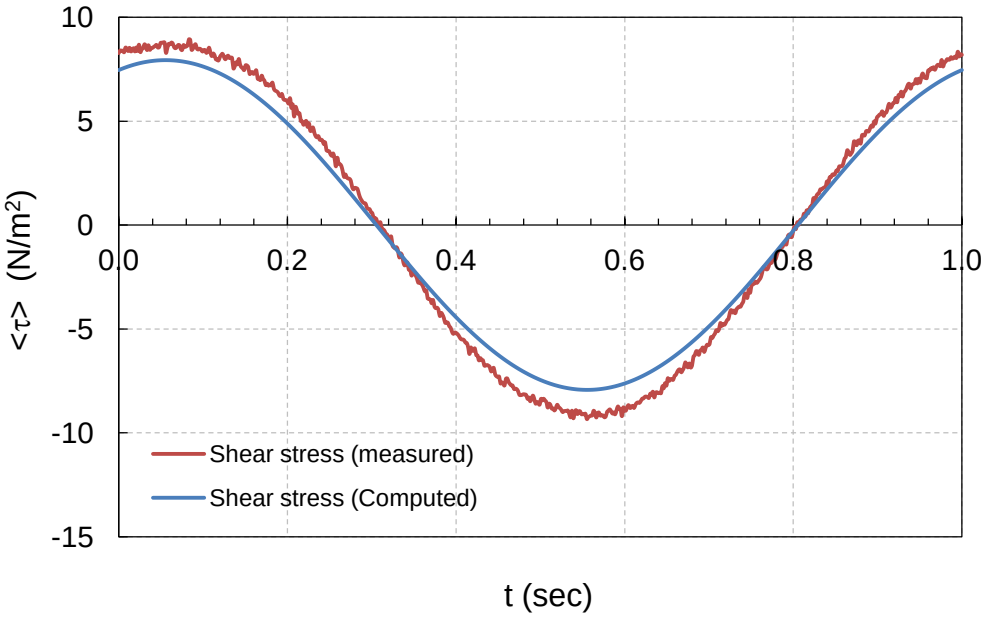

Figure 5.2: Shear stress computed using $<\tau>=0.5 f_w \rho U_m^2 \cos(\omega t)$ superimposed on measured shear stress profile, $<\tau>$ for H=8cm, T=1.0 sec., h=40cm.

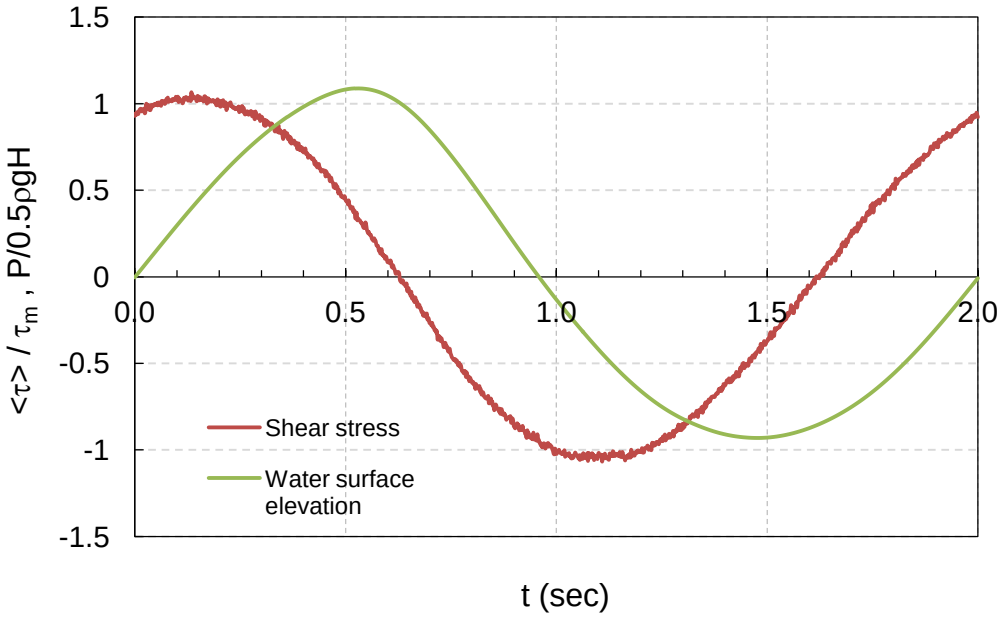

Figure 5.3: Shear stress variation. H=8cm, T=2.0 sec., h=40cm. Shear stress leads the water surface elevation by an average 64 degrees.

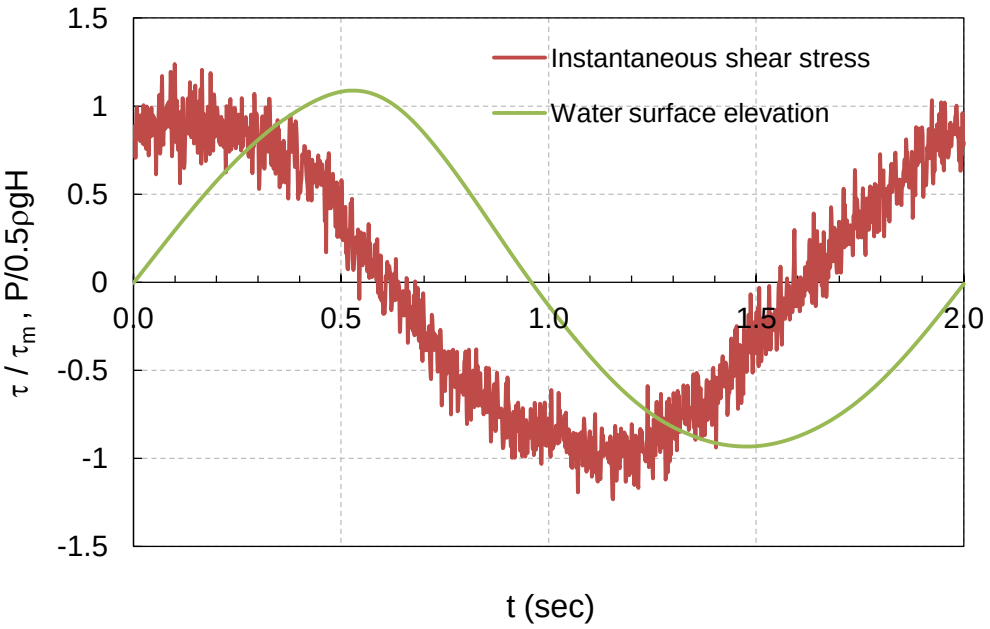

Figure 5.4: Variation of instantaneous shear stress, τ. H=8cm, T=2.0 sec., h=40cm.

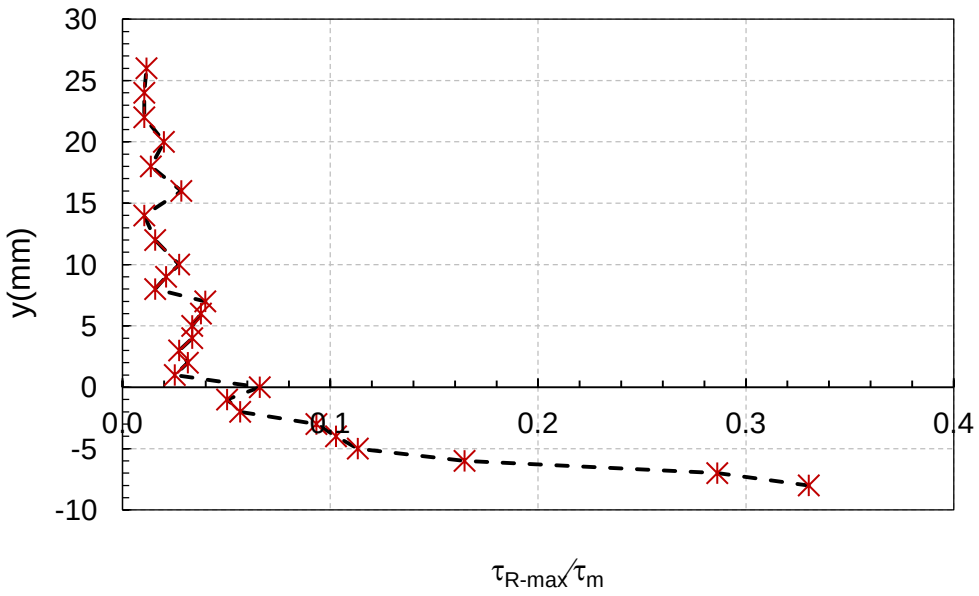

Figure 5.5: Maximum Reynolds stress magnitude measured from the crest level of the roughness elements, $\tau_{R\text{-}max}$. H=8cm, T=2.0 sec., h=40cm.

The maximum Reynolds stress magnitude, $\tau_{R\text{-}max}$, averaged over 50 cycles plotted against elevation, y, from the bed level, is shown in Figure 5.5. The maximum Reynolds stress occurs below the bed level (this is consistent with the observations of Dixen *et al*., 2008). The Reynolds stress is only a fraction of the shear stress, i.e. $\tau_{R\text{-}max}/\tau_m$=0.33 at a level 0.16d below the top of the roughness elements. Looking at the data of Sleath (1987), the same ratio is ~0.19.

5.3.1 Phase lead by shear stress

It was found that the shear stress leads the surface water elevation by an average angle of 62-67deg. Nielsen (1992) reported a value of 45 deg for laminar flow and noted that the bed shear stress in laminar flow is simple harmonic. Jonsson & Carlsen (1976) reported a phase lag of maximum 31deg. for smaller roughness heights (a/k_s). However, the present data agree with the recent bed shear stress measurements by Seelam *et al.* (2011) using a shear cell apparatus for a solitary wave. They reported that the total shear stress on a smooth bed (i.e., sum of the skin friction plus Froude-Krylov force) had a mean phase shift of 50deg with the free stream velocity (ranging 40-70deg). The phase shift of the skin friction shear stress had an average 30deg (ranging 5-50 deg). These tests were conducted in laminar and transitional flow regions.

Table 5.2: Phase lead (deg) by the shear stress.

Test	H (cm)	T (sec)	h (cm)	a/k_s	ϕ_c^0 (crest)	ϕ_t^0 (trough)	ϕ^0 (average)
PM1	6	1	40	0.09	60.5	72.6	66.6
PM2	8	1	40	0.12	54.1	71.4	62.8
PM3	8	1.6	40	0.32	58.0	69.8	63.9
PM4	10	1.6	40	0.40	61.9	69.1	65.5
PM5	12	1.6	40	0.48	54.7	74.5	64.6
PM6	5	2	40	0.27	59.9	64.5	62.2
PM7	8	2	40	0.44	59.0	68.3	63.7
PM8	10	2	40	0.55	60.2	65.1	62.7
PM9	12	2	40	0.65	65.0	67.1	66.1

Therefore, the test results exhibit characteristics of laminar flow viewed from the present knowledge (i.e. shear stress is sinusoidal and the phase lead is greater than 45deg). Though the flow is within the rough turbulent regime on account of roughness Reynolds number, $u_* k_s/\nu$ > 200, the flow near the individual elements may not have been fully developed. This is because of the rapid flow reversal as well as the oscillatory nature of the flow, where actual velocities remain relatively small during a larger portion of the wave half cycle. The flow Reynolds number during the tests, $Re=aU_m/\nu$, varied between laminar and transitional regimes (i.e. 7.5 $X10^2$ - 2.0 $X10^4$. The previous parameters describing the shear stress variation (shape and phase lag) were based on turbulence measurements whereas this study followed a different approach, i.e. direct pressure measurement. Therefore, it would be important to observe the shear stress variation for higher Reynolds number ($Re=aU_m/\nu$) flows using the present apparatus.

5.4 Normal stress

The normal stress is defined here as the net vertical force per unit area. In order to determine the normal stress, the net vertical force, ΔF_L was divided by the effective planar area of the sphere, $2\sqrt{3}$ R^2.

Figure 5.6 compares the normal stress with the shear stress (both were ensemble-averaged, over 50 cycles).

The instantaneous normal shear stress, τ_{nt}, is plotted in Figure 5.7.

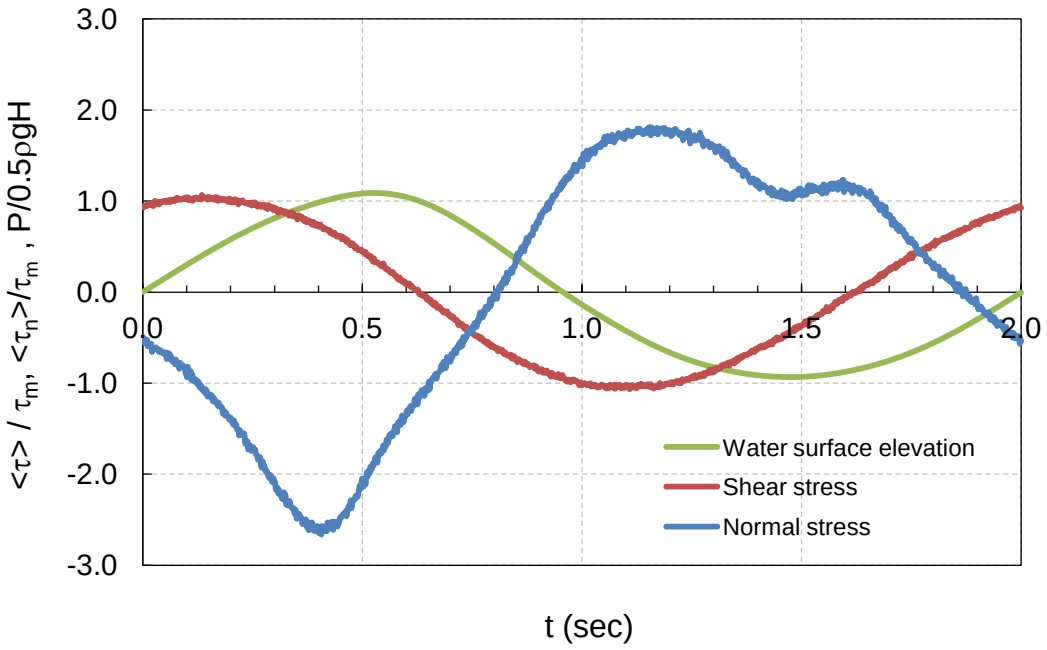

Figure 5.6: Shear stress, <τ> and normal stress, <τ_n> variation. H=8cm, T=2.0 sec., h=40cm.

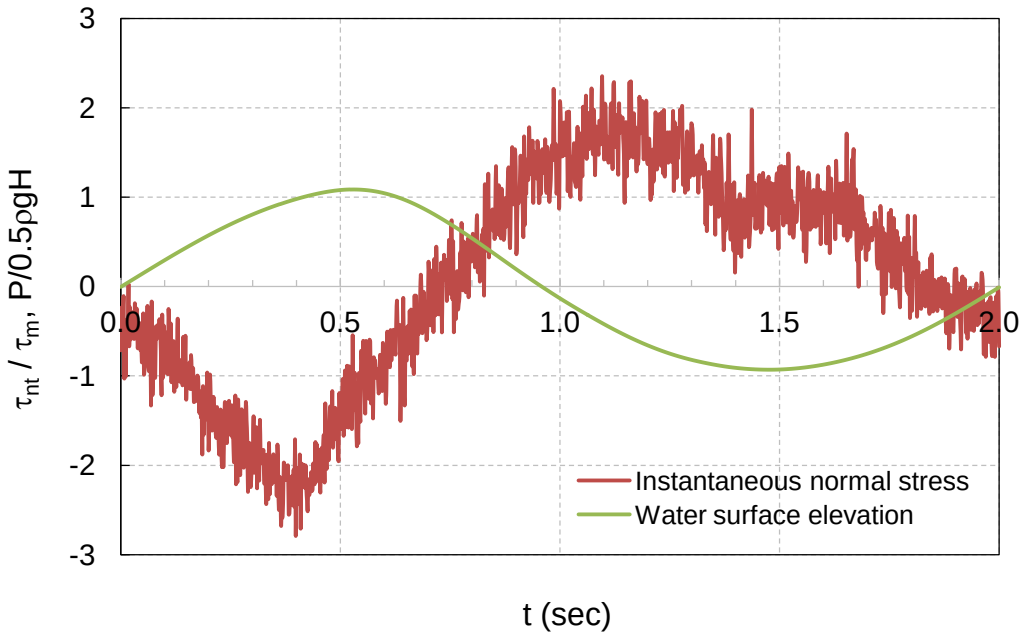

Figure 5.7: Variation of instantaneous normal stress, τ_{nt}. H=8cm, T=2.0 sec., h=40cm.

The relative amplitude of the normal stress, $\tau_{nm}/\tau_{m,}$ for the H=8cm and T=2 sec was quite asymmetrical with a value of 2.61 and 1.8 for the crest and trough half cycles respectively (Figure 5.6). This is due to the fact that the relative water depth (h/L) was shallow and non-linear terms dominate for the case with T=2.0 sec. For the case of H=8cm and T=1.0 sec, τ_{nm}/τ_{m}=1.26 was observed (Figure 5.9).

It was found that the ensemble-averaged normal stress can be fitted to a $<\tau_n>=<\tau_{nm}>cos(\omega t)$ type equation (Figure 5.9).

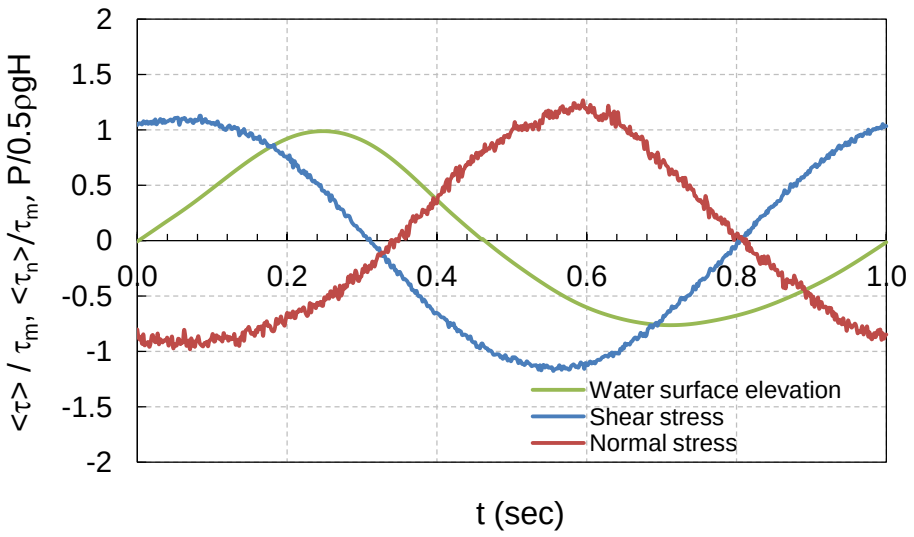

Figure 5.8: Shear stress, $<\tau>$ and normal stress, $<\tau_n>$. H=8cm, T=1.0 sec., h=40cm.

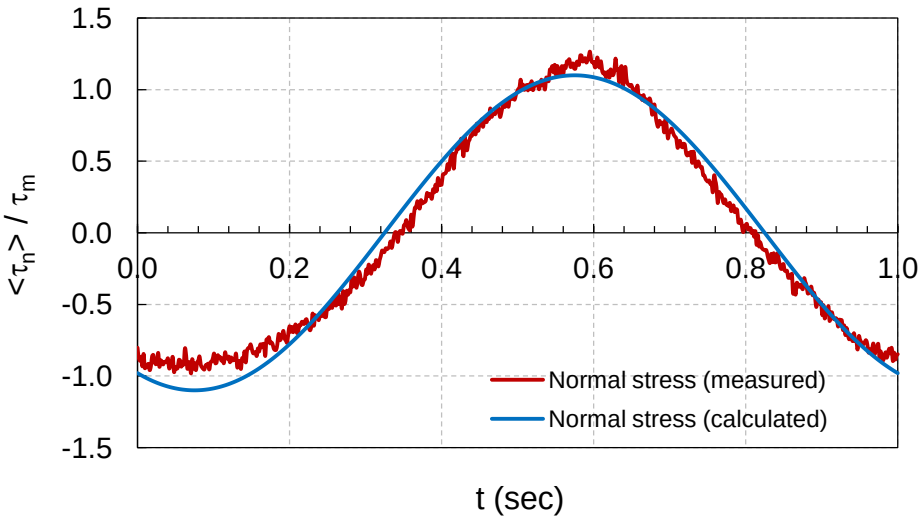

Figure 5.9: Normal stress computed using $<\tau_n>=<\tau_{nm}>\cos(\omega t)$ superimposed on measured normal stress profile, $<\tau>$ for H=8cm, T=1.0 sec., h=40cm.

5.5 Friction factor

The wave friction factor, f_w, was calculated using the relation:

$$f_w = \frac{< \tau_m >}{0.5\rho U_m^2} \tag{5.1}$$

Where, $< \tau_m >$ is the ensemble-averaged peak shear stress. Figure 5.10 shows the friction factor for different relative roughness values. The data were fitted to a power relationship with a good correlation (i.e., R^2=0.99).

$$f_w = 0.33\left(\frac{a}{k_s}\right)^{-0.9} \; ; \; 0.09 < \frac{a}{k_s} < 0.65 \tag{5.2}$$

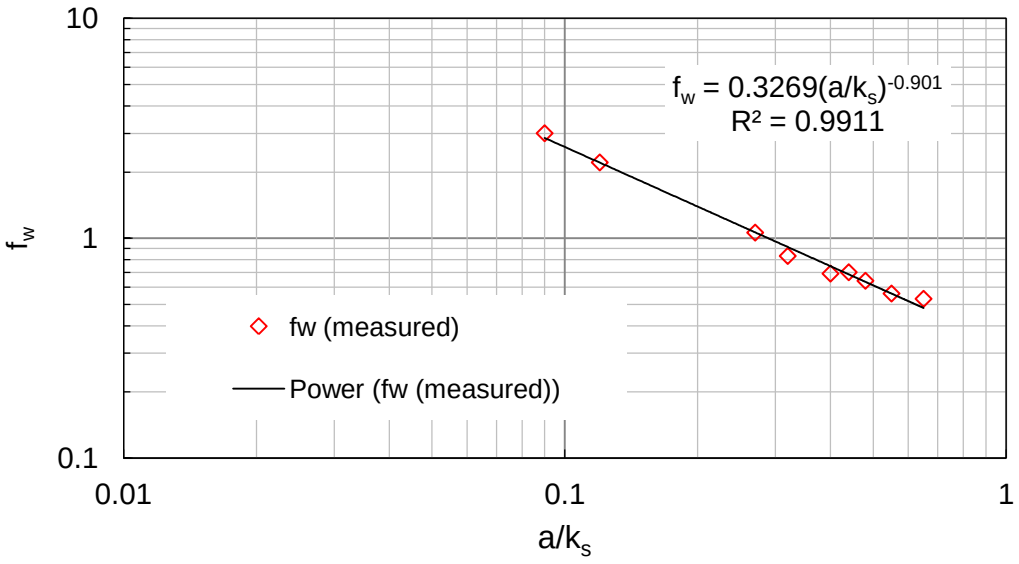

Figure 5.10: Measured friction factor against relative roughness.

The measured friction factor data also agreed well with the relationships of Simons *et al.* (2000) in Figure 5.11 and Kamphuis (1975) and Dixen *et al.* (2008) in Figure 5.12.

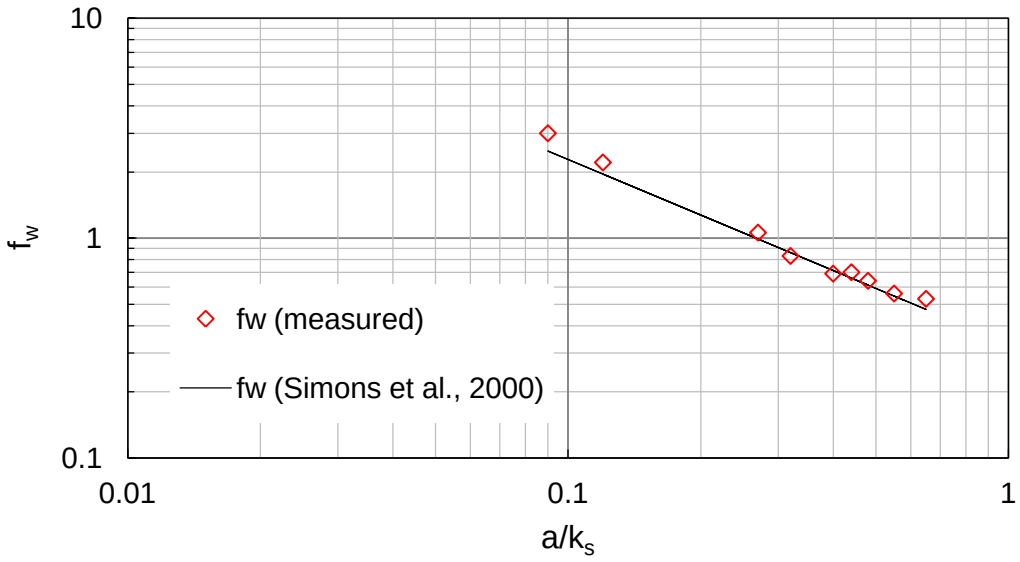

Figure 5.11: Measured friction factor compared with the relationship, $f_w=0.33(a/k_s)^{-0.84}$ of Simons et al. (2000).

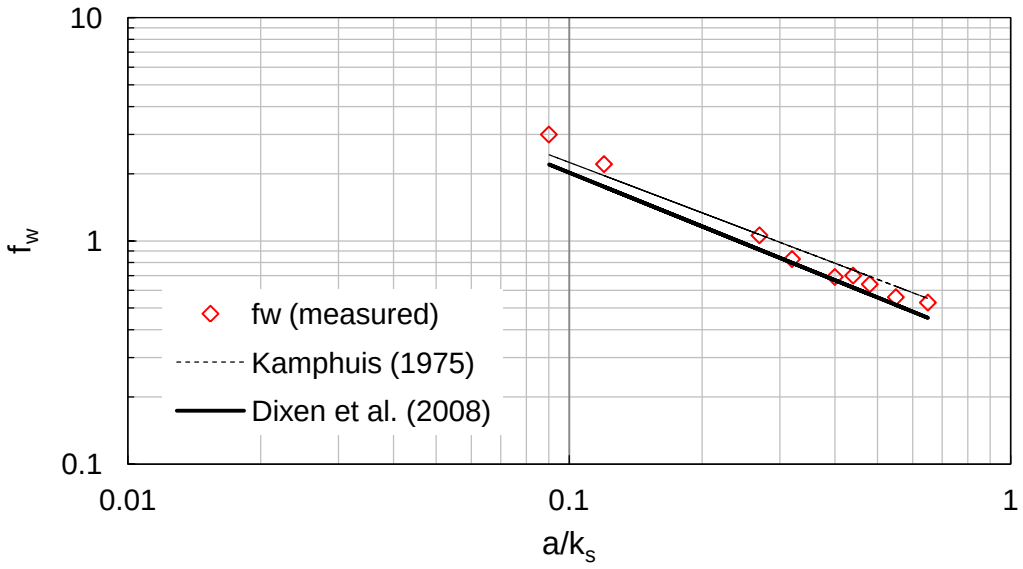

Figure 5.12: Measured friction factor compared with the relationship $f_w=0.4(a/k_s)^{-0.75}$ of Kamphuis (1975) and $f_w=0.32(a/k_s)^{-0.8}$ of Dixen et al. (2008).

5.6 Theoretical bed level

Opinions differ as to where the theoretical bed level of a rough bed is located. Following a suggestion of Einstein (1950), Sleath (1987) assumed that the theoretical bed level is located 0.35d below the crest level of roughness elements. Dixen *et al.* (2008) proposed an average value of 0.24d (see Section 2.8.4).

In order to obtain the shear stress and hence, the friction factor shown in Figure 5.10, the pressure on the spherical test element was integrated assuming that the theoretical bed level is located at 0.35d below the crest level of the roughness elements. That is, only the pressure data and surface area above this level were used in the calculation. Interestingly, the friction factor derived based on this assumption matched well with the equation, $f_w=0.33(a/k_s)^{-0.84}$ of Simons et al. (2000).

The tests of Simons *et al.* (2000) were conducted for a rough bed consisting of 2D roughness elements of 6mm square. They used the UCL shear cell to directly measure the shear stress. Also their equation matched well with the data of Kamphuis (1975) who used natural stones for the rough bed. Dixen *et al*. (2008) used ping-pong balls (glued to the flume bed) and natural stones for the rough bed and found the equation, $f_w=0.32(a/k_s)^{-0.8}$. Dixen *et al.* compared the relation with the data of Kamphuis (1975), Sleath (1987) and Simons *et al.* (2000) and found good agreement (see Figure 5.12).

In order to check the sensitivity of the assumed theoretical bed level on the results, the shear stress and hence, the friction factor was calculated

assuming that the theoretical bed level is located 0.25d below the crest level of the roughness elements as shown in Figure 5.13. The agreement of the data with the curves of Simons *et al.* (2000) and Dixen *et al.* (2008) was poor, with the data shifted to the lower part of the graph.

Therefore, this observation suggests that, for all roughness types (i.e., 2D roughness elements, natural rocks, spherical elements), the theoretical bed level is located 0.35d below the crest of the roughness elements.

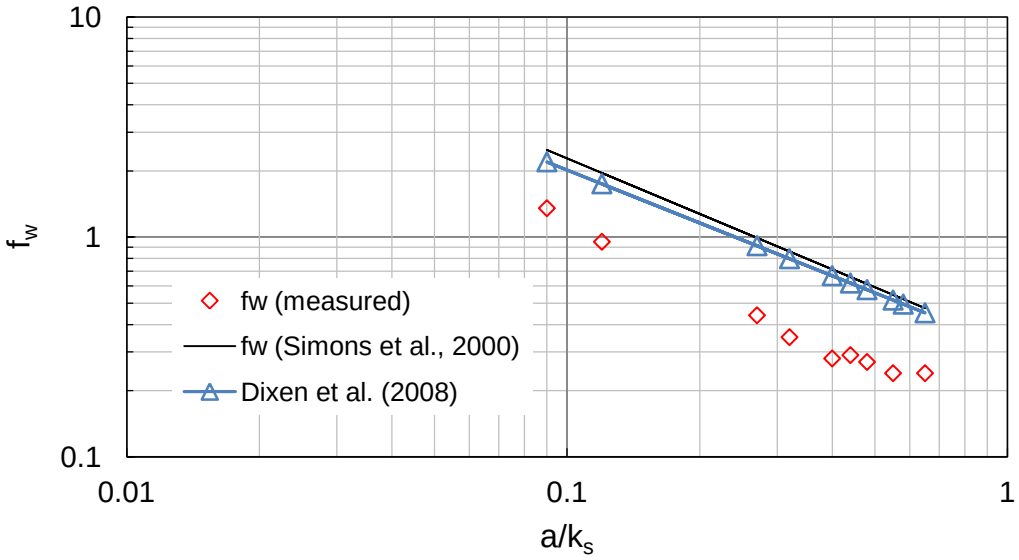

Figure 5.13: Measured friction factor based on pressure integration on a spherical bed element. Theoretical bed level was assumed at 0.25d below crest level of the roughness elements.

5.7 Variation of friction factor with Reynolds number

The wave friction factor is a function of both the relative roughness, a/k_s, and the flow Reynolds number, $Re=aU_m/\nu$ (see Section 2.9.6). The present experiments were conducted in the Re = 7.5 X 10^2 – 2 X10^4 range in the

rough turbulent flow regime, i.e. $u_* k_s/\nu \geq 200$ for $a/k_s \leq 100$ according to Kamphuis (1975).

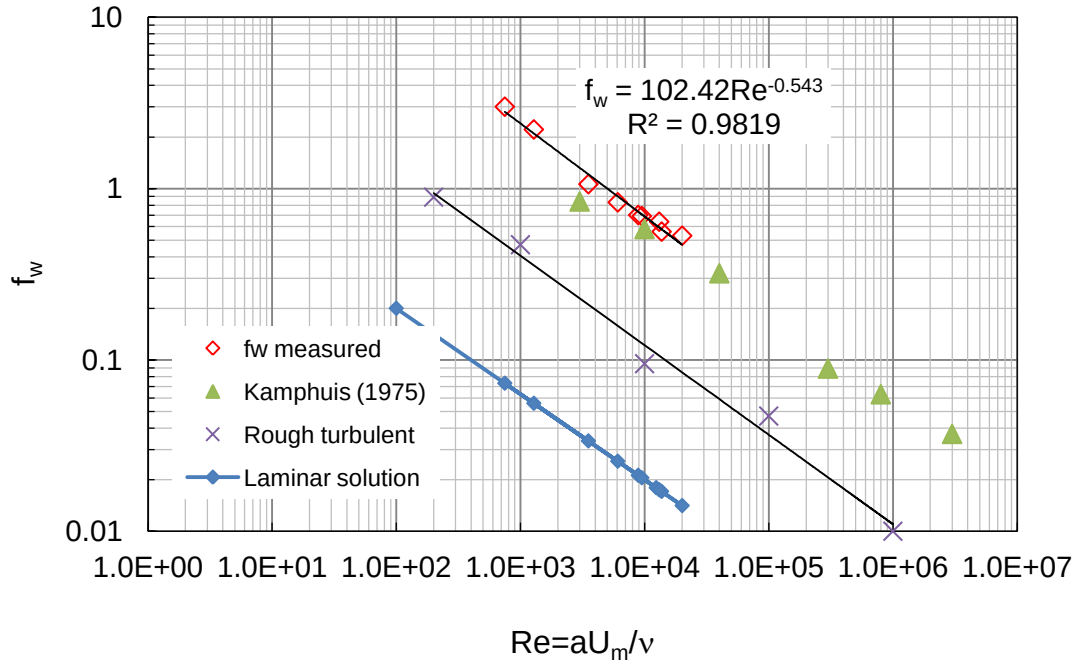

Figure 5.14: Measured friction factor against Reynolds number. Laminar solution is given by $f_w=2/\sqrt{Re}$. (x) – Lower limit of the rough turbulent flow region from Kamphuis (1975).

As shown in Figure 5.14, the f_w data of the present experiments were plotted against $Re=aU_m/\nu$. The friction factor for laminar flows, i.e., $f_w=2/\sqrt{Re}$ and the lower limit of the rough turbulent flow regime obtained from Kamphuis (1975) as shown in Figures 2.23 and 2.24 are also plotted on the same graph. The data of the present tests are located well above the lower limit for rough turbulent flow. They are also slightly above the test results of Kamphuis (1975) shown by triangles. A power relation for the variation of f_w with $Re=aU_m/\nu$ was established.

$$f_w = 102.42\, Re^{-0.543} \qquad (5.2)$$

5.8 Fluctuation in bed shear stress

The turbulent fluctuation in the measured bed shear stress, $\tau'=\tau-<\tau>$ was normalised using, $\tau_m=0.5f_w\rho U_m^2$ and plotted as shown in Figures 5.15 and 5.16. For steady flow, the r.m.s fluctuation, $(<\tau'^2>)^{1/2}/\tau_0$ is about 0.4, with the lower and upper limits of 0.3 and 0.6, respectively (Sumer *et al*., 2001). In the present tests for regular waves, the upper limit of $(<\tau'^2>)^{1/2}/\tau_m$ was found to be 0.28 and 0.44 for T=2 sec and T=1 sec waves, respectively. The relatively large r.m.s value $'$ for T=1 sec waves could be due to the rapid stirring effect by the shorter period waves. The peak in the r.m.s. fluctuation in the shear stress that occurred in the trough half cycle after the maximum horizontal deceleration, is slightly higher (about 5-8%) than during the crest half cycle as shown in Table 5.3.

Table 5.3: Maximum r.m.s.fluctuation in the shear stress.

Test	H (cm)	T (cm)	h (cm)	r.m.s. fluctuation in the shear stress, $(<\tau'^2>)^{1/2}/\tau_m$		% increase
				Crest	Trough	
PM2	8	1	40	0.42	0.44	4.8
PM7	8	2	40	0.26	0.28	7.7

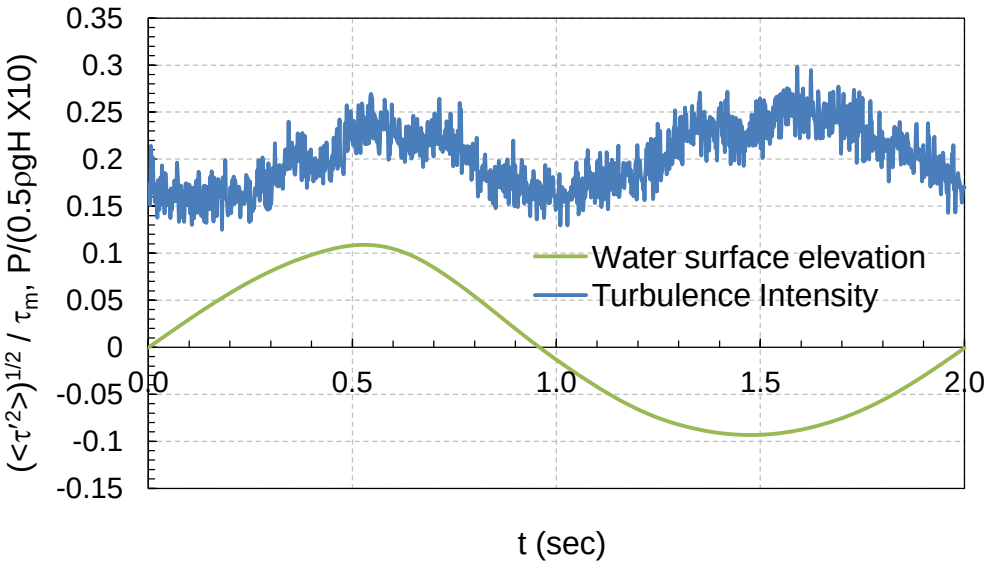

.

(a)

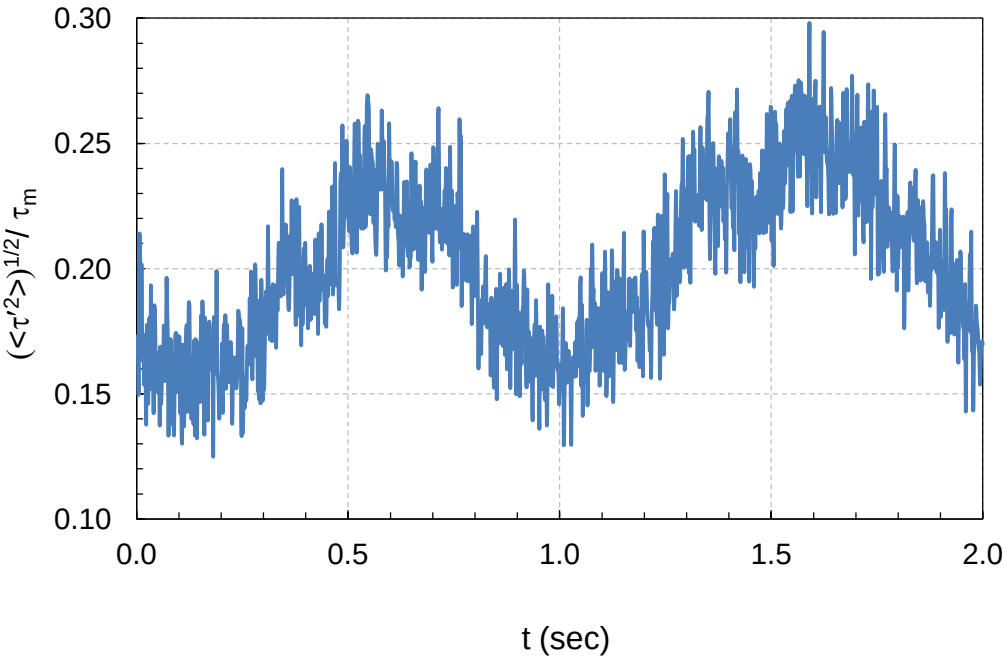

(b)

Figure 5.15(a),(b): Variation of $(<\tau'^2>)^{1/2}$during the course of the wave cycle. H=8cm, T=2 sec, h=40cm.

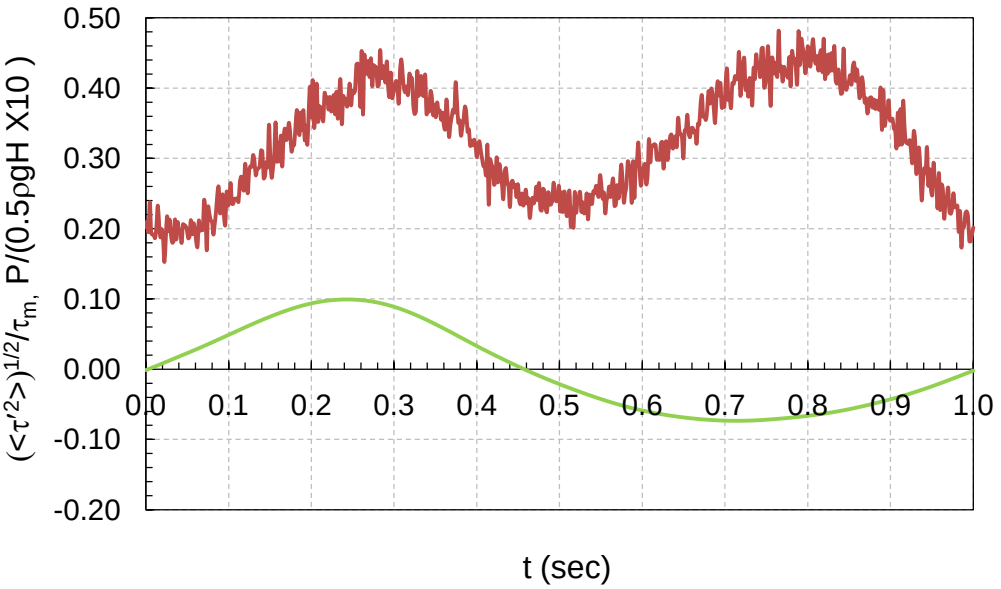

(a)

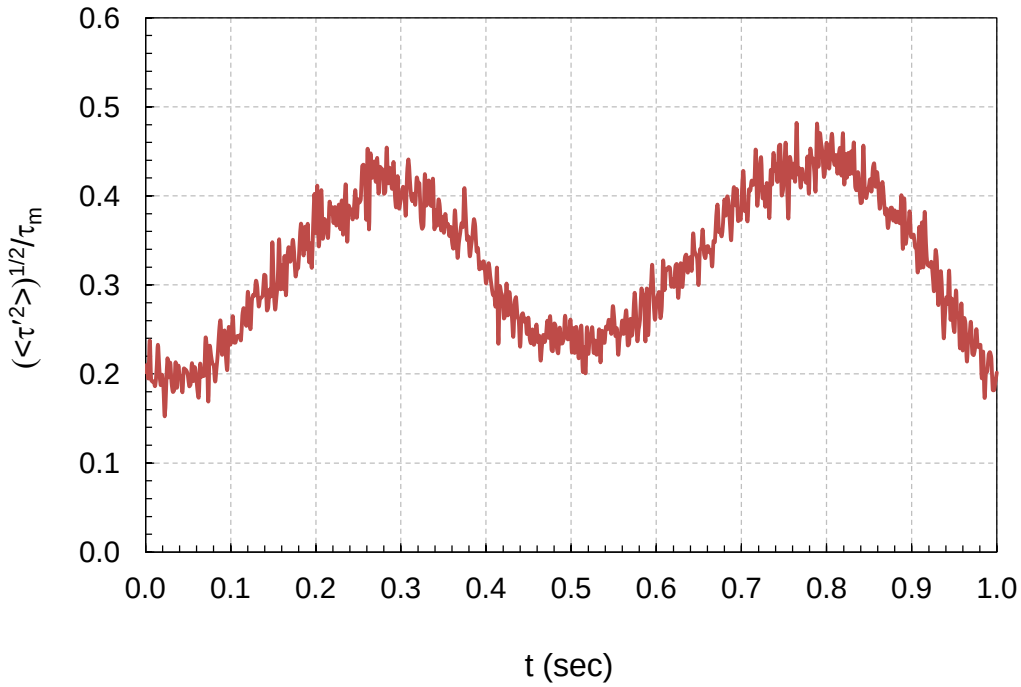

(b)

Figure 5.16(a),(b): Variation of $(<\tau'^2>)^{1/2}$ during the course of the wave cycle. H=8cm, T=1 sec, h=40cm.

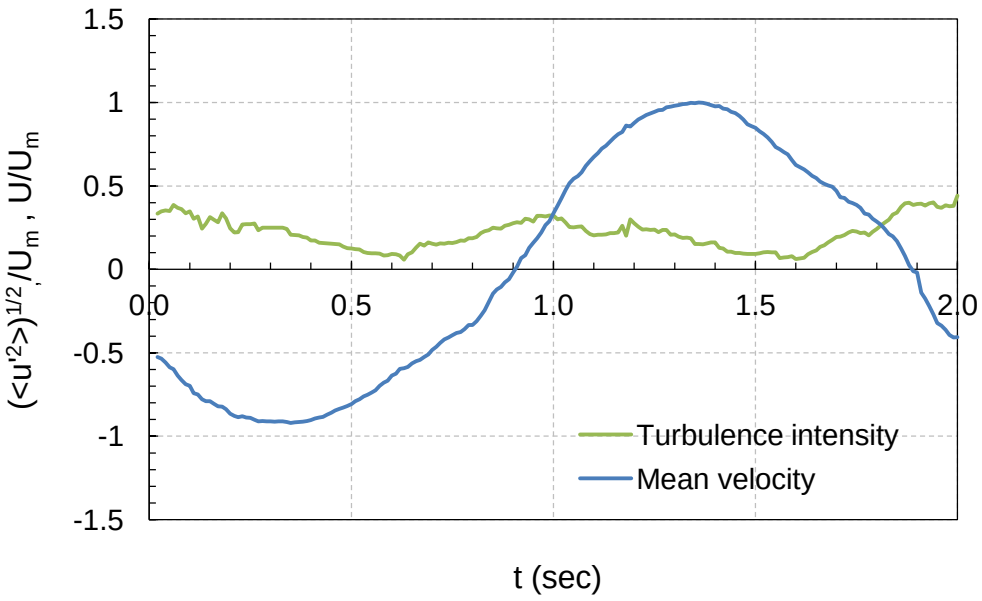

Figure 5.17: Variation of turbulence intensity ($\langle u'^2 \rangle)^{1/2}/U_m$ during the course of the wave cycle. H=8cm, T=2 sec, h=40cm. y=1mm above the bed.

Kemp & Simons (1982) observed that the horizontal component of the turbulence intensity is largest at the maximum horizontal deceleration during the decelerating part of the cycle with a small peak during the accelerating phase.

Figure 5.17 seems to agree with this observation. $(\langle u'^2 \rangle)^{1/2}/U_m$ reached a peak of 0.4 at the maximum horizontal deceleration. It was 0.28 at the maximum accelerating phase in the crest half cycle. This is an increase of approximately 43% in the turbulence intensity.

However, the corresponding peak in the r.m.s. shear stress fluctuation (see Figures 5.15 and 5.16) appears late in the record, i.e. about 60-90deg delayed, relative to the phase of the maximum horizontal deceleration.

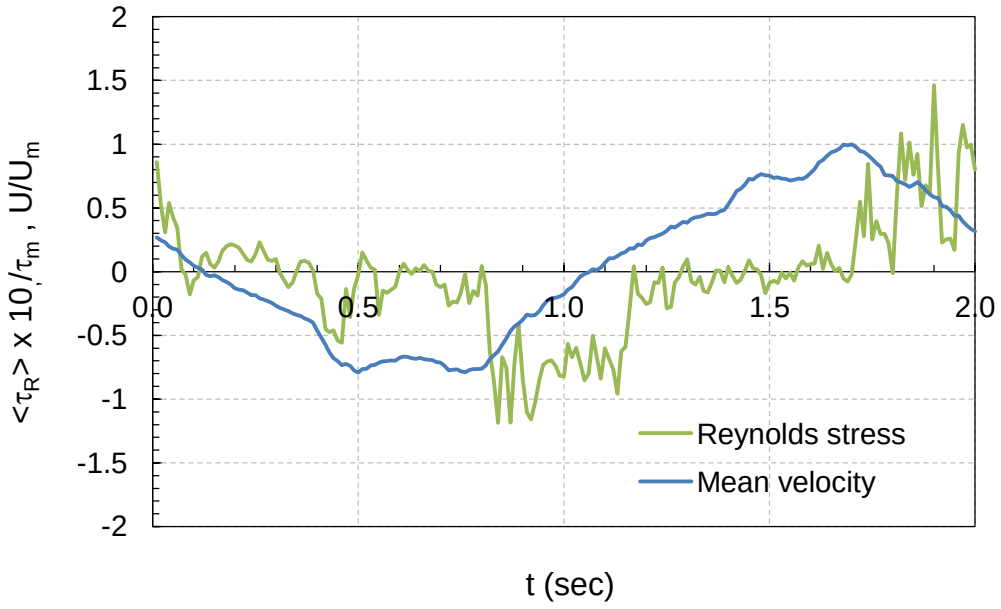

.

(a)

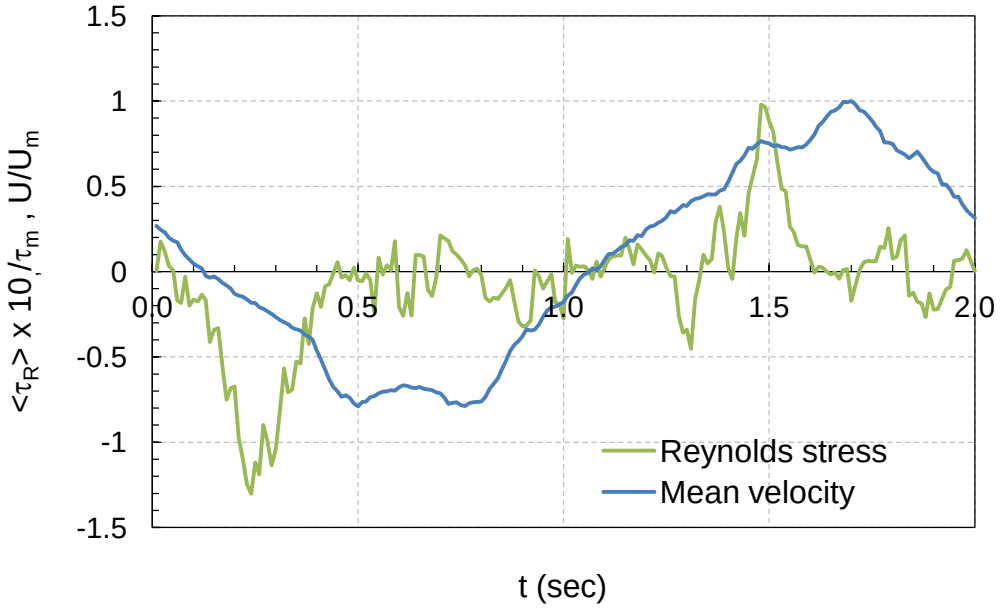

(b)

Figure 5.18(a),(b): Variation of Reynolds stress $<\tau_R>=-\rho<u'v'>$ during the course of the wave cycle. H=8cm, T=2 sec, h=40cm. y=1mm above the bed.

The Reynolds stress 1mm above the bed is shown in Figure 5.18. Large peaks in the Reynolds stress appear just after the flow reversal. It is larger during the deceleration phase and after flow reversal in the trough half cycle than in the acceleration phases closer to the bed and may reach 10 -15% of the peak shear stress amplitude, τ_m. Different shapes in the mean oscillatory velocity profiles observed in Figures 5.17 and 5.18 are due to the different points of measurement on the bed.

A 43% increase in the turbulence intensity near maximum deceleration and after flow reversal during the trough half cycle is quite significant for the stability of stone. One of the reasons for the increase in the turbulence intensity during the deceleration phases could be due to the bursting of turbulent ‘spots’ which is known to register shear stress magnifications as much as by a factor of 3 to 4. The emergence of turbulent ‘spots’ marks the onset of turbulence. For low Reynolds numbers these features appear during the late deceleration phase and can appear early (at the passage of the crest) for high Reynolds number flows (Carstensen, 2010).

Another reason could be due to the residual vorticity remaining from the late acceleration phases. Flow visualisation tests showed that the vortex ejection from the roughness elements occurs predominantly during the acceleration phases and this process is suppressed during the deceleration phases. The flow visualisation tests also suggested that the vortices can maintain their shape longer and return to the same position with the reversing flow.

5.9 PDF of shear stress fluctuation

The measured shear stress fluctuation, τ', during 50 wave cycles was fitted to standard normal distribution as shown in Figures 5.19. For the test PM7 for example, the number of data points in the sample were 62500 (i.e., 625Hz data sampling). It was found that for all tests, the shear stress fluctuation can be fitted to a standard normal distribution with good agreement.

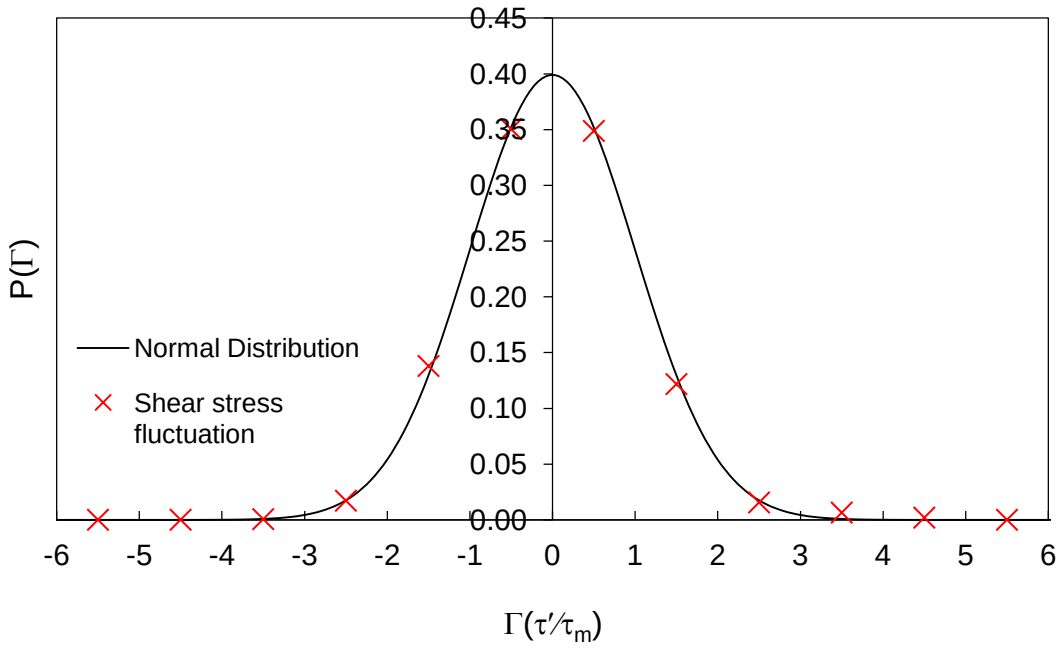

Figure 5.19(a): PDF of instantaneous shear stress fluctuation, τ'. H=8cm, T=2 sec, h=40cm. Skewness=0.34, Kurtosis=0.92.

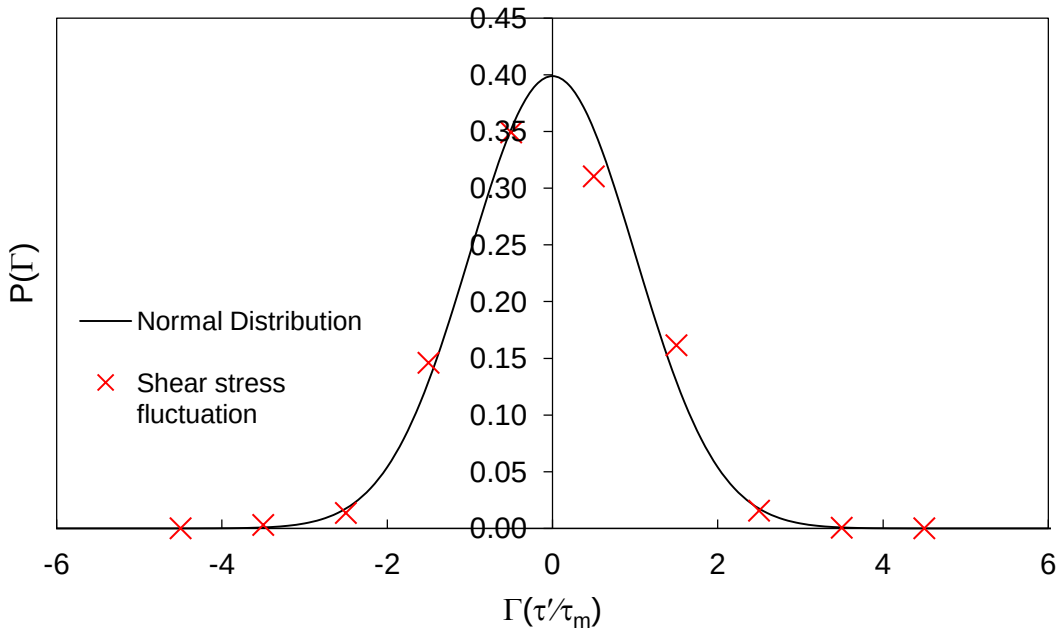

Figure 5.19(b): PDF of instantaneous shear stress fluctuation, τ'. H=8cm, T=1 sec, h=40cm. Skewness= -0.04, Kurtosis= -0.25.

Table 5.4: Statistics of shear stress fluctuation, τ'.

Test	H (cm)	T (s)	h (cm)	τ'/τ_m				$\Gamma=[(\tau'/\tau_m) - \mu]/\sigma$			
				min	max	μ	σ	min	max	μ_s	σ_s
PM2	8	1.0	40	-1.33	1.21	0.0	0.33	-3.99	3.64	0.0	1.0
PM3	8	1.6	40	-0.91	0.78	0.0	0.27	-3.42	2.92	0.0	1.0
PM7	8	2.0	40	-0.80	1.02	0.02	0.20	-4.02	4.92	0.0	1.0

Note: Sample duration = 50 wave cycles, sampling rate = 625Hz, $\tau'=\tau-<\tau>$, $\tau_m=0.5f_w\rho U_m^2$, μ = statistical mean, σ = standard deviation.

The average minimum and maximum values were found to be τ'/τ_m=-1.01 and τ'/τ_m=1.00. This means that the fluctuation in shear stress can be as large as the shear stress amplitude, τ_m itself. These intermittent peak turbulent events may occur only momentarily. However, their impact on the stability of the bed could be significant. The mean and standard deviation of

the normalised shear stress fluctuation (τ'/τ_m) were found to be 0 and 0.27 as an average of the above three tests.

5.10 PDF of normal stress fluctuation

The turbulent fluctuation of the normal stress, τ'_n/τ_m was also fitted to a standard normal probability distribution as shown in Figure 5.20. A summary of the parameters of the distribution is shown in Table 5.5.

Table 5.5: Statistics of normal stress fluctuation, τ'_n.

Test	H (cm)	T (s)	h (cm)	τ'_n/τ_m				$\Gamma=[(\tau'_n/\tau_m) - \mu]/\sigma$			
				min	max	μ	σ	min	max	μ_s	σ_s
PM2	8	1.0	40	-1.43	1.24	0.0	0.31	-4.63	4.02	0.0	1.0

Note: Sample duration = 50 wave cycles, sampling rate = 625Hz, $\tau'_n=\tau_n-<\tau_n>$, $\tau_m=0.5f_w\rho U_m^2$, μ = statistical mean, σ = standard deviation.

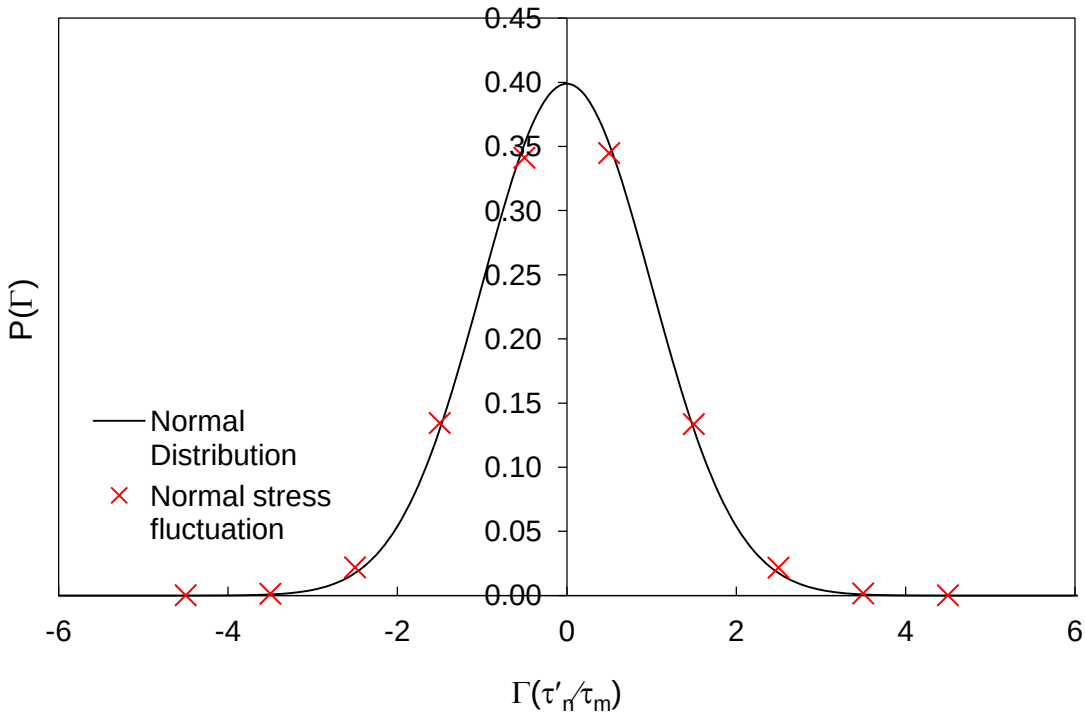

Figure 5.20: PDF of instantaneous normal stress fluctuation, τ'_n. H=8cm, T=1 sec, h=40cm. Skewness= 0, Kurtosis= 0.02.

5.11 Summary

In order to measure the wave-induced bed shear stress, researchers have previously used, turbulence measurements (i.e., Reynolds stress, momentum integration) and direct measurement using shear cell, hot film techniques etc. In the present study a different approach was adopted using direct measurement and integration of the pressure on the surface of a spherical element embedded in a coplanar bed of the same diameter spherical elements set in a hexagonal array. Based on the results of these experiments the following observations are made:

1 For regular waves, the measured mean shear stress profile agreed well with the sinusoidal relationship, $\tau_m = 0.5 f_w \rho U_m^2 \cos(\omega t)$.

2 The shear stress showed an average phase lead of between 62deg and 67deg relative to the water surface elevation for relative roughness, $a/k_s = 0.09 – 0.65$.

3 When viewed from the present knowledge, the measured shear stress profile exhibits characteristics of laminar flow, i.e., sinusoidal variation with a phase shift greater than 45deg (Nielsen, 1992). However, the existing parameters describing the shape and phase of the bed shear stress have been derived mostly indirectly, using turbulence measurements and not by pressure measurement on a bed element such as in the present tests. Therefore, further research on the shear stress at high Reynolds numbers using the present apparatus is required.

4 The measured wave friction factor data fitted well to the power relationship, $f_w=0.33(a/k_s)^{-0.9}$. Data also matched the equation, $f_w=102.42Re^{-0.543}$. This reconfirms the dependence of f_w on both the relative roughness and Reynolds number (aU_m/ν).

5 The measured wave friction factor data agreed well with the previous relationships of Kamphuis (1975), Simons *et al.* (2000) and the more recent work of Dixen *et al.* (2008).

6 Good agreement of the wave friction factor data with previous studies was obtained when the pressure was integrated above the theoretical bed level assumed to be located 0.35d below the crest level of the roughness elements. Previously published studies used various types of roughness elements (2D square roughness elements, natural stones, spheres). The agreement of the present data with previous studies on rough beds suggests that for all types of roughness, the theoretical bed is located 0.35d below the crest level of the roughness elements.

7 The maximum turbulent fluctuation in the shear stress, τ' is in the order of τ_m (i.e., $\tau'/\tau_m \cong 1.00$) with the possibility of reaching $1.5\tau_m$. The mean and standard deviation of the same parameter are 0 and 0.27 on average.

8 The turbulent fluctuation in the shear and normal stresses follows a normal probability distribution.

9 The maximum Reynolds stress occurs below the bed level and is only a fraction of the total shear stress, i.e., approximately 33% of the peak shear stress, τ_m. It is about 10-15% at the bed level.

10 The turbulence intensity is largest near the maximum horizontal deceleration in the crest half cycle and just after the flow reversal suggesting that the inception of turbulence occurs in this part of the wave cycle. The turbulence intensity increased 43% at the maximum horizontal deceleration compared to the value at maximum acceleration. Peaks in the Reynolds stress were observed just after the flow reversal in the trough half cycle and were larger in magnitude than in the other phases suggesting that bursting of turbulent ‘spots’ may have contributed to the intense turbulence.

11 The residual vorticity from the late acceleration phases, could also have contributed to the heightened turbulence levels during the deceleration phases.

12 The overall peak in the turbulent fluctuation in bed shear stress occurred closer to the trough of the wave. The r.m.s. value of the turbulent fluctuation in shear stress, τ', is between 5-8% higher at the trough than at the crest, showing a clear shift during the trough half cycle.

13 The methodology used in the present study, i.e., direct pressure measurement and integration on a sphere to find the net horizontal force per unit area, with the effective planar area of the test sphere

assumed as $2\sqrt{3}\ R^2$, gives consistent results compared with other studies that used different techniques to measure bed shear stress. In this instance forces measured at individual bed element level has been extended to find the average wave-induced force per unit area on the entire bed.

6 Incipient motion of idealised stones

6.1 Introduction

It is the primary objective of this research to study the effect of stone protrusion on the incipient motion of rock armour under regular waves. Tests were conducted in the wave-current flume at the UCL Fluid Mechanics Laboratory using the apparatus described in Chapter 3. Some preliminary tests on a coplanar bed were carried out in the Mechanical Engineering Fluids Laboratory. The bed consisted of loose glass marbles of 19mm diameter arranged in a hexagonal array. Rock armour was idealised using light weight spherical particles of different size and density. Spherical elements were chosen due to a number of reasons (i) the effect of shape can be removed from the test results (ii) forces on the element can be easily quantified (iii) the amount of stone protrusion can be accurately controlled in the experiments (iv) a sphere is the most unstable of all shapes and hence offers a bottom line for threshold shear stress. The test stone was supported on three 19mm acrylic spheres screwed to a circular disk which is, in turn, fitted flush with the flume bed. Waves were generated at two water depths, i.e., 30cm and 40cm. For a particular wave period, the wave height was gradually increased in 0.5cm increments until the test stone started rocking and then displaced from its pocket. The critical wave height and period at which the first stone movement occurred, was recorded to calculate the horizontal orbital velocity using linear wave theory and then the shear stress

via equation $\tau_m=0.5f_w\rho U_m^2$ was calculated also. Table 6.1 gives a summary of the test conditions.

Table 6.1: Incipient motion tests - summary of test parameters.

Parameter	**Range**
Water depth, h (cm)	30 and 40
Wave height, H (cm)	3.5 – 16.5
Wave period, T (sec)	1 – 2.5
Test stone size, d_1 (mm)	Acrylic - 9.5, 12.7, 15.9, 19, 25.3, 31.8 Other materials – 19
Specific gravity of test stone	1.19 – 2.65
Bed material size, d_2 (mm)	19 (glass marbles)

6.2 Stability of stones on a coplanar bed

Fluid exerts a major portion of the force on the projected part of a rock element above the mean bed level. In a coplanar bed, this projection or the protrusion is zero. This means that the force applied on a perfectly flat/levelled bed should be negligibly small (see Figure 4.16). Therefore, a coplanar bed, with little force to destabilise a stone and a large pivot angle, should be more stable than one having a finite stone protrusion.

To test this hypothesis, a number of tests were carried out for different wave conditions. The bed consisted of two layers of 19mm diameter glass marbles spread on a 90cm x 45cm area, whilst the test section consisted of 19mm acrylic spheres of specific gravity, s=1.19. The pressure on top of the

test element was measured using a Honeywell 40PC006G2A type transducer.

6.2.1 Test CP-1A: Coplanar bed of lightweight stones

It was observed that for varying wave heights, periods and water depths as shown in Table 6.2, the test elements were remarkably stable. In the absence of exposure to significant streamwise forces, the primary mode of stone entrainment in a coplanar bed should be by uplift. However, no such instability was observed for the lightweight elements with specific gravity of 1.19 for the applied Shields shear stress as high as 0.4. The test runs were carried out for a duration of 10-15 minutes.

6.2.2 Test CP-2A: Effect of stone density on stability

Two lightweight 19mm diameter spherical stones X, Y close to the neutral buoyancy condition with a specific gravity, s=1.04 were placed on the coplanar bed in place of two acrylic stones. The same test conditions as in the Test CP-1A were applied. The X,Y positions were also changed to different locations. However, the tests showed that the X,Y spheres were very stable for all test conditions.

6.2.3 Test CP-3A: Effect of sheltering by overlying elements

Several glass spheres with a specific gravity, s=2.65, were rested above the coplanar bed in an overlying position several diameters apart across the width of the test section so as not to influence each other. The aim was to see if the overlying glass spheres would have any effect on the lightweight

spheres (s=1.19) on the lee side in their wake. There was no change to the stable condition observed in test CP-1A for the test conditions.

Two glass spheres were then placed in front of the neutrally buoyant X,Y spheres (s=1.04) embedded in the top layer. The centre to centre distance between the overlying glass sphere and the neutrally buoyant one was 1.0d. On this occasion one of the X,Y spheres was displaced out of its pocket for the test condition, H=20cm, T=2 sec, h=30cm. Increasing the distance to 1.5d made the X,Y stones stable again.

This instability is considered to be due to the effect of the low pressure region developed in the wake behind the upstream glass sphere and also the uplift forces created by vortex shedding by the overlying glass sphere. Comparing the pressure time-series records with and without an upstream sphere, a sharp drop in peak pressure over the sheltered/hidden sphere was observed when an upstream overlying sphere was present.

The extraction of neutrally buoyant X,Y stones due to the influence of an upstream overlying glass sphere confirms that, given the right hydrodynamic conditions, the spheres would be displaced by uplift and there is no particular aspect of the apparatus that had made the spheres particularly stable in the previous tests.

6.2.4 Test CP- 4A: Effect of sphere roughness

Two spheres, 19mm diameter, were roughened by gluing sand onto their surfaces and placing them on the coplanar bed in place of the smooth

spheres. The aim was to investigate the effect of roughness on particle stability in a coplanar bed. A range of waves was then generated but there was no instability, even for waves with the highest horizontal orbital velocity.

6.2.5 Tests CP- 1B, 2B, 3B, 4B: Effect of bed arrangement

A series of tests were carried out using a cubic arrangement of the sphere matrix as opposed to the hexagonal arrangement in the previous tests. The tests carried out for same conditions as in the previous tests CP-1A,2A,3A,4A showed that there is no change to the observations made in a hexagonal bed arrangement and the coplanar bed is very stable for the cubic bed arrangement.

Table 6.2: Tests on a coplanar bed.

Test	H (cm))	T (s)	h (cm)	U_m (m/s)	a/k_s (-)	Re_d (-)	Re^* (-)	Re (-)	KC (-)	Ψ (-)
M.191007.A1	10	2	40	0.21	1.44	4069	1420	14601	23	0.158
M.191007.A2	10	1.1	40	0.14	0.51	2610	1411	3304	8	0.156
M.191007.A3	15	1.2	40	0.23	0.93	4374	1835	10122	15	0.263
M.191007.A4	20	1.7	40	0.40	2.30	7682	2198	44231	36	0.378
M.191007.A5	20	2	40	0.43	2.87	8138	2123	58402	45	0.353
M.191007.A8	10	1	40	0.12	0.39	2218	1336	2169	6	0.140
M.191007.A9	10	2	30	0.26	1.72	4883	1579	21027	27	0.195
M.191007.A10	15	2	30	0.39	2.58	7325	1997	47312	41	0.312
M.191007.A11	15	1	30	0.26	0.86	4852	2104	10379	13	0.346
M.191007.A14	10	1.7	30	0.25	1.41	4692	1652	16502	22	0.213
M.191007.A15	18	2.5	30	0.49	4.09	9273	2085	94771	64	0.340
M.191007.A16	18	1.7	30	0.44	2.53	8446	2322	53466	40	0.422
M.191007.A17	15	1.7	30	0.37	2.11	7038	2089	37129	33	0.341
M.191007.A18	15	0.8	30	0.17	0.45	3213	1820	3642	7	0.259
M.191007.A19	6	1	30	0.10	0.34	1941	1237	1661	5	0.120
M.221007.A4	10	1.3	30	0.22	0.94	4113	1712	9695	15	0.229
M.221007.A5	15	1.3	30	0.32	1.41	6169	2166	21814	22	0.367
M.221007.A6	10	1.1	30	0.19	0.70	3600	1700	6285	11	0.226
M.221007.A7	20	2	30	0.51	3.44	9767	2360	84110	54	0.436
M.221007.A8	18	2.5	30	0.49	4.09	9273	2085	94771	64	0.340
M.221007.A9	15	2.5	30	0.41	3.41	7727	1876	65813	54	0.275
M.221007.A10	18	2	30	0.46	3.10	8790	2220	68129	49	0.385
M.221007.A12	18	1.25	30	0.38	1.59	7222	2413	28740	25	0.455
M.221007.A13	15	1	40	0.18	0.59	3327	1691	4880	9	0.224
M.221007.A15	10	0.8	40	0.06	0.17	1179	1017	490	3	0.081
M.221007.A16	10	1.3	40	0.17	0.73	3183	1476	5808	11	0.170
M.221007.A17	15	1.36	40	0.26	1.20	4998	1881	14979	19	0.277
M.221007.A18	10	1.5	40	0.19	0.94	3564	1484	8402	15	0.172
M.221007.A19	15	2.5	40	0.34	2.84	6445	1688	45789	45	0.223
M.221007.A20	18	2	40	0.39	2.58	7325	1997	47306	41	0.312
M.221007.A21	15	2	40	0.32	2.15	6104	1797	32851	34	0.253

6.3 Variation of Shields critical shear stress with relative protrusion

In the preceding section, it was observed that a coplanar bed is remarkably stable. The results for the present tests conducted for varying finite protrusion levels under waves and published data for currents are shown in

Figure 6.1. The incipient motion data showed that the Shields critical shear stress has an exponential relationship (Figure 6.2) with the critical shear stress with the latter increasing when the relative protrusion decreased. The lowest critical shear stress was observed for a fully exposed stone (i.e. relative protrusion, p/d_1=0.82 and higher).

For relative protrusion values 0 (coplanar bed), 0.17 and 0.21 a stone was remarkably stable even for the largest shear stresses that could be produced in the wave flume (see Table 6.3). The stone started to move again when the relative protrusion was increased to 0.24. Therefore, the value of p/d_1=0.21 appears to be the threshold relative protrusion below which stones are stable. Therefore, the test results suggest that a 'no mobility' condition of a bed protection can be achieved when the relative protrusion is within the range $0<p/d_1<0.21$.

This finding is of significance in coastal engineering practice, i.e., if a rock armour scour protection can be levelled to an optimum protrusion of 0.21d or less, the bed damage can be reduced to a desirable level.

The present test results and the data of Fenton & Abbot (1977) and Chin & Chiew (1993) for uni-directional currents were plotted on the same Figure 6.1, for comparison. In particular, the study of Chin & Chiew (1993) used an apparatus similar to the present research with spherical glass and steel particles as test stones. The incipient motion data for waves in the present tests lie above the data for currents. This seems to suggest, from a first observation, that stones are more stable under the action of waves.

Table 6.3: Incipient motion of stones of relative protrusion $0<p/d_1<0.24$. $d_1=d_2=19mm$, specific gravity =1.19 (acrylic).

Test no.	p/d_1 (-)	H (cm)	T (s)	h (cm)	U_m (cm/s)	Ψ_{cr} (-)	Re (-)	Re_* (-)	Re_d (-)	Remarks
W5	0.24	13.5	2.5	30	36.6	0.24	1.1×10^5	1454	6954	Displaced
W6	0.24	14.5	2.0	40	31.1	0.24	5.0×10^4	1675	5890	Displaced
W110908.10	0.21	13	2	40	27.8	0.21	4.0×10^4	1647	5269	Stable
W110908.11	0.21	12	2.5	40	27.1	0.17	5.7×10^4	1478	5137	Stable
W110908.4	0.17	13	2	40	27.8	0.21	4.0×10^4	1647	5269	Stable
W110908.6	0.17	12	2.5	40	27.1	0.17	5.7×10^4	1478	5137	Stable
B2.221007.A8	0	18	2.5	30	48.8	0.34	2.0×10^5	2076	9229	Stable
B2.221007.A9	0	15	2.5	30	40.6	0.27	1.4×10^5	1868	7691	Stable

However, it appears that, rather than inherent differences in the flow structure of waves and currents as assumed at the beginning of this research, this discrepancy is due to the effect of the chosen model scale that has contributed to laminar flow effects resulting in the apparent stability of stones under waves.

There exists a unique curve for each wave period (Figure 6.*2*). When, the magnitude of the wave period is increased, the curves appear to flatten and fall back on the position for currents. The difference in the wave and current curves is smallest for a fully exposed stone ($p/d_1> 0.82$). When the relative protrusion decreased, the two curves diverged.

In the wave flume the maximum sustainable wave period that can be generated without breaking due to spilling was 2.5 seconds (Simons *et al*., 2000 mentioned a working range of 0.8 - 3.0 sec). Moreover, the wave generator became unstable leading to sudden stoppage at wave periods larger than 2.5 sec. Therefore, tests were limited to wave periods of 1 – 2.5

seconds. The flow visualisation tests described in Chapter 7 show that for smaller particles of the order of 19mm diameter, under the wave periods used, the flow is not fully developed (see Figures 7.23-727). That is, flow reversal occurs before the separation and detachment of the lee-wake vortices (before turbulent separation).

Therefore, the behaviour shown under waves in the present tests, and which contrasts with currents, is related to the insufficient flow development due to (i) rapid flow reversal (ii) reduced size of the protruding element (iii) Reynolds number flow regime at the inception of motion – for a light weight fully exposed particle of the same diameter at laminar (unseparated) flow, the critical shear stress reached a high 0.1 (tests W128 and W129) whereas for glass marbles at relatively high Reynolds number a critical shear stress of 0.02-0.03 was observed (tests W113 and W116 – see Table 6.4).

The longer the wave period, the flatter is the Ψ_{cr} vs p/d_1 curve. The curve for waves approaches the position of the current for larger wave periods. Therefore, extrapolating to conditions typical to those experienced in engineering practice where longer wave periods often exceeding 8 seconds and fully developed rough turbulent flow exists, the curves of Fenton & Abbot (1977) and Chin & Chiew (1993) derived for currents should be applicable.

Table 6.4: Incipient motion of stones - test results.

Test	p/d_1 (-)	d_1 (mm)	s (-)	H (cm)	T (s)	h (m)	U_m (m/s)	a (mm)	a/k_s (-)	f_w (-)	Ψ (-)	Re_* (-)	KC (-)
W5	0.24	19	1.19	13.5	2.5	0.3	0.36	143	3.0	0.13	0.238	1454	47
W6	0.24	19	1.19	14.5	2	0.4	0.31	99	2.1	0.18	0.243	1675	33
W7	0.24	19	1.19	13	2.5	0.4	0.29	117	2.5	0.15	0.189	1477	39
W10	0.32	19	1.19	13.5	2.5	0.3	0.36	143	3.0	0.13	0.238	1574	47
W11	0.32	19	1.19	11.5	2.5	0.4	0.26	103	2.2	0.17	0.164	1305	34
W17	0.40	19	1.23	14	2	0.4	0.30	95	2.0	0.18	0.196	1699	32
W18	0.41	19	1.36	12.5	2	0.4	0.27	85	1.8	0.20	0.108	1616	28
W19	0.41	19	1.2	10.5	2	0.4	0.22	72	1.5	0.23	0.159	1461	24
W20	0.41	19	1.19	9.5	2	0.4	0.20	65	1.4	0.25	0.149	1379	21
W21	0.41	19	1.38	14.5	2	0.4	0.31	99	2.1	0.18	0.121	1762	33
W22	0.41	19	1.19	10.5	2	0.4	0.22	72	1.5	0.23	0.167	1216	24
W31	0.51	19	1.19	14	1	0.3	0.24	38	0.8	0.40	0.320	1728	13
W32	0.51	19	1.19	11	2	0.3	0.28	90	1.9	0.19	0.218	1426	30
W33	0.51	19	1.19	9	2	0.4	0.19	61	1.3	0.27	0.140	1142	20
W34	0.56	19	1.19	13	1	0.3	0.22	35	0.7	0.42	0.293	1613	12
W35	0.56	19	1.19	10.5	2	0.3	0.27	86	1.8	0.20	0.206	1352	28
W36	0.56	19	1.19	15	1	0.4	0.18	28	0.6	0.52	0.224	1408	9
W37	0.56	19	1.19	8.5	2	0.4	0.18	58	1.2	0.28	0.131	1076	19
W38	0.56	19	1.19	7	2.5	0.4	0.16	63	1.3	0.26	0.092	904	21
W39	0.60	19	1.23	13	1	0.4	0.15	24	0.5	0.58	0.159	1531	8
W40	0.60	19	1.23	7.5	2	0.4	0.16	51	1.1	0.31	0.095	1183	17
W41	0.60	19	1.36	9.5	2	0.4	0.20	65	1.4	0.25	0.078	1379	21
W53	0.61	19	1.19	9.5	2	0.3	0.24	78	1.6	0.22	0.184	1310	26
W113	0.81	19	2.65	14	2.5	0.3	0.37	148	3.1	0.13	0.029	1565	49
W116	0.81	19	2.65	12.5	2.5	0.4	0.28	112	2.4	0.16	0.021	1298	37
W128	0.82	19	1.19	5	1	0.3	0.09	14	0.3	0.95	0.097	977	4
W129	0.82	19	1.19	4.5	1.3	0.3	0.10	20	0.4	0.68	0.091	946	7

$k_s = 2.5d_2$, d_2=19mm. This Table contains only data for d_1=19mm. Complete list of the tests is provided in Appendix-B.

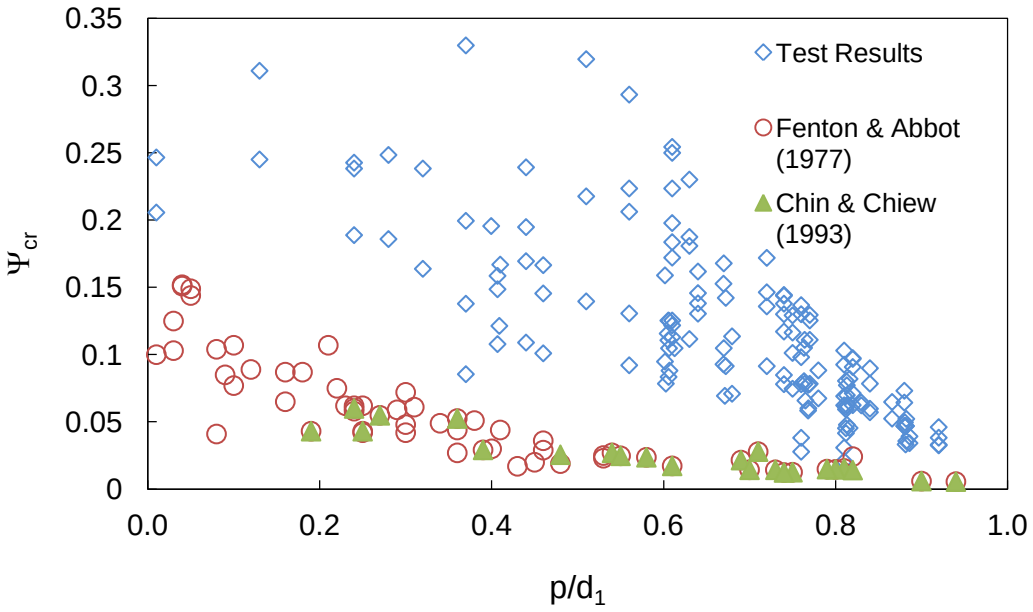

Figure 6.1: Variation of critical shear stress with stone protrusion. Data for uni-directional currents from Fenton & Abbot (1977) and Chin & Chiew (1993) are also plotted in the same figure for comparison.

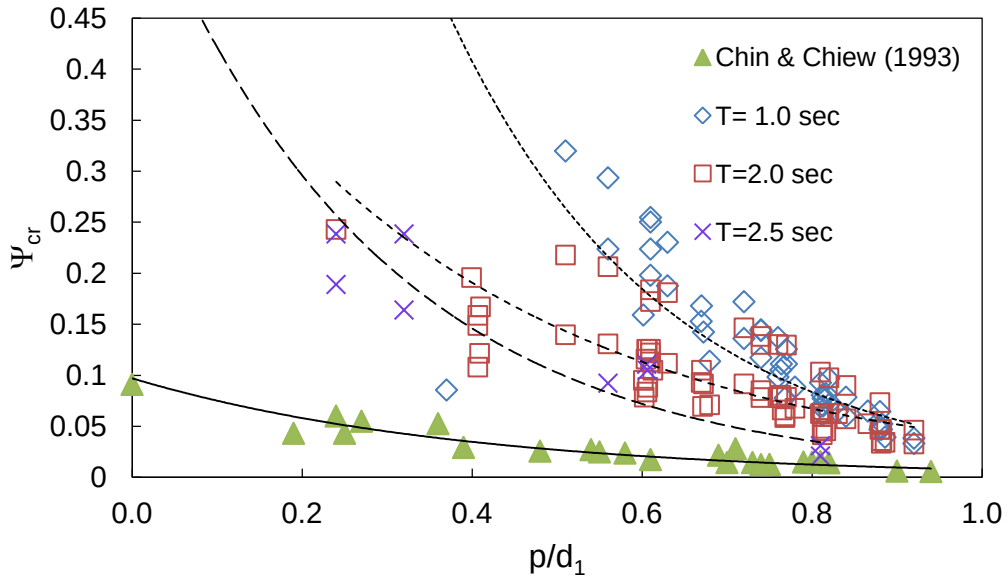

(a)

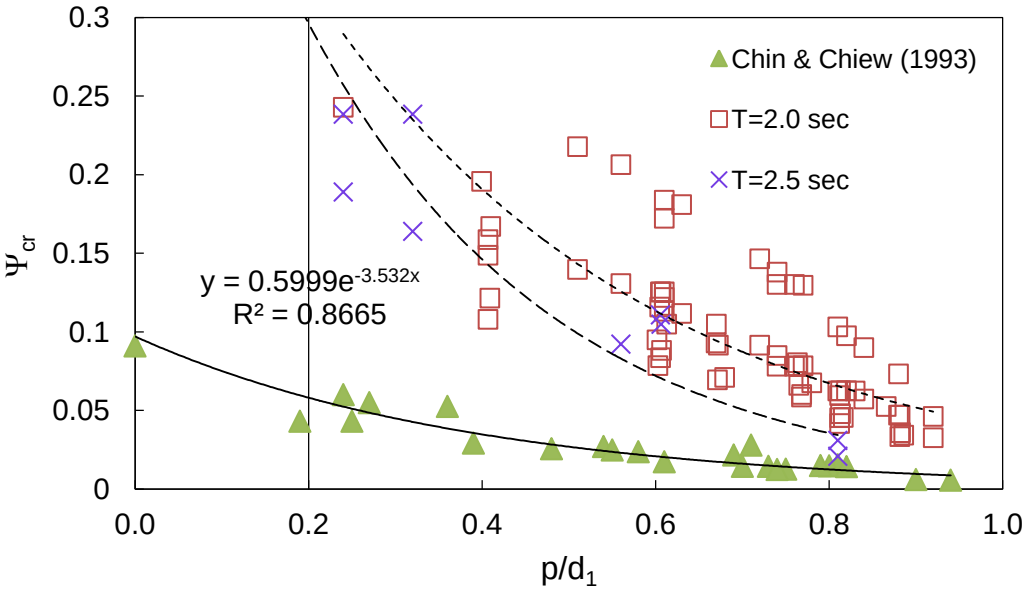

(b)

Figure 6.2a,b: Critical shear stress data for different wave periods and for currents (Chin & Chiew, 1993) fitted to exponential equation.

Figure 6.1 shows wide scatter of data. This is due to factors like different wave periods, water depths, stone size, density etc. The Shields critical shear stress was slightly modified to reduce this scatter based on consideration of turbulence length scales. It is known from existing literature that large scale turbulent sweep events are primarily responsible for the displacement of stones.

The orbital amplitude, “a” has the length scale of the wave-induced turbulence. It is also known from the work of various researchers (Nezu & Nakagawa, 1993; Davidson, 2004; Hofland, 2005), that the large scale turbulent eddies that cause stone displacement have a length scale of the order of the water depth, “h”. A modification to the critical shear stress, introduced using water depth, appeared to reduce the scatter to some extent (see Figure 6.3). Therefore, the following modified Shields parameter is proposed:

$$\Psi'_{cr} = \sqrt{\Psi_{cr} \frac{h}{d_1}} \qquad (6.1)$$

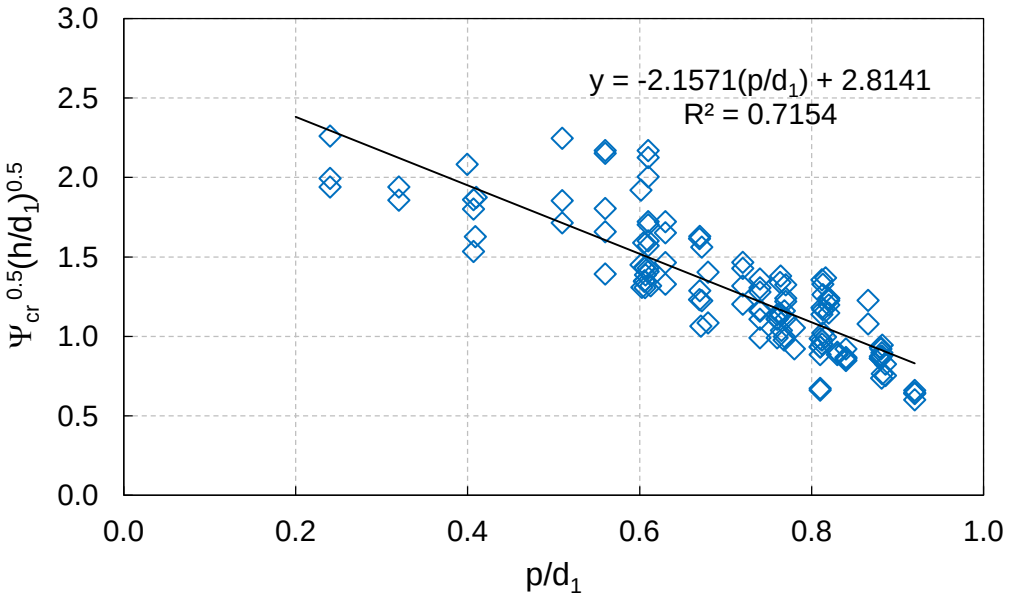

Figure 6.3: Modified Shields critical shear stress against relative protrusion.

6.4 Effect of stone size

In the tests to measure threshold stone displacement, a solid test sphere with diameter d_1, was placed over the interstice formed by three spheres of diameter, d_2=19mm. The supporting spheres themselves were located in part of a rough bed of 19mm glass marbles forming a hexagonal matrix. The tests can be divided into two types based on particle size.

I. The diameter of the test sphere is equal to or larger than the diameter of the spherical elements forming the rough bed, i.e. $d_1 \geq d_2$.

II. The diameter of the test sphere is equal to or smaller than the diameter of the spherical elements forming the rough bed, i.e. $d_1 \leq d_2$.

The tests described in the preceding sections refer to the test type (I). The data for test particles smaller than the bed material (d_2=19mm) are plotted

as a separate data set in Figure 6.4. They show significant scatter particularly for small relative protrusion levels less than 0.5. Test particles displaced even when the relative protrusion was in the region between 0 and 0.2, where no mobility was observed for larger particles (i.e. $d_1>d_2$).

The increased scatter of data indicates that, for smaller stones, in addition to the shear stress in the streamwise direction, there is another mechanism involved in the displacement of particles. This can be due to the increasing influence of the normal stress (uplift) as the dominant force as opposed to the shear stress at the moment of entrainment. This is because hiding increases due to small stone size and decreasing protrusion, reducing the exposed frontal area for the fluid to act on.

Moreover, the pivot angle becomes larger for small particles, increasing the stone's resistance to displace by rolling over another stone. Therefore, the main mode of displacement for smaller stones should be by uplift motion.

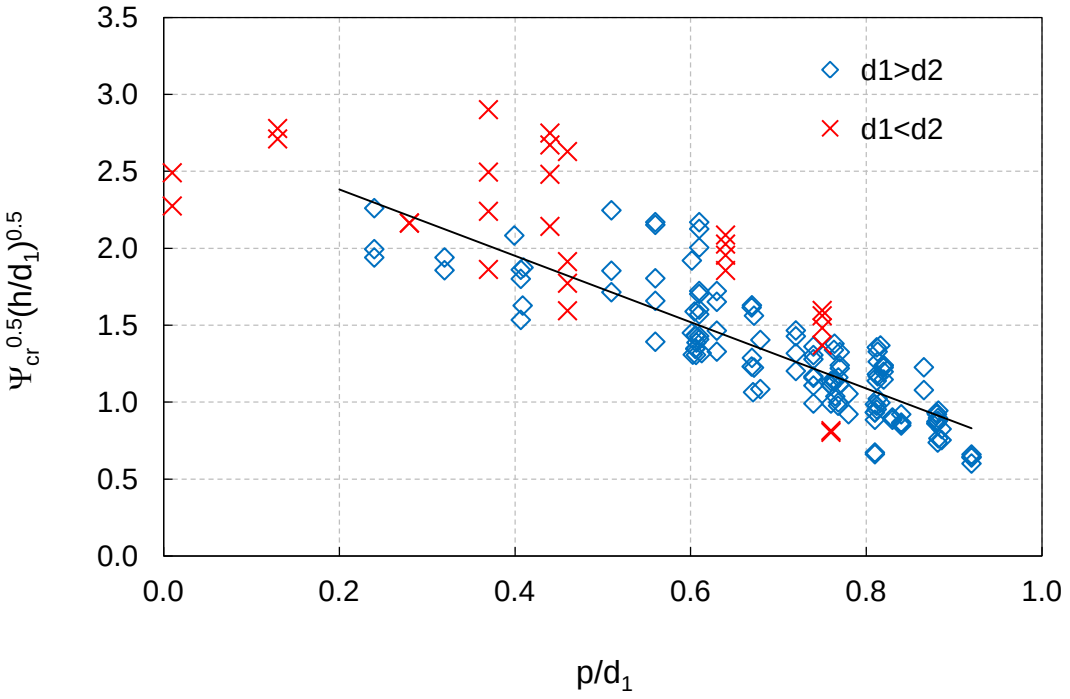

Figure 6.4: Modified Shields critical shear stress against relative protrusion. (X)- Acrylic particles of diameter, d_1=9.5, 12.7, 15.9, 16mm, specific gravity =1.19, (◊) – particles of various specific gravity, s=1.19-2.65, d_1=19, 25.3, 31.8mm. Particle size of bed material, d_2=19mm.

6.5 Effect of the flow regime

In addition to the wave period, the strength of the flow and turbulence (reflected in the flow Reynolds number, $Re=aU_m/\nu$ and $Re_d=U_md/\nu$) is of importance. For example, as shown in Table 6.5, fully exposed particles of the same size and relative protrusion (d_1=19mm, $p/d_1\cong0.82$) and different density materials showed different Shields critical shear stress values. This is because, for a light weight acrylic particle, the flow strength at stone displacement (i.e., Re = 6361, Re_d=2686) was less than that for a Glass marble (i.e., Re = 31798, Re_d=5371). That is, the flow strength is an order of magnitude larger for glass marbles. For higher Reynolds number flow just

prior to stone displacement, turbulent flow separation on the glass sphere would have occurred resulting in increased form drag being exerted compared to an acrylic sphere.

Fenton & Abbot (1977) used two test spheres of 3.8cm diameter by filling table tennis balls with homogeneous mixtures of lead shot, polystyrene grains and sand. Chin & Chiew (1993) used 16.5mm diameter glass marbles and steel balls with diameters between 6.3-13.5mm. The results of the present tests and the published data from the above authors for currents are compared in Table 6.5.

Table 6.5: Reynolds number at threshold stone movement for a fully exposed stone.

Details of the test	Present Tests with regular waves			Uni-directional current	
	acrylic	PVC	glass	Fenton & Abbot (1977)	Chin & Chiew (1993)
Test no.	W130	W127	W116	C3	M7
d1(mm)	19	19	19	38	16.5
d2(mm)	19	19	19	38	16.5
s (-)	1.19	1.4	2.65	-	2.64
p/d1 (-)	0.82	0.82	0.81	0.82	0.81
$Re=aU_m/\nu$ (-)	6361	6169	31798	-	-
Re* (-)	980	1106	1298	1760	1009
$Re_d=U_md/\nu$ (-)	2686	2645	5371	-	-
KC (-)	15	15	37	-	-
Ψ_{cr} (-)	0.097	0.045	0.021	0.0104	0.0154

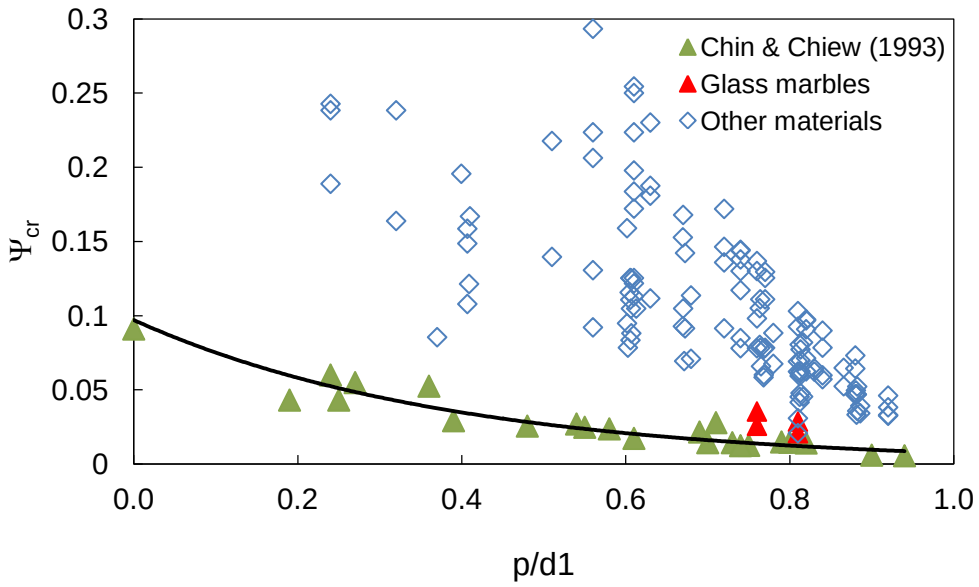

Figure 6.5: Threshold shear stress for glass marbles (in red) compared with currents.

For a relative protrusion of ≅0.82 under currents, the Shields critical shear stress for marbles of different material density lies very close to 0.01. In the present tests, the threshold stress for glass marbles lies within 0.02-0.03, which is closer to data for currents. The Reynolds number (Re_d) at the first displacement is larger for glass than for other light weight particles (Figure 6.7).

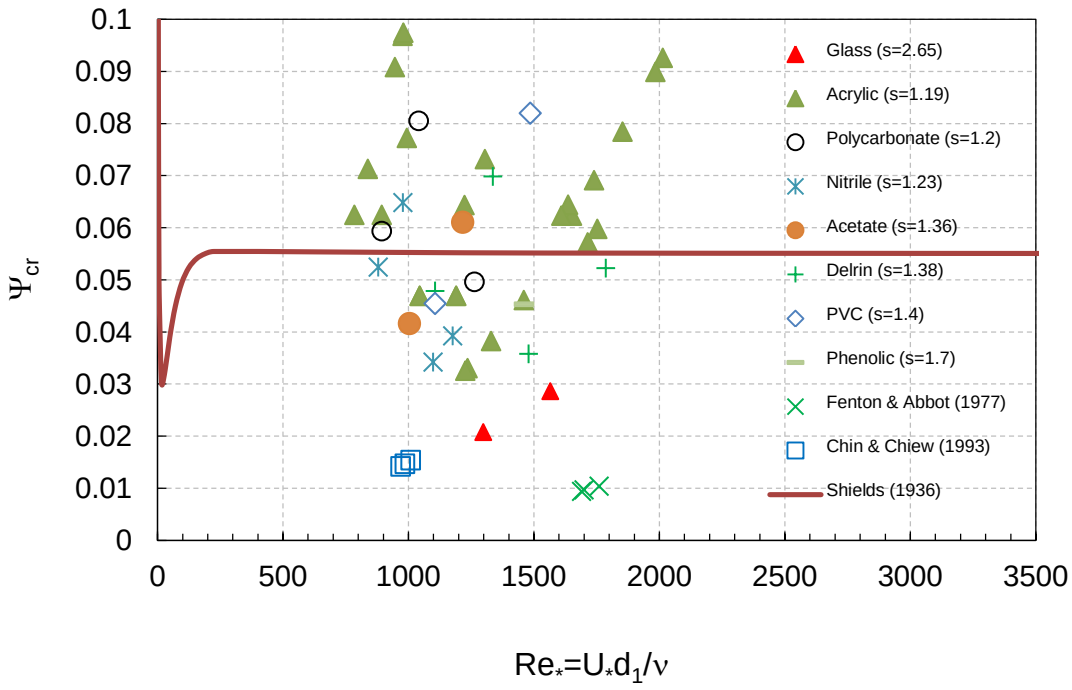

Figure 6.6: Shields critical shear stress against particle Reynolds number, Re, for the present tests and for uni-directional currents (Fenton & Abbot, 1977; Chin & Chiew, 1993). Fully exposed particles (p/d_1=0.82).*

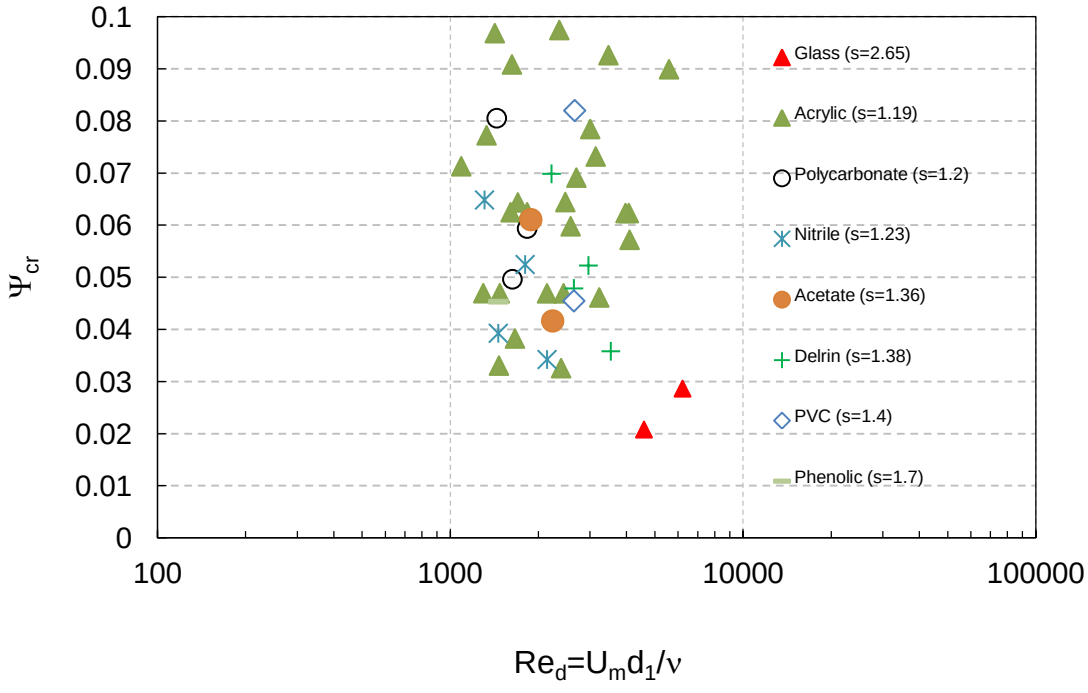

Figure 6.7: Shields critical shear stress against Reynolds number, Re_d, for the present tests and for uni-directional current (Fenton & Abbot, 1977; Chin & Chiew, 1993). Fully exposed particle (p/d_1=0.82).

Laminar flow separation on a free sphere occurs at $Re_d \approx 1000$ at 80^0 from the front stagnation point. As shown in Figure 2.28, the transition from laminar to turbulent flow occurs at a critical Reynolds number, Re_d=2000. About half of the data set lies within the laminar flow region ($Re_d < 2000$) where the drag coefficient is dependent on the Reynolds number (Schlichting, 1968; Massey & Ward-Smith, 1998). The majority of the data lies in the region Re_d=1000 – 3000 and, therefore, should be in the laminar or transition flow regions.

The Reynolds number, $Re_d=U_m d/\nu$ is based on the maximum orbital velocity, U_m, which is achieved only momentarily. A good portion of the wave half cycle is, therefore, under lower velocities. Given the short time period of the oscillatory flow (1-2.5 sec) the flow reverses before the flow separation.

As can be seen from the flow visualisation tests in Chapter 7, flow separation and a clearly defined lee-wake region was not established for a 19mm diameter fully exposed spherical stone (see Section 7.4.1). One can only see an upward directed residual vorticity structure on top of the sphere instead of a wake region on the downstream side as observed for a free sphere under steady flow (Figures 2.25 and 2.26).

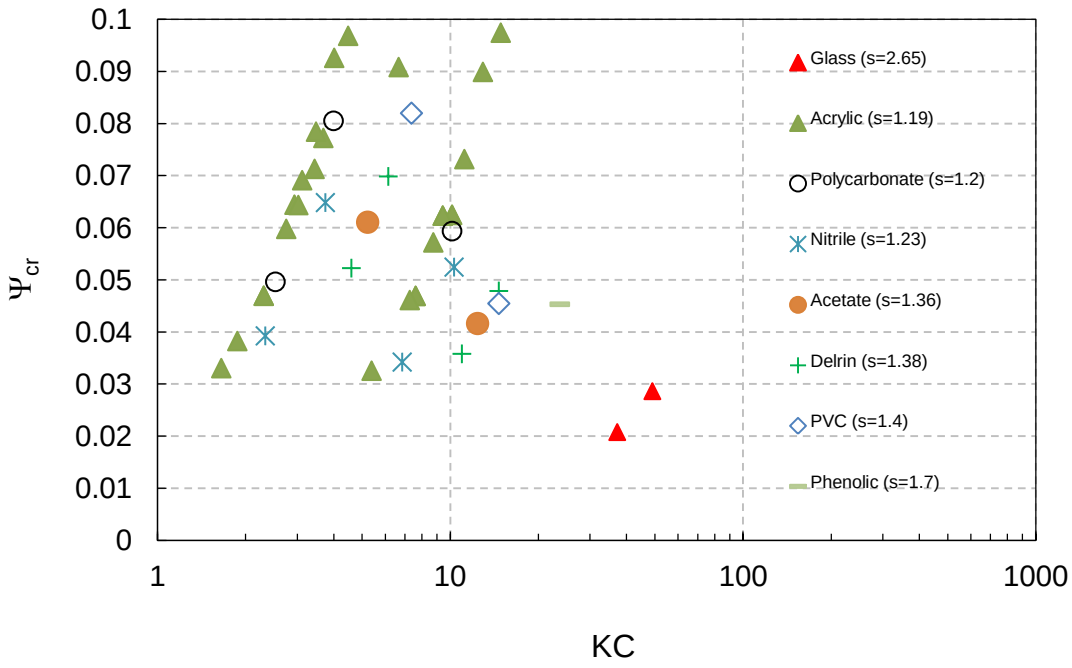

Figure 6.8: Shields critical shear stress against KC number for the present tests. Fully exposed particle (p/d_1=0.82).

The majority of the data lies in the region KC<10 (Figure 6.8). Flow separation will be inhibited when the KC number is low.

Therefore, the apparent stability of stones (high Shields critical shear stress) observed for waves in the present tests, is due to the lack of flow development. At high Reynolds numbers, the Shields critical shear stress should reach that observed for currents.

6.6 Applicability of test results under field conditions

Shields (1936) found that the non-dimensional critical shear stress remains constant (Ψ_{cr}=0.06) for fully rough turbulent flow (Re*>1000). However, Fenton & Abbot (1977) suggested that this critical value is dependent on the

particle protrusion above mean bed level and for a fully exposed stone, the threshold stress must be as low as 0.01. Therefore, for higher Reynolds number flows the shear stress should be independent of the Reynolds number.

The Shields parameter (Ψ) for typical field conditions and test data are compared with the Shields curve (Figure 6.9). Re* for typical field conditions vary from 1.8 X 10^5 to 2.5 X10^5. Present experiments were in the range Re*= 800 – 2200 (i.e., order of 10^3) and D* =200-450. Most of the previously published incipient motion data for waves, correspond to D*<700 (see Figure 2.5, Soulsby & Whitehouse, 1997). Based on Shields (1936), it has been widely assumed in the literature that the critical shear stress is constant when Re* $\rightarrow\infty$ and hence, laboratory results for Re*>1000 have been extrapolated to field conditions. The majority of the data in the present tests are in the region Re*>1000.

However, most of the test results, except for the glass spheres, exhibit the characteristics of laminar flow. Low values of critical shear stress as obtained for currents, can be observed for large period waves for which fully developed flow conditions will be achieved. Therefore, data for high Reynolds number flow, i.e. glass marbles, from the present tests are valid for field conditions.

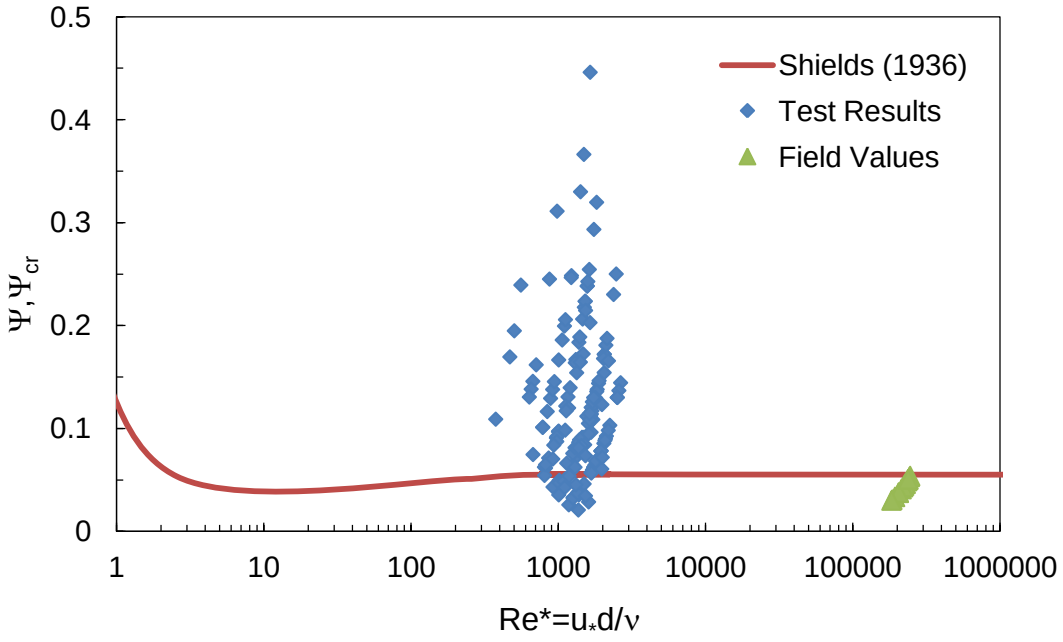

Figure 6.9: Shields parameter values for typical field conditions.

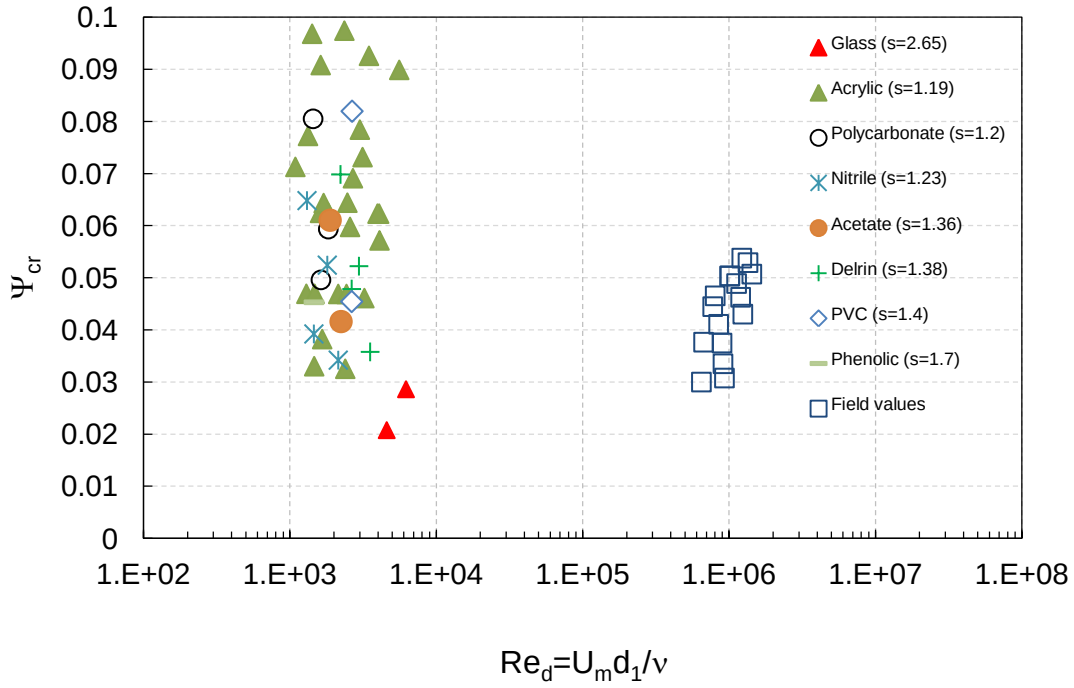

Figure 6.10: Shields parameter values for typical field conditions.

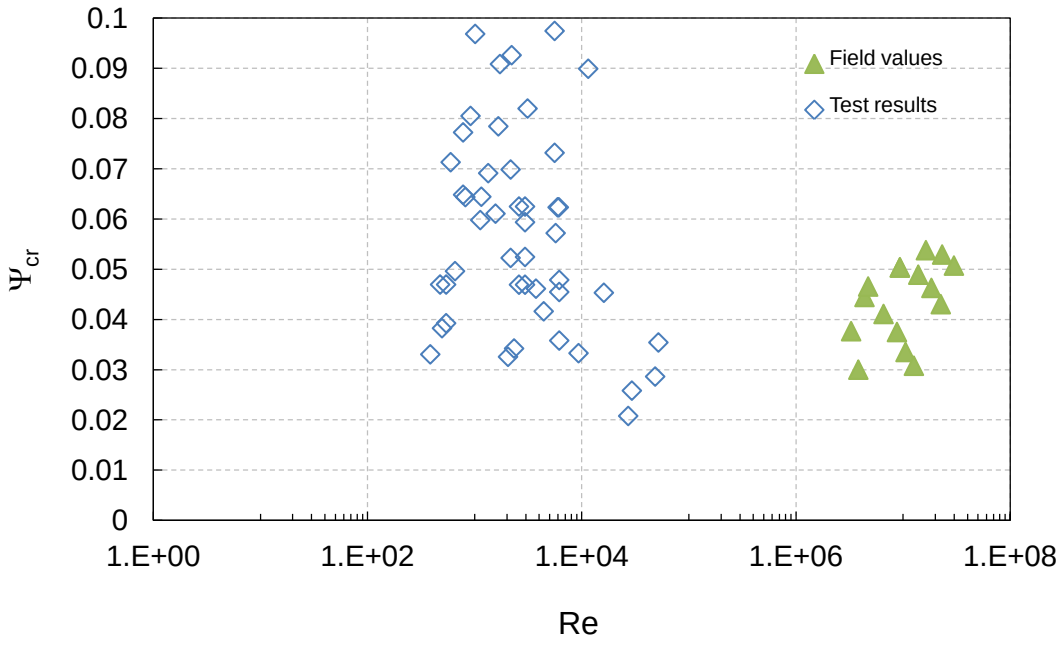

Figure 6.11: Shields parameter values for typical field conditions.

Table 6.6: Typical flow parameters under field conditions.

H (m)	T (s)	h (m)	U_m (m/s	a (m	d (m)	k_s (m	a/k_s (-)	f_w (-)	Re_d (-)	Re* (-)	Re (-)	KC (-)	Ψ (-)
2.5	10	5	1.6	2.6	0.4	1.1	2.3	0.1	6.5E+0	1.8E+0	3.8E+0	37	0.0
5	8	10	2.0	2.5	0.4	1.1	2.2	0.1	7.7E+0	2.2E+0	4.4E+0	35	0.0
5	10	10	2.1	3.4	0.4	1.1	3.1	0.1	8.5E+0	2.1E+0	6.6E+0	49	0.0
5	12	10	2.3	4.3	0.4	1.1	3.9	0.1	9.0E+0	2.1E+0	8.8E+0	62	0.0
5	14	10	2.3	5.1	0.4	1.1	4.6	0.0	9.1E+0	1.9E+0	1.1E+0	73	0.0
5	16	10	2.3	6.0	0.4	1.1	5.4	0.0	9.3E+0	1.9E+0	1.3E+0	85	0.0
10	8	20	2.0	2.6	0.4	1.1	2.3	0.1	8.1E+0	2.3E+0	4.7E+0	37	0.0
10	10	20	2.6	4.1	0.4	1.1	3.6	0.1	1.0E+0	2.4E+0	9.3E+0	58	0.0
10	12	20	2.8	5.4	0.4	1.1	4.9	0.0	1.1E+0	2.3E+0	1.4E+0	77	0.0
10	14	20	3.0	6.7	0.4	1.1	6.1	0.0	1.2E+0	2.3E+0	1.8E+0	96	0.0
10	16	20	3.1	8.0	0.4	1.1	7.2	0.0	1.2E+0	2.2E+0	2.3E+0	11	0.0
15	8	30	1.7	2.2	0.4	1.1	1.9	0.1	6.7E+0	2.1E+0	3.3E+0	31	0.0
15	10	30	2.6	4.1	0.4	1.1	3.6	0.1	1.0E+0	2.4E+0	9.4E+0	58	0.0
15	12	30	3.1	5.9	0.4	1.1	5.3	0.0	1.2E+0	2.5E+0	1.6E+0	84	0.0
15	14	30	3.4	7.6	0.4	1.1	6.8	0.0	1.3E+0	2.4E+0	2.3E+0	10	0.0
15	16	30	3.6	9.2	0.4	1.1	8.3	0.0	1.4E+0	2.4E+0	3.0E+0	13	0.0

Ψ was calculated based on a rock size d_{n50}=0.44m with W_{50}=230kg.

6.7 Force balance at incipient motion

Morison's equation was used to calculate the in-line and uplift forces on a fully exposed (p/d=0.82) spherical stone of 19mm diameter sitting on a coplanar bed made up of glass marbles of the same diameter (see Table 6.7). Morison's force coefficients derived in Chapter 4 by curve fitting to measured forces were used in the calculation. In calculating in-line force only the inertia term was used as it was found earlier in Chapter 4 that the contribution of the drag force to the total force for KC<10 is not significant. According to the theory, the ratio of disturbing moment to restoring moment around a pivot point should approach unity at the threshold stone displacement (M_D/M_R=1, see Section 3.2.3 and Appendix-A). However, the majority of the data lie between M_D/M_R =1.7 to 4.2. In the stability equation, $M_D/M_R=F_H\ (L_2)/(F_W-F_L)L_1$, the denominator, $M_R=(F_W-F_L)\ L_1$ is the restoring moment caused by the difference between the gravity force and the uplift force and the numerator is the moment caused by the horizontal force. Here, the ensemble-average of the lift force, F_L, at the time of the peak horizontal force, $F_{H\text{-}max}$, was used in the calculation. Morison's equation calculates the quasi-steady forces without considering the turbulent fluctuation.

The root mean square turbulent fluctuation of the horizontal and uplift forces was calculated based on the pressure measurement on a 50mm spherical stone for a wave height of 8cm and period of 2 sec at a 40cm water depth. The rms fluctuations in the horizontal and uplift forces were found to be 0.0013N and 0.0027N, respectively. This means that the fluctuation in the

uplift force is twice that of the horizontal force. The analysis was based on 50 wave cycles and a data capturing rate of 625Hz.

Figures 6.12 and 6.13 show the variation of the M_D/M_R ratio with the Reynolds and Keuligan-Carpenter numbers. Although there is substantial scatter, the trend generally shows that the M_D/M_R ratio decreases when the Reynolds number increases and the flow regime moves into fully developed turbulence.

The disturbing moment was plotted against the restoring moment in Figure 6.14. The graph deviated from the theoretical $M_D=M_R$. With $a/k_s \approx 1.0$ and $Re=O(10^4)$ the flow regime of the tests is in the transition to rough turbulent flow region (Kamphuis, 1975). For an individual sphere, the transition to turbulence occurs at $Re_d=U_m d/\nu \approx 2300$ (Schlichting, 1968). The majority of the tests were conducted below this critical Re_d value. For oscillatory flow, rapid flow reversal inhibits full development of the flow. Therefore, the fact that the flow is in the laminar and transitional flow regimes could have contributed to the increased stability (i.e., $M_D/M_R>1$) when $Re < 2 \times 10^4$ and $KC < 35$ and for the deviation of the observed M_D/M_R ratio from the theoretical value (Figure 6.14).

Table 6.7: Incipient motion test conditions and M_D/M_R ratio.

Test no.	Specific gravity (-)	H (cm)	T(sec)	h(cm)	M_D/M_R (-)	KC (-)	Re_d (-)
W89	1.19	6	1	40	4.0	3.6	1189
W90	1.19	4.5	2	40	2.7	10.2	1666
W94	1.19	5.6	1	30	3.7	3.4	1110
W95	1.19	4.5	2	40	2.7	10.2	1666
W120	1.2	6.5	1	40	4.2	3.9	1288
W121	1.2	4.5	2	40	2.5	10.2	1666
W137	1.36	8.5	1	40	2.9	5.1	1685
W138	1.36	5.5	2	40	1.7	12.4	2037
W143	1.38	6.5	2	40	1.9	14.7	2407
W144	1.38	10	1	40	3.3	6.0	1982
W148	1.4	12	1	40	3.9	7.2	2378
W149	1.4	6.5	2	40	1.8	14.7	2407
W152	1.7	10.5	2	40	1.8	23.7	3888
W156	2.53	12.5	2.5	40	0.8	37.2	4887

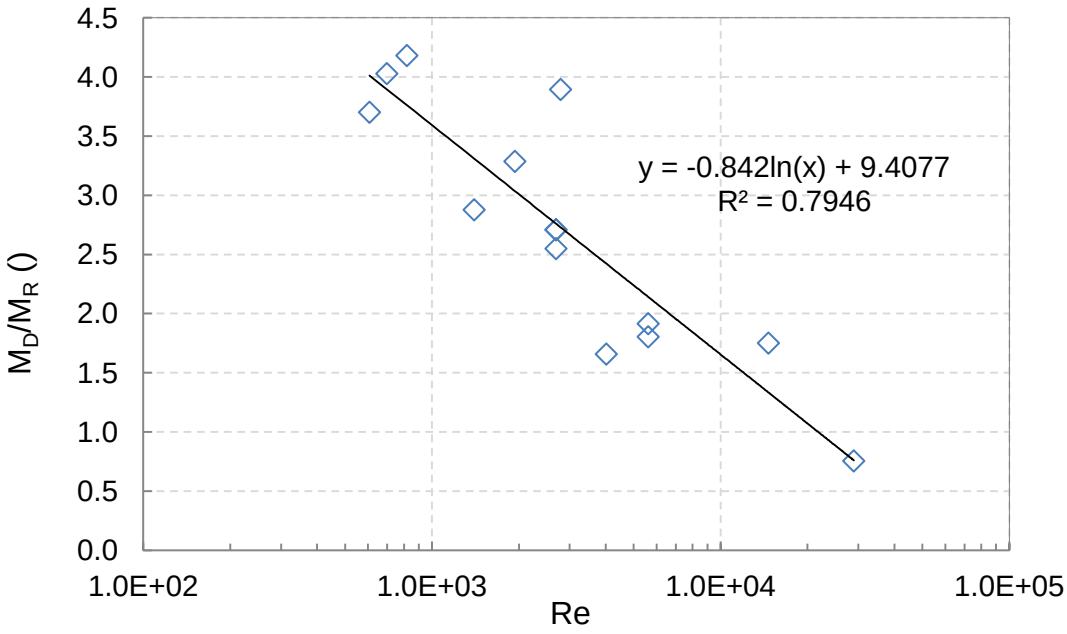

Figure 6.12: Variation of disturbing moment to restoring moment ratio with Re.

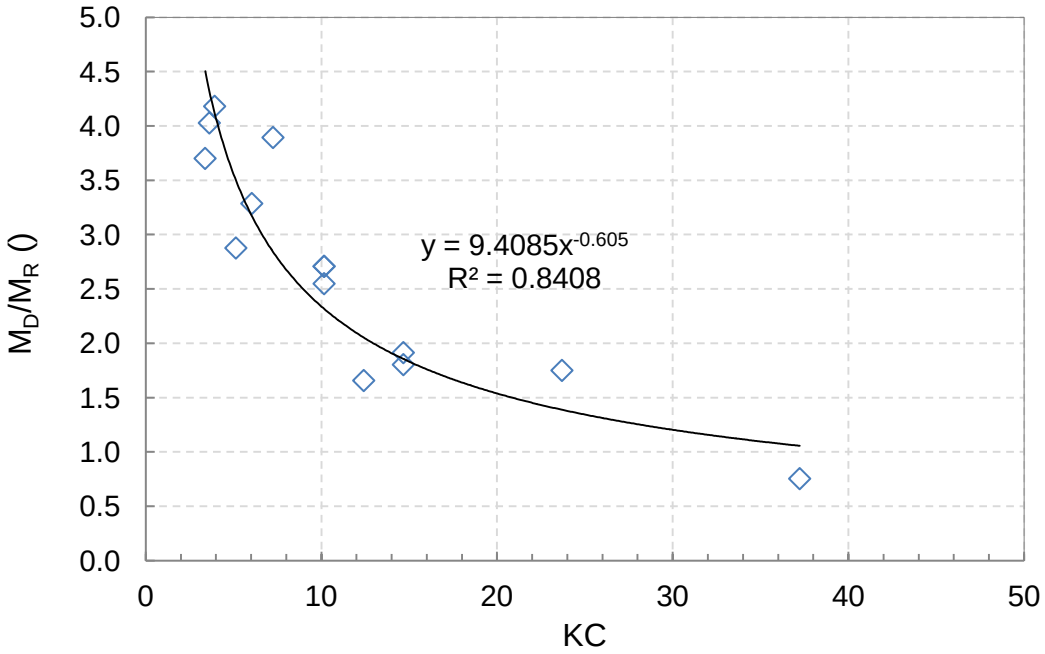

Figure 6.13: Variation of disturbing moment to restoring moment ratio with KC.

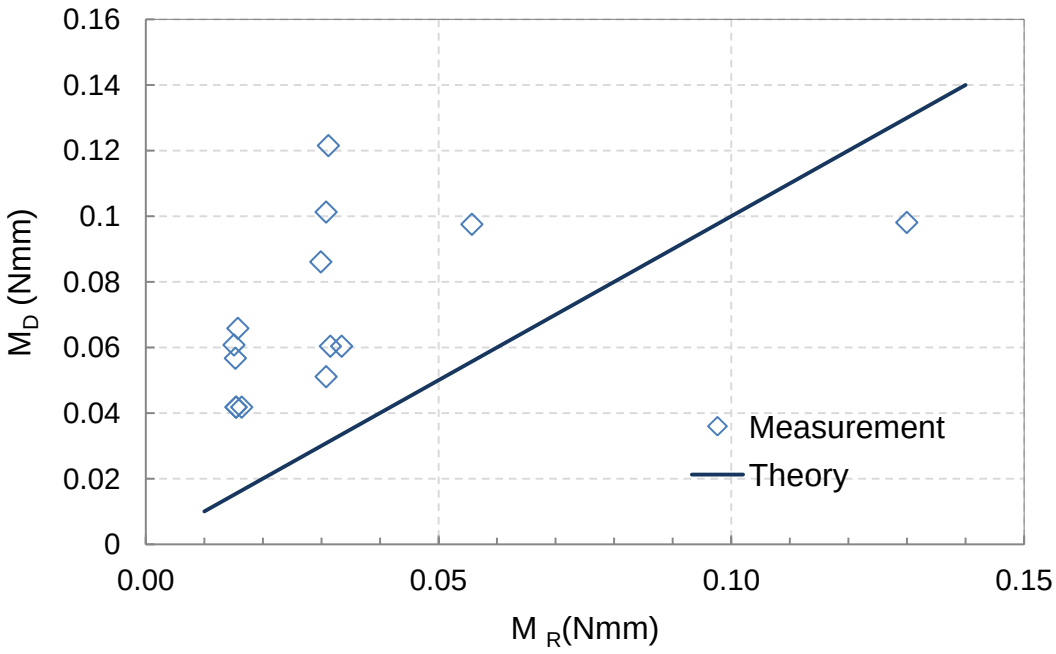

Figure 6.14: Disturbing moment against restoring moment at threshold stone movement.

6.8 Phases of stone movement in the wave cycle - visual observations

Displacement of fully exposed 19mm diameter spherical elements made of different material resting on a rough bed consisting of glass marbles of the same diameter, was observed through video recording. Figure 6.15 shows a frame from the video at the time of displacement. A scale glued to the face of the flume was used to measure the surface elevation. Several tests were carried out to obtain a statistically representative result.

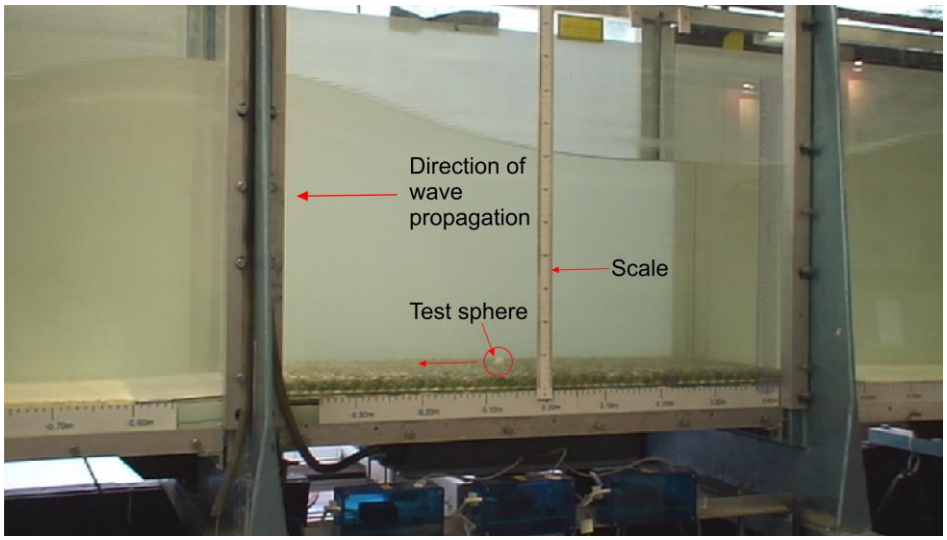

Figure 6.15: Visual observation of incipient motion.

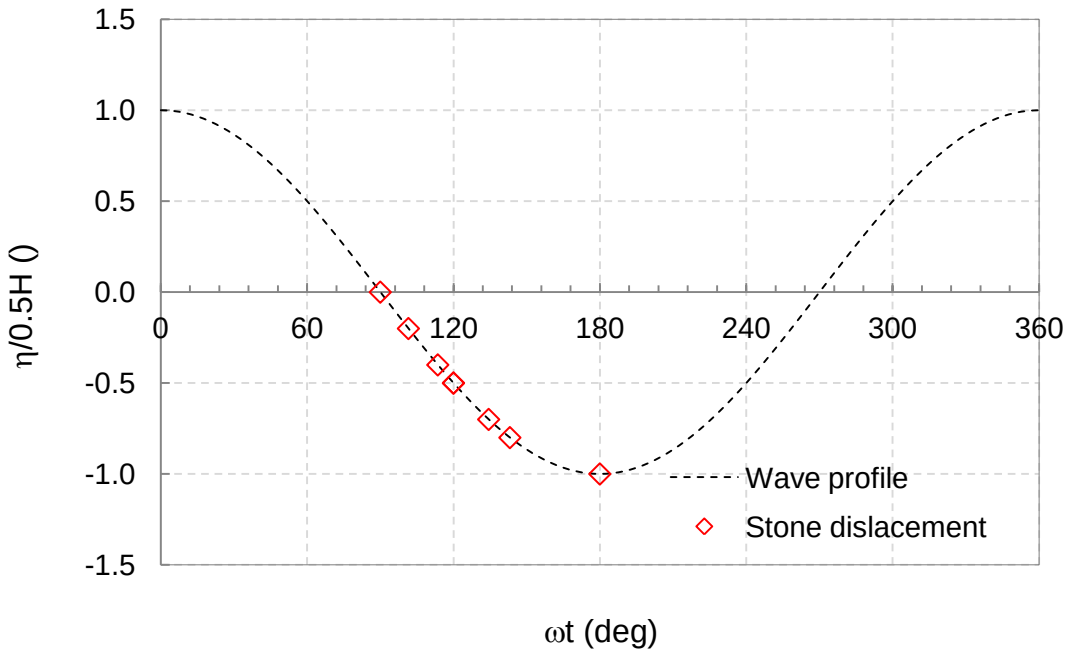

Figure 6.16: Phases of stone displacement within the course of wave cycle.

The phase of the stone displacement is shown in Figure 6.16. All displacements occurred within the trough half cycle near and after the flow reversal. The quasi-steady uplift is positive (beneficial) for the displacement during this phase (Figure 4.1). Moreover, the turbulence intensity at the bed

is higher (about 43%) during the decelerating part of the wave cycle and after the flow reversal compared to the accelerating phase (Figure 5.17). Therefore, there are favourable conditions for stone displacement during the trough half cycle.

Figure 6.16 shows that stone displacement can occur at any point in the trough half cycle between $\omega t=90^0$-180^0. For that to happen, the existence of a positive uplift force is essential. The flow visualisation tests in Chapter 7 showed that at the inception of motion, a stone required the aid of an instantaneous uplift force induced by a moving vorticity structure, acting simultaneously with the shear stress.

The peak shear stress, $\tau_m=0.5f_w\rho U_m^2$ has been traditionally used to define the bed shear stress in the Shields parameter. The measured shear stress, τ/τ_m varied between 0.95 and 0.43 within the $\omega t=90^0$-180^0 range where the stones were most likely to be displaced (Figure 5.6). Therefore, an average shear stress of $0.69\tau_m$ would be more appropriate to describe the shear stress at the point of incipient motion. Using a value of shear stress of $\tau=0.69\tau_m$ in the Shields parameter, the data for glass marbles were plotted in Figure 6.17 together with published data for currents (Chin & Chiew, 1993). This improved the agreement with the curve for currents.

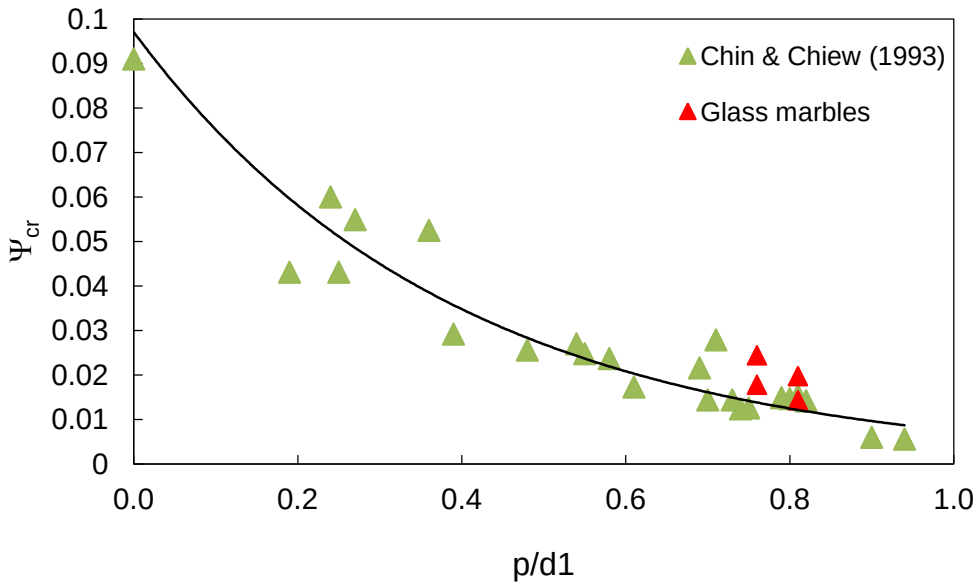

Figure 6.17: Shields critical shear stress against relative protrusion for glass marbles under waves after using $\tau=0.69\tau_m$. Data for currents are plotted for comparison.

6.9 Comparison with previous studies

Soulsby & Whitehouse (1997) plotted the Shields critical shear stress for existing incipient motion data from various published studies for currents and waves against the non-dimensional grain diameter D_* (see Figures 2.4 and 2.5). Much of the data for currents were below the Shields curve and the data for waves were scattered and located above the curve.

Figure 6.18 shows the critical shear stress data for spherical stones of different density from the present tests plotted against the non-dimensional grain diameter. Only the data for fully exposed stones p/d=0.82 were chosen, to reduce the effect of protrusion. The Shields curve is shown on the same graph for comparison. Though there is significant scatter of data, the general trend of the Shields critical shear stress is to decrease for

increasing D* reaching a lowest value at 0.02 at D*=432. The scattered data tend to reach a Shields value of 0.1 as an upper bound. This is due to the effect of Reynolds number on the inception of stone motion as discussed in Section 6.5 and 6.8 respectively. It appears that for larger D* values or higher Reynolds number flows, for a fully exposed stone, the Shields critical shear stress approaches the value for current.

The data set of Rance and Warren (1969) is particularly relevant for this study as the authors used a bed of coarse material ranging from 0.4 cm to 4.8cm. They included limestone chips primarily (d=0.32-2.5cm), concrete cubes, coal, glass spheres, Perspex cubes and coarse quartz sand. The period of oscillation was 5 – 15 seconds. The authors made visual observations on the first movement of particles in a bed of 2-4 stones deep, 2.44m long and 45cm wide set up in an oscillating water tunnel. In these tests different particles on the bed must have had varying stone protrusion levels. Therefore, the scatter of the data and the larger Shields values observed is considered to be due to the effect of the wave period and relative protrusion (see Figure 2.5). Any deviations due to the choice of friction factor/bed shear stress calculation method would not arise in this case as this data set is from the same series of experiments.

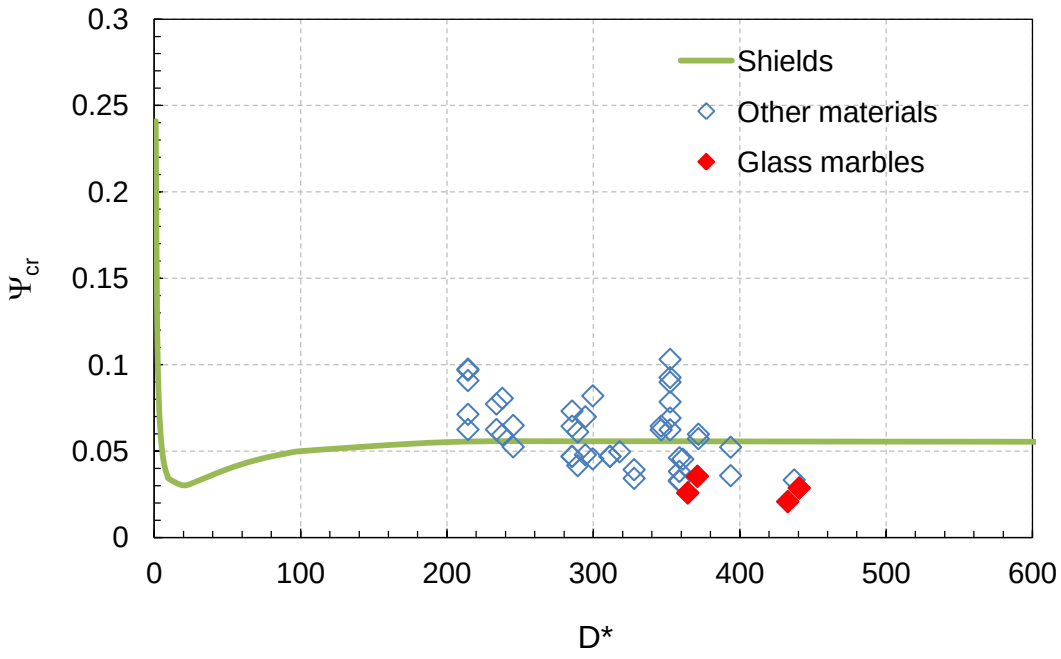

Figure 6.18: Critical shear stress against non-dimensional particle diameter for p/d=0.82.

Therefore, based on the results of the present study, the difference between the Shields curve and the various published data reviewed by Soulsby & Whitehouse (1997) could be attributed primarily to: (i) the effect of particle protrusion; and (ii) the Reynolds number regime at the inception of motion.

6.10 Summary

Laboratory tests were carried out using spherical stones to study the effect of the varying relative protrusion on stone movement. The rough bed consisted of 19mm diameter glass marbles. Test stones were of different materials with specific gravity ranging from 1.19 (acrylic) to 2.65 (glass). In terms of the stone size, tests can be categorised into two types: (i) the test

stone diameter is equal to or larger than that of the material forming the bed, i.e. $d_1 \geq d_2$; and (ii) the test stone diameter is smaller than that of the bed material, i.e. $d_1 < d_2$.

1 The Shields critical shear stress for waves increased when the relative stone protrusion decreased. The data strongly correlated to the relative stone protrusion exhibiting an exponential relationship.

2 The critical shear stress data for waves lie above the data for currents, giving an impression, on first observation, that the stones are more stable under waves than currents. This discrepancy is due to processes that inhibit turbulent separation rather than due to an inherent difference in the vertical structure of waves and currents as assumed initially. They are (i) rapid flow reversal due to the small wave periods used (i.e., 1-2.5 sec), (ii) the reduced element size exposed to the flow when the protrusion was decreased and, (iii) the Reynolds number flow regime at the inception of motion – light weight acrylic particles displaced under laminar flow while glass marbles displaced at a relatively high Reynolds number. Majority of the data were in the region KC<10. At high Reynolds number, the critical shear stress approached 0.02-0.03 - closer to the value observed by previous researchers for currents (i.e., 0.01 by Fenton & Abbot, 1977 and Chin & Chiew, 1993).

3 The Shields critical shear stress is strongly dependent on the wave period as well as the relative protrusion. A set of critical shear stress

versus relative protrusion curves for different wave periods was identified. When the wave period increased, this curve became flatter and approached the position for currents. This suggests, by extrapolation, that the incipient motion data obtained for currents in previous studies are applicable to high Reynolds number oscillatory flows that exist under field conditions.

4 Good correlation between the critical shear stress and the relative protrusion data was obtained when the test stone diameter is equal to or larger than the diameter of the glass marbles that make up the rough bed ($d_1 \geq d_2$). When, smaller diameter test stones were used ($d_1 < d_2$), the scatter of the data increased, indicating the influence of another mechanism other than the shear stress. When the data is in the range $0<p/d_1<0.5$, the scatter is significant. In this range, the influence of the shear stress in the stone displacement appears to diminish as hiding increases. Therefore, for smaller particles at lower protrusion levels, the uplift force should play a dominant role in the stone displacement.

5 Stones in a coplanar bed (p/d=0) were remarkably stable even for the largest bed shear stresses that could be produced in the wave flume. This is despite the use of lightweight stones of specific gravity 1.19 and neutral buoyancy in the tests. It was observed that the stones did not move and exhibited the same behaviour as a coplanar bed when the stone protrusion was increased to 0.17d and 0.21d. The stone started moving again when the protrusion was increased to 0.24d.

Therefore, 0.21d is considered to be the threshold protrusion below which stones in a bed protection are stable.

6 The ratio of the disturbing moment to the restoring moment on a stone due to the horizontal and uplift forces should approach unity at the moment of incipient motion. However, this ratio, computed based on the force balance on a fully exposed stone using inertia term of the Morison's equation, varied between 1.7 - 4.2 for $Re < 2 \times 10^4$ and $KC < 35$. This deviation is likely due to the fact that the majority of the tests were carried out in the laminar and transitional flow regions. However, this ratio approached unity for larger Re and KC values.

7 Visual observation of stone displacement using video recordings showed that the displacement is most likely to occur during the trough half cycle between the phases of flow reversal and peak velocity. This could be due to (i) the existence of positive (beneficial) uplift; and (ii) increased turbulence intensity during these phases.

8 The peak shear stress, $\tau_m=0.5f_w\rho U_m^2$, has most commonly been used in the Shields parameter to describe the threshold of movement. The visual observations showed that stone displacement could occur any time during the decelerating phases of the trough half cycle in which the measured shear stress varied from $0.43\tau_m$ to $0.95\tau_m$. Therefore, this indicates that the use of an average value in the Shields shear stress parameter would be more suitable.

7 Flow visualisation

7.1 Introduction

Flow visualization around an idealised spherical stone sitting on a rough bed of similar stones, was carried out in a wave flume using the Volumetric Three-component Velocimetry (V3V) system to study the flow features contributing to stone displacement. The water depth was maintained at 40cm for all tests. The rough bed consisted of billiard balls of 50mm diameter and glass marbles of 19mm diameter spread across the 45cm flume width over a 90cm length.

The flow features over a coplanar bed were studied in Tests FV1 and FV5 (Section 7.2). Flow around a fully exposed 50mm sphere (p/d=0.82) is shown in Test FV2 (Section 7.3).

It was observed in Chapter 6 that stones are more stable under the action of waves than currents. It was one of the objectives in the flow visualisation tests to understand the reason behind this phenomenon. With this objective, flow around a fully exposed and partially exposed 19mm diameter glass marble was studied in Test FV8 and FV7, respectively (Section 7.4).

To gain insight into the initiation of motion and entrainment process, it is important to understand the flow features near a stone just before, during and after the first stone displacement. With this objective, V3V images were

captured for a light weight PVC sphere of 19mm diameter at the moment of incipient motion (Section 7.5).

7.2 Oscillatory flow over a coplanar bed

7.2.1 Rough bed of 19mm spherical elements

The measured wave surface profile and a raw image of the bed taken from the V3V camera probe are shown in Figure 7.1 and 7.2, respectively. The measured wave height, period and water depth were 10.1cm, 2.5 seconds and 40cm respectively. The flow Reynolds number was Re=1.9 x 10^4 and the roughness Reynolds number was $u_* k_s/\nu$ =3 x 10^3.

Figures 7.3 to 7.6 show the V3V images of the flow over a rough bed of 19mm diameter glass marbles set in coplanar bed. The 3D vorticty isosurface (in red) patterns show different types of coherent vortex structures; i.e., spherical blobs of water, doughnut shaped vortex rings, hairpin vortices, horse-shoe vortices being shed from the bed elements. The size of these vortices appears to be of the size of the glass marbles. The ejected vortices are lifted off and move up to join the flow above which is shown by streamlines. The legend shows the velocity and vorticity magnitude. The streamlines are represented by the streaks.

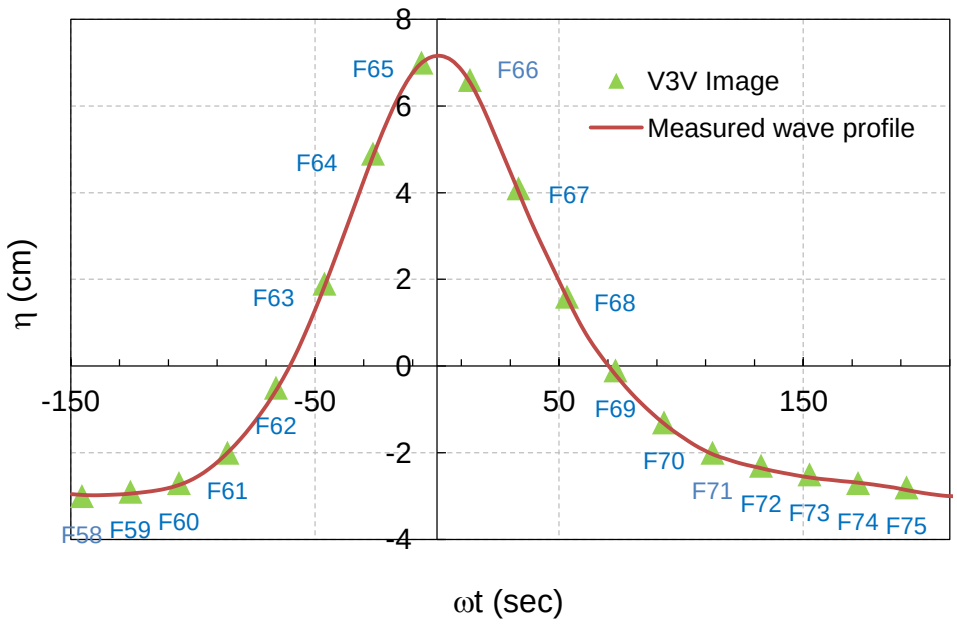

Figure 7.1: Measured wave profile. Test FV5, H=10.1cm, T=2.5, h=40cm.

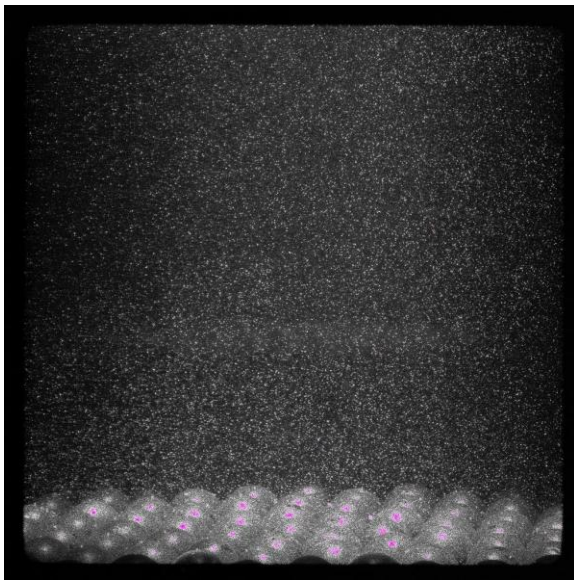

Figure 7.2: Raw V3V image of the rough bed consisting of 19mm diameter elements.

Vortex formation and ejection activity from the roughness elements is dominant during the acceleration phases (Figures 7.3 and 7.4). During the

deceleration phases, vortex shedding is not very significant and the vortices already shed from the elements appear to move back and forth with the wave-induced flow (Figures 7.5 and 7.6).

This finding is quite paradoxical. The turbulent intensity showed a 43% increase during the deceleration phase and just after flow reversal. Yet, vortex ejection is suppressed during this phase. Therefore, it could be argued that this increase in turbulence intensity is generated by another mechanism other than vortex ejection. Two possible causes could be: (i) residual vorticity remaining from the acceleration phases; and, (ii) bursting of turbulent 'spots'.

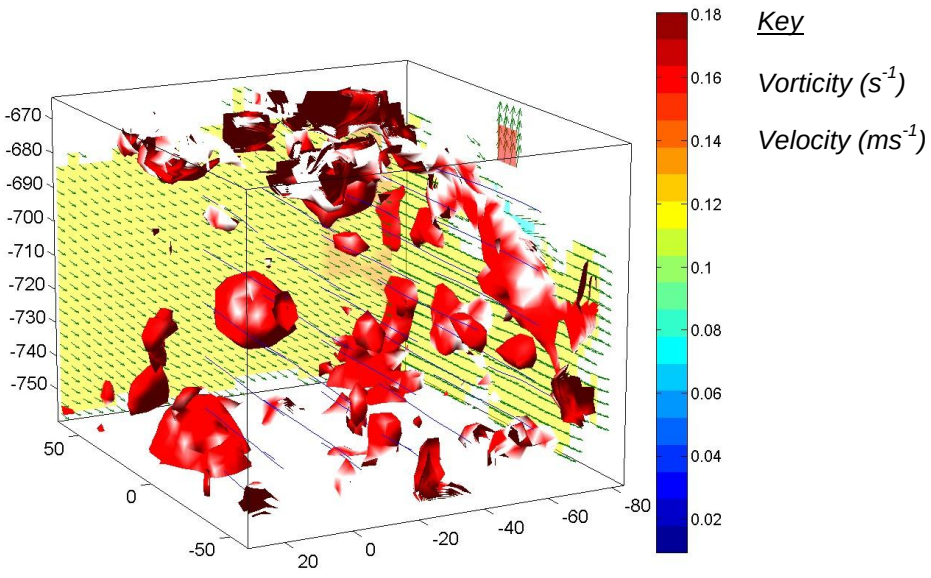

Figure 7.3: Vorticity isosurface and velocity vectors/contours. Test FV5, Frame 59, $\omega t = -125.5^0$.

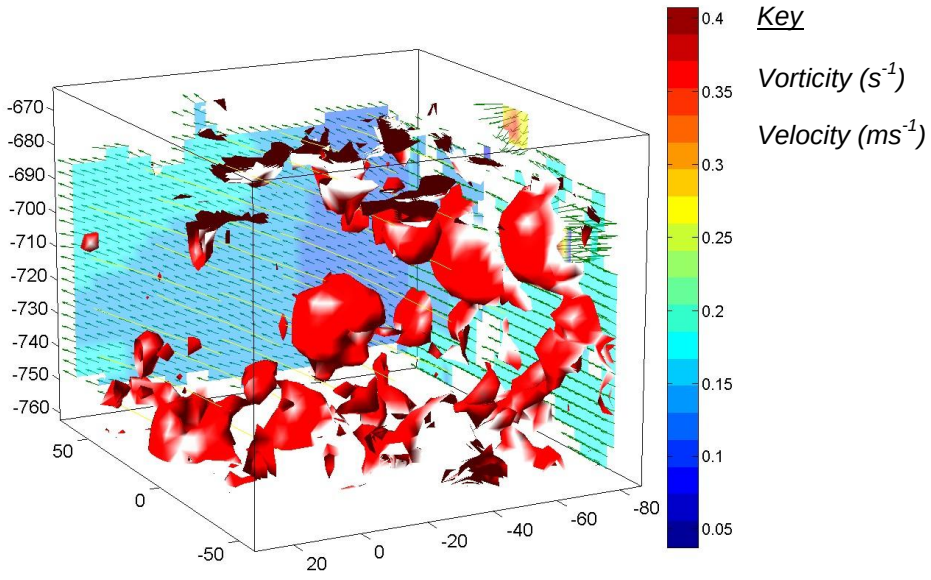

Figure 7.4: Vorticity isosurface and velocity vectors/contours. Test FV5, Frame 64. ωt= -26.2^0.

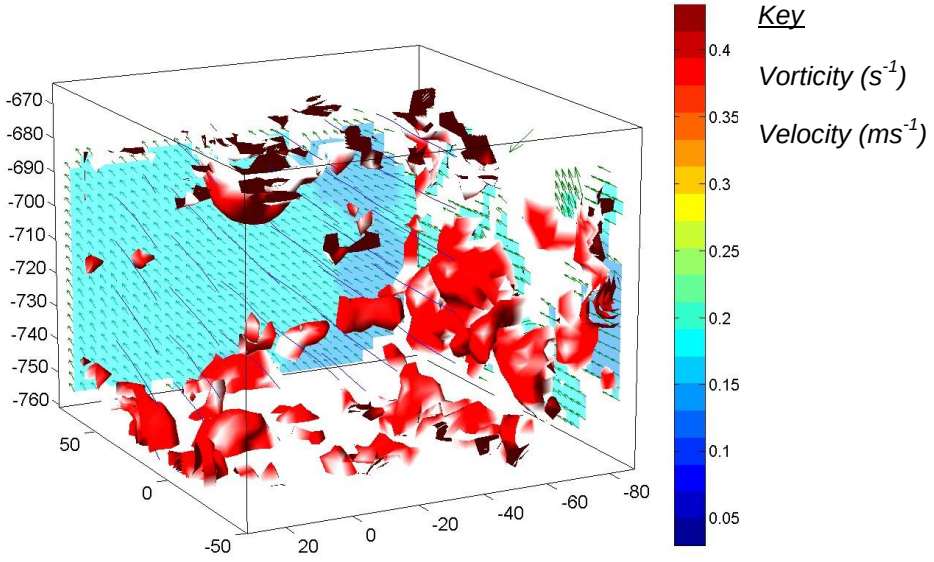

Figure 7.5: Vorticity isosurface and velocity vectors/contours. Test FV5, Frame 67, ωt= 33.4^0.

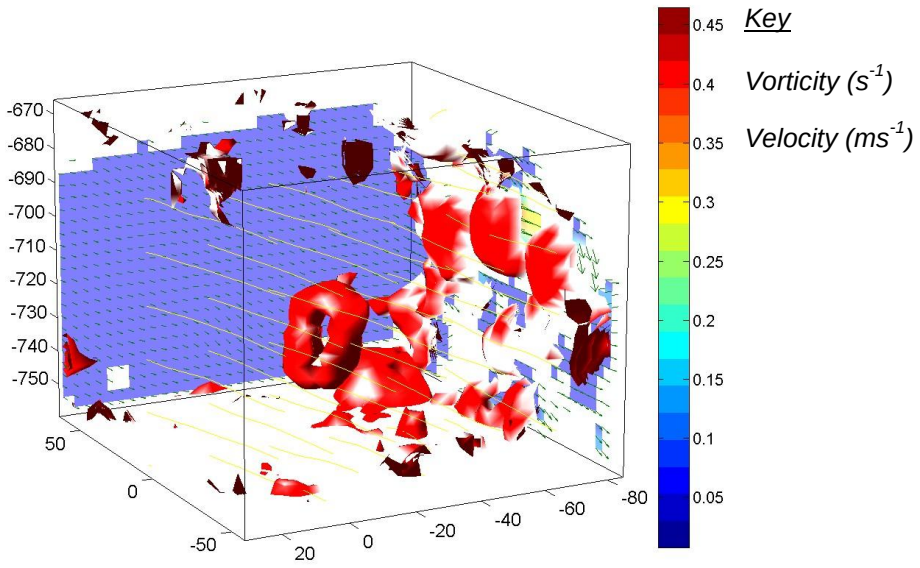

Figure 7.6: Vorticity isosurface and velocity vectors/contours. Test FV5, Frame 70, ωt= 93.0^0.

7.2.2 Rough bed of 50mm spherical elements

Figures 7.9 to 7.12 show the 3D flow information over a rough bed consisting of 50mm diameter spheres (billiard balls) set within a coplanar hexagonal bed arrangement. The measured wave height and period were 11.63cm and 2 seconds in a 40cm still water depth and with a flow Reynolds number of Re=1.8 x10^4 and a roughness Reynolds number of $u_* k_s/\nu$ =1.4 x 10^4.

Coherent vortices shed from the roughness elements are larger than for 19mm diameter spheres and hence, were more visible. Significant turbulence was observed in the region 100mm above the bed (about two

stone diameters). Vortices ejected from the bed elements are shown to move away from the bed to join the flow above.

Vortex formation and ejection is dominant in the acceleration phases, very similar to the observations made in tests on a coplanar bed of 19mm diameter marbles described in the preceding section (Figures 7.9 and 7.10). Vortex shedding was not very pronounced in the decelerating phases and after flow reversal, though vortex formation and ejection did not completely cease (Figures 7.11 and 7.12). It appears that vortices already shed are being transported back and forth during these phases.

Flow reversal occurs closer to Frame no. 13 and 20 (Figures C.21 and C.28, respectively, in Appendix C). Though the mean velocity approaches zero at the flow reversal, the near-bed turbulence does not cease. The turbulence is still strong within a region about one diameter (50mm) above the bed level. Kajiura (1968) assumed that for rough beds, the cycle-averaged eddy viscosity is a constant within a region $0.5k_s$ above the bed (i.e. $\cong$ 1.0d). The results of the present measurements appear to suggest that the eddy viscosity is a non-zero quantity throughout the wave cycle giving credence to the above assumption.

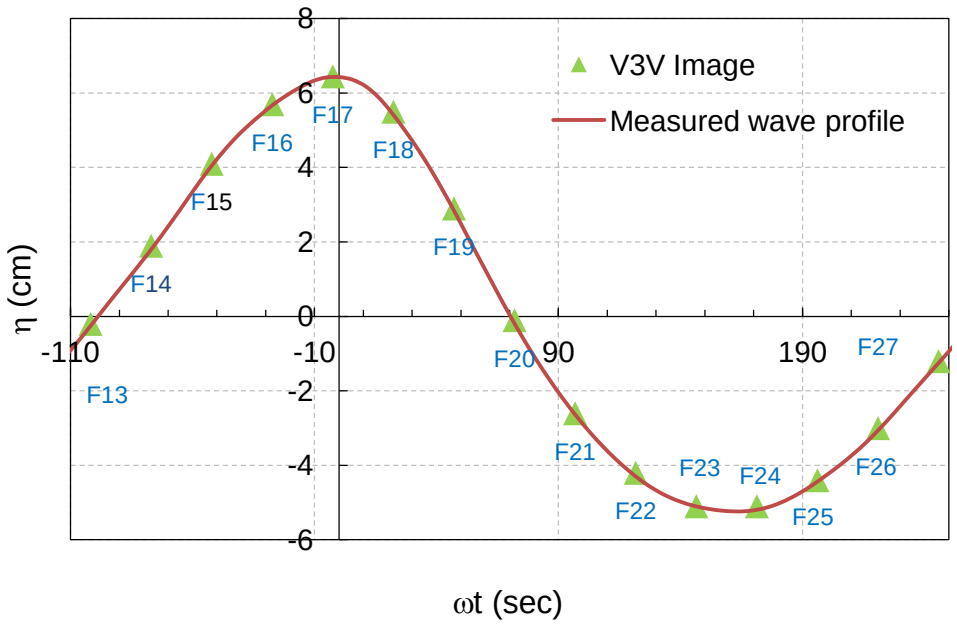

Figure 7.7: Measured wave profile, Test FV1, H=11.63cm, T=2 sec, h=40cm.

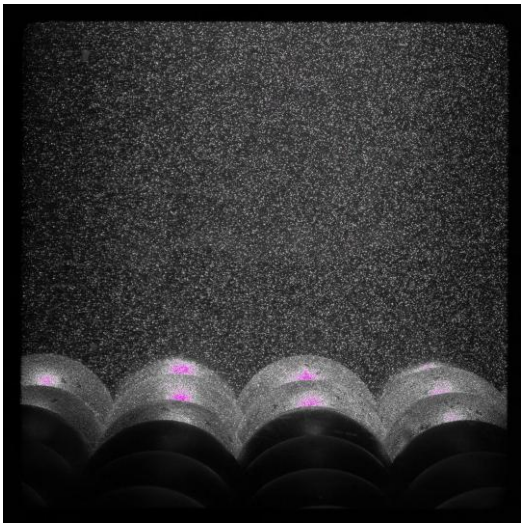

Figure 7.8: Raw V3V image of the rough bed consisting of 50mm elements.

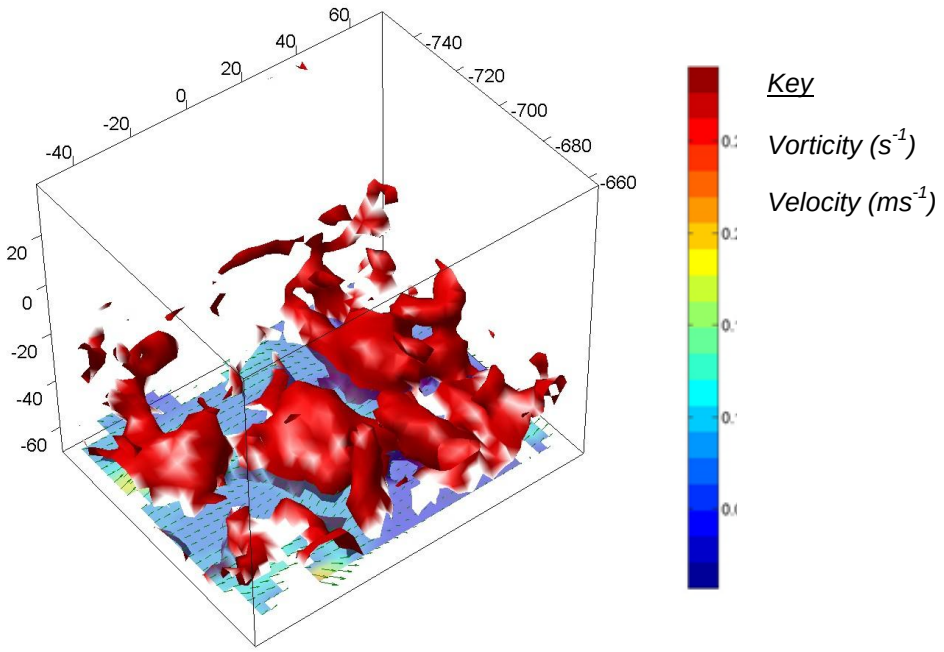

Figure 7.9: Vorticity isosurface and velocity. Test FV1, Frame 14. ωt= -76.9^0.

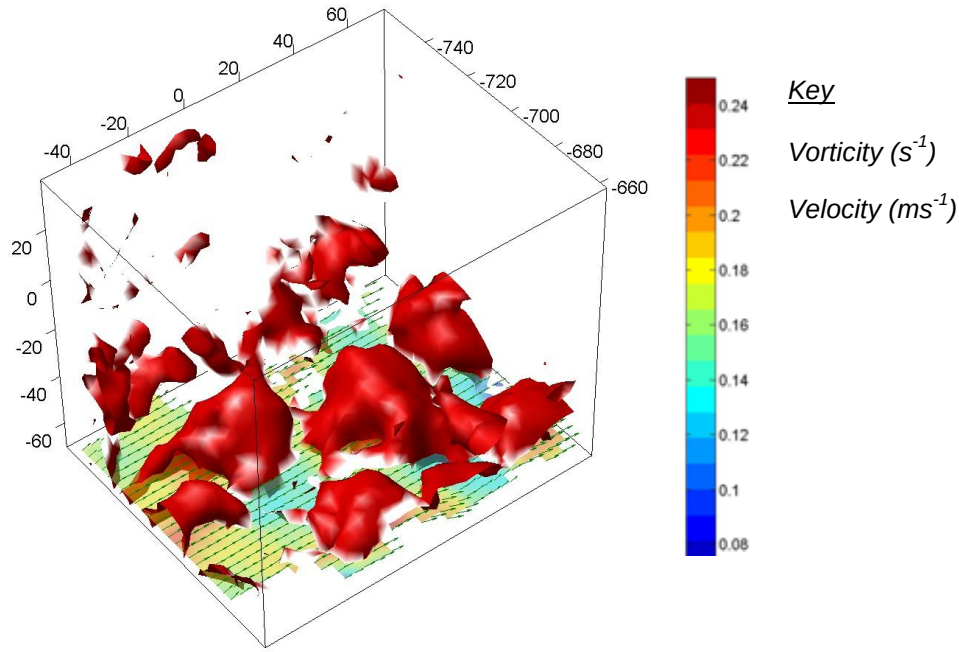

Figure 7.10: Vorticity isosurface and velocity. Test FV1, Frame 15, ωt= -52.1^0.

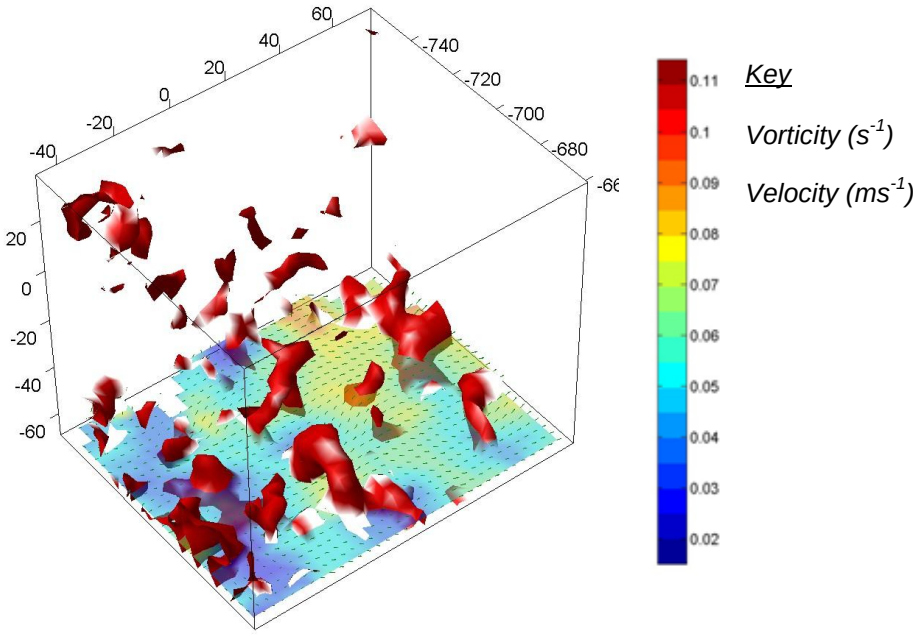

Figure 7.11: Vorticity isosurface and velocity. Test FV1, Frame 20. $\omega t = 72.0^0$.

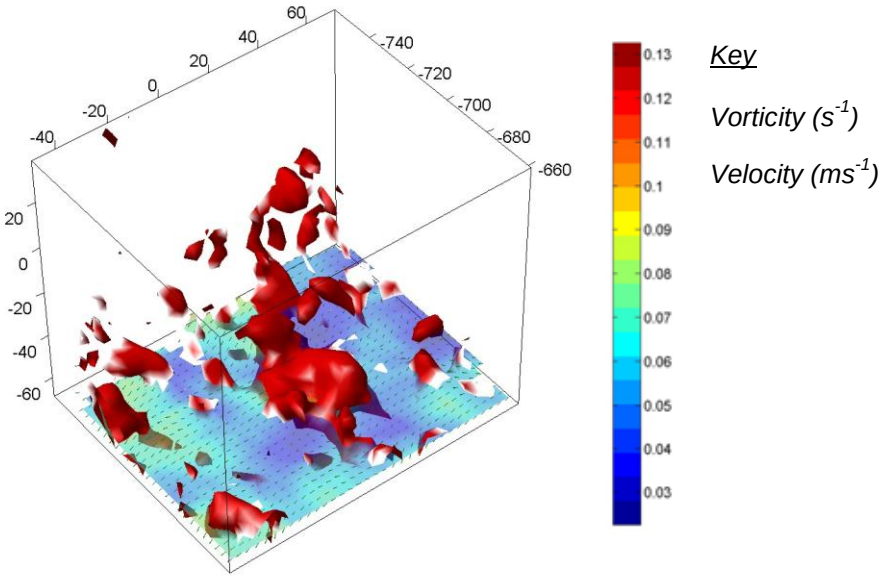

Figure 7.12: Vorticity isosurface and velocity. Test FV1, Frame 21, $\omega t = 96.9^0$.

7.3 Flow around a fully exposed 50mm sphere

Visualisation of flow past a free sphere can be found in classical books on fluid mechanics (i.e., Schlichting, 1968). However, the details of the three dimensional flow field around a sphere resting on a coplanar bed of similar spheres subject to oscillatory flow from the point of view of large particle sediment transport, is not available in the literature to the author's knowledge. However, there are many studies on cylinders.

Figures 7.15 to 7.17 show a 3D view of the formation and detachment of coherent vortices from the spheres. The flow reverses at Frame 60 (start of the crest half cycle) and vortex starts to develop from Frame 61 and 62. At Frame 63 vortex is about to be detached and at Frame 64 (wave crest phase) the vortex is completely detached. The velocity vectors on the side view in Figures 7.18 and 7.19 seem to follow the curvature of the sphere showing an unseparated flow pattern and there is no wake region formed on the lee side of the sphere.

Planar and sectional views in Section C.3 (Appendix - C) show that the flow is detached from the outer surface of the sphere rather than forming a vortex ring around the exposed surface as observed for a free sphere. This could be due to the low flow velocities during most of the wave half cycle and rapid flow reversal leading to sub-critical flow. The flow Reynolds number at the peak velocity is $Re = 1.8 \times 10^4$, approximately, the stone Reynolds number is $Re_d = U_m d/\nu = 1.1 \times 10^4$ and the Keulegan-Carpenter number is KC=10.

Further, the proximity to the bed and surrounding spheres may have inhibited the vortex shedding.

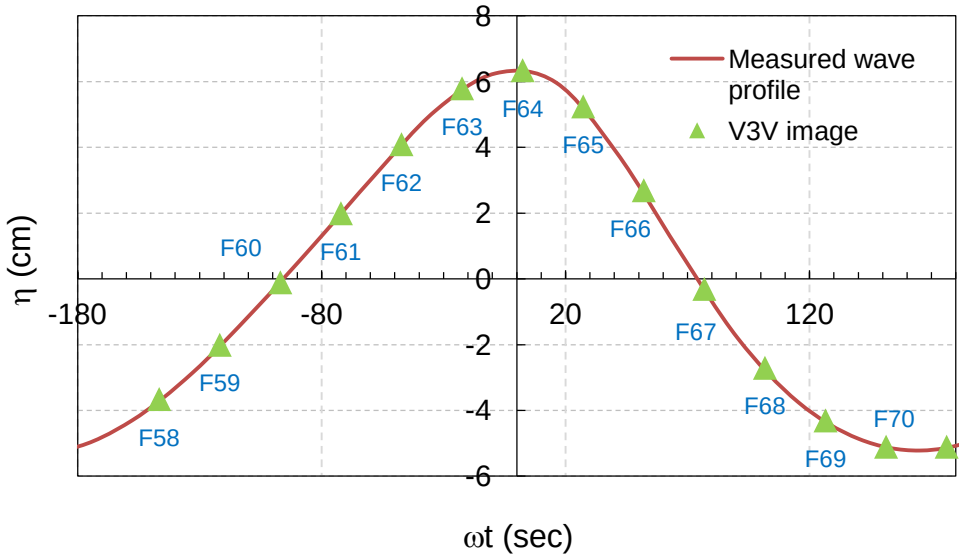

Figure 7.13: Measured wave profile, Test FV2, H=11.6cm, T=2 sec.

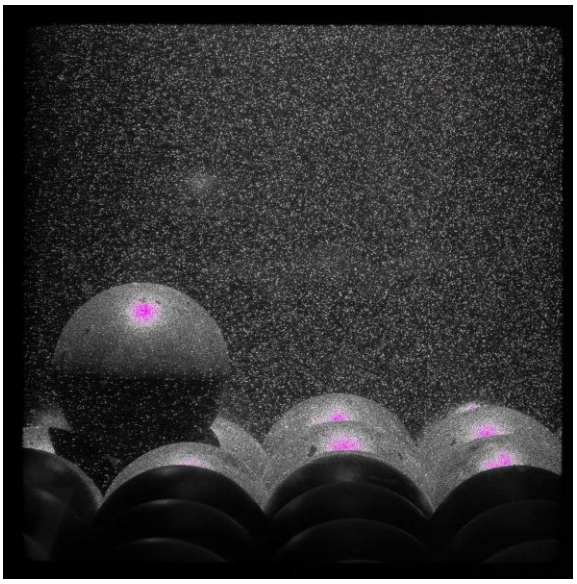

Figure 7.14: Raw V3V image of the overlying 50mm sphere.

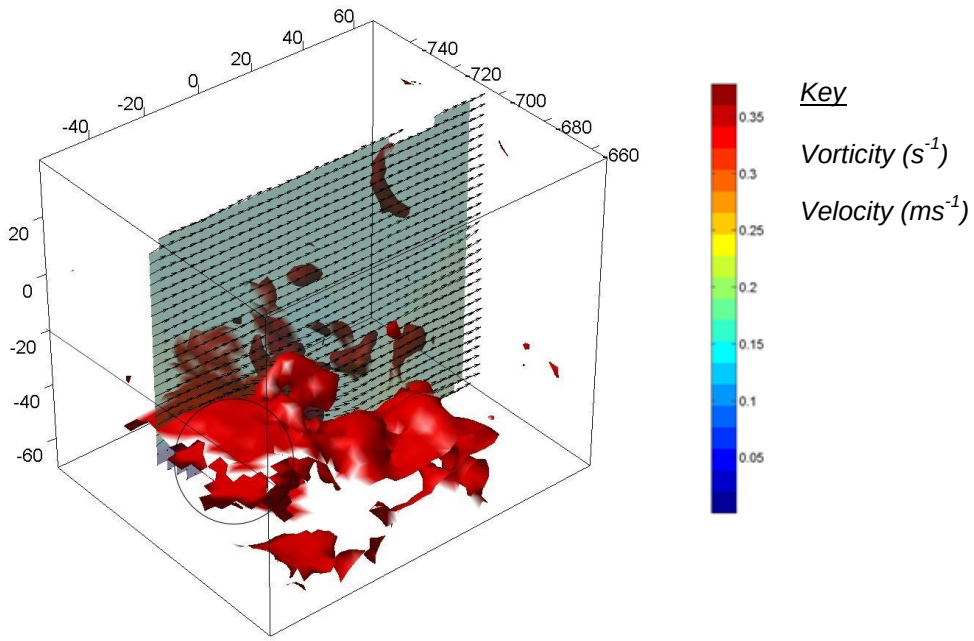

Figure 7.15: Vorticity isosurface and velocity around 50mm sphere. Test FV2, Frame 62, ωt=-47.2^0.

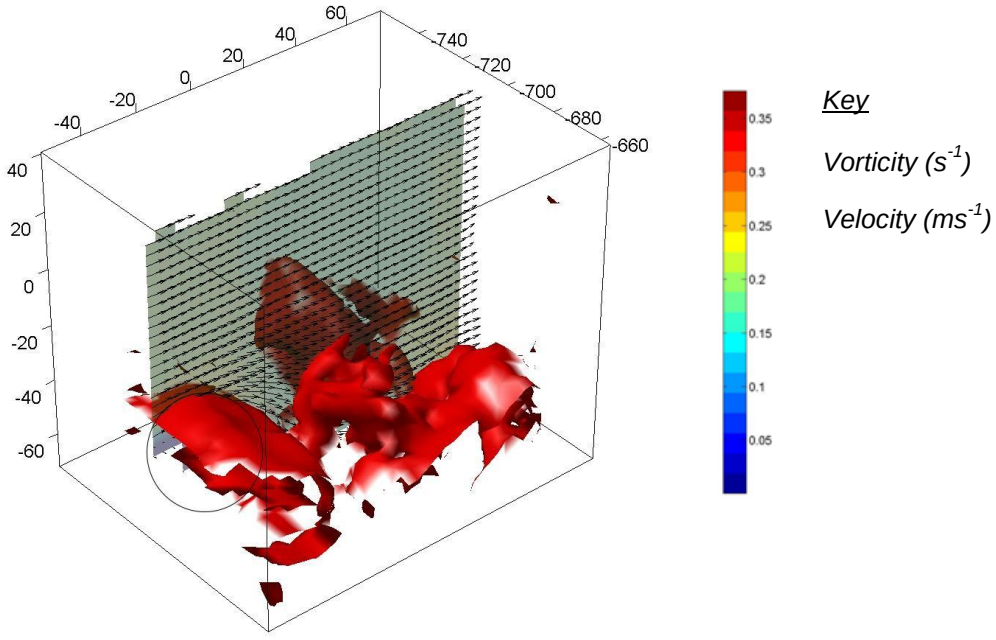

Figure 7.16: Vorticity isosurface and velocity around 50mm sphere. Test FV2, Frame 63, ωt= -22.4^0.

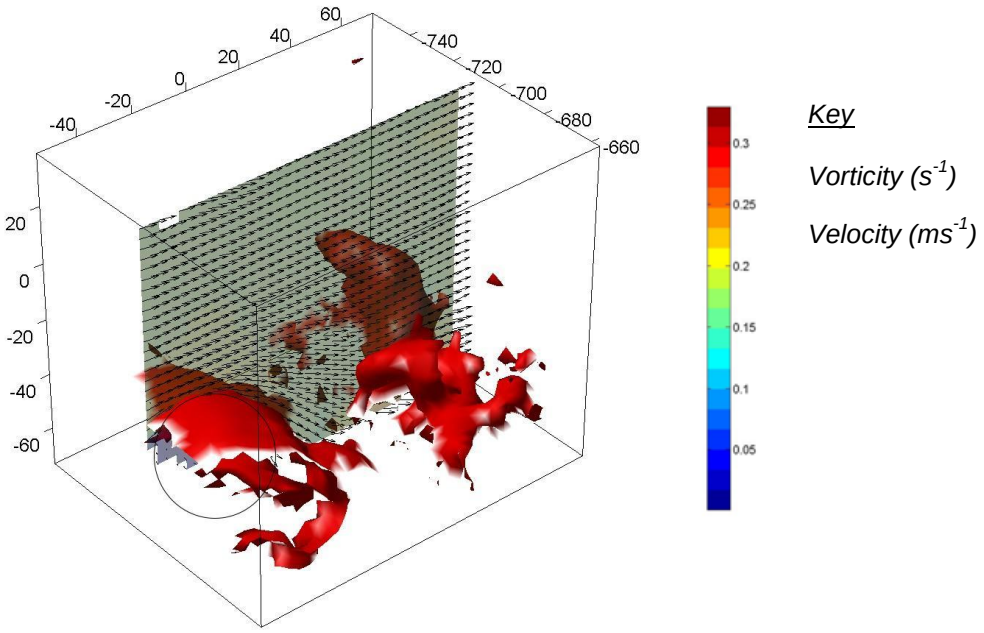

Figure 7.17: Vorticity isosurface and velocity around 50mm sphere. Test FV2, Frame 64, $\omega t = 2.4^0$.

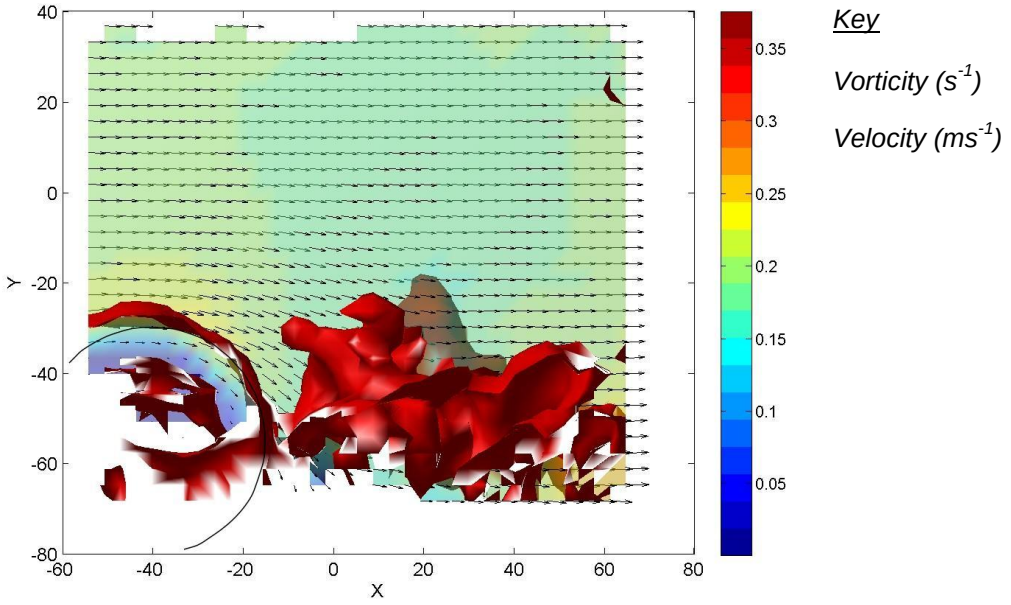

Figure 7.18: Vorticity isosurface and velocity (side view) just before the vortex detachment. Test FV2, Frame 63, $\omega t = -22.4^0$.

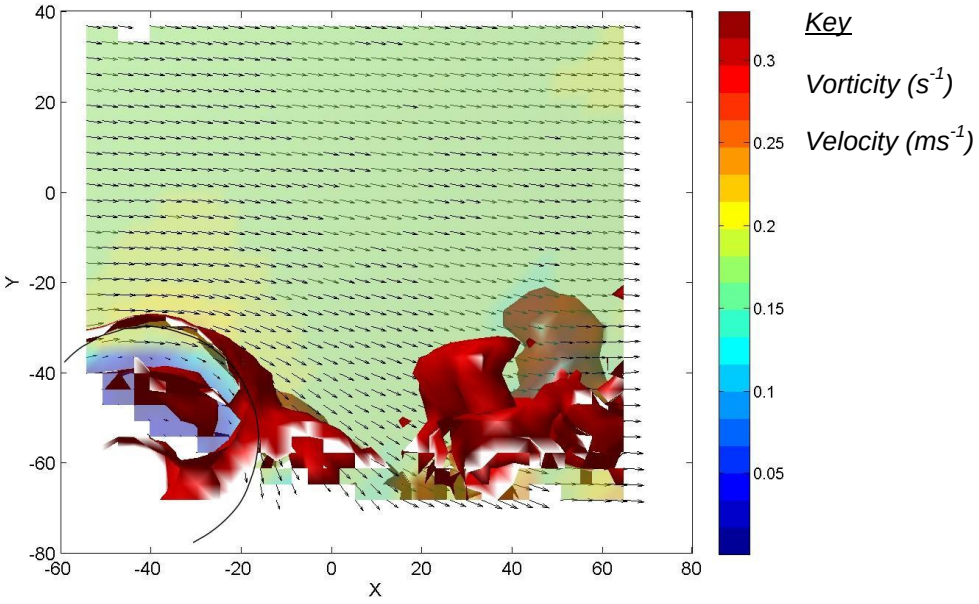

Figure 7.19: Vorticity isosurface and velocity (side view) just after vortex detachment at the wave crest. Test FV2, Frame 64, $\omega t = 2.4^0$.

7.4 Flow around a 19mm spherical stone at varying protrusion levels

In Chapter 6 on the incipient motion of stones, particles were tested for stability at different stone protrusion levels. Their specific gravity varied from 1.19 (acrylic) to 2.65 (glass) and the particle diameter varied from 9.5mm to 31.8mm. The majority of the tests were carried out using 19mm diameter spherical elements.

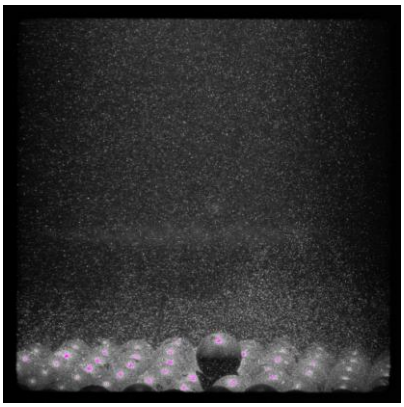

Figure 7.20: Raw V3V image for a fully exposed 19mm spherical stone sitting on a bed of same diameter elements in a hexagonal array.

When compared with the published data for currents, a relatively large Shields critical shear stress was observed for particles under regular waves in the present tests for different protrusion levels, with threshold shear stress data lying above the Shields curve. That is, for oscillatory flow under the present test conditions, particles were more stable. Therefore, flow visualisation tests were carried out for 19mm diameter glass marbles with the objective of understanding the cause behind this behaviour. This section describes the flow visualisation tests carried out for a fully exposed (p/d=0.82) and partially exposed (p/d=0.5) stones (Figure 7.21).

(a)

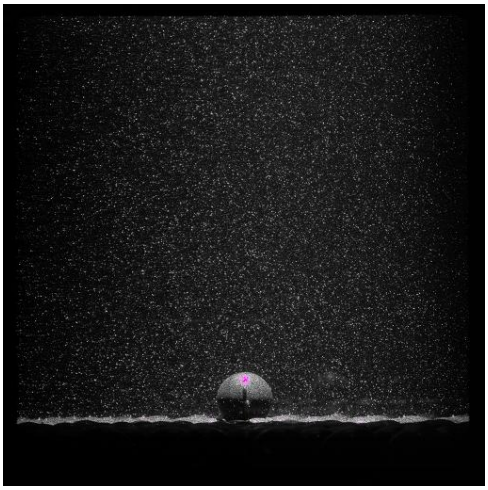

(b)

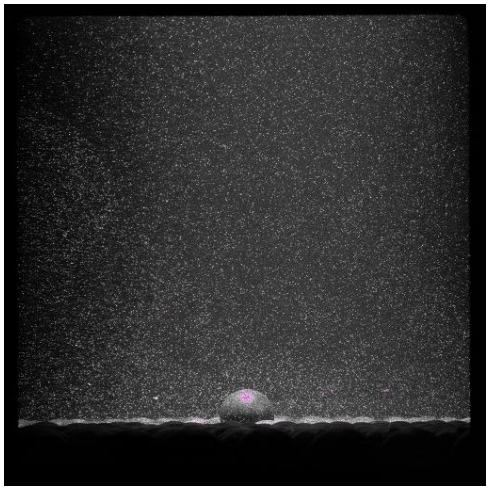

(c)

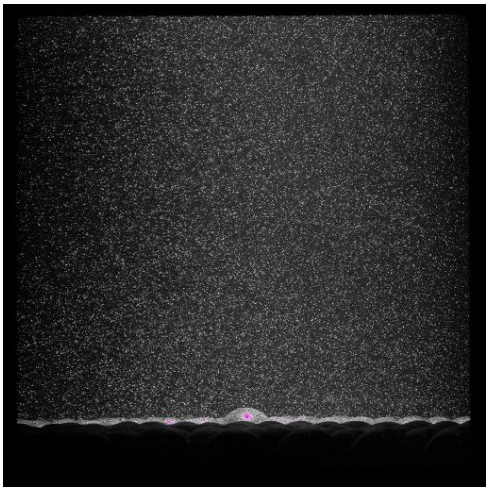

Figure 7.21: Raw V3V images of the bed for (a) p/d_1=0.82 (b) p/d_1=0.5 (c) p/d_1=0.2.

7.4.1 Fully exposed stone (p/d=0.82)

Figures 7.23 to 7.26 show 3D images of the flow around a 19mm diameter glass sphere resting on a coplanar bed of similar sized spheres. A clearly defined lee wake region downstream of the stone was not established over the course of the wave cycle. Instead, a residual vorticity structure was observed on top of the sphere.

Figure 7.27 shows side and sectional views of the vorticity structure on top of the stone. Due to the low pressure region within the core of the vortex, the uplift force would have been significant compared to the horizontal force and hence, the uplift force would have contributed more to the displacement of the stone.

Non-existence of a lee-wake region on the downstream side of the stone is due to the rapid flow reversal for short period waves used in the laboratory (i.e., 1.0 - 2.5 sec). The flow reverses before the full development of the lee-wake region. Velocities remain low for the most part of the wave cycle. Therefore, relatively high Reynolds numbers are achieved only for the peak velocity, which lasts for a fraction of the wave period.

Therefore, the increased stability of particles observed in the incipient motion tests is considered to be due to the lack of flow development.

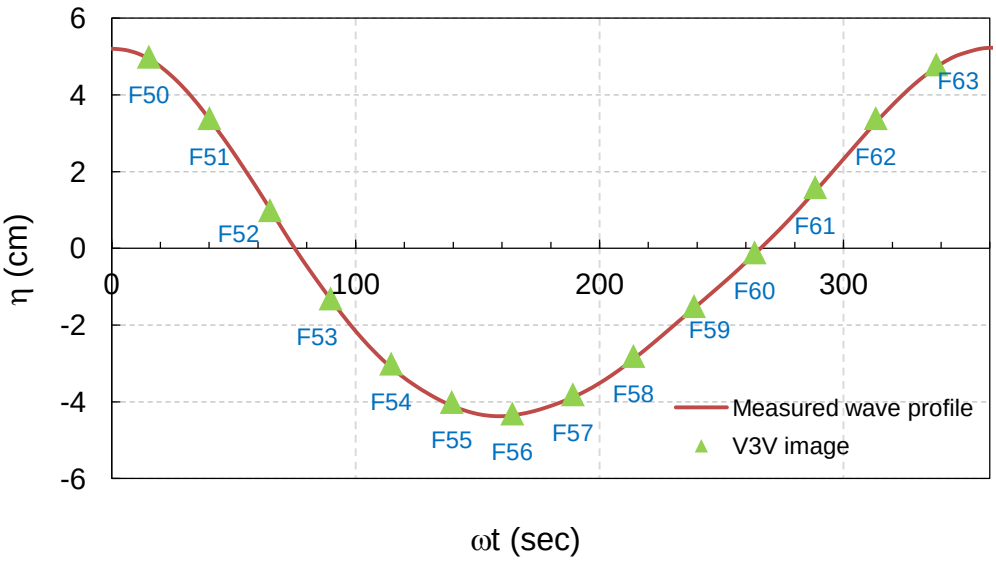

Figure 7.22: Measured wave profile, Test FV8, H=9.5cm, T=2 sec.

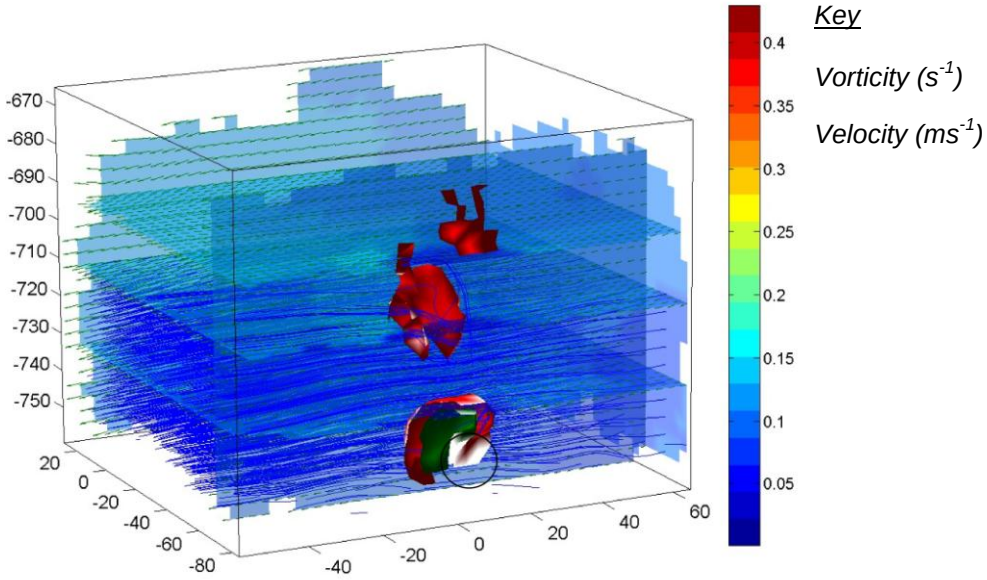

Figure 7.23: Vorticity isosurface, velocity vectors/contours and stream lines. Test FV8, Frame 54, $\omega t = 114.6^0$.

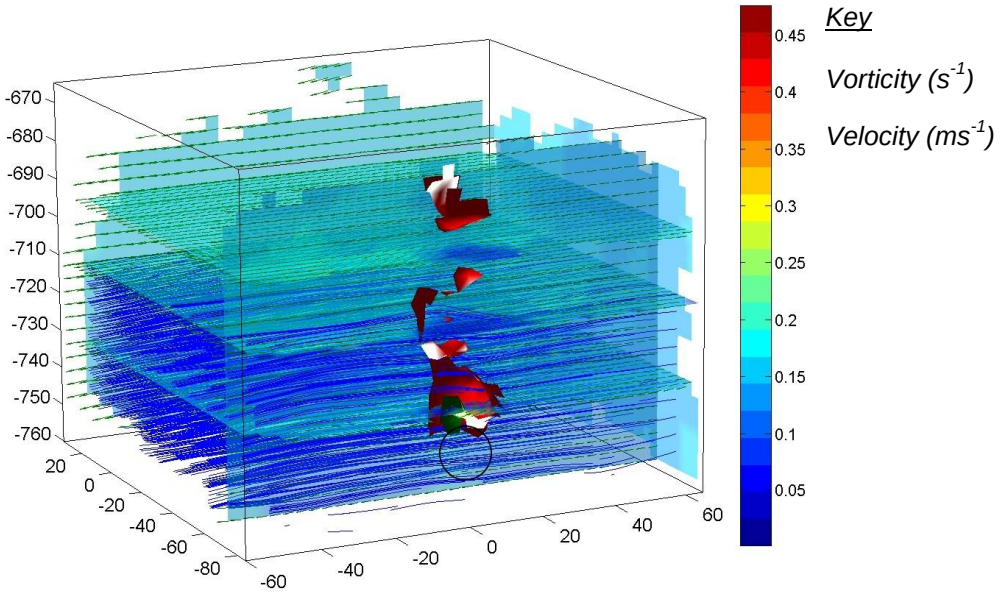

Figure 7.24: Vorticity isosurface, velocity vectors/contours and stream lines. Test FV8, Frame 55, $\omega t = 139.4^0$.

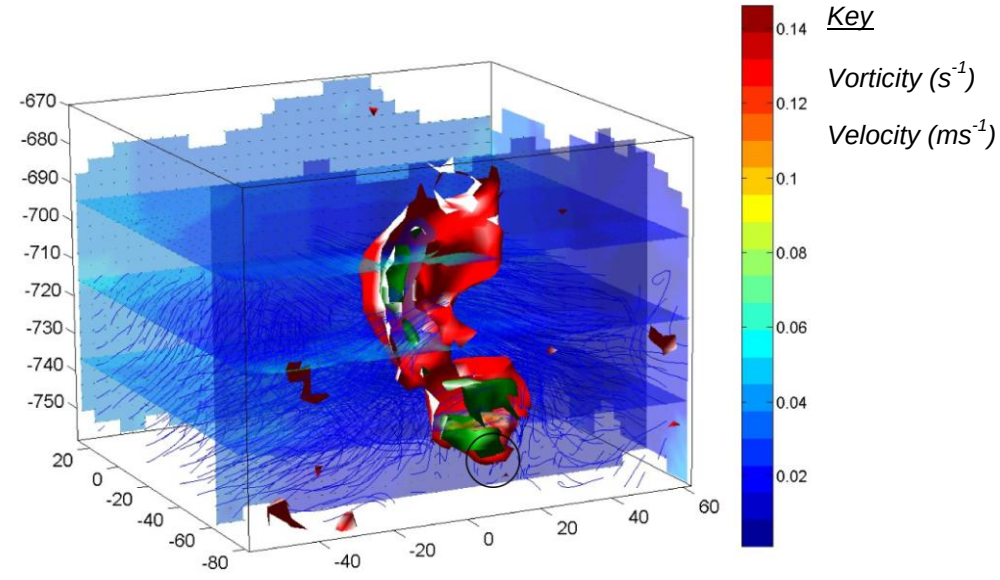

Figure 7.25: Vorticity isosurface, velocity vectors/contours and stream lines. Test FV8, Frame 60, $\omega t = 263.6^0$.

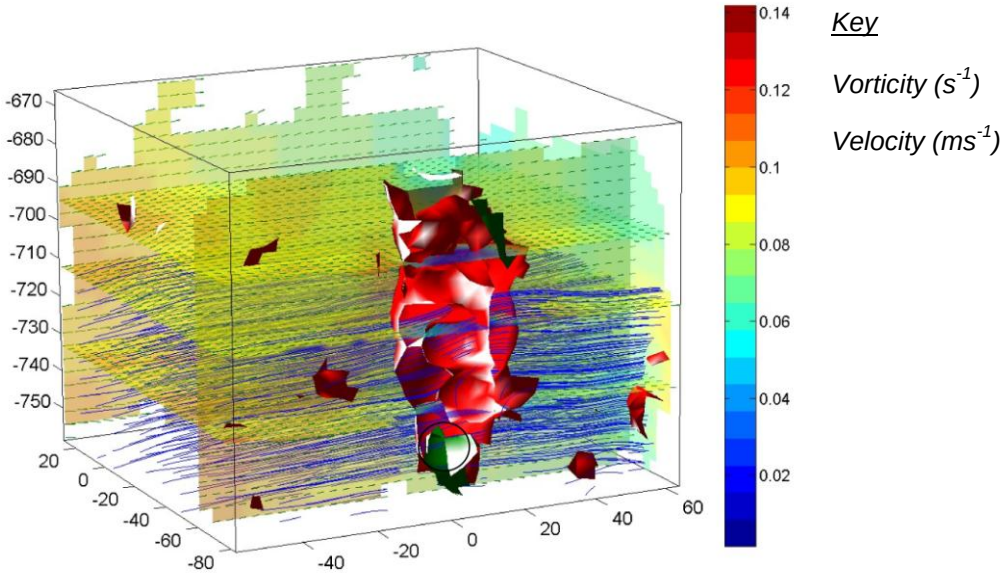

Figure 7.26: Vorticity isosurface, velocity vectors/contours and stream lines. Test FV8, Frame 61, $\omega t = 288.4^0$.

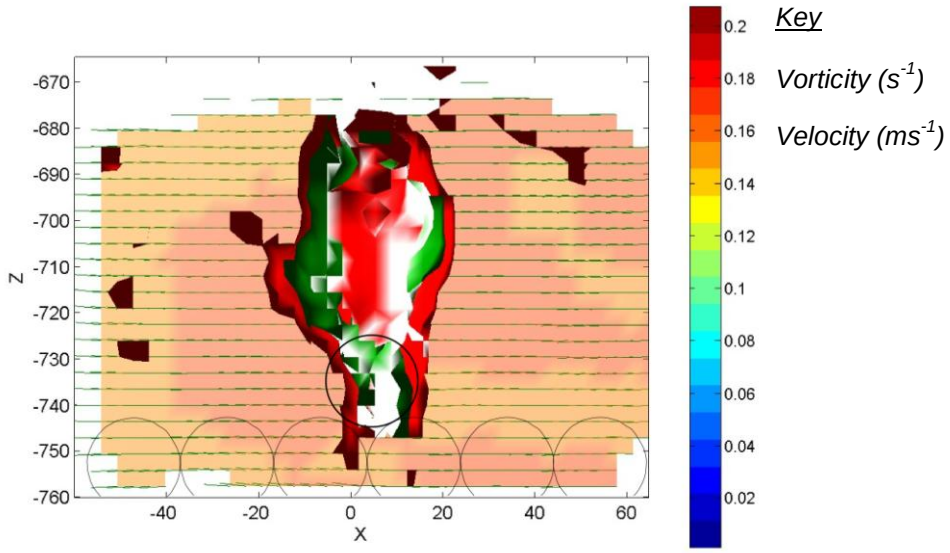

(a)

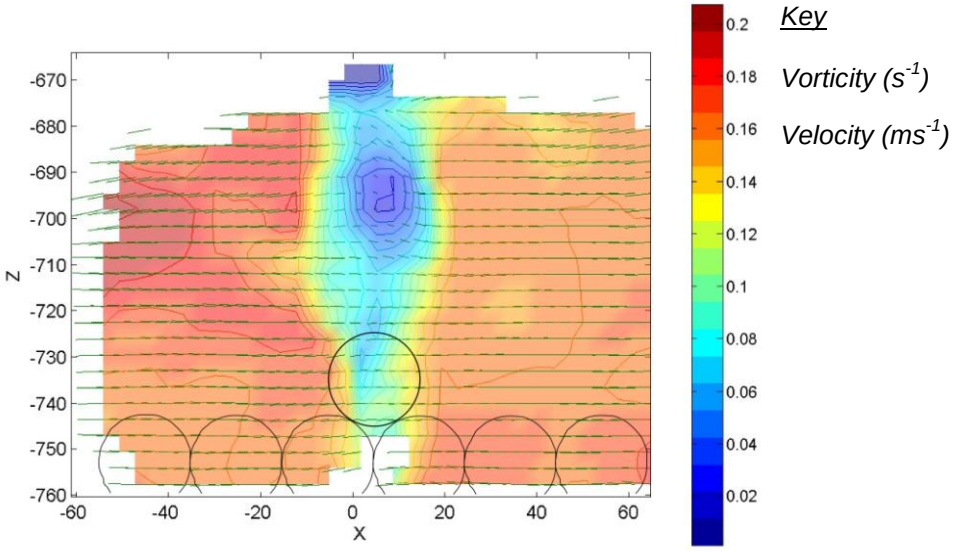

(b)

Figure 7.27: Residual vorticity structure above the stone (a) side view (b) section through the midpoint. Test FV8, Frame 56, $\omega t=164.3^0$.

7.4.2 Partially exposed stone (p/d=0.5)

Vortex shedding from a stone with relative protrusion, p/d=0.5 is shown in Figures 7.28. Similar to a fully exposed stone in the preceding section, the vortices are shed from the top of the stone rather than from the lee side in the streamwise direction. Figure 7.29 shows a sectional view of the vorticity structure. Similar to the flow around a fully exposed stone described in the preceding section, the residual vorticity at the crest of the stone is due to the lack of flow development as the flow reversal occurs within a short time.

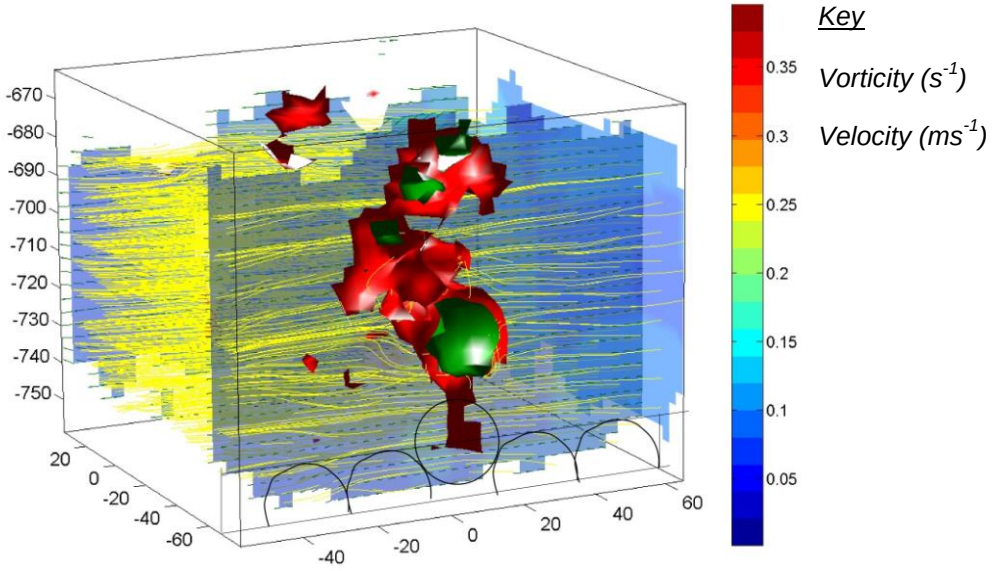

(a)

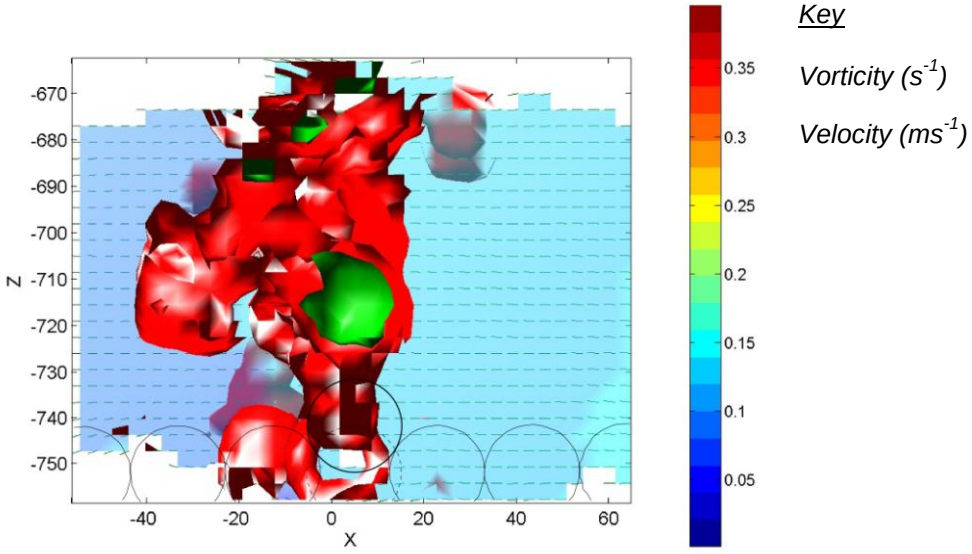

(b)

Figure 7.28: Residual vorticity structure above the stone (a) 3D view (b) side view. Test FV7, Frame 24.

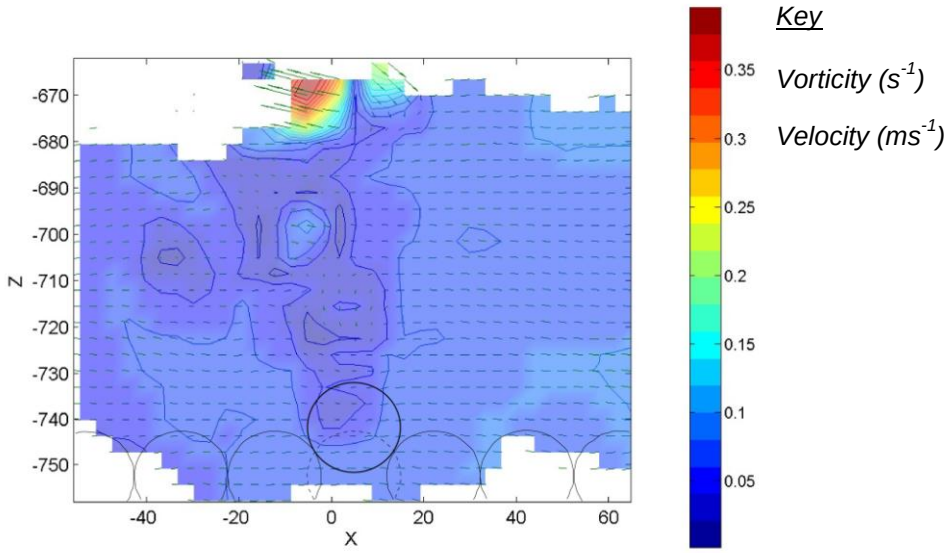

Figure 7.29: Residual vorticity structure – a section through the midpoint, Test FV7, Frame 24.

7.5 Flow around a light weight stone at incipient movement

Consecutive snap shots showing the sequence of movement of a light weight 19mm diameter sphere made of PVC (specific gravity = 1.4) are shown in Figure 7.30. Image (a) refers to the stable position just before the movement. The stone starts moving at (b). (c) shows the rolling motion and the stone comes to rest at (d) in a new position.

Figures 7.31 to 7.33 show vortex shedding before the movement. It was observed in the incipient motion tests that stones often undergo a rocking motion just before their movement. Vortex shedding is likely to contribute to this rocking movement.

At the moment of stone displacement (Frame 116), the stone comes within the region of influence of a moving vorticity structure (Figure 7.34). The low pressure region (eye) of the vortex moved from Position-A in Frame 115 (Figure 7.35) to Position-B in Frame 116 (Figure 7.36). The size of the vorticity structure is approximately of the size of the PVC test sphere. Therefore, this vorticity structure must have induced a sufficient lift force contributing to the displacement of the stone.

The movement occurred at Frame 116 (7.30*b*), 15.863 seconds after the start of the wave run (H=8.8cm, T=1.6). That is, for approximately 10 wave cycles (20 peaks in velocity), the stone did not move. It moved only when the uplift induced by the moving eddy and horizontal force/shear stress due to the peak streamwise velocity (between 0.175-0.2 m/s) coincided. Therefore, the probability of stone displacement is considered to be a

function of the probability of joint occurrence of an uplift force sufficient to give a lift to the stone simultaneously with a significant in-line force.

(a)

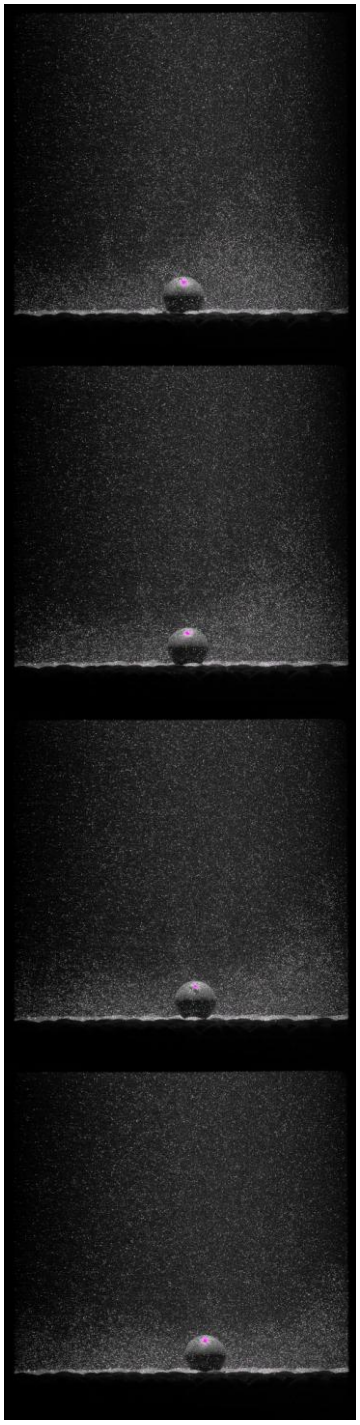

t=15.725 sec

(b)

t=15.863 sec

(c)

t=16.001 sec

(d)

t=16.139 sec

Figure 7.30: Displacement of a stone. Raw V3V images for consecutive frame nos. (a) 115-stable, rocking (b) 116- start of movement (c) 117- rolling (d) 118 – stable new position.

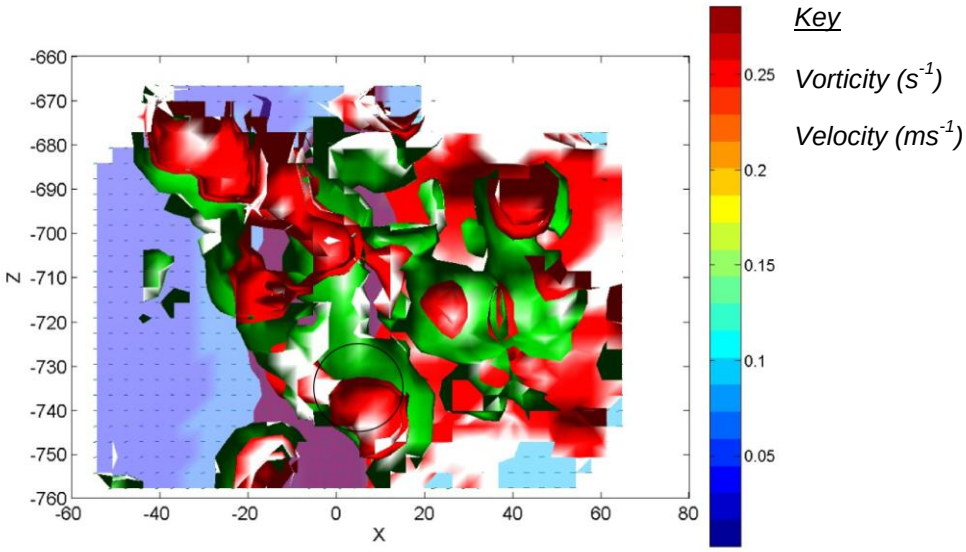

Figure 7.31: Vortex shedding before displacement, Test FV9, Frame 113.

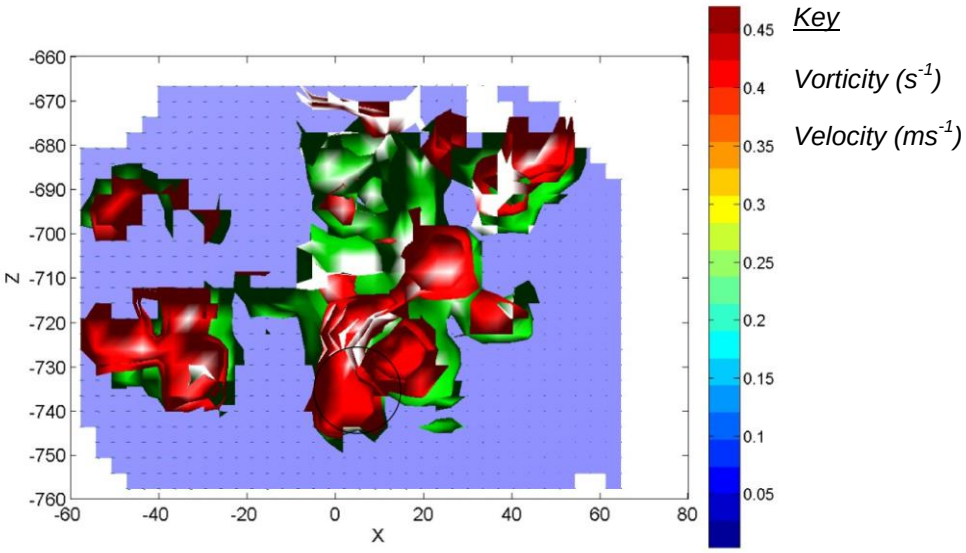

Figure 7.32: Vortex shedding before displacement, Test FV9, Frame 114.

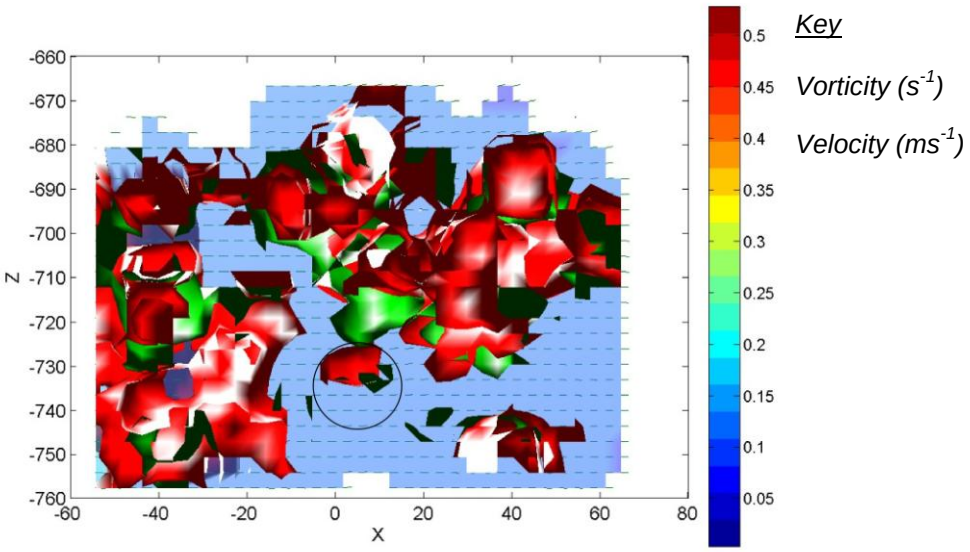

Figure 7.33: Vortex shedding just a moment before displacement, Test FV9, Frame 115.

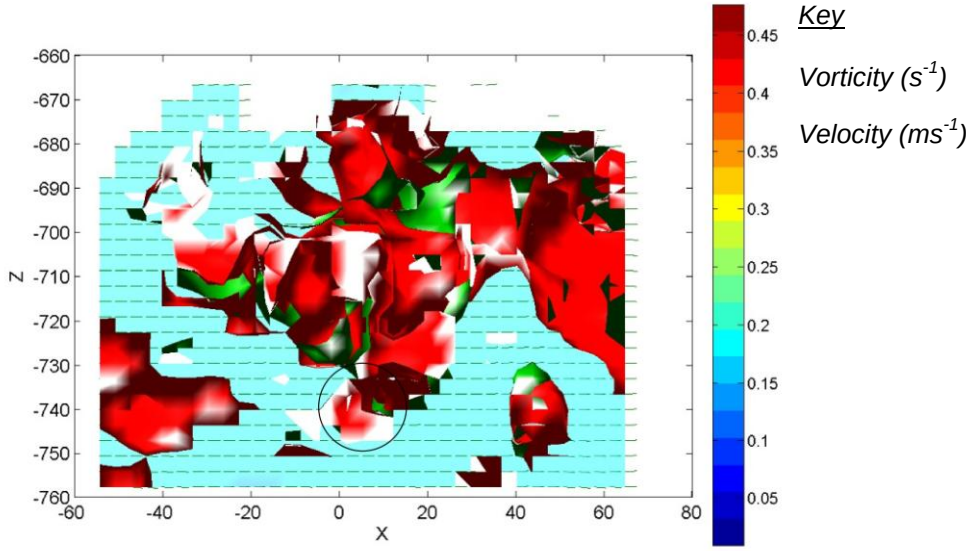

Figure 7.34: Moment of stone displacement, Test FV9, Frame 116.

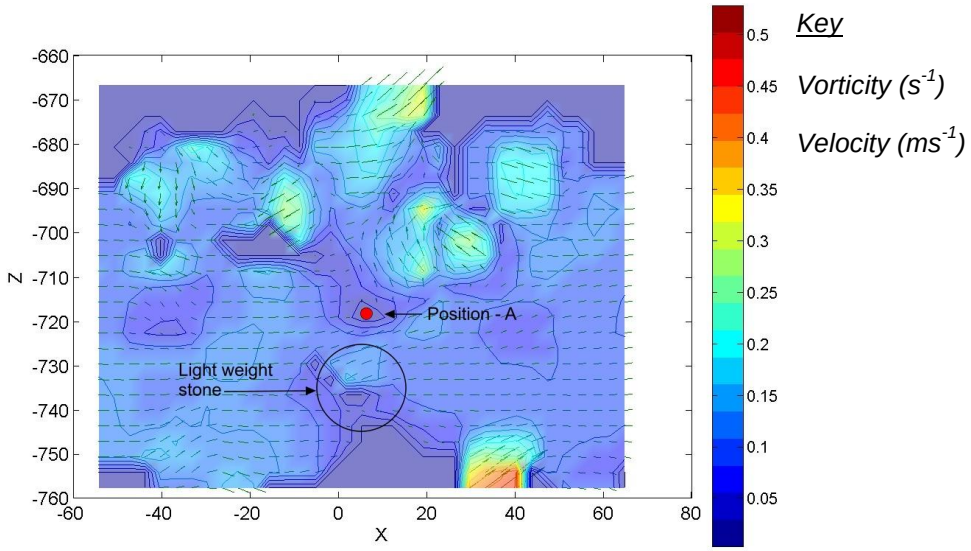

Figure 7.35: Vorticity structures just a moment before incipient movement, Test FV9, Frame 115.

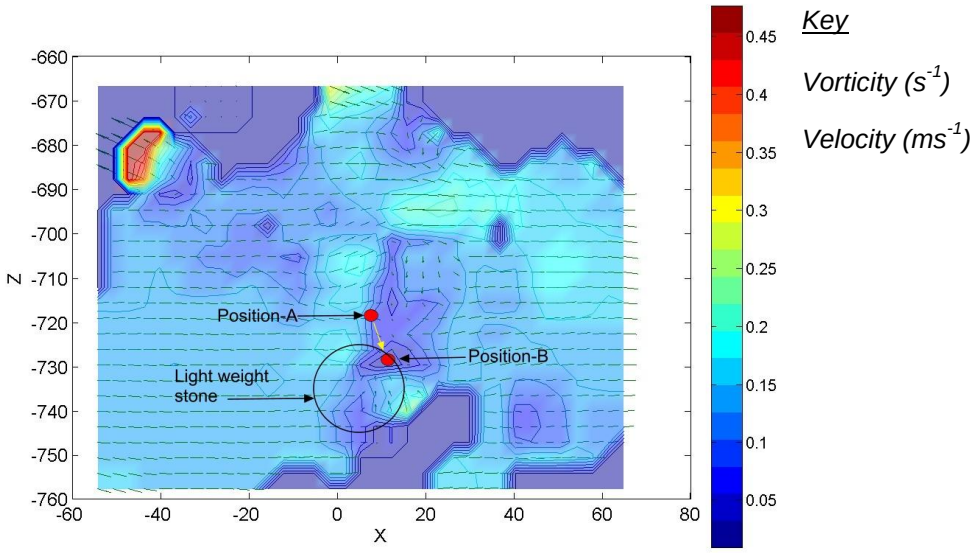

Figure 7.36: Vorticity structures at the time of stone displacement, Test FV9, Frame 116.

7.6 Summary

A summary of the observations made in the flow visualisation tests is given below:

1 Tests on a coplanar bed of spherical roughness elements showed that, various types of vortices, i.e., spherical blobs, hair pins, horse shoe, doughnut shaped rings etc., are detached from the top of the roughness elements and ejected into the flow above. These momentum rich parcels of fluid could contribute to the fluctuations in the Reynolds stresses.

2 Vortex shedding is dominant during the acceleration phases of the wave cycle.

3 Over the course of the wave cycle, near-bed turbulence does not cease even when flow reversal occurs and the mean velocities approach zero. The presence of turbulent eddies in significant density, was observed within a distance $\sim$ 1.0d from the bed at flow reversal. Therefore, the eddy viscosity in a rough bed should be a non-zero quantity within a one stone diameter distance from the bed. This observation is consistent with the assumption of Kajiura (1968) that for rough beds, the cycle-averaged eddy viscosity is a constant within a height $0.5k_s$ from the bed.

4 A residual vorticity structure on top of a 19mm diameter fully and partially exposed glass marble was observed instead of a fully

developed lee-wake region and ejection of vortex rings in the downstream side of the stone as typically observed for a free sphere. This suggests that the apparent stability of stones observed under waves is because the flow around the stone was not fully developed.

5 An otherwise stable test stone was displaced when it came under the influence of a moving eddy structure. Therefore, uplift forces generated by large scale moving vortices contribute significantly to the displacement of stones. The in-line force created by the peak velocity amplitude alone is not sufficient to move a stone. Probability of the threshold of movement depends on the probability of the joint occurrence of the horizontal and uplift forces simultaneously.

6 The threshold stone movement occurred at the peak orbital velocity, U_m. This is consistent with the observations made in the incipient motion tests.

8 Modelling of wave-induced damage to a bed protection

8.1 Introduction

In the preceding chapter on the incipient motion of stones, it was observed that the threshold of movement is strongly influenced by a stone's protrusion above the mean bed level, which in turn depends on its position in the bed surface. That is, a fully exposed stone lying on top of similar stones is more easily displaced than one in a co-planar bed. As the stone protrusion varies over the bed, the threshold shear stress should also vary, following a probability distribution. Turbulent fluctuations in shear and normal stresses applied by the fluid on the bed follow normal probability distributions (see Chapter 5 for a discussion). Therefore, threshold movement of a stone depends on the exceedence probability of the critical shear stress by the applied shear stresses.

A model that mimics the stochastic processes involved in the entrainment of a stone was set up to randomly generate stone size, protrusion (hence, threshold shear stress) and turbulence fluctuation in shear stress using the Monte Carlo simulation method.

8.2 The model

The following assumptions were made in formulating the model:

1. A stone will be displaced when the shear stress applied by the fluid just exceeds its critical value, i.e. $\Psi_t > \Psi_{cr}$ where, $\Psi_t = \tau_t/(s-1)\rho g d_i$, $\tau_t(t) = \tau_m \cos(\omega t) + \tau'$.

2. However, the rocks move only during the half cycle when there is a positive (upward) lift. Negative lift tends to stabilise the bed. Having a periodic peak shear stress alone would not be sufficient to remove a stone (see discussion in Section 7.5). It should be aided by a positive uplift force. Therefore, it was assumed that the instantaneous normal stress relative to the peak shear stress should exceed a certain threshold value, i.e., $\tau_{nt}/\tau_m > \lambda_{UL}$, at the moment of the threshold movement where $\tau_{nt}(t) = \tau_{nm} \cos(\omega t + \pi) + \tau_n'$.

3. A stone will move if the instantaneous normal stress integrated over the footprint (planar) area of the stone exceeds its submerged weight, W'.

4. Protrusion above the mean bed level of each stone, i (i=1….N), varies according to position on the bed. The critical shear stress for each stone, was related to the relative protrusion through an equation obtained from the incipient motion tests discussed in Chapter 6. These tests were conducted using light weight spheres which are

more easily removed than natural rocks, as the latter have to overcome inter-granular friction. Due to irregular shape and sharp edges, a natural rock can be interlocked more tightly than a sphere. Hence, a factor to increase the critical shear stress, $\lambda_{\Psi\text{-}cr}$ was applied.

5. The mean applied shear and normal stresses follow a cosine variation with peaks at crest and trough half cycles. The turbulent fluctuations of the shear and normal stresses follow a normal PDF. For each passing wave, j (j=1,2,3…M) , turbulent events were generated at a sampling frequency, f, at equal intervals, r (r=1,2,3…R). For example, if the sampling frequency is 50Hz, for a 2 sec wave period, the number of turbulent events per wave cycle is R=2 X 50 =100.

6. The rock size, $d_{i,}$ follows a normal PDF.

7. The relative particle protrusion was represented by a probability histogram derived from bed elevation measurements in a: (a) randomly placed bed; and, (b) a levelled bed constructed in the laboratory.

The schematic of the model implementation is shown in the flow chart in Figure 8.1.

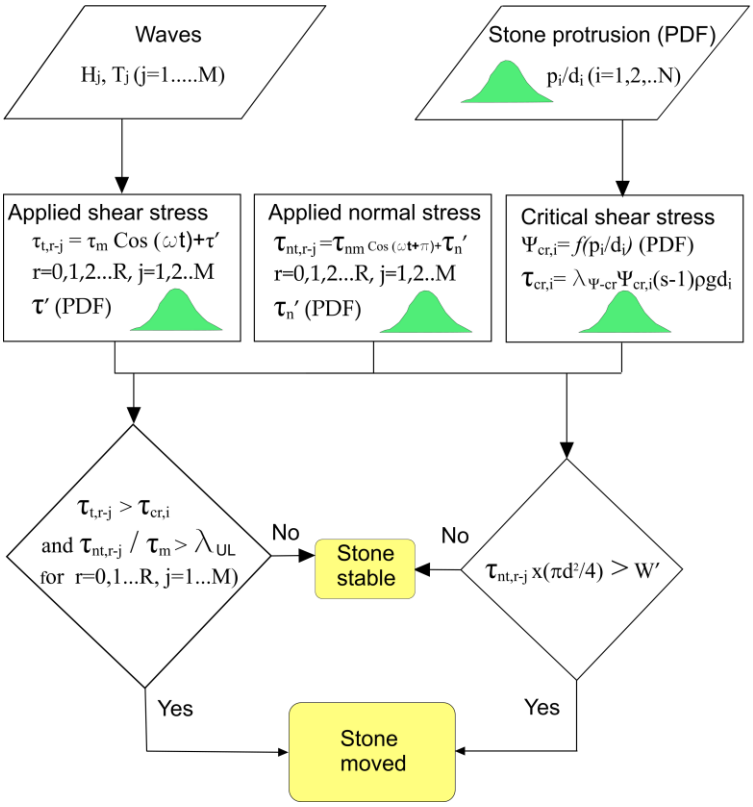

Figure 8.1: Stochastic model schematic.

8.2.1 Shear stress

As shown in Chapter 5, the wave-induced mean shear stress can be represented by a cosine function, $\tau=\tau_m\cos(\omega t)$. The instantaneous shear stress is given as $\tau_t=\tau+\tau'$ where, τ' is the turbulent fluctuation in the shear stress and $\tau_m=0.5f_w\rho U_m^2$. τ' follows a normal probability distribution as shown in Figure 5.19 in Chapter 5. Based on experimental observations in the present tests, a mean and standard deviation of 0 and 0.27 respectively

for the parameter τ'/τ_m, were used to generate the turbulence-induced shear stress fluctuations in this model.

8.2.2 Normal stress

It was found that the mean wave induced normal stress can be represented by a cosine relationship, $\tau_n=\tau_{nm}\cos(\omega t)$. The peak normal stress relative to peak shear stress, τ_{nm}/τ_m was found to be equal to 1.26 from the present measurements and was used in this model. Instantaneous shear stress is defined as $\tau_{nt}=\tau_n+\tau_n'$ where τ_n' is the turbulent fluctuation. τ_n'/τ_m follows a normal probability distribution with a mean and standard deviation 0 and 0.31 respectively (see Figure 5.20 in Chapter 5).

8.2.3 Simulated shear and normal stresses

Figure 8.2 shows the time-series of the simulated shear and normal stresses. The turbulence fluctuation was randomly generated following a normal PDF. The sampling time of the turbulence was assumed as 50Hz. Based on the observed variation of shear and normal stress as measured and presented in Chapter 5, it was assumed that the shear stress leads the normal stress by 180 degrees. The positive lift force (upward) occurs during the trough half cycle. The negative lift force (downward) tends to make a stone stable. Therefore, during the positive lift force time window, it was assumed that a stone has a relatively high probability to be displaced, with the shear stress and the positive lift force acting simultaneously.

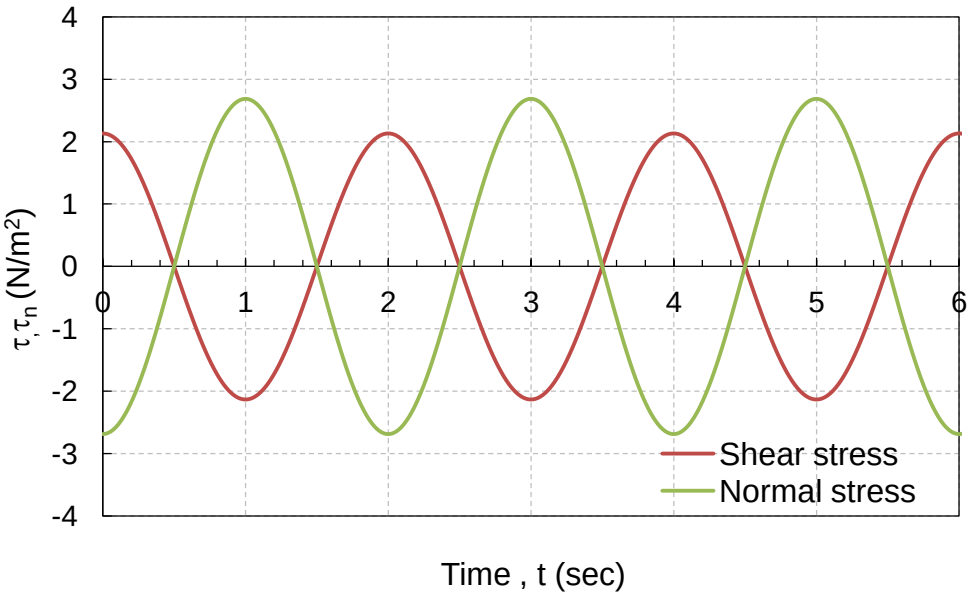

(a)

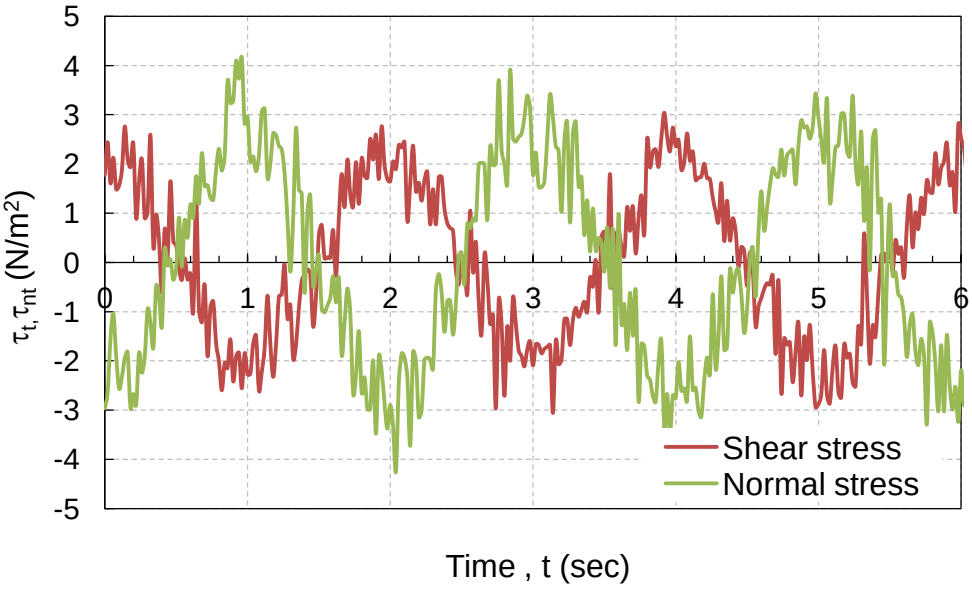

(b)

Figure 8.2: Simulated (a) mean (b) instantaneous shear and normal stress time series.

8.2.4 Stone protrusion and critical shear stress

Previous studies on currents (Fenton & Abbot, 1977; Chin & Chiew, 1993) and the present study on waves (see Chapter 6) showed that the critical shear stress has a strong dependence on the relative stone protrusion level. As the critical shear stress becomes asymptotic at p/d=0.2, a continuous exponential curve would have been more appropriate to represent the relationship. However, due to the wide scatter in the data due to water depth and wave period effects, good correlation could not be obtained. Therefore, a linear equation provided a good fit when p/d>0.2, and hence it was used in the model (Figure 8.3).

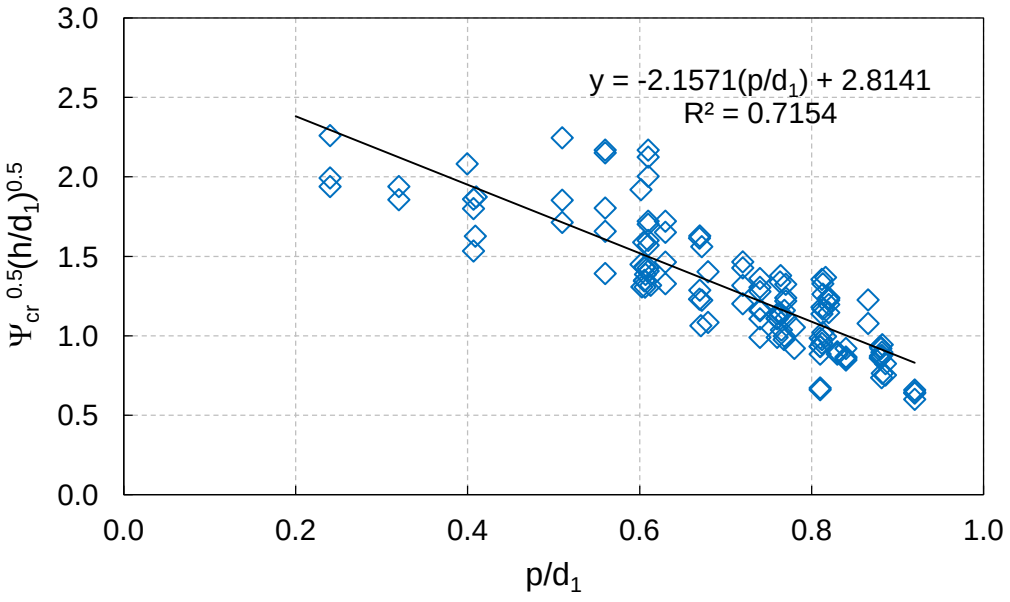

Figure 8.3: Modified Shields critical shear stress against relative protrusion.

In the above relationship, the critical shear stress is based on the mean value (phase-averaged). In order to add the effect of turbulence, the rms value of the turbulent fluctuation was added to the shear stress (Figure 8.4).

From the measurements presented in Chapter 5 (see Table 5.4), it was found that $<\tau'^2>^{1/2}/\tau_m=0.375$.

Therefore, the modified Shields parameter was assumed as:

$$\Psi_{k-cr} = \left(\tau_m + <\tau'^2>^{\frac{1}{2}}\right)/(s-1)\rho g d \qquad (8.1)$$

$$\sqrt{\frac{\Psi_{k-cr} h}{d_1}} = -2.529\left(\frac{p}{d}\right) + 3.3 \qquad (8.2)$$

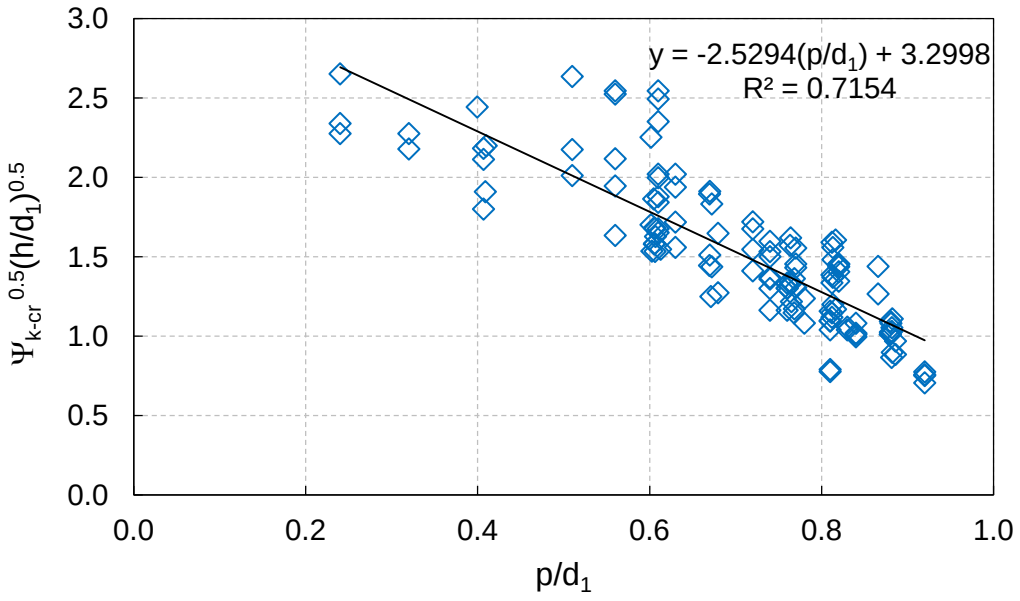

Figure 8.4: Modified Shields critical shear stress accounting for the effect of turbulence intensity plotted against relative protrusion.

8.2.4.1 Randomly placed bed

Rocks were dropped from a 40cm height (which is the water line when the flume is filled) above the flume bed to construct the bed protection. This was intended to simulate the dumping of rocks on the seabed in marine construction.

A 3D digital surface model of the bed was obtained using a laser scanner (Figure 3.31). Three cross-sections from this digital surface model were extracted to obtain the surface elevation profile. The points on the surface profile, η_{bi}were averaged to obtain the mean bed level $\bar{\eta}_b$. The protrusion was obtained by the relation, $p = \eta_{bi} - \bar{\eta}_b$.

A close-up photo of the granular bed, a 3D representation of the bed, cross-sectional views of the bed obtained from the digital surface elevation model and the probability histogram for the relative protrusion p/d_{n50} are shown in Figures 8.5 to 8.9.

Figure 8.5: Close up view of the granular bed consisting of anthracite rocks.

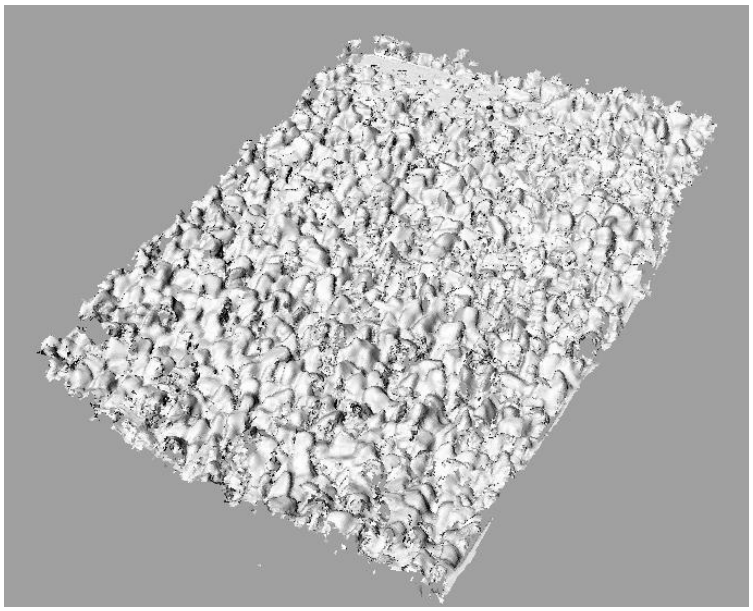

Figure 8.6: The digital surface elevation model of the randomly placed bed.

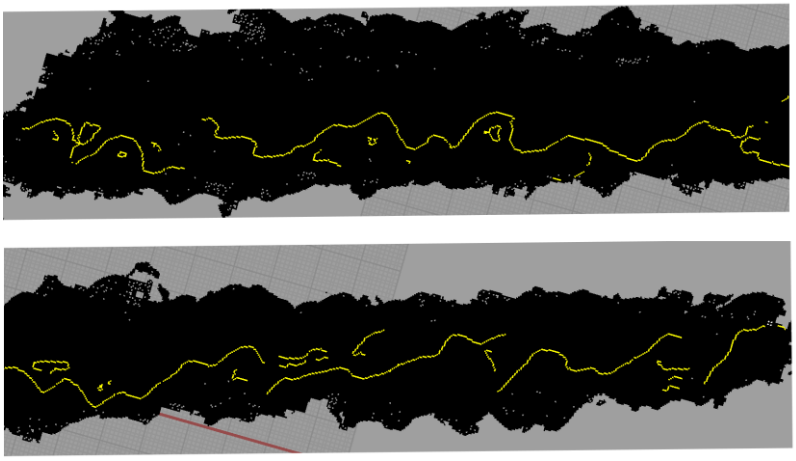

Figure 8.7: A cross-section of the randomly placed bed obtained from the digital surface elevation model.

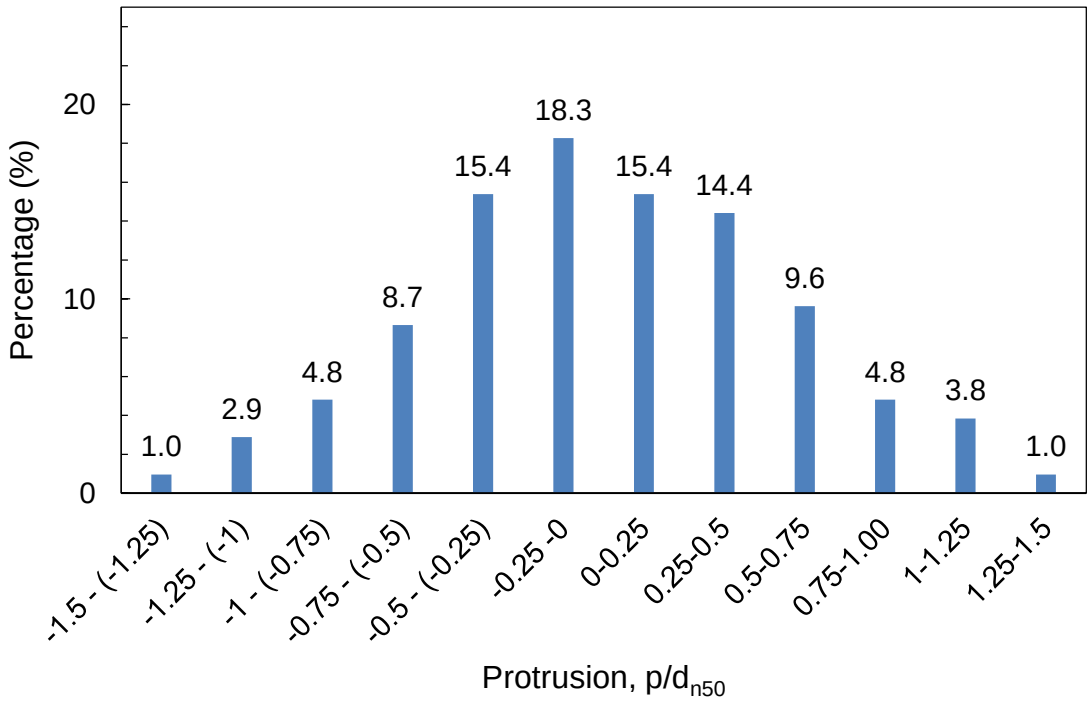

Figure 8.8: Probability histogram of the relative protrusion of stones – randomly placed bed.

The data did not fit a normal PDF. As the model was set up using spreadsheets only the functions available for random number generation within the spreadsheet program could be used. For this reason, the probabilities in this specific histogram found above were multiplied by the total number of rocks on the bed to obtain the number of protrusions falling within a given range, i.e. p/d=0-0.25, 0.25- 0.5 etc.

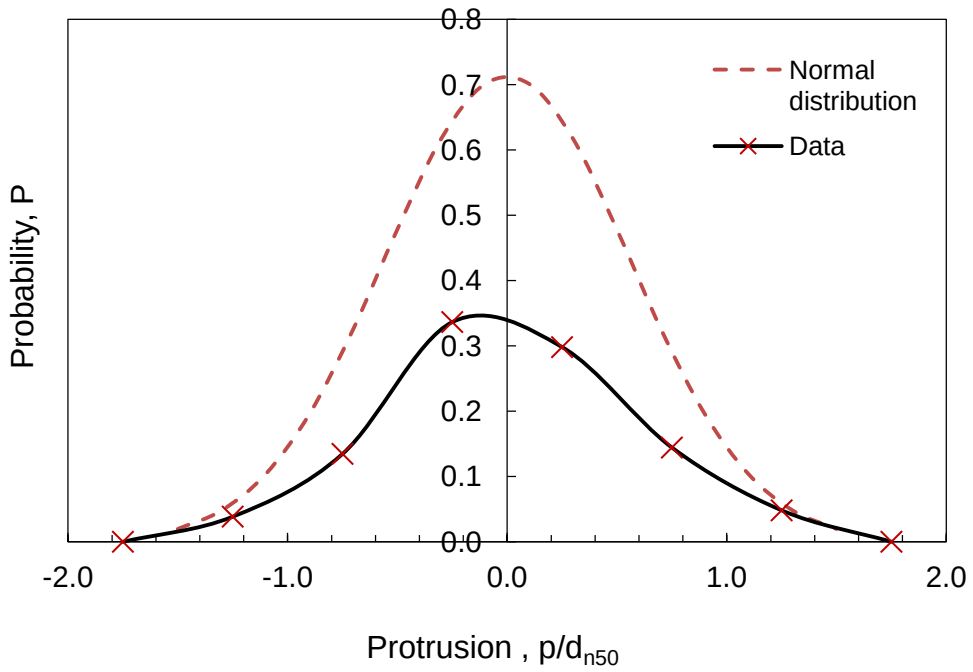

Figure 8.9: Probability distribution of relative protrusion compared with normal PDF.

8.2.4.2 Levelled bed

It is one of the objectives of this research to study the effect of reduced stone protrusion on bed damage. For this purpose, the bed was levelled with the aid of a straight edged timber plank and a tubular spirit level. The same procedure was followed as for the random bed to obtain the probability histogram of the relative stone protrusion.

A 3D perspective, cross-sectional views of the levelled bed obtained from the digital surface elevation model and the probability histogram for the relative protrusion p/d_{n50} are shown in Figures 8.10 to 8.12.

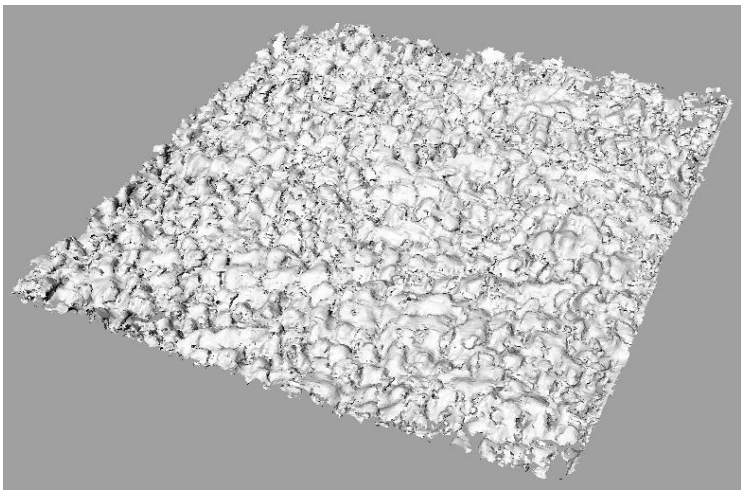

Figure 8.10: The digital surface elevation model of the levelled bed.

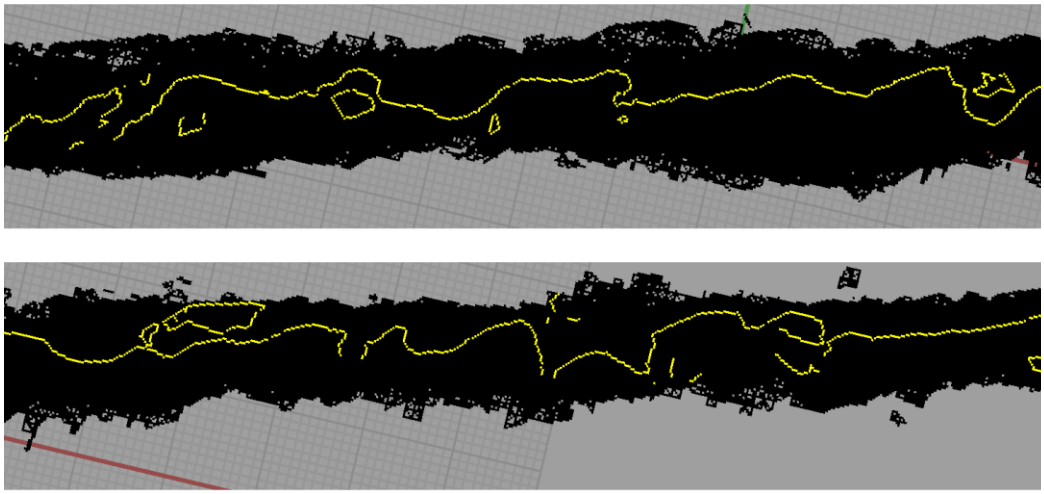

Figure 8.11: A cross-section of the levelled bed obtained from digital surface elevation model.

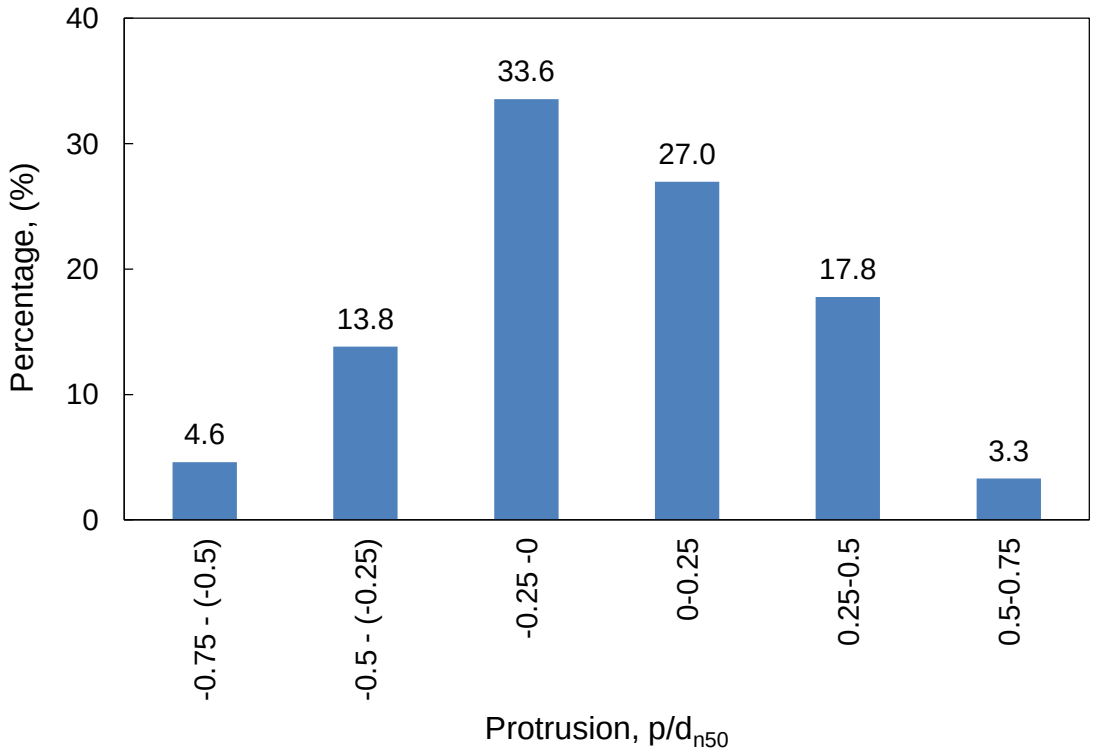

Figure 8.12: Probability histogram of the relative protrusion of stones – levelled bed.

8.2.5 Stone size, shape and density

8.2.5.1 Rock size

A sample of natural rock (anthracite) was sieved using 8mm and 12mm mesh sizes to obtain a uniform grading. Particles larger than 12mm and smaller than 8mm were rejected. From the sieved rocks, a sample consisting of 220 particles were weighed and the three dimensions, i.e. longest, shortest, and the intermediate were measured using a Vernier calliper. The nominal diameter was calculated using the relationship, $d_n=(M/\rho)^{1/3}$. Figure 8.13 shows the grading curve thus obtained.

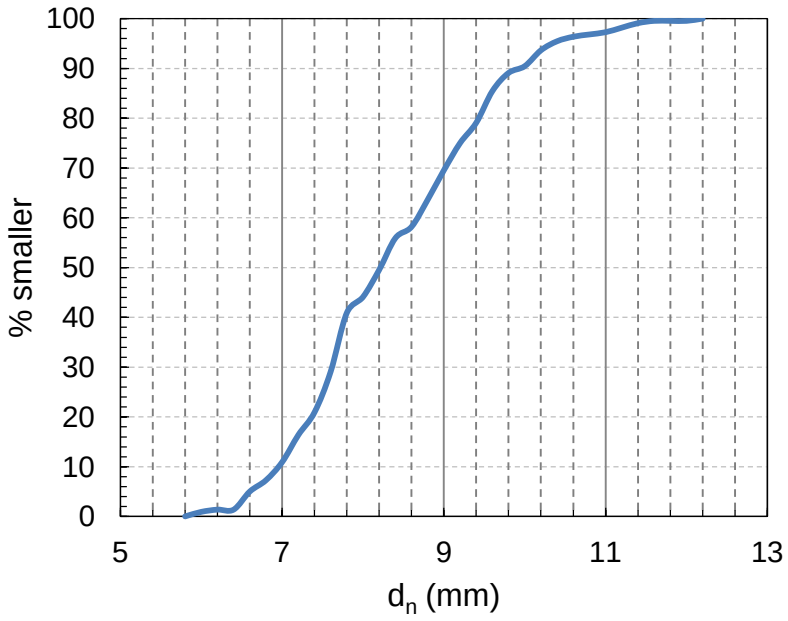

Figure 8.13: Grading curve of anthracite particles.

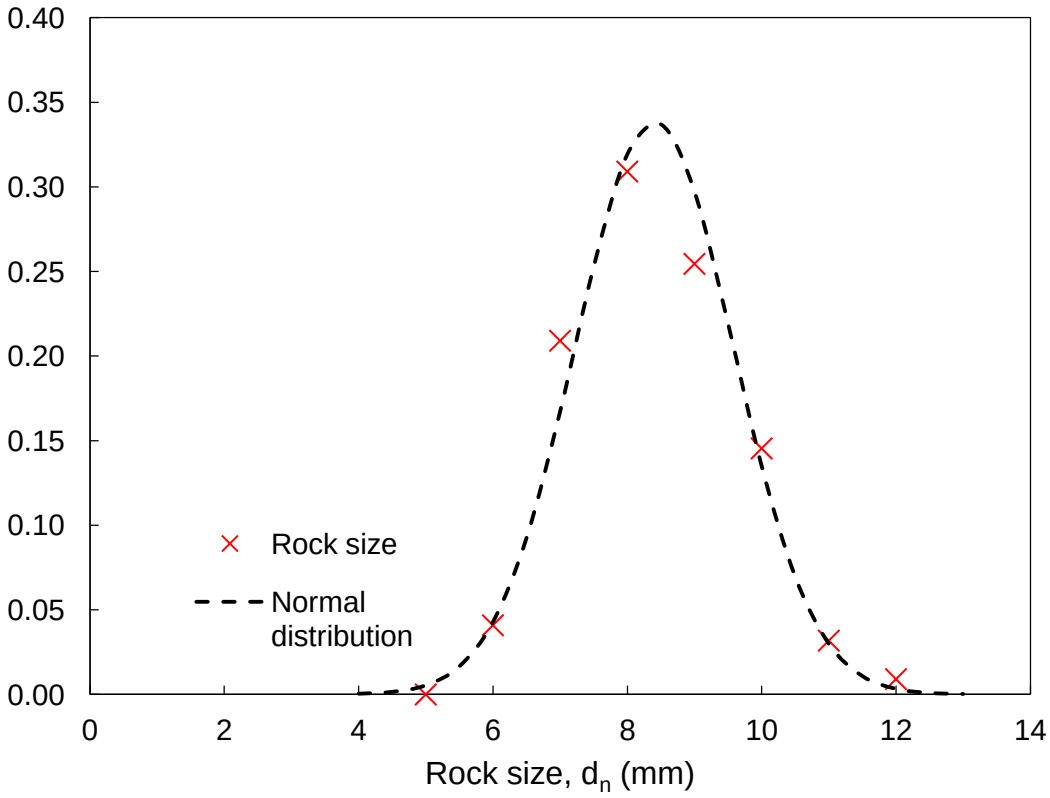

Figure 8.14: The PDF of the rock size in a sample.

The grading curve gives the 50% passing nominal diameter, d_{n50}=8.2mm. The mean and standard deviation of the rock sample diameter were found to be 8.4mm and 1.18mm, respectively.

The measured uniformity ratio, d_{85}/d_{15}=9.6mm/7.2mm=1.33, falls into the narrow grading (i.e. <1.5). A narrow grading is used for most top armour layers in coastal engineering applications.

8.2.5.2 Shape

The average shape factor of rocks computed based on $SF=a/(bc)^{1/2}$ was found to be equal to 0.58. This is close to the value SF=0.6 for graded stones given in CIRIA Rock Manual (1991). The dimensions a, b and c correspond to shortest, intermediate and longest lengths of a rock, respectively.

8.2.5.3 Density

A graduated glass beaker was partially filled with water. Washed and weighed samples of rock were placed in the beaker. The displaced volume was then calculated based on water level change. The mass of the rock sample was then divided by the displaced volume to find the density of rocks, which was found to be 1.35g/cm^3. This agreed with the supplier's specification.

8.2.6 Excel functions for random number generation

Table 8.1 lists the Excel functions used to generate random values for the model parameters.

Table 8.1: Excel functions used to generate random numbers.

Parameter	PDF	Excel function
Turbulent fluctuation in shear and normal stress (τ', τ'_n)	Standard normal	NORMSINV(RAND())
Stone size (d_i)	Normal	NORMINV(RAND())
Stone protrusion $(p/d)_i$	Probability histogram	RAND()*[(p/d)max-(p/d)min]+(p/d)min Where (p/d) max and (p/d)min are upper and lower limits of a class

8.3 Comparison of model results

8.3.1 Model calibration

The physical model test RS1 was run for 30 mins (900 waves) and photographs of the bed were taken at 10 sec intervals from an overhead camera fixed above the test section. The number of rocks displaced after 30 mins were counted using the photographic information.

The stochastic model was run for the same period, with the turbulent events being generated at 50Hz, i.e., at every time-step (0.02sec interval) a turbulent fluctuation was generated.

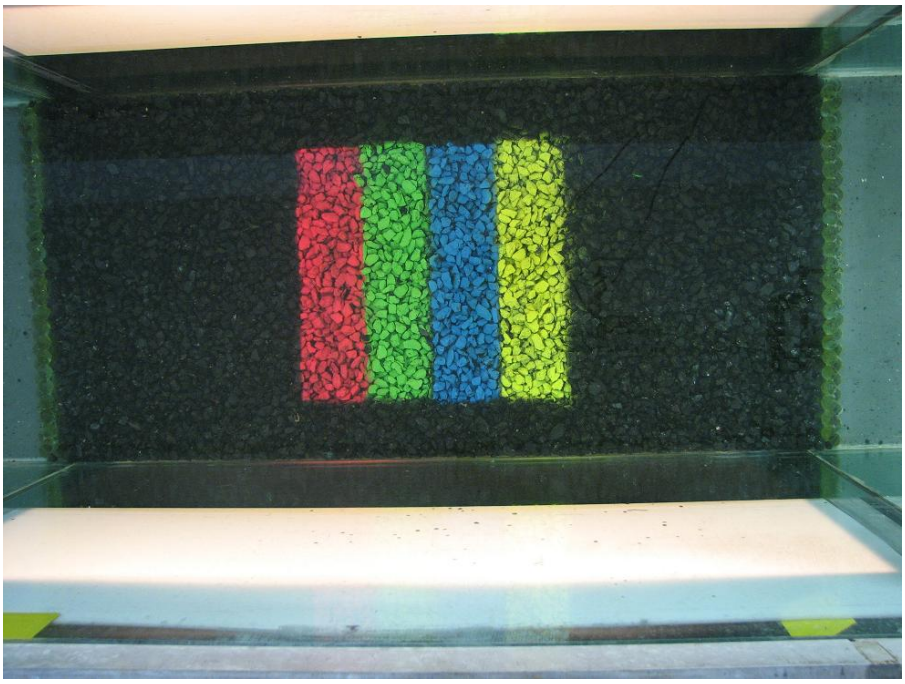

Figure 8.15: The 30cm X 30cm test section at t=0. Test RS1.

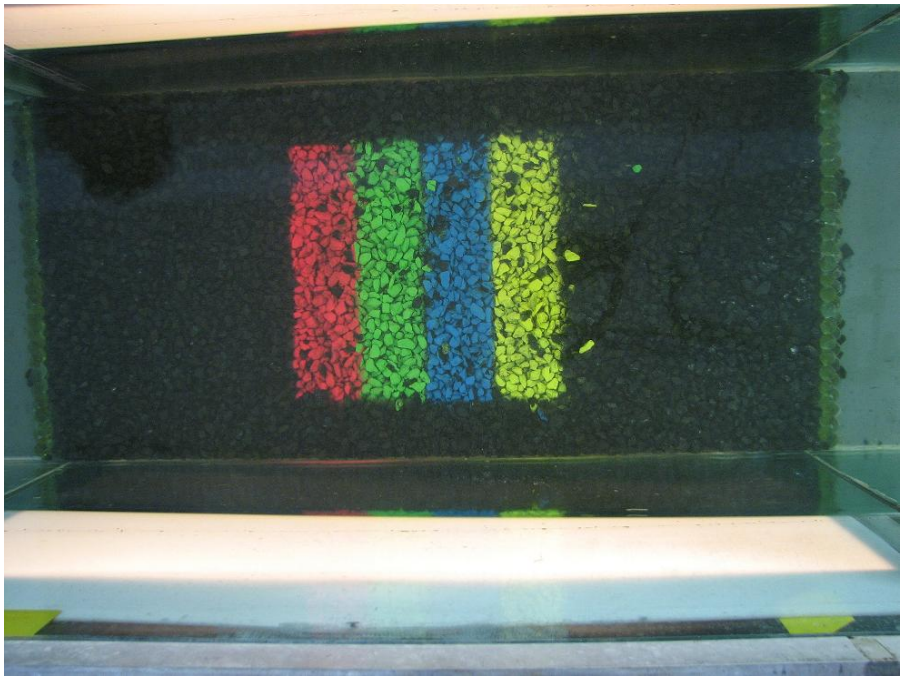

Figure 8.16: Bed damage after t=30 mins (900 waves). Test RS1.

It was assumed that the stones will not be displaced without the aid of a significant uplift force (see Chapter 7.5 for a discussion). The shear stress and the normal stress (positive uplift) should act simultaneously to displace a stone. It was assumed that the instantaneous normal stress should exceed a certain threshold limit, $\tau_{nt}/\tau_m > \lambda_{UL}$ to lift a particle from its pocket and this limit is an unknown parameter. Therefore, this threshold value was used as a calibration coefficient. That is, the λ_{UL} value is used to best fit the stochastic model results to the physical model results, and the value will then be used to predict the bed damage in the other tests.

The other calibration coefficient used was $\lambda_{\Psi\text{-cr}}$, which was an enhancement factor to the critical shear stress. The relationship obtained for the critical shear stress as a function of the relative protrusion was derived in Chapter 6 using light weight spherical elements which are more easily displaced than natural rocks. Therefore, the critical shear stress value obtained from equation 8.2 was multiplied by $\lambda_{\Psi\text{-cr}}$ to apply to a bed of natural rocks.

The number of rocks displaced was more sensitive to a change in the parameter λ_{UL} than for a similar percentage change in $\lambda_{\Psi\text{-cr}}$.

Table 8.3 shows the test conditions and number of rocks displaced in the physical model test RS1 which was used to calibrate the model. Table 8.4 presents the predicted results of the calibrated stochastic model.

Table 8.2: Physical model test conditions and observed bed damage – Test RS1.

Test no.	H (cm)	T (sec)	h (cm)	Total number of rocks in the test area	No. of rocks displaced	% removed
RS1	8	2	40	760	52	6.84

Table 8.3: Stochastic model prediction – Test RS1.

p/d	No. of rocks in the range	No. of rocks displaced		
		Run 1	Run 2	Run 3
0 – 0.25	117	0	0	0
0.25 – 0.5	109	0	1	2
0.5 – 0.75	73	15	25	15
0.75 – 1.0	36	17	14	19
1.0 – 1.25	29	15	8	10
1.25 – 1.5	8	5	2	5
Total		52	50	51
Prediction error, %		0	-3.8	-1.9

The model results were matched to the physical model results (i.e., 52 rocks or 6.84% displaced) by changing the calibration coefficients, mainly, λ_{UL}. The coefficient that gives the best fit of the model result to the bed damage observed in the physical model was chosen as the calibration factor.

Table 8.4: Stochastic model calibration factors deduced.

$\lambda_{\Psi\text{-cr}}$	λ_{UL}
1.1	2.45

8.3.2 Randomly placed bed

The stochastic model calibrated for physical model test RS1 in the preceding section (i.e. H=8cm, T=2 sec) was used to predict the number of rocks displaced in Test RS7 (H=10cm, T=2 sec, Table 8.5). The model was run 5 times to obtain an average value (Table 8.6). The prediction error for individual runs varied from -4.8% to 40.5%. However, the average of 5 model runs gave a 21.4% error when compared with the number of rocks displaced in the physical model.

Table 8.5: Physical model test conditions and observed bed damage – Test RS7. Randomly placed bed.

Test no.	H (cm)	T (sec)	h (cm)	Total number of rocks in the test area	No. of rocks displaced	% removed
RS7	10	2	40	571*	42	7.36

* without accounting for the red strip as it showed unrealistically large damage.

Table 8.6: Stochastic model prediction – Test RS7.

p/d	No. of rocks in the range	No. of rocks displaced					
		Run 1	Run 2	Run 3	Run 4	Run 5	Average
0 – 0.25	88	0	0	0	0	0	0
0.25 – 0.5	82	9	11	10	7	8	9
0.5 – 0.75	55	23	20	18	17	19	19
0.75 – 1.0	27	15	8	11	8	17	12
1.0 – 1.25	22	10	8	9	8	9	9
1.25 – 1.5	6	2	4	1	0	3	2
Total		59	51	49	40	56	51
Prediction error, %		40.5	21.4	16.7	-4.8	33.3	21.4

8.3.3 Levelled bed

The calibrated model was applied to predict the number of rocks displaced from the levelled bed in test RS8 (Table 8.7). Five model runs were carried out (Table 8.8). The prediction error in the individual runs varied from -40% to 0%. The average of the five model runs gave a prediction error of -24%.

Table 8.7: Physical model test conditions and observed bed damage – Test RS8 - Levelled bed.

Test no.	H (cm)	T (sec)	h (cm)	Total number of rocks in the test area	No. of rocks displaced	% removed
RS8	10	2	40	718	25	3.48

Table 8.8: Stochastic model prediction – Test RS8.

p/d		No. of rocks displaced					
	No. of rocks in the range	Run 1	Run 2	Run 3	Run 4	Run 5	Average
0 – 0.25	194	1	1	0	4	0	1
0.25 – 0.5	128	10	6	13	12	14	11
0.5 – 0.75	24	8	8	12	4	3	7
Total		19	15	25	20	17	19
Prediction error, %		-24.0	-40.0	0.0	-20.0	-32.0	-24.0

8.3.4 Bed damage progression with time and the effect of sampling rate on damage prediction

Figure 8.17 shows the damage progression in Test RS7 plotted against the number of wave cycles. The stochastic model predicted bed damage poorly up to about 680 wave cycles (after 22.7 mins) where the two curves representing physical model results and model prediction cross.

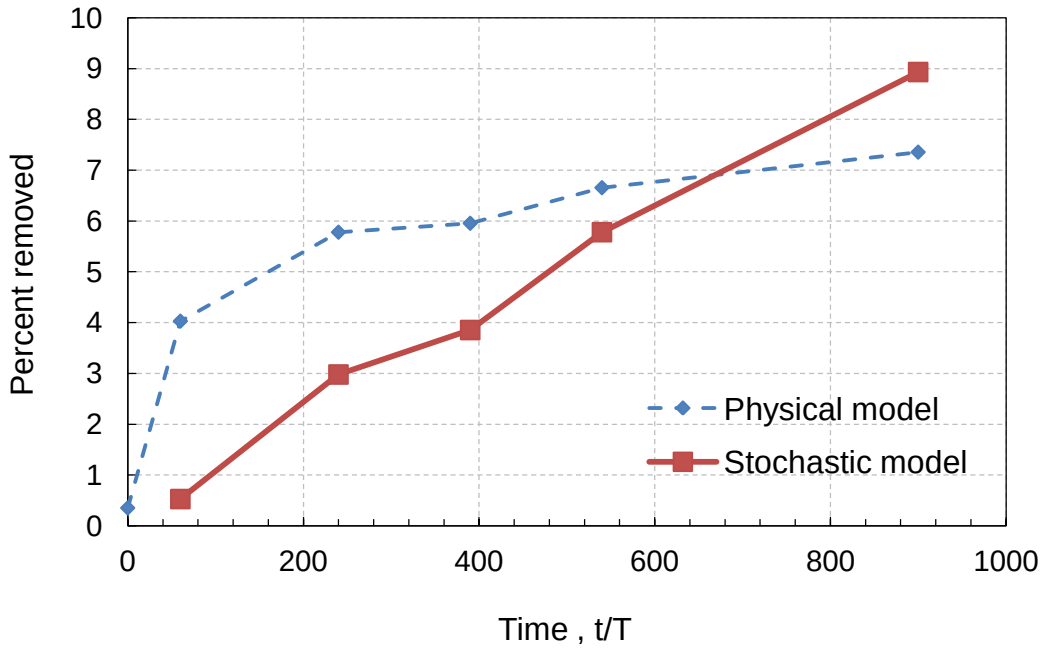

Figure 8.17: Bed damage progression with time.

Table 8.9: Effect of turbulence sampling frequency on prediction accuracy.

Turbulence Sampling frequency (Hz)	100	50	25
Rocks displaced in the physical model in 30 mins	42		
Rocks displaced in the stochastic model**	76	51	31
Error in the prediction, %	80.9	21.4	-26.2

** Average of 5 runs

The model was calibrated for a sampling frequency of 50Hz and a model run time of 30 mins. It appears that when the chosen calibration factors are used for predicting bed damage for smaller time periods or for different sampling frequencies different to the calibration conditions, the prediction error increases.

Despite this disadvantage, the model predicts the bed damage reasonably well for the calibrated period and sampling frequency (i.e. within ±25% error). Hoan *et al.* (2008) reported a 50% error in his bed damage prediction model. Therefore, the prediction error achieved in this study is improved above those previously presented for a bed damage prediction. It appears that the statistical accuracy in the prediction is increased after a large number of waves are allowed to pass. A possible application of this model would be when a large number of physical model runs in the laboratory have to be carried out to optimise a bed protection solution. One or few preliminary physical model tests can be used for calibration of the stochastic model. The calibrated model could then be used for further tests instead of running the physical model.

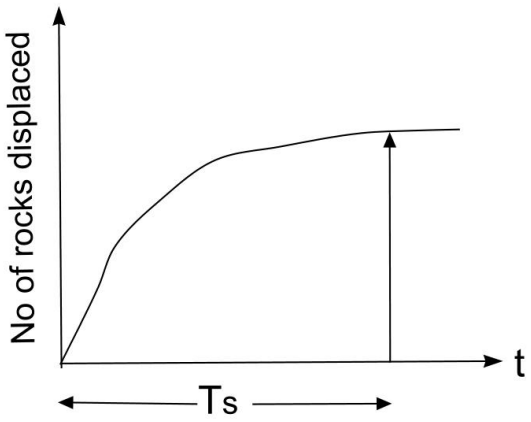

Figure 8.18: Sketch of bed damage progression.

The model does not take into account stone consolidation, bed armouring etc., the processes of which will increase the resistance of the bed to damage with time. It was assumed that the bed updating is not important as a scour protection is designed for low mobility conditions. However, in the physical model tests, it was observed that the rate of rock displacement gradually decreases with time and the bed will reach a stable condition. Therefore, the prediction model is valid only up to the time when the rate of stone entrainment first approaches a zero value at $t=T_s$. The stochastic model will continue to displace rocks even when the bed is stable (i.e. when $t>T_s$) as the increasing bed resistance is not factored into the model. This limitation should be considered when selecting the time duration for model calibration and bed damage prediction.

8.3.5 Effect of stone placement method on the stability of a bed protection

One of the key objectives of this study is to emphasise the importance of stone protrusion on the bed damage of a scour protection. From the experiments conducted it was observed that a levelled bed is more stable, with almost 50% less damage compared to a bed prepared by dropping rocks randomly from a height of 40cm, i.e. water depth (see Table 8.10). An explanation for this phenomenon can be given in terms of the probability of occurrence of exposed stones. In Figure 8.8, for a randomly placed bed, the probability of occurrence of fully exposed stones (p/d_{n50}=0.75-1.0) is 4.8% whereas this is zero for a levelled bed (Figure 8.12). Stones in the p/d_{n50}=0.5-0.75 range occupy 9.6% in the randomly placed bed. However,

this is only 3.3% in the levelled bed. Therefore, the lower the probability of occurrence of exposed stones, the lower is the percentage bed damage.

In the histogram for the levelled bed (Figure 8.12) the total number of stones in the p/d_{n50} = 0 – 0.25 range is 27%. This is 15% in the randomly placed bed (Figure 8.8). In the levelled bed, 21.1% of the stones exceeded p/d_{n50}=0.25. In contrast, 33.6% of the stones exceeded this value in a randomly placed bed.

Stones with the highest exposure have a high probability of displacement. For a randomly placed bed the number of stones falling within p/d_{n50}=0.5-1.0 is 14.4%. This is only 3.3% in a levelled bed.

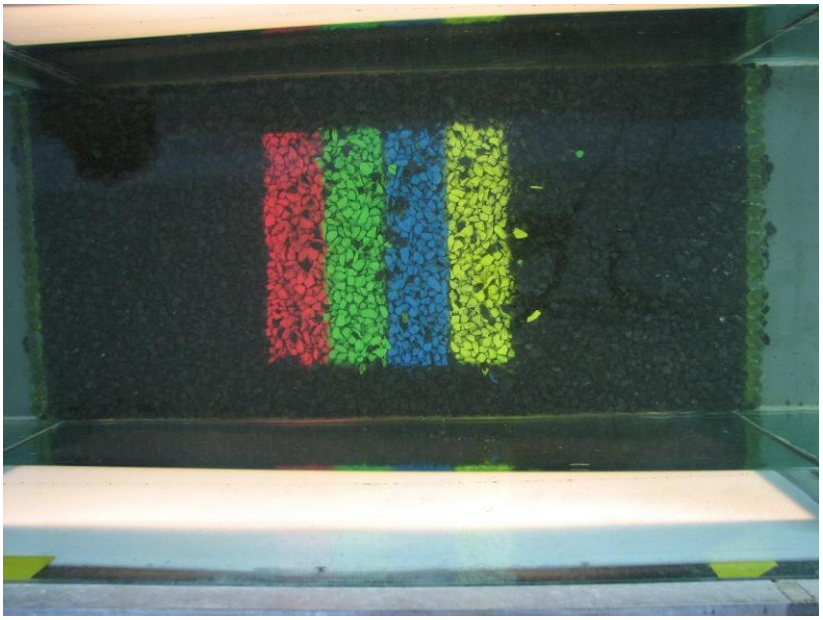

(a)

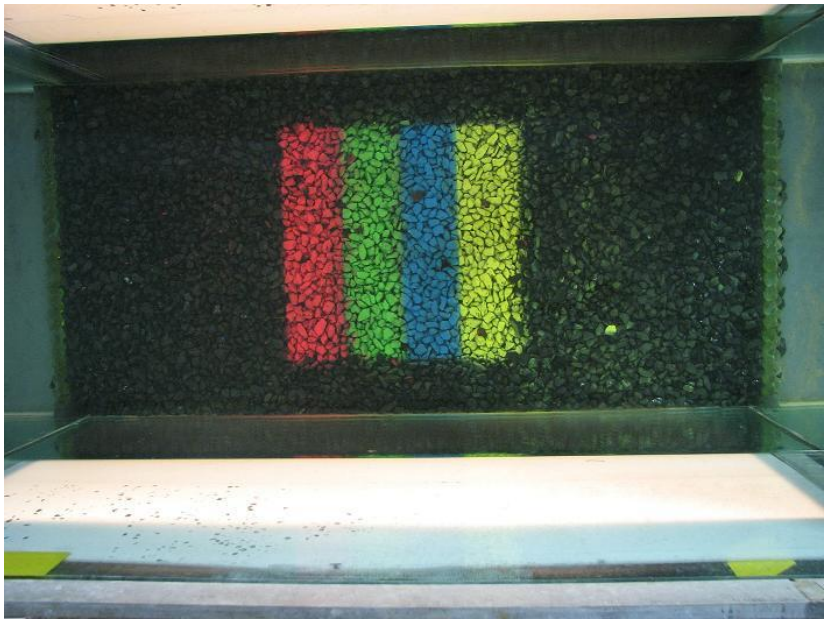

(b)

Figure 8.19: Damage to (a) randomly placed bed (b) levelled bed after 30 mins.

Table 8.10: Summary of physical model test conditions and bed damage observations: Storm duration is 30mins (900 waves).

Test no.	Placement	H (cm)	T (sec)	h (cm)	Total number of rocks in the test area	No. of rocks displaced	% removed
RS1	Random	8	2	40	760	52	6.84
RS7	Random	10	2	40	571*	42	7.36
RS8	Levelled	10	2	40	718	25	3.48

* One strip was not counted due to errors caused by unrealistic bed damage.

Damage to a randomly placed bed and a levelled bed is shown in Figure 8.19 for comparison.

8.4 Scour protection around a monopile

Wind energy farms consisting of hundreds of monopiles are being constructed presently in the North Sea. Engineers have to provide bed protection around every monopile founded on erodible seabed or allow for scour in the monopole design. Therefore, due to the practical relevance, it was decided to make a brief comment on the scour protection design problem around a cylindrical monopole.

The bed protection around a monopile of diameter, D=100mm was constructed by (a) randomly dumping rocks from a 40cm height equal to the water depth and (b) levelling the bed with the aid of a straight edged timber plank and a spirit level. Both were subjected to the same wave conditions and model run time of 30mins.

Figure 8.20: Bed protection around a monopile before the start of model run.

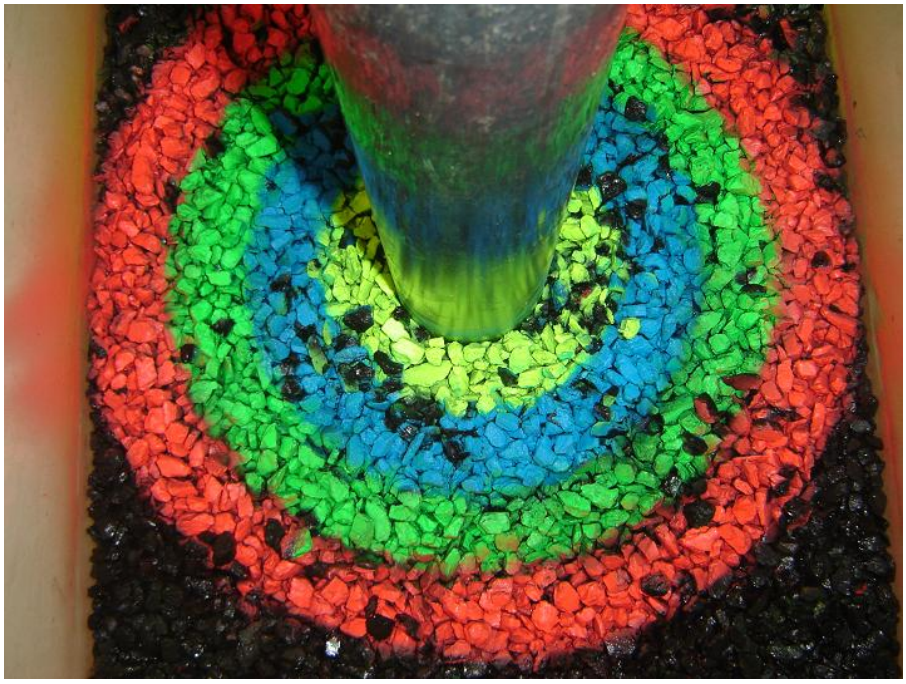

Figure 8.21: Damage to randomly placed bed protection.

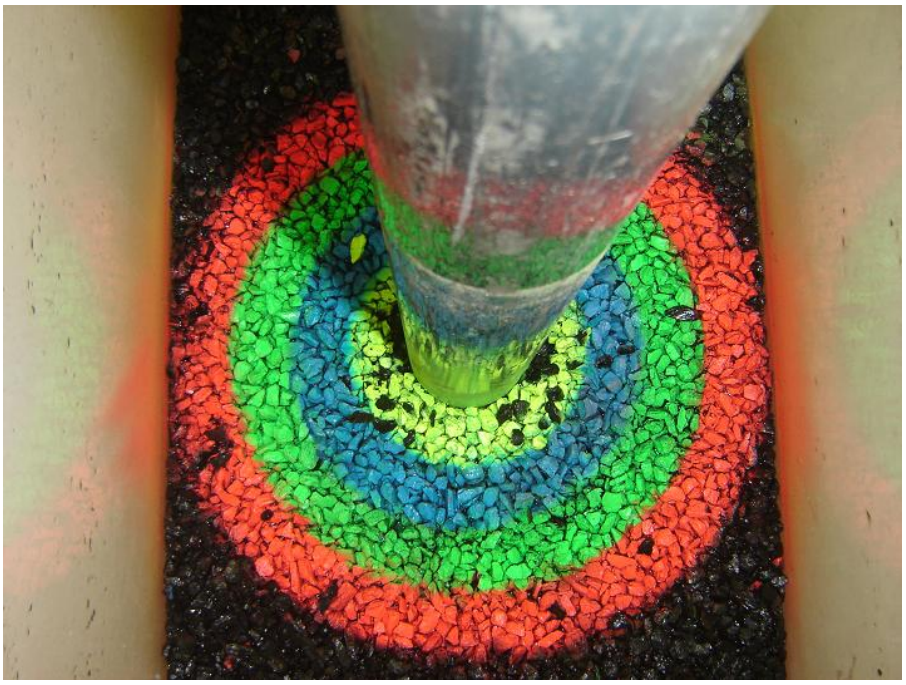

(a)

(b)

Figure 8.22 (a),(b): Damage to a levelled bed protection confined to the region 0.5D distance from the pile (i.e. yellow coloured area).

Damage to the randomly placed bed (Figure 8.21) spread to all 4 circular rings each of 50mm (0.5D) width. Significant damage was observed within an area 1.0D from the monopile and some damage in the area from 1.0D-2.0D.

However, damage to the levelled bed (Figure 8.22) was confined largely to the first circular ring with a width equivalent to half the diameter of the monopile (yellow coloured area). Within this 0.5D wide area, damage is mostly confined to the area where flow accelerates around the pile and where turbulence is magnified.

Therefore, again this observation reminds the engineer of the importance of the construction of the bed protection to achieve a level surface, rather than random dumping of rocks where the probability of occurrence of large protrusions of the size of the rock, is high. As observed in the tests on incipient motion of spherical elements in Chapter 6, if a bed protection can be constructed to have an optimum relative protrusion of p/d=0.21, the damage to a bed protection can be significantly reduced.

8.5 Summary

In this chapter the effect of the stone placement method on wave-induced damage to a bed protection has been investigated through laboratory tests and stochastic modelling using the Monte Carlo Simulation. The key observations in this chapter were:

1. The method of stone placement crucially influences the stability of a bed protection. Wave-induced damage to a 'levelled' bed protection was found to be 50% less than in a bed prepared by dropping stones randomly from a height equal to water depth.

2. The stochastic model developed, based on exceedance probability of the critical shear stress, predicted damage to a bed protection reasonably well (i.e. within an error of $\pm$25%).

3. The stochastic model has its limitations. The model needs to be calibrated against a known bed damage scenario. The calibration coefficients are valid only for the turbulence sampling frequency and the time period corresponding to that used within the calibration test. The model does not include bed updating, consolidation and armouring processes that happen over time increasing the resistance of the bed. The physical model tests showed that the rate of stone entrainment decreases with time. Therefore, the model is valid for a period until the rate of stone displacement first approaches a zero value.

4. Damage to a levelled bed protection placed around a monopile with diameter D, was limited largely to a local area close to the pile within a ring of 0.5D from the monopile. Random placement showed significant damage within 1.0D area and some damage between 1.0D to 2.0D area spreading damage to the full width of the scour protection apron.

9 Concluding Remarks

9.1 Overview

The research project described within this thesis has sought to investigate the effect of stone protrusion on the incipient motion of rock armour in a scour protection. In scour protection construction around structures in the marine environment, rock armour is randomly dumped from above using side stone dumping vessels, barge or flexible fallpipes. These methods of placement will create more stone protrusions and make the rocks prone to displacement under wave loading. However, if the bed can be laid to an optimum uniform protrusion, ideally a coplanar bed, exposure can be reduced increasing the stability of the bed.

The motivation for this research comes from the challenges and difficulties faced by the author himself in the design of scour protection for offshore meteorological masts and wind energy farms in the North Sea while working for engineering consultants. Some of the questions that often come to the mind of a designer are: (i) to what extent is the Shields parameter valid and what threshold value is to be used to determine the stable rock size in a wave environment ?. (ii) what effect will the use of a single threshold stress have on bed damage ?. (iii) what is the optimum vertical rock placement tolerance/ stone protrusion to minimise the bed damage ?. The research focused on finding answers to those practical questions while addressing some of the general scientific questions.

The starting point of this research has been the work of Fenton & Abbot (1977) and Chin & Chiew (1993) who investigated the effect of particle protrusion on the Shields critical shear stress. They concluded that Shields in his original experiments used a 'levelled' bed and the threshold stress of 0.06 refers to a relative protrusion (p/d) of between 0 - 0.2. Therefore, for a fully exposed stone (p/d=0.82), they recommended a value of 0.01 for the threshold stress in the design of bed protections. However, it was not clear whether the same design criteria can be applied for waves.

Rock armour was idealised as spheres in this study for a number of reasons: (i) it is easier to control the protrusion (ii) the need to exclude the shape effect (iii) it is easier to calculate forces on a sphere than on an irregular shaped rock element (iv) a sphere is the most unstable and hence, gives the bottom line for the threshold stress.

The incipient motion of spherical stones made of different density material resting on a rough bed of similar particles, was observed in the wave flume. The tests showed that the threshold stress data lie above the Shields curve. It is concluded that this behaviour is due to a majority of the tests being conducted in the laminar and transitional flow regimes. The flow visualisation tests showed that the flow around the stone in the majority of tests does not develop into fully developed turbulence. This is because (i) rapid flow reversal inhibits the flow development and (ii) the majority of the tests were conducted at low stone exposure levels.

Shields' critical shear stress is strongly correlated to the stone protrusion through an exponential relationship. It is also dependent on the wave period.

There is a unique critical shear stress versus relative stone protrusion curve for each wave period. For higher Reynolds number flows with longer wave periods, the data for the waves coincided with the data for currents. Therefore, for the design of stable rock armour size under the action of waves at high Reynolds number flow, i.e., in field conditions where the design wave periods typically exceed 8 seconds, the curve of Fenton & Abbot (1977) and Chin & Chiew (1993) is applicable.

It was one of the objectives to determine the optimum stone protrusion to which rocks should be laid in a bed protection to increase the stability. A coplanar bed with zero exposure to flow would have been ideal. However, in practice, this is difficult to achieve with irregular shaped rocks. In the present tests a coplanar bed of light weight spheres exhibited remarkable stability under the largest bed shear stresses that could be generated in the flume. The sphere exhibited the same amount of stability when the protrusion level increased to 0.17d and 0.21d. The sphere was displaced when its protrusion was increased to 0.24d. Therefore, it appears that 0.21d is the threshold level, below which there is no stone movement. If rock armour can be laid at or less than this protrusion level, storm-induced bed damage can be minimised. It was observed that the force on a stone with finite protrusion, p/d=0.216, is only marginally higher than that on a stone in a coplanar bed. The measured pressure distribution around the stone followed the same trend.

The test program consisted of incipient motion tests using mostly 19mm diameter spherical test stones with varying density, as well as pressure

measurements on a 50mm diameter sphere set in a rough bed of similar spheres, turbulence measurement using Laser Doppler Velocimetry (LDV) and flow visualisation using Volumetric Three component Velocimetry (V3V). The pressure measurement was crucial in this study as the forces and shear stresses were obtained by the integration of the pressure on a sphere. A special apparatus, with pressure tappings on the surface of a 50mm diameter sphere connected to pressure sensors, was developed. The data, captured via a data logger, was calibrated in a still water tank. The instrument was validated using linear wave theory and used to obtain pressure readings on the test sphere.

In the past, researchers have used various techniques to measure bed shear stress applied by the fluid flow. They include turbulence measurement, direct measurement of shear using a shear cell and hot film techniques. In the present tests, a different method – direct measurement of pressure and hence, the force on an individual roughness element, was used to deduce the average force on the bed. The calculated shear stress and hence, the wave friction factor agreed well with the published data of Kamphuis (1975) and Simons *et al.* (2000). This agreement was obtained when it was assumed that the theoretical bed level (origin, y=0) is at 0.35d below the average crest level of the roughness elements. Sleath (1987) first assumed this level as the hydraulic origin following a suggestion of Einstein (1950). The roughness elements used by the above authors included 2D square elements as well as 3D elements such as natural rocks, spheres etc. The fact that the wave friction factor data in the present tests agree well with

published data suggests that, irrespective of the type of roughness elements, the theoretical bed level is located around 0.35d below the average crest level of the roughness elements.

V3V images showed that the ejection of vortices from the roughness elements occurs during the acceleration phases. Ejected vortices moving upward may enhance the Reynolds stresses. Such production of vortices (turbulence) and their ejection was not significant during the decelerating phase and the first half of the trough half cycle. Paradoxically, the measured turbulence intensity was higher ($\cong$ 43%) in these phases (ωt=90-180deg) than in the acceleration phases. This enhancement of turbulence intensity could be due to (i) bursting of turbulent 'spots' and (ii) the residual vorticity that remains from the accelerating phases. Moreover, near-bed turbulence never ceased within a region 1.0d thick over the wave cycle. This phenomenon could give credence to Kajiura's (1968) assumption of the region of constant eddy viscosity within a height $0.5k_s$ above the bed.

Reynolds stresses 1mm above the crest of the roughness elements remained 10-15% of the maximum shear stress amplitude, τ_m. The maximum of 33% τ_m was found at 0.16d below the roughness apex level. These observations are consistent with the measurements of Sleath (1987).

How and when a stone would displace is of practical importance to determine damage to a scour protection as well as for the science of predicting sediment transport. Flow visualisation tests suggest that forces on a stone due to shear and normal (uplift) stresses should act simultaneously to displace a stone. Visual observations of the incipient motion through video

recording and measured shear and normal stress variation over the wave cycle showed that rather than at the time of peak shear stress amplitude, displacement can occur at any time in the decelerating phases when there are favourable conditions - positive uplift and high turbulence intensity. A stone which would not move otherwise, despite being subjected to peak oscillatory shear stresses, was displaced when it came under the influence of a moving vorticity structure as shown earlier in Figures 7.33 and 7.34. This suggests that the probability of stone displacement is dependent on the joint probability of occurrence of the lateral and uplift forces. A stone moved when the bed shear stress ranged from $0.4\tau_m$ to $0.93\tau_m$. Therefore, rather than using a peak shear stress amplitude in the Shields parameter to represent the threshold condition, the use of an average, i.e., $0.67\tau_m$ or lower value, i.e. $0.5\tau_m$, would be more appropriate. Van Rijn (1993) and Soulsby & Whitehouse (1997) were among the first to offer answers to this question on the appropriate shear stress magnitude.

The protrusion of rock armour in a bed protection varies in space and hence, follows a probability distribution. Consequently, the critical shear stress can also be represented by a probability distribution. It was also found, by measurement, that the turbulent fluctuation in the bed shear stress and normal stress (uplift) applied by the flow can be represented by normal probability distributions. Therefore, rather than designing a bed protection for a single threshold shear stress, designing for an acceptable damage criterion would be realistic. To study the influence of the probabilistic processes on bed damage, a stochastic model was constructed and run

using a Monte Carlo simulation method subject to the following conditions: (i) that the stone will move when the applied shear stress just exceeds the critical shear stress and; (ii) the stone will move during the phases of positive uplift subject to the exceedance of a threshold uplift. It was found that the model predicted the observed bed damage within a ±25% error margin. Physical model tests using a horizontal bed of a crushed natural rocks (anthracite coal), showed that a 50% reduction in bed damage can be achieved by 'levelling' the bed compared to a bed protection constructed by random dumping of rocks from the still water level.

The fraction of rocks within the relative protrusion range, p/d_{n50}=0-0.25 in a randomly placed bed was 15%. This increased to 27% after 'levelling'. The occurrence of a large number of exposed stones will increase the probability of damage to a bed protection. The number of exposed stones in the range p/d_{n50}=0.5-1.0 was reduced to 3.3% after levelling from 14.4% in a randomly placed bed. Therefore, the fraction of exposed stones can be reduced and the fraction of stones in the 'immobile' range can be increased by 'levelling' of the bed, resulting in a significant reduction to the bed damage as observed in the present tests.

9.2 Conclusions

This work has revealed a number of phenomena related to the incipient motion of rock armour in bed protection. Particularly, the research focused on the effect of stone protrusion on the Shields critical shear stress and its

practical implications in the engineering design of scour protection. The main findings are listed below.

1. The Shields critical shear stress has a strong exponential relationship with relative stone protrusion. It is also dependent on the wave period. There is a unique critical shear stress versus relative protrusion curve for each wave period. At high Reynolds number flow with large wave periods, these curves coincide with the curve for uni-directional currents. Therefore, the design threshold shear stress for currents is valid for waves at high Reynolds numbers.

2. Stones in a coplanar bed are remarkably stable under wave action. The threshold protrusion below which a bed protection is stable was found to be 0.21d.

3. The oscillatory shear stress is not sufficient on its own and requires the simultaneous occurrence of an uplift force in order to displace a stone. These uplift forces can be induced by the quasi-steady mechanism due to the flow around it and/or the stone coming under the influence of large-scale moving vortices. Uplift induced by vortex shedding also adds to the total uplift force.

4. The formation and ejection of vortices from the roughness elements occurs mainly during the acceleration phases. However, the peak in turbulence intensity is 43% higher during the deceleration phases compared to the acceleration phases. This enhancement could be

due to (i) bursting of turbulent ‘spots’ and (ii) residual vorticity remaining from the acceleration phases.

5. Incipient movement of stones can occur any time during the decelerating phases in the trough half cycle where favourable conditions exist (i.e., positive uplift, enhanced turbulence intensity). During this phase, the measured bed shear stress varied from $0.4\tau_m$ to $0.93\tau_m$, indicating that the use of the peak shear stress amplitude, τ_m, in the Shields parameter will result in an under design. Therefore, use of an average value is recommended.

6. The measured bed shear stress, and hence, the wave friction factor agrees well with the published data of Kamphuis (1975) and Simons *et al*. (2000). This agreement supports the view that the theoretical bed level is located 0.35d below the average crest level of the roughness elements irrespective of the type of bed material.

7. Turbulent fluctuations in shear and normal stresses follow normal probability distributions.

8. The maximum turbulent fluctuation in the bed shear stress is approximately equal to $1.0\tau_m$ when averaged and can reach up to a maximum $1.5\tau_m$. Therefore, the occurrence of instantaneous shear stresses twice the magnitude of the peak shear stress amplitude is possible. This highlights the importance of accounting for turbulence in bed damage prediction models.

9. The measured peak Reynolds stress is only a fraction of the peak bed shear stress amplitude, τ_m. It is approximately 10-15% at the crest level of the roughness elements and 33% about 8mm (0.16d) below this level.

10. Vorticity (turbulence) is observed continuously over the wave cycle within a region approximately one diameter above the bed and hence, this is a positive (non-zero) quantity. This observation supports the constant eddy viscosity hypothesis within a height equal to $0.5k_s$ (Kajiura, 1968).

11. Morison's inertia force matched well with the horizontal force measured in the present tests for KC<10. This indicates the dominance of the inertia force within this range. The uplift force was not predicted well. Force transfer coefficients were much larger, being closer to the laminar solution. This is due to (i) the wall proximity and (ii) laminar effects.

12. The method of rock armour placement is crucially important for the stability of a bed protection. The damage to a model bed protection in the wave flume consisting of crushed natural rocks, reduced by 50% when the bed was 'levelled' compared to a bed prepared by random dumping of rocks from the still water level.

13. Stochastic modelling using a Monte Carlo simulation method is a useful tool to predict storm-induced damage to a bed protection.

9.3 Further work

The work presented in this thesis covers a number of sub-topics including: the incipient motion of coarse sediment, turbulence, bed shear stresses, fluid flow around submerged spheres, rock armour bed protection and construction. There is scope to continue the work carried out in the present study. Some of the possible avenues requiring further investigation include:

1. Incipient motion tests for varying stone protrusion levels and pressure measurement on a spherical roughness element need to be carried out at high Reynolds number for large wave periods. This will provide a data set applicable directly to field conditions.

2. The present tests on incipient motion of spherical particles should be repeated for angular natural rocks. Crushed natural rock armour used for bed protections in the field, are, in general, angular in shape.

3. The effect of random waves and combined wave-current flows on incipient motion need to be investigated for different stone protrusion levels. The assumption of regular-waves in the present research is only a simplification to the actual field conditions.

4. The bed shear stress calculation should be carried out using the same pressure measurement apparatus developed in the present study under random waves and wave-current flows as more understanding on the flow behaviour around roughness elements of the scale, a/k_s =O(1) and high Re number will be valuable for

extending laboratory data into field scale and explaining some of the conclusions in previous studies on combined wave-current flow.

5. Scale effects on incipient motion tests require further investigation. This knowledge is important in extending laboratory results to field scale.

6. The stochastic model needs further refinement. It assumes a threshold value of instantaneous normal stress (uplift) above which it begins to aid the incipient motion by simultaneously acting with the shear stress. This threshold value was calibrated based on preliminary tests and a better way to define this parameter is required.

7. A numerical model to simulate the bottom turbulence over a rough bed should be developed, with the V3V flow visualisation images from the present study used for model verification.

8. The effect of other parameters on the critical shear stress, i.e., shape, size, orientation, etc., needs to be investigated. This will allow the most dominant parameter/s to be included in this incipient motion models.

Bibliography

AIRY, G.B. 1841. Tides and waves. *Encyclopaedia Metropolitana* (1817–1845), *Mixed Sciences*, Vol. 3, ed. HJ Rose, et al. Also *Trigonometry, On the Figure of the Earth, Tides and Waves.* 396 pp. C Plates.

ARNSKOV, M.M., FREDSOE, J. AND SUMER, B.M. 1993. Bed shear stress measurement over a smooth bed in three-dimensional wave-current motion. *Coastal Engineering*, **20**, 277-316.

BAGNOLD, R.A. 1946. Motion of waves in shallow water. Interaction between waves and sand bottoms. In: *Proc. Roy. Soc.*, Ser.A, **187**,1-15.

BAGNOLD, R.A. 1963. Mechanics of marine sedimentation. In: *The Sea*, M.N.Hill (ed.). New York:Interscience.

BAILARD, J.A. AND INMAN, D.L. 1981. An energetics bed load model for plane sloping beach: Local transport. *Journal of Geophys. Res*., **86**(C3), 2035-2043.

BAYAZIT, M. 1976. Free surface flow in a channel of large relative roughness. *Journal of Hydraulic Research*, **14**(2),115-125.

BAYAZIT, M. 1983. Flow structure and sediment transport mechanics in steep channels. Mechanics of Sediment Transport, In: *Proc. of Euromech 156*, Istanbul, 12-14 July. Rotterdam:A.A.Balkema, 197-206.

BENEDICT, B.A. AND CHRISTENSEN, B.A. 1972. Hydrodynamic lift on a stream bed. In: H.W.Shen (ed.), *Sedimentation*, Symposium to honour Prof. H.A.Einstein.

BOUSSINESQ, J. 1877. Théorie de l'écoulement tourbillant. *Mém. Prés. Acad. Sci. XXIII*, **46**, Paris.

BREUSERS, H.N.C. 1965. Gradual closure VI, influence of shape and grading on the stability of riprap. Tech Report M731, Delft: WL | Delft Hydraulics. In Dutch.

BREUSERS, H.N.C. AND SCHUKKING, W.H.P. 1971. *Begin van beweging van bodemmateriaal (Incipient motion of bed material)*. Report S159-I, Delft: Delft Hydraulics.

BUFFINGTON, M.J. 1999. The legend of A.F.Shields. *Journal of Hydraulic Engineering*, **125**(4), 376-387.

BURCHARTH, H.F. AND LIU, Z. 1993. Design of dolos armour units. In: B.L.EDGE, ed., *Proc. 23rd Int. Conf. Coastal Eng*., 1992, Venice. New York:ASCE, **1**,1053-1066.

CARLING, P.A., KELSEY, A. AND GLAISTER, M.S. 1992. Effect of bed roughness, particle shape and orientation on initial motion criteria. In: *Dynamics of Gravel-bed Rivers*, P. Billi *et al*., eds. New York:Wiley, 23-37.

CARSTENSEN, S., SUMER, B.M. AND FREDSØE, J. 2010. Coherent structures in wave boundary layers. *Journal of Fluid Mechanics*, 646, 169-206.

CHAKRABARTI, S.K. 1973. Wave forces on submerged objects of symmetry flow. *Journal of the Waterways, Harbours and Coastal Eng. Div.*, ASCE, **99**(WW2), 147-163.

CHENG, N., AND CHIEW, Y. 1998. Pickup probability for sediment entrainment. *Journal of Hydraulic Eng*., **124**(2), 232-235.

CHEPIL, W.S. 1958. The use of evenly spaced hemispheres to evaluate aerodynamic forces on a soil surface. *Transactions, American Geophysical Union*, **39**(3), 397- 404.

CHEUNG, J.C.K. AND MELBOURNE, W.H. 1983. Turbulence effects on some aerodynamic parameters of a circular cylinder at supercritical Reynolds numbers. *Journal of Wind Engineering and Industrial Aerodynamics, **14**, 399-410.*

CHIN, C.O. AND CHIEW, Y.M. 1993. Effect of bed surface structure on spherical particle stability. *Journal of Waterway, Port, Coastal and Ocean Engineering*, **113**(3), 231-242.

CIRIA/CUR 1991. *Manual on the use of rock in coastal and shoreline engineering*. CUR Report 154, London: CIRIA.

CIRIA 2007. *The Rock Manual : The use of rock in hydraulic engineering*. 2nd ed. Report no. C638. London: CIRIA.

COLEMAN, N.L. 1967. A theoretical and experimental study of drag and lift forces acting on a sphere resting on a hypothetical streambed. In: *Proc. 12th IAHR Congress*, Port Collins, Col., **3**, 185-192.

COLEMAN, N.L. 1972. The drag coefficient of a stationary sphere on a boundary of similar spheres. *Houille Blanche*, **1**,17-21.

CRAIK, A.D.D. 2004. The origins of water wave theory. *Annual Reviews of Fluid Mechanics*, **36**, 1-28.

DAVIDSON, P.A. 2004. *Turbulence; an introduction for scientists and engineers*. Oxford University Press.

DEAN, R.G. 1965. Stream function representation of nonlinear ocean waves. *Journal of Geo. Phys. Res.*, **70**, 4561-4572.

DEAN, R.G. AND PERLIN, M. 1986. Intercomparison of near-bottom kinematics by several wave theories and field laboratory data. *Coastal Engineering*, **9**, 399-437.

DE BOER, G.M. 1998. *Transport of stones on a granular bed-protection*. Thesis(M.Sc.) (In Dutch), Delft University of Technology.

DE JONG, T.J. 1996. Stability of Tetrapods at front crest and rear of a low crested breakwater. Thesis (M.Sc.), Delft University of Technology.

DIXEN, M., HATIPOGLU, F., SUMER, B.M. AND FREDSOE, J. 2008. Wave boundary layer over a stone-covered bed. *Coastal Engineering*, **55**(1), 1-20.

DURST, F. 1981. *Principles and practice of Laser-Doppler Anemometry, 2nd edn. Academic Press.*

EGIAZAROFF, I.V. 1965. Calculation of non-uniform sediment concentrations. *Journal of Hydraulic Division*, **4**(91), 225-247.

EINSTEIN, H.A. 1942. Formulae for the transportation of bed-load. *Trans. ASCE*, **107**, 561-577.

EINSTEIN, H.A. 1950. *The bed-load function for sediment transport in open channel flows*. US. Dept. of Agriculture, Soil Conservation Service, Washington D.C., Tech. Bull. no. 1026.

EINSTEIN, H.A. AND EL-SAMNI, E.A. 1949. Hydrodynamic forces on a rough wall. *Review of Modern Physics*, **21**(3), 520-524.

ENGELUND, F. AND HANSEN, E. 1972. *A monograph on sediment transport in alluvial streams*. Copenhagen: Teknisk Forlag.

FENTON, J.D. AND ABBOT, J.E. 1977. Initial movement of grains in a stream bed: the effect of relative protrusion. In: *Proc. of the Royal Society of London*, Series A, Mathematical and Physical Sciences, **352**(1671), 523-537.

FISCHER, P.F., LEAF, G.K. AND RESTREPO, J.M. 2002. Forces on particles in oscillatory boundary layers. *Journal of Fluid Mechanics*, **468**, 327-347.

FRIJLINK, H.C. 1952. Discussion des formules de Debit Solide de Kalinske, Einstein et Meyer-Peter et Mueller compte tenue des mesures recentes de dans rivieres Neerlandaises. *2eme Journal Hydraulique*, Soc. Hydraulique de France, Grenoble, 98-103.

GODDET, J. 1960. Etude du debut dentrainement des materiaux mobiles sous laction de la houle. *La Houille Blanche*, **2**, 122-135.

GOGUS, M. AND DEFNE, Z. 2005. Effect of shape on incipient motion of large solitary particles. *Journal of Hydraulic Engineering*, **131**(1), 38-45.

GRASS, A.J. 1970. Initial instability of fine bed sand. *Journal of the Hydraulics Division*, ASCE, **96**(3), 619-632.

GRASS, A.J. 1971. Structural features of turbulent flow over smooth and rough
boundaries. *Journal of Fluid Mechanics*, **50**, 233-255.

GRASS, A.J., SIMONS, R.R. MACIVER, R.D., MANSOUR TEHRANI, M. AND KALOPEDIS, A. 1995. Shear cell for direct measurement of fluctuating bed shear stress vector in combined wave current flow. In: *Proc. 26 th IAHR Congress HYDRA 2000*, London, 11-15 Sept.

HOAN, N.T. 2008. *Stone stability under non-uniform flow*. Thesis (Ph.D.), Delft University of Technology.

HOAN, N.T., BOOIJ, R., HOFLAND, B., STIVE, M.J.F., VERHAGEN, H.J. 2008. Estimation of bed protection damage using numerical flow modelling, COPEDEC VII, Dubai, UAE, Paper no 096.

HOFLAND, B. 2005. *Rock and roll - turbulence induced damage to granular bed protections*. Thesis (Ph.D.), Delft University of Technology.

HOFLAND, B. AND BATTJES, J.A., AND BOOIJ, R. 2005. Measurement of fluctuating pressures on coarse bed material. Journal *of Hydraulic Engineering*,
131(9), 770-781.

HOFLAND, B. AND BATTJES, J.A. 2006. Probability density function of instantaneous drag forces and shear stresses on a bed. *Journal of Hydraulic Engineering*, **132**(11), 1169-1175.

HOLTZHAUZEN, A.H. 1996. Effective use of concrete for breakwater armour units. *Bulletin, no 90*, PIANC, Brussels, 23-28.
HORIKAWA, K. 1978. *Coastal Engineering, an introduction to Ocean Engineering*. New York: Wiley.

HUDSON, R.Y. 1959. Laboratory investigation of rubble-mound breakwaters. *Journal of the Waterways, Harbors and Coastal Engineering Division*, ASCE, **85**(WW3), 93-121.

HUGHES, S.A. 1993. *Physical models and laboratory techniques in coastal engineering*. Singapore: World Scientific.

IPPEN, A.T. 1966. *Estuary and Coastline Hydrodynamics*. New York: McGraw-Hill.

ISOBE, M. AND HORIKAWA, K. 1982. Study on water particle velocities of shoaling and breaking waves. *Coastal Engineering*, Japan, **25**, 109-123.

IWATA, N., AND MIZUTANI, N. 1989. Experimental study on wave force acting on a submerged sphere. In: *Proc. of the Eighth International Conference on Offshore Mechanics and Arctic Engineering*. Hague, The Netherlands, March 1989, 145-152.

IWATA, K. AND MIZUTANI, N. 1991. Proximity effects of bottom and free surface boundaries to wave forces acting on a submerged sphere. In: *Proc. of the First International Offshore and Polar Engineering Conference*, Edinburgh, United Kingdom, 11-16 August, III,163-171.

IZBASH, S.V. AND KHALDRE, K.Y. 1970. *Hydraulics of river channel closure.* London: Butterworths.

JACKSON, P.S. 1981. On the displacement height in the logarithmic velocity profile. *Journal of Fluid Mechanics*, **111**, 15-25.

JENSEN, B.L. 1989. *Experimental investigation of turbulent oscillatory boundary layers*. Series Paper 45, Institute of Hydrodynamics and Hydraulic Engineering (ISVA), Technical University of Denmark.

JENSEN, B.L., SUMER, B.M. AND FREDSØE, J. 1989. Turbulent oscillatory boundary layers at high Reynolds numbers. *Journal of Fluid Mechanics*, **206**, 265-297.

JONGELING, T.H.G., BLOM, A., JAGERS, H.R.A. AND STOLKER, C. 2003. *Design method granular protections* (Technical Report Q2933 / Q3018). WL|Delft Hydraulics. In Dutch.

JONSSON, I.G. 1963. Measurements in the turbulent wave boundary layer. In: *Proc. 10 th Congress IAHR*, London, 85-92.

JONSSON, I.G. 1966. Wave boundary layers and friction factors. In: *Proc. 10 th Int. Conf. Coastal Eng.*, Tokyo, 127-148.

JONSSON, I.G. AND CARLSEN, N.A. 1976. Experimental and theoretical investigation in an oscillatory turbulent boundary layer. *Journal of Hydr. Res.*, **14**(1):45-60.

KAJIURA, K. 1968. A model of the bottom boundary layer in water waves. *Bulletin Earthquake Res. Inst.*, **46**, 75-123.

KALINSKE, A.A. 1942. Criteria for determining sand-transport by surface creep and saltation. *Trans. Am. Geophys. Union*, **23**, 639-643.

KALINSKE, A.A. 1947. Movement of sediment as bed-load in rivers. *Trans. Am. Geophys. Union*, **28**(4), 615-620.

KAMPHUIS, J.W. 1975. Friction factors under oscillatory waves. *Journal of Waterways, Harbors and Coastal Eng. Div.*, ASCE, **101**(2), 135-144.

KANG, S., PATIL, B. AND ROY, R.P. 2001. Effects of coincidence window and measuring volume size on laser Doppler velocimetry measurement of turbulence. *Experiments in Fluids*, **30**(4), 365-370.

KEMP, P.H. AND SIMONS, R.R. 1982. The interaction between waves and a turbulent current: waves propagating with the current. *Journal of Fluid Mechanics*, **116**, 227-250.

KEMP, P.H. AND SIMONS, R.R. 1983. The interaction between waves and a turbulent current: waves propagating against the current. *Journal of Fluid Mechanics*, **130**, 73-89.

KENNEDY, J. F. 1995. The Albert Shields story. *Journal of Hydraulic Engineering*, ASCE, **121**(11), 766–772.

KIRCHNER, J.W., DIETRICH, W.E., ISEYA, F. AND IKEDA., H. 1990. The variability of critical shear stress, friction angle, and grain protrusion in water worked sediments. *Sedimentology*, **37**, 647-672.

KIRKGOZ, M.S. 1986. Particle velocity prediction at the transformation point of plunging breakers. *Coastal Engineering*, **10**, 139-147.

KIM, H.T., KLINE, S.J. AND REYNOLDS, W.C. 1971. The production of turbulence near a smooth wall in a turbulent boundary layer. *Journal of Fluid Mechanics*, **50**(1), 133-160.

KLINE, S.J., REYNOLD, W.C., SCHRAUB, F.A. AND RUNSTADLER, P.W. 1967. The structure of turbulent boundary layers. *Journal of Fluid Mechanics*, **30**(4), 741-7.

KOMAR, P.D., AND INMAN, D.L. 1970. Longshore sand transport on beaches. *Journal of Geophys. Res.*, **75**(30), 5914-5927.

KRAMER, H. 1932. *Modellgeschiebe und schleppkraft*, Doktor-Ingenieurs dissertation, Technischen Hochschule, Dresden, Germany (in German).

KRAMER, H. 1935. Sand mixtures and sand movement in fluvial models. *Trans.*, ASCE, **100**(1909), 798–838.

LAAN, G.J. 1981. *The relation between shape and weight of pieces of rock*. Report MAW-R-81079 (in Dutch), Rijkswaterstaat, Delft, The Netherlands.

LAI, W., PAN, G., MENON, R., TROOLIN, D., GRAFF, E., GHARIB, M., AND PEREIRA, F. 2008. Volumetric Three-Component Velocimetry: a new tool for 3D flow measurement. In: *Proc. 14th Int. Symposium on Applications of laser Techniques to Fluid Mechanics,* Lisbon, Portugal, 07-10 July, 2008.

LAMB, S.H. 1932. *Hydrodynamics*. 6th ed. Cambridge University Press.

LATHAM, J.P., MANNION, M.B., POOLE, A.B., BRADBURY, A.P. AND ALLSOP, N.W.H. 1988. *The influence of armour stone shape and rounding on the stability of breakwater armour layers*. Report no.1, Coastal Engineering Research Group, Queen Mary College, University of London and Hydraulics Research Ltd, Wallingford.

LE MÉHAUTÉ, B. 1976. *An introduction to hydrodynamics and water waves*. Dusseldorf: Springer-Verlag.

LOFQUIST, K.E.B. 1980. Measurements of oscillatory drag on sand ripples. In: *Proc. 17 th Int. Conf. Coastal Eng.*, Sydney, 3087-3106.

LOFQUIST, K.E.B. 1986. *Drag on naturally rippled beds under oscillatory flows*. Misc. Paper, CERC, 86-13.

LONGUET-HIGGINS, M.S. 1953. Mass transport in water waves. *Philosophical Transactions of the Royal Society of London*, Series A, **245**, 535-581.

LOSADA, M.A. AND DESIRE, J.M. 1985. Incipient motion on a horizontal granular bed in non-breaking water waves. *Coastal Engineering,* **9**, 535-581.

LOSADA, M.A., DESIRE, J.M. AND MERINO, J. 1987. An energy approach to non-breaking wave-induced motion of bottom sediment particles. *Coastal Engineering,* **11**, 159-173.

MADSEN, O.S. AND GRANT, W.D. 1976. Quantitative description of sediment transport by waves. In: *Proc. 15th Coastal Engineering Conf.*, Honolulu, **2**, 1093-1112.

MANOHAR, M. 1955. *Mechanics of bottom sediment movement due to wave action*. U.S. Army Corps of Eng., Beach Erosion Board, Tech.Memo.75.

MASSEY, B. AND WARD-SMITH, J. 1998. *Mechanics of Fluids*. Oxon: Spon Press.

MEI, C.C AND LIU, P.L.-F 1993. Surface waves and coastal dynamics. *Annual Reviews of Fluid Mechanics*, **25**, 215-40.

MEYER-PETER, E. AND MULLER, R. 1948. Formulas for bed load transport. In: *Proc. 2nd Meeting, International Association for Hydraulic Research*, Delft, The Netherlands, 39-64.

MILLER, R.L. AND BYRNE, R.J. 1966. The angle of repose for a single grain on a fixed rough bed. *Sedimentology*, **6**, 303-314.

MIZUTANI, N. AND IWATA, K. 1993. Estimation method on wave force acting on a submerged sphere. In: *Proc. of the Third International Offshore and Polar Engineering Conference*. Singapore, June 1993, 184 -191.

MORISON, J.R., O'BRIEN, M.P., JOHNSON, J.W. AND SCHAAF, S.A. 1950. The wave force exerted by surface wave on piles. *Petroleum Trans.*, AIME, **189**, 149-157.

MUNEKATA, M., OHBA, H., AND KAZUYOSHI, M. 2001. A study on Reynolds shear stress measurement by LDV. *Journal of Thermal Science*, **10**(1), 20-25.

MYRHAUG, D., SLAATTELID, O.H. AND LAMBRAKOS, K.F. 1998. Seabed shear stresses under random waves: Predictions vs estimates from field measurements. Ocean Engineering, **25**(10), 907-916.

NAHEER, E. 1979. Incipient motion of arbitrary shape particles under solitary waves. *Coastal Engineering*, **2**, 277-296.

NEZU, I. AND NAKAGAWA, H. 1993. *Turbulence in open channel flows*. Rotterdam: Balkema.

NIELSEN, P. 1992. *Coastal bottom boundary layers and sediment transport*. Singapore: World Scientific.

NIKORA, V.I., GORING, D.G. AND BIGGS, B.J.F. 1998. On gravel-bed roughness characterization. *Water Resources Research*, **34**(3), 517-527.

NIKURADSE, J. 1933. Stromungsgesetze in Rohren. *VDI-Forschungsheft 361*, Berlin. NACA (Trans.), Laws of flow in rough pipes, NACA, Washington, November, 1950.

PAINTAL, A. S. 1971a. Concept of critical shear stress in loose boundary open channels. *Journal of Hydraulic Research*, **9**(1), 911-13.

PAINTAL, A. S. 1971b. A stochastic model of bed-load transport. *Journal of Hydraulic Research*, **9**(4), 527-554.

PAPANICOLAOU, A.N., DIPLAS, P., EVAGGELOPOULOS, N., AND FOTOPOULOS, S. 2002. Stochastic incipient motion criterion for spheres under various bed packing conditions. *Journal of Hydraulic Engineering*, **128**(4), 369-380.

PARKER, G. 1979. Hydraulic geometry of active gravel rivers. In: *Proc. ASCE*, **105**(HY9), 1185-1201.

PATNAIK, P.C., VITTAL, N. AND PANDE, P.K. 1992. Drag coefficient of a stationary sphere in gradient flow. *Journal of Hydraulic Research*, **30**(2), 389-402.

PEREIRA, F., STUER, H., GRAFF, E.C., GHARIB, M. 2006. Two-frame 3D particle tracking. *Measurement Science and Technology*, **17**, 1680-1692.

PHILLIPS, O.M. 1974. The dynamics of the upper ocean. 2nd ed., Cambridge Univ. Press.

PHILLIPS, O.M. 1977. Nonlinear dispersive waves. *Annual Reviews of Fluid Mechanics*, **6**, 93-110.

POTHOS, S., TROOLIN, D., LAI, W. AND MENON, R. 2009. V3V-Volumetric Three Component Velocimetry for 3D flow measurements – main principle, theory and applications. *Termotehnica*, 2/2009.

RANCE, P.J. AND WARREN, N.F. 1969. The threshold of movement of coarse material in oscillatory flow. In: *Proc. 11th Coastal Eng. Conf.*, ASCE, New York, 487-491.

RAUDKIVI, A.J. 1998. *Loose boundary hydraulics*. Rotterdam: A.A.Balkema.

RIGLER, J.K. AND COLLINS, M.B. 1984. Initial grain motion under oscillatory flow: a comparison of some threshold criteria. *Geo-Marine Letters*, **3**(1), 43-48.

RIEDEL, H.P. 1972. *Direct measurement of bed shear stress under waves*. Thesis (Ph.D.), Dept. of Civil Eng., Queen's University, Kingston, Ontario.

ROBINSON, T.O. 2006. Gravity currents in the presence of water waves. Thesis (Ph.D), University College London, University of London.

ROSENTHAL, G.N. AND SLEATH, J.F.A. 1986. Measurement of lift in oscillatory flow. *Journal of Fluid Mechanics*, **164**, 449-467.

RUNSTADLER, P.W., KLINE, S.J. AND REYNOLDS, W.C. 1963. *An experimental investigation of the flow structure of the turbulent boundary layer*. Report MD-8, Department of Mechanical Engineering, Stanford University.

RUSSELL, R.C.H. AND OSORIO, J.D.C. 1957. An experimental investigation of drift profiles in a closed channel. In: *Proceedings of the 6th Coastal Engineering Conference*, ASCE, 171-183.

SARPKAYA, T. 1975. Forces on cylinders and spheres in a sinusoidally oscillating fluid. Transaction of the ASME, *Journal of Applied Mechanics*, 32-37.

SARPKAYA, T. 1977. In-line and transverse forces on cylinders near a wall in oscillatory flow at high Reynolds numbers. OTC Paper No. 2898, Houston, TX.

SARPKAYA, T. AND ISSACSON, M. 1981. *Mechanics of wave forces on off shore structures*. Van Nostrand Reinhold.

SCHLICHTING, H. 1968. *Boundary layer theory*. McGraw-Hill Inc.

SCHWARTZ, L. W. AND FENTON, J.D. 1982. Strongly nonlinear waves. *Annual Reviews of Fluid Mechanics*, **14**, 39-60.

SEELAM, J.K, GUARD, P.A. AND BALDOCK, T.E. 2011. Measurement and modeling of bed shear stress under solitary waves. *Coastal Engineering*, **58**, 937-947.

SHIELDS., A. 1936. Application of similarity principles and turbulence research to bed-load movement. In: *Mitteilunger der Preussischen Versuchsanstalt für Wasserbau und Schiffbau*, Berlin. Translated by W.P.OTT AND J.C.VAN UCHELEN, California Inst. of Technology, Pasadena, Calif., Report no. 167.

SIMONS, R., MYRHAUG, D., THAIS, L., CHAPALAIN, G., HOLMEDAL, L.-E., AND MACIVER, R. 2000. Bed friction in combined wave-current flows. In: *Proc. 27th Int. Conf. on Coastal Eng.*, ASCE, July 16-21, Sydney, 1, 216-226.

SLEATH, J.F.A. 1978. Measurements of bed load in oscillatory flow. *Journal of Waterway, Port, Coastal and Ocean Eng. Div.*, ASCE, **104**(WW3), 291-307.

SLEATH, J.F.A. 1987. Turbulent oscillatory flow over rough beds. *Journal of Fluid Mechanics*, **82**, 360-409.

SLEATH, J.F.A., 1991. Velocities and shear stresses in wave-current flows. *Journal of Geophysical Research*, **96**(C), 15237-15244.

SOULSBY, R.L., HAMM, L., KLOPMAN, G., MYRHAUG, D., SIMONS, R.R. AND THOMAS, G.P. 1993. Wave-current interaction within and outside the bottom boundary layer. *Coastal Engineering*, **21**, 41- 49.

SOULSBY, R.L. AND WHITEHOUSE, R.J.S. 1997. Threshold Sediment Motion in Coastal Environments. In: *Proc. of Combined Australasian Coastal Eng. and Ports Conf.*, Christchurch, **2**, 149-154.

STOKES, G. 1847. On the theory of oscillatory waves. *Transcript of Cambridge Philosophical Society,* **8**, 441-445.

SWART, D.H. 1974. *Offshore sediment transport and equilibrium beach profiles*. Publication no. 131., Delft Hydraulics Lab.

SUMER, B.M AND FREDSØE, J. 2006. *Hydrodynamics around cylindrical structures*. Singapore: World Scientific.

SUMER, B.M AND FREDSØE, J. 2002. *The mechanics of scour in the marine environment*. Singapore: World Scientific.

SUMER, B.M, WHITEHOUSE, R.J.S AND TØRUM, A. 2001. Scour around coastal structures: a summary of recent research. *Coastal Engineering*, **44**, 153-190.

TERRILE, E., RENIERS, A.J.H.M., STIVE, M.J.F., TROMP, M., VERHAGEN, H.J. 2006. Incipient motion of coarse particles under regular shoaling waves. *Coastal Engineering*, **53**, 81-92.

THOMPSON, C.E.L., WILLIAMS, J.J., METJE, N., COATS, L.E. AND PACHECO, A. 2012. Turbulence based measurements of wave friction factors under irregular waves on a gravel bed. *Coastal Engineering*, **63**, 39-47.

TØRUM, A. 1994. Wave-induced forces on armor unit on berm breakwater. *Journal of Waterway, Port, Coastal, and Ocean Eng.*, **120**, 251-268.

U.S. Army Corps of Engineers (USACE) 2006. The Coastal Engineering Manual.

VAN DER MEER, J.W. 1988. Rock slopes and gravel beaches under wave attack. Thesis (Ph.D.), Delft University of Technology, Delft. Also Delft Hydraulics publication no 396.

VAN DER MEER, J.W. 1993. Conceptual design of rubble mound breakwaters. Publication no. 483, WL| Delft Hydraulics, Delft.

VAN RIJN, L.C., 1993. Principles of sediment transport in rivers, estuaries and coastal seas. Amsterdam: Aqua Publications.

VINCENT, G.E. 1957. Contribution to the study of sediment transport on a horizontal bed due to wave action. In: *Proc. 6th Coastal Eng. Conf.*, ASCE, New York, 326-355.

WATTERS, G.Z. AND RAO, M.V.P. 1971. Hydrodynamic effects of seepage on bed particles. *Journal of the Hydraulics Division*, Proc. of ASCE, **97**(HY3):421- 439.

WHITEHOUSE, R.J.S. 1995. In: STIVE, M.J.F., *et al*., ed. The transport of sandy sediments over sloping beds in *Advances in Coastal Morphodynamics*. Delft, Netherlands: Delft Hydraulics.

WHITEHOUSE, R. 1998. Scour at marine structures: A manual for practical applications. London: Thomas Telford.

WILBERG, P.L. AND SMITH, J.D. 1985. A theoretical model for saltating grains in water. Journal of Geophysical Res., **90**(C4), 7341-7354.

WILLIS, D.H. 1978. Sediment load under waves and currents. In: *Proc. 16th Coastal Eng. Conf.*, ASCE, New York, II:1626-1637.

WOLFRAM, J. AND NAGHIPOUR, M. 1999. On the estimation of Morison Force Coefficients and their predictive accuracy for very rough circular cylinders, *Applied Ocean Research*, **21**, 311-328.

WU, F. AND YANG, K. 2004. Entrainment probabilities of mixed-size sediment incorporating near-bed coherent flow structures. *Journal of Hydraulic Engineering*, **130**(12),1187-1197.

XINGKUI, W. AND FONTIJN, H.L. 1993. Experimental study of the hydrodynamic forces on a bed element in an open channel with a backward-facing step. *Journal of Fluid Structures*, **7**, 299-318.

YALIN, M.S. AND KARAHAN, E. 1979. Inception of sediment transport, Journal of Hydraulic Division, ASCE, **105**(11), 1433-1443.

Appendices

Appendix A: An analytical model for force balance of a spherical stone

This analysis implies that the exposed particle rolls over the surrounding particles at the threshold condition. Figure A.1 shows the definition sketch of the inter-particle geometry of an exposed particle with diameter, d_1 and supporting particles with diameter, d_2. Two pivot points P_b and P_c exist at the threshold condition.

By taking moments around pivot point P_b we get

$$F_H(e + L_2) = (F_w - F_V)L_1 \qquad (A.1)$$

$$\frac{M_D}{M_R} = 1 = \frac{F_H(e + L_2)}{(F_w - F_V)L_1} \qquad (A.2)$$

Where M_D is disturbing moment and M_R is restoring moment.

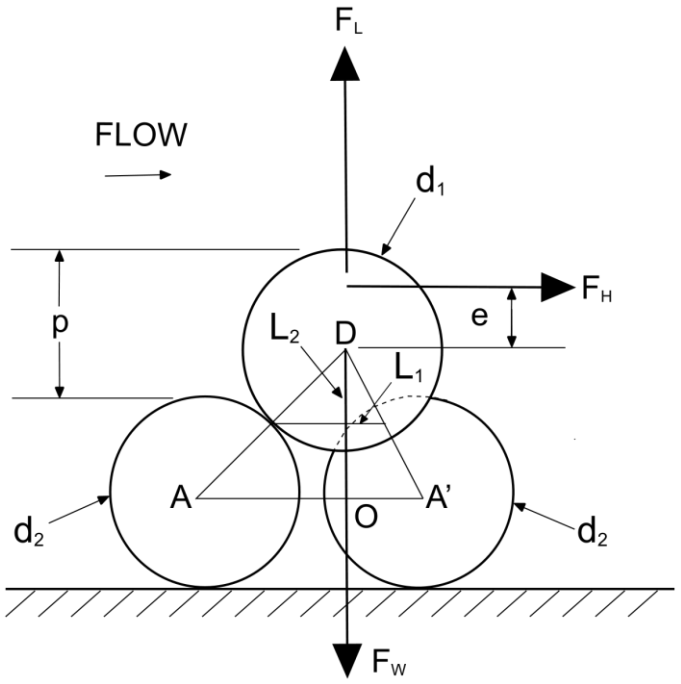

(a)

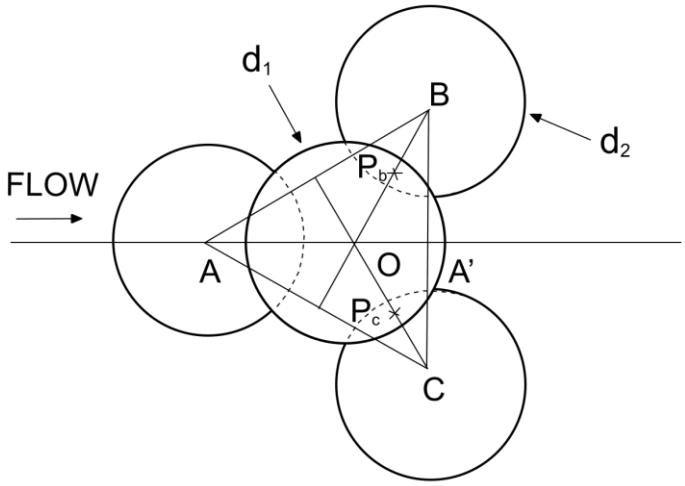

(b)

Figure A.1: Definition sketch of inter particle geometry (a) section at the middle (b) plan view.

Consider triangle AA'B

$$AB = (d_2 + s) \tag{A.1}$$

$$A'B = \frac{1}{2}(d_2 + s) \tag{A.2}$$

$$AA'^2 = AB^2 - A'B^2 \tag{A.3}$$

Therefore,

$$AA' = \frac{\sqrt{3}}{2}(d_2 + s) \tag{A.4}$$

$$AO = \frac{2}{3}AA' = \frac{1}{\sqrt{3}}\,(d_2 + s) \tag{A.5}$$

$$A'O = \frac{1}{3}AA' = \frac{1}{2\sqrt{3}}\,(d_2 + s) \tag{A.6}$$

Consider triangle AOD:

$$AD = \frac{1}{2}(d_1 + d_2) \tag{A.7}$$

$$OD^2 = AD^2 - AO^2 \tag{A.8}$$

$$OD = \hat{\lambda} = \sqrt{\frac{1}{4}(d_1 + d_2)^2 - \frac{1}{3}(d_2 + s)^2} \tag{A.9}$$

Consider similar triangles AOD and A'OD:

$$\frac{L_1}{L_2} = \frac{OA'}{OD} = \frac{d_2 + s}{2\sqrt{3}\hat{\lambda}} \tag{A.10}$$

$$\frac{L_2}{OD} = \frac{d_1}{d_1 + d_2} \qquad (A.11)$$

Hence, we get for L_1:

$$L_1 = \frac{1}{2\sqrt{3}}\left(\frac{d_1}{d_1 + d_2}\right)(d_2 + s) \qquad (A.12)$$

The pivot angle, ϕ is given by:

$$\tan\phi = \frac{L_1}{L_2} \qquad (A.13)$$

Appendix B: Incipient motion data

Test	p/d_1 (-)	d_1 (mm)	s (-)	H (cm)	T (s)	h (m)	U_m (m/s)	a (mm)	a/k_s (-)	f_w (-)	Ψ_{cr} (-)	Re_* (-)	KC (-)
W1	0.01	15.9	1.19	12	2.5	0.4	0.27	108	2.3	0.17	0.206	1034	43
W2	0.01	15.9	1.19	14	1	0.4	0.16	26	0.5	0.55	0.247	1132	10
W3	0.13	12.7	1.19	11.5	2.5	0.4	0.26	103	2.2	0.17	0.245	849	51
W4	0.13	12.7	1.19	12	2.5	0.3	0.32	127	2.7	0.14	0.311	957	63
W5	0.24	19	1.19	13.5	2.5	0.3	0.36	143	3.0	0.13	0.238	1454	47
W6	0.24	19	1.19	14.5	2	0.4	0.31	99	2.1	0.18	0.243	1675	33
W7	0.24	19	1.19	13	2.5	0.4	0.29	117	2.5	0.15	0.189	1477	39
W8	0.28	15.9	1.19	11	2.5	0.4	0.25	99	2.1	0.18	0.186	1009	39
W9	0.28	15.9	1.19	12	2.5	0.3	0.32	127	2.7	0.14	0.248	1166	50
W10	0.32	19	1.19	13.5	2.5	0.3	0.36	143	3.0	0.13	0.238	1574	47
W11	0.32	19	1.19	11.5	2.5	0.4	0.26	103	2.2	0.17	0.164	1305	34
W12	0.37	15.9	1.19	10.5	2	0.4	0.22	72	1.5	0.23	0.200	1018	28
W13	0.37	15.9	1.19	8.5	2.5	0.4	0.19	76	1.6	0.22	0.138	846	30
W14	0.37	15.9	1.19	16	1	0.3	0.27	43	0.9	0.36	0.446	1522	17
W15	0.37	15.9	1.19	13.5	2	0.3	0.35	110	2.3	0.16	0.330	1309	44
W16	0.37	31.8	1.19	7	1	0.3	0.12	19	0.4	0.71	0.085	1935	4
W17	0.40	18.7	1.23	14	2	0.4	0.30	95	2.0	0.18	0.196	1699	32
W18	0.41	19	1.36	12.5	2	0.4	0.27	85	1.8	0.20	0.108	1616	28
W19	0.41	19	1.2	10.5	2	0.4	0.22	72	1.5	0.23	0.159	1461	24
W20	0.41	19	1.19	9.5	2	0.4	0.20	65	1.4	0.25	0.149	1379	21
W21	0.41	19	1.38	14.5	2	0.4	0.31	99	2.1	0.18	0.121	1762	33
W22	0.41	19	1.19	10.5	2	0.4	0.22	72	1.5	0.23	0.167	1216	24
W23	0.44	9.5	1.19	5.5	2	0.3	0.14	45	0.9	0.35	0.195	490	30
W24	0.44	9.5	1.19	6	1	0.3	0.10	16	0.3	0.81	0.239	543	11
W25	0.44	9.5	1.19	6.5	1	0.4	0.08	12	0.3	1.04	0.170	457	8
W26	0.44	9.5	1.19	4	2	0.4	0.09	27	0.6	0.53	0.109	366	18
W27	0.46	15.9	1.19	6.5	2.5	0.4	0.15	58	1.2	0.28	0.101	806	23
W28	0.46	15.9	1.19	8	2	0.4	0.17	55	1.1	0.29	0.146	967	22
W29	0.46	15.9	1.19	13.5	1	0.3	0.23	37	0.8	0.41	0.366	1416	14
W30	0.46	15.9	1.19	8.5	2.5	0.3	0.23	90	1.9	0.19	0.167	955	36
W31	0.51	19	1.19	14	1	0.3	0.24	38	0.8	0.40	0.320	1728	13
W32	0.51	19	1.19	11	2	0.3	0.28	90	1.9	0.19	0.218	1426	30
W33	0.51	19	1.19	9	2	0.4	0.19	61	1.3	0.27	0.140	1142	20
W34	0.56	19	1.19	13	1	0.3	0.22	35	0.7	0.42	0.293	1613	12
W35	0.56	19	1.19	10.5	2	0.3	0.27	86	1.8	0.20	0.206	1352	28

Test	p/d_1 (-)	d_1 (mm)	s (-)	H (cm)	T (s)	h (m)	U_m (m/s)	a (mm)	a/k_s (-)	f_w (-)	Ψ_{cr} (-)	Re_* (-)	KC (-)
W36	0.56	19	1.19	15	1	0.4	0.18	28	0.6	0.52	0.224	1408	9
W37	0.56	19	1.19	8.5	2	0.4	0.18	58	1.2	0.28	0.131	1076	19
W38	0.56	19	1.19	7	2.5	0.4	0.16	63	1.3	0.26	0.092	904	21
W39	0.60	18.7	1.23	13	1	0.4	0.15	24	0.5	0.58	0.159	1531	8
W40	0.60	18.7	1.23	7.5	2	0.4	0.16	51	1.1	0.31	0.095	1183	17
W41	0.60	19	1.36	9.5	2	0.4	0.20	65	1.4	0.25	0.078	1379	21
W42	0.60	19	1.2	8	2	0.4	0.17	55	1.1	0.29	0.116	1248	18
W43	0.61	25.3	1.19	10.5	2	0.4	0.22	72	1.5	0.23	0.125	1945	18
W44	0.61	25.3	1.19	10.5	2.5	0.4	0.24	94	2.0	0.19	0.111	1828	23
W45	0.61	19	1.38	10.5	2	0.4	0.22	72	1.5	0.23	0.083	1461	24
W46	0.61	25.4	1.2	11	2	0.4	0.24	75	1.6	0.22	0.125	2006	19
W47	0.61	25.4	1.2	10.5	2.5	0.4	0.24	94	2.0	0.19	0.105	1835	23
W48	0.61	19	1.4	11.5	2	0.4	0.25	78	1.7	0.22	0.088	1540	26
W49	0.61	19	1.19	13.5	1	0.4	0.16	25	0.5	0.56	0.198	1590	8
W50	0.61	19	1.19	7.5	2	0.4	0.16	51	1.1	0.31	0.113	1202	17
W51	0.61	19	1.19	11.5	1	0.3	0.20	31	0.7	0.47	0.254	1542	10
W52	0.61	25.3	1.19	14.5	1	0.3	0.25	39	0.8	0.39	0.250	2288	10
W53	0.61	19	1.19	9.5	2	0.3	0.24	78	1.6	0.22	0.184	1310	26
W54	0.61	25.3	1.19	11.5	2	0.3	0.30	94	2.0	0.19	0.172	1898	23
W55	0.61	19	1.19	15	1	0.4	0.18	28	0.6	0.52	0.224	1565	9
W56	0.61	19	1.19	8	2	0.4	0.17	55	1.1	0.29	0.122	1155	18
W57	0.61	25.3	1.19	10.5	2	0.4	0.22	72	1.5	0.23	0.125	1849	18
W58	0.61	25	1.23	10.5	2	0.4	0.22	72	1.5	0.23	0.105	1922	18
W59	0.63	25.3	1.19	13.5	1	0.3	0.23	37	0.8	0.41	0.230	2377	9
W60	0.63	25.3	1.19	12	2	0.3	0.31	98	2.1	0.18	0.181	2107	24
W61	0.63	25.3	1.19	16.5	1	0.4	0.19	31	0.6	0.48	0.188	2145	8
W62	0.63	25.3	1.19	9.5	2	0.4	0.20	65	1.4	0.25	0.112	1655	16
W63	0.64	12.7	1.19	5.5	1	0.3	0.09	15	0.3	0.87	0.162	690	7
W64	0.64	12.7	1.19	5.5	2	0.3	0.14	45	0.9	0.35	0.146	655	22
W65	0.64	12.7	1.19	7	1	0.4	0.08	13	0.3	0.98	0.138	638	6
W66	0.64	12.7	1.19	6	2	0.4	0.13	41	0.9	0.37	0.131	620	20
W67	0.67	25.4	1.2	14.5	1	0.4	0.17	27	0.6	0.53	0.153	2216	7
W68	0.67	25.4	1.2	8.5	2	0.4	0.18	58	1.2	0.28	0.093	1728	14
W69	0.67	25.3	1.19	15	1	0.4	0.18	28	0.6	0.52	0.168	1875	7
W70	0.67	25.3	1.19	9	2	0.4	0.19	61	1.3	0.27	0.105	1481	15

Test	p/d_1 (-)	d_1 (mm)	s (-)	H (cm)	T (s)	h (m)	U_m (m/s)	a (mm)	a/k_s (-)	f_w (-)	Ψ_{cr} (-)	Re_* (-)	KC (-)
W71	0.67	25.4	1.38	11.5	2	0.4	0.25	78	1.7	0.22	0.069	2059	19
W72	0.67	25.3	1.19	13	1	0.4	0.15	24	0.5	0.58	0.142	2072	6
W73	0.67	25.3	1.19	8	2	0.4	0.17	55	1.1	0.29	0.091	1662	14
W74	0.68	25	1.23	12.5	1	0.4	0.15	23	0.5	0.60	0.114	2001	6
W75	0.68	25	1.23	7.5	2	0.4	0.16	51	1.1	0.31	0.071	1582	13
W76	0.72	25.3	1.19	10.5	1	0.3	0.18	28	0.6	0.51	0.172	1947	7
W77	0.72	25.3	1.19	10	2	0.3	0.26	82	1.7	0.21	0.146	1797	20
W78	0.72	25.3	1.19	12.5	1	0.4	0.15	23	0.5	0.60	0.136	1731	6
W79	0.72	25.3	1.19	8	2	0.4	0.17	55	1.1	0.29	0.091	1420	14
W80	0.74	25.3	1.19	9	1	0.3	0.15	24	0.5	0.58	0.144	1735	6
W81	0.74	31.8	1.19	11	1	0.3	0.19	30	0.6	0.49	0.144	2450	6
W82	0.74	25.3	1.19	9.5	2	0.3	0.24	78	1.6	0.22	0.138	1699	19
W83	0.74	31.8	1.19	11	2	0.3	0.28	90	1.9	0.19	0.130	2325	18
W84	0.74	25.3	1.19	11	1	0.4	0.13	20	0.4	0.67	0.117	1566	5
W85	0.74	25.3	1.19	7.5	2	0.4	0.16	51	1.1	0.31	0.085	1333	13
W86	0.74	31.8	1.19	8.5	2	0.4	0.18	58	1.2	0.28	0.078	2056	11
W87	0.75	15.9	1.19	5.5	1	0.3	0.09	15	0.3	0.87	0.129	864	6
W88	0.75	15.9	1.19	5.5	2	0.3	0.14	45	0.9	0.35	0.116	820	18
W89	0.75	15.9	1.19	6.5	1	0.4	0.08	12	0.3	1.04	0.101	765	5
W90	0.75	15.9	1.19	4.5	2	0.4	0.10	31	0.6	0.48	0.075	657	12
W91	0.76	16	2.65	14.5	2.5	0.3	0.39	154	3.2	0.12	0.035	1345	60
W92	0.76	16	2.65	13	2.5	0.4	0.29	117	2.5	0.15	0.026	1118	46
W93	0.76	31.8	1.19	10.5	1	0.3	0.18	28	0.6	0.51	0.137	2582	6
W94	0.76	31.8	1.19	11	2	0.3	0.28	90	1.9	0.19	0.130	2518	18
W95	0.76	31.8	1.19	11.5	1	0.4	0.13	21	0.4	0.65	0.098	2187	4
W96	0.76	31.8	1.19	8.5	2	0.4	0.18	58	1.2	0.28	0.078	1951	11
W97	0.76	25.4	1.2	10.5	1	0.4	0.12	20	0.4	0.70	0.105	1838	5
W98	0.76	25.4	1.2	7.5	2	0.4	0.16	51	1.1	0.31	0.080	1607	13
W99	0.76	25.3	1.19	10.5	1	0.4	0.12	20	0.4	0.70	0.111	1831	5
W100	0.76	25.3	1.19	7	2	0.4	0.15	48	1.0	0.33	0.078	1538	12
W101	0.76	25.4	1.38	11	2	0.4	0.24	75	1.6	0.22	0.066	2006	19
W102	0.77	25.4	1.52	13	2	0.4	0.28	89	1.9	0.20	0.058	2211	22
W103	0.77	25	1.23	9	1	0.4	0.11	17	0.4	0.79	0.078	1654	4
W104	0.77	25	1.23	6.5	2	0.4	0.14	44	0.9	0.35	0.060	1456	11
W105	0.77	25.3	1.19	8	1	0.3	0.14	22	0.5	0.64	0.125	1663	5

Test	p/d_1 (-)	d_1 (mm)	s (-)	H (cm)	T (s)	h (m)	U_m (m/s)	a (mm)	a/k_s (-)	f_w (-)	Ψ_{cr} (-)	Re_* (-)	KC (-)
W106	0.77	25.3	1.19	9	2	0.3	0.23	74	1.6	0.23	0.130	1690	18
W107	0.77	25.3	1.19	10.5	1	0.4	0.12	20	0.4	0.70	0.111	1695	5
W108	0.77	25.3	1.19	7	2	0.4	0.15	48	1.0	0.33	0.078	1424	12
W109	0.78	31.8	1.19	10.5	1	0.4	0.12	20	0.4	0.70	0.088	1916	4
W110	0.78	31.8	1.19	7.5	2	0.4	0.16	51	1.1	0.31	0.068	1675	10
W111	0.81	31.8	1.19	7.5	1	0.3	0.13	20	0.4	0.67	0.093	2014	4
W112	0.81	31.8	1.19	9	2	0.3	0.23	74	1.6	0.23	0.103	2124	15
W113	0.81	19	2.65	14	2.5	0.3	0.37	148	3.1	0.13	0.029	1565	49
W114	0.81	31.8	1.19	8.5	1	0.4	0.10	16	0.3	0.83	0.069	1740	3
W115	0.81	31.8	1.19	7	2	0.4	0.15	48	1.0	0.33	0.062	1652	9
W116	0.81	19	2.65	12.5	2.5	0.4	0.28	112	2.4	0.16	0.021	1298	37
W117	0.81	19	1.7	10.5	2	0.4	0.22	72	1.5	0.23	0.045	1461	24
W118	0.81	19	1.36	8.5	1	0.4	0.10	16	0.3	0.83	0.061	1216	5
W119	0.81	19	1.36	5.5	2	0.4	0.12	37	0.8	0.40	0.042	1004	12
W120	0.81	19	1.2	6.5	1	0.4	0.08	12	0.3	1.04	0.081	1041	4
W121	0.81	19	1.2	4.5	2	0.4	0.10	31	0.6	0.48	0.059	894	10
W122	0.81	19	1.38	6.5	2	0.4	0.14	44	0.9	0.35	0.048	1106	15
W123	0.81	19	1.38	10	1	0.4	0.12	19	0.4	0.73	0.070	1336	6
W124	0.81	19	1.19	6	1	0.4	0.07	11	0.2	1.12	0.077	994	4
W125	0.81	19	1.19	4.5	2	0.4	0.10	31	0.6	0.48	0.062	894	10
W126	0.82	19	1.4	12	1	0.4	0.14	22	0.5	0.62	0.082	1485	7
W127	0.82	19	1.4	6.5	2	0.4	0.14	44	0.9	0.35	0.045	1106	15
W128	0.82	19	1.19	5	1	0.3	0.09	14	0.3	0.95	0.097	977	4
W129	0.82	19	1.19	4.5	1.3	0.3	0.10	20	0.4	0.68	0.091	946	7
W130	0.82	19	1.19	5.5	2	0.3	0.14	45	0.9	0.35	0.097	980	15
W131	0.82	19	1.19	5.6	1	0.4	0.07	10	0.2	1.18	0.071	838	3
W132	0.82	19	1.19	4.5	2	0.4	0.10	31	0.6	0.48	0.062	785	10
W133	0.83	31.8	1.19	8	1	0.4	0.09	15	0.3	0.88	0.064	1636	3
W134	0.83	31.8	1.19	7	2	0.4	0.15	48	1.0	0.33	0.062	1609	9
W135	0.84	31.8	1.19	6.5	1	0.3	0.11	18	0.4	0.76	0.078	1853	3
W136	0.84	31.8	1.19	8	2	0.3	0.21	65	1.4	0.25	0.090	1984	13
W137	0.84	31.8	1.19	7.5	1	0.4	0.09	14	0.3	0.92	0.060	1753	3
W138	0.84	31.8	1.19	6.5	2	0.4	0.14	44	0.9	0.35	0.057	1714	9
W139	0.87	18.7	1.23	6	1	0.4	0.07	11	0.2	1.12	0.065	978	4
W140	0.87	18.7	1.23	4.5	2	0.4	0.10	31	0.6	0.48	0.052	880	10

Test	p/d_1 (-)	d_1 (mm)	s (-)	H (cm)	T (s)	h (m)	U_m (m/s)	a (mm)	a/k_s (-)	f_w (-)	Ψ_{cr} (-)	Re_* (-)	KC (-)
W141	0.88	25.3	1.19	4.5	1	0.3	0.08	12	0.3	1.03	0.064	1224	3
W142	0.88	25.3	1.19	5.5	2	0.3	0.14	45	0.9	0.35	0.073	1305	11
W143	0.88	25.3	1.19	5	1	0.4	0.06	9	0.2	1.30	0.047	1045	2
W144	0.88	25.3	1.19	4.5	2	0.4	0.10	31	0.6	0.48	0.047	1045	8
W145	0.88	25.4	1.2	5.5	1	0.4	0.06	10	0.2	1.20	0.050	1263	3
W146	0.88	25.4	1.52	8	2	0.4	0.17	55	1.1	0.29	0.033	1668	13
W147	0.88	25.3	1.19	5	1	0.4	0.06	9	0.2	1.30	0.047	1190	2
W148	0.88	25.3	1.19	4.5	2	0.4	0.10	31	0.6	0.48	0.047	1190	8
W149	0.88	25.4	1.38	6.5	2	0.4	0.14	44	0.9	0.35	0.036	1479	11
W150	0.88	25.4	1.38	10	1	0.4	0.12	19	0.4	0.73	0.052	1787	5
W151	0.89	25	1.23	5	1	0.4	0.06	9	0.2	1.30	0.039	1176	2
W152	0.89	25	1.23	4	2	0.4	0.09	27	0.6	0.53	0.034	1098	7
W153	0.92	31.8	1.19	3.5	1	0.3	0.06	9	0.2	1.28	0.038	1329	2
W154	0.92	31.8	1.19	4.5	2	0.3	0.12	37	0.8	0.41	0.046	1460	7
W155	0.92	31.8	1.19	4.5	1	0.4	0.05	8	0.2	1.42	0.033	1236	2
W156	0.92	31.8	1.19	4	2	0.4	0.09	27	0.6	0.53	0.033	1227	5

Appendix C: Flow visualisation

C.1 Vortex ejection from a rough bed of 19mm spherical elements

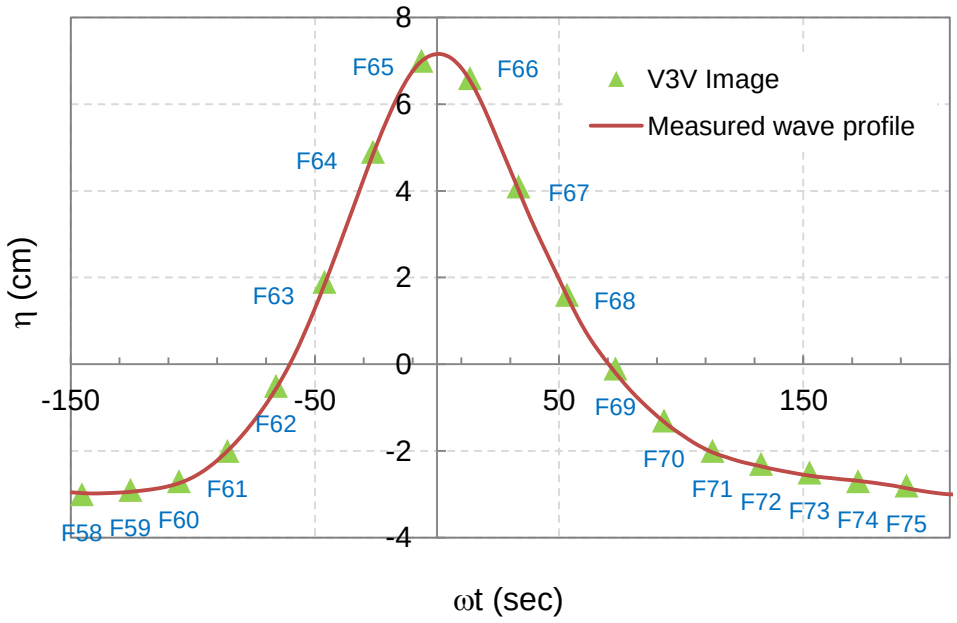

Figure C.1: Measured wave profile. Test FV5, H=10.1cm, T=2.5, h=40cm.

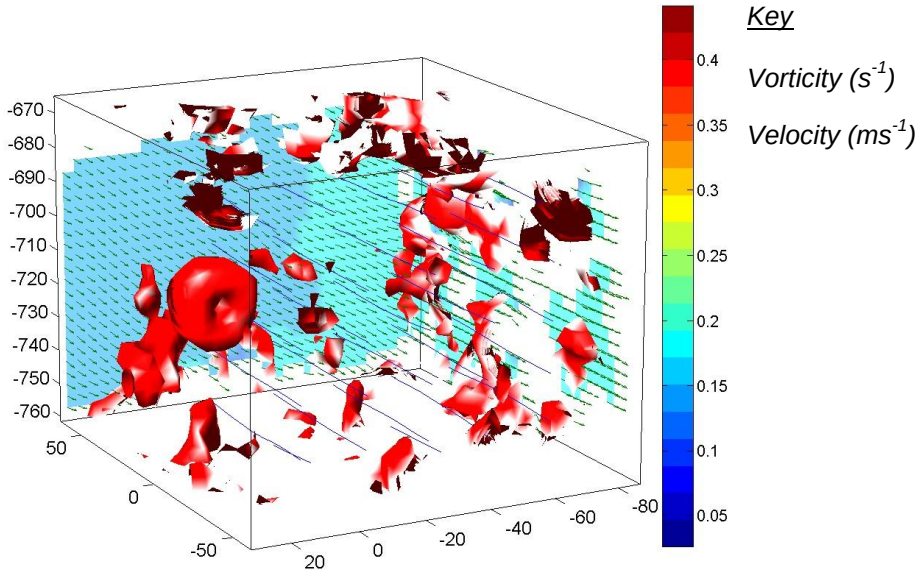

Figure C.2: Vorticity isosurface and velocity. Test FV5, Frame 58, ωt= -145.4^0.

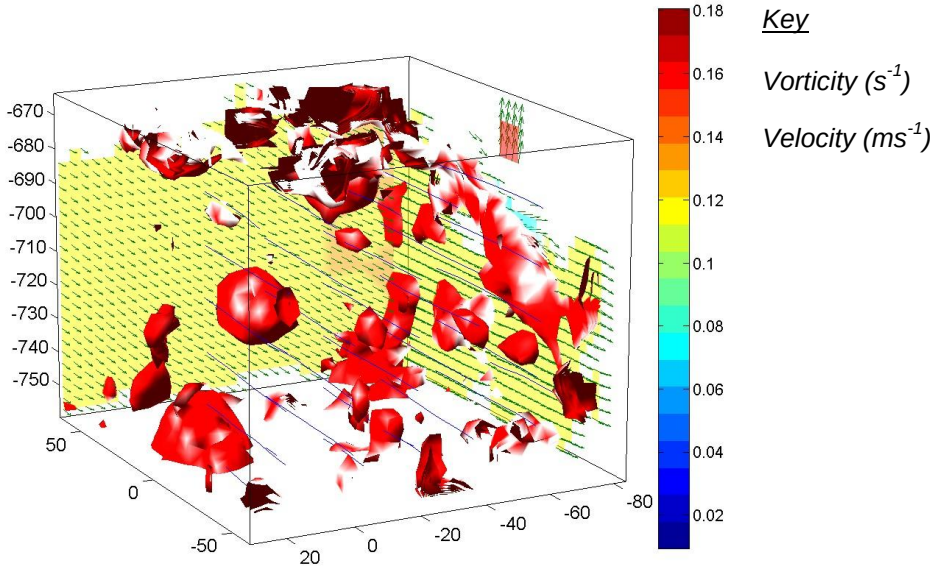

Figure C.3: Vorticity isosurface and velocity. Test FV5, Frame 59, ωt= -125.5^0.

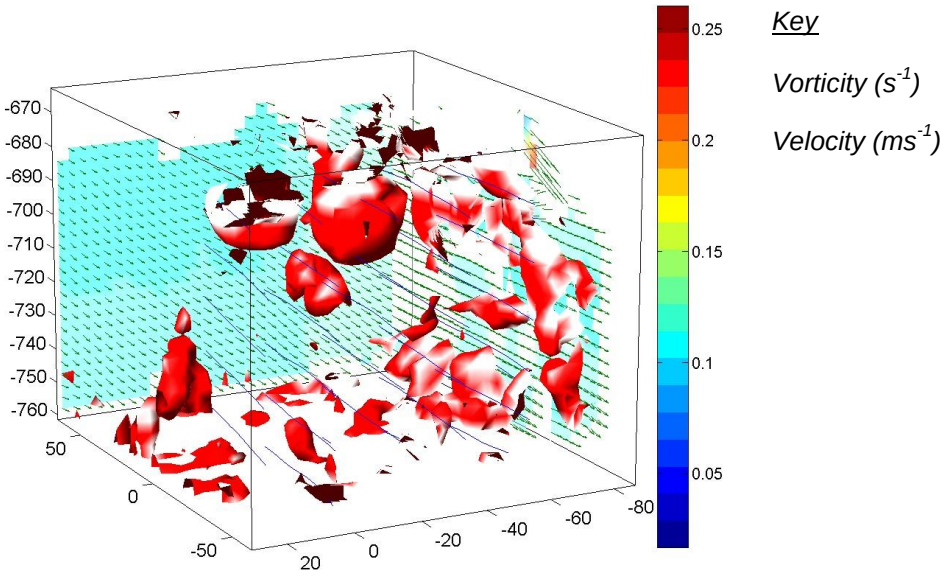

Figure C.4: Vorticity isosurface and velocity. Test FV5, Frame 60. ωt= -105.6^0.

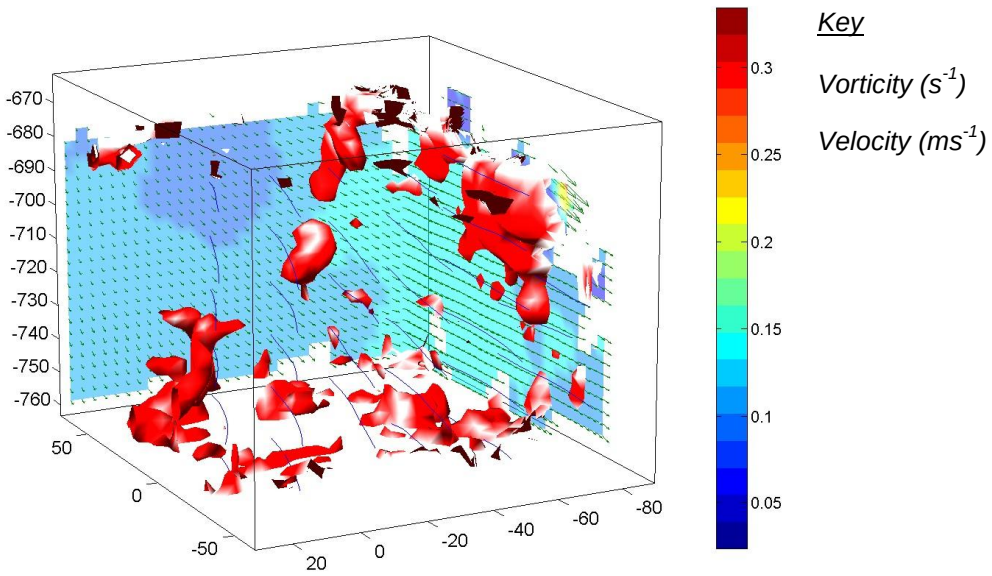

Figure C.5: Vorticity isosurface and velocity. Test FV5, Frame 61, ωt= -85.8^0.

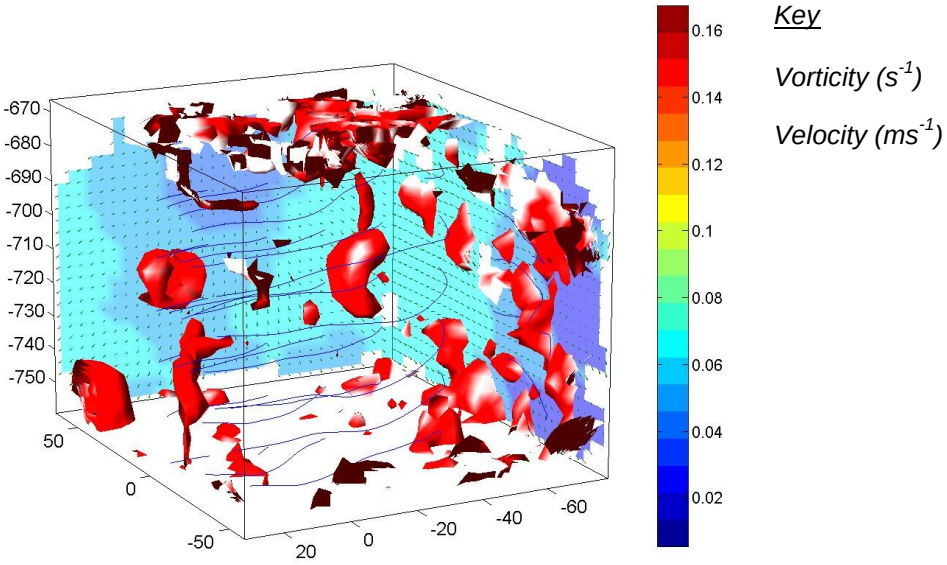

Figure C.6: Vorticity isosurface and velocity. Test FV5, Frame 62, ωt= -65.9^0.

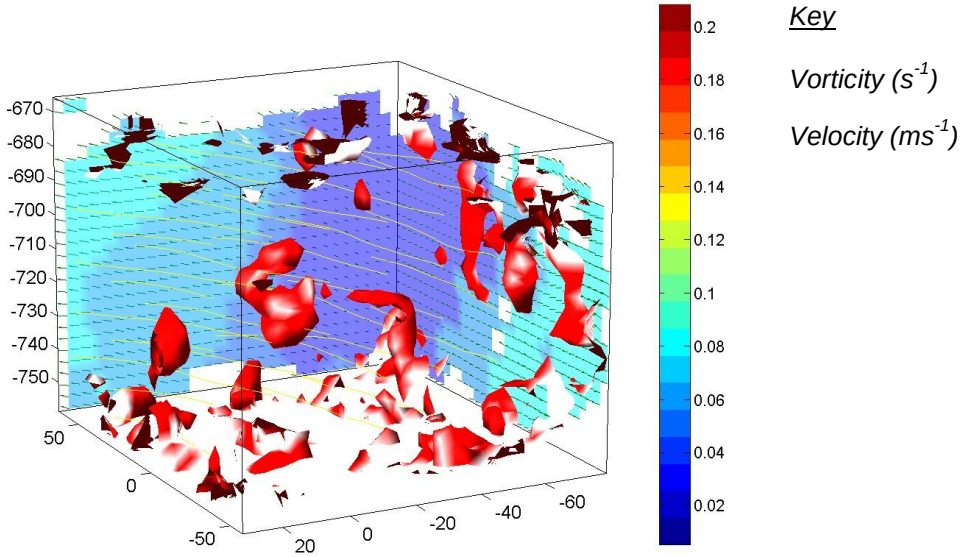

Figure C.7: Vorticity isosurface and velocity. Test FV5, Frame 63, ωt= -46.1^0

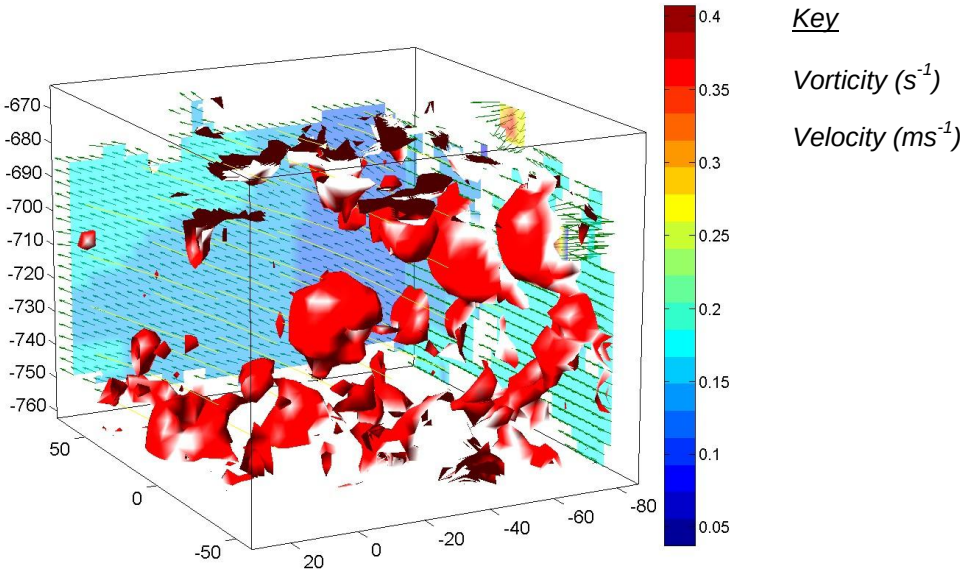

Figure C.8: Vorticity isosurface and velocity. Test FV5, Frame 64. ωt= -26.2^0.

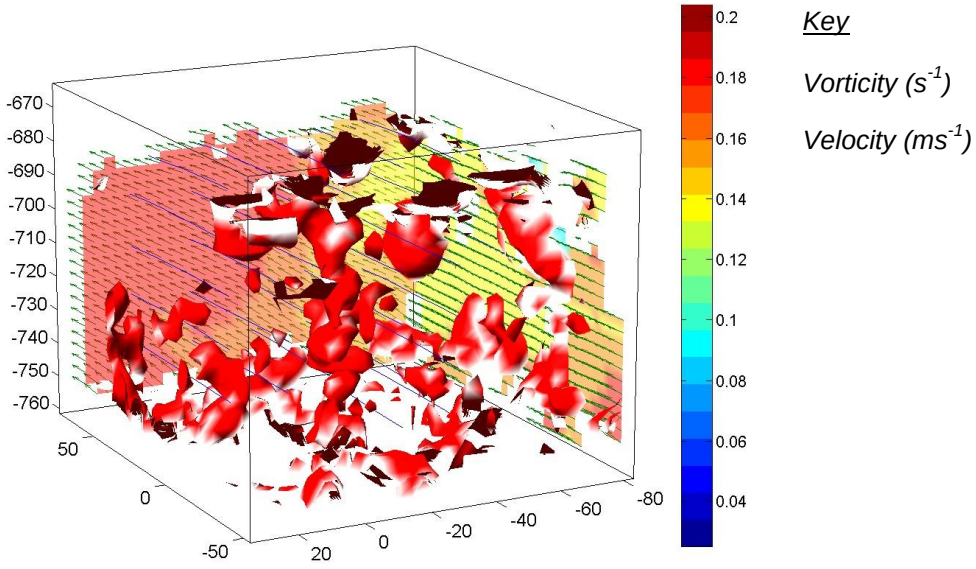

Figure C.9: Vorticity isosurface and velocity. Test FV5, Frame 65. ωt= -6.3^0.

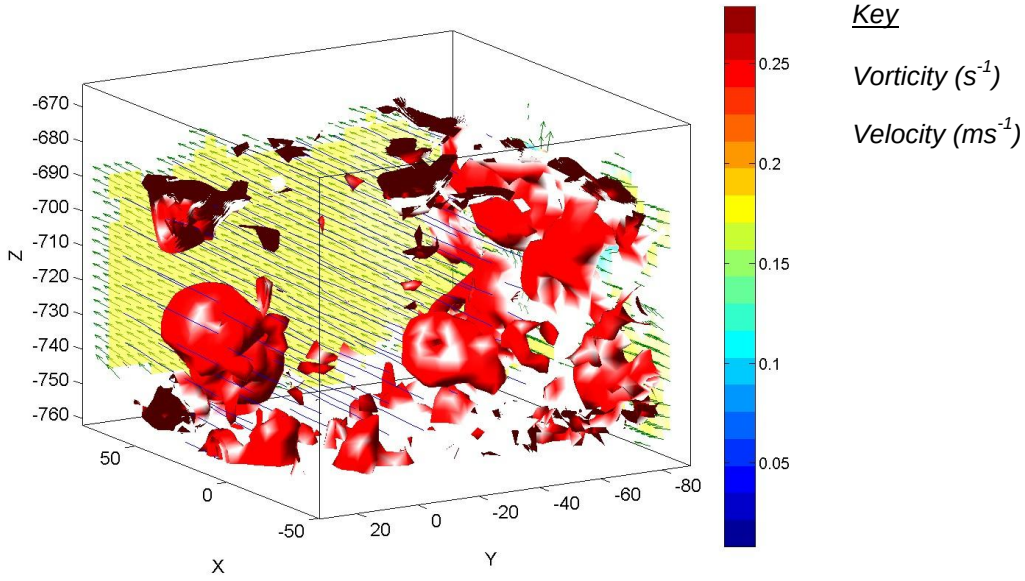

Figure C.10: Vorticity isosurface and velocity. Test FV5, Frame 66, ωt= 13.5^0.

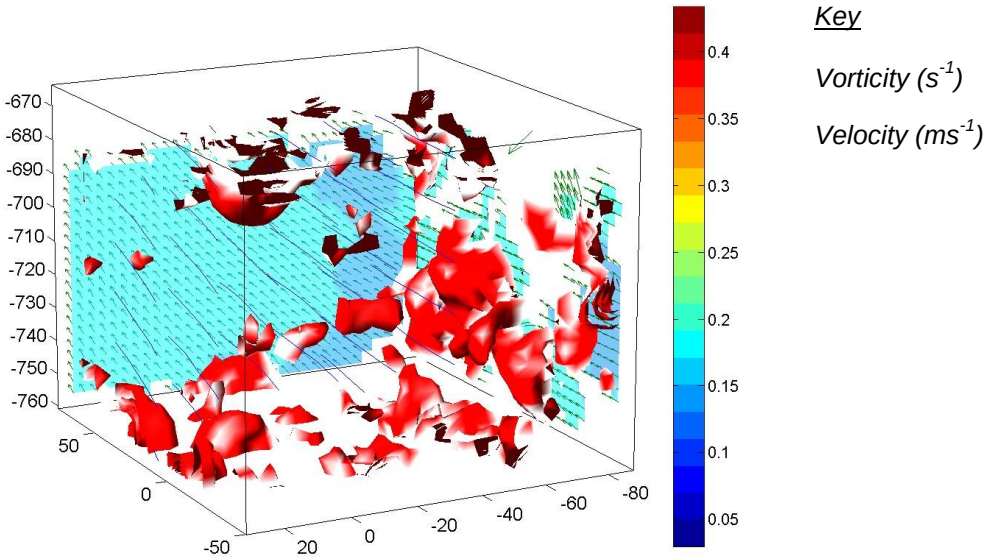

Figure C.11: Vorticity isosurface and velocity. Test FV5, Frame 67, $\omega t = 33.4^0$.

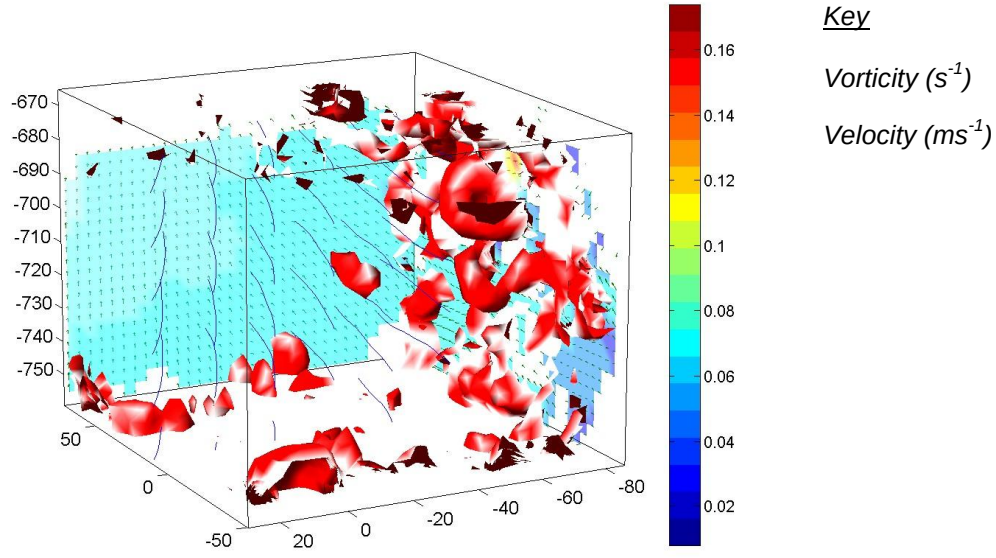

Figure C.12: Vorticity isosurface and velocity. Test FV5, Frame 68, $\omega t = 53.3^0$.

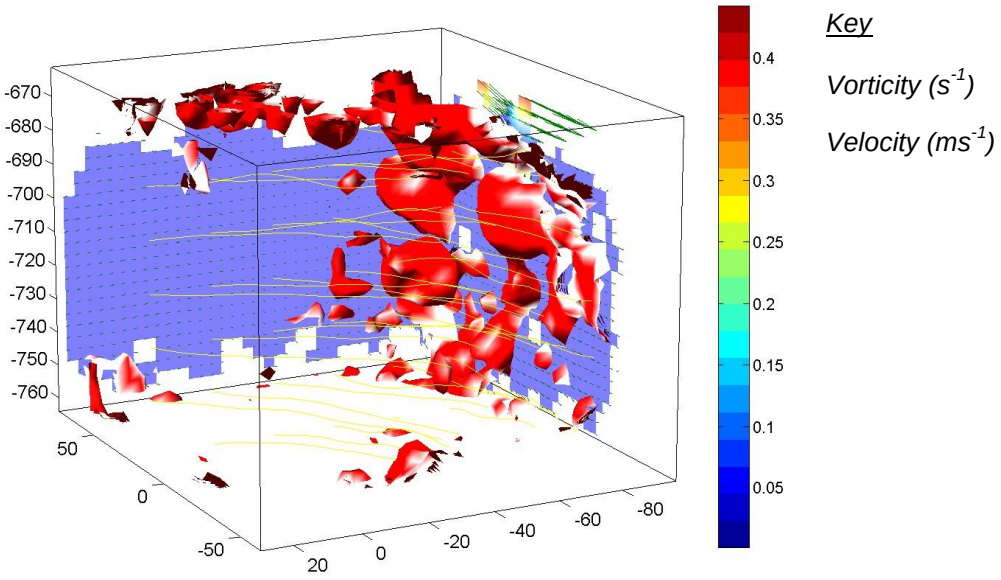

Figure C.13: Vorticity isosurface and velocity. Test FV5, Frame 69. $\omega t = 73.1^0$.

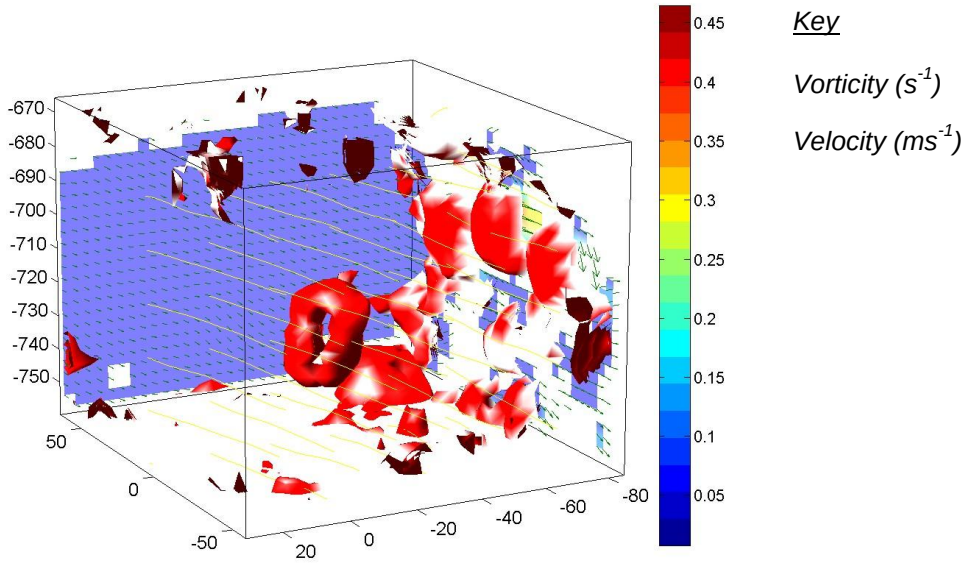

Figure C.14: Vorticity isosurface and velocity.Test FV5, Frame 70, $\omega t = 93.0^0$.

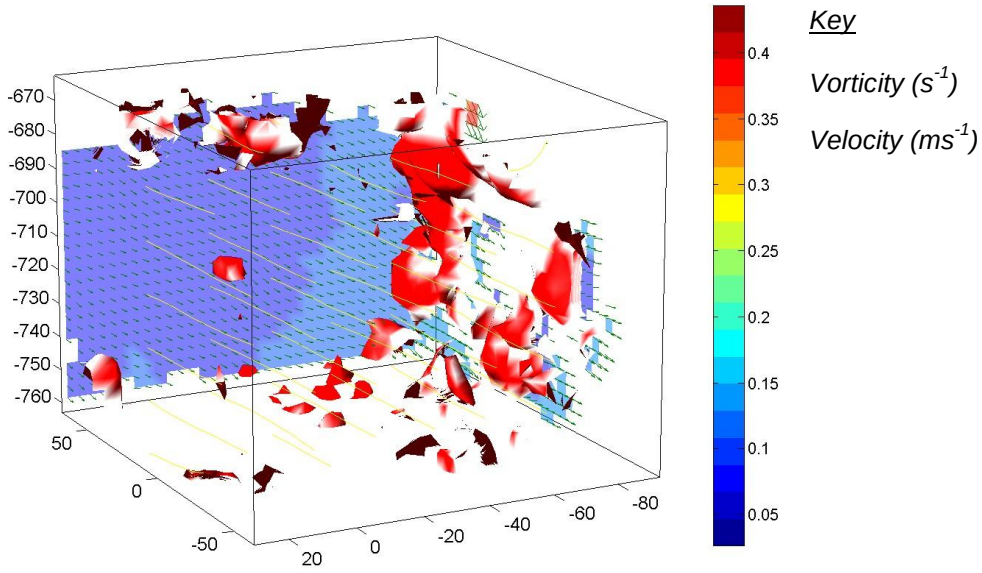

Figure C.15: Vorticity isosurface and velocity. Test FV5, Frame 71, ωt= 112.8^0.

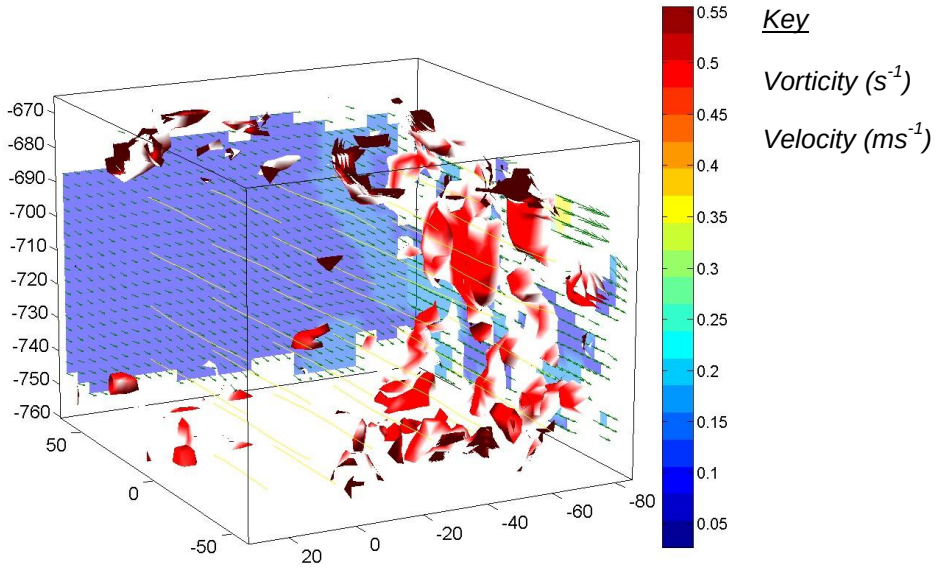

Figure C.16: Vorticity isosurface and velocity. Test FV5, Frame 72. ωt= 132.7^0.

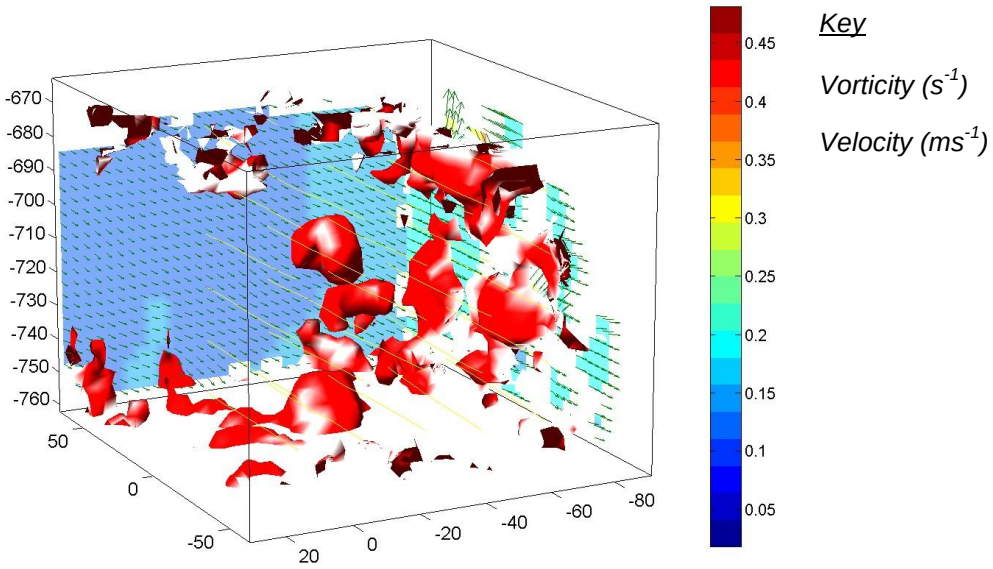

Figure C.17: Vorticity isosurface and velocity. Test FV5, Frame 73, $\omega t = 152.6^0$.

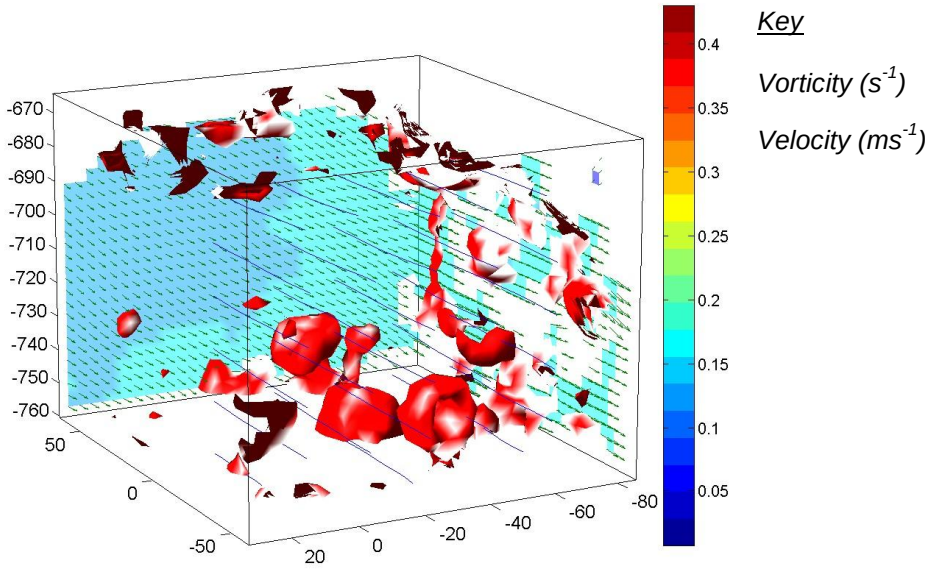

Figure C.18: Vorticity isosurface and velocity. Test FV5, Frame 74, $\omega t = 172.4^0$.

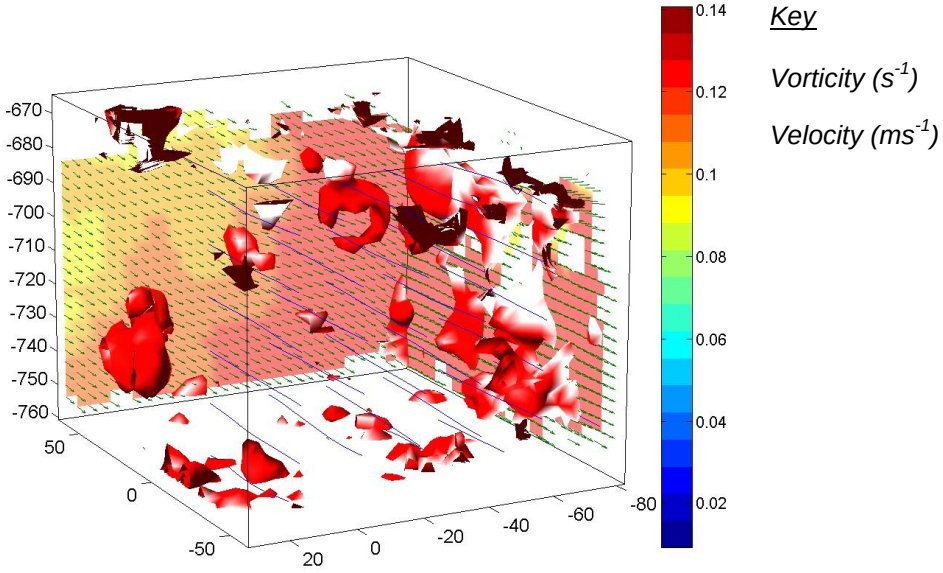

Figure C.19: Vorticity isosurface and velocity. Test FV5, Frame 75, ωt= 192.3^0.

C.2 Vortex ejection from a rough bed of 50mm spherical elements

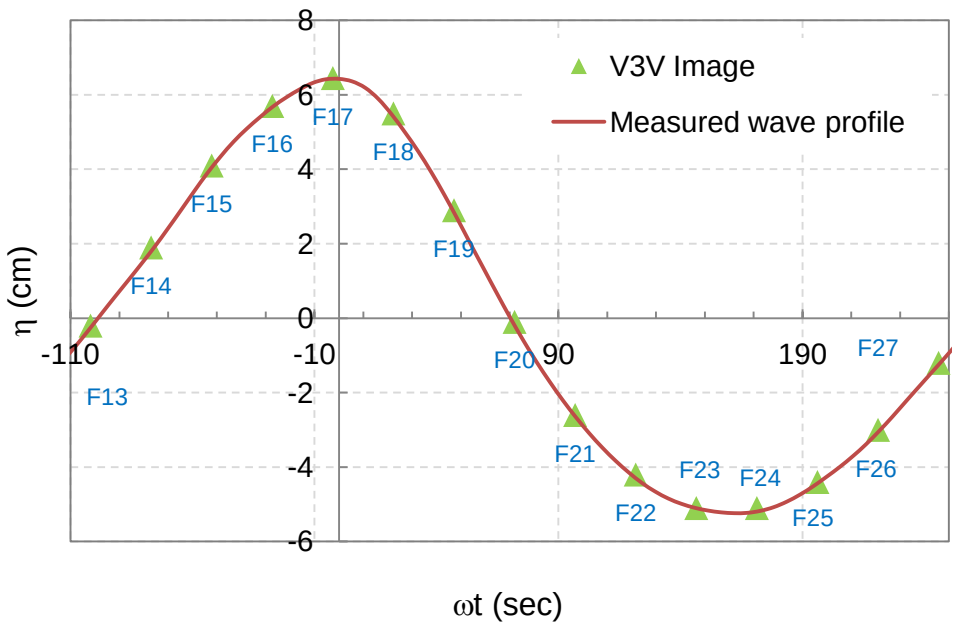

Figure C.20: Measured wave profile, Test FV1, H=11.63cm, T=2 sec, h=40cm.

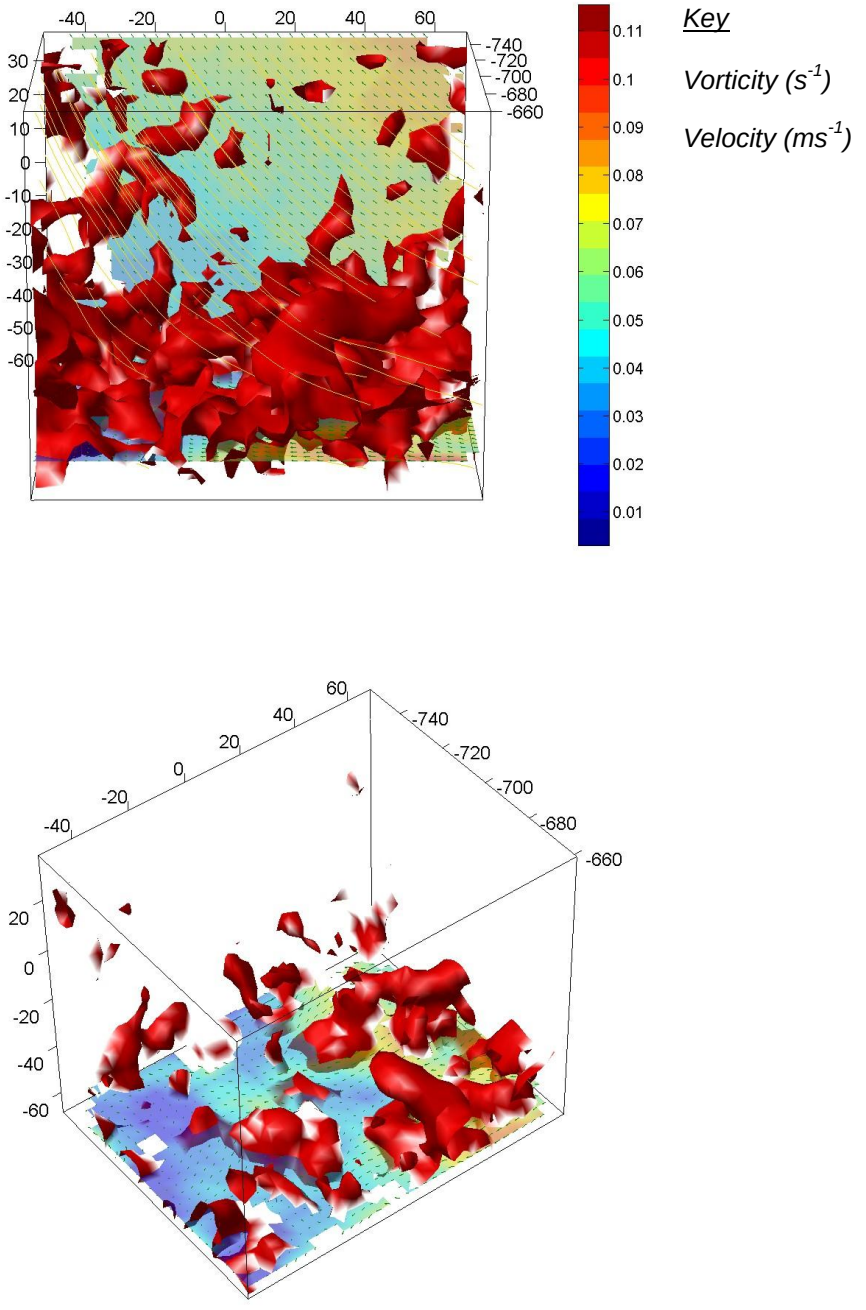

Figure C.21: Vorticity isosurface and velocity. Test FV1, Frame 13. ωt=-101.8^0.

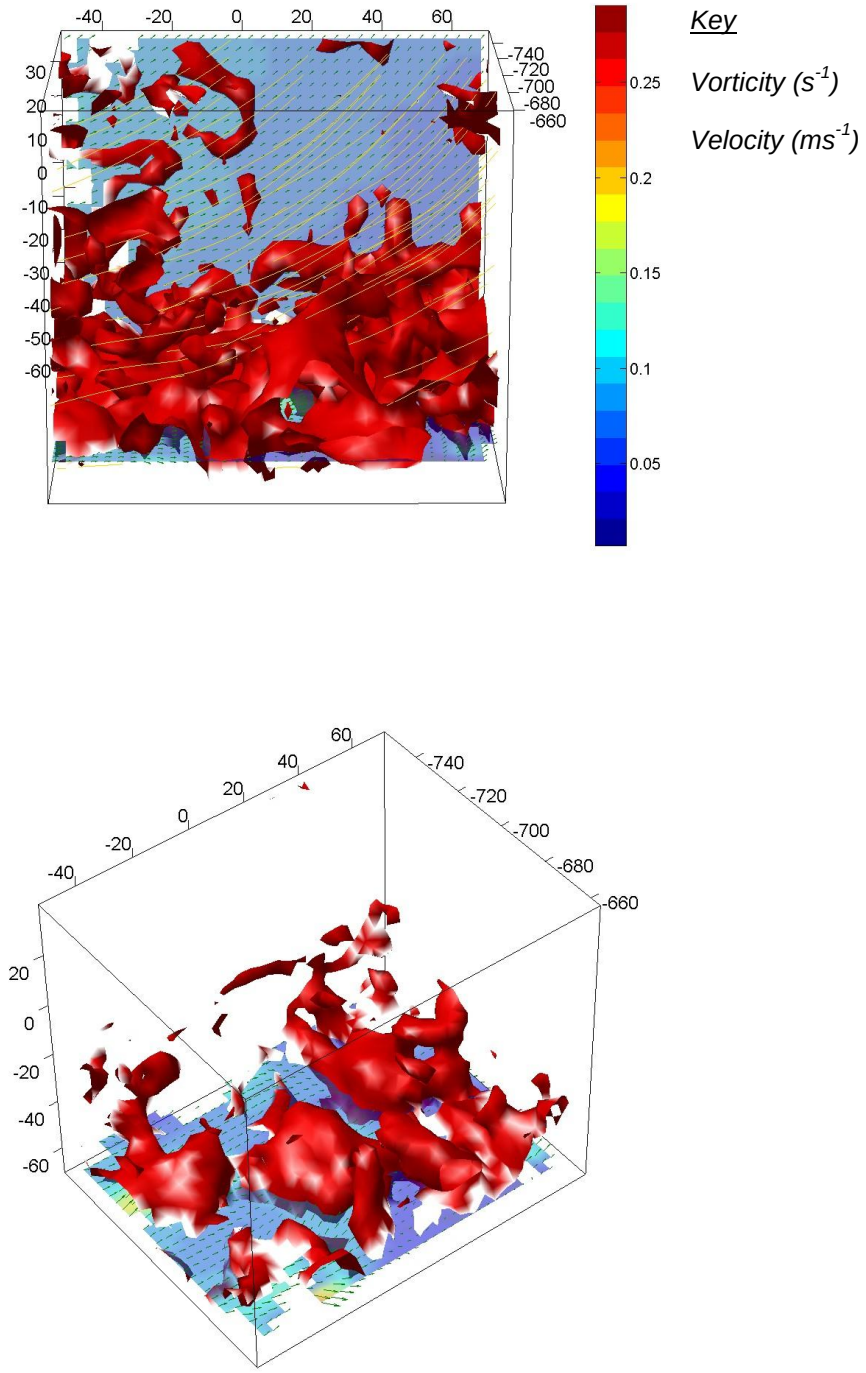

Figure C.22: Vorticity isosurface and velocity. Test FV1, Frame 14. ωt= -76.9^0.

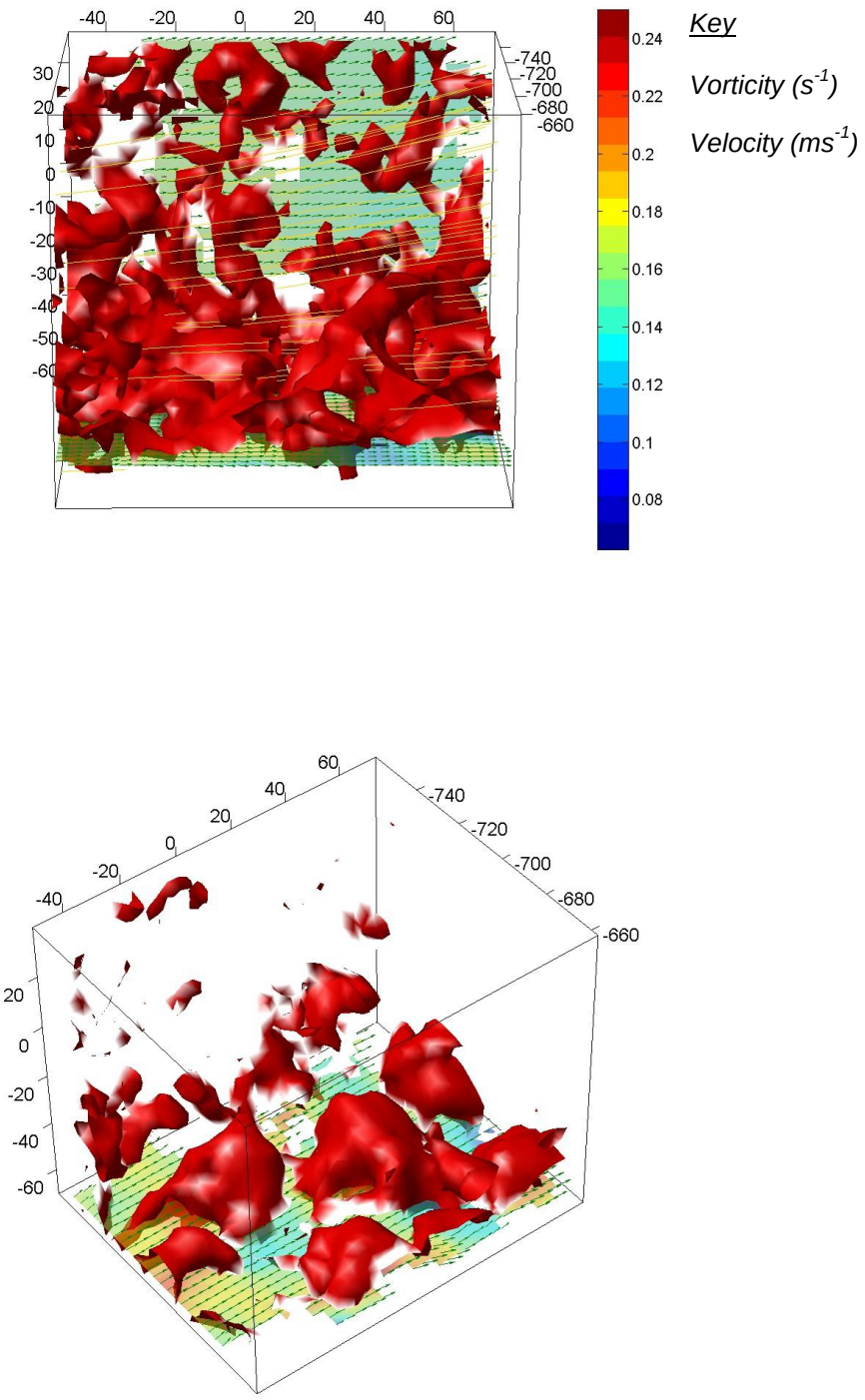

Figure C.23: Vorticity isosurface and velocity.Test FV1, Frame 15, ωt= -52.1^0.

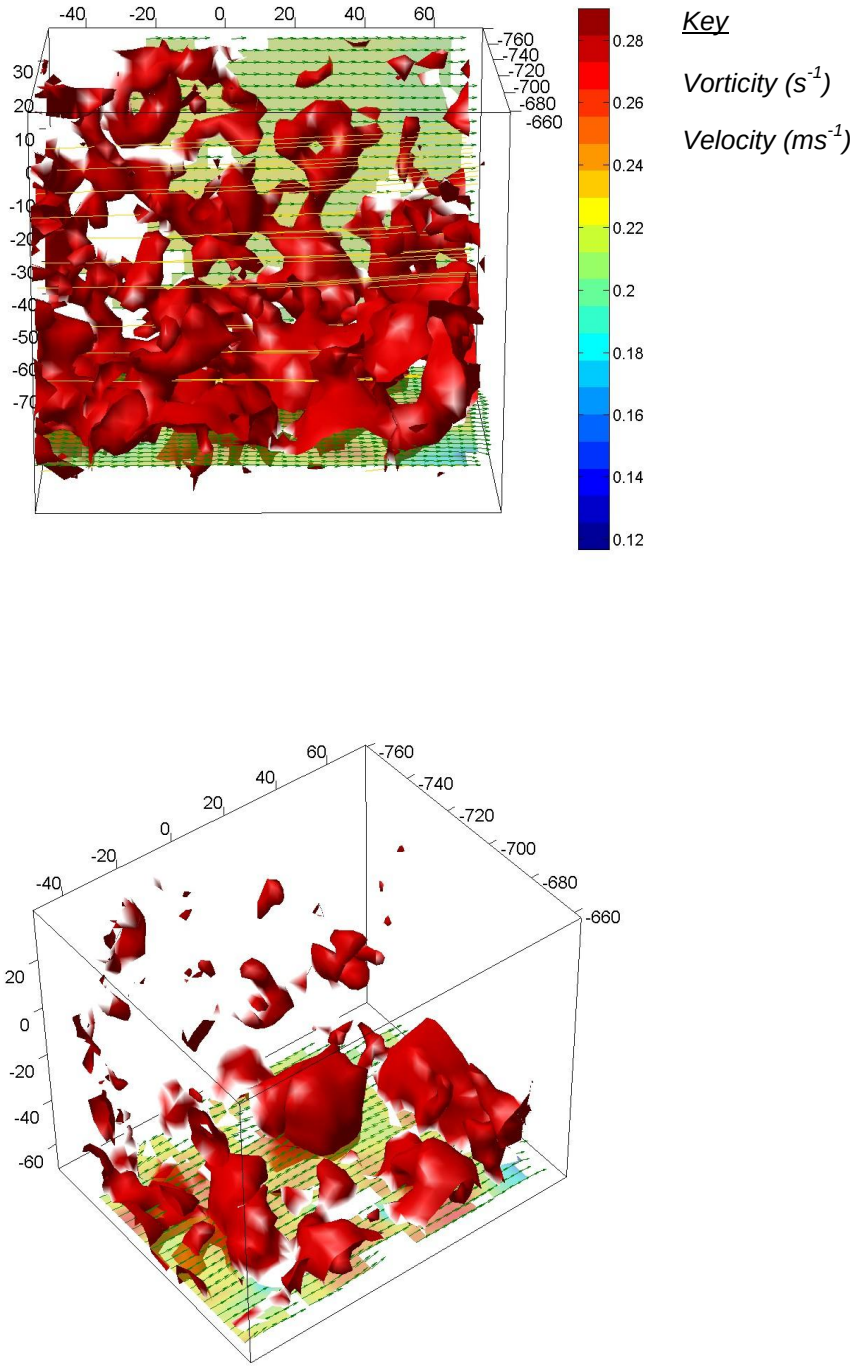

Figure C.24: Vorticity isosurface and velocity. Test FV1, Frame 16. ωt= -27.3^0.

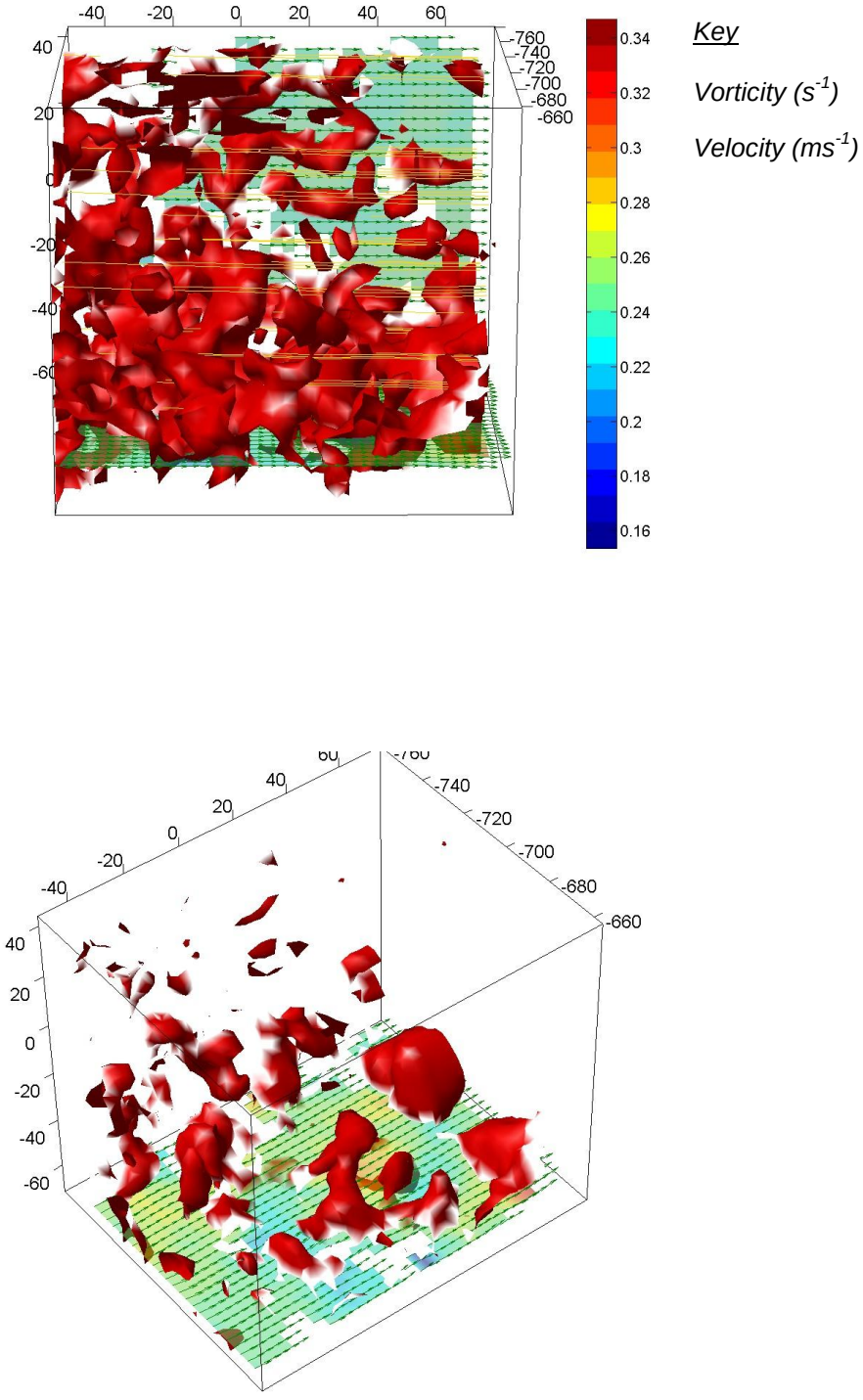

Figure C.25: Vorticity isosurface and velocity. Test FV1, Frame 17, ωt= -2.4^0.

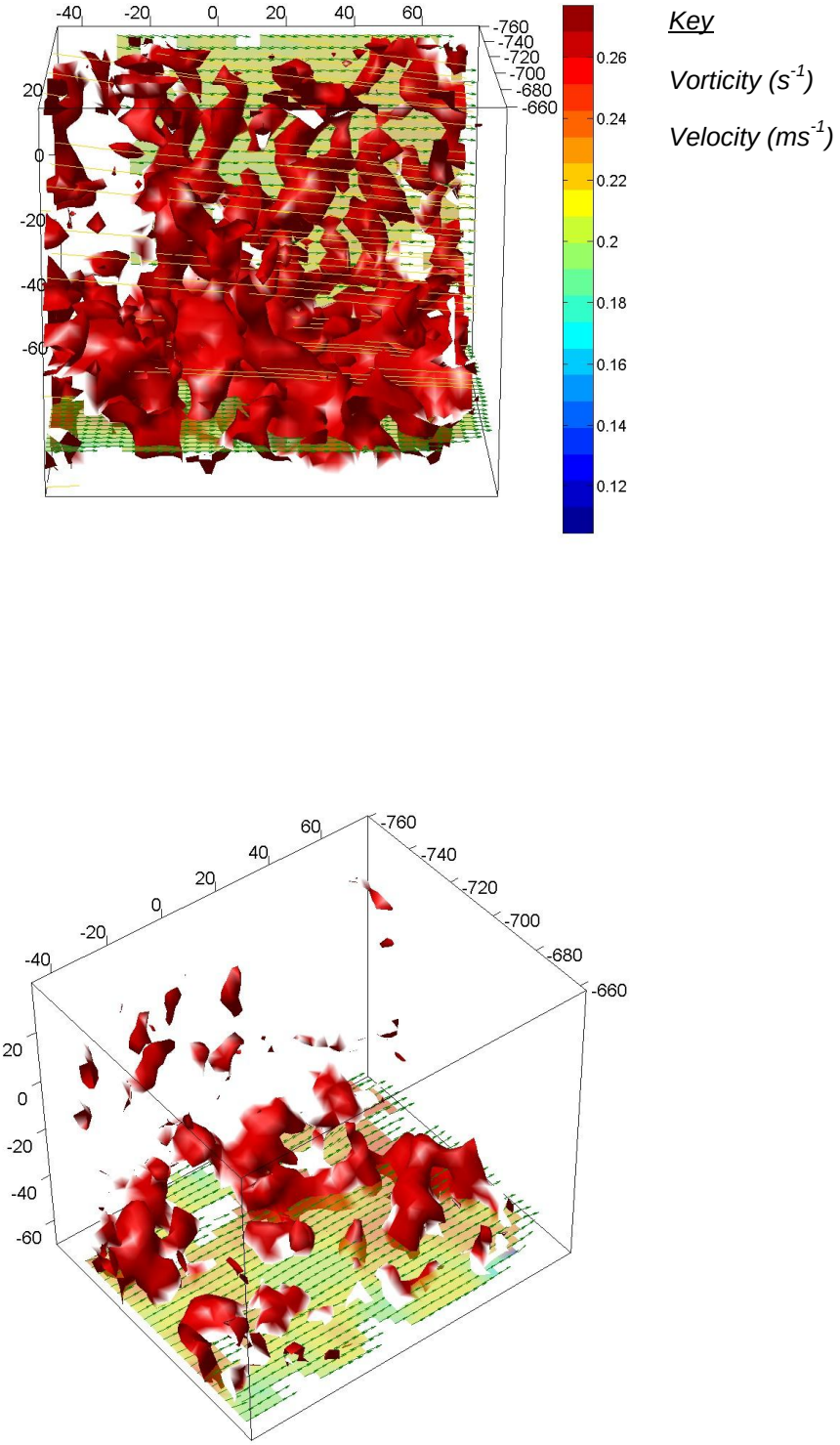

Figure C.26: Vorticity isosurface and velocity. Test FV1, Frame 18. $\omega t = 22.4^0$.

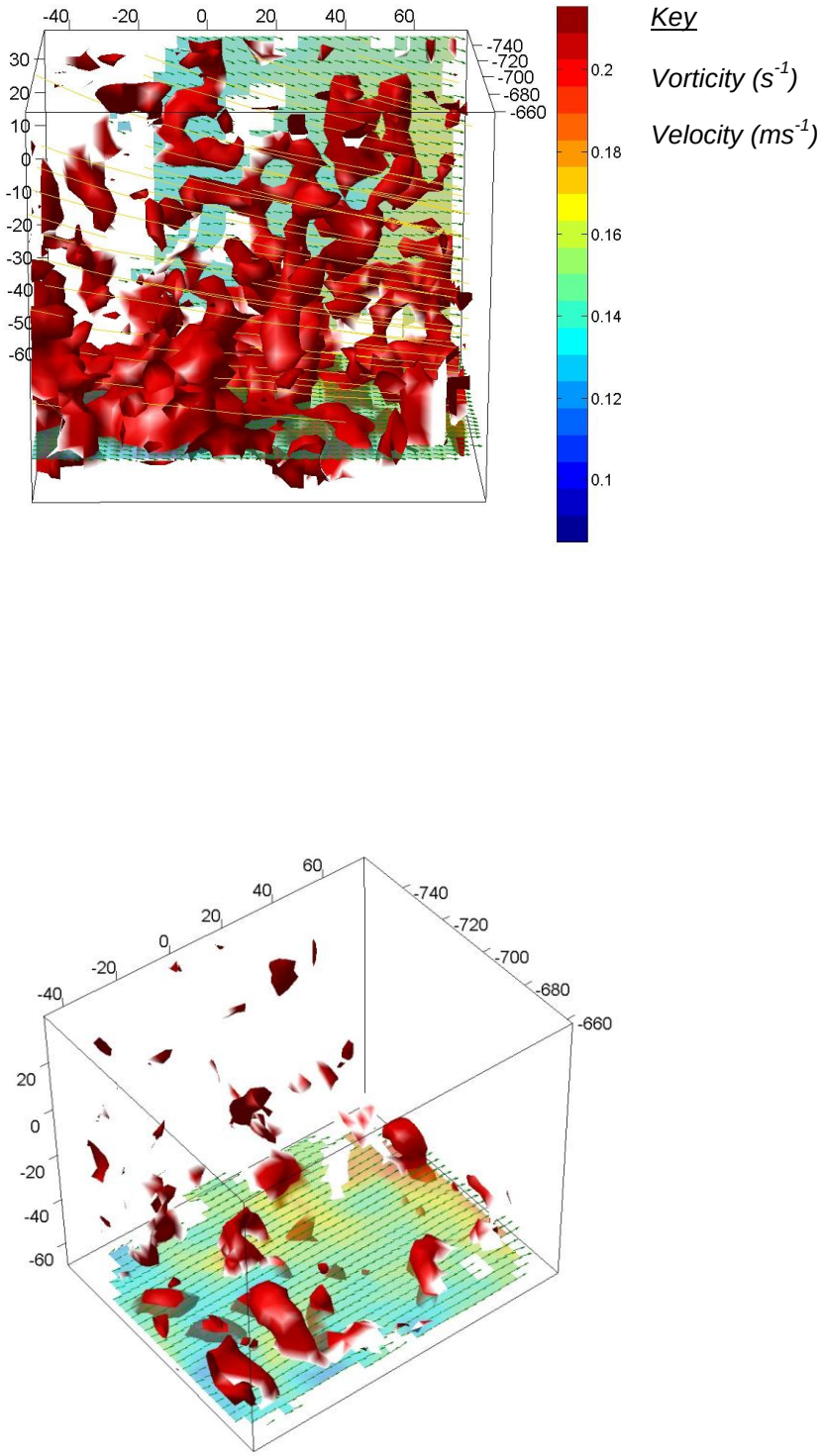

Figure C.27: Vorticity isosurface and velocity. Test FV1, Frame 19, ωt= 47.2^0.

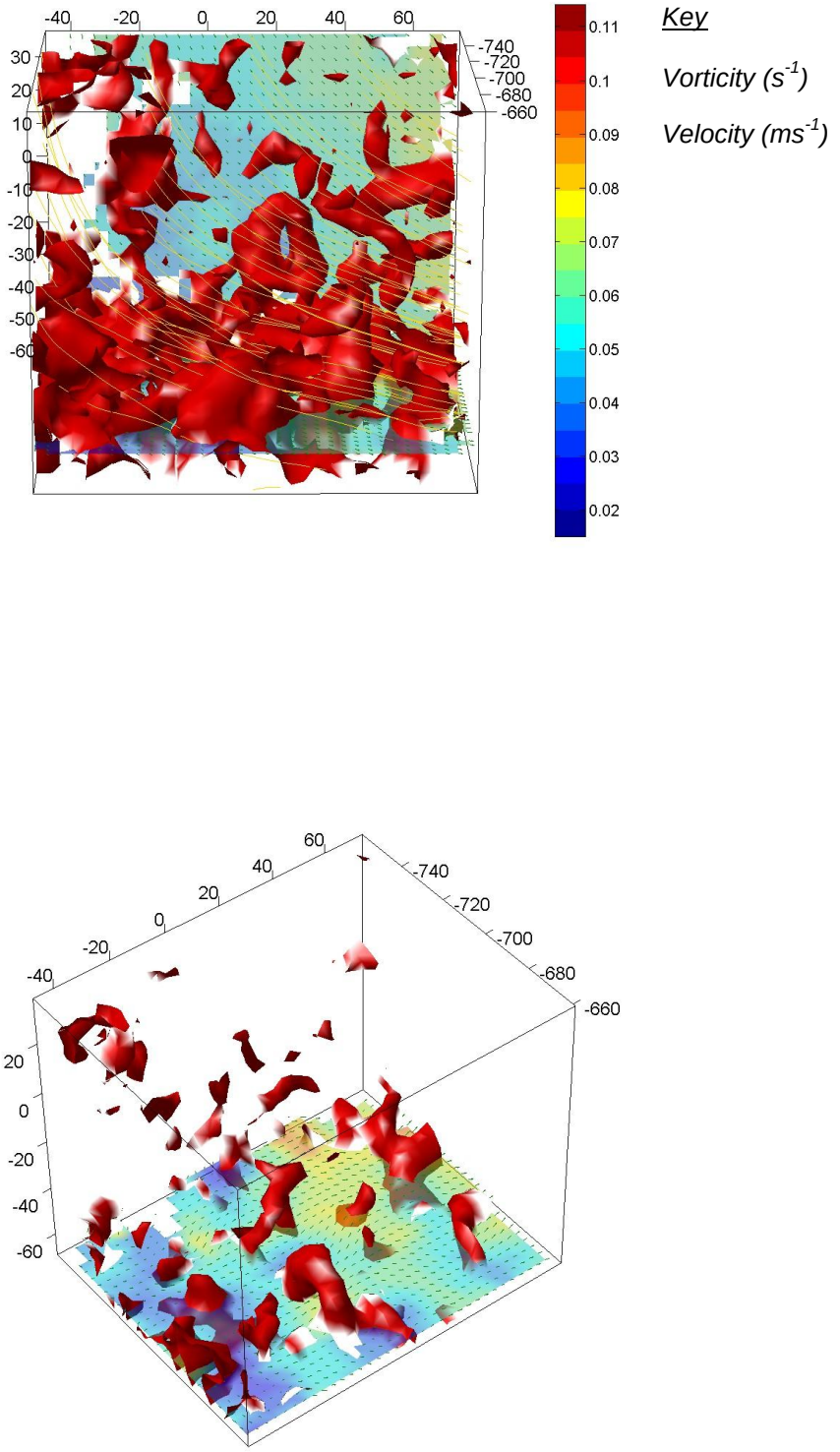

Figure C.28: Vorticity isosurface and velocity. Test FV1, Frame 20. $\omega t = 72.0^0$.

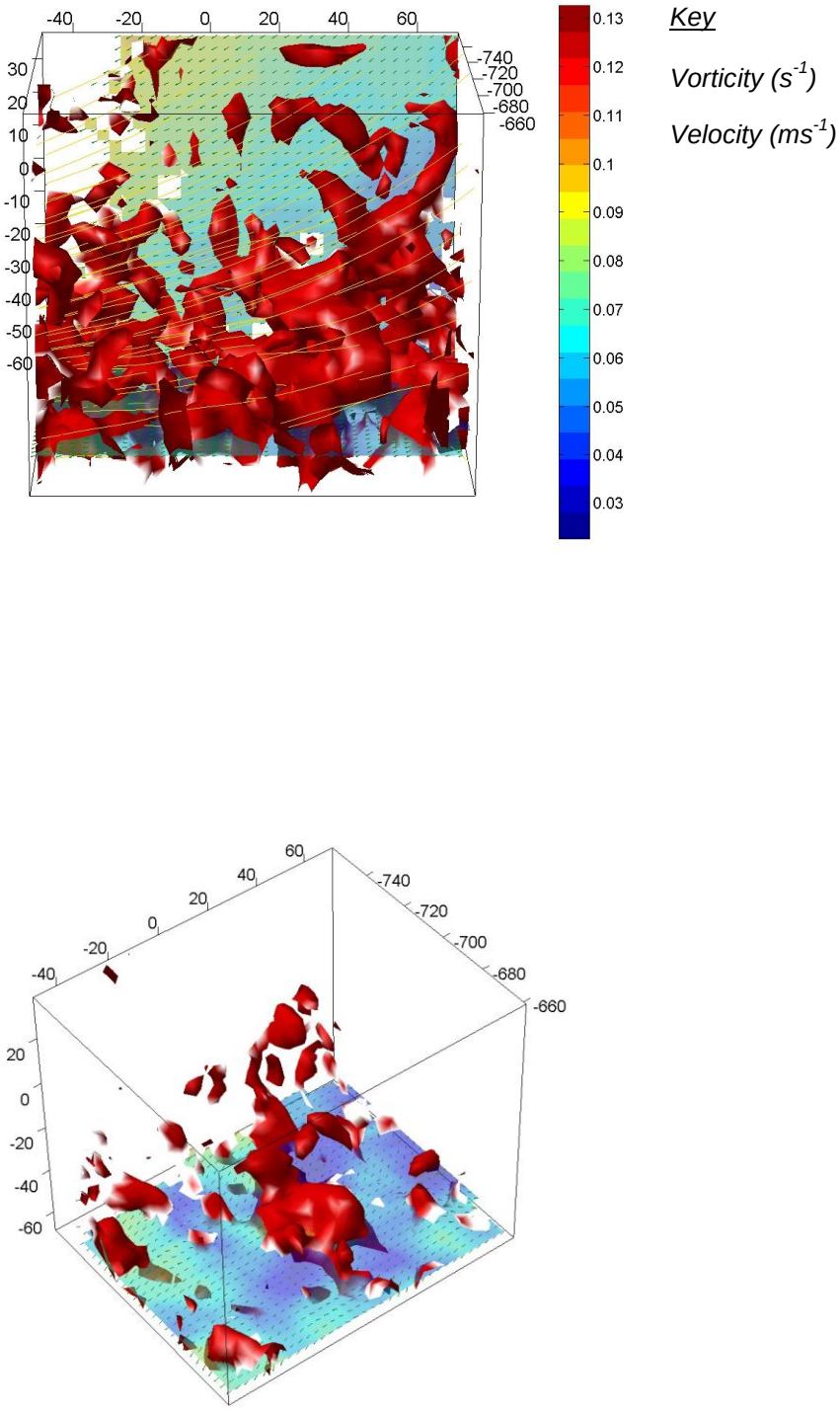

Figure C.29: Vorticity isosurface and velocity. Test FV1, Frame 21, $\omega t = 96.9^0$.

C.3 Vortex ejection from a 50mm sphere

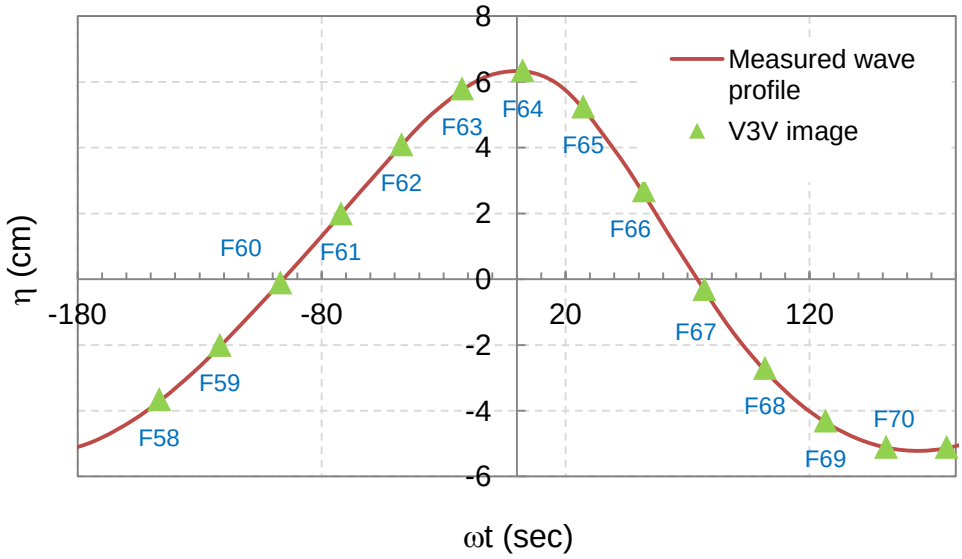

Figure C.30: Measured wave profile, Test FV2, H=11.6cm, T=2 sec.

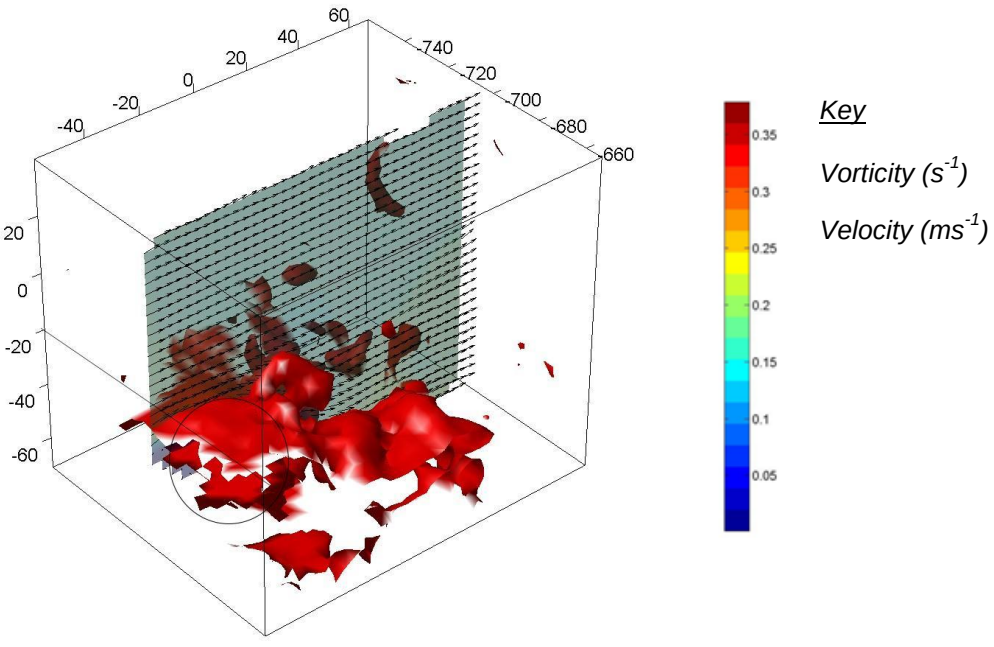

Figure C.31: Vorticity isosurface and velocity around 50mm sphere. Test FV2, Frame 62, ωt=-47.2^0.

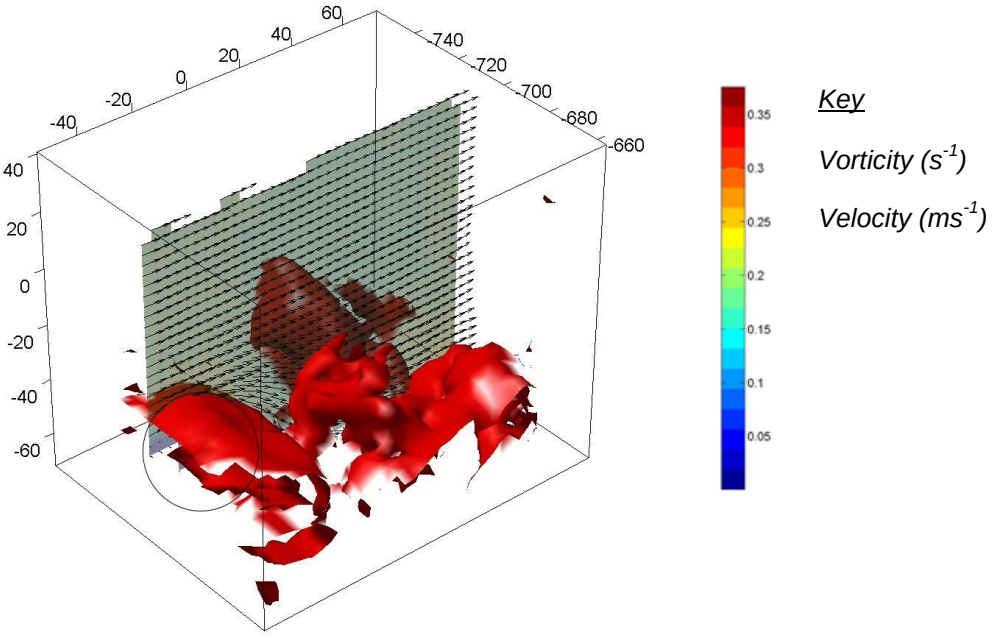

Figure C.32: Vorticity isosurface and velocity around 50mm sphere. Test FV2, Frame 63, ωt= -22.4^0.

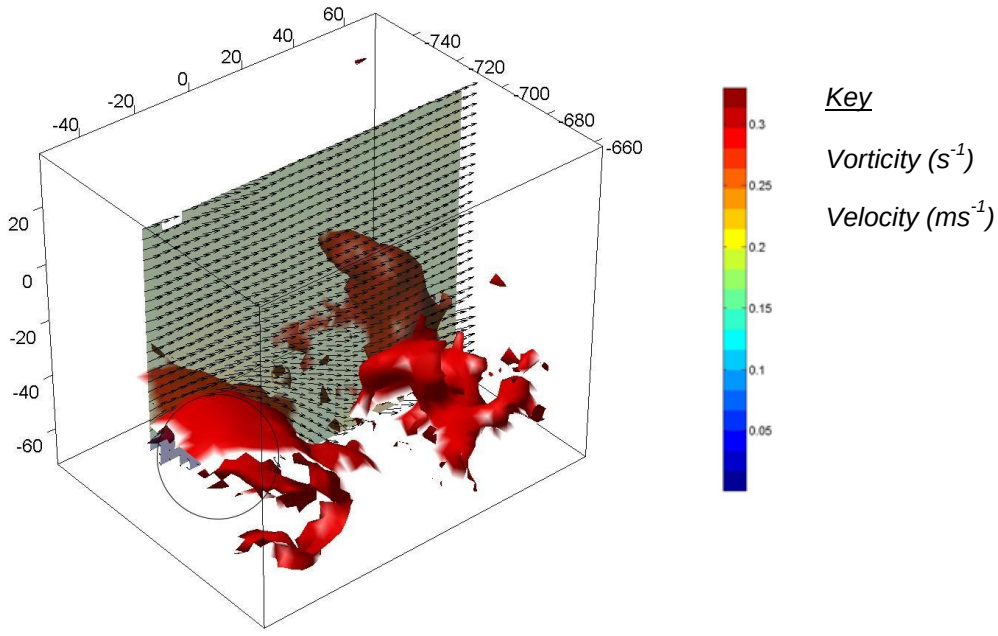

Figure C.33: Vorticity isosurface and velocity around 50mm sphere. Test FV2, Frame 64, ωt= 2.4^0.

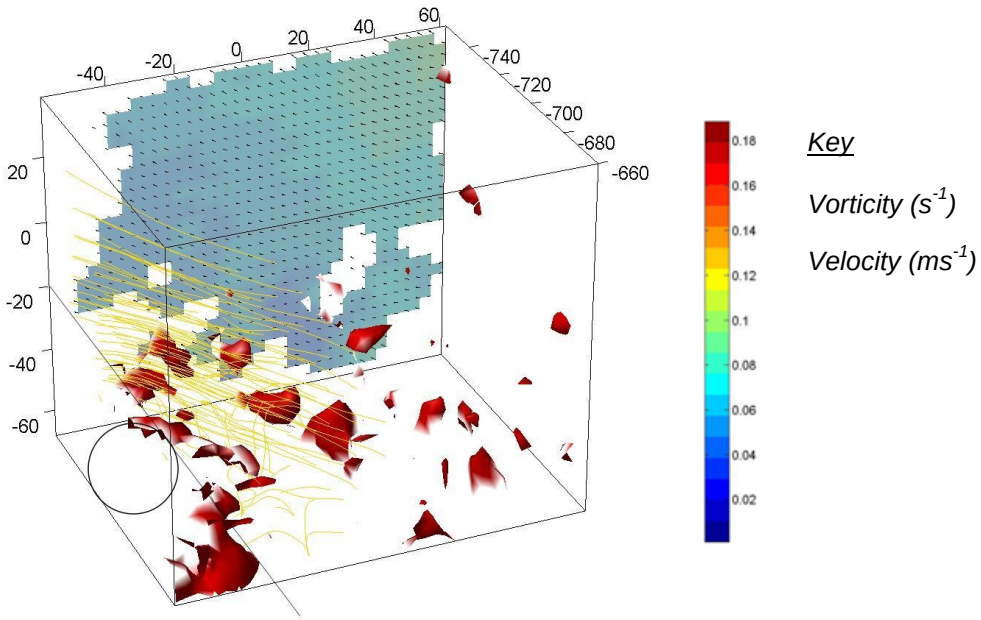

Figure C.34: Vorticity isosurface and velocity with stream lines. Test FV2, Frame 59. $\omega t = -121.7^0$.

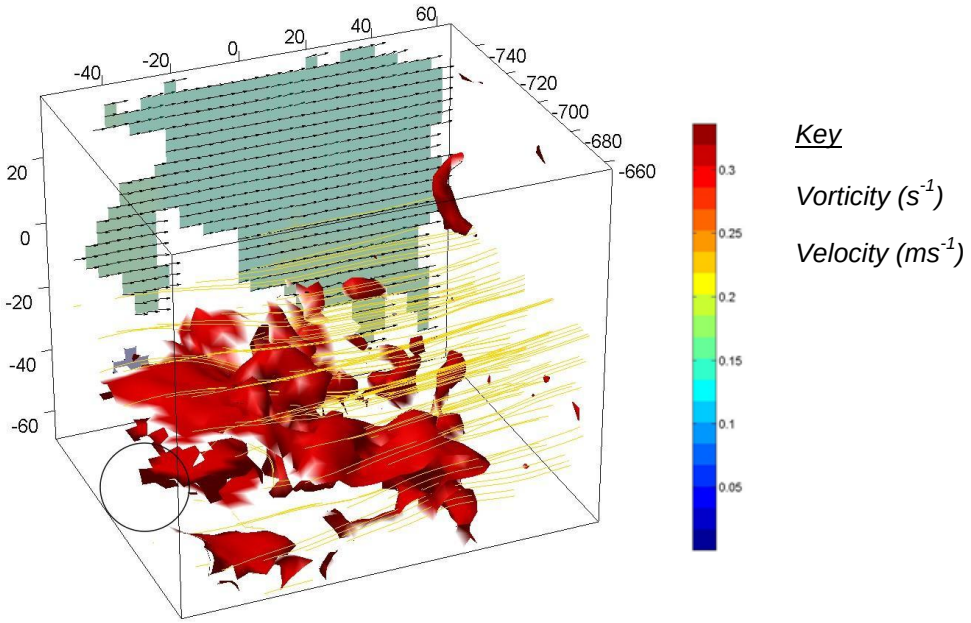

Figure C.35: Vorticity isosurface and velocity with stream lines. Test FV2, Frame 60, $\omega t = -96.9^0$.

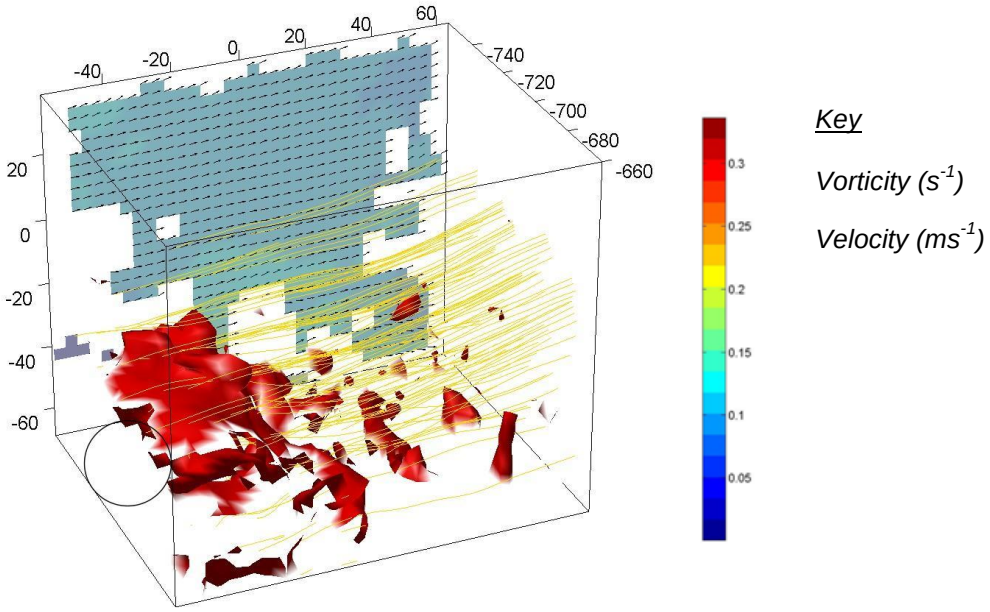

Figure C.36: Vorticity isosurface and velocity with stream lines. Test FV2, Frame 61, $\omega t = -72.0^0$.

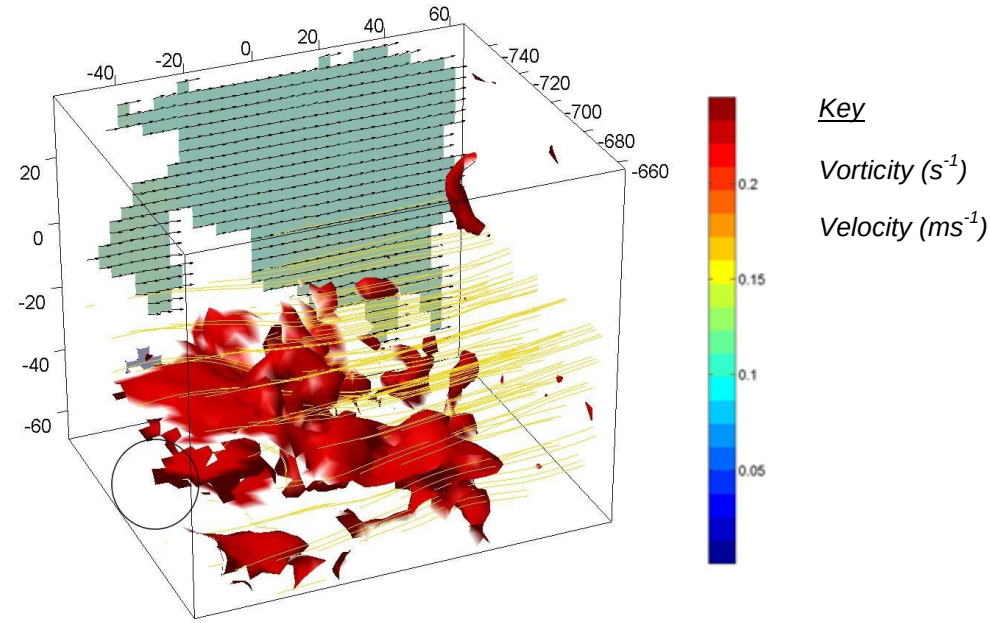

Figure C.37: Vorticity isosurface and velocity stream lines. Test FV2, Frame 62, $\omega t = -47.2^0$.

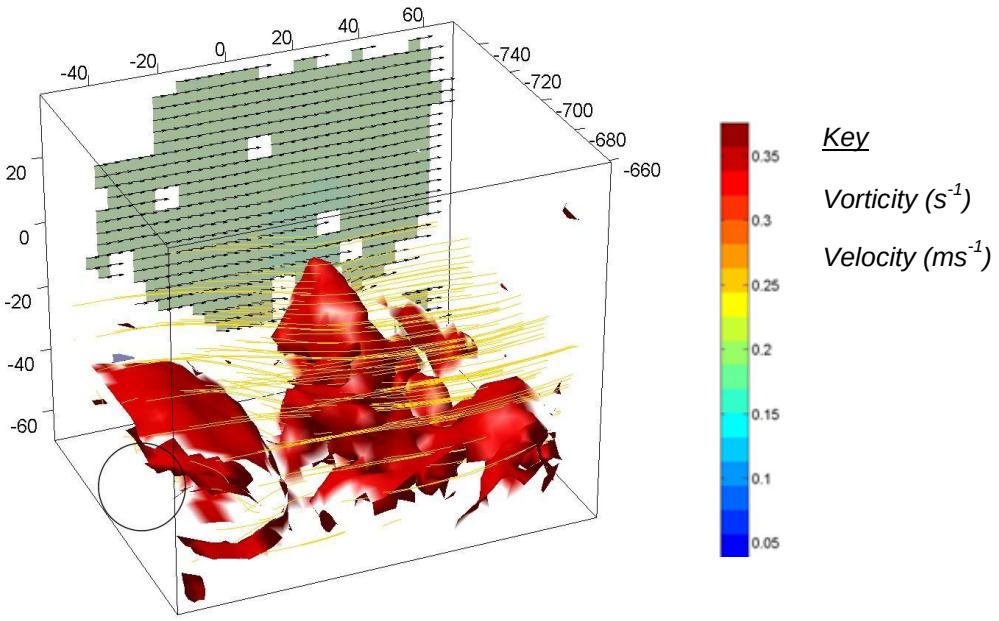

Figure C.38: Vorticity isosurface and velocity with stream lines. Test FV2, Frame 63, ωt= -22.4^0.

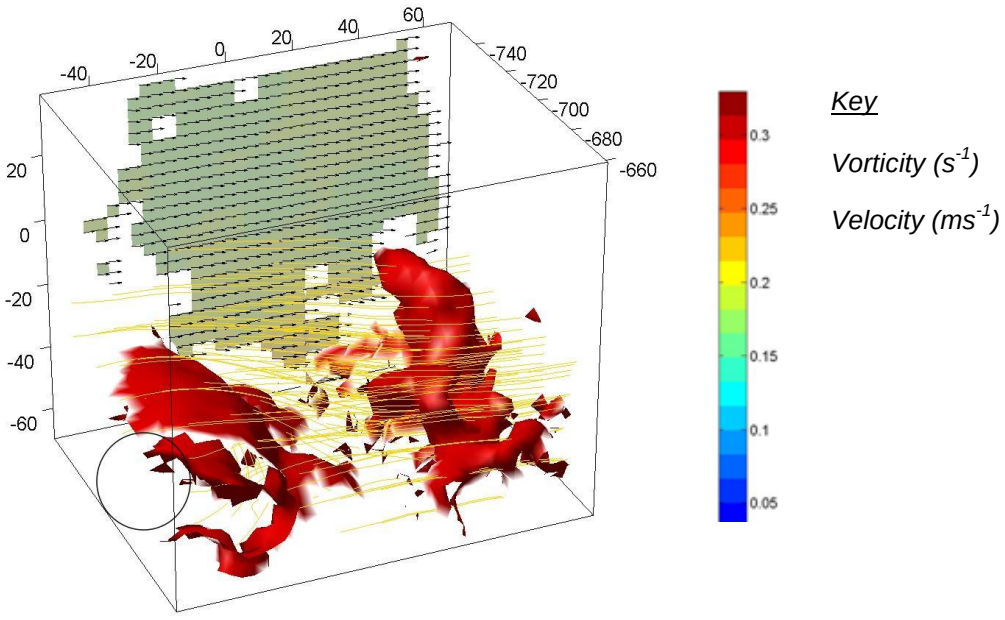

Figure C.39: Vorticity isosurface and velocity with stream lines. Test FV2, Frame 64, ωt= 2.4^0.

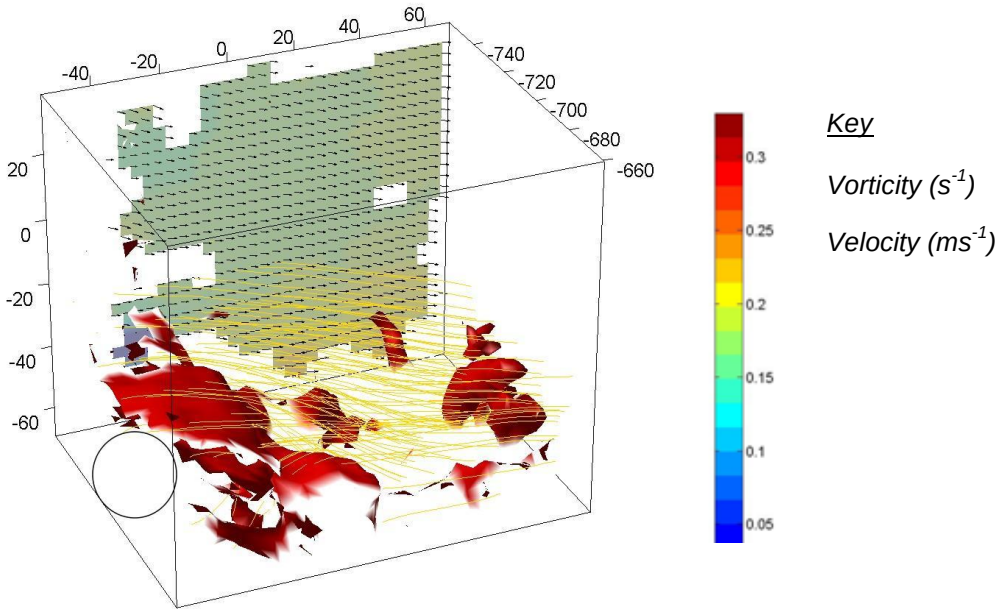

Figure C.40: Vorticity isosurface and velocity with stream lines. Test FV2, Frame 65. $\omega t = 27.3^0$.

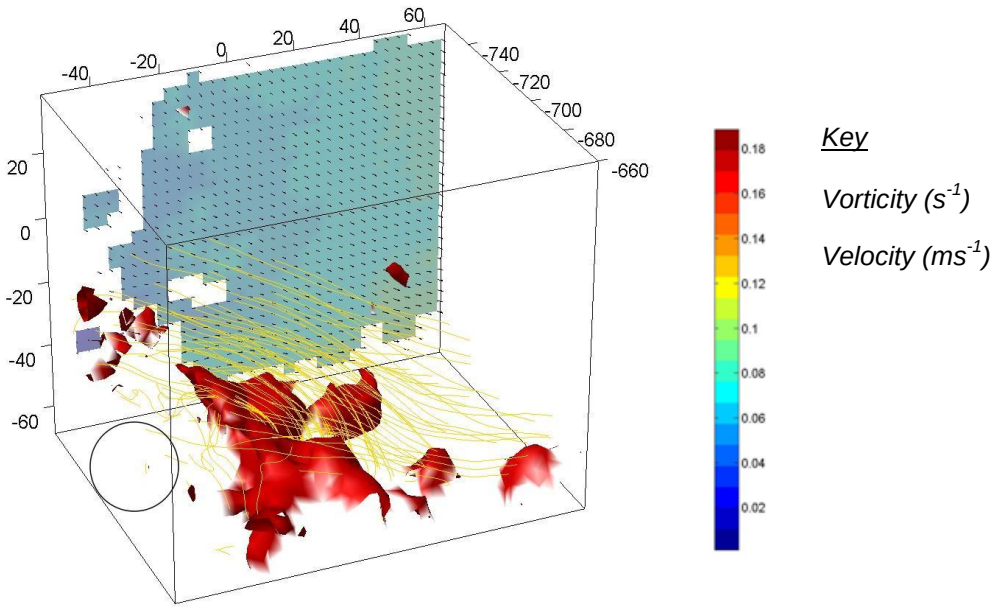

Figure C.41: Vorticity isosurface and velocity with stream lines. Test FV2, Frame 66, $\omega t = 52.1^0$.

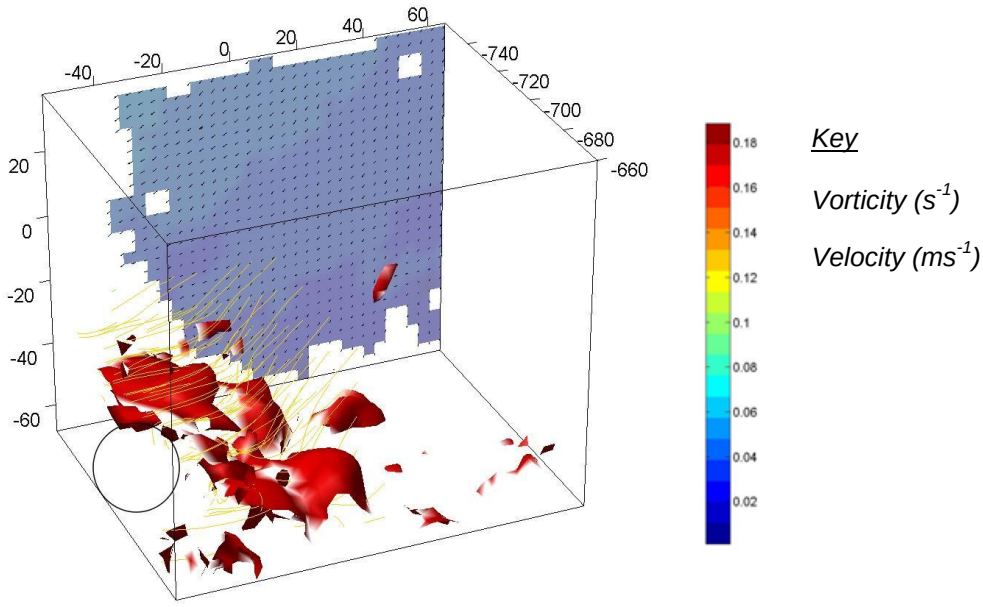

Figure C.42: Vorticity isosurface and velocity with stream lines. Test FV2, Frame 67. $\omega t = 76.9^0$.

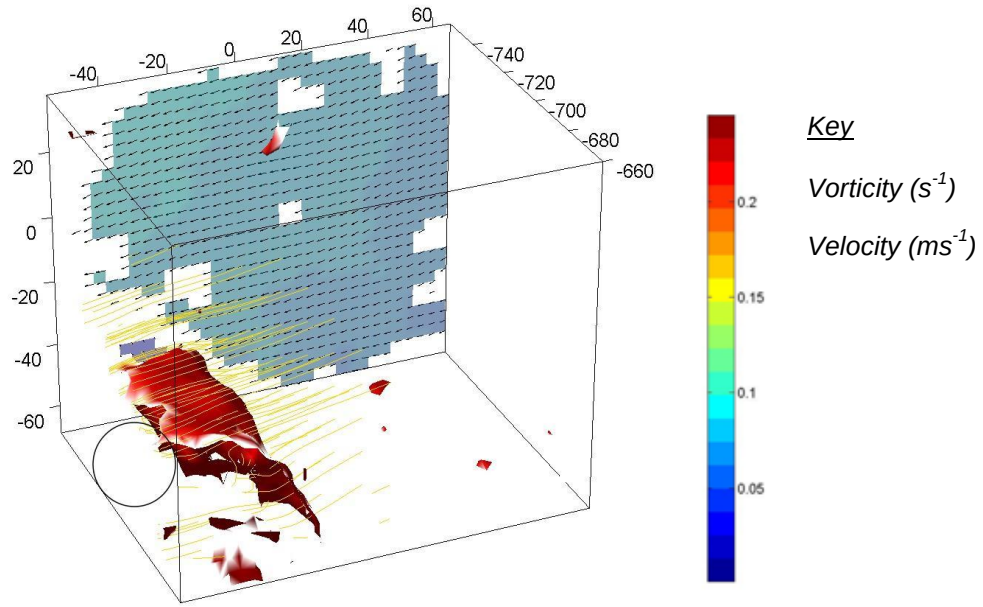

Figure C.43: Vorticity isosurface and velocity with stream lines. Test FV2, Frame 68, $\omega t = 101.8^0$.

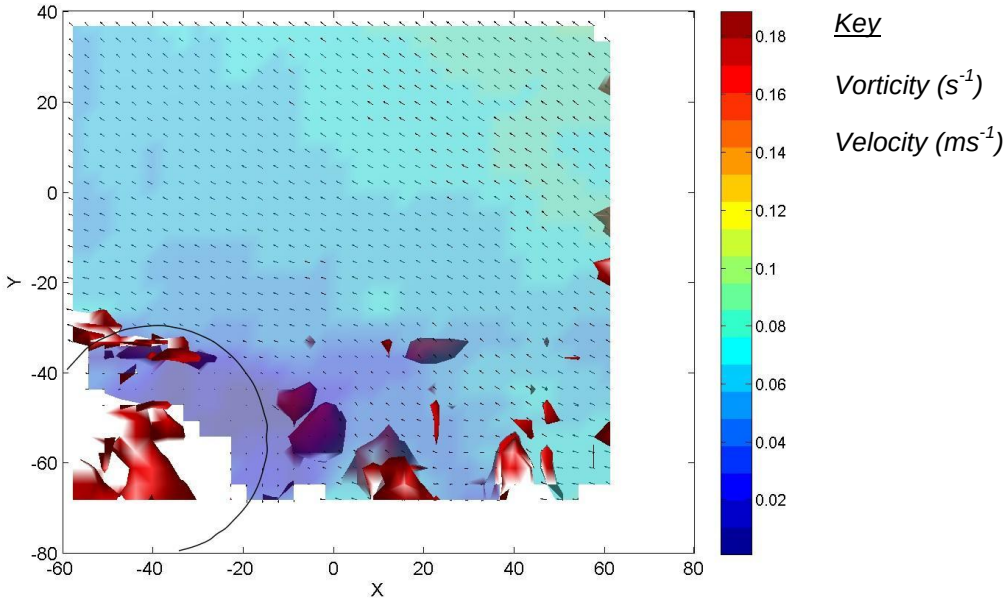

Figure C.44: Vorticity isosurface and velocity (side view). Test FV2, Frame 59, ωt= -121.7^0.

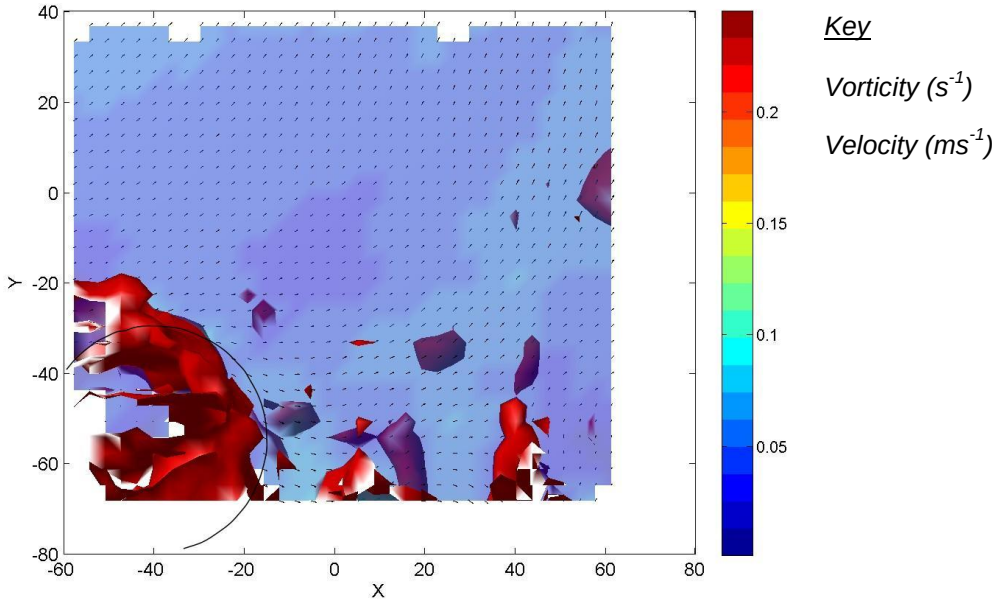

Figure C.45: Vorticity isosurface and velocity (side view) at flow reversal. Test FV2, Frame 60, ωt= -96.9^0.

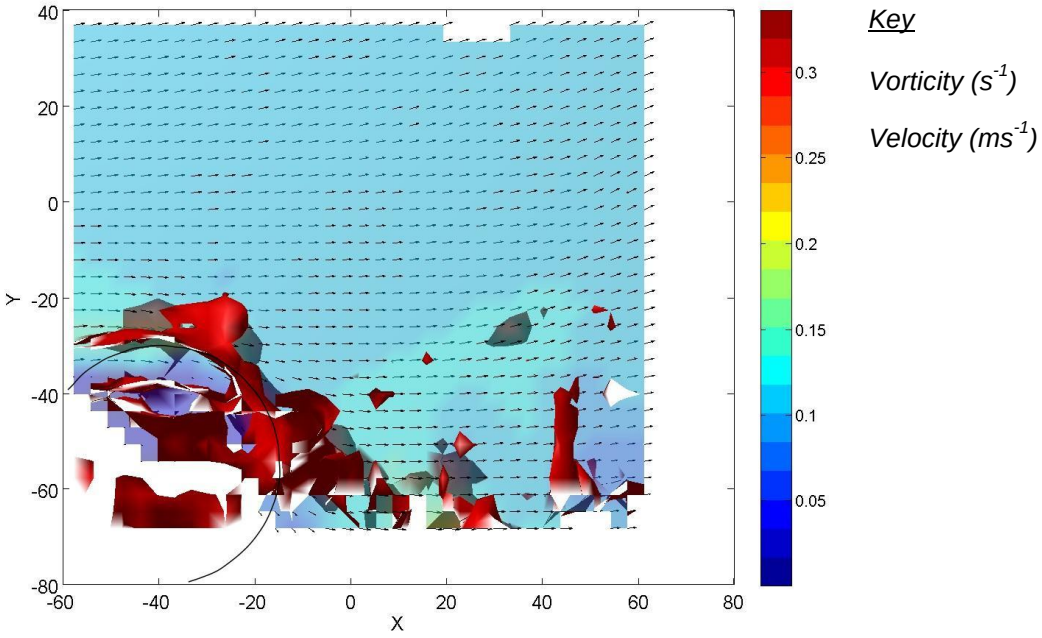

Figure C.46: Vorticity isosurface and velocity (side view). Lee vortex starts developing at the start of the crest half cycle. Test FV2, Frame 61, ωt= -72.0^0.

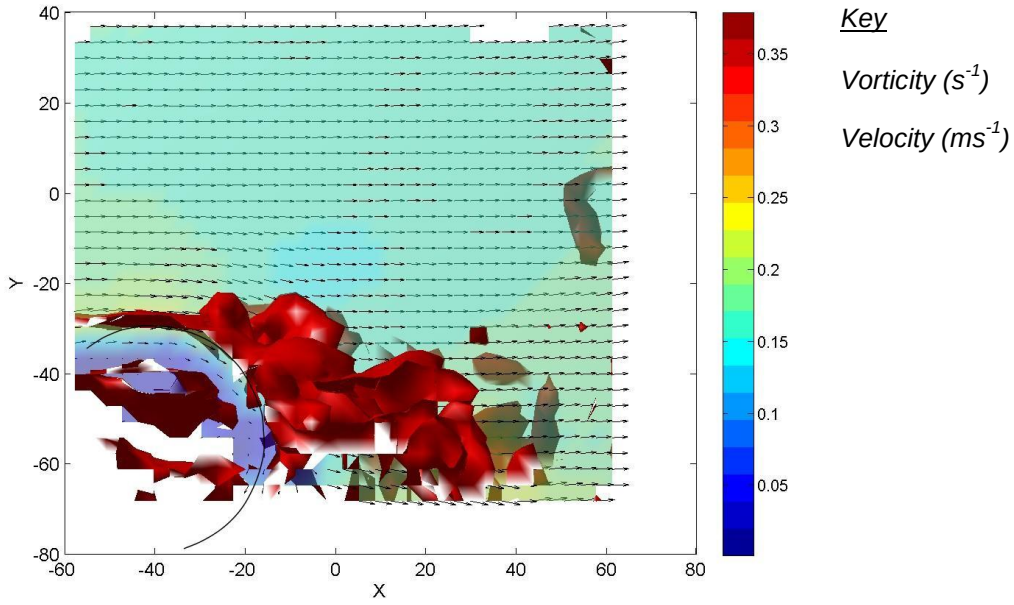

Figure C.47: Vorticity isosurface and velocity (side view). Test FV2, Frame 62, ωt= -47.2^0.

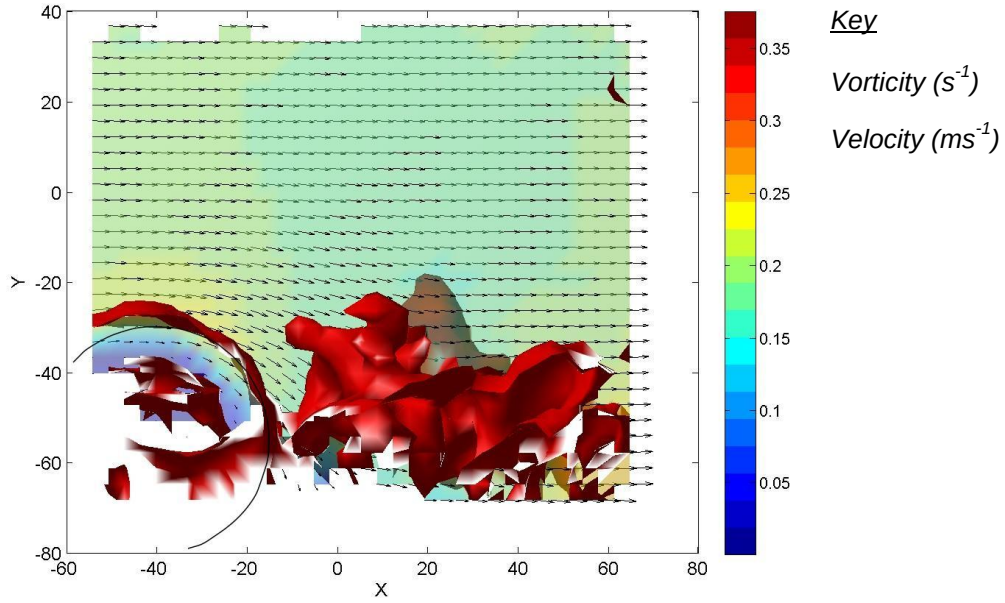

Figure C.48: Vorticity isosurface and velocity (side view) just before the vortex detachment. Test FV2, Frame 63, $\omega t = -22.4^0$.

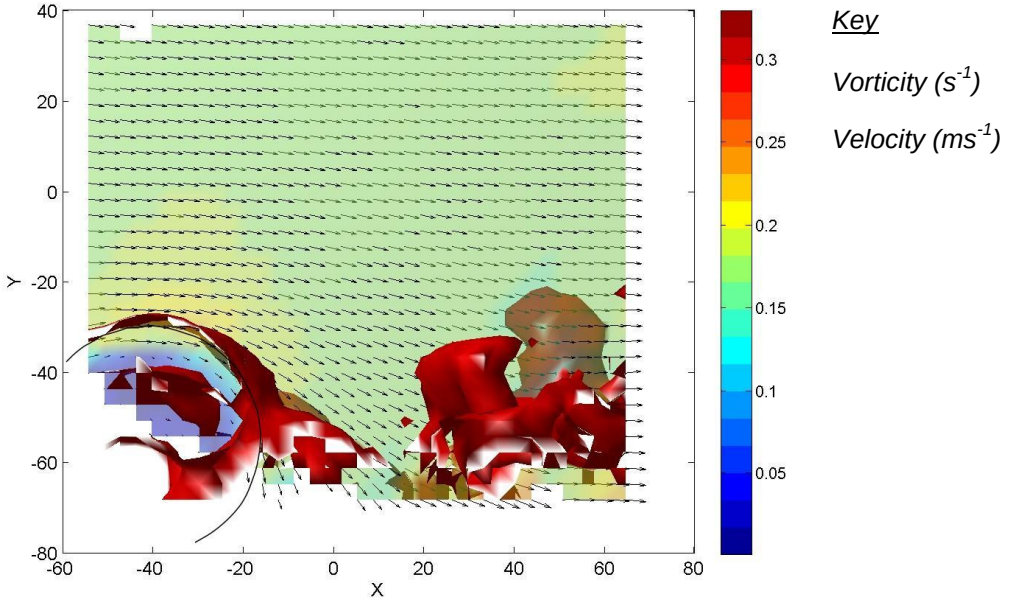

Figure C.49: Vorticity isosurface and velocity (side view) just after vortex detachment at the wave crest. Test FV2, Frame 64, $\omega t = 2.4^0$.

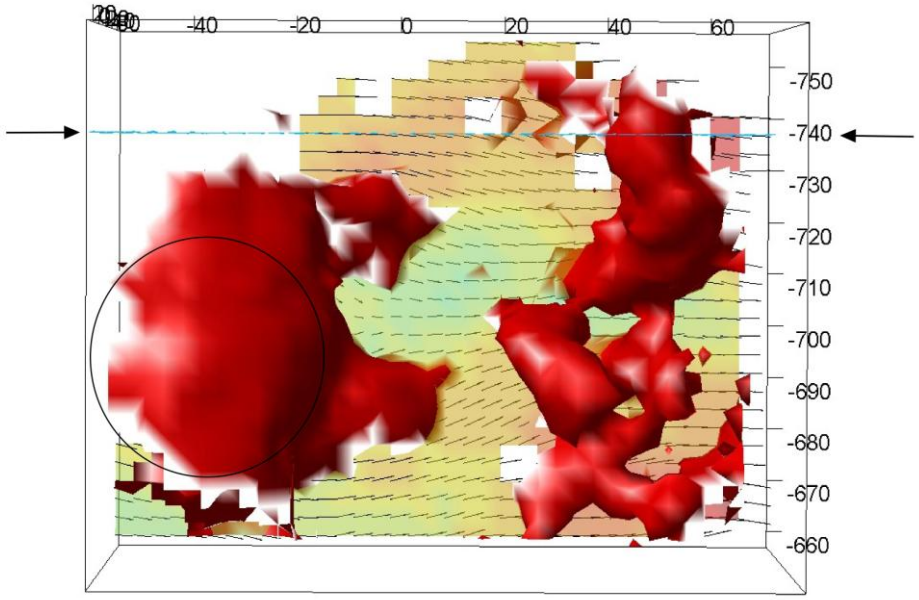

(a)

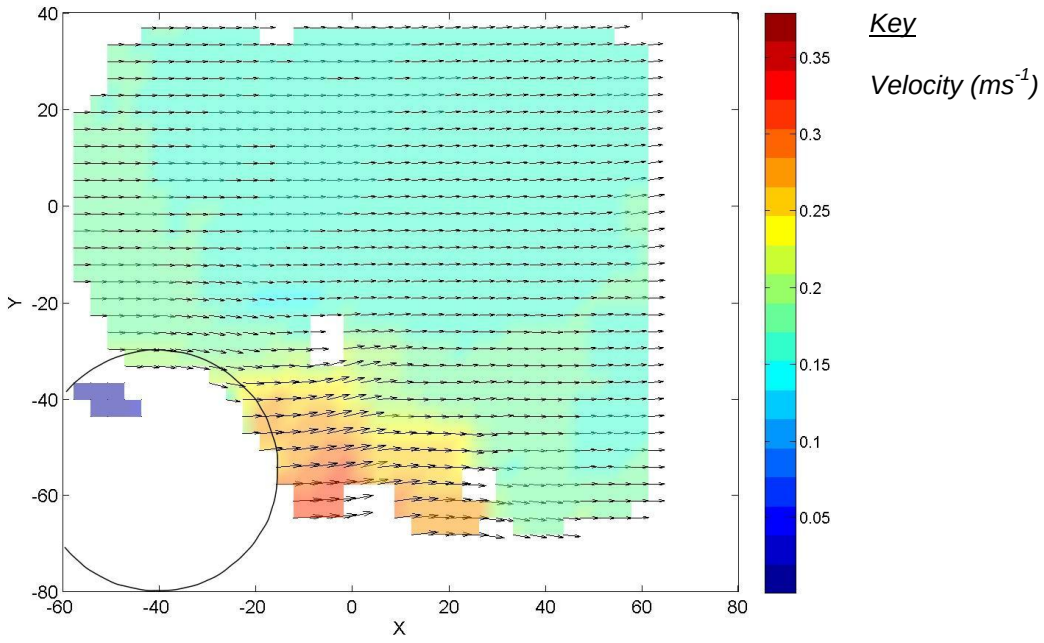

(b)

Figure C.50: Velocity contours and vectors, Test FV2, Frame 62, ωt= -47.2^0.

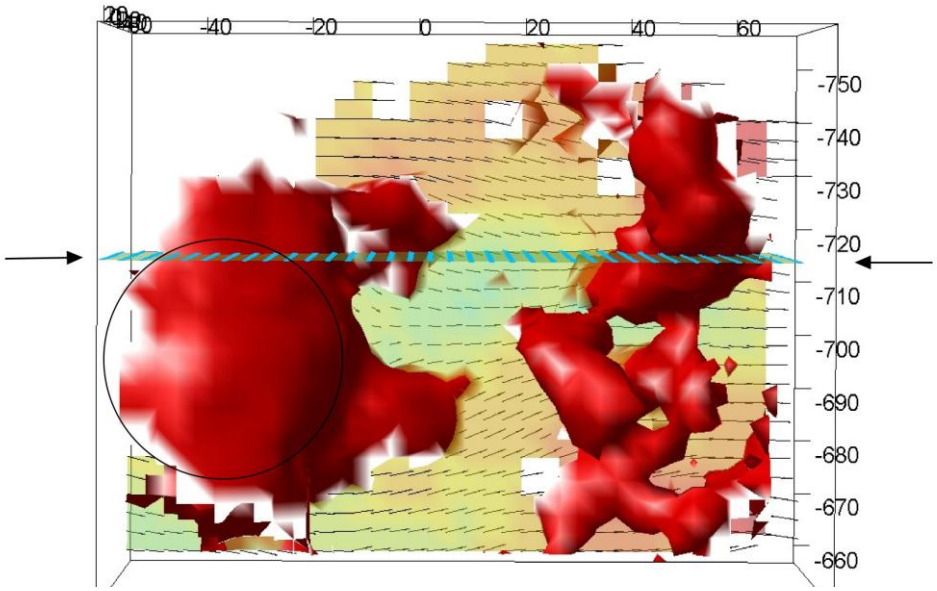

(a)

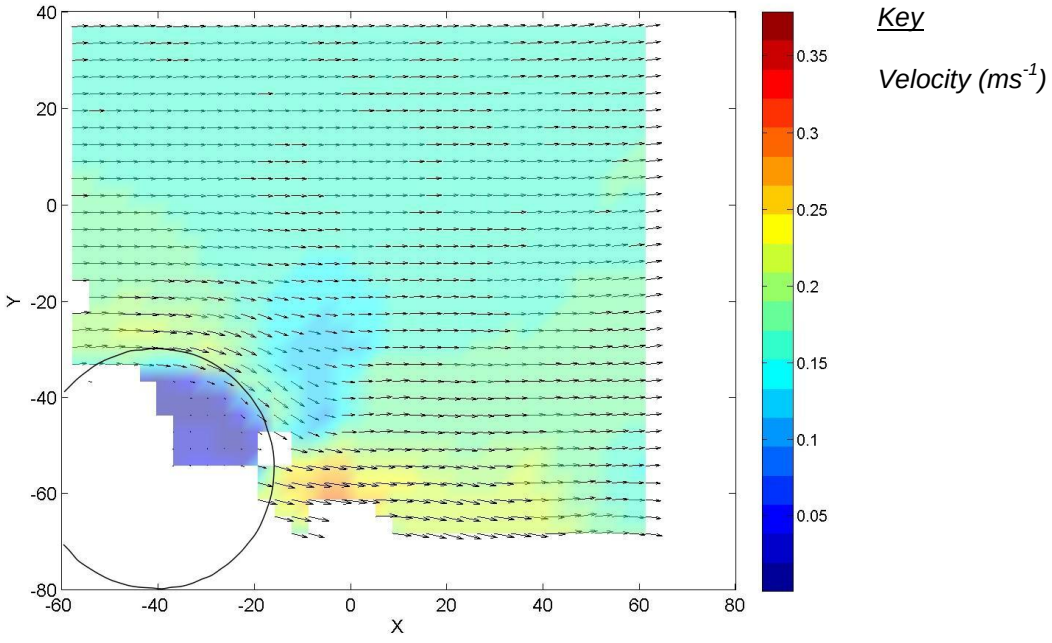

(b)

Figure C.51: Velocity contours and vectors, Test FV2, Frame 62, ωt= -47.2^0 (a) plan view (b) section at ~ 0.5d from the centre of the sphere.

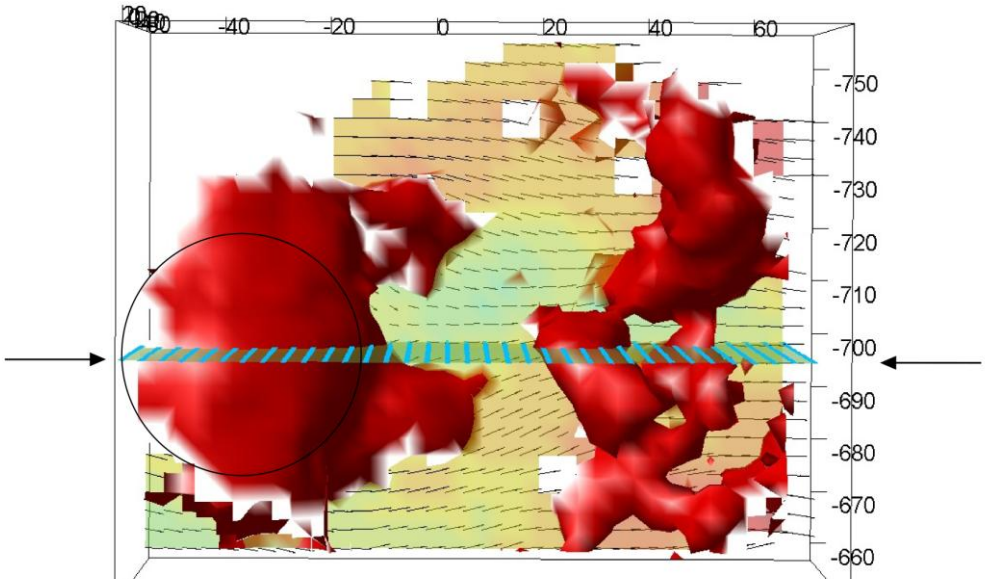

(a)

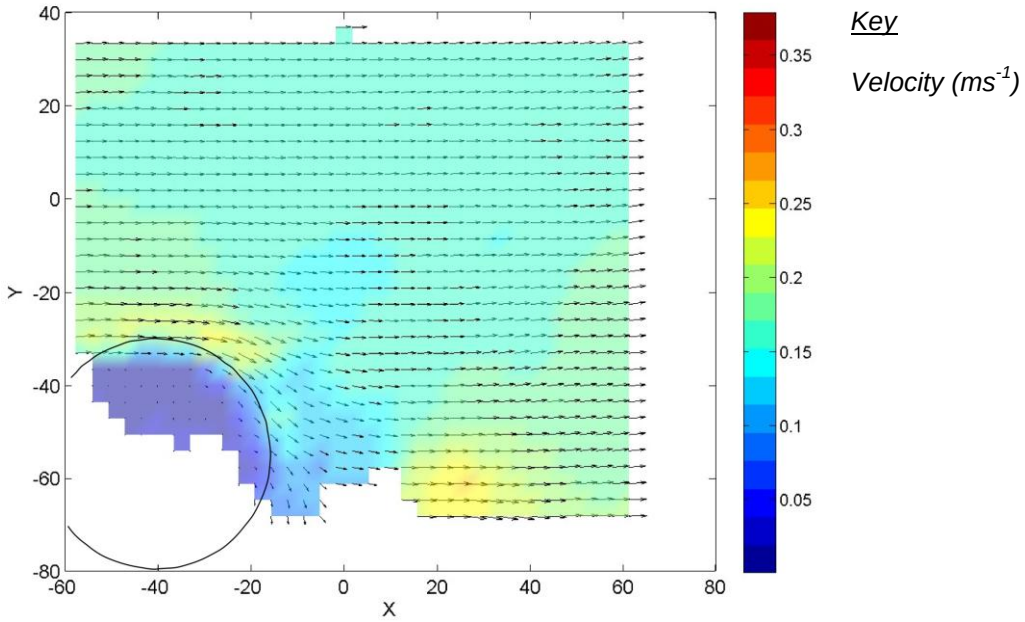

(b)

Figure C.52: Velocity contours and vectors, Test FV2, Frame 62, ωt= -47.2^0 (a) plan view (b) section at the centre of the sphere.

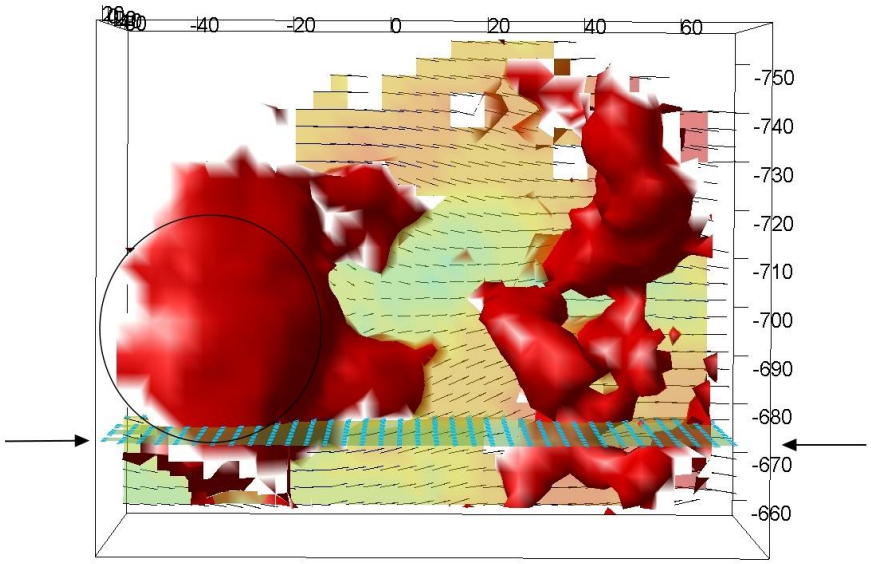

(a)

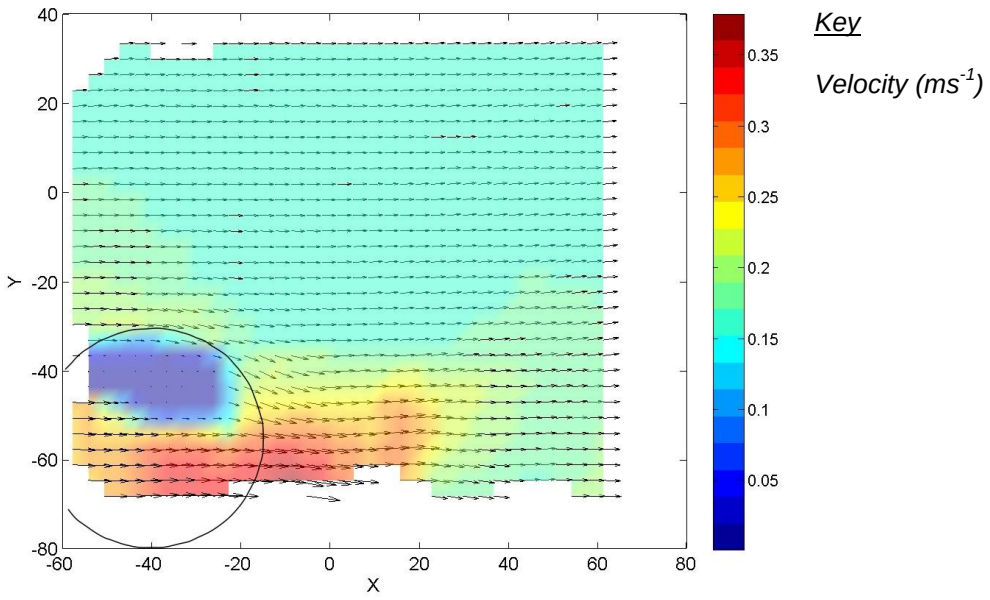

(b)

Figure C.53: Velocity contours and vectors, Test FV2, Frame 62, $\omega t = -47.2^0$ (a) plan view (b) section at ~ 0.5d from the centre of the sphere.

C.4 Flow around a 19mm fully exposed sphere (p/d=0.82)

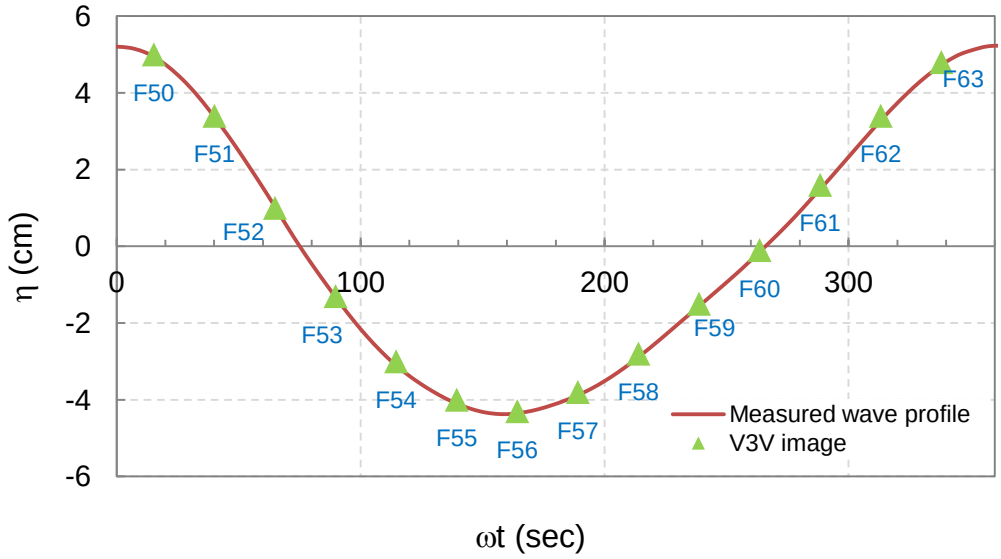

Figure C.54: Measured wave profile, Test FV8, H=9.5cm, T=2 sec.

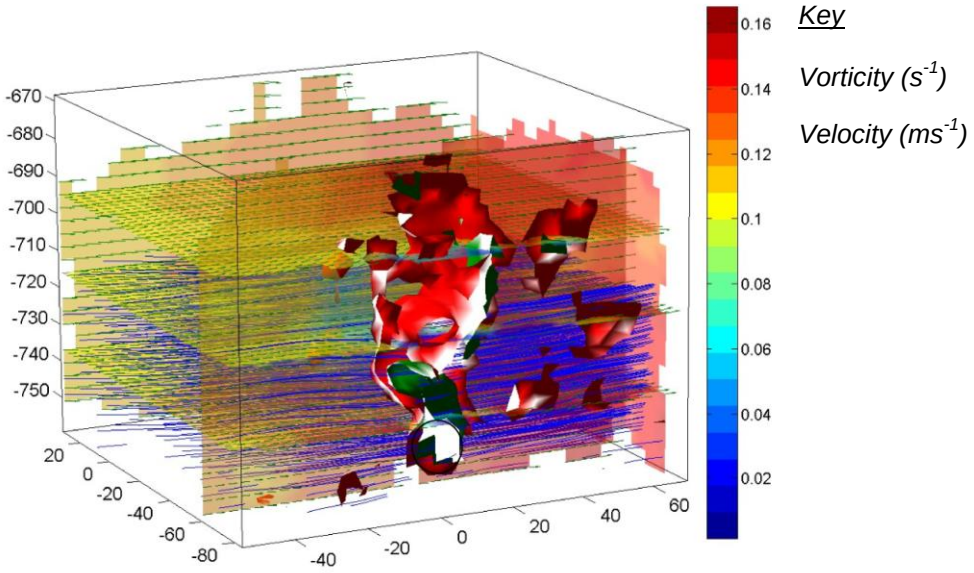

Figure C.55: Vorticity isosurface, velocity vectors/contours and stream lines. Test FV8, Frame 51, $\omega t = 40.1^0$.

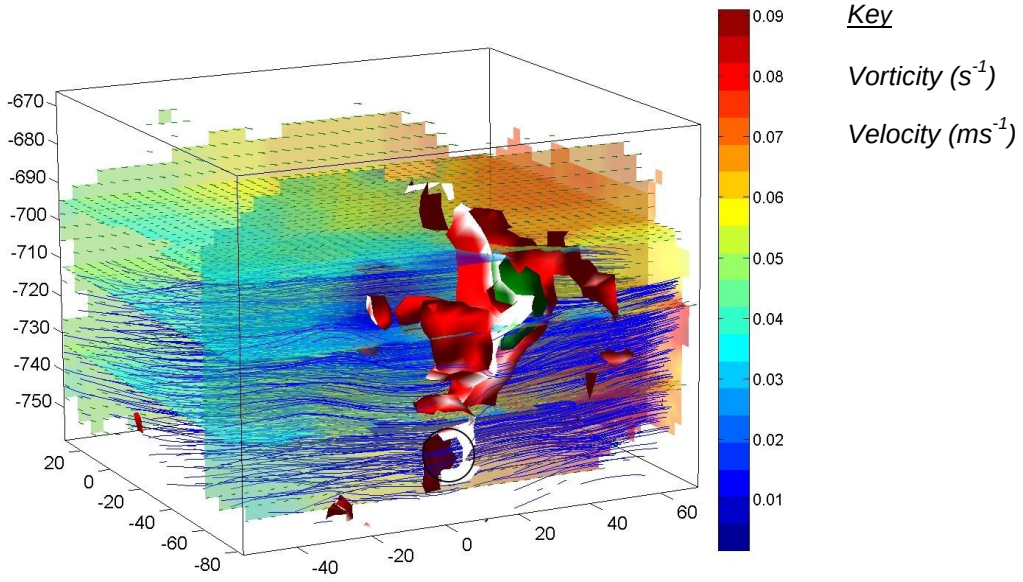

Figure C.56: Vorticity isosurface, velocity vectors/contours and stream lines. Test FV8, Frame 52, $\omega t = 64.9^0$.

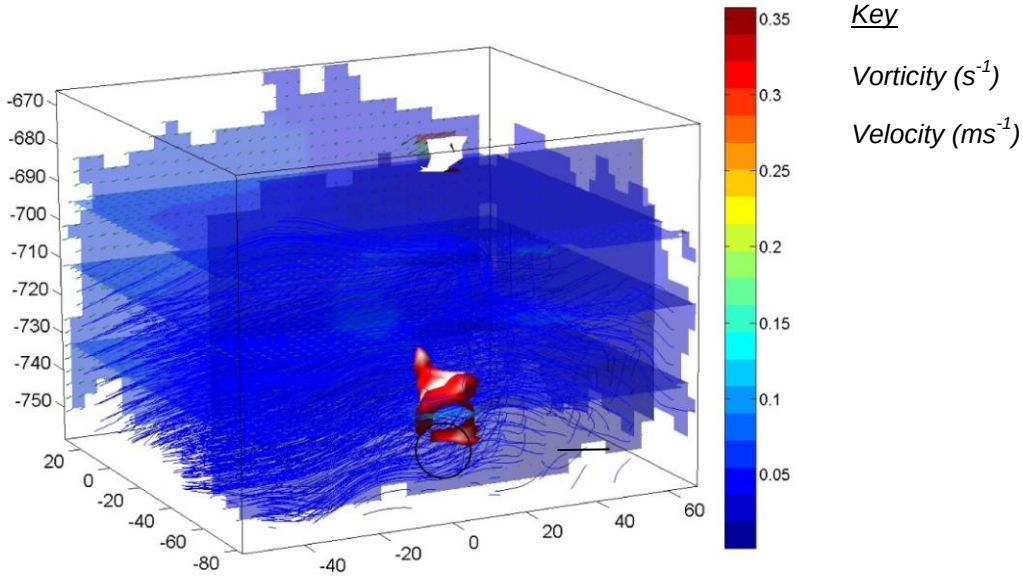

Figure C.57: Vorticity isosurface, velocity vectors/contours and stream lines. Test FV8, Frame 53, $\omega t = 89.8^0$.

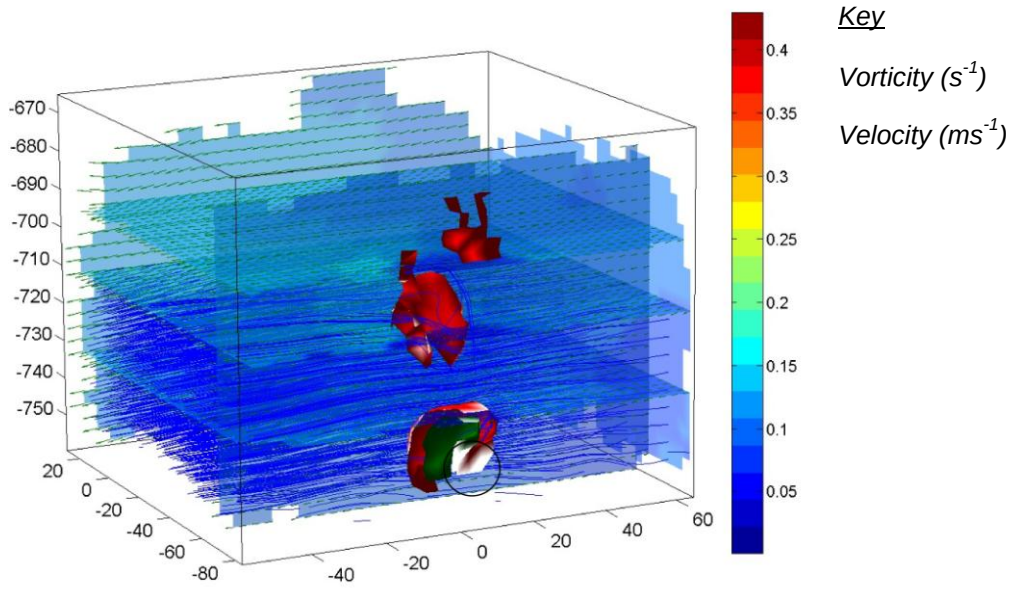

Figure C.58: Vorticity isosurface, velocity vectors/contours and stream lines. Test FV8, Frame 54, $\omega t = 114.6^0$.

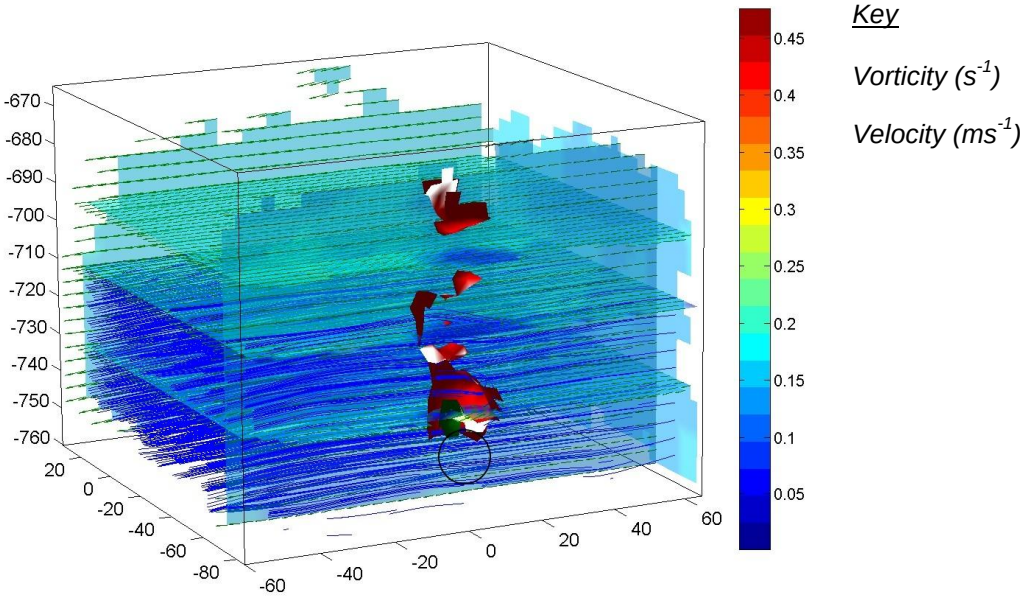

Figure C.59: Vorticity isosurface, velocity vectors/contours and stream lines. Test FV8, Frame 55, $\omega t = 139.4^0$.

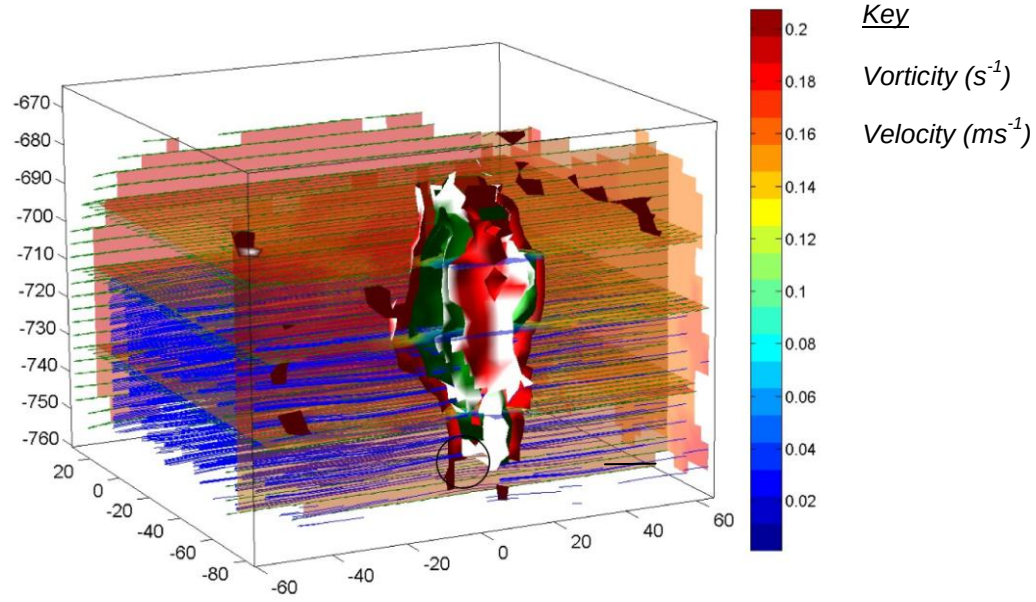

Figure C.60: Vorticity isosurface, velocity vectors/contours and stream lines. Test FV8, Frame 56, $\omega t = 164.3^0$.

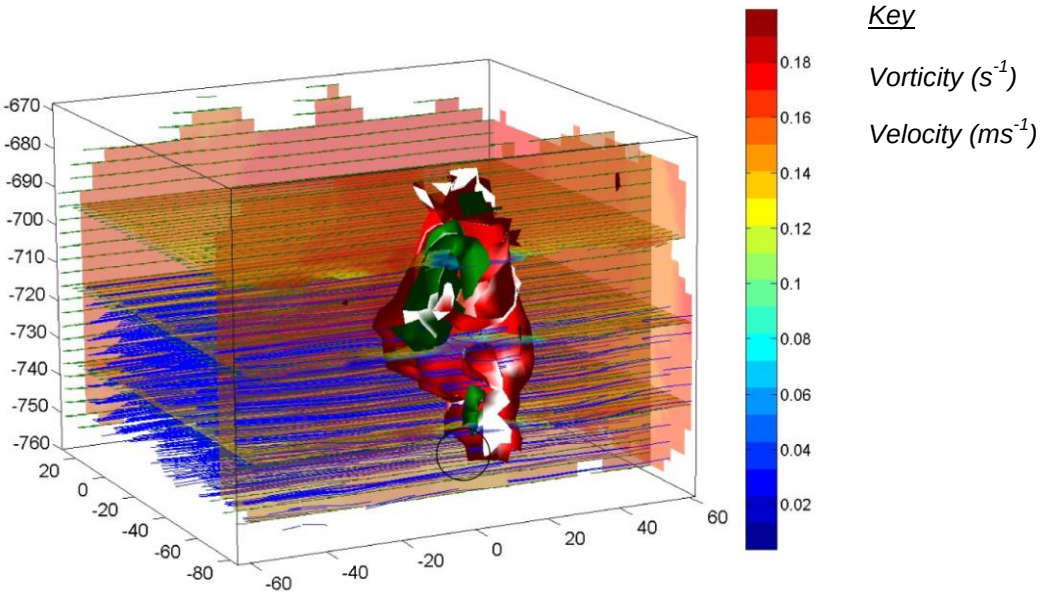

Figure C.61: Vorticity isosurface, velocity vectors/contours and stream lines. Test FV8, Frame 57, $\omega t = 189.1^0$.

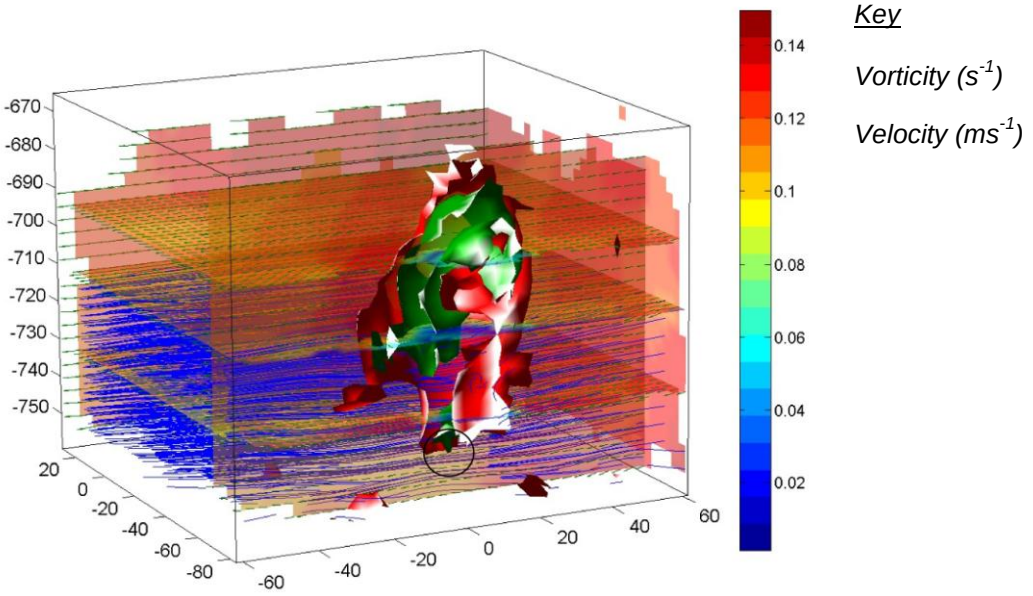

Figure C.62: Vorticity isosurface, velocity vectors/contours and stream lines. Test FV8, Frame 58, $\omega t = 213.9^0$.

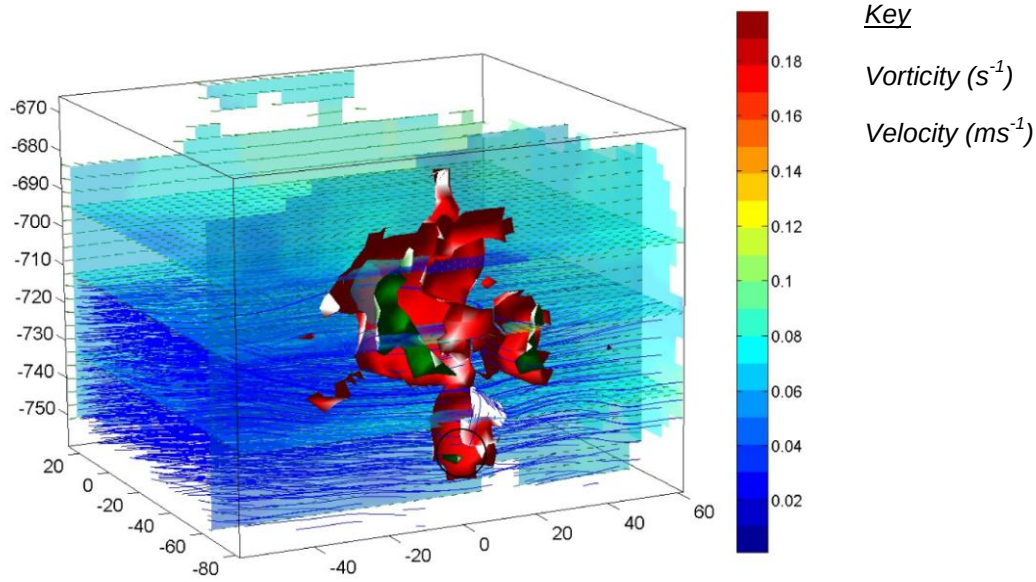

Figure C.63: Vorticity isosurface, velocity vectors/contours and stream lines. Test FV8, Frame 59, $\omega t = 238.7^0$.

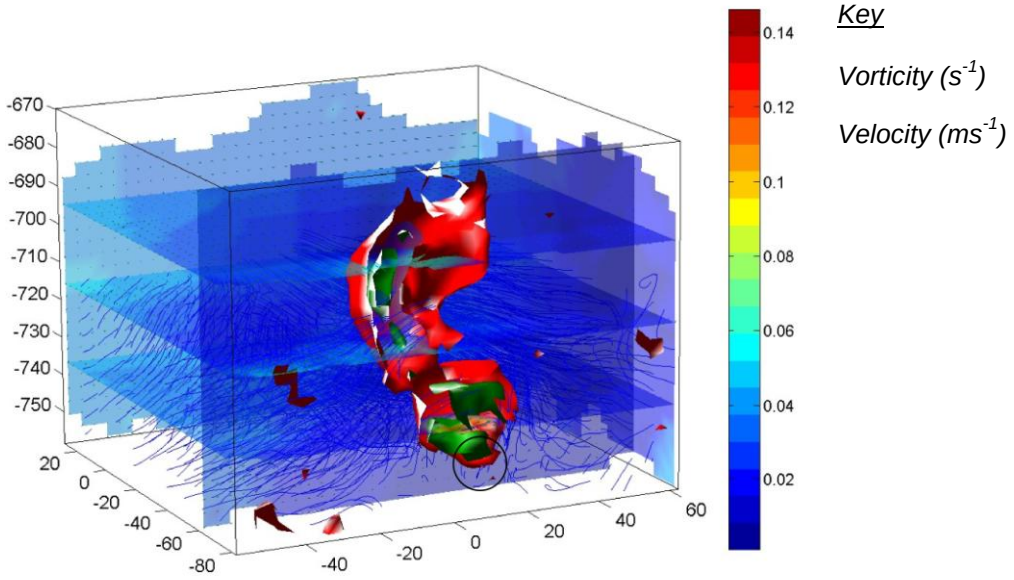

Figure C.64: Vorticity isosurface, velocity vectors/contours and stream lines. Test FV8, Frame 60, $\omega t = 263.6^0$.

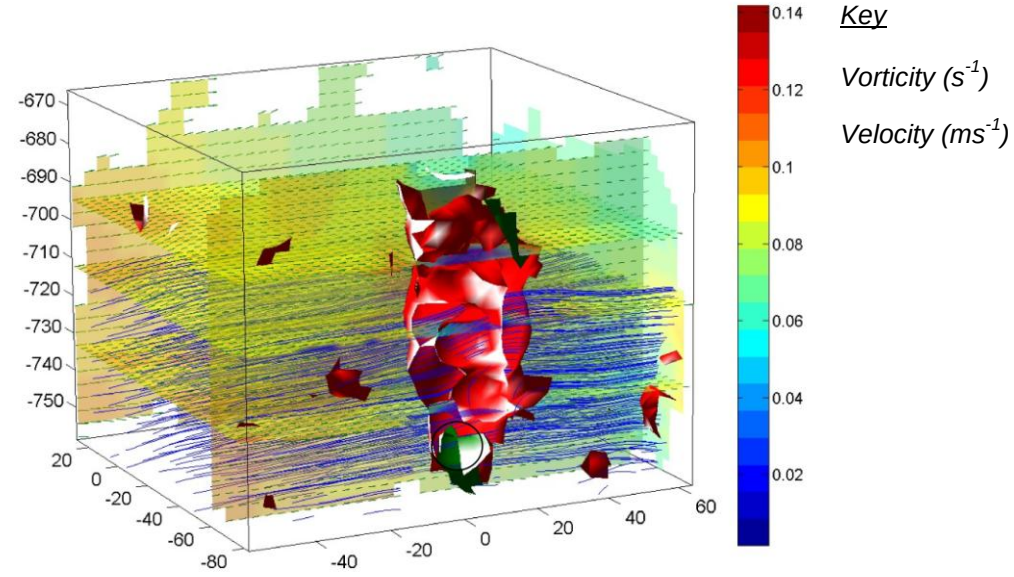

Figure C.65: Vorticity isosurface, velocity vectors/contours and stream lines. Test FV8, Frame 61, $\omega t = 288.4^0$.

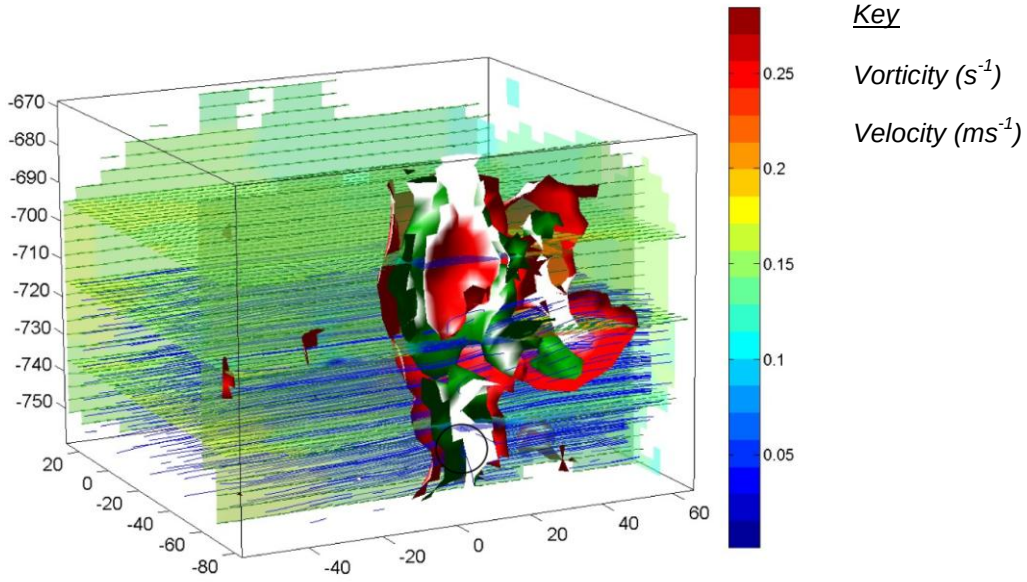

Figure C.66: Vorticity isosurface, velocity vectors/contours and stream lines. Test FV8, Frame 62, $\omega t = 313.2^0$.